I. R. IRAN

ISSN: 1728-1431
e-ISSN: 1735-9244

International Journal of Engineering

Journal Homepage: www.ije.ir

MERC

TRANSACTIONS A: Basics

Volume 34, Number 01, January 2021

Materials and Energy Research Center

In the Name of God

INTERNATIONAL JOURNAL OF ENGINEERING
Transactions A: Basics

International **J**ournal of **E**ngineering *Transactions A: Basics* (ISSN 1728-1431) (EISSN 1735-9244)
International **J**ournal of **E**ngineering *Transactions B: Applications* (ISSN 1728-144X) (EISSN 1735-9244)
International **J**ournal of **E**ngineering *Transactions C: Aspects* (ISSN 2423-7167) (EISSN 1735-9244)
Web Sites: www.ije.ir & www.ijeir.info E-mails: ije.editor8@gmail.com, Tel: (+9821) 88771578, Fax: (+9821) 88773352
Materials and Energy Research Center (MERC)

ISSN: 1728-1431, e-ISSN: 1735-9244

International Journal of Engineering, Volume 34, Number 1, January 2021

CONTENTS:

Transactions A: Basics

ISSN: 1728-1431, e-ISSN: 1735-9244

International Journal of Engineering, Volume 34, Number 1, January 2021

ISSN: 1728-1431, e-ISSN: 1735-9244

International Journal of Engineering, Volume 34, Number 1, January 2021

International Journal of Engineering

Journal Homepage: www.ije.ir

Titanium Dioxide Nanotubes Incorporated Bioactive Glass Nanocomposites: Synthesis, Characterization, Bioactivity Evaluation and Drug Loading

O. Saneei Siavashy[a], N. Nabian*[a], S. M. Rabiee[b]

[a] *Department of Chemical Engineering, University of Science and Technology of Mazandaran, Behshahr, Iran*
[b] *Department of Mechanical Engineering, Babol Noshirvani University of Technology, Babol, Iran*

PAPER INFO

Paper history:
Received 06 July 2020
Received in revised form 20 October 2020
Accepted 21 October 2020

Keywords:
Bioactive Nanocomposites
Titanium Dioxide Nanoubes
Bioactivity Evaluation
Drug Loading

ABSTRACT

Nano bioactive glasses are known as suitable alternatives to repair the damaged bone tissues. In this research, novel sol-gel derived bioactive glass composites were synthesized through a reduction in the common weight percent of SiO_2 substituted by 15 wt% of titanium dioxide nanotubes (TNTs) at two different steps by the synthetic procedure. The morphology, crystalline structure, and functional groups of the composites were evaluated through scanning electron microscopy (SEM), X-ray diffraction (XRD) and Fourier transform infrared (FTIR) analyses. Based on the SEM images, the step in which TNTs were added to the solution completely changed the morphology of the composite. Bioactivity tests were carried out by soaking the samples in the simulated body fluid (SBF) at the intervals of 14 and 28 days followed by the investigation of hydroxyapatite (HA) layer formation on the surface of the samples. According to XRD peaks at 2-theta angle of around 31 and 40 degrees, it was found that the presence of titanium dioxide nanotubes improved bioactivity after 14 days of immersion and both 58S-TNT composites were more bioactive than 58S bioglass, while 58S bioactive glass possessed more intense peaks of HA after 28 days of immersion in SBF. Furthermore, the drug loading characteristic of the prepared composites was examined and the results showed that the addition of nanotubes improved the drug loading performance of bioactive composites containing TNTs up to 70% compared to the 58S bioglass with 37% drug loading.

***doi**: 10.5829/ije.2021.34.01a.01*

NOMENCLATURE

°C	Degree celcius	M	Molar concentration
λ	Wavelength	wt%	Weight percent
$	U.S Dollar	kV	Kilovolt
°	Degree	θ	diffration angle (in X-Ray Diffraction)

1. INTRODUCTION

Tissue engineering is an interdisciplinary field involving life sciences, medicine, material sciences, and engineering [1]. The development of practical substitutes for damaged tissues is the main purpose of tissue engineering. The global market of tissue engineering and cell therapy was appraised in 2014 at about $15 billion. Tissue engineering and regenerative medicine solutions can also be used for any tissue, although the levels of complexity of targets are different [2].

Bone tissue engineering is a complex and dynamic process that begins by transferring and utilizing osteogenic cells after proliferation, differentiation, matrix formation, and bone regeneration [3]. As a tissue or a critical organ in the human body, the bone not only plays an essential role in protecting the organs within the body but also causes the stability of the body and provides the mineral reserves of the body [4].

Natural bone is a composite material consisting of organic and mineral substances. Organic substances mainly include collagen fibers that cause bone hardness. In contrast, minerals mainly include calcium and

*Corresponding Author Institutional Email: nimanabian@mazust.ac.ir (N. Nabian)

Please cite this article as: O. Saneei Siavashy, N. Nabian, S. M. Rabiee, Titanium Dioxide Nanotubes Incorporated Bioactive Glass Nanocomposites: Synthesis, Characterization, Bioactivity Evaluation and Drug Loading, International Journal of Engineering, Transactions A: Basics Vol. 34, No. 01, (2021) 1-9

phosphorus in the form of hydroxyapatite crystals and, along with them, sodium, potassium, magnesium, fluoride, chlorine, carbonate, and some elements in small quantities such as silicon, strontium, iron, and zinc are the cause of bone strength [5].

Unlike some tissues, the bones have the potential to regenerate and repair against injury. However, when the demand for bone regeneration is more than average potentials, such as extensive bone defects that are caused after trauma, infection, and tumor removal or skeletal abnormalities, bone grafting is required [6]. Bone grafting, which can be used as an autograft [7], allograft [8], or xenograft [9], is applied when a part of the bone is destroyed. It is required to fill the gaps after injuries and accidents or after tumor removal. However, the use of the above methods is limited due to the lack of connective tissues for all patients, as well as the likelihood of recoil by the immune system. There is also the possibility of infection and disease transmission from the donor person to the patient. Bone tissue engineering is looking for methods to replace the damaged bone tissue of the human body by combining the cells of living organisms in an artificial or natural substance. This strategy introduces a good solution for the treatment of diseases and injuries of bone tissue. Alternative materials used in bone tissue engineering can be classified into polymers, including natural and synthetic polymers, ceramics including calcium phosphates and bioactive glasses, metals, and composites [10].

Bioglass is a material with high biocompatibility which has significant osteoconductivity, osteoinductivity, and controllable biodegradability. Bioglass, which is a material with high biocompatibility, remarkable osteoconductivity, significant osteoinductivity, and controllable biodegradability, was originally developed by Larry Hench. In an aqueous environment, this material can form hydroxycarbonate apatite, which is similar to biological minerals, and thus was widely used in the regeneration of bone and tissue engineering [11, 12].

Typically, glass is made through melting or the sol-gel method. In the melting method, the bioactive glass can be obtained by melting a mixture of raw materials and then cooling [13]. The sol-gel method is a wet chemical process for producing materials such as bioactive glass, using materials such as silicate compounds and metal ions. This process mainly involves hydrolysis, condensation of raw materials, drying, and calcination [14, 15]. By controlling the process parameters, it is possible to control properties such as morphology and composition [16]. The results of in vitro and in vivo tests indicate the superiority of sol-gel bioglass to melt-drived bioglass in bioactivity [17]. For the synthesis of bioactive glass by the sol-gel method, mostly, tetraethyl orthosilicate (TEOS) is used as a source of silica. Also, water or ethanol is used as a solvent [18]. The sol-gel method, according to the catalyst used in synthesis, can be divided into two acid and base catalytic methods that can affect the properties of the resulting materials. Metal ions can be added during the hydrolysis and condensation of tetraethyl orthosilicate, or after the formation of silicon-oxide nanoparticles. After drying and calcination of resulting nanoparticles, the bioactive glass is obtained. For particle shaping or dispersion improvement, it is possible to add other organic material during synthesis to the solution [18].

To ensure the effectiveness and safety of bone tissue substitutes, they should be tested in vitro and in vivo before testing in the human body. To avoid the high cost of in vivo tests, several types of in vitro tests are used to predict the in-vitro bioactivity of bioceramics. The purpose of in vitro bioactivity tests is to select the most appropriate biomaterial to continue its development [19, 20].

Currently, the most common in vitro bioactivity test is the soaking of the ceramics in the simulated body fluid [21]. In this method, the hydroxyapatite layer is formed on the surface of the bioactive material, after immersion in the simulated fluid of the bodies' plasma. Materials that a layer of hydroxyapatite is formed on their surface after immersion in simulated body fluids, but they are not implanted in the body, are known as in vitro bioactive [19]. Simulated body fluid which proposed by Kokubo et al. [22] is an ionic solution, which is similar to human plasma and is fixed in the physiological acidity by Tris Buffer. The formation of a layer of hydroxyapatite on the surface of bioactive glass is a sign of readiness for transplantation into living bone tissue [23]. The composition of the glass, the particle size, and finally their surface area are known as the factors that have the greatest impact on the formation of the hydroxyapatite layer and bone graft [18].

One of the fundamental challenges of implantation is controlling the infection caused by the bacterial load, which can create immune problems and eventually lead to the rejection of the implant [24]. To overcome the implant-related infection and the bacterial load on the implant, an incorporation combination of antibiotic drugs is recommended [25].

However, there are some limitations to the application of common medicinal drugs like toxicity in non-objective tissues, low efficiency, biological distribution, absence of selectivity, and overdose of medication [26]. To overcome these abovementioned restrictions and to reduce the side effects of medications, the local delivery of the drugs to bone tissue was considered as a suitable candidate [27]. Local delivery of medication to the desired tissues not only maintains the healthy cells unaffected but also provides the optimal amount of generally expensive related drugs with no drug dilution throughout the body, which results in bioavailability optimization of drugs [28].

The fabrication of nanostructures with physical properties such as pore size, pore volume and suitable surface area will improve the adsorption of guest particles such as drugs on the nanostructures [29]. Tetracycline (TC) is an effective antibiotic that is widely used in the treatment of infectious diseases. There is a very high tendency for TC towards calcified tissues like bone and teeth [30].

To enhance the bioactivity of bioactive glasses, some groups of researchers impregnated various types of metal oxides such as TiO_2. To do this, different sources of titanium were substituted for one of the common constituents of bioactive glass (SiO_2–CaO–P_2O_5). In most cases, researchers used Tetrabutyl Titanate as the Ti precursor and fabricated quaternary bioactive glasses without the direct utilization of TiO_2 particles [31, 32]. During the last decades, it has been proven that titania nanotubes (TNT) have desirable properties such as biocompatibility, high surface area, controllable pores size, chemical stability, mechanical strength, excellent accretion to bone tissue, and ability to promote hydroxyapatite growth [33, 34]. To the best of our knowledge, no research reported the application of titanium oxide nanoparticles directly in the common structure of 58S bioactive glass by decreasing the weight percent of SiO_2.

In this study, the 58S bioactive glass and a novel bioactive glass, which is synthesized by using TiO_2 nanotubes as one of the raw materials in the synthesis of bioglass, were produced by the sol-gel method. Furthermore, functional groups, phase structures, and bioactivity of samples, as well as tetracycline loading on the glasses, were investigated.

2. EXPERIMENTAL

2. 1. Materials The chemicals used in this study was tetraethyl orthosilicate (TEOS) as Si source, triethyl phosphate (TEP) as a P source, nitric acid (HNO_3) (70%), ammonia (NH_4OH) (25%), and ethanol (C_2H_5OH) were purchased from Merck (Germany), and calcium nitrate tetrahydrate ($Ca(NO_3)_2{\cdot}4H_2O$)) as Ca source was supplied from Carlo Erba, Spain. TiO_2 nanotubes (TNT) were purchased from Day Petronic Company (Iran), and tetracycline hydrochloride was purchased from Razak Laboratory Company (Iran).

2. 2. Glass Preparation The 58S bioactive glass was prepared by a quick alkali-mediated sol-gel method as described in a previous publication [35, 36]. Briefly, 21.6 ml of tetraethyl orthosilicate, 13.9 ml of deionized water, and 2.8 ml of nitric acid were dissolved in 50 ml of ethanol. This solution was stirred at room temperature for 30 minutes to complete the hydrolysis of tetraethyl orthosilicate. After this stage, 2.2 ml of triethyl phosphate was added to the previous solution and stirred for 20 minutes. Next, 14.04 g of calcium-nitrate was added to the solution and stirred for 20 minutes. The 2 M ammonia solution was then added dropwise to the solution, so that the viscosity of the solution increased slowly, and the solution became a gel. Ammonia was used as an accelerating agent in the gelation process. The resulting gel was then placed in an oven at 60 °C for one day for drying the gel and evaporating the alcoholic and water compounds, and the gel was obtained in a powder form. Subsequently, The resulting powder was placed in a furnace with a temperature of 600 °C for 2 hours at the 3 °C/min to remove its nitrate compounds (sample code: 58S).

For the synthesis of novel modified bioactive glass with titanium dioxide nanotubes, the synthesis method was similar to the 58S biglass synthesis, while 15 wt% of titanium dioxide nanotubes were incorporated into the solution by reducing the weight percent of SiO_2. In other words, the amount of used TEOS was reduced to 16.02 ml and instead, 0.755 g of titanium dioxide nanotube was added to the solution. Moreover, for better evaluation of the TNTs role in the modifid bioactive glasses, TNTs were added to the solution in two different steps:

1. after hydrolysis step of TEOS (sample code: 58S-15TNT);
2. before ammonia solution addition (sample code: 58S-TNT15).

The weight percent composition of the synthesized nanocomposites as well as the nanotube addition step are presented in Table 1.

2. 3. Characterization The X-ray diffraction (XRD) analysis of powdered bioactive glasses was performed on Inel EQUINOX 3000 diffractometer using CuKα radiation ($\lambda = 1.54$) with 0.032 step size over a range of $20<2\theta<60$. The Fourier transform infrared spectroscopy (FT-IR) absorption spectra of the samples were recorded with an ABB Bomem MB Series spectrometer at room temperature in the 400–4000 cm^{-1} range with a resolution of 4 cm^{-1} and 25 scans per minute. The morphologies of prepared samples were investigated using KYKY EM3200 scanning electron microscope (SEM) operating at the accelerating voltage of 30 kV. Before SEM analysis, the samples were covered with gold.

TABLE 1. Compositions of bioactive nanocomposites

	SiO_2	TiO_2	CaO	P_2O_5
58S	58	-	33	9
58S-15TNT	43	15	33	9
58S-TNT15	43	15	33	9

2. 4. Bioactivity Evaluation The in vitro bioactivity of samples was investigated by immersion of the samples in the simulated body fluid (SBF). The composition of the simulated body fluid is according to the method proposed by kokubo et al. [22]. Powders were immersed in the simulated body fluid and were placed in an incubator at 37 °C for 14 and 28 days. The mass of powder per volume of SBF was 25 mg/ml. Also, to maintain the concentration of ions in the solution, the previous solution was replaced by the fresh simulated body fluid. Finally, the powders were dried in an oven at 60 °C and then were analyzed by XRD, FTIR, and SEM.

2. 5. Drug Loading Drug loading analysis was carried out using the immersion of samples in the drug solution. Initially, 2000 mg/ml drug solution was prepared by mixing of tetracycline hydrochloride and deionized water for 5 minutes. The bioglass powders were added to the drug solution with 10 mg/ml concentration and stirred at room temperature for one day using a magnetic stirrer. Afterward, the absorbance of the dissolved solution was determined by Unico 2100 UV-Vis spectrometer at 383 nm [37] after the solution was centrifugated. Using the calibration curve, the concentration of the soluble drug was calculated after the loading process. This concentration is related to the residual drug in the loading solution, and the decrease in the drug concentration is assigned to the drug adsorption by the bioglass powders.

The calibration curve of Tetracycline concentration was determined at room temperature by plotting absorbance versus different concentrations of tetracycline hydrochloride solution including 18.75, 37.5, 50, 75, 100, 125, 150, 200 ppm. The calibration curve was obtained based on the lambert-beers law.

3. RESULTS AND DISCUSSION

3. 1. Phase Structure Analysis Figure 1 shows the scanning electron microscopy (SEM) images of the prepared samples. As shown in the SEM picture of *58S* bioactive glass, this synthesized material possessed spherical nanoparticles, while the addition of titanium dioxide had a significant effect on the morphology of the composites. Moreover, the step in which titanium dioxide nanotubes were added to the solution completely changed the composite morphology. In other words, the SEM picture of 58S-15TNT composite shows that titanium dioxide nanotubes were impregnated through the composite surface with no considerable spherical particles, while the 58S-TNT15 SEM image displays that needle-like titanium dioxide nanotubes were formed on the spherical bioactive glass composite.

XRD patterns for 58S, 58S-15TNT, and 58S-TNT15 samples are shown in Figure 2. There are no obvious

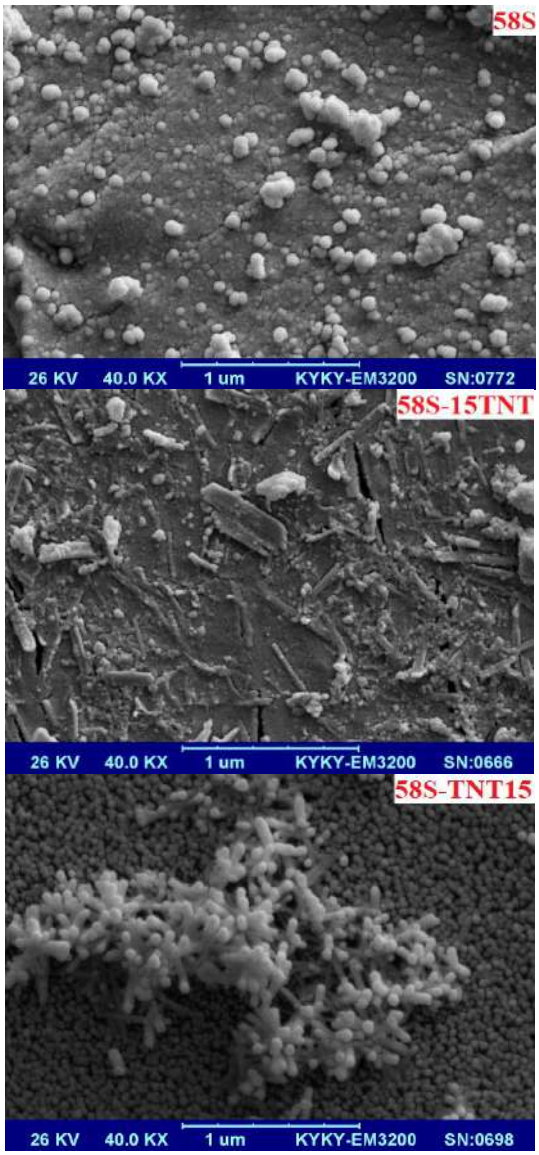

Figure 1. SEM images of 58S, 58S-15TNT, and 58S-TNT15

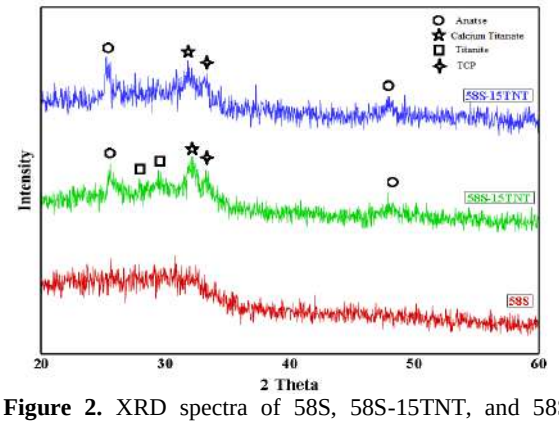

Figure 2. XRD spectra of 58S, 58S-15TNT, and 58S-TNT15

peaks in the 58S XRD pattern, which indicates that this bioglass was amorphous. By incorporation of titanium dioxide nanotubes in the bioactive composites, two characteristic peaks of this material appeared at approximate angles of 25° and 48°, which represents the presence of anatase TiO_2. The peak appeared at an approximate angle of 34° may be due to tricalcium phosphate [38]. A peak created around an angle of 32.5°, is related to the formation of calcium titanate phase.

Also, two peaks shown at about angles of 27° and 29° correspond to the titanite [39, 40]. The formation of these new compounds can be attributed to the reaction of titanium dioxide nanotubes with functional groups of bioactive glass. As shown in this figure, the 58S-TNT15 XRD pattern has stronger TiO_2 peaks compared to that of 58S-15TNT. This may be due to the weaker interaction between TNTs and the functional groups involved in the synthesis of 58S-15TNT biocomposite due to the step of TNTs addition. In addition, the lack of calcium titanium silicate phase in the XRD pattern of the 58S-TNT15 sample confirms this finding.

Figure 3 shows the FTIR absorption spectra of the 58S, 58S-15TNT, and 58S-TNT15 bioglasses. The band at 468 cm^{-1} is attributed to Si-O-Si bending vibration, while the peak at 1099 cm^{-1} is ascribed to Si-O-Si asymmetric stretching vibration [41]. Due to the addition of TNTs, a band appeared at around 940 cm^{-1}, which can be assigned to Si-O stretching vibration in Si-O-Ti groups [42].

3. 2. In Vitro Bioactivity Figure 4 shows XRD patterns of 58S, 58S-15TNT, and 58S-TNT15 samples after immersion in SBF for 14 and 28 days. Two weak peaks observed at approximate angles of 31.5° and 40° in 58S XRD pattern indicates the onset of hydroxyapatite formation after 14 days of immersion [43]. At an around angle of 35°, a new peak was generated that may be due to the formation of tricalcium phosphate [38]. Furthermore, the peak observed for all samples at an about angle of 30° can be assigned to wollastonite formation [44].

Due to the increase in the number of peaks related to hydroxyapatite as well as their intensity after 28 days of immersion in SBF compared to 14 days, it can be concluded that increasing the soaking time enhanced the formation of hydroxyapatite and subsequently the bioactivity of samples. Furthermore, based on the intensity of hydroxyapatite peaks at 31.5° and 40° shown in the XRD patterns of composites containing titanium dioxide nanotubes, it can be understood that the presence of titanium dioxide nanotubes improved the bioactivity after 14 days of immersion and both 58S-TNT composites were more bioactive than 58S bioglass. Although the 58S-15TNT sample was the more bioactive sample after 14 days of soaking in SBF, 58S bioactive glass possessed more intense peaks of HA after 28 days of immersion in SBF.

Figure 5 shows the FTIR absorption spectra of the 58S, 58S-15TNT, and 58S-TNT15 composites after 14 and 28 days of immersion in SBF. The peaks at 567 cm^{-1} and 604 cm^{-1} can be assigned to the bending mode of the O-P-O bond [43]. Another peak that appeared at 961

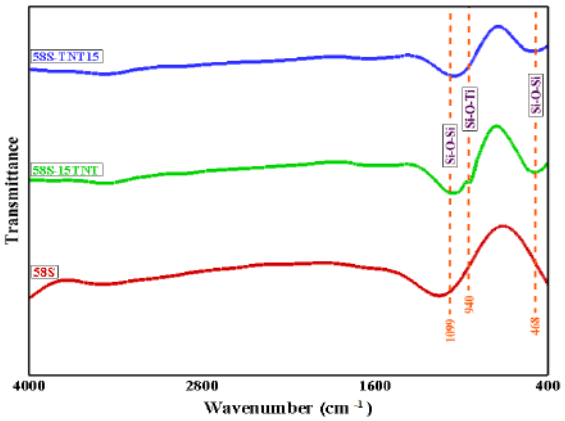

Figure 3. FTIR spectra of 58S, 58S-15TNT, and 58S-TNT15

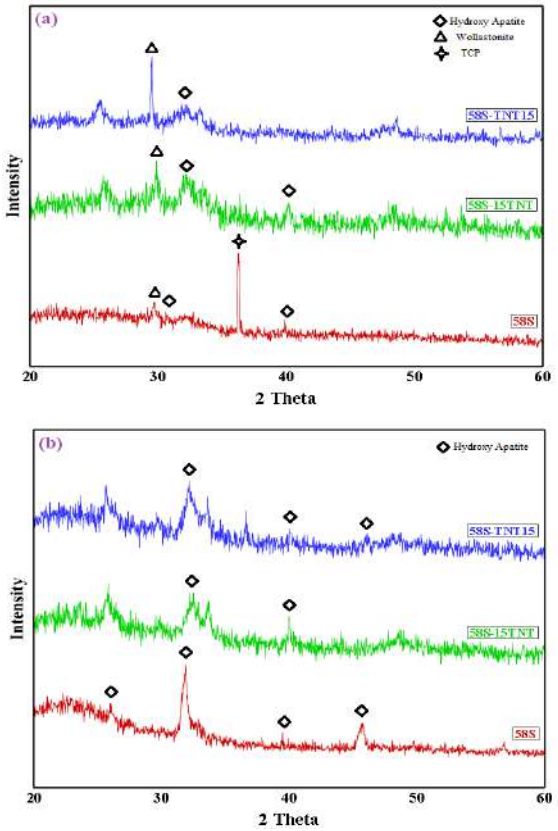

Figure 4. XRD patterns of 58S, 58S-15TNT, and 58S-TNT15 samples after a) 14 and b) 28 days of immersion in SBF

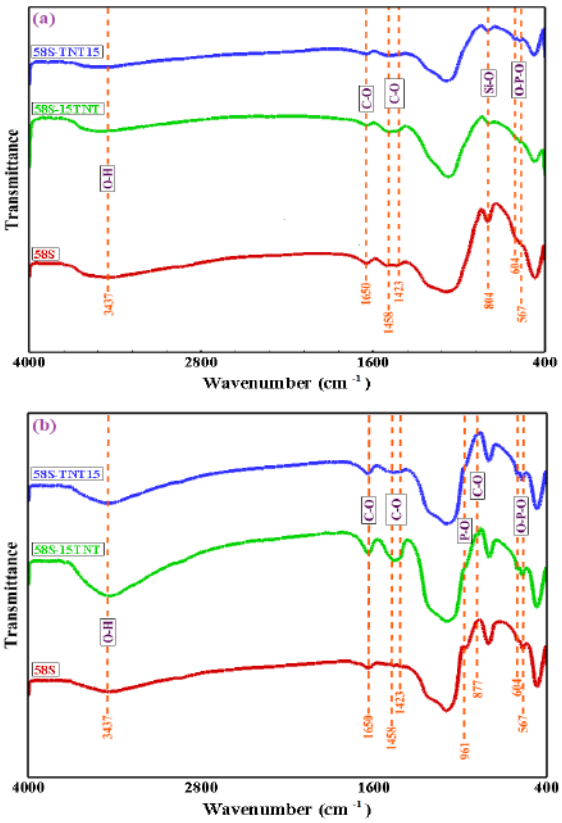

Figure 5. FTIR spectra of 58S, 58S-15TNT, and 58S-TNT15 samples after a) 14 and b) 28 days of immersion in SBF

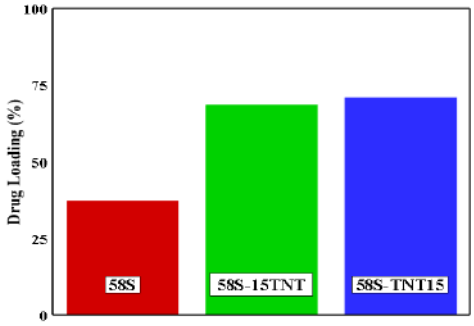

Figure 6. TC loading capacity on of 58S, 58S-15TNT, and 58S-TNT15 samples

cm^{-1} is attributed to the symmetric stretching mode of the P–O bond of the phosphate group [43]. The peak that appeared at 877 cm^{-1} corresponds to the symmetric vibrational.

C-O [45]. A new peak appeared at 961 cm^{-1} is assigned to P-O stretching vibration. The peak at 1650 cm^{-1} can be ascribed to the vibration of CO_3^{2-} and the twin peaks located at 1423 cm^{-1} and 1458 cm^{-1} can be attributed to C-O asymmetric stretching vibration due to the presence of CO_3^{2-} in site PO_4^{3-} [43, 46]. The peak at 3437 cm^{-1} could be ascribed to O-H bond [47].

According to the peaks shown in the FTIR spectra of the composite containing titanium dioxide nanotubes, it can be perceived that the intensity of peaks present in the FTIR spectrum of 58S-15TNT is higher than that of the 58S-TNT15 sample, which again confirms better bioactivity of 58S-15TNT.

3. 3. Drug Loading The drug loading performance of each sample is shown in Figure 6. As shown in this bar chart, with an addition of the TNT to the structure of 58 base bioglass, the drug loading capacity of samples increased more than 2 times. The dominant mechanism of drug loading on the bioactive nanocomposites is adsorption in which the active sites of the composites are occupied by tetracycline particles during the process [48]. The composites containing titanium dioxide nanotubes showed a higher value of tetracycline loading compared to 58S bioactive glass due to a better adsorption capacity of TNTs present in the matrix of nanocomposites [49]. The slightly better performance of 58S-TNT15 in comparison with 58S-15TNT may be attributed to its higher surface area due to the presence of needle-like titanium dioxide nanotubes formed on the spherical bioactive glass composite as shown in the SEM picture of the final product.

3. 4. Comparison of the Results As described in this study, navel nano bioactive nanocomposites were synthesized by the incorporation of titanium dioxide nanotubes into the bioglass structure. As mentioned in the introduction section, The literature review in this area shows that no research reported the direct substitution of SiO_2 with titanium dioxide nanotubes in the bioglass composition. Based on the results obtained in this study, it is clear that the presence of titanium dioxide nanotubes resulted in better bioactivity of samples after 14 days of soaking in the SBF solution compared to 58S bioglass. However, Ni et al. [30] investigated the effect of adding TiO_2 to a bioactive glass compound. They reported that the addition of TiO_2 reduced the rate of hydroxyapatite formation, but this effect diminished in a long time and did not affect the growth of the apatite layer after long periods of soaking. Moreover, Heidari et al. [32] assessed the replacement of CaO with TiO_2 in 45S5 bioactive glass synthesized by sol-method. They reported that despite the slowdown of hydroxyapatite formation in the early days in titanium-containing samples, the bioactivity results were almost the same over the 14 days. Therefore, it is worth mentioning that direct utilization of titanium dioxide nanotubes as a titanium precursor, applied in this study, was more effective in increasing the bioactivity of the composites than other titanium sources such as Tetrabutyl Titanate used by other researchers.

4. CONCLUSION

In this study, novel sol-gel derived modified bioactive glasses incorporated by titanium dioxide nanotubes were synthesized by reducing the amount of SiO_2 present in the structure of common 58S. According to the SEM images of the modified bioglasses, it was found that the addition of TiO_2 nanotubes caused a change in the morphology of samples and also new crystalline phases such as titanite ($CaTiSiO_5$) and calcium titanate ($CaTiO_3$) were generated. Comparing XRD and FTIR patterns of the modified samples before and after in vitro bioactivity tests revealed that the hydroxyapatite was formed on both composites containing titanium dioxide nanotubes. However, there was a decrease in the bioactivity behavior of the modified bioglasses compared to 58S base bioglass after 28 days of immersion in simulated body fluid. Moreover, the 58S-15TNT composite showed better bioactivity than the 58S-TNT15 sample after 28 days of soaking in SBF. The results of drug loading on the modified bioglasses also indicated that the presence of titanium dioxide nanotubes in the structure of bioactive composites was effective and these composites possessed better drug loading performance due to an increase in the tetracycline loading. Therefore, TNT incorporated bioactive composites have the potential for extensive research in the regeneration of bone defects and local drug delivery.

5. REFERENCES

1. Chiu, L. L. Y., Chu, Z., Radisic, M., Mozafari, M., "Tissue Engineering, Reference Module in Materials Science and Materials Engineering", Elsevier, (2017).
2. Hasan, A., "Tissue Engineering for Artificial Organs: Regenerative Medicine, Smart Diagnostics and Personalized Medicine", Vol. 2, Wiley, Weinheim, (2017).
3. T. Gong, J. Xie, J. Liao, T. Zhang, S. Lin, Y. Lin, "Nanomaterials and bone regeneration", ***Bone Research***, Vol. 3, (2015), 1-7. doi: 10.1038/boneres.2015.29
4. Maksimkin, A.V., Senatov, F.S., Anisimova, N.Y., Kiselevskiy, M.V., Zalepugin, D.Y., Chernyshova, I.V., Tilkunova, N.A. and Kaloshkin, S.D., "Multilayer porous UHMWPE scaffolds for bone defects replacement", ***Materials Science and Engineering: C***, Vol. 73, (2017), 366-372. doi: 10.1016/j.msec.2016.12.104
5. Gao, C., Peng, S., Feng, P. and Shuai, C., "Bone biomaterials and interactions with stem cells", ***Bone Research***, Vol. 5, (2017), 1-33. doi: 10.1038/boneres.2017.59
6. Kim, T., See, C.W., Li, X. and Zhu, D., "Orthopedic implants and devices for bone fractures and defects: Past, present and perspective", ***Engineered Regeneration***, Vol. 1, (2020), 6-18. doi: 10.1016/j.engreg.2020.05.003
7. Shin, S. Y., Rios, H. F. Giannobile, W. V., Oh, T. -J., "Stem Cell Biology and Tissue Engineering in Dental Sciences", in: Vishwakarma, A., Sharpe, P., Shi, S., Ramalingam, M. (Ed.), Academic Press, Boston, (2015), 459-469, (Chapter 36).
8. Yoshida, R., Baron, S., Rodner, C. and Ferreira, J., "Biologics in Orthopaedic Surgery", in: Mazzocca, A. D., Lindsay A. D. (Ed.), Elsevier, Philadelphia, (2019), 135-139, (Chapter 13).
9. Shibuya, N. and Jupiter, D.C., "Bone graft substitute: Allograft and xenograft", ***Clinics in Podiatric Medicine and Surgery***, Vol. 32, No. 1, (2015), 21-34. doi: 10.1016/j.cpm.2014.09.011
10. Nikolova, M.P. and Chavali, M.S., "Recent advances in biomaterials for 3D scaffolds: A review", ***Bioactive Materials***, Vol. 4, (2019), 271-292. doi: 10.1016/j.bioactmat.2019.10.005
11. Diaz-Rodriguez, P., Sánchez, M. and Landin, M., "Drug-loaded biomimetic ceramics for tissue engineering", ***Pharmaceutics***, Vol. 10, No. 4, (2018), 272. doi: 10.3390/pharmaceutics10040272
12. Bargavi, P., Ramya, R., Chitra, S., Vijayakumari, S., Riju Chandran, R., Durgalakshmi, D., Rajashree, P. and Balakumar, S., "Bioactive, degradable and multi-functional three-dimensional membranous scaffolds of bioglass and alginate composites for tissue regenerative applications", ***Biomaterials Science***, Vol. 8, No. 14, (2020), 4003-4025. doi: 10.1039/D0BM00714E
13. Kaur, G., Pickrell, G., Sriranganathan, N., Kumar, V. and Homa, D., "Review and the state of the art: Sol–gel and melt quenched bioactive glasses for tissue engineering", ***Journal of Biomedical Materials Research Part B: Applied Biomaterials***, Vol. 104, No. 6, (2016), 1248-1275. doi: 10.1002/jbm.b.33443
14. Rabiee, S.M., Nazparvar, N., Azizian, M., Vashaee, D. and Tayebi, L., "Effect of ion substitution on properties of bioactive glasses: A review", ***Ceramics International***, Vol. 41, No. 6, (2015), 7241-7251. doi: 10.1016/j.ceramint.2015.02.140
15. Derhambakhsh, M., Novinrooz, J. and Tohidi, S.H., "Preparation and study of molecular structure of copper ions doped in a silica xerogel matrix", ***International Journal of Engineering, Transactions A: Basics***, Vol. 19, No. 1, (2006), 53-60.
16. Zheng, K. and Boccaccini, A.R., "Sol-gel processing of bioactive glass nanoparticles: A review", ***Adv Colloid Interface Sci***, Vol. 249, (2017), 363-373. doi: 10.1016/j.cis.2017.03.008
17. Nabian, N., Delavar, M., Rabiee, S.M. and Jahanshahi, M., "Quenched/unquenched nano bioactive glass-ceramics: Synthesis and in vitro bioactivity evaluation in ringer's solution with BSA", ***Chemical Industry and Chemical Engineering Quarterly***, Vol. 19., No. 2, (2013), 231-239. doi: 10.2298/CICEQ120323057N
18. Vichery, C. and Nedelec, J.-M., "Bioactive glass nanoparticles: From synthesis to materials design for biomedical applications", ***Materials***, Vol. 9, No. 4, (2016), 288. doi: 10.3390/ma9040288
19. Salinas, A.J. and Vallet-Regí, M., "Bioactive ceramics: From bone grafts to tissue engineering", ***RSC Advances***, Vol. 3, No. 28, (2013), 11116-11131. doi: 10.1039/C3RA00166K
20. Wu, C. and Xiao, Y., "Article commentary: Evaluation of the in vitro bioactivity of bioceramics", ***Bone and Tissue Regeneration Insights***, Vol. 2, (2009), 25-29. doi: 10.4137/BTRI.S3188
21. Saebnoori, e. and vali, I., "Surface activation of niti alloy by using electrochemical process for biomimetic deposition of hydroxyapatite coating", ***International Journal of Engineering, Transactions A: Basics***, Vol. 27, No. 10, (2014), 1627-1634. doi: 10.5829/idosi.ije.2014.27.10a.17
22. Kokubo, T. and Takadama, H., "How useful is SBF in predicting in vivo bone bioactivity?", ***Biomaterials***, Vol. 27, No. 15, (2006), 2907-2915. doi: 10.1016/j.biomaterials.2006.01.017
23. Sorrell, C.C., Saeri, M.R., Ehsani, N., Afshar, A. and Ghorbani, M., "Interface characterization of plasma sprayed hydroxyapatite coat on Ti 6Al 4V ", ***International Journal of Engineering, Transactions B: Applications***, Vol. 15, No. 2, (2002), 173-182.
24. Abbaspour, S. and Sadrnezhaad, S.K., "Loading drug on nanostructured Ti6Al4V-HA for implant applications", ***International Journal of Engineering, Transactions B: Applications***, Vol. 31, No. 8, (2018), 1159-1165. doi: 10.5829/ije.2018.31.08b.01
25. Turkyilmaz, I., "Current concepts in dental implantology, IntechOpen, (2015).

26. Rubiana, M.M. and Luciano, P.S., "Drug delivery systems: Past, present, and future", ***Current Drug Targets***, Vol. 5, No. 5, (2004), 449-455. doi: 10.2174/1389450043345407
27. Porter, J.R., Ruckh, T.T. and Popat, K.C., "Bone tissue engineering: A review in bone biomimetics and drug delivery strategies", ***Biotechnology Progress***, Vol. 25, No. 6, (2009), 1539-1560. doi: 10.1002/btpr.246
28. Wu, P. and Grainger, D.W., "Drug/device combinations for local drug therapies and infection prophylaxis", ***Biomaterials***, Vol. 27, No. 11, (2006), 2450-2467. doi: 10.1016/j.biomaterials.2005.11.031
29. Bavnhøj, C.G., Knopp, M.M., Madsen, C.M. and Löbmann, K., "The role interplay between mesoporous silica pore volume and surface area and their effect on drug loading capacity", ***International Journal of Pharmaceutics: X***, Vol. 1, (2019), 100008. doi: 10.1016/j.ijpx.2019.100008
40. Seok, H., Kim, S.-G., Kweon, H., Jo, Y.-Y., Lee, K.-G., Kang, T.Y., Chae, W.-S., Min, S.-K., Ahn, J.-H., Park, J.-W. and Choi, D.-J., "Comparison of different concentrations of tetracycline-loaded silk fibroin membranes on the guided bone regeneration in the rat calvarial defect model", ***Tissue Engineering and Regenerative Medicine***, Vol. 11, No. 6, (2014), 476-482. doi: 10.1007/s13770-014-9057-3
31. Ni, S., Du, R. and Ni, S., "The influence of Na and Ti on the in vitro degradation and bioactivity in 58S sol-gel bioactive glass", ***Advances in Materials Science and Engineering***, Vol. 2012, No., (2012), 730810. doi: 10.1155/2012/730810
32. Heidari, S., Hooshmand, T., Yekta, B.E., Tarlani, A., Noshiri, N. and Tahriri, M., "Effect of addition of titanium on structural, mechanical and biological properties of 45S5 glass-ceramic", ***Ceramics International***, Vol. 44, No. 10, (2018), 11682-11692. doi: 10.1016/j.ceramint.2018.03.245
33. Aw, M.S., Khalid, K.A., Gulati, K., Atkins, G.J., Pivonka, P., Findlay, D.M. and Losic, D., "Characterization of drug-release kinetics in trabecular bone from titania nanotube implants", ***International Journal of Nanomedicine***, Vol. 7, (2012), 4883-4892. doi: 10.2147/IJN.S33655
34. Hassanzadeh Nemati, N., Ghasempour, E. and Zamanian, A., "Effect of dual releasing of β-glycerophosphate and dexamethasone from Ti nanostructured surface for using in orthopedic applications", ***International Journal of Engineering, Transactions A: Basics***, Vol. 32, No. 10, (2019), 1337-1344. doi: 10.5829/ije.2019.32.10a.01
35. Xia, W. and Chang, J., "Preparation and characterization of nano-bioactive-glasses (NBG) by a quick alkali-mediated sol–gel method", ***Materials Letters***, Vol. 61, No. 14, (2007), 3251-3253. doi: 10.1016/j.matlet.2006.11.048
36. Taghian Dehaghani, M. and Ahmadian, M., "Fracture mechanism of CoCrMo porous nano-composite prepared by powder metallurgy route", ***International Journal of Engineering, Transactions A: Basics***, Vol. 31, No. 1, (2018), 19-24. doi: 10.5829/ije.2018.31.01a.03
37. Andrade, A.L., Souza, D.M., Vasconcellos, W.A., Ferreira, R.V. and Domingues, R.Z., "Tetracycline and/or hydrocortisone incorporation and release by bioactive glasses compounds", ***Journal of Non-Crystalline Solids***, Vol. 355, No. 13, (2009), 811-816. doi: 10.1016/j.jnoncrysol.2009.01.015
38. Gallinetti, S., Canal, C., Ginebra, M.-P. and Ferreira, J., "Development and characterization of biphasic hydroxyapatite/β-TCP cements", ***Journal of the American Ceramic Society. American Ceramic Society***, Vol. 97, No. 4, (2014), 1065-1073. doi:10.1111/jace.12861
39. Hu, W., Liu, H., Hao, H., Yao, Z., Cao, M., Wang, Z. and Song, Z., "Influence of Tio_2 additive on the microwave dielectric properties of α-$CaSiO_3$–Al_2O_3 ceramics", ***Ceramics International***, Vol. 41, (2015), 510-514. doi: 10.1016/j.ceramint.2015.03.138
40. Zhu, W., Jiang, H., Sun, S., Jia, S. and Liu, Y., "Effect of Tio_2 content on the crystallization behavior and properties of Cao-Al_2O_3-SiO_2 glass ceramic fillers for high temperature joining application", ***Journal of Alloys and Compounds***, Vol. 732, (2018), 141-148. doi: 10.1016/j.jallcom.2017.10.166
41. Letaïef, N., Lucas-Girot, A., Oudadesse, H., Dorbez-Sridi, R. and Boullay, P., "Investigation of the surfactant type effect on characteristics and bioactivity of new mesoporous bioactive glass in the ternary system SiO_2–CaO–P_2O_5: Structural, textural and reactivity studies", ***Microporous and Mesoporous Materials***, Vol. 195, (2014), 102-111. doi: 10.1016/j.micromeso.2014.03.035
42. Taloş, F., Senilă, M., Frentiu, T. and Simon, S., "Effect of titanium ions on the ion release rate and uptake at the interface of silica based Xerogels with simulated body fluid", ***Corrosion Science***, Vol. 72, (2013), 41-46. doi: 10.1016/j.corsci.2013.03.003
43. Mezahi, F.Z., Oudadesse, H., Harabi, A., Lucas-Girot, A., Le Gal, Y., Chaair, H. and Cathelineau, G., "Dissolution kinetic and structural behaviour of natural Hydroxyapatite vs. Thermal treatment", ***Journal of Thermal Analysis and Calorimetry***, Vol. 95, No. 1, (2008), 21-29. doi: 10.1007/s10973-008-9065-4
44. Mokhtari, H., Ghasemi, Z., Kharaziha, M., Karimzadeh, F. and Alihosseini, F., "Chitosan-58S bioactive glass nanocomposite coatings on TiO_2 nanotube: Structural and biological properties", ***Applied Surface Science***, Vol. 441, (2018), 138-149. doi: 10.1016/j.apsusc.2018.01.314
45. Sossa, P.A.F., Giraldo, B.S., Garcia, B.C.G., Parra, E.R. and Arango, P.J.A., "Comparative study between natural and synthetic hydroxyapatite: Structural, morphological and bioactivity properties", ***Matéria (Rio de Janeiro)***, Vol. 23, No. 4, (2018). doi: 10.1590/s1517-707620180004.0551
46. Chen, J., Zeng, L., Chen, X., Liao, T. and Zheng, J., "Preparation and characterization of bioactive glass tablets and evaluation of bioactivity and cytotoxicity in vitro", ***Bioactive Materials***, Vol. 3, No. 3, (2018), 315-321. doi: 10.1016/j.bioactmat.2017.11.004
47. Nabian, N., Jahanshahi, M. and Rabiee, S.M., "Synthesis of nano-bioactive glass–ceramic powders and its in vitro bioactivity study in bovine serum albumin protein", ***Journal of Molecular Structure***, Vol. 998, No. 1, (2011), 37-41. doi: 10.1016/j.molstruc.2011.05.002
48. Zhao, L., Yan, X., Zhou, X., Zhou, L., Wang, H., Tang, J. and Yu, C., "Mesoporous bioactive glasses for controlled drug release", ***Microporous and Mesoporous Materials***, Vol. 109, No. 1, (2008), 210-215. doi: 10.1016/j.micromeso.2007.04.041
49. Delavar, M., Bakeri, G., Hosseini, M. and Nabian, N., "Fabrication and characterization of polyvinyl chloride mixed matrix membranes containing high aspect ratio anatase titania and hydrous manganese oxide nanoparticle for efficient removal of heavy metal ions: Competitive removal study", ***The Canadian Journal of Chemical Engineering***, Vol. 98, No. 7, (2020), 1558-1579. doi: 10.1002/cjce.23725

Persian Abstract

چکیده

کامپوزیت‌های شیشه زیست‌فعال جدیدی با روش سل-ژل، از طریق کاهش درصد وزنی سیلیس و جایگزینی آن با ۱۵ درصد وزنی از نانولوله‌های اکسید تیتانیوم سنتز شده‌اند که این مواد در دو مرحله متفاوت در فرآیند سنتز اضافه شده‌اند. خواص زیست‌فعالی، مورفولوژی، ساختار کریستالی، گروه‌های عاملی کامپوزیت‌ها از طریق میکرو سکوپ الکترون روبشی (SEM) و آنالیزهای پراش اشعه ایکس (XRD) و تبدیل فوریه مادون قرمز (FTIR) مورد ارزیابی قرار گرفتند. بر اساس تصاویر SEM، مرحله‌ای که در آن نانولوله‌های اکسید تیتانیوم به محلول اضافه می شود، به طور کامل مورفولوژی کامپوزیت را تغییر داده است. آزمون زیست‌فعالی بیرون‌تنی با غوطه‌ور کردن نمونه‌ها در مایع شبیه‌سازی‌شده بدن برای بازه‌های ١٤ و ٢٨ روزه و با توجه به تشکیل لایه هیدروکسی‌آپاتیت روی سطح نمونه‌ها انجام شد. با توجه به پیک‌های XRD در زاویه دوتا حدود ٣١ و ٤٠ درجه، مشخص گردید حضور نانولوله‌های اکسید تیتانیوم منجر به بهبود زیست‌فعالی نمونه‌ها بعد از ١٤ روز گردیده است و هر دو کامپوزیت حاوی نانولوله‌های اکسید تیتانیوم از نمونه 58S زیست‌فعالی بیشتری داشته‌اند، در حالیکه بعد از ٢٨ روز غوطه‌وری در SBF، شیشه زیست‌فعال 58S پیک‌های هیدروکسی‌آپاتیت با شدت بیشتری را نشان داده است. به علاوه، ویژگی بارگذاری دارو کامپوزیت‌های تهیه‌شده ارزیابی شدند و نتایج مربوطه نشان دادند که اضافه نمودن نانولوله‌ها در مقایسه با بیوگلس 58S با بارگذاری داروی ٣٧ درصد، عملکرد کامپوزیت‌های زیست‌فعال حاوی نانو لوله‌های اکسید تیتانیوم را تا ٧٠ درصد بهبود بخشیده است.

International Journal of Engineering

Journal Homepage: www.ije.ir

Influence of Bi-directional Fibreglass Grid Reinforcement on Drying Shrinkage and Mechanical Properties of Lightweight Foamed Concrete

S. B. Wani*

Department of Civil Engineering, B. S. Abdur Rahman Crescent Institute of Science & Technology Chennai, India

P A P E R I N F O

Paper history:
Received 26 August 2020
Received in revised form 18 September 2020
Accepted 26 October 2020

Keywords:
Drying Shrinkage
Durability
Foamed Concrete
Strain
Textile Fabric

A B S T R A C T

This experimental work is about the study of drying shrinkage followed by strength testing of lightweight foamed concrete (LFC) specimens with the confinement of woven fiberglass mesh (FGM) at three different densities. The LFC specimens were wrapped with 1-layer to 3-layer(s) of FGM for cube and cylinder specimens and in beam specimens, it was centrally spread along the longitudinal axis. The specimens were cured under air storage conditions and the drying shrinkage test was carried following ASTM C157/C 157M specification on three prism-shaped '75mmx75mmx285mm' specimens. NORAITE PA-1 foaming agent was used to produce the desired density of LFC. All of 324 specimens were cast and tested for mechanical properties at 7days, 28days and 56days respectively. In compression strength test, cube dimensions of 100mm side following BS EN 12390-3:2009 was adopted. The flexural strength was conducted on '100mmx100mmx500mm' beam specimens following BS ISO 1920-8:2009. The specimens '100mm in diameter and 200mm in height' were tested for split tensile strength considering ASTM C496/ C496M-04e1 specifications. The results showed that confinement with 160g/m^2 (GSM) of FGM significantly restricts the drying shrinkage of LFC specimens compared to control specimens and it decreased with the increases in layer(s) from l-layer to 3-layer(s) and density of LFC. The testing of the mechanical properties of LFC showed a direct proportionality between strength and LFC density and confinement layer(s). The failure pattern observed in all specimens was either by debonding or splitting of fibers of FGM. Thus, LFC at 1600kg/m^3 density confined/reinforced with 3-layers of FGM conquers the good performance in drying shrinkage and strength properties while the poor performance was shown by the unconfined LFC at 600kg/m^3 density.

***doi**: 10.5829/ije.2021.34.01a.02*

1. INTRODUCTION

Lightweight foamed concrete (LFC) is a cellular concrete prepared by combination of foam of desired density in a cement-based slurry. The foam enriches the workability property of slurry due to the thixotropic behaviour of the foam bubbles, allowing it to be easily poured and transported into the desired moulds of any shape. The technical terms used for labelling LFC include reduced self-weight for lower densities [1, 2], which is essential for restoration or to reduce the dead loads on structural elements of buildings, thermal and acoustic insulation [3], partition walls, enhance fire resistance [4], sub-base in highways, insulation of floor and roof screeds, bridge approaches/embankments [5], prefabricated structures and many more.

Choi and Ma [6] engaged LFC to serve in tunnel drainage and it was implemented in a two-lane highway tunnel in South Korea. LFC results in sustainable [7, 8] and economical construction due to use of less labour, easy transportation and low operating costs [2, 6]. In addition to this, the provision of partial replacement of traditional aggregates used in foamed-concrete by fly ash and silica fumes [9, 10] or recycled ingredients like glass and foundry or electric arc furnace slag [11, 12] is possible which can further reduce the cost. In practice, the LFC has found numerous application in the construction field in countries like UK, Turkey, Philippines, Canada, Malaysia, Korea and Thailand [13, 14].

One of the prevalent downsides of LFC is its early age drying shrinkage [15]. The reason being the expulsion of

*Corresponding Author Email: *shoibbwani@gmail.com* (Shoib B Wani)

Please cite this article as: Shoib. B Wani, Influence of Bi-directional Fibreglass Grid Reinforcement on Drying Shrinkage and Mechanical Properties of Lightweight Foamed Concrete, International Journal of Engineering, Transactions A: Basics, Vol. 34, No. 1, (2021) 10-18

water from the capillaries of the concrete mixture [16]. Once the water evaporates, it is impossible to replace it. This problem causes the LFC made elements to shrink and reduce in volume leading to cracking and decreasing overall performance. Kearsley [17] stated that the LFC is noticed to be weak and non-durable due to its characteristic high shrinkage value which can lead to change in dimensions and cracks in the matrix. Besides this, the average percentage of drying shrinkage in LFC is about two to three times greater than conventional concrete. Roslan et al. [18] revealed that the "typical range of drying shrinkage value in LFC is in between 0.1% to 0.35% of the total volume of the hardened concrete matrix". As reported by Fedorov and Mestnikov [19], the highest values of shrinkage deformations lead to low strength characteristics in LFC. The explanation by Rai and Kumar [20] about "high drying shrinkage of LFC due to the absence of coarse aggregates where the result is up to 10 times greater than has been observed in the normal concrete". The examination of the shrinkage behaviour of LFC, moisture content and composition are the basic responsible factors as stated by Nambiar and Ramamurthy [21]. Amran et al. [22] stated that drying shrinkage in LFC can be controlled by the type of material used in matrix design, greater cement, water proportion and admixtures. Namsone et al. [23] also justified that the possible shrinkage problem in LFC is caused by carbonation which leads to cracking and its durability loss. Also, the high volume of voids is the prime cause for increased drying shrinkage proportion in LFC. As reported by Zamzani [24], the drying shrinkage of LFC is radically greater in the beginning till 30 days and then continues to grow gradually. The reason being at the early age of the test, the specimens are not fully hardened, and the lowest percentage of drying shrinkage value is achieved at a higher density of LFC.

Since the drying shrinkage of LFC is higher compared to conventional concrete. Either synthetic or natural fibers like alkali-resistant glass, kenaf, steel, oil palm fiber, and polypropylene fiber [25–27] can be used in LFC to reduce the drying shrinkage and improve its mechanical properties. This paper focuses on the confinement of woven fiberglass mesh (FGM) by 1layer to 3layers(s) in LFC to study the drying shrinkage behaviour followed by basic mechanical property testing of specimens for validation. Three different densities of LFC were chosen based on the application categorized which were 600kg/m^3 for non-structural building material, 1100kg/m^3 for semi-structural while 1600kg/m^3 for structural building material in real practice.

2. MATERIALS AND MIX DESIGN

There are four basic materials utilized in the production of LFC which were cement, fine aggregate (FA), potable-water, and foam. Besides, 160g/m^2 (GSM) of FGM was employed in this research to investigate its functionality to restrict the drying shrinkage and enhance strength aspects of LFC. 53-grade OPC, commercially known by 'Ultra Tech' brand, following the specifications of category 1 portland cement in ASTM C150-04 [28] was used. Table 1 includes the basic chemical configuration of used cement and the reference Type 1 cement as specified.

The FA utilized in this research was restricted to less than 1.18mm diameter with a specific gravity of 2.74 and fineness modulus of 1.35. The grading limits was according to ASTM C778-06 [29]. FA is suitable for producing the LFC as the presence of coarse aggregate creates bigger voids, sinks to the bottom of moulds, affects its flowability resulting in an inconsistent mix and thereby affects the LFC properties.

The presence of water is necessary to mix the cement and FA to form the cement slurry which by a chemical reaction will lead to the hardened mortar paste complied with ASTM C1602-C05 [30]. 'Protein-based foaming agent, NORAITE PA-1' was utilized as a foaming agent that was added into the cement slurry to get the desired density. 1kg of the foaming agent was diluted into 30L of water as shown in Figure 1 before supplied to the foam generator as shown in Figure 2.

Furthermore, the FGM as shown in Figure 3 also known as the textile fabric was used as a confinement/reinforcement. This mesh is categorized as synthetic, lightweight, flexible, eco-friendly and alkali-resistant fiber. Table 2 shows the physical properties of 160 g/m^2 (GSM) woven FGM and Table 3 displays its composition.

TABLE 1. Basic chemical composition of OPC

Chemical compound (%)	OPC	Specification limit as per ASTM C150-04 [10]	
		Max	Min
SiO_2	16.00		20.00
Al_2O_3	3.90	6.0	
Fe_2O_3	2.90	6.0	
MgO	1.50	6.0	
SO_3	3.10	3.0	

Figure 1. Foaming agent dilution into the water

Figure 2. Foam generator

Figure 3. 160 GSM woven FGM

TABLE 2. Physical properties of FGM

Properties	160 GSM woven fiberglass mesh
Mesh size	4.0mm x 5.0mm
Colour	White
Coating type	Alkali resistance
Mass (g/m^2)	160±5
Ignition point	759.2ºF/ 404ºC
Melting point	320.0ºF /160ºC
Tensile strength (MPa)	1407
Elongation at break (%)	3.07%
Compliance	ASTM C1116-02

TABLE 3. Composition of FGM

Oxide components (AR-glass)	Percentage by weight (%)
SiO_2	65.4
ZrO_2	17.3
TiO_2	1.2
Al_2O_3	1.6
Fe_2O_3	1.7
CaO	7.2
MgO	0.7
Na_2O	0.6
K_2O	0.4
B_2O_3	2.2
Li_2O	0.3
F_2	0.5
Others	0.9

The mix proportioning of the LFC as shown in Table 4 was prepared at three different densities: 600kg/m^3, 1100kg/m^3 and 1600kg/m^3 with the confinement of 1-layer to 3-layers of FGM. 1L-FGM specifies1-layer, 2L-FGM for 2-layer and 3L-FGM for 3-layers of FGM. The water to cement proportion was fixed to 0.45 as suggested by Talaei et al. [31] and Kearsley and Visagie [32]. Also, the cement to FA ratio was fixed to 1:1.5.

3. EXPERIMENTAL PROGRAMME

The drying shrinkage test was conducted by using a Mitutoyo brand digital indicator (accuracy up to 0±0.001 mm) with a 298mm reference bar. The test was performed according to ASTM C157/C157M [33] where three prism-shaped '75mmx75mmx285mm' specimens with mesh confinement about the longitudinal lateral surface were installed with a pair of steel screw and cap nut. After demolding, LFC specimens were placed in the length comparator; a setup is shown in Figure 4(a) and rotated anti-clockwise to get the data. The readings were taken and recorded. Then, the steps were repeated for the next age of testing, which was on day 1, 3, 7, 14, 21, 28, and 56.

The strength tests were conducted on 324 specimens, 3 specimens in each category for each test. The different categories were: control,1L-FGM, 2L-FGM and 3L-FGM. The cast specimens were put to test at 7days, 28days and 56days. In compression strength test, cube dimension of 100mm side following BS EN 12390-3:2009 [34] was used. The flexural strength was conducted on '100mmx100mmx500mm' beam specimens following BS ISO 1920-8:2009 [35] and

TABLE 4. Mix design of LFC confined with FGM

Sample	Mix density (kg/m^3)	Cement/ Sand	Water/ Cement	Mix proportion (kg/m^3)		
				Cement	Sand	Water
Control	600	1:1.5	0.45	230.24	345.36	103.61
	1100	1:1.5	0.45	410.79	616.18	184.86
	1600	1:1.5	0.45	591.34	887.01	266.10
1L-FGM	600	1:1.5	0.45	230.24	345.36	103.61
	1100	1:1.5	0.45	410.79	616.18	184.86
	1600	1:1.5	0.45	591.34	887.01	266.10
2L-FGM	600	1:1.5	0.45	230.24	345.36	103.61
	1100	1:1.5	0.45	410.79	616.18	184.86
	1600	1:1.5	0.45	591.34	887.01	266.10
3L-FGM	600	1:1.5	0.45	230.24	345.36	103.61
	1100	1:1.5	0.45	410.79	616.18	184.86
	1600	1:1.5	0.45	591.34	887.01	266.10

(a)

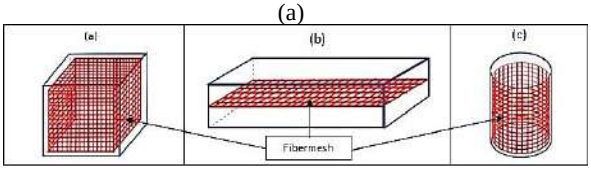

(b)

Figure 4. (a) The instrument for drying shrinkage test; (b) Placement of mesh

lastly, split tensile test was conducted on '100mm diameter and 200mm height' cylindrical specimens considering ASTM C496/C496M-04e1 [36]. The specimens in compressive strength test and split tensile test were confined along the lateral surface and in the flexural test, the mesh was spread in the longitudinal direction at the center of the height of the specimen. Figure 4(b) shows the FGM placement in specimens.

3. RESULTS AND DISCUSSION

3. 1. Drying Shrinkage Figures 5, 6, and 7 depict the graphical development of drying shrinkage results for LFC confined with 160 g/m^2 (GSM) woven FGM. The test results revealed that the control specimens have the uppermost shrinkage strain when compared to the confined LFC specimens for the three respective densities. The drying shrinkage was in indirect relation with LFC density and the layer(s) of FGM. At 600kg/m^3 density of LFC confined with 1-layer FGM, the drying shrinkage was restricted by 48%, while for LFC density of 1100kg/m^3 and 1600 kg/m^3 by 57% and 43% compared to the unconfined specimen at 56days. When the number of layer(s) of FGM was increased by 2-layers and 3-layers, the drying shrinkage behaviour also decreased by 52% to 77% than the unconfined specimens.

At the early stage of the test, all the specimens show inconsistent drying shrinkage measurement as the specimens were not fully hardened. However, on day-30 and above the graph shows only a slight increment in drying shrinkage for the confined LFC while the control specimen shows a noticeable increase. Besides, Karim et al. [37] also clarified that the rapid "increase of drying shrinkage at the early age is due to the rapid loss of moisture from the surface of the specimen while for the later ages, the rate of increase of drying shrinkage is reduced with time depending on the moisture movement of concrete".

The FGM not only prevents the water diffusion from the cement matrix, but it also avoids the loss of existing water in LFC. This also has been proved by Falliano et al. [38] stating that the "unreinforced specimens exhibit a shrinkage that decreases with increasing dry density". Namsone et al. [23, 39] also concluded that the addition of fiber can reduce the risk of shrinkage and stabilize the fresh mix.

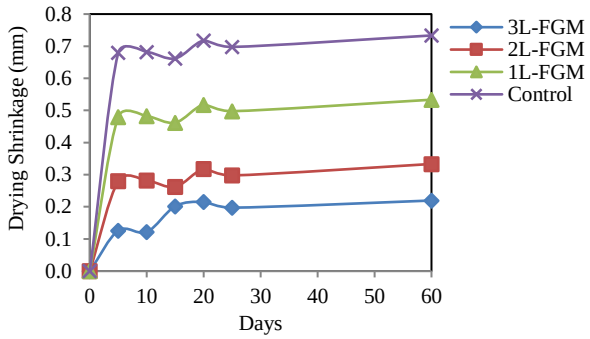

Figure 5. Drying shrinkage results of 600kg/m^3 density LFC confined with a different number of layer(s) of fibreglass mesh

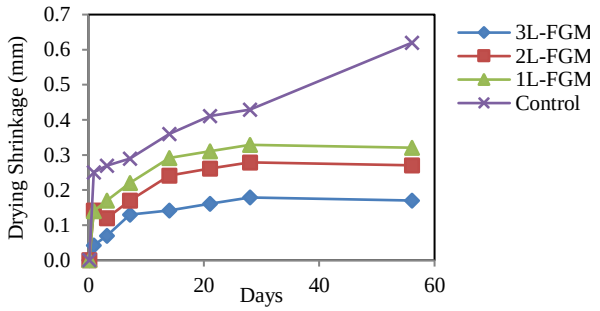

Figure 6. Drying shrinkage results of 1100kg/m^3 density LFC confined with a different number of layer(s) of fibreglass mesh

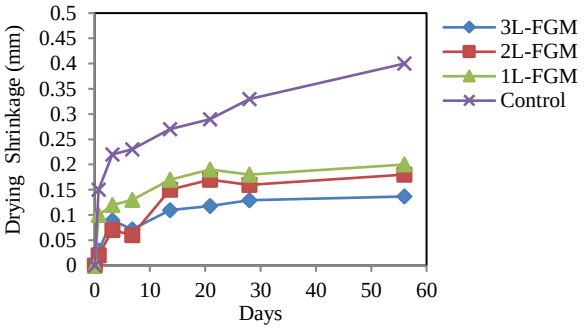

Figure 7. Drying shrinkage results of 1600kg/m^3 density LFC confined with different number of layer(s) of fiberglass mesh

3. 2. Compressive Strength The compressive strength test (CT) results of LFC specimens of density 600kg/m^3, 1100kg/m^3 and 1600kg/m^3 respectively are displayed in Figures (8,9 and 10) indicating the test outcomes at 7days, 28days and 56 days. It was found that the compressive strength in all cases increases with age and is in direct correlation with LFC density and layer(s) of confinement in the specimens as supported by the literature [40]. The 56th day compressive strength of LFC specimens confined with 1L-FGM,2L-FGM and 3L-FGM at 600kg/m^3 density was +58.94%, +137.89% and +168.42% respectively greater than unconfined/control specimens. Similarly, the 56th day compressive strength of 1100kg/m^3 and 1600kg/m^3 LFC specimens was found in a range of +38.42% to +94.65% greater than unconfined specimens.

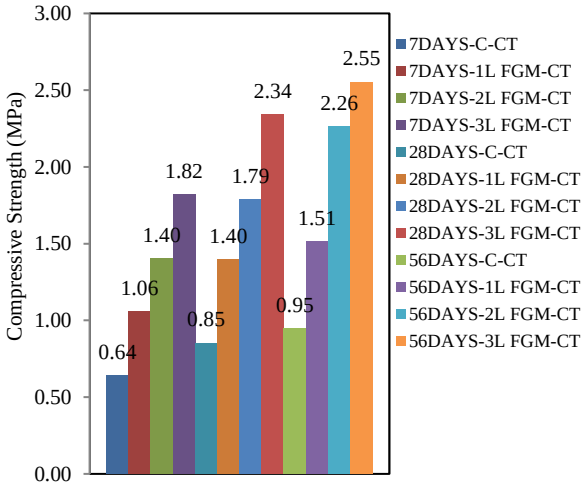

Figure 8. Comparative compressive strength of LFC of 600kg/m^3 density with different layer(s) of FGM

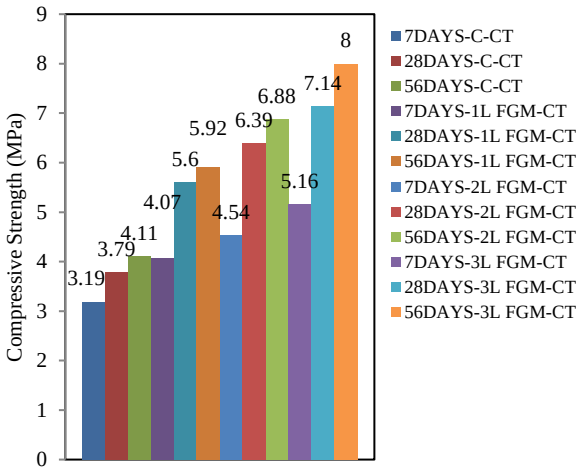

Figure 9. Comparative compressive strength of LFC of 1100kg/m^3 density with different layer(s) of FGM

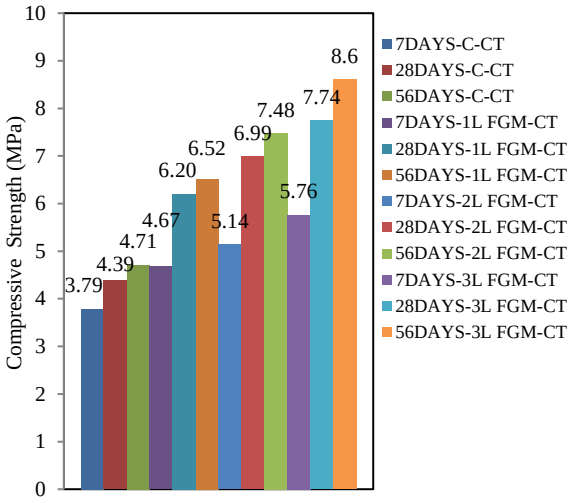

Figure 10. Comparative compressive strength of LFC of 1600kg/m^3 density with different layer(s) of FGM

3. 3. Flexural Strength Figures 11, 12 and 13 present the results of the flexural strength test (FST) at 7days, 28days and 56days. The test results showed a direct correlation between LFC density and the layer(s) of confinement of FGM. Thus flexural strength in LFC can be improved by an appreciable proportion of flexural members of a structure as supported by findings of Musa et al. [41]. The 56th day flexural strength of LFC specimens reinforced with 1L-FGM,2L-FGM and 3L-FGM at 600kg/m^3 was +103.70%, +151.85% and +385.18% respectively greater than control specimens. Similarly, for 1100kg/m^3 and 1600kg/m^3 density LFC specimens, the respective increment in flexural strength after 56days was in a range of +119.54% to +256.32% greater than control specimens.

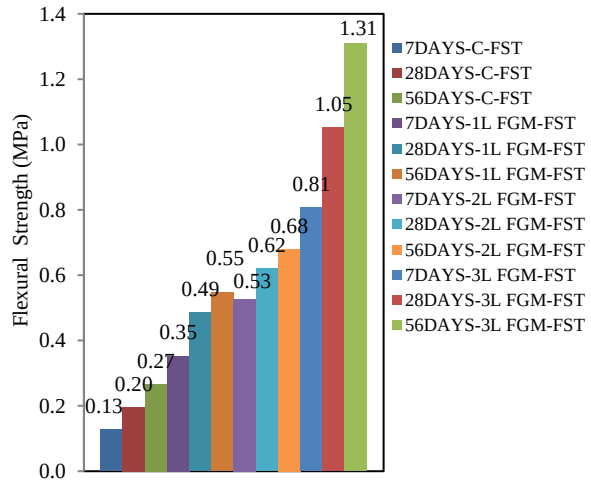

Figure 11. Comparative flexural strength of LFC of 600kg/m^3 density with different layer(s) of FGM

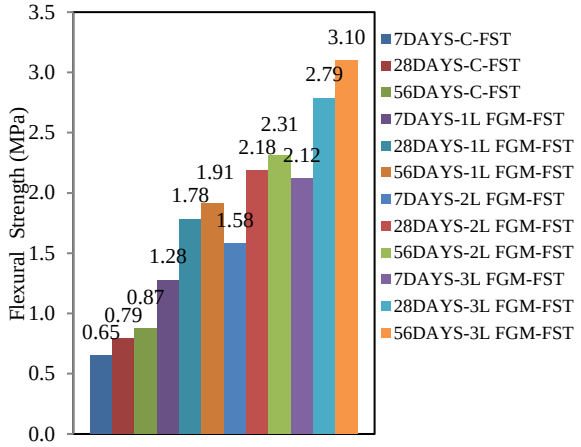

Figure 12. Comparative flexural strength of LFC of 1100kg/m^3 density with different layer(s) of FGM

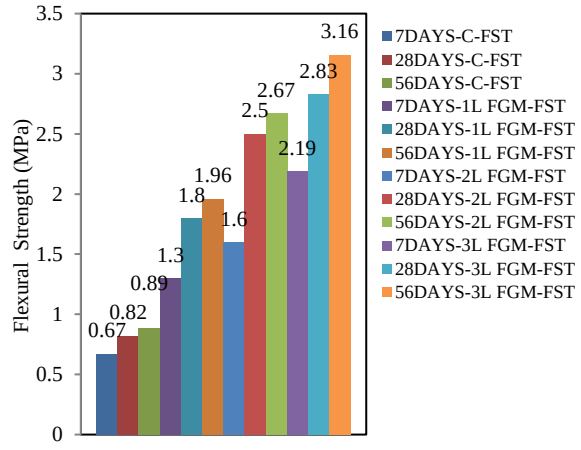

Figure 13. Comparative flexural strength of LFC of 1600kg/m^3 density with different layer(s) of FGM

3. 4. Split Tensile Strength Figures 14, 15 and 16 present the results of the split tensile strength(STS) test at 7days, 28days and 56days. The 3L-FGM performed outstandingly followed by 2L-FGM and 1L-FGM confinement in all the foam densities. The test results were approved by the finding of [42, 43]. The 56th day split tensile strength test of LFC specimens confined with 1L-FGM,2L-FGM and 3L-FGM at 600kg/m^3 was +157.14%, +242.85% and +471.42% respectively greater than unconfined specimens. Similarly, for 1100kg/m^3 and 1600kg/m^3 density LFC specimens, the corresponding increment in split tensile strength after 56days was in a range of +98.63% to +354.16% greater than unconfined specimens. It was noticed that the appearance of crack was vertical and progress was slow and linear. The failure load of the specimens created a wide crack departing the specimen longitudinally.

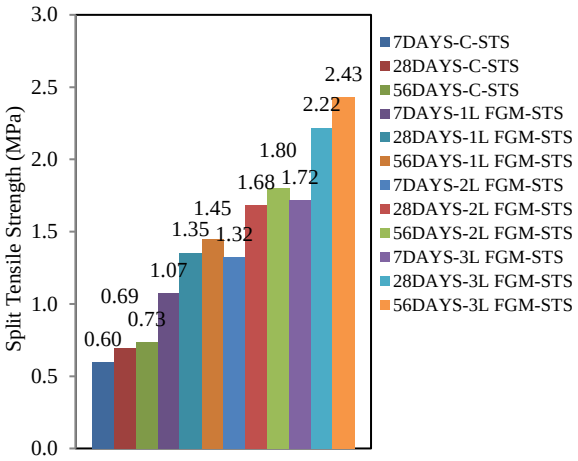

Figure 14. Comparative split tensile strength of LFC of 600kg/m^3 density with different layer(s) of FGM.

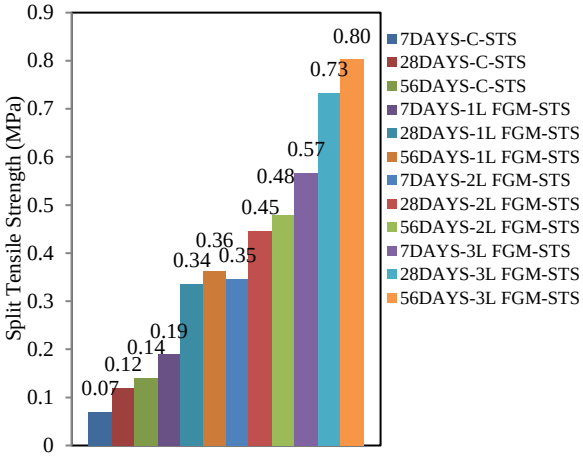

Figure 15. Comparative split tensile strength of LFC of 1100kg/m^3 density with different layer(s) of FGM

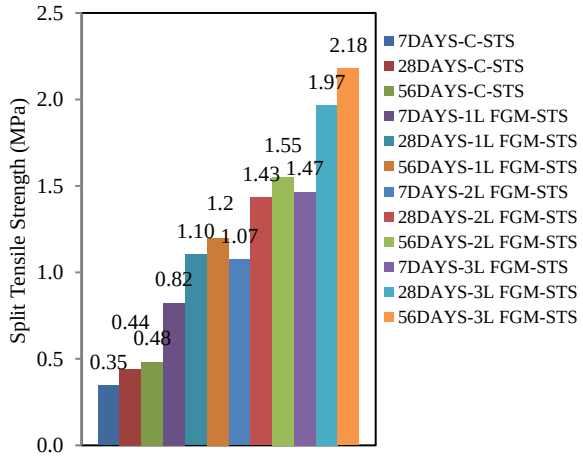

Figure 16. Comparative split tensile strength of LFC of 1600kg/m^3 density with different layer(s) of FGM

After testing the mechanical properties of specimens, the common failure pattern observed in all cases was either by debonding or splitting of fibers of the mesh. Figure 17 shows the scanning electron microscope(SEM) images indicating the typical failure of the specimens.

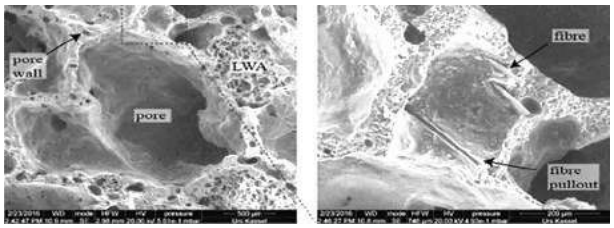

Figure 17. SEM images of failure of specimens

4. CONCLUSIONS

This paper presents the shrinkage behaviour of lightweight foamed concrete (LFC) confined with a different number of layer(s) of woven fiberglass mesh (FGM). Furthermore, to evaluate the strength aspects of LFC specimens, compressive strength, flexural strength and tensile strength tests were conducted. The variables in the study include control specimens, 1layered, 2layered,3 layered FGM specimens with foam density of 600kg/m^3, 1100kg/m^3 and 1600kg/m^3. Thus, based on the interpretation of the data obtained, few conclusions were observed as follows:

1. The higher drying shrinkage was obtained at the low density of LFC and vice versa, which was correlated to the volume of foam added. The utilization of FGM significantly reduces the drying shrinkage issue in LFC.
2. At 600kg/m^3 density of LFC confined with 1-layer FGM, the drying shrinkage was restricted by 48%, while for LFC density of 1100kg/m^3 and 1600 kg/m^3 by 57% and 43% compared to the unconfined specimen at 56th day. When the number of layer(s) of FGM was increased by 2-layers and 3-layers, the drying shrinkage behaviour also decreased by 52% to 77% than the unconfined/control specimens.
3. The early age drying shrinkage results showed inconsistency and on 30th day and after the confined LFC specimens showed a low-rate of drying shrinkage increment while unconfined LFC specimens showed a noticeable high-rate of drying shrinkage growth for the respective densities.
4. Even though many factors can influence the drying shrinkage behaviour in LFC as reported in the previous investigations. However, it can be suggested that the major influences to the drying shrinkage behaviour are: (1) the density of LFC and (2) the number of layer(s) of FGM confinement. Thus, at density 1600kg/m^3 LFC confined with 3-layers FGM conquers the good performance of drying shrinkage while the poor performance was shown by the unconfined LFC at density 600kg/m^3.
5. The testing of mechanical properties like compressive strength, flexural strength and split tensile strength of LFC showed a direct correlation of strength with age, confinement layer(s) and foam density. The type of failure of specimens in all cases was either by debonding or by splitting of fibers.

5. REFERENCES

1. Yang, K. H., Lee, K. H., Song, J. K., and Gong, M. H., "Properties and sustainability of alkali-activated slag foamed concrete", ***Journal of Cleaner Production***, Vol. 68, (2014), 226–233. doi:10.1016/j.jclepro.2013.12.068
2. Wei, S., Yiqiang, C., Yunsheng, Z., and Jones, M. R., "Characterization and simulation of microstructure and thermal properties of foamed concrete", ***Construction and Building Materials***, Vol. 47, (2013), 1278–1291. doi:10.1016/j.conbuildmat.2013.06.027
3. Kim, H. K., Jeon, J. H., and Lee, H. K., "Workability, and mechanical, acoustic and thermal properties of lightweight aggregate concrete with a high volume of entrained air", ***Construction and Building Materials***, Vol. 29, (2012), 193–200. doi:10.1016/j.conbuildmat.2011.08.067
4. Vilches, J., Ramezani, M., and Neitzert, T., "Experimental investigation of the fire resistance of ultra-lightweight foam concrete", ***International Journal of Advanced Engineering Applications***, Vol. 1, No. 4, (2012), 15–22
5. Zhang, Z., Provis, J. L., Reid, A., and Wang, H., "Mechanical, thermal insulation, thermal resistance and acoustic absorption properties of geopolymer foam concrete", ***Cement and Concrete Composites***, Vol. 62, (2015), 97–105. doi:10.1016/j.cemconcomp.2015.03.013
6. Choi, H., and Ma, S., "An optimal lightweight foamed mortar mix suitable for tunnel drainage carried out using the composite lining method", ***Tunnelling and Underground Space Technology***, Vol. 47, (2015), 93–105. doi:10.1016/j.tust.2014.12.002
7. Siram, K. K. B., and Raj, K. A., " Concrete+ Green= Foam Concrete", ***International Journal of Civil Engineering and Technology,*** Vol. 4, No. 4, (2013), 179–184
8. Moon, A. S., and Varghese, V., "Sustainable construction with foam concrete as a green building material", ***International Journal of Modern Trends in Engineering and Research***, Vol. 2, No. 2, (2014), 13–16
9. Durack, J. M., and Weiqing, L., " The properties of foamed air cured fly ash based concrete for masonry production", Proceedings of the Fifth Australasian Masonry Conference, (1998), 129–138.
10. Ramamurthy, K., Kunhanandan Nambiar, E. K., and Indu Siva Ranjani, G., "A classification of studies on properties of foam concrete", ***Cement and Concrete Composites***, Vol. 31, No. 6, (2009), 388–396. doi:10.1016/j.cemconcomp.2009.04.006
11. Jones, M. R., Mccarthy, A., and Dhir, R. K., Recycled and Secondary Aggregates in Foamed Concrete, (2005), The Waste & Resources Action Programme.
12. De Domenico, D., Faleschini, F., Pellegrino, C., and Ricciardi, G., "Structural behavior of RC beams containing EAF slag as recycled aggregate: Numerical versus experimental results", ***Construction and Building Materials***, Vol. 171, (2018), 321–337. doi:10.1016/j.conbuildmat.2018.03.128

13. Weigler, H., and Karl, S., "Structural lightweight aggregate concrete with reduced density- lightweight aggregate foamed concrete", ***International Journal of Cement Composites and Lightweight Concrete***, Vol. 2, No. 2, (1980), 101–104. doi:10.1016/0262-5075(80)90029-9
14. Favaretto, P., Hidalgo, G., Sampaio, C., Silva, R., and Lermen, R., "Characterization and Use of Construction and Demolition Waste from South of Brazil in the Production of Foamed Concrete Blocks", ***Applied Sciences***, Vol. 7, No. 10, (2017), 1090. doi:10.3390/app7101090
15. McGovern, G., "Manufacture and supply of ready-mix foamed concrete", One-Day Awareness Seminar on Foamed Concrete: Properties, Applications and Potential, (2000), 12–22.
16. Al-Haidary, M. H. M. H., "Shrinkage in Lightweight Foam Concrete, Universiti Sains Malaysia", (2010).
17. Kearsley, E. P., "Just Foamed Concrete - An Overview", Specialist Techniques and Materials for Concrete Construction, (1999), 227–237 Thomas Telford Publishing. doi:10.1680/stamfcc.28258.0022
18. Roslan, A. F., Awang, H., and Mydin, M. A. O., "Effects of various additives on drying shrinkage, compressive and flexural strength of lightweight foamed concrete (LFC)", ***Advanced Materials Research***, Vol. 626, (2013), 594–604, Trans Tech Publications Ltd, 594–604. doi:10.4028/www.scientific.net/AMR.626.594
19. Fedorov, V., and Mestnikov, A., "Influence of cellulose fibers on structure and properties of fiber reinforced foam concrete", MATEC Web of Conferences, Vol. 143, (2018), 02008. doi:10.1051/matecconf/201814302008
20. Rai, A., and Kumar, M., "Experimental study on compressive and split tensile strength of foamed concrete using stone dust", ***International Research Journal of Engineering and Technology***, Vol. 4, No. 5, (2017), 1377–1382
21. Nambiar, E. K. K., and Ramamurthy, K., "Shrinkage Behavior of Foam Concrete", ***Journal of Materials in Civil Engineering***, Vol. 21, No. 11, (2009), 631–636. doi:10.1061/(asce)0899-1561(2009)21:11(631)
22. Amran, Y. H. M., Farzadnia, N., and Ali, A. A. A., (, December 30)"Properties and applications of foamed concrete; A review", ***Construction and Building Materials***, Vol. 101, (2015), 990–1005. doi:10.1016/j.conbuildmat.2015.10.112
23. Namsone, E., Korjakins, A., Sahmenko, G., and Sinka, M., "The environmental impacts of foamed concrete production and exploitation", ***IOP Conference Series: Materials Science and Engineering***, Vol. 251, No. 1, (2017), 012029. doi:10.1088/1757-899X/251/1/012029
24. Zamzani, N., "Characterization Of Durability And Mechanical Properties Of 'Cocos Nucifera Linn'Fibre (Cnf) Reinforced Foamcrete And Its Performance At Elevated Temperatures, Doctoral dissertation, Universiti Sains Malaysia", (2019).
25. Akil, H. M., Omar, M. F., Mazuki, A. A. M., Safiee, S., Ishak, Z. A. M., and Abu Bakar, A., (, September 1)"Kenaf fiber reinforced composites: A review", ***Materials and Design***, Vol. 32, Nos. 8–9, (2011), 4107–4121. doi:10.1016/j.matdes.2011.04.008
26. Bing, C., Zhen, W., and Ning, L., "Experimental Research on Properties of High-Strength Foamed Concrete", ***Journal of Materials in Civil Engineering***, Vol. 24, No. 1, (2012), 113–118. doi:10.1061/(asce)mt.1943-5533.0000353
27. Panesar, D. K., "Cellular concrete properties and the effect of synthetic and protein foaming agents", ***Construction and Building Materials***, Vol. 44, (2013), 575–584. doi:10.1016/j.conbuildmat.2013.03.024
28. ASTM C150-04. Standard Specification for Portland Cement C150-04. Annual Book of ASTM Standards, 04(02), (2009), 1–8.
29. ASTM C778-06. Standard Specification for Standard Sand C778-06. Annual Book of ASTM Standards, (2006).
30. ASTM C1602-C05. Standard Specification for Mixing Water Used in Production of Hydraulic Cement Concrete C1602. Annual Book of ASTM Standards, (2006).
31. Talaei, S., Jafari, M., Tarfan, S., and Hashemlou, H., "The effect of ratio of aggregate to cement paste volume on structural lightweight concrete strength, viscosity, density and cost", ***Research Journal of Environmental and Earth Sciences***, Vol. 6, No. 9, (2014), 443–450
32. Kearsley, E. P., and Visagie, M., "Micro-properties of Foamed Concrete", In RK Dhir, NA Handerson (Eds.), Proceedings of Congress on Creating with Concrete (Conference on Specialist Technology and Materials for Concrete Construction), (1999), 173–184
33. ASTM C157/C157M. Standard Test Method for Length Change of Hardened Hydraulic-Cement Mortar and Concrete. Annual Book of ASTM Standards, C, (2005), 1–10.
34. BSI, BS EN 12390-3: 2009: Testing hardened concrete. Compressive Strength of Test Specimens, (2009).
35. The International Organization of Standardization, ISO 1920-8:2009 Testing of Concrete -Part 8: Determination of drying shrinkage of concrete for samples prepared in the field or in the laboratory, (2009).
36. ASTM C496/C496M-04e1 Standard Test Method for Splitting Tensile Strength of Cylindrical Concrete Specimens. Annual book of ASTM standards, (2008).
37. Karim, H., Khalid, H., and Sahii, S., "Behavior of Light Weight Concrete Using Polymer Materials", The 2nd International Conference of Buildings, Construction and Environmental Engineering (BCEE2-2015), (2015), 79–84, 79–84
38. Falliano, D., De Domenico, D., Ricciardi, G., and Gugliandolo, E., "Compressive and flexural strength of fiber-reinforced foamed concrete: Effect of fiber content, curing conditions and dry density", ***Construction and Building Materials***, Vol. 198, (2019), 479–493. doi:10.1016/j.conbuildmat.2018.11.197
39. Namsone, E., Šahmenko, G., and Korjakins, A., "Durability Properties of High Performance Foamed Concrete", ***Procedia Engineering***, Vol. 172, No. 172, (2017), 760–767. doi:10.1016/j.proeng.2017.02.120
40. Momoh, E. O., and Osofero, A. I., (, February 1)"Recent developments in the application of oil palm fibers in cement composites", ***Frontiers of Structural and Civil Engineering***, Vol. 14, No. 1, (2020), 94–108, Higher Education Press, 94–108. doi:10.1007/s11709-019-0576-9
41. Musa, M., Othuman Mydin, A., and Abdul Ghani, A. N., "Optimization of mechanical properties in foamcrete reinforced with raw oil palm empty fruit bunch (EFB) fiber", ***MATEC Web of Conferences***, Vol. 250, (2018), 05004. doi:10.1051/matecconf/201825005004
42. Serudin, A. M., Azree, M., Mydin, O., Naser, A., and Ghani, A., "Significance of Woven Fiberglass Mesh addition to Lightweight Foamed Concrete on its Flexural and Tensile Strengths", ***Journal of Xi'an University of Architecture & Technology***, Vol. XII, No. IV, (2020), 1566–1571
43. Falliano, D., De Domenico, D., Ricciardi, G., and Gugliandolo, E., "Improving the flexural capacity of extrudable foamed concrete with glass-fiber bi-directional grid reinforcement: An experimental study", ***Composite Structures***, Vol. 209, (2019), 45–59. doi:10.1016/j.compstruct.2018.10.092

Persian Abstract

چکیده

این کار آزمایشی در مورد مطالعه جمع‌شدگی خشک شدن و به دنبال آن آزمایش مقاومت نمونه‌های بتن سبک کف (LFC) با محصور شدن شبکه فایبرگلاس بافته شده (FGM) در سه تراکم متفاوت است. نمونه‌های LFC با نمونه‌های مکعبی و استوانه‌ای با ۱ لایه تا ۳ لایه (FGM) پیچیده شده و در نمونه پرتو، بطور مرکزی در امتداد محور طولی پخش شد. نمونه‌ها تحت شرایط ذخیره‌سازی هوا درمان شده و آزمایش انقباض خشک شدن به دنبال مشخصات ASTM C157 / C 157M بر روی سه نمونه منشوری شکل ۷۵mmx75mmx285mm انجام شد. برای تولید چگالی مطلوب LFC از ماده کف‌کننده NORAITE PA-1 استفاده شد. در مجموع ۳۲۴ نمونه برای خواص مکانیکی LFC مورد آزمایش قرار گرفتند. نمونه‌های بازیگران در ۷ روز، ۲۸ روز و ۵۶ روز مورد آزمایش قرار گرفتند. در آزمون مقاومت فشاری، ابعاد مکعب ضلع ۱۰۰ میلی متر به دنبال BS EN 12390-3: 2009 به تصویب رسید. مقاومت خمشی بر روی نمونه‌های پرتو be 100mmx100mmx500mm به دنبال BS ISO 1920-8: 2009 انجام شد. نمونه‌ها با قطر ۱۰۰ میلی‌متر و ارتفاع ۲۰۰ میلی‌متر با توجه به مشخصات ASTM C496 / C496M-04e1 از نظر مقاومت کششی تقسیم شدند. نتیجه نشان داد که حبس با ۱۶۰ گرم در مترمربع (GSM) از FGM به طور قابل توجهی جمع شدن خشک شدن نمونه‌های LFC را در مقایسه با نمونه‌های کنترل محدود می‌کند و با افزایش لایه (لایه‌ها) از لایه L به ۳ لایه و تراکم کاهش می‌یابد. از LFC. آزمایش خصوصیات مکانیکی LFC تناسب مستقیمی بین قدرت و تراکم LFC و لایه(های) حبس نشان داد. الگوی شکست مشاهده شده در همه نمونه‌ها یا با تجزیه یا تقسیم الیاف FGM بود. بنابراین، LFC با تراکم ۱۶۰۰ کیلوگرم در متر مکعب با ۳ لایه FGM محدود / تقویت‌شده عملکرد خوبی را در خواص انقباض و مقاومت خشک کردن تسخیر می‌کند در حالی که عملکرد ضعیف توسط LFC غیرقابل کنترل در تراکم ۶۰۰ کیلوگرم در متر مکعب نشان داده شد.

International Journal of Engineering

Journal Homepage: www.ije.ir

Influence of Chemical Admixtures on Geotechnical Properties of Expansive Soil

R. Suresh*, V. Murugaiyan

Department of Civil Engineering, Pondicherry Engineering College, Puducherry, India

P A P E R I N F O

Paper history:
Received 06 July 2020
Received in revised form 03 September 2020
Accepted 26 October 2020

Keywords:
Expansive Soil
Ultra-fine Slag
Calcium Chloride
Unconfined Compressive Strength

A B S T R A C T

The present study is to elucidate and efficacy of Ultra-fine slag and Calcium Chloride in improving the Engineering characteristics of expansive soil. An experimental program has evaluated the effects of Ultra-fine slag 3%, 6%, 9% and $CaCl_2$ 0.25%, 0.5%, 1.0%, Free swell index, swelling potential, swell pressure, plasticity, compaction, strength, hydraulic conductivity, Cation Exchange Capacity and microstructural XRD, SEM tests of expansive soil. Both admixtures were added independently and blended to the expansive soil. Mixing of Ultra-fine slag, $CaCl_2$ and expansive soil results have shown that plasticity index, hydraulic conductivity, swelling properties of blends decreased and dry unit weight and unconfined compressive strength is increased in combination of soil +6% of Ultra-fine slag + 1% $CaCl_2$. The unconfined compressive strength (UCS) of the samples is again found to decrease slightly beyond 6% Ultra-fine slag and 1% $CaCl_2$. It was found that the optimum quantity of material for a favorable combination of soil +6% of Ultra-fine slag + 1% $CaCl_2$ was taken for further study in view of its economy due to lower $CaCl_2$ content.

doi: *10.5829/ije.2021.34.01a.03*

NOMENCLATURE

W_L	Liquid limit	MDD	Maximum dry density
W_P	Plastic limit	UCS	Unconfined Compressive Strength
W_S	Shrinkage limit	$CaCl_2$	Calcium chloride
FSI	Free swell index	G_s	Specific gravity (g/cc)
W_A	Water absorption	ρ	Bulk Density (kg/m^3)
CEC	Cation Exchange Capacity	PI	Plasticity Index
OMC	Optimum Moisture Content	CNS	Cohesive non-swelling soil

1. INTRODUCTION

Expansive soils are known worldwide for their volume change behaviour due to moisture fluctuation because of their intrinsic mineralogical behaviour [1]. These types of soils are found mainly in the arid and semi-arid regions [2] such as Australia, Canada, China, India, South Africa, and the United States. India has an extensive track of expansive soils known as black cotton soil covers about twenty percentage of the total land area [3]. Due to its black colour which is a result of high iron and magnesium minerals acquire from basalt [4]. Expansive soils are clayey soils are the extensive specific surface area and high cation exchange capacity [5, 6]. Expansive soil contains clayey minerals such as montmorillonite which increases in volume during wetting. This volume change can exert sufficient stress on a building, sidewalk, driveways, basement floors, pipelines, and foundations to cause damages. Since the expansive soils are found worldwide, the challenges to the Civil Engineers in one felt around the globe. If not adequately treated, expansive soils may act as natural hazards resulting in damages to structures [7, 8]. The annual cost of damages to the Civil Engineering structures is estimated at 150 million in the

*Corresponding Author Institutional Email: *rangasuresh307@pec.edu* (R. Suresh)

Please cite this article as: R. Suresh, V. Murugaiyan, Influence of Chemical Admixtures on Geotechnical Properties of Expansive Soil, International Journal of Engineering, Transactions A: Basics, Vol. 34, No. 1, (2021) 19-25

United States and many billions of dollars worldwide [9]. Under the moisture ingress and digress, a building founded on expansive soil undergoes differential movements caused by alternate swell/shrink behaviour of soil causing several structural damages. Many reported data are available on the heave profile of soil at the surface, at various depths from the ground surface and on covered areas [10, 11] it is generally observed that the amplitude of soil movement decreases with depth and there is an increase in time lag with movement at depth compared with that at the surface. To date, distress problems related to this type of soils are quite immense to have ensued in the loss of billions of dollars in repairs and rehabilitation [12].

Many Researchers used the strong electrolytes such as potassium Chloride, Magnesium Chloride, Zinc Chloride, Sodium hydroxide, Ferric Chloride, and Calcium Chloride could be tried instead of lime [13]. strong electrolytes are readily soluble in water and hence could supply adequate cations for exchange reactions. Industrial by-product material such as flyash [14], GGBS [15], cement kiln dust, limestone dust [16] as additives are becoming more popular due to their relatively low cost additionally CO_2, emission can be reduced significantly by the increased use of such supplementary cementing materials currently wasted in lagoons and landfill sites. The most important feature in the stabilization of clay soils is the ability of the stabilizer to provide a sufficient amount of Calcium [17]. Stabilizers can be amended with activators like lime or cement to enhance their cementitious and pozzolanic properties.

The purpose of this study is to investigate the influence of the inclusion of Ultra-fine slag in conjunction with Calcium Chloride ($CaCl_2$) in the stabilization of expansive soils. In India, an industrial by-product Ultra-fine slag material is manufactured by Ambuja cement private limited. The majority of Ultra-fine slag material is utilized in the high-performance concrete structures either as a cement replacement or as an additive to improve concrete properties in both fresh and hardened states and soil stabilization purpose [18], while $CaCl_2$ is mainly used to reduce the swelling and increase the shear strength of expansive soil for soil stabilization. These Ultra-fine slag and $CaCl_2$ have also great potential to be used as stabilizing agents. The main reason for their underutilization is the lack of pozzolanic reactivity [19].

Ultra-fine slag is ultrafine ground granulated blast furnace slag, performs a superior to all other mineral admixtures used in India [20–22]. On the other hand, $CaCl_2$ is the hygroscopic material and hence is pre-eminently suited for stabilization of expansive soils, because it absorbs water from the atmosphere and prevents shrinkage cracks occurring in expansive soils during summer season. The combination of the two materials can be more beneficial when used as a stabilizing agent than using the individual. However, no studies on the joint activation of Ultra-fine slag and $CaCl_2$ as stabilizing agents for expansive soils have been published to date.

2. MATERIALS

2. 1. Expansive Soil The expansive clay soil is collected from Kirumambakkam, is located in Puducherry, India. The soil is collected in a dry condition at a depth of 1 meter below the ground level and preserved in the laboratory. Identified the index and engineering properties of expansive soils as shown in Table 1.

2. 2. Alccofine-1203 Alccofine-1203 is ultrafine slag, manufactured by Ambuja cement private limited in India. Ultra-fine slag and Ultra-fine slag-1101 are two types with low calcium silicate and high calcium silicate respectively. Ultra-fine slag has the lime binder 34% and average particle size of 4 microns (Range 0-17microns). Chemical composition and physical properties are tested by Ultra-fine slag micro materials, Pissurlem, Goa. Ultra-fine slag properties are given in Table 2.

2. 3. Calcium Chloride The chemical formula of Calcium Chloride is $CaCl_2$. It is a hygroscopic material and hence, it is pre-eminently suited for stabilization of

TABLE 1. Physical properties of soil

Properties of soil	Results
Sand (%)	12
Silt (%)	30
Clay (%)	58
Specific gravity	2.60
Liquid limit (W_L)	59%
Plastic limit (W_P)	34.5%
Shrinkage limit (W_S)	12.5%
Free swell index (FSI)	25%
Water absorption (W_A)	53.69%
Cation exchange capacity (CEC) meq/100g	55
Unified soil classification (USCS)	CH
OMC (%)	18.19
MDD (kN/m^3)	15.73
UCS (kPa)	157
Swell potential (%)	5.29
Swell pressure (kPa)	150
Hydraulic conductivity cm/sec	$1.58x10^{-6}$

TABLE 2. Physical and chemical properties of Ultra-fine slag

Properties	Results
Physical properties	
Particle size Distribution(mm)	
D10	1.5
D50	4.3
D90	9.0
Specific gravity (g/cc)	2.88
Bulk density (kg/m^3)	680
Chemical properties	
SiO_2	35.6%
Al_2O_3	21.4%
Fe_2O_3	1.3%
CaO	33.6%
SO_3	0.12%
MgO	7.98%

black cotton soil (expansive soil), because it absorbs water from the atmosphere and releases heat when it is dissolved in water. Calcium Chloride is obtained from Sri Rajendra Scientific and Surgicals Pvt Ltd. Pondicherry, India.

3. RESULTS AND DISCUSSION

3. 1. Index and Compaction Tests The influence of Ultra-fine slag and $CaCl_2$ on Atterberg limits (liquid limit, plastic limit, and shrinkage limit) of expansive soil is shown in Table 3. Results show that liquid limit decreases and plastic limit increases; hence, the difference between liquid limit and plastic limit is the plasticity index. The plasticity index is reduced by about 67% when the soil is blended with 6% Ultra-fine slag + $CaCl_2$ 1%.

The compaction characteristics of untreated and treated soils are shown in Table 3. The results of compaction show that the maximum dry density is increased from 15.73 kN/m^3 to 16.92 kN/m^3 and optimum moisture content is reduced from 18.19% to 16.5% with an increase of 6% Ultra-fine slag and 1% $CaCl_2$ binder; that is, for sample which shows maximum strength.

3.2. Unconfined Compression Strength Unconfined compressive strength (UCS) tests were conducted with Ultra-fine slag and $CaCl_2$ was added. Independently and blended to the expansive soil samples. UCS tests were performed on both intrinsic soil and chemically treated soil. The UCS value for intrinsic soil is 157 kPa. The percentage of Ultra-fine slag (3, 6 and 9%) and $CaCl_2$ (0.25, 0.5 and 1.0%) were added by dry weight of the soil. The UCS values are shown in Table. 3. The optimum increase was noticed at 6% Ultra-fine slag and 1% $CaCl_2$. The UCS strength was an increase from 157 kPa to 418 kPa. Beyond 6% of Ultra-fine slag with 1%, $CaCl_2$ resulted in a slight decrease in UCS values.

3. 3. Swell Behavior The swell behavior of soil and mixed with different percentages of Ultra-fine slag and $CaCl_2$ is presented in Table. 3. The maximum swell potential of intrinsic soil is 5.29% and swell pressure is 150 kPa. The swell of intrinsic soil is mainly due to the presence of montmorillonite mineral. With the addition of various percentages of Ultra-fine slag and $CaCl_2$, the swell of the soil decreases gradually and completely brings to halt beyond the addition of Ultra-fine slag 6% with 1% of $CaCl_2$. Beyond Ultra-fine slag 6% with 1% of $CaCl_2$, complete elimination of swell is due to the availability of adequate calcium, not only for cation exchange reaction but also for the formation of pozzolanic reaction compounds. Pozzolanic reaction binds the flocculated soil particles, and thereby, the formation of strong flocculated fabric, leading to the reduction in a swell of soil.

3. 4. Mineralogical and Microstructural Analysis

3. 4. 1. SEM Analysis Changes in surface matrix and chemical composition due to reaction between minerals of soil-Ultra-fine slag-$CaCl_2$ were performed with SEM and EDAX techniques, respectively. EVO 18 Carl Zeiss is used for the SEM and EDAX studies. The analysis for clay soil, Ultra-fine slag and clay soil + Ultra-fine slag 6% + $CaCl_2$ 1% are shown in Figure 1 (a, b, c).

These studies were carried out in order to observe the individually and changes in the soil are blended with an admixture of 0 days. Eminent peaks Fe, Au, Al are observed in 1(a) and Fe, Au, Al, Si are observed in clay soil. In Ultra-fine slag (1b) Ca, Mg, Si, Al eminent peaks are observed. In combination of soil blended with admixture (1c) is observed eminent peaks are Fe, Au, Si, O, Al. The test was performed mainly for the identification of the various cementations compounds on the soil stabilized with 6% Ultra-fine slag + $CaCl_2$ 1% binder; that is, for sample which shows maximum strength. The formation of aggregation or flocs is mainly responsible for the reduction of the swelling in expansive soil [8]. Cement hydration materials such as C-S-H gel is mixed with calcium hydroxide, aggregation can be observed in the SEM-micrograph. The hydration products are usually intermixed with pore spaces that are not empty but occupied by hardened epoxy resin [22].

TABLE 3. Effects of soil-admixtures blended on Index and Engineering properties

$CaCl_2$ (%)	Ultra-fine slag (%)	Liquid limit (%)	Plastic limit (%)	Shrinkage limit (%)	Plasticity index (%)	MDD (%)	OMC (%)	UCS (kPa) 0 days	Swell characteristics		W_A (%)
									Swell potential (%)	Swell pressure (kPa)	
0	0	59.0	34.5	12.5	24.5	15.73	18.19	157	5.29	150	53.69
	3	55.0	35.0	13.3	20.0	15.85	17.75	216	3.22	120	50.05
	6	49.0	35.5	16.0	13.5	15.95	17.45	245	1.23	095	44.59
	9	47.0	36.0	22.5	11.0	16.15	17.24	241	0.75	075	42.77
0.25	0	54.0	37.0	14.0	17.0	15.85	18.05	245	2.17	115	49.14
	3	51.0	38.5	15.0	12.5	16.05	17.76	300	1.02	098	46.41
	6	49.0	39.0	19.0	10.0	16.30	17.25	327	0.59	065	44.59
	9	48.0	39.0	24.5	9.0	16.45	17.10	324	0.46	096	43.68
0.5	0	52.5	38.0	14.5	14.5	15.90	17.65	306	1.47	045	47.77
	3	50.4	38.5	16.0	11.9	16.34	17.34	359	0.90	038	45.86
	6	48.0	40.0	18.8	8.0	16.70	16.80	384	0.34	022	43.68
	9	49.0	41.0	24.0	8.0	16.90	16.40	376	0.11	018	44.59
1.0	0	51.0	39.0	18.0	12.0	15.80	17.40	352	0.78	032	45.68
	3	49.0	41.0	21.0	8.0	16.30	16.80	401	0.17	012	44.59
	6	47.0	39.0	22.5	8.0	16.92	16.50	418	0	0	42.77
	9	49.0	42.0	22.8	7.0	16.95	16.24	406	0	0	44.59

Note: W_L = Liquid limit; W_P = Plastic limit; W_S = Shrinkage limit; PI = Plasticity index; MDD = Maximum dry density; OMC = Optimum moisture content; UCS = Unconfined compressive strength; W_A = Absorption water content.

TABLE 4. Properties Obtained for Optimum Soil-Ultra-fine slag-$CaCl_2$ Mix

Properties	Soil	93% soil+1% $CaCl_2$+6% Ultra-fine slag
Sand (%)	12	10.30
Silt (%)	30	35.20
Clay (%)	58	54.50
Specific gravity	2.60	2.72
Liquid limit (W_L)	59%	47%
Plastic limit (W_P)	34.5%	39%
Shrinkage limit (W_S)	12.5%	22.50%
Plasticity Index (PI)	25%	8%
Water absorption (W_A)	53.69%	42.77%
Cation exchange capacity (CEC) meq/100g	55	18
Unified soil classification	CH	CI
OMC (%)	18.19	16.50
MDD (kN/m^3)	15.73	16.92
UCC (kPa)	157	418
Free swell index (FSI)	25%	0
Swell potential (%)	5.29	0
Swell pressure (kPa)	150	0
Hydraulic conductivity cm/sec	$1.58x10^{-6}$	$4.3x10^{-5}$

3. 4. 2. XRD The results of experimental and XRD analysis that most of the Calcium is consumed to alter the physical behavior of soil by short-term process. However, peaks related to clay soil are [d = 3.38Å, 2.29Å, and 2.96Å]. The X-ray diffraction peaks identify for clay soil, Ultra-fine slag and clay soil + Ultra-fine slag 6% + $CaCl_2$ 1%. The most important peak traced was related to CH, which was identified at 2Θ =26° to 36° [20].

As can be seen from Figure 2 (a, b, c); the addition of Ultra-fine slag and $CaCl_2$ in the soil causes CH related peaks to appear at the aforementioned 2Θ. It has been carried out to confirm the formation of new minerals, which can play a significant role in strength improvement behavior Calcium stabilized for soil admixture. The intensity has increased for Calcium Chloride and Ultra-fine slag materials treated when compared with the clay soil, which is all-evident from X-ray data. The hydration products as a result of pozzolanic reactions primarily consist of C-S-H gel and calcium hydroxide (CH) [21]. The most important peak traced was related to CH which were identified at 2Θ=26° to 36° [22].

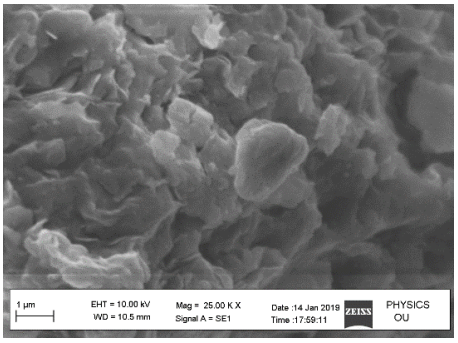

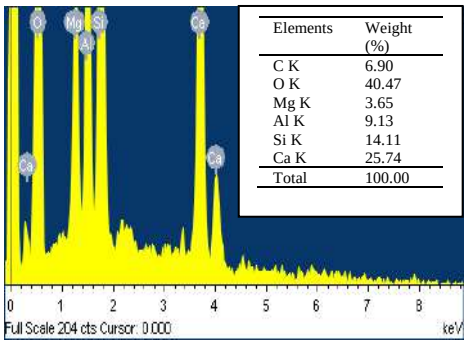

Elements	Weight (%)
C K	6.90
O K	40.47
Mg K	3.65
Al K	9.13
Si K	14.11
Ca K	25.74
Total	100.00

(a) SEM with EDAX analysis for soil

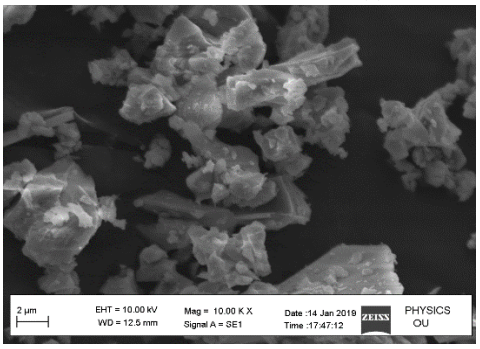

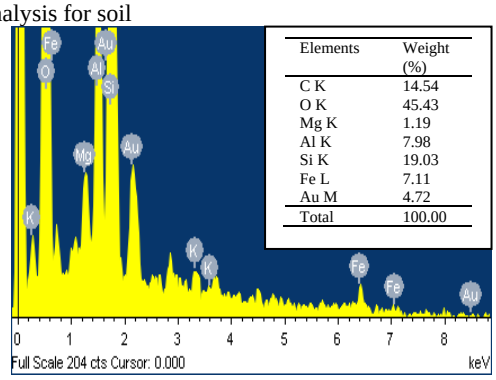

Elements	Weight (%)
C K	14.54
O K	45.43
Mg K	1.19
Al K	7.98
Si K	19.03
Fe L	7.11
Au M	4.72
Total	100.00

(b) SEM with EDAX analysis for Ultra-fine slag

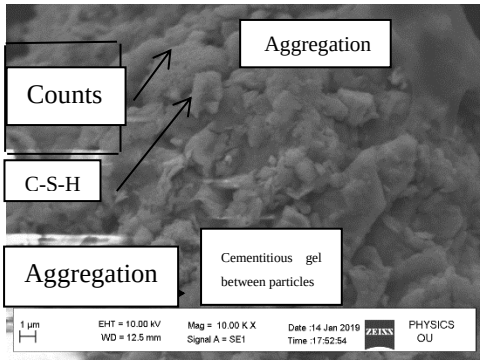

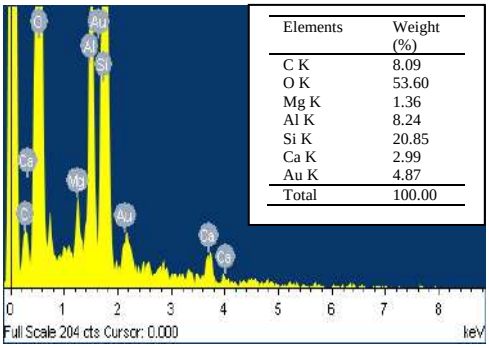

Elements	Weight (%)
C K	8.09
O K	53.60
Mg K	1.36
Al K	8.24
Si K	20.85
Ca K	2.99
Au K	4.87
Total	100.00

(c) SEM with EDAX analysis for soil + Ultra-fine slag1203+ CaCl2 0 day

Figure 1. (a) SEM with EDAX analysis for soil; (b) SEM with EDAX analysis for ultra-fine slag 1203; (c) SEM with EDAX analysis for soil + Ultra-fine slag1203+$CaCl_2$ 0 days

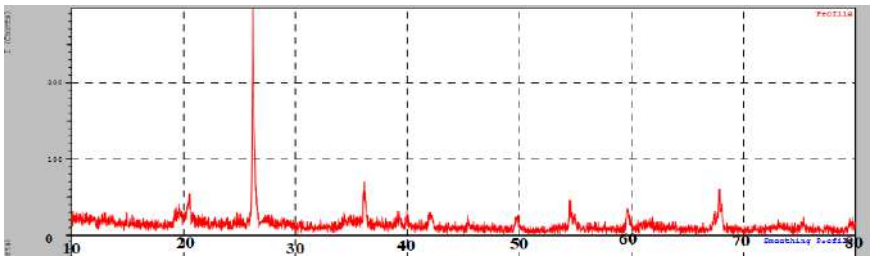

(a) Soil

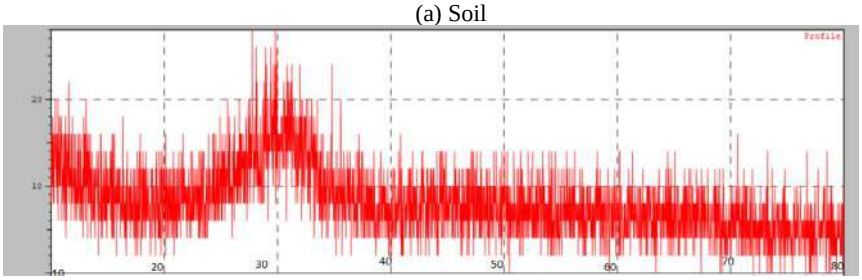

(b) Ultra-fine slag

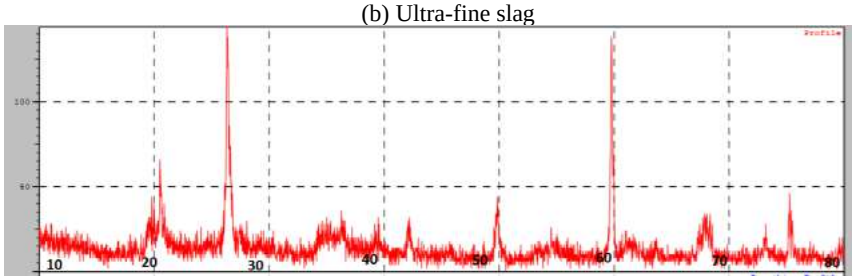

(c) soil+6%Ultra-fine slag+1%$CaCl_2$

Figure 2. XRD analysis for(a)soil;(b) Ultra-fine slag;(c)soil+6%Ultra-fine slag+1%$CaCl_2$

4. CONCLUSION

In this study, based on the laboratory investigation, a series of tests were performed to study the effect of $CaCl_2$ and Ultra-fine slag on the swelling properties and strength behavior of soils. Based on the results presented in this paper, the following conclusions are made:

1. The optimum moisture content (OMC) was found to decrease 18.19% to 16.5% while the maximum dry density (MDD) increases from 15.73kN/m^3 to 16.92kN/m^3 with binding content.
2. The unconfined compressive strength (UCS) tests were conducted with Ultra-fine slag and $CaCl_2$ were added independently and blended to the expansive soil samples. The UCS strength was an increase from 157 kPa to 418 kPa. Beyond 6% of Ultra-fine slag with 1% $CaCl_2$ resulted in a slight decreased in UCS values.
3. The swell behaviour of soil; the swell potential is reduced from 5.29% to zero and swell pressure is reduced from 150kPa to completely bring to halt beyond addition of Ultra-fine slag 6% with 1% of $CaCl_2$.
4. SEM and XRD studies confirm the formation of reaction products such as Ca, Mg and Si to contribute to strength significantly. In XRD the addition of Ultra-fine slag and $CaCl_2$ in the soil causes CH related peaks to appear at the aforementioned 2Ɵ.

In the view of severe scarcity for suitable cohesive non-swelling soils (CNS) at several project sites, an alternative cushion material is proposed to be prepared at the site using the intrinsic soil (expansive soil) by admixing with it 6% Ultra-fine slag and 1% $CaCl_2$ by dry weight of the soil. Based on the favorable results obtained, it can be concluded that the expansive soil with Ultra-fine slag and $CaCl_2$ can be considered as an effective cohesive non-swelling soil (CNS) for pavements, sidewalks, and floorings.

5. Funding

This research is financially supported by Council of Scientific and Industrial Research (CSIR), New Delhi, India. (Acknowledgement no. 141268/2K18/1; File no. 08/518(0001)/2019 EMR-1.

6. REFERENCES

1. Murty, V. R., and Krishna, P. H., "Stabilisation of expansive clay bed using calcium chloride solution", ***Proceedings of the Institution of Civil Engineers - Ground Improvement***, Vol. 10, No. 1, (2006), 39–46. doi:10.1680/grim.2006.10.1.39

2. Mishra, A. K., Dhawan, S., and Rao, S. M., "Analysis of swelling and shrinkage behavior of compacted clays", ***Geotechnical and Geological Engineering***, Vol. 26, No. 3, (2008), 289–298. doi:10.1007/s10706-007-9165-0
3. Murty, V. R., and Praveen, G. V., "Use of Chemically Stabilized Soil as Cushion Material below Light Weight Structures Founded on Expansive Soils", ***Journal of Materials in Civil Engineering***, Vol. 20, No. 5, (2008), 392–400. doi:10.1061/(asce)0899-1561(2008)20:5(392)
4. Lal, R., "Encyclopedia of Soil Science." Volume 1, CRC Press, Boca Raton. (2007).
5. Nalbantoğlu, Z., "Effectiveness of class C fly ash as an expansive soil stabilizer", ***Construction and Building Materials***, Vol. 18, No. 6, (2004), 377–381. doi:10.1016/j.conbuildmat.2004.03.011
6. Nalbantoglu, Z., and Gucbilmez, E., "Improvement of calcareous expansive soils in semi-arid environments", ***Journal of Arid Environments***, Vol. 47, No. 4, (2001), 453–463. doi:10.1006/jare.2000.0726
7. Zhang, G., Robertson, P. K., and Brachman, R. W. I., "Estimating liquefaction-induced ground settlements from CPT for level ground", ***Canadian Geotechnical Journal***, Vol. 39, No. 5, (2002), 1168–1180. doi:10.1139/t02-047
8. Al-Rawas, A. A., Taha, R., Nelson, J. D., Al-Shab, T. B., and Al-Siyabi, H., "A comparative evaluation of various additives used in the stabilization of expansive soils", ***Geotechnical Testing Journal***, Vol. 25, No. 2, (2002), 199–209. doi:10.1520/gtj11363j
9. Puppala, A. J., Intharasombat, N., and Vempati, R. K., "Experimental Studies on Ettringite-Induced Heaving in Soils", ***Journal of Geotechnical and Geoenvironmental Engineering***, Vol. 131, No. 3, (2005), 325–337. doi:10.1061/(asce)1090-0241(2005)131:3(325)
10. Nelson, J.D., Miller. D.J., "Expansive soils: Problems and practices in Foundation and Pavemet Engineering". John Wiley & Sons Inc. (1992).
11. Rao, S. M., and Subba Rao, K. S., "Ground heave from caustic soda solution spillage-a case study", ***Soils and Foundations***, Vol. 34, No. 2, (1994), 13–18. doi:10.3208/sandf1972.34.2_13
12. Çokça, E., "Use of Class C Fly Ashes for the Stabilizationof an Expansive Soil", ***Journal of Geotechnical and Geoenvironmental Engineering***, Vol. 127, No. 7, (2001), 568–573. doi:10.1061/(asce)1090-0241(2001)127:7(568)
13. Ferguson, G., "Use of Self-Cementing Fly Ashes as a Soil Stabilization Agent Fly Ash for Soil Improvement." ASCE Geotechnical Special Publication, Vol 36. (1993), Doi: 10.14256/JCE.1281.2014
14. Phani Kumar, B. R., and Sharma, R. S., "Effect of Fly Ash on Engineering Properties of Expansive Soils", ***Journal of Geotechnical and Geoenvironmental Engineering***, Vol. 130, No. 7, (2004), 764–767. doi:10.1061/(asce)1090-0241(2004)130:7(764)
15. Cokca, E., Yazici, V., and Ozaydin, V., "Stabilization of expansive clays using granulated blast furnace slag (GBFS) and GBFS-Cement", ***Geotechnical and Geological Engineering***, Vol. 27, No. 4, (2009), 489–499. doi:10.1007/s10706-008-9250-z
16. Higging, D., "Soil Stabilization with Ground Granulated Blast furnace slag". UK Cementations slag Markets Association (CSMA). (2005).
17. Miller, G. A., and Azad, S., "Influence of soil type on stabilization with cement kiln dust", ***Construction and Building Materials***, Vol. 14, No. 2, (2000), 89–97. doi:10.1016/S0950-0618(00)00007-6
18. Brooks, R., Udoeyo, F. F., and Takkalapelli, K. V., "Geotechnical Properties of Problem Soils Stabilized with Fly Ash and Limestone Dust in Philadelphia", ***Journal of Materials in Civil Engineering***, Vol. 23, No. 5, (2011), 711–716. doi:10.1061/(asce)mt.1943-5533.0000214
19. Nadiger, A., and Madhavan, M. K., "Influence of Mineral Admixtures and Fibers on Workability and Mechanical Properties of Reactive Powder Concrete", ***Journal of Materials in Civil Engineering***, Vol. 31, No. 2, (2019), 04018394. doi:10.1061/(asce)mt.1943-5533.0002596
20. Reddy, P. N., and Naqash, J. A., "Experimental study on TGA, XRD and SEM Analysis of Concrete with Ultra-fine Slag", ***International Journal of Engineering, Transactions B: Applications***, Vol. 32, No. 5, (2019), 679–684. doi:10.5829/ije.2019.32.05b.09
21. Reddy, P. N., and Naqash, J. A., "Effect of Alccofine on Strength and Durability Index Properties of Green Concrete", ***International Journal of Engineering, Transactions C: Aspects***, Vol. 32, No. 6, (2019), 813–819. doi:10.5829/ije.2019.32.06c.03
22. Diamond, S., "The microstructure of cement paste and concrete - A visual primer", ***Cement and Concrete Composites***, Vol. 26, No. 8, (2004), 919–933. doi:10.1016/j.cemconcomp.2004.02.028

Persian Abstract

چکیده

مطالعه حاضر برای روشن‌سازی و کارایی سربارهٔ فوق‌العاده ریز و کلرید کلسیم در بهبود خصوصیات مهندسی خاک گسترده است. یک برنامه آزمایشی اثرات سربارهٔ فوق‌العاده ریز ۳ ٪، ۶ ٪، ۹ ٪ و $CaCl_2$ ۰/۲۵ ٪، ۰/۵ ٪، ۱/۰ ٪ شاخص تورم آزاد، پتانسیل تورم، فشار تورم، خاصیت انعطاف‌پذیری، تراکم، مقاومت، هدایت هیدرولیکی، ظرفیت تبادل کاتیونی و آزمایشات XRD، SEM ریزساختاری خاک گسترده و همچنین از یک ابزار آماری برای پیش‌بینی مقادیر آزمایشی مقاومت فشاری غیر محدود خاک استفاده شد. هر دو مواد افزودنی به طور مستقل اضافه شده و به خاک وسیع مخلوط می‌شوند. اختلاط سربارهٔ فوق‌العاده ریز، $CaCl_2$ و نتایج گسترده خاک نشان داد که شاخص پلاستیکی، هدایت هیدرولیکی، خصوصیات تورم مخلوط کاهش یافته و وزن واحد خشک و مقاومت فشاری غیر محدود در ترکیب خاک ۶٪+ سربارهٔ فوق العاده ریز ۱٪+ $CaCl_2$ افزایش می یابد. مقاومت فشاری نامشخص (UCS) نمونه‌ها مجدداً کمی فراتر از ۶٪ سربارهٔ فوق العاده ریز و ۱٪ $CaCl_2$ کاهش می‌یابد. مشخص شد که مقدار مطلوب مواد برای ترکیبی مطلوب از خاک ۶٪+ سربارهٔ فوق العاده ریز ۱٪+ $CaCl_2$ برای مطالعه بیشتر با توجه به اقتصاد آن به دلیل محتوای کم $CaCl_2$ مورد بررسی قرار گرفت.

International Journal of Engineering

Journal Homepage: www.ije.ir

Durability and Mechanical Properties of Self-compacting Concretes with Combined Use of Aluminium Oxide Nanoparticles and Glass Fiber

H. Heidarzad Moghaddam[a], M. A. Lotfollahi-Yaghin*[b], A. Maleki[a]

[a] *Department of Civil Engineering, Maragheh Branch, Islamic Azad University, Maragheh, Iran*
[b] *Faculty of Civil Engineering, University of Tabriz, Tabriz, Iran*

PAPER INFO

Paper history:
Received 07 September 2020
Received in revised form 25 September 2020
Accepted 26 October 2020

Keywords:
Aluminium Oxide Nanoparticles
Durability Properties
Glass Fiber
Mechanical Properties
Rheological Properties
Self-compacting Concrete

ABSTRACT

The presence of fibers in concrete specimens has an effective role on how the specimens were failed. In this study, the effects of aluminium oxide nanoparticles on the workability, mechanical and, durability properties of SCCs containing glass fibers were investigated. Glass fibers contents of 0, 0.5, 1, and 1.5 % by volume of concrete and aluminium oxide nanoparticles contents of 0, 0.5, 1, 1.5, 2, and 3 % by weight of cement were used. The properties of fresh concrete were evaluated according to EFNARC consideartions. The mechanical properties were evaluated by compressive strength, splitting tensile strength, and ultrasonic pulse velocity tests. The durability of the specimens was also measured using water absorption tests, water penetration depth and, electrical resistivity. Combined use of 2% aluminium oxide nanoparticles and 1% glass fiber has increased the compressive and tensile strengths of SCCs by 59% and 119.2%, respectively. Aluminium nanoparticles have a very high specific surface area and their reactivity causes them to react rapidly with calcium hydroxide to produce silicate-hydrate gels. Therefore, calcium hydroxide crystals are reduced and the cavities in the cement gel are filled and the compressive strength is increased. The use of aluminium oxide nanoparticles along with glass fibers reduces the water absorption rate compared to the sample without these materials. This is one of the effective properties of aluminium oxide nanoparticles, which increases the resistance to adverse environmental factors by reducing water absorption.

***doi**: 10.5829/ije.2021.34.01a.04*

1. INTRODUCTION

Today, the use of nanotechnology in the construction of concrete has good practical potential and has different features [1-4]. Brittleness of concrete limits its use for parts that are completely or locally under tension. In practice, this fundamental defect of concrete is resolved by reinforcing it by installing steel rebars in the direction of tensile forces. In order to create isotropic conditions and reduce the brittleness of concrete, glass fibers can be used in concrete [5].

On the other hand, the use of nanoparticles in concrete has attracted the attention of many researchers in recent years. Silva et al. (2016) examined the effect of silica and aluminium oxide nanoparticle additives with steel fibers on the behaviour of RC beams. They showed that nanoparticles can improve the performance of RC beams [6]. Joshaghani et al. (2020) showed that titanium, aluminium, and iron oxide nanoparticles can improve mechanical and durability and reduce workability [7]. Mohammed et al. (2020) investigated calcium and aluminium oxide on the physical attributes of cementitious mortar. For this purpose, different percentages of calcined eggshell powder were used along with 1% of aluminium oxide nanoparticles. The experiments showed that the combined use of aluminium oxide nanoparticles and eggshell powder reduced the compressive strength and density, but increased the percentage of water absorption [8]. Ansari rad et al. (2020) studied the properties of basalt fiber reinforced concrete containing silica nanoparticles and aluminium nanoparticles. Basalt fibers reduced the flowability of

*Corresponding Author Email: *Ma_lotfollahi_yaghin@yahoo.com* (M. A. Lotfollahi-Yaghin)

Please cite this article as: H. Heidarzad Moghaddam, A. Maleki, M. A. Lotfollahi-Yaghin, Durability and Mechanical Properties of Self-compacting Concretes with Combined Use of Aluminium Oxide Nanoparticles and Glass Fiber, International Journal of Engineering, Transactions A: Basics, Vol. 34, No. 1, (2021) 26-38

self-compacting specimens and have little effect on improving compressive strength [9]. Zin al-Abedini et al. (2020) showed that the concrete made of nanolime showed higher resistance than nano-silica and this type of concrete can be considered in the group of high performance and high strength concrete [10].

There have also been several studies on the use of fibers in concrete. Ganesh (2016) examined self-compacting concrete containing glass fibers. The length of fibers added to the mixture was 1.2, 1.8, and 2.4 mm, respectively, and the percentage of fibers were 0%, 0.25, 0.5%, 0.75%, and 1%. The highest compressive strength was obtained in a specimen containing 1% fiber [11]. Soratur et al. (2018) stated that glass fiber and foundry sand can lead to a significant improvement in mechanical characteristics of concrete [12]. Alex and Arunachalam (2018) conducted an experimental study of steel fibers and glass fibers on the attributes of lightweight concrete. The use of glass fibers and steel fibers improved tensile and flexural strength of specimens [13]. Vasu et al. (2019) used 0.1, 0.2 and 0.3% of glass fibers. They indicated that glass fibers could improve the mechanical characteristics of concrete [14]. Hemavathi et al. (2020) examined the properties of concrete reinforced with glass fibers containing silica fume. For this purpose, different percentages of "manufactured sand" (30, 40, 70, and 100%) were replaced with natural sand. It was shown that glass fiber and silica fume in concrete containing 30% sand and 70% natural sand can be effective [15]. Kwan et al. (2018) examined the durability of high-strength self-compacting concrete specimens in corrosive environments. For this purpose, glass fibers were used at a rate of 0.6 to 2.40%. Specimens in which more glass fibers were used showed greater resistance to adverse environmental conditions [16]. Tabkhi Wayghan et al. (2019) investigated the contribution of GFRP bars on the compressive strength of concrete columns with circular cross section. It has been shown that these rebars can contribute significantly to compressive strength of concrete columns if the column confinement is provided sufficiently [17]. Ali et al. (2019) investigated the influence of glass fibers on mechanical properties of concrete with recycled coarse aggregates (RCA) and normal coarse aggregates (NCA). The results indicated that the addition of glass fibers was very useful in enhancing the split tensile and flexural strength of both RCA and NCA concrete [18]. Shadmand et al. (2020) investigated the use of steel fiber in concrete jacket with the purpose of retrofitting RC beams. They showed that steel fiber-can improve the concrete jacket performance and it is an adequate choice for reinforcing the concrete of RC jacket [19].

In general, the results of the mentioned studies show that the use of various fibers in concrete reduces cracks and improves tensile strength. But the addition of some fibers, along with their benefits, has drawbacks that can affect their performance. For example, steel fibers have a higher density than other fibers and are relatively more expensive to make. In addition, steel fibers do not function well in corrosive atmospheric conditions and can affect the durability of concrete. However, fibers such as polypropylene, carbon, basalt and glass do not have these weaknesses.

On the other hand, in the area between the cement paste and the aggregate surfaces and the boundary areas between the fibers and the aggregates, there are always cracks that in the long run can lead to porosity in concrete and reduce strength. The use of pozzolans can overcome this weakness by strengthening the mentioned boundary areas. The results of various studies show that aluminium oxide nanoparticles have an effective role in improving the mechanical properties of concrete and their use can lead to increase adhesion between concrete and rebar in concrete [2, 6]. Also, these nanoparticles have a relatively higher resistance to heat caused by fire compared to other nanoparticles [20-22].

The combined use of different fibers and nanoparticles in concrete is considered as an effective step in preventing the spread of microcracks and cracks and compensating for the weak tensile strength of concrete. From an economic point of view, the use of fibers and nanoparticles depends on the application and conditions of the project. Fiber has already found its place in construction projects and its economic evaluation is more related to the type of fiber which is used and how to use it. However, in cases where fibers are used instead of steel reinforcing mesh, not only equal price of fibers and steel mesh but also skilled manpower, tools, equipment, material storage space, etc are considered and even this issue can be looked at with foresight. Maintenance costs, weather conditions and future applications of the structure that may have in the future are all the factors that can justify the use of fibers economically or vice versa. In some cases, project scheduling may be very important and the use of fibers can speed up the process and save a lot of money and this can lead to abundant economic savings.

Therefore, in this study, the combined use of glass fibers and aluminium oxide nanoparticles on the workability, mechanical, and durability properties has been evaluated. Glass fiber volume fractions between 0% to 1.5% in combination with 0% to 3% aluminium oxide nanoparticles were used. For this purpose, the properties of fresh concrete were determined by conventional experiments which were introduced by EFNARC [23], and the mechanical properties were determined by performing compressive strength and tensile strength tests. The durability properties were performed by water absorption, electrical resistivity and water penetration tests. Also, non-destructive properties were evaluated using ultrasonic pulse velocity (UPV). The flowchart of the experimental tests is presented in Figure 1.

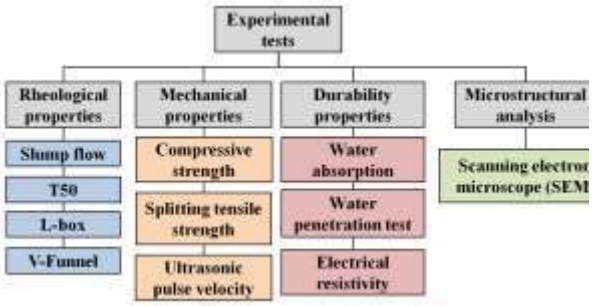

Figure 1. Flowchart of the experimental tests

2. EXPERIMENTAL STUDY

2. 1. The Used Materials Materials include cement, sand, gravel, glass fiber, aluminium oxide nanoparticles, water, and superplasticizer. Portland cement (Type II) was used. Its chemical properties were presented in Table 1.

The gradation of sand and gravel curve is within the allowable range of ASTM C33 [24] (Figure 2). The used sand is a river type with a density of 2640 kg/m^3. The coarse aggregate is a broken type with a density of 2580 kg/m^3 and its size is between 4.75 and 19 mm.

TABLE 1. Chemical attributes of aluminium oxide nanoparticles and cement

Components	Cement type II	Components	AL_2O_3
SiO_2 %	21.27	Al_2O_3	99≥%
Al_2O_3 %	4.95	Ca	25ppm ≤
Fe_2O_3 %	4.03	Fe	80ppm ≤
CaO %	62.95	Cr	4ppm ≤
MgO%	1.55	Na	70ppm ≤
SO_3 %	2.26	Mn	3ppm ≤
K_2O %	0.65	Co	2ppm ≤
Na_2O %	0.49		

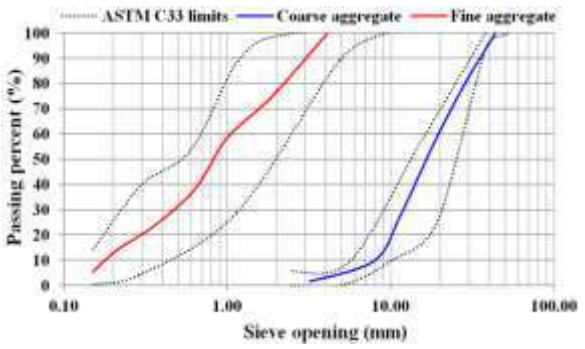

Figure 2. Aggregates grading diagram

The length and diameter of glass fibers were considered 12 and 0.02 mm, respectively. Also, tensile strength and density of glass fibers were 14000 kg/cm^2 and 2.44 kg/cm^3, respectively. Aluminium oxide nanoparticles are artificial and white matter which is composed of very tiny AL_2O_3 particles. The alumina which is used in nano- aluminium powder in this study was more than 99%. The density and specific surface area of aluminium oxide nanoparticles were 3.89 g/cm^3 and 138 g/cm^2, respectively. Also, the diameter of its solid particles was about 20 nanometers. The chemical properties of aluminium oxide nanoparticles were presented in Table 1. The water which was used for making and curing specimens was under the criterion recommended by ASTM D1129 [25]. In this study, the third generation superplasticizer based on carboxylic ether with the brand name of GLENIUM_110P was used. This material is opaque and cloudy in color and its density at a temperature of 20 degrees Celsius is 1.1 g/cm^3.

2. 2. Experiments In order for self-compacting concrete to be used in a variety of projects, it must be evaluated in terms of the parameters such as stability and filling ability. Each of these parameters is estimated by one or more experiments [26]. In this study, according to the considered abilities, slump flow test was selected to appraise the flowability, T50, and V funnel tests were selected to assess the viscosity and L-box test was selected to evaluate the transmission capability. In the slump flow experiment, the diameter of the circle that the concrete forms after spreading will be the criterion of examining filling ability. The appropriate range for slump flow based on EFNARC [23] is considered between 650 and 850 mm. Self-compacting concrete with this range of slump flow is suitable for use in a variety of conventional applications of self-compacting concrete such as use in beams or building columns. Concrete viscosity is the strength against fresh concrete flow and is usually evaluated by T50 and V funnel tests.

Concrete viscosity should usually be considered for areas with heavy reinforcement and when concrete pouring levels are required. The time which is needed for reaching the slump flow of specimen with a diameter of 50 cm is called T50. T50 FLow time can cause separation and high T50 time can cause concrete blockage. To determine the time of V-funnel, first, the inner surface and the funnel valve were cleaned and moistened. The moment of the complete evacuation of concrete from the funnel is called V funnel time. The L-box test is applied to determine the passing properties of specimens in the presence of reinforcement without separation or blockage. In L-box, two or three rebars with a certain diameter and distance can be used, depending on the density of the reinforcement at the execution site. The values of H2 (concrete height at the end of the set-up) and

H1 (concrete height behind the gate) were calculated. The H_2/H_1 proportion indicates the blocking ratio. Figure 3 shows the images of fresh concrete experiments.

Compressive strength experiments were conducted using 300×150 mm cylindrical specimens [27]. During testing, the sample was located along the center of the top plate of set-up and loading was conducted continuously at a rate of 0.125 cm/min.

Standard cylindrical specimens of 300×150 mm were pressed along the diameter of the specimen [28]. Splitting tensile strength was determined from Equation (1):

$$f_t = \frac{2P}{\pi Ld} \quad (1)$$

The parameters of Equation (1) are presented below:
f_t: Tensile stress; P: Failure load; L: Length; D: Diameter

The non-destructive properties of concrete were evaluated by UPV test in accordance with ASTM C597 [29]. For this purpose, specimens with dimensions of 10×10×10 cm were made and tested at the age of 28 days (Figure 4).

The water absorption of concrete specimens indirectly indicates the porosity and extent of capillary cavities in it [30]. Water absorption test was performed on 10 cm cubic specimens at age of 28 days in accordance with ASTM C1585-04 [31]. Three cubic samples were made from each mixture and the final water absorption was calculated based on the average of the water absorption values obtained from the specimens.

There are no specific instructions in the various standards for determining the electrical resistivity of concrete specimens [32], and therefore special equipment has been used to perform this test. Thus, a device for determining the electrical resistivity with a frequency of 1 Hz and a final capacity of 1 MΩ with two copper plates has been used. In order to connect and establish proper flow between the main sample (cement paste or intermediate hardened concrete) and copper plates, some fresh cement paste is placed and spread evenly by the spatula. Also, to prevent short circuits and inaccurate responses, the dough protruding from the copper plates and the sample should be removed with a cloth. Finally, by connecting each of the wires of the device to one of the plates, the amount of electrical resistivity is recorded. Figure 5 shows how to measure the electrical resistivity of concrete specimens and copper plates and additional specimens (to prevent connection to the workbench and ground).

The water penetration depth is a parameter for comparing the performance of the specimens against the penetration of destructive ions. The lower permeability of one concrete specimen than another specimen may indicate that destructive ions and the extent of their damage are less likely to penetrate the concrete specimen. Water penetration test was conduted according to DIN 1048 [33] on cubic specimens with a dimension of 15 cm. These specimens were cured in saturated lime water until 28 days and then placed in a water permeation tester (Figure 6).

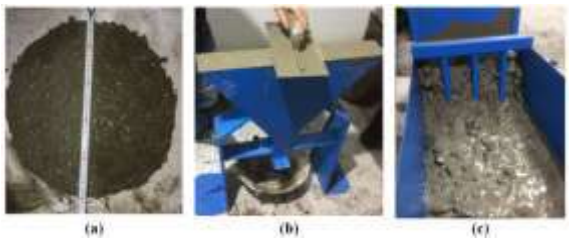

Figure 3. Fresh concrete experiments a: Slump flow b: V funnel c: L-box

Figure 4. UPV test

Figure 5. Electrical resistivity test

Figure 6. Water pentration test

In this device, water with a pressure of 5 bar acts on the specimens for three days. According to the standard, the surface of the specimen that is affected by water pressure should be slightly roughened with a wire brush. The water infiltration was determined after three days.

2. 3. Mixed Design 24 types of mixed designs were investigated. The variables included glass fibers (0, 0.5, 1 and 1.5% by concrete volume) and aluminium oxide nanoparticles (0, 0.5, 1, 1.5, 2 and 3% by weight of cement|), respectively. The mixed design was considered in accordance with ACI211-1-89 [34]. First, the aggregates were mixed and then the fibers that previously had been separated by sieve were added. At this stage, a mixture of aluminium oxide nanoparticles and cement were combined, and after mixing, water was added along with a superplasticizer. In order to prevent the fibers from sticking together and to create the balling phenomenon, as well as to prevent the formation of separate granules of aluminium oxide nanoparticles due to contact with water, the mixed design operation was carried out carefully. For each mixed design of compressive, tensile, and flexural strength tests, three cylindrical specimens were made and their mean was evaluated as the final result .The environment of concrete curing was drinking water with a temperature of about 20 degrees Celsius. Table 2 presents the values of used materials for each design separately.

TABLE 2. Mixed design (kg/m^3)

Mix code	C	W	AL	FA	CA	GF	SP
NA0-F0	450	216	0	700	955	0	7
NA0-F0.5	450	216	0	700	945	12.2	7
NA0-F1	450	216	0	700	930	24.4	7
NA0F1.5	450	216	0	700	920	36.3	7
NA0.5-F0	447.75	216	2.25	700	955	0	7
NA0.5-F0.5	447.75	216	2.25	700	945	12.2	7
N0.50-F1	447.75	216	2.25	700	930	24.4	7
NA0.5-F1.5	447.75	216	2.25	700	920	36.3	7
NA1-F0	445.5	216	4.5	700	955	0	7
NA1-F0.5	445.5	216	4.5	700	945	12.2	7
NA1-F1	445.5	216	4.5	700	930	24.4	7
NA1-F1.5	445.5	216	4.5	700	920	36.3	7
NA1.5-F0	443.25	216	6.75	700	955	0	7
NA1.5-F0.5	443.25	216	6.75	700	945	12.2	7
NA1.5-F1	443.25	216	6.75	700	930	24.4	7
NA1.5-F1.5	443.25	216	6.75	700	920	36.3	7
NA2-F0	441	216	9	700	955	0	7
NA2-F0.5	441	216	9	700	945	12.2	7
NA2-F1	441	216	9	700	930	24.4	7
NA2-F1.5	441	216	9	700	920	36.3	7
NA3-F0	436.5	216	13.5	700	955	0	7
NA3-F0.5	436.5	216	13.5	700	945	12.2	7
NA3-F1	436.5	216	13.5	700	930	24.4	7
NA3-F1.5	436.5	216	13.5	700	920	36.3	7

C: Cement, W: Water, GF: Glass fiber, FA: Fine aggregates, CA: Fine aggregates, AL: Aluminium oxide nanoparticles, SP: Superplasticizer

3. RESULTS AND DISCUSSION

3. 1. Rheological Properties The results of fresh concrete tests and the allowable range of EFNARC [23] are presented in Table 3. EFNARC has classified self-compacting concrete in terms of slump flow into three categories: SF1, SF2, and SF3. The slump flow of the specimens in this study are in the range of 657 to 749 mm. Therefore, the specimens are classified as SF2 and can be used in structural members with high-density. With increasing glass fibers and aluminium oxide nanoparticles, the slump flow in self-compacting concrete decreased. For the slump flow to be within the allowable range, more superplasticizer must be used. On the other hand, if the used superplasticizer exceeds the amount recommended by the manufacturer, it will have a negative effect on the attributes of concrete. The highest value of slump flow is related to NA0-F0 design (749 mm) and its lowest value is related to NA3-F1.5 design (657 mm). The allowable range of T50 is between 2 and 5 seconds that the specimens under study are within this range. The decrease in slump flow and the increase in T50 time due to the presence of fibers and nanoparticles have been observed in the studies of Mazaheripour et al. (2011) [35], Mohsenzadeh et al. (2019) [5], and Faez et al. (2019) [2]. Considering the changes of slump flow in the specimens, it can be stated that by increasing the accuracy in the method of adding superplasticizer, a desirable result can be achieved.

Self-compacting concrete is divided into PA1 and PA2 based on the ability to pass. Because the purpose is to consider the access to concrete with the ability to pass through compacting rebars, three rebars were used in the L-box test. The blocking ratio of the specimens are within the range of 0.8 to 0.97 and are in the PA2 category. In general, fibers and nanoparticles lead to slow concrete movement, which can be overcome by using the allowable value of a superplasticizer.

Self-compacting concrete based on its viscosity is divided into two categories, VS1/VF1 and VS2/VF2. Self-compacting concrete in the VS1/VF1 category even has a good filling ability in the presence of large rebars. The passing time from V funnel for the specimens is in the range of 7.4 to 11.1 seconds, and the T50 time is in

TABLE 3. Fresh concrete results

Mix code	Slump flow (mm)	T50 (s)	V_{funnel} (s)	L_{box} (H_2/H_1)
NA0-F0	749	2.9	7.4	0.8
NA0-F0.5	740	3.4	7.9	0.83
NA0-F1	726	3.6	8.3	0.85
NA0F1.5	716	3.7	8.9	0.87
NA0.5-F0	726	3.1	7.6	0.84
NA0.5-F0.5	708	3.5	8.2	0.85
N0.50-F1	702	3.7	8.5	0.86
NA0.5-F1.5	684	3.8	9.1	0.89
NA1-F0	714	3.2	7.8	0.89
NA1-F0.5	694	3.6	8.5	0.91
NA1-F1	683	3.9	8.8	0.91
NA1-F1.5	674	4	9.4	0.92
NA1.5-F0	699	3.3	8.1	0.9
NA1.5-F0.5	693	3.7	8.9	0.92
NA1.5-F1	687	4	9.9	0.93
NA1.5-F1.5	675	4.1	10.1	0.94
NA2-F0	689	3.4	8.5	0.91
NA2-F0.5	681	3.8	9.6	0.93
NA2-F1	671	4.1	10.4	0.95
NA2-F1.5	669	4.2	10.6	0.96
NA3-F0	671	3.7	8.9	0.94
NA3-F0.5	665	3.9	10.1	0.95
NA3-F1	660	4.4	11.2	0.96
NA3-F1.5	657	4.9	11.1	0.97
EFNARC	SF1: 550-650 SF2: 660-750 SF3: 760-850	VS1: ≤ 2 VS2: >2	VF1: < 8 VF2: 9-25	PA2 ≥ 0.8 (with three bars)

the range of 2.9 to 4.9 seconds. Therefore, in terms of viscosity, it can be stated that most of the specimens are in the VS1/VF1 category. With increasing glass fibers and nanoparticles, the viscosity of concrete specimens increased. For example, the V-funnel time of the specimen containing 3% of aluminium oxide nanoparticles and 1.5% of glass fiber increased by 50%. In general, considering the results, it can be stated that the concrete specimens made in the present study have the necessary self-compaction.

3. 2. Hardened Concrete Results

3. 2. 1. Compressive Strength Table 4 presents the results of compressive test of cylindrical specimens at 28 days for 24 mixed designs in MPa. In this table, the percentage of compressive strength changes of the specimens containing aluminium oxide nanoparticles and glass fibers compared to the control specimen is presented. The lowest and highest compressive strengths were 41.8 MPa (NA0-0F0) and 68.2 MPa (NA2-F1), respectively, and the lowest and highest splitting tensile strength were 2.6 MPa (NA0-0F0) and 5.7 MPa (NA3-F1.5), respectively. Figure 7 shows the compressive strength of the specimens and their increased percentage. As can be seen, glass fibers have little effect on increasing compressive strength. For example, in specimens without alumina oxide nanoparticles, the compressive strength of the specimens reinforced with 1% glass fiber increased by a maximum of 1.9%. Also, in specimens containing nanoparticles, the addition of glass fiber has increased the compressive strength by a maximum of about 2.5%. However, the addition of aluminium oxide nanoparticles to concrete has

TABLE 4. Compressive and tensile strength of specimens

Mix code	Compressive strength (MPa)		Splitting tensile strength (MPa)	
	Strength (MPa)	Variations (%)	Strength (MPa)	Variations (%)
NA0-F0	41.8	0.0	2.6	0.0
NA0-F0.5	42.4	1.4	2.9	11.5
NA0-F1	42.6	1.9	3.4	30.3
NA0F1.5	42.2	1.0	3.7	41.0
NA0.5-F0	48.1	15.1	2.9	9.6
NA0.5-F0.5	48.7	16.5	3.3	14.0
N0.50-F1	49.1	17.5	3.9	48.7
NA0.5-F1.5	48.4	15.8	4.4	66.7
NA1-F0	54.3	29.9	3.1	19.2
NA1-F0.5	55	31.6	3.6	38.3
NA1-F1	55.6	33.0	4.4	69.0
NA1-F1.5	54.7	30.9	4.8	83.5
NA1.5-F0	61.1	46.2	3.5	34.5
NA1.5-F0.5	61.8	47.8	4.0	52.5
NA1.5-F1	62.8	50.2	4.6	77.0
NA1.5-F1.5	61.5	47.1	5.1	95.4
NA2-F0	66.5	59.1	3.7	41.8
NA2-F0.5	67.2	60.8	4.2	60.9
NA2-F1	68.2	63.2	5.0	90.0
NA2-F1.5	66.9	60.0	5.4	106.5
NA3-F0	64.3	53.8	3.9	47.9
NA3-F0.5	65.1	55.7	4.4	66.7
NA3-F1	65.9	57.7	5.2	97.3
NA3-F1.5	64.7	54.8	5.7	119.2

significantly increased compressive strength. In specimens without glass fiber, the use of 0.5, 1, 1.5, 2, and 3% aluminium oxide nanoparticles increased the compressive strength by 15.1, 29.9, 46.2, 59.1, and 53.8%, respectively. Therefore, according to the mentioned values, the use of only aluminium oxide nanoparticles as a replacement to a part of cement in increasing the compressive strength of the studied concrete specimens is more effective than using only glass fibers in concrete; So that the maximum increase in compressive strength of the samples in which the fibers are only used is 2.5% and the maximum compressive strength of the specimens in which the aluminium oxide nanoparticles are only used is 59.1%. The reason for this increase could be the appropriate reactivity of aluminium nanoparticles with Portland cement during the cement hydration process; Aluminium nanoparticles have a very high specific surface area and their reactivity causes them to react quickly with calcium hydroxide $Ca(OH)_2$ and produce silicate-hydrate gel (C-S-H). Thus, the $Ca(OH)_2$ crystals are decreased and the cavities in the cement gel are filled and the compressive strength is increased [2, 36-39].

SEM images of the specimens presented in Figure 8 also confirm the mentioned result. The control specimen contains numerous air cavities that the use of nanoparticles fills these cavities and increases the bond between cement and aggregates. The use of aluminium oxide nanoparticles in cement not only improves the structure due to the filling of the pores but also makes the pozzolanic reactions more active.

Figure 8 clearly shows the microstructure difference between concrete with and without aluminium oxide nanoparticles and glass fibers after 28 days. The increase of compressive strength due to the addition of aluminium oxide nanoparticles has also been reported in related studies. Arefi et al. (2011) [40] reported that the use of 3% aluminium oxide nanoparticles increases the compressive strength by 63%. The mentioned results can confirm the validity of the compressive strength test performed in the present study.

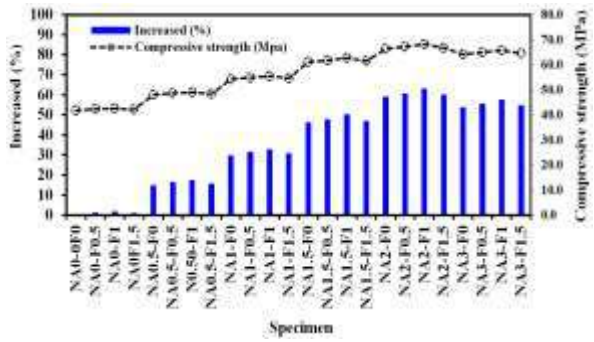

Figure 7. 28-day compressive strength of cylindrical specimens and their percentage increase compared to the control specimen

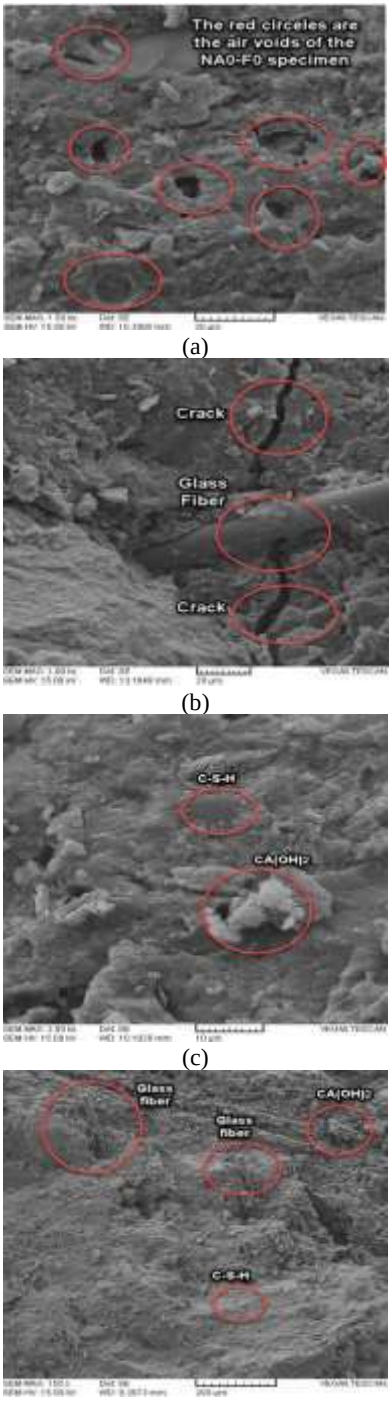

Figure 8. Microstructural images of 4 specimens examined at 28 days a: NA0-F0 b: NA0-F1.5 c: NA3-F0 d: NA3-F1.5

3. 2. 2. Splitting Tensile Strength Table 4 and Figure 9 show the splitting tensile strength at 28 days. The combined use of nanoparticles and glass fiber has a very efficient impress in improving the splitting tensile strength; In specimens without glass fibers, the use of 0.5, 1, 1.5, 2 and 3% aluminium oxide nanoparticles

increased the splitting tensile strength by 9.6, 19.2, 34.5, 41.8 and 47.9%, respectively. In specimens without nanoparticles, the use of 0.5, 1, and 1.5% glass fibers increased the splitting tensile strength by 11.5, 30.3, and 41%, respectively.

The presence of glass fibers in the brittle binder matrix reduced crack width and thus increased the splitting tensile strength. The combined use of 1.5% glass fiber and 3% aluminium nanoparticles increased the tensile strength by 119.2%. Therefore, according to the obtained values, it can be stated that the combined use of glass fibers and aluminium oxide nanoparticles has a greater efficacy on increasing splitting tensile strength compared to the use of only one of them. The presence of fibers in concrete specimens had an effect on the failure of specimens. In the specimens without glass fiber, the failure was done abruptly, and with the separation of the two pieces, and in the concrete specimens containing 1 and 1.5% of fiber, the failure was done gradually. Also, the combined use of aluminium oxide nanoparticles and glass fibers increased the interaction between cement particles and fibers. This can lead to an increase in density and splitting tensile strength.

In a study by Sivkumar et al. (2018), it was shown that the use of 0.8% glass fiber increases the tensile strength by 18% [41]. Hilles and Ziara (2018) also found that the use of 1.2% of glass fibers can increase the tensile strength by about 63% [42]. In general, it can be stated that the strengths obtained in this study and their variations are in the range of similar studies and the difference between the results is due to the quality of the materials, curing environment, accuracy of measuring set-ups and type of cement.

Changes in the cylindrical compressive strength against the splitting tensile strength of the self-compacting specimens containing glass fibers and aluminium oxide nanoparticles are presented in Figure 10.

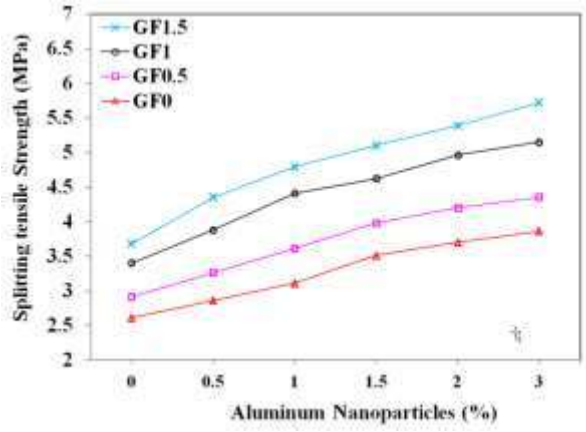

Figure 9. Comparison of splitting tensile strength of specimens at 28 days

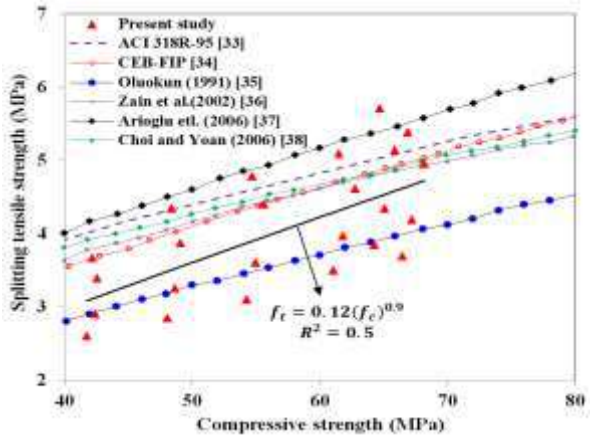

Figure 10. The correlation between splitting tensile and compressive strengths

Figure 10 also shows the proposed relationships by ACI 318-R [43] and CEB-FIP [44] and a number of studies [45-48] on high-strength concrete. As can be seen, the slope of the diagram for the results of the present study is almost the same as the slope of the various diagrams presented. The correlation analysis coefficient (R2) [49] between splitting tensile and compressive strengths of the studied specimens is presented in Equation (2).

$$f_t = 0.12(f_c)^{0.9} \quad (2)$$

3. 2. 3. UPV Figure 11 compares the UPV vs compressive strength of the specimens. In samples without nanoparticles, the addition of glass fibers had little effect on changes of the UPV. Minor changes in UPV of concrete due to the addition of glass fibers have also been observed in the studies of Rath et al. (2017) [50] and Hedjazi and Castillo (2020) [51]. The combined use of aluminium oxide nanoparticles and glass fibers has an effect on increasing the UPV. The UPV of the NA0-F0 and NA2-F1 specimens are 4.10 and 5.15 km/s, respectively. In fact, the combined use of 2% aluminium oxide nanoparticles and 1% glass fiber has increased the UPV by about 26%. Increasing the aluminium oxide nanoparticles will increase the UPV, but when the amount of aluminium oxide nanoparticles in the mixture increases too much, it will reduce the UPV.

By increasing the percentage of nanomaterials more than the optimum value, the compressive strength and UPV decrease. This may be due to the fact that increasing the amount of nanopowder to its optimum limit causes the nanoparticles to not disperse well. The accumulation of nanoparticles creates a weak zone in the form of a cavity and consequently, the microstructure of the cement hydrate cannot be formed, which in turn reduces the compressive strength.

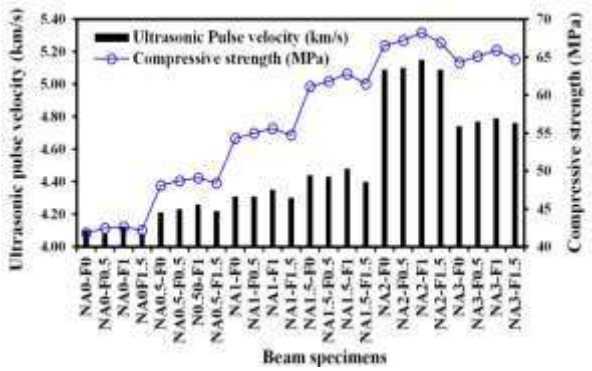

Figure 11. UPV vs compressive strength of the specimens

3. 3. Durability Properties

3. 3. 1. Water Absorption Figure 12 compares the water absorption of the specimens. According to CEB [52], concrete specimens are divided into three groups according to water absorption percentage: good, medium and poor. Most of the studied specimens are in the medium range. Addition of aluminium oxide nanoparticles reduced the water absorption of the specimens containing glass fibers by about 10 to 46%, depending on the fibers contents compared to the control specimen. The lowest water absorption decrease is related to the specimen in which 3% aluminium oxide nanoparticles are used (N3-F0) and the highest water absorption is related to the sample in which 1.5% glass fibers are used (N0-F1.5). The use of aluminium oxide nanoparticles has reduced the voids of the specimens due to the formation of hydrated silicate gel and thus significantly reduced water absorption. Considering the changes in water absorption of self-compacting concrete specimens containing glass fibers and aluminium oxide nanoparticles, it can be concluded that the use of glass fibers along with aluminium oxide nanoparticles causes the water absorption rate to be less compared to specimens without these materials. This is one of the effective properties of aluminium oxide nanoparticles, which increases the resistance to adverse environmental factors by reducing water absorption.

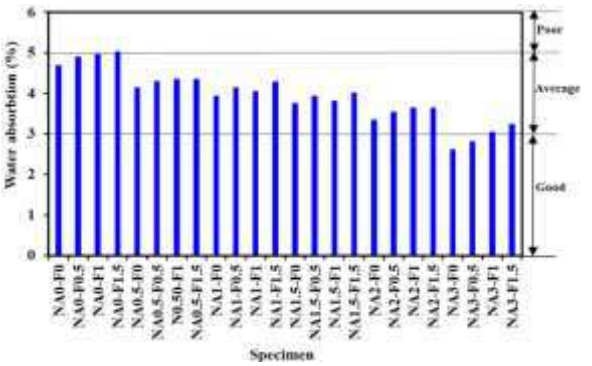

Figure 12. Water absorption of the specimens

3. 3. 2. Electrical Resistivity Figure 13 compares the electrical resistivity of the specimens at the age of 28 days. Higher electrical resistivity indicates that concrete is more durable. Song and Saraswathy (2007) [53] and Elkey and Sellevold (1995) [54] divide concrete into four categories in terms of corrosion probability (Figure 13). Specimens without nanoparticles are in the high range and specimens containing nanoparticles are in the Low to moderate range. The addition of aluminium oxide nanoparticles to concrete specimens containing glass fibers was effective and increased the electrical resistivity by about 98 to 265% compared to the control specimen.

The addition of aluminium oxide nanoparticles to specimens with and without glass fibers greatly increases the electrical resistivity. The extremely fast reactivity of aluminium oxide nanoparticles causes it to react with calcium hydroxide and produce hydrated calcium silicate, which by filling small cavities and increasing the density of concrete, prevents more ions from moving in the concrete, thus increase the electrical resistivity of concrete and concrete corrosion is reduced. The electrical resistivity of all fiber specimens is lower than the control sample. The fibers in the concrete increase the air and thus reduce the electrical resistivity.

Figure 14 presents the results of water penetration depth concrete for 24 specimens at the age of 28 days. The addition of aluminium oxide nanoparticles to self-compacting concrete specimens containing glass fibers has significantly reduced the water penetration depth. The addition of 0.5, 1, 1.5, 2 and 3% aluminium oxide nanoparticles to the specimens without fiber reduced the water penetration depth by 4, 19, 23, 34 and 38%, respectively. Addition of 0.5, 1, 1.5, 2 and 3% aluminium oxide nanoparticles to specimens containing 0.5% fibers reduced the water penetration depth by 6, 20, 24, 33 and 37%, respectively. The addition of 0.5, 1, 1.5, 2 and 3% aluminium oxide nanoparticles to specimens containing 1% fiber reduced the water penetration depth by 8, 20, 24, 31 and 37%, respectively. Also, adding 0.5, 1, 1.5, 2 and 3% of aluminium oxide nanoparticles to specimens

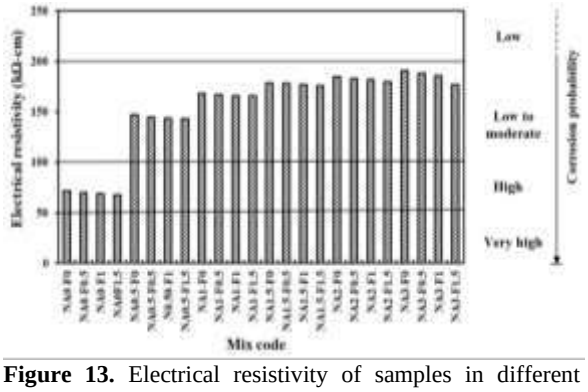

Figure 13. Electrical resistivity of samples in different specimens

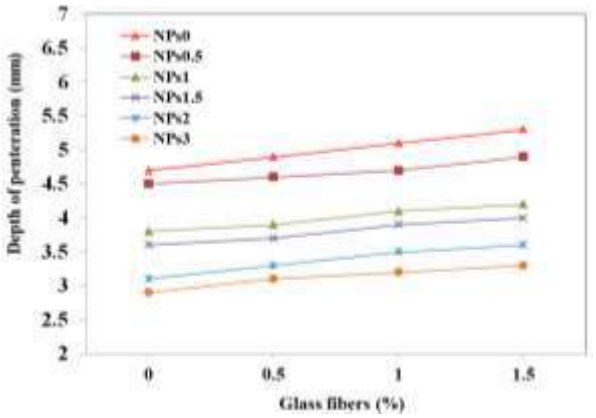

Figure 14. Depth of penetration

containing 1% fibers reduced the water penetration depth by 8, 21, 25, 32 and 38%, respectively. Powder effect and pozzolanic reaction rate of nanoparticles are among the reasons for reducing water penetration inside concrete samples. The decrease in permeability with the increase of aluminium oxide nanoparticles up to 3% by weight of cement is related to the reduction of cracks due to the flooding of concrete and the filling of pores in nano and micro dimensions in concrete.

4. CONCLUSION

In the present study, the combined use of glass fibers and aluminum oxide nanoparticles on rheological, mechanical, durability and, microstructure properties of self-compacting concrete was investigated. In previous studies, the use of only each of these materials was considered. The distinguishing feature of this study from other similar studies was the combined use of glass fibers and aluminum oxide nanoparticles. In this section, the most important results are presented:

- The maximum increase in compressive strength of the specimens in which fibers are only used is 2.5% and the maximum compressive strength of the specimens in which the aluminium oxide nanoparticles are only used is 59.1%. The reason for this increase could be the reactivity of aluminium nanoparticles to Portland cement during the cement hydration process.
- SEM images show that the control specimen contains numerous air cavities and the use of nanoparticles fills these cavities and increases the bond between cement and aggregates.
- The combined use of 1.5% glass fiber and 3% aluminium nanoparticles increased the tensile strength by 119.2%. The combined use of glass fibers and aluminium oxide nanoparticles has a greater effect on increasing tensile strength compared to use only one of them.
- The presence of fibers in concrete specimens with and without nanoparticles had an effect on the failure of specimens. In the specimens without glass fiber, the failure was done abruptly, and with the separation of the two pieces, and in the concrete specimens containing 1 and 1.5% of the fiber, the failure was done gradually.
- The combined use of aluminium oxide nanoparticles and glass fibers has caused the interaction surface between cement particles and fibers to increase.
- Adding aluminium oxide nanoparticles to the specimens also results in more C-H-S gel, which increases the strength of the matrix in the concrete. Also, part of the tensile stress is also borne by the glass fibres.
- The use of nanoparticles in self-compacting concretes containing glass fibers improves the UPV. For example, the addition of 2% of aluminium oxide nanoparticles to specimens containing 1% glass fibers increased the UPV by about 26%.
- The use of glass fibres along with aluminium oxide nanoparticles causes the water absorption rate to be less compared to specimens without these materials. This is one of the effective properties of aluminium oxide nanoparticles, which increases the resistance to adverse environmental factors by reducing water absorption.
- The utilization of glass fibers alongside aluminium oxide nanoparticles decreased water absorption and water penetration compared to specimens without these materials. This advantage makes it possible to use concretes in environments that are exposed to water flow.

In general, the results showed that the combined use of glass fibers and aluminum oxide nanoparticles has a positive effect on improving the properties of self-compacting concrete and they can be more useful in projects in which high tensile and flexural strengths are considered. The application of these materials can reduce the use of steel rebar in reinforced concrete and it may be more cost-effective.

Also, the results showed that the use of glass fibers alone does not seem very suitable in terms of permeability and water absorption. Aluminium oxide nanoparticles can compensate for this weakness and improve the durability properties of concrete. On the other hand, glass fibers increase the tensile strength of concrete by increasing the cracking resistance. Therefore, the combined use of these two materials is effective and can improve the mechanical properties and durability of concrete

The use of other fibers such as steel fibers, nylon fibers, polypropylene fibers, carbon fibers in the composition of aluminum oxide nanoparticles in different types of concretes is the topics that can be investigated in future studies.

5. REFERENCES

1. Niewiadomski, P., Stefaniuk, D. and Hoła, J., "Microstructural Analysis of Self-compacting Concrete Modified with the Addition of Nanoparticles". ***Procedia Engineering***, Vol. 172, (2017), 776-783. doi:org/10.1016/j.proeng.2017.02.122.
2. Faez, A., Sayari, A. and Manie, S. "Mechanical and Rheological Properties of Self-Compacting Concrete Containing Al2O3 Nanoparticles and Silica Fume". Iranian Journal of Science and Technology, ***Iranian Journal of Science and Technology, Transactions of Civil Engineering***, (2020). doi: org/10.1007/s40996-019-00339-y
3. Ghanbari, M., Kohnehpooshi, O., & Tohidi, M. (2020). "Experimental Study of the Combined Use of Fiber and Nano Silica Particles on the Properties of Lightweight Self Compacting Concrete". ***International Journal of Engineering, Transactions B: Applications***, Vol. 33, No. 8, (2020), 1499-1511. doi: 10.5829/ije.2020.33.08b.08
4. Kebria, M. S., & Jahanshahi, M. "Nanofiltration membranes synthesized from polyethyleneimine for removal of MgSO4 from aqueous solution (Research Note). ***International Journal of Engineering, Transactions B: Applications***, Vol. 27, No. 8, (2014), 1173-1178. doi: 10.5829/idosi.ije.2014.27.08b.02
5. Mohsenzadeh, S., Maleki, A., and Lotfollahi-Yaghin, M. A, "Experimental and Numerical Study of Energy Absorption Capacity of Glass Reinforced SCC Beams". ***International Journal of Engineering, Transactions C: Aspects***, Vol. 32, No. 12, (2019), 1733-1744. doi: 10.5829/IJE.2019.32.12C.06
6. Silva, J. V., Ismael, R., Carmo, R. N. F., Lourenço, C., Soldado, E., Costa, H., and Júlio, E. "Influence of nano-SiO2 and nano-Al_2O_3 additions on the shear strength and the bending moment capacity of RC beams". ***Construction and Building Materials***, Vol. 123, (2016), 35-46. doi: 10.1016/j.conbuildmat.2016.06.132
7. Joshaghani, A., Balapour, M., Mashhadian, M., and Ozbakkaloglu, T. "Effects of nano-TiO_2, nano-Al_2O_3, and nano-Fe_2O_3 on rheology, mechanical and durability properties of self-consolidating concrete (SCC): An experimental study". ***Construction and Building Materials***, Vol. 245, (2020), 118444. doi:org/10.1016/j.conbuildmat.2020.118444
8. Mohammed, R. K., Kamal, H. M., and Kadhim, M. J., "Study the effect of calcium and nano Al_2O_3 oxide powders on the mechanical and physical properties of cement mortar", In AIP Conference Proceedings, Vol. 2213, No. 1, (2020), 020135. doi:org/10.1063/5.0000393
9. Ansari rad, T, Tanzadeh, J, Azin pourdada., "Laboratory evaluation of self-compacting fiber-reinforced concrete modified with hybrid of nanomaterials". ***Construction and Building Materials***,Vol.232,(2020),117211.doi:org/10.1016/j.conbuildmat.2019.117211
10. Zeinolabedini, A., Tanzadeh, J., and Mamodan, M., "Laboratory investigation of ultra-high–performance fiber-reinforced concrete modified with nanomaterials", ***Journal of Testing and Evaluation,*** Vol. 49, No. 1, (2021). doi: 10.1520/JTE20180806.
11. Ganesh, L. M., (2016), "Experimental methods of investigation on glass fiber reinforced self-compaction concrete", ***Journal of Chemical and Pharmaceutical Sciences***, Vol. 9, No. 3, (2016), 1504-1510.
12. Soratur, A., Ajay, B. K., Hiremath, S. P., Maganur, T. P., and Rajesh, S. J. "An experimental investigation on properties of concrete with foundry sand and glass fiber", ***International Research Journal of Engineering and Technology (IRJET),*** Vol. 5, No. 5, (2018), 2176-2179.
13. Alex, X., and Arunachalam, K. "Experimental Investigation of Steel and Glass Fiber Reinforced Light Weight Concrete". ***Journal of Computational and Theoretical Nanoscience***, Vol. 16, No. 1, (2018), 47-52. doi: org/10.1166/jctn.2018.7054
14. Vasu, K., Krishna, P. M., Rupa, J. S., Kumar, A. V., and Janardhan, N. "An Experimental Investigation on the Mechanical Properties of Glass Fiber Reinforced Concrete". ***IUP Journal of Structural Engineering***, Vol. 12, No. 1, (2019), 22-33. doi: 10.1088/1757-899X/114/1/012118
15. Hemavathi, S., Kumaran, A. S., and Sindhu, R. "An experimental investigation on properties of concrete by using silica fume and glass fibre as admixture". ***Materials Today: Proceedings***, Vol. 21, (2020), 456-459. doi: org/10.1016/j.matpr.2019.06.558
16. Kwan, W. H., Cheah, C. B., Ramli, M., and Chang, K. Y. "Alkali-resistant glass fiber reinforced high strength concrete in simulated aggressive environment", ***Materials de Construction,*** Vol. 68, No. 329, (2018), 147. doi: org/10.3989/mc.2018.13216
17. Wayghan, A. R. T., Mofid, M., Ravandi, B. B., & Yazdi, S. M. Z. "Increasing the contribution of gfrp bars on the compressive strength of concrete columns with circular cross section". ***Civil Engineering Journal***, Vol. *5 No.* 8, (2019), 1850-1862. doi: 10.28991/cej-2019-03091377
18. Ali, B., Qureshi, L. A., Raza, A., Nawaz, M. A., Safi Ur, R., & Rashid, M. U. "Influence of glass fibers on mechanical properties of concrete with recycled coarse aggregates". ***Civil Engineering Journal***, Vol. 5, No. 5, (2019), 1007-1019. doi: 10.28991/cej-2019-03091307
19. Shadmand, M., Hedayatnasab, A., Kohnehpooshi, O. "Retrofitting of Reinforced Concrete Beams with Steel Fiber Reinforced Composite Jackets". ***International Journal of Engineering, Transactions B: Applications***, Vol. 33, No. 5, (2020), 770-783. doi: 10.5829/ije.2020.33.05b.08
20. Esmaeilnia, O.M., Pashakhani, A., Fekri, S. "Investigation of the effect of different percentages of nanosilica, nano-Aluminium and microsilica on the compressive strength of lightweight structural concrete exposed to fire", ***Second National Congress of Construction Engineering and Evaluation of Civil Projects***, Semnan, Iran. (2015).
21. Ribeiro, M. C. S., Pereira, C. M. C., Sousa, S. P. B., Nóvoa, P. R. O., and Ferreira, A. J. M. "Fire reaction and mechanical performance analyses of polymer concrete materials modified with micro and nano alumina particles***", Restoration of Buildings and Monuments***, Vol. 19, No.2-3, (2013), 195-202. doi: org/10.1515/rbm-2013-6595
22. Elsayd, A. A., and Fathy, I. N. "Experimental Study of Fire Effects on Compressive Strength of Normal-Strength Concrete Supported With Nanomaterials Additives". ***IOSR Journal of Mechanical and Civil Engineering (IOSR-JMCE)***, Vol. 16, No. 1, (2019), 28-37.
23. Self-Compacting Concrete European Project Group. The European guidelines for self-compacting concrete: Specification, production and use. International Bureau for Precast Concrete (BIBM). (2005).
24. ASTM Standard C33/C33M-18. Standard specification for concrete aggregates. ASTM International, West Conshohocken PA, (2018).
25. ASTM D1129-13, Standard Terminology Relating to Water, ASTM International, West Conshohocken, PA, (2013).
26. Ranjbar, M. M., Madandoust, R., Mousavi, S. Y., and Yosefi, S. "Effects of natural zeolite on the fresh and hardened properties of self-compacted concrete". ***Construction and Building Materials***, Vol. 47, (2013), 806-813. doi:10.1016/j.conbuildmat.2013.05.097
27. ASTM Standard C39/C39M-18, Standard test method for compressive strength of cylindrical concrete specimens, ASTM International, West Conshohocken PA, (2018).

28. ASTM Standard C496/C496M-17 Standard test method for splitting tensile strength of cylindrical concrete specimens, ASTM International, West Conshohocken PA, (2017).
29. ASTM C597-09, Standard Test Method for Pulse Velocity Through Concrete, ASTM International, West Conshohocken, PA, (2009).
30. Babu, K. G., and Babu, D,S., "Performance of fly ash concrete containing lightweight EPS aggregates", ***Cement and Concrete Composites***, Vol. 12, (2004), 279-222. doi.org/10.1016/S0958-9465(03)00034-9
31. ASTM C1585-04, Standard Test Method for Measurement of Rate of Absorption of Water by Hydraulic-Cement Concretes, ASTM International, West Conshohocken, PA, (2004).
32. McCarter W. J., Starrs G., Kandasami S., Jones R., and Chrisp M., "Electrode configurations for resistivity measurements on concrete", ***ACI Materials Journal***, Vol. 106, No. 3, (2009), pp. 258-264. doi :10.14359/56550
33. DIN 1048 part 5, Testing of concrete, Testing of hardened concrete (Specimens prepared in mould). German standards, (1991).
34. ACI Committee 211, American Concrete Institute, Farmington Hills, Michigan, (1991).
35. Mazaheripour, h., Gandarpour, S., Mirmoradi, SH., Hosseinpour, I. "The effect of polypropylene fibers on the properties of fresh and hardened lightweight selfcompacting concrete'', ***Constructin and Building Materials***, Vol. 25, (2011), 351-8. doi: org/10.1016/j.conbuildmat.2010.06.018
36. Li, H., Xiao, H.G., Yuan J. and Ou J., "Microstructure of cement mortar with nano-particles***", Composites: Part B***, Vol. 35, (2005), 185-189. doi: org/10.1016/S1359-8368(03)00052-0
37. Ji, T., "Preliminary study on the water permeability and microstructure of concrete incorporating nano-SiO_2", ***Cement and Concrete Research***, Vol. 35, (2005), 1943-1947. doi: org/10.1016/j.cemconres.2005.07.004
38. Li, H., Xiao, H.G., Yuan, J., and Ou, J., "Microstructure of cement mortar with nano-particles", ***Composites: Part B***, Vol. 35, (2005), 185-189. doi: org/10.1016/S1359-8368(03)00052-0
39. Nazari, A., Riahi, S., Riahi, S., Shamekhi, SF., Khademno, A., "Influence of Al_2O_3 nanoparticles on the compressive strength and workability of blended concrete", ***Journal of American Science,*** Vol. 6, No. 5, (2010), 6–9.
40. Arefi, M., Javeri, M., Mollaahmadi, E., "To study the effect of adding Al_2O_3 nanoparticles on the mechanical properties and microstructure of cement mortar". ***Life Science Journal***, Vol. 8, No. 4, (2011), 613-617.
41. Sivakumar, V. R., Kavitha, O. R., Arulraj, G. P., and Srisanthi, V. G. "An experimental study on combined effects of glass fiber and Metakaolin on the rheological, mechanical, and durability properties of self-compacting concrete". ***Applied Clay Science***, Vol. 147, (2017), 123-127. doi: org/10.1016/j.clay.2017.07.015
42. Hilles, M. M., and Ziara, M. M., "Mechanical behavior of high strength concrete reinforced with glass fiber". ***Engineering Science and Technology, An International Journal***, Vol. 22, No. 3, (2019), 920-928. doi: org/10.1016/j.jestch.2019.01.003
43. ACI 318-99, Building Requirements for Structural Concrete and Commentary, American Concrete Institute, Farmington Hills, Michigan, 393, (1999).
44. CEB-FIP Model code. Comite Euro-International du Beton. London: Thomas Telford.Olukan, (1990).
45. Oluokun, F. A. "Prediction concrete tensile strength from its compressive strength: evaluation of existing relations for normal weight concrete". ***ACI Materials Journal***, Vol. 88, No. 3, (1991), 302-309.
46. Zain, M.F.M., Mahmud, H.B., Ilham A, Faizala, M., "Prediction of splitting tensile strength of high-performance concrete", ***Cement and Concrete Research***, Vol. 32, No. 8, (2002), 1251-1258. doi:org/10.1016/S0008-8846(02)00768-8
47. Arío glu, N., Girgin, ZC., Arío glu, E., "Evaluation of ratio between splitting tensile strength and compressive strength for concrete up to 120 MPa and its application in strength criterion". ***ACI Materials Journal,*** Vol. 103, No. 1, (2006), 18-24.
48. Choi, Y and Yuan, RL. "Experimental relationship between splitting tensile strength and compressive strength of GFRC and PFRC". ***Cement and Concrete Research,*** Vol. 35, No. 8, (2006), 1587-1591. doi:org/10.1016/j.cemconres.2004.09.010
49. Mohammadi, J., Ataei, M., Kakaei, R. K., Mikaeil, R., & Haghshenas, S. S., "Prediction of the production rate of chain saw machine using the multilayer perceptron (MLP) neural network". ***Civil Engineering Journal***, Vol. 4, No. 7, (2018), 1575-1583. doi: 10.28991/cej-0309196
50. Rath, B., Deo, S., Ramtekkar, G., "Durable Glass Fiber Reinforced Concrete with Supplimentary Cementitious Materials". ***International Journal of Engineering, Transactions A: Basics***, Vol. 30, No. 7, (2017), 964-971. doi: 10.5829/ije.2017.30.07a.05
51. Hedjazi, S., & Castillo, D., "Relationships among compressive strength and UPV of concrete reinforced with different types of fibers". ***Heliyon***, Vol. 6, No. 3, (2020). doi: org/10.1016/j.heliyon.2020.e03646
52. CEB–FIP. Diagnosis and assessment of concrete structures – state of art report. CEB Bulletin, Euro-International Concrete Committee (Comité Euro- International du Béton***)***, (1989), 83–85.
53. Song, H. W., and Saraswathy, V., "Corrosion monitoring of reinforced concrete structures-a review," ***International Journal of Electrochemical Science***, Vol. 2, (2007), 1–28.
54. Elkey, W., and Sellevold E. J., (1995). "Electrical Resistivity of Concrete", supplement 80, Norwegian Road Research Laboratory, Oslo, Norway.

Persian Abstract

چکیده

نانو ذرات به عنوان افزودنی‌های جدید و تأثیرگذار در کنار الیاف، می‌توانند به نحو مطلوبی خواص بتن خودتراکم را بهبود بخشند. در مطالعه حاضر به بررسی اثرات نانو ذرات اکسید آلومینیوم بر کارایی، خصوصیات مکانیکی و دوام بتن‌های خودتراکم حاوی الیاف شیشه پرداخته شد. الیاف شیشه به مقدار ۰، ۰/۵، ۱ و ۱/۵ درصد و نانوذرات اکسید آلومینیوم به مقدار ۰، ۰/۵، ۱ و ۱/۵، ۲ و ۳ درصد وزنی سیمان استفاده شد. خواص بتن تازه، با آزمایش‌های اسلامپ، T50، قیف V و جعبه L ارزیابی شد. خصوصیات مکانیکی با انجام آزمایش‌های مقاومت فشاری و مقاومت کششی ارزیابی شد. خواص غیر مخرب بتن با استفاده از آزمایش التراسونیک بررسی شد. همچنین دوام نمونه‌ها با استفاده از آزمایش‌های جذب آب، عمق نفوذ آب و مقاومت الکتریکی سنجیده شد. نتایج نشان داد استفاده ترکیبی از نانوذرات و الیاف شیشه نقش تاثیر گذاری بر بهبود خواص مکانیکی بتن دارد؛ بطوریکه به عنوان مثال استفاده ترکیبی از ۲ درصد نانوذرات اکسید آلومینیوم و ۱ درصد الیاف شیشه مقاومت‌های فشاری و کششی بتن‌های خودتراکم را به ترتیب ۵۹ و ۱۱۹/۲ درصد افزایش داده است. نانوذرات آلومینیوم دارای سطح ویژه بسیار بالایی می‌باشند و واکنش‌پذیری آنها سبب می‌شود که با هیدروکسید کلسیم به سرعت واکنش داده و ژل سلیکات- هیدرات تولید کنند. از این رو کریستال‌های هیدروکسید کلسیم کاهش می‌یابد و حفرات موجود در ژل سیمانی پر شده و مقاومت فشاری افزایش می‌یابد. همچنین الیاف شیشه نیز با محدود کردن امتداد ترک‌ها می‌تواند گزینه مناسبی در ترکیب با نانوذرات اکسید آلومینیوم با هدف افزایش مقاومت کششی بتن‌های خودتراکم باشد. استفاده از نانوذرات اکسید آلومینیوم در کنار الیاف شیشه سبب می‌شود که میزان جذب آب در مقایسه با نمونه فاقد این مواد کمتر شود. این مسئله از خواص موثر نانوذرات اکسید آلومینیوم می باشد که سبب می‌شود با کاهش جذب آب، مقاومت در مقابل عوامل نامساعد محیطی افزایش یابد. افزودن نانوذرات اکسید آلومینیوم به نمونه‌های حاوی و فاقد الیاف شیشه باعث افزایش خیلی زیاد مقاومت الکتریکی شد. نانوذرات اکسید آلومینیوم با پر کردن حفرات ریز و افزودن بر تراکم بتن، مانع تحرک هر چه بیشتر یون‌ها در بتن گردید و بدین ترتیب خوردگی بتن کاهش یافت.

IJE TRANSACTIONS A: Basics Vol. 34, No. 01, (January 2021) 39-45

International Journal of Engineering

Journal Homepage: www.ije.ir

Structural Behavior of Hollow-core One Way Slabs of High Strength Self-compacting Concrete

A. A. Mahdi*, M. A. Ismael

Civil Engineering Department, College of Engineering, University of Diyala, Diyala, Iraq

P A P E R I N F O

Paper history:
Received 09 May 2020
Received in revised form 06 August 2020
Accepted 26 August 2020

Keywords:
Hollow-core Slab
High Strength
Reinforced Concrete
Self-compacting Concrete

A B S T R A C T

Reinforced concrete hollow-core slab (HCS) is a new type of lightweight slabs in which the longitudinal voids provide the ability to reduce the concrete amount. Reducing the concrete amount causes a reduction of the dead loads which consequently leads to cost-saving, fast construction, and getting long-span. The experimental program includes constructing and testing slab species with dimensions 1700×435×125mm to investigate the effect of eliminating concrete ratio by changing the size of the longitudinal void and the number of longitudinal voids on the performance of HCS. The experimental results showed that elimination of the concrete with percentages 10.83, 17.20 and 24.37% from the hollow-core high strength slabs using three longitudinal voids of diameters 50, 63, and 75mm, respectively, resulted in saving the ultimate strength by 90.06, 87.84 and 85.07%, and increasing the ultimate deflection by 5.48, 10.80 and 17.44%. While, elimination of the concrete with percentages 16.25, 24.37 and 32.50% from the hollow-core high strength slabs using two, three, and four longitudinal voids of 75mm diameter resulted in saving the ultimate strength with percentages 89.29, 85.07 and 80.61%, and increasing the ultimate deflection with percentages 7.57, 17.44 and 22.81% respectively when compared with the reference solid slab.

***doi**: 10.5829/ije.2021.34.01a.05*

NOMENCLATURE

Hollow-core slab	HCS	American Society for Testing and Materials	ASTM
Near-surface mounted	NSM	Shear span to effective depth ratio	a/d
Concrete compressive strength	*fc*	American Concrete Institute	ACI
Linear variable deflection transducer	LVDT	British Standards	BS
Solid slab	**SS**		

1. INTRODUCTION

Reinforced concrete slabs are the members that used as floors and roofs in the building and used in the decks of bridges [1]. The floor system can tack many forms such as solid slabs, precast slabs, and ribbed slabs, the slabs may be supported on a concrete beam, steel beam, and wall or directly on the column [1]. Several attempts in the past have been carried out on reinforced concrete slabs to reduce its self-weight with a minimum reduction in the flexural capacity of the slabs, the reduction in the self-weight of the slab will reduce the deflection and will make slabs with larger span length without using intermediate supports [2]. Waffle, Bubbled and Hollow-core slabs were used to reduce the slab self-weight and to provide slabs with a long span [2]. Hollow-core slab (HCS) is a concrete slab with continuous voids that extend through the long direction of the slab, these voids provided for reducing the weight and cost of the slabs and for running the mechanical or electrical facilities. The HCS provides high structural efficiency with low material consumption [3]. Pajari [4] has made an experimental program to study the pure torsion tests on pre-stressed hollow-core slabs, the result showed that the

*Corresponding Author Email: ahmad_abbas_87@yahoo.com (A. A. Mahdi)

Please cite this article as: A. A. Mahdi, M. A. Ismael, Structural Behavier of Hollow-core One Way Slabs of High Strength Self-compacting Concrete, International Journal of Engineering, Transactions A: Basics Vol. 34, No. 01, (2021) 39-45

torsional stiffness of the hollow-core with 400mm depth was so close to the predicted values of the elementary calculation. Cuenca and Serna [5] studied the effect of steel fiber on the behavior of hollow-core slabs, the result showed that using the steel fiber in the hollow-core slabs gives higher shear capacity than slabs without steel fibers and increased the ductile behavior of the hollow-core slab. Sarma and Prakash [6] studied the effect of cut-outs (openings) on the pre-stressed hollow-core slabs, the test results showed that presence of the opening at the center of slabs causes a reduction in the ultimate load by 44% due to the local cracks around the opening and failure of the slab. Kankeri and Prakash [7] studied strengthening the hollow-core slab by bonded overlay and by near-surface mounted (NSM) glass fiber reinforced polymer bar, the researcher found that Strengthening the hollow-core slabs by hybrid the NSM with the bonded overly increase the ultimate load by 238% without compromise the ductility when compared with the reference slab. Al-Azawi and Abdul Al-Aziz [8] have made an experimental program to study the lightweight aggregate hollow-core slabs, the test result showed that using the lightweight aggregate hollow-core slabs with constant (a/d=2.9) gives a reduction in self-weight by 32.92% and reduction in the ultimate load and the first crack load by 5.18% and 12%, respectively when compared with the solid slab. Khalil, et al. [9] studied the shear behavior in composite hollow-core Slab, the researcher found that using the longitudinal steel reinforcement in the hollow-core slab delayed the apparition of the shear crack and reduce the crack width. Lee, et al. [10] studied the shear performance of hollow core slab, the researcher found that the shear performance satisfied the requirements of ACI 318-19. Mahdi and Ismael [11] studied normal strength hollow core slabs, the result thowed that using the HCS can save the ultimate load by 82.92 to 93.47%, but the ultimate deflection increased by 6.58 to 28.31%. From the previous studies which dealt with the field of the structural behavior of hollow-core slabs, it can be noted that most of these studies focused on investigating the effect of using concrete topping, strengthening, using steel fiber, cutout (opening), and some other parameters, but did not study the effect of the reduction the concrete volume on the structural behavior of hollow-core high strength slabs. Therefore, this paper presents an experimental study to investigate the effect of eliminating concrete ratio by changing the size of the longitudinal void (50mm, 63mm, and 75mm) and the number of longitudinal voids (two, three, and four) on the structural behavior of hollow-core high strength self-compacted concrete slabs. In hollow-core slabs, the recycled plastic pipes were placed in the middle of the slab thickness where the flexural stress is minimum, to eliminate some amount of concrete. This process leads to reduce the self-weight of the slabs and therefore it leads to reducing the embedded energy and the CO_2 emission from the cement industry and this process is considered environmental-friendly action which contributes to the sustainability process. Figure 1 shows the research methodology of this paper.

2. EXPEREMENTAL PROGRAM

2. 1. Slabs Description The experimental program includes casting and testing six reinforced high strength self-compacted concrete one-way slabs, all the slab have 1700mm length, 435mm width, and 125mm thickness, these slabs were divided into two groups as they are presented in Table 1. The first group consists of one solid slab as a control slab and three hollow-core slabs which have three longitudinal voids with a different diameter (50mm, 63mm, and 75mm) with designation names 3V50, 3V63, and, 3V75, chosen these diameters due to existent these pip diameters in the market. Also, these diameters satisfy the planned percentages of eliminating concrete. The purpose of this group is to study the effect of longitudinal voids diameter on the structural behavior of high strength hollow-core slabs, and the second group consists of the same solid slab in group one and three

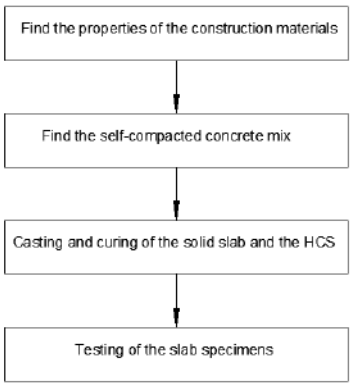

Figure 1. The research methodology

TABLE 1. Experimental parameters details

Group No.	Parameter	Slab designation	Number of longitudinal vids	Diameter of longitudinal voids (mm)
1	Longitudinal voids diameter	SS	---	---
		3V50	3	50
		3V63	3	63
		3V75	3	75
2	Longitudinal voids number	SS	---	---
		2V75	2	75
		3V75	3	75
		4V75	4	75

hollow-core slabs with different numbers of 75mm diameter longitudinal voids (two, three, and four) with designations name 2V75, 3V75, and 4V75 respectively. The slab 3V75 is the same slab in the first group, the purpose of this group is to study the effect of longitudinal voids numbers on the structural behavior of high strength hollow-core slab. Figures 2-4 show details of the solid and hollow-core slabs in groups one and two, respectively.

2. 2. Materials

• Cement: The ordinary Portland cement (type I) was used in this work. This cement has physical properties and chemical composition which confirm according to British Standards Institution (BS 12) [12].

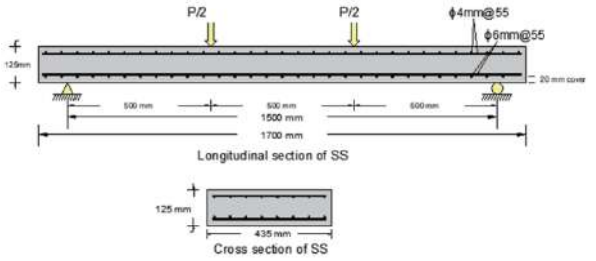

Figure 2. Details of the solid slab

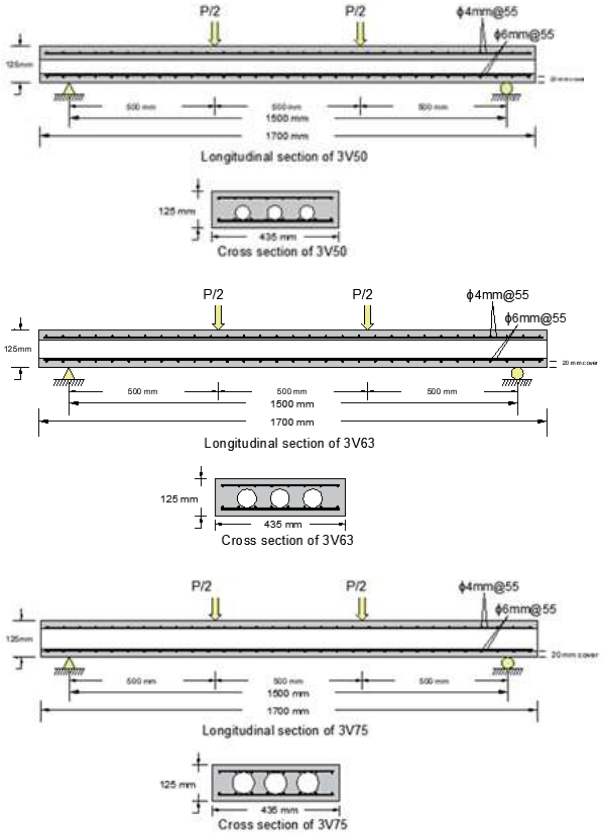

Figure 3. Details of the HCS slabs in group one

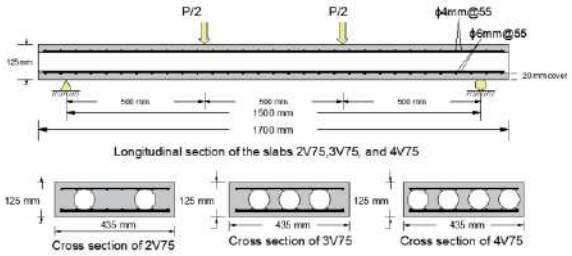

Figure 4. Details of the HCS slabs in group two

• Fine Aggregate: The used fine aggregate has 2.38 fineness modulus, the grading and the physical properties of this fine aggregate indicated that it is within the Limits of B.S.882 [13].

• Coarse Aggregate: The maximum size of the used coarse aggregate is 14mm, the grading and the physical properties of this coarse aggregate are within the Limits of B.S.882 [13].

• Limestone Powder: The ground limestone powder was used in this work as a filler to get better cohesiveness and better segregation resistance, it has a particle size less than 0.125mm according to EFNARC, [14]

• Superplasticizer: The third generation of high-performance superplasticizers (ViscoCrete®-5930L) was used for producing self-compacted concrete. This superplasticizer meets the requirement of ASTM C494 type F [15].

• Steel Reinforcement: Deformed steel bars with diameters of 6mm and yield stress of 497Mpa were used as main steel reinforcement and deformed steel bars with a diameter of 4mm and yield stress of 430Mpa were used as secondary steel reinforcement, the steel reinforcement bars were tested according to ASTM A615/A &M [16]

• Plastic Pipes: The recycled plastic pipes were used to create the longitudinal voids in the hollow-core slabs, these pipes have different diameters (50mm, 63mm, and 75mm).

2. 3. Concrete Mixture In this study, the trail mixes were made many times to obtain the concrete mixture which has 60.8MPa compressive strength at 28 days, these concrete mixture satisfied the requirement of the high strength self-compacted concert according to EFNARC [14] and European guidelines [17]. Table 2 shows the concrete mixture of quantities. Measuring the concrete compressive strength (*fc*) is done by testing three cylindrical concrete for each slab specimens with dimensions 150mm and 300mm according to ASTM C39/C39M-15a [18].

2. 4. Test Specimens The slab specimens were tested by using a universal hydraulic machine with a capacity of 600kN. Before starting the applied load, the linear variable deflection transducer sensor (LVDT) was fixed in the bottom mid-span slabs to measure the

TABLE 2. Quantities of the concrete mixture per cubic meter

Materials	Cement	Sand	Gravel	Limestone powder	Water	Superplasticizer
Quantities (kg/m^3)	550	855	767	50	150	20

deflection. Also, an electrical strain gauge was fixed in the center of top mid-span slabs to measure the concrete strain during increasing the applied load. The slabs were tested as a simply supported slab under two-point loads with a clear span of 1500mm as shown in Figure 5.

3. RESULTS AND DISCUSSION

3. 1. First Crack Load and Ultimate Load Capacity

Table 3 shows the first crack load and the ultimate strength of all the tested slabs, it can be noted that elimination of the concrete with percentages 10.83, 17.20 and 24.37% from the hollow-core high strength slabs 3V50, 3V63, and 3V75, respectively cause a reduction in cracking load by 5.58, 8.37 and 13.49%, and reduction in ultimate strength by 9.94, 12.16 and 14.93%. Also, elimination the concrete with percentages 16.25, 24.37 and 32.50% from the hollow-core high strength slabs 2V75, 3V75, and 4V75 with two, three, and four longitudinal voids with diameter 75mm, respectively; resulted in reducing the first crack load with percentages 8.84, 13.49 and 17.21%, and reducing the ultimate strength with percentages 10.71, 14.93 and 19.39%. These decreases can be attributed to the presence of the longitudinal voids which leads to decrease the moment of inertia of the beam section; thus, the flexural rigidity will decrease with increasing diameter or number of longitudinal voids in the hollow core slabs. Figure 6 shows the reduction in ultimate load of the hollow core slabs with different diameter and number of longitudinal voids, it can be noted in this figure that increasing diameter of longitudinal voids has more effect on the reduction in ultimate load than increasing number of longitudinal voids due to increase in approaching the longitudinal voids from the compression zone with increasing the diameter of longitudinal voids, so, the optimum slab in this study was the slab 3V50 to preserve the ultimate strength and satisfy the economical consideration.

Figure 5. Testing of the slab specimens

3. 2. Load-deflection Relationship

Figures 7 and 8 show the load-deflection curve of the solid and hollow-core high strength slabs with different diameter and number of longitudinal voids, respectively; it can be noted that elimination of the concrete with percentages 10.83, 17.20 and 24.37% from the hollow-core high strength slabs 3V50, 3V63, and 3V75, respectively cause an increase in the ultimate deflection by 5.48%, 10.80 and 17.44%. Also, elimination the concrete with percentages 16.25, 24.37 and 32.50% from the hollow-core high strength slabs 2V75, 3V75, and 4V75 with two, three, and four longitudinal voids with diameter 75mm, respectively; result in increased the ultimate

TABLE 3. The first crack load and ultimate strength of all the tested slabs

Group No.	Slab designation	Elimination concrete (%)	Cracking load Pcr (kN)	Decrease (%)	Ultimate load Pu (kN)	Decrease in Pu%
	SS	---	21.5	---	71.32	---
1	3V50	10.83	20.3	5.58	64.23	9.94
	3V63	17.20	19.7	8.37	62.73	12.16
	3V75	24.37	18.6	13.49	60.67	14.93
	SS	---	21.5	---	71.32	---
2	2V75	16.25	19.6	8.84	63.68	10.71
	3V75	24.37	18.6	13.49	60.67	14.93
	4V75	32.50	17.8	17.21	57.49	19.39

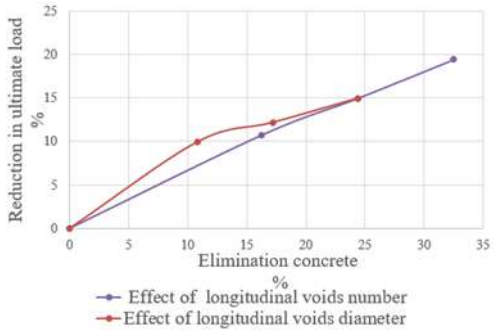

Figure 6. The reduction in ultimate load of HCS with different diameter and number of longitudinal voids

deflection with percentages 7.57, 17.44 and 22.81%, this increase in the ultimate deflection of the HCS belong to the presence of the longitudinal voids which leads to decrease the moment of inertia of the beam section thus, the flexural rigidity will decrease with increasing diameter or number of longitudinal voids.

3. 3. Load-strain Relationship Figure 9 shows the effect of longitudinal voids diameter on the concrete compressive strain and steel tensile strain of the hollow-core high strength slabs. It can be noted that elimination of the concrete with percentages 10.83, 17.20 and 24.37% from the hollow-core high strength slabs 3V50, 3V63, and 3V75 with three longitudinal voids with diameter 50, 63, and 75mm, respectively; resulted in increased the ultimate concrete strain with percentages 14.14, 24.14 and 30.40%, and decreased the ultimate steel strain with percentages 10.59, 13.36 and 16.56%. Figure 10 shows the effect of longitudinal voids number on the concrete compressive strain and steel tensile strain of the HCS. It can be noted that elimination the concrete with percentages 16.25, 24.37 and 32.50% from the hollow-core high strength slabs 2V75, 3V75, and 4V75 with two, three, and four longitudinal voids with diameter 75mm, respectively; resulted in increased the ultimate concrete compressive strain with percentages 22.95, 30.40 and 38.95%, and decreased the ultimate steel strain with percentages 9.81, 16.56 and 32.25%. Increasing the concrete compression strain belong to the presence of the longitudinal voids in the hollow-core slabs which leads to eliminating part of concrete from the middle of the slabs and focusing the stress in the region between the plastic pipes. Decreasing the steel tensile strain of hollow-core slabs can be attributed to reducing the ultimate strength of the hollow-core high strength slabs with increasing diameter or number of longitudinal voids.

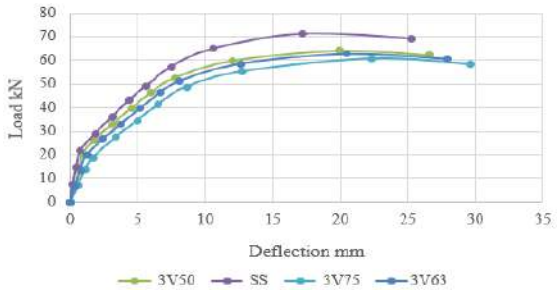

Figure 7. Effect of longitudinal voids diameter on the load-deflection curve of hollow-core high strength slabs

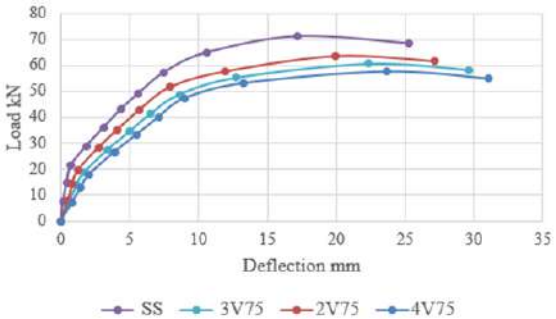

Figure 8. Effect of longitudinal voids number on the load-deflection curve of hollow-core high strength slabs

3. 4. Crack Pattern and Failure Mode The first observed crack is first seen in the middle bottom at the

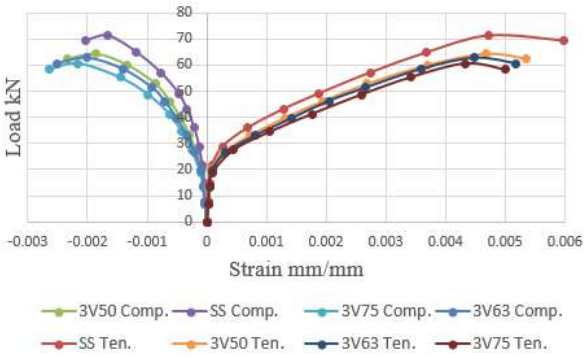

Figure 9. Effect of longitudinal voids diameter on the concrete compressive strain and steel tensile strain of the HCS

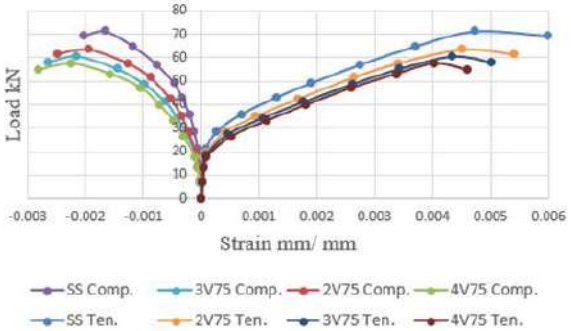

Figure 10. Effect of longitudinal voids number on concrete compressive strain and steel tensile strain of the HCS

tension zone of all the slabs when the concrete tensile stress exceeds the value of its tensile strength, after increasing the applied load other cracks appeared at right and left of the first crack, these cracks extended upward and the flexural shear cracks appear in the hollow-core slabs. The flexural failure occurred in all the slabs when one of the cracks in the middle of slabs split into two directions before it reaches the upper face of the slab. The increasing diameter of longitudinal voids in hollow-core high strength slabs decrease the number of crack from 13 in the solid slab to 12, 12, and 11 in hollow-core slabs (3V50, 3V63, and 3V75), and increases the crack width of the hollow-core slabs at yield load by 13.83, 27.4 and 39.13%, respectively when compared with the solid slab. Also, an increasing number of longitudinal voids in the hollow-core slabs from two to three and four decreases the number of cracks from 13 in the solid slab to 12, 11, and 8 respectively in hollow-core slabs (2V75, 3V75, 4V75), but the crack width of the hollow-core slabs at yield load increased by 21.74, 39.13 and 56.52%, respectively when compared with the reference solid slab. Extend the cracks up will be gradually in the solid slab, but in the hollow-core slabs extended the cracks will be opposed by the plastic pipes, so the path of the cracks deviate around the plastic pipes, this leads to increase length and width of the cracks and delay the spread of the cracks and that lead to decrease the number of cracks in hollow-core slabs. Figures 11 and 12 show the effect of longitudinal voids diameter and number respectively on the crack pattern of hollow-core high strength slabs.

Figure 11. Effect of longitudinal voids diameter on crack pattern of hollow-core high strength slabs

Figure 12. Effect of longitudinal voids number on crack pattern of hollow-core high strength slabs

4. CONCLUSION

Using the hollow-core slab was a very effective method to reduce the self-weight of the slabs with maintaining most of the structural behavior of the solid slabs as they are presented below:

1. Elimination of the concrete with percentages 10.83, 17.20 and 24.37% from the hollow-core high strength slabs with three longitudinal voids with diameter 50, 63, and 75mm respectively gives a reduction in cracking load by 5.58, 8.37 and 13.49%, saving the ultimate strength by 90.06, 87.84 and 85.07%, and increasing the ultimate deflection by 5.4, 10.80 and 17.44%.
2. Elimination of the concrete with percentages 16.25, 24.37 and 32.50% from the hollow-core high strength slabs with two, three, and four longitudinal voids with diameter 75mm respectively, resulted in reducing the first crack load with percentages 8.84, 13.49 and 17.21%, saving the ultimate strength with percentages 89.29, 85.07, 80.61%, and increasing the ultimate deflection with percentages 7.57, 17.44 and 22.81%.
3. The ultimate concrete compressive strain of the high strength hollow-core slabs was larger than the ultimate strain in solid slab and increased with increasing diameter or number of longitudinal voids.
4. The high strength hollow-core slabs make a reduction in ultimate steel tensile strain by 10.59%, 13.36%, and 16.56% with an increasing diameter of longitudinal voids, and by 9.81%, 16.56%, and 23.25%, respectively; with increasing number of longitudinal voids.
5. Increasing the diameter of longitudinal voids have more effect on the reduction in the ultimate load than the increasing number of longitudinal voids.

6. There is a good agreement with existing reported data in terms of saving the ultimate load and the load-deflection relationship
7. The crack width increased and the number of cracks decreased with increasing diameter or number of longitudinal voids.

5. REFERENCES

1. Mosley, W. H. & Bungey, J. H., "Reinforced Concrete Design", Third edition, Macmillan, (2012).
2. Marais, C. C., "Design Adjustment Factors and the Economical Application of Concrete Flat-slabs with Internal Spherical Voids in South Africa" (Doctoral dissertation, University of Pretoria), (2009).
3. Stephen, C., "Hollow Core Manufacturing and Factory Design", ***Indian Concrete Journal***, (2013), 20-25.
4. Pajari, M., "Pure Torsion Tests on Single Hollow Core Slabs" ***Espoo VTT Tiedotteita***, Vol. 2273, (2004), 28-29.
5. Cuenca, E., & Serna, P., "Failure Modes and Shear Design of Prestressed Hollow Core Slabs Made of Fiber-reinforced Concrete", ***Composites Part B: Engineering***, Vol. 45, No. 1, (2013), 952-964, doi: 10.1016/j.compositesb.2012.06.005.
6. Sarma, P. S. K., & Prakash, S. S., "Performance of Prestressed Hollow Core Slabs with and without Cutouts", ***International Journal of Research in Engineering and Technology***, Vol. 4, No. 13, (2015), 443-447, doi: 10.15623/ijret.2015.0425066.
7. Kankeri, P., & Prakash, S. S., "Experimental Evaluation of Bonded Overlay and NSM GFRP Bar Strengthening on Flexural Behavior of Precast Prestressed Hollow Core Slabs", ***Engineering Structures***, Vol. 120, (2016), 49-57, doi: 10.1016/j.engstruct.2016.04.033.
8. Al-Azzawi, A. A., & Abdul Al-Aziz, M. A., "Behavior of Reinforced Lightweight Aggregate Concrete Hollow-core Slabs", ***Computers and Concrete***, Vol. 21, No. 2, (2018), 117-126.
9. Khalil, A. A., El Shafiey, T. F., Mahmoud, M. H., Baraghith, A. T., & Etman, A. E., "Shear Behavior of Innovated Composite Hollow Core Slabs", International Conference on Advances in Structural and Geotechnical Engineering, (2019).
10. Lee, Y. J., Kim, H. G., Kim, M. J., Kim, D. H., & Kim, K. H., "Shear Performance for Prestressed Concrete Hollow Core Slabs", ***Applied Sciences***, Vol. 10, No. 5, (2020), 1636, doi: 10.3390/app10051636.
11. Mahdi, A. A. and Ismael M. A., "Structural Behaviour of Hollow Core Reinforced Self Compacting Concrete One Way Slabs", IOP Conference Series: Materials Science and Engineering, Vol. 888 (2020), 10.1088/1757-899X/888/1/012019.
12. BS 12, "Specification for Portland cement" British Standard Institution, (1996), doi: 10.3403/00662547.
13. B.S. 882, "Specification for Aggregates from Natural Sources for Concrete", British Standard Institution, 3-9, (1992), doi: 10.3403/00047290u.
14. EFNARC, F., "Specification and Guidelines for Self-compacting Concrete", European federation of specialist construction chemicals and concrete system, (2002).
15. ASTM C-494/C-494M, "Standard Specification for Chemical Admixtures for Concrete", American Society for Testing and Materials, (2015), doi: 10.1520/c0494_c0494m-15a.
16. ASTM A 615/A 615M, "Standard Specification for Deformed and Plain Billet-Steel Bars for Concrete Reinforcement" American Society for Testing and Materials, (2009), doi: 10.1520/a0706_a0706m-08a.
17. Self-Compacting Concrete European Project Group, "The European guidelines for self-compacting concrete: Specification, production and use", International Bureau for Precast Concrete (BIBM), (2005).
18. ASTM C39/C39M, "Standard Test Method for Compressive Strength of Cylindrical Concrete Specimens", American Society for Testing and Materials, (2015), doi: 10.1520/c0039_c0039m-15a.

Persian Abstract

چکیده

دال هسته توخالی بتن آرمه (HCS) نوع جدیدی از اسلب های سبک است که در آن حفره های طولی توانایی کاهش مقدار بتن را فراهم می کنند. کاهش مقدار بتن باعث کاهش بارهای تلف شده می شود که در نتیجه منجر به صرفه جویی در هزینه ها ، ساخت سریع و طولانی شدن مدت می شود. این برنامه آزمایشی شامل ساخت و آزمایش گونه های دال با ابعاد ۱۷۰۰×٤۳٥× ۱۲٥ میلی متر برای بررسی اثر حذف نسبت بتن با تغییر اندازه خلا طولی و تعداد حفره های طولی بر عملکرد HCS است. نتیجه آزمایشی نشان داد که حذف بتن با درصد ۱۰,۸۳٪ ، ۱۷,۲۰٪ و ۲٤,۳۷٪ از اسلبهای با مقاومت بالا در هسته توخالی با استفاده از سه حفره طولی به قطر ٥۰ ، ٦۳ و ۷٥ میلی متر به ترتیب باعث صرفه جویی در مقاومت نهایی توسط ۹۰,۰٦، ۸۷,۸٤ و ۸٥,۰۷٪ و افزایش انحراف نهایی ٥,٤۸، ۱۰,۸۰ و ۱۷,٤٤٪. در حالی که ، حذف بتن با درصد ۱٦/۲٥، ۲٤/۳۷ و ۳۲/٥۰ ٪ از اسلبهای با مقاومت بالا در هسته توخالی با استفاده از دو حفره طولی دو ، سه و چهار طول قطر ۷٥ میلی متر منجر به صرفه جویی در مقاومت نهایی با درصد ۸۹/۲۹ ، ۸٥/۷ درصد گردید ، و ۸۰,٦۱، ، و افزایش انحراف نهایی به ترتیب با درصد ۷,٥۷، ، ۱۷,٤٤، و ۲۲,۸۱ در مقایسه با دال جامد مرجع گردید.

International Journal of Engineering

Journal Homepage: www.ije.ir

Blast Demand Estimation of RC-moment-resisting Frames using a Proposed Multi-modal Adaptive Pushover Analysis Procedure

K. K. Kiran[a], E. Noroozinejad Farsangi*[b]

[a] *SJB Institute of Technology, Bangalore, Karnataka, India*
[b] *Faculty of Civil and Surveying Engineering, Graduate University of Advanced Technology, Kerman, Iran*

P A P E R I N F O

Paper history:
Received 16 September 2020
Received in revised form 23 October 2020
Accepted 26 October 2020

Keywords:
Blast Load
Drift Ratio
Modal Pushover Analysis
Multi-mode Adaptive Pushover
Nonlinear Response History Analysis
Storey Drift

A B S T R A C T

The procedure of estimating the RC moment-resisting frames under blast loading using a multi-mode adaptive pushover (MADP) analysis is investigated in the current study. The main advantage of the proposed procedure is the combination of the multi-mode and adaptive pushover analysis approaches, which has not been done in the past for blast loadings. To investigate the efficiency of the proposed approach, several RC moment-resisting frames (RC-MRFs) of the 4-, 8-, and 20- storey are considered in the study. For a better comparison, the conventional modal pushover analysis (MPA), nonlinear response history analysis (NRHA), and the proposed approach are considered in the simulations. To this end, various influential parameters including the lateral force, floor displacement, storey drift, storey drift ratio, etc. are considered. For all models, the first three mode shapes were considered in the analysis procedure, while for the case of 20 storey RC-MRF, the torsional effect is included as well. The results indicated that the proposed MADP procedure has adequate accuracy and efficiency to estimate the blast loading demand on RC-MRFs.

doi: *10.5829/ije.2021.34.01a.06*

1. INTRODUCTION[1]

The process of evaluation and design of a structure or elements due to imposed loading can be performed by pushover analysis [1]. The loading pattern for assessing the two- or three-dimensional structures due to lateral loadings which includes linear or nonlinear responses, is mainly based on inertia forces obtained at masses [2]. The structure will then be pushed under these load patterns to reach a pre-defined target displacement [3]. The strength and deformation demands are estimated for the compared available capacities can also be calculated by the inertial forces and deformations at the target displacement levels. This phenomenon is known as pushover analysis [4].

In turkey, the structures are constructed by using precast concrete technologies. These structures were subjected to seismic load and the peak responses were obtained [5].

In some previous studies, the influence of vertical and plan irregularities of the building has been carried out. In the next stage, the results obtained from inelastic dynamic analysis such as inter-storey drifts and plastic rotations correlates by the modified pushover analysis [6]. Many researchers have also considered a single degree of freedom (SDOF) system to estimate the collapse capacity of a structural system due to seismic loading by considering the P-Δ effect [7–13]. In another research, different building structures collapse capacities were analyzed by pushover analysis, and results were compared with nonlinear incremental dynamic analysis. The pushover analysis is simple, efficient, accurate, and lucid while predicting the collapse capacity of different types of structures [2]. Hasan et al. have investigated the nonlinear, inelastic, ideal, rigid, or pinned connections frame structure under earthquake loadings by pushover analysis [14].

Hundreds of different properties and the number of stories of a generic structure were developed in the study of Manafpour and Jalikhani. All structures were exposed to seismic loading and analyses were carried out by

*Corresponding Author Institutional Email: *noroozinejad@kgut.ac.ir* (E. Noroozinejad Farsangi)

Please cite this article as: K. K. Kiran, E. Noroozinejad Farsangi, Blast Demand Estimation of RC-moment-resisting Frames using a Proposed Multi-modal Adaptive Pushover Analysis Procedure, International Journal of Engineering, Transactions A: Basics, Vol. 34, No. 1, (2021) 46-55

pushover analysis. The authors have estimated the median seismic collapse capacity by pushover analysis without considering dynamic analysis [15].

In another study by Rahmania et al., the seismic behavior of tall inelastic structures considering higher modes was studied by pushover analysis. The responses of progressive changes in dynamic properties have been identified. To this aim, two steel frames were analyzed by various methods such as upper bound, adaptive upper bound, modal pushover analysis, and nonlinear time history analysis. Among the investigated methods, adaptive upper bound analysis has given the most accurate results [16, 17]. In another study, the lateral displacement profile of the moment-resisting frame structure is estimated by mechanics-based procedure or pushover analysis [18]. In the study of Hall, the seismic analysis of a twenty storey building was analyzed by nonlinear pushover analysis approach [19]. Nonlinear static pushover analysis has also been used to analyze the high-rise structures exposed to seismic force by considering the torsion factor [20].

In the study of Hassan and Reyes, the mid-rise special moment-resisting frames exposed to seismic loadings were analyzed by using modal pushover analysis. The results showed the accuracy of the method compared to nonlinear response history analysis [21]. The limitation of the nonlinear static analysis in terms of the computational effort is saved by modal pushover analysis. The symmetrical and unsymmetrical plan multi-story concrete buildings exposed to seismic force were analyzed by modal pushover analysis in several references [22–27].

The multi-storey structures responses exposed to seismic load were calculated by the Newmark-β method [28–30]. The response due to blast load on a single degree of freedom structures is shown in [31]. The use of damper devices and base isolations techniques were investigated to reduce the responses [32, 33].

The accuracy of the modified modal pushover analysis of a different frame building with ground motion is compared by modal pushover analysis. The higher vibration modes with a linear elastic frame are analyzed by modified modal pushover analysis. The modified pushover analysis saves computational time and effort compare to modal pushover analysis [34]. The higher mode of vibrations of the midrise base isolation system with seismic load response can be calculated by using modal pushover analysis [35, 36]. MPA gives superior results for the response of two actual buildings of 19 and 52 stories with seismic force [37]. The three-steel frames of 3, 9, and 20 stories structures with seismic load analysis were carried out using the floor response spectrum approach. The floor response spectrum is the advanced version of the modal pushover analysis [38]. The three-dimensional analysis for an unsymmetrical both plan and elevations of a frame structure exposed to ground motions data considering two horizontal components is analyzed by modal pushover analysis and the results show the accuracy compare to nonlinear static pushover analysis [39–41]. The unsymmetrical plan for 10, 15, and 20 storey models considering soil-structure interactions were analyzed by consecutive modal pushover analysis [42].

In the study of Maysam Jalilkhani et al, the seismic analysis was carried out by multi-mode adaptive pushover analysis (MADP) for RC moment resisting frames of 4-,8-,12- and 20- stories [43].

Saedi-Daryan et al., the detailed stepwise procedure was explained for the response of the structure exposed to blast load by MPA [44]. The eight-storey structure with shear wall exposed to blast load response was calculated and compared with other methods of nonlinear dynamic analysis [45].

The influence of blast load waves on nonlinear structure responses was calculated by differential equations. The responses were calculated for different mode shapes [45, 46].

Antoniou and Pinho proposed the displacement-based adaptive based pushover analysis method for the response of the MDOF system exposed to seismic loading [47]. Balram Gupta and Sashi K Kunnath proposed the adaptive pushover analysis method for determining the response of mid-rise and high rise structures exposed to seismic load by considering the higher modes [45, 48]. Adaptive based pushover analysis method is considered for obtaining the nonlinear seismic response of structures [49, 50].

The current study is focused on three different frame types that are low rise, mid-rise, and high-rise RC-MRFs under blast loading. To this end, the blast loading effect on 4-, 8- and 20 storey RC-MRFs were carried out by three different analyses approaches. The investigated methods have been the modal pushover analysis (MPA), non-linear response history analysis (NRHA), and the proposed multi-mode adaptative pushover analysis (MADP). Simulations have been carried out using the MATLAB platform and the results indicated the accuracy and efficiency of the proposed MADP procedure for RC-MRFs.

2.TORSION

The torsional effect of the lateral coupling is considered for the analysis of the RC-MRF. The irregularity indices and torsional factors are considered. The following equations are used to calculate the eccentricity of a given storey in the X and Y directions [51–54]:

$$e_{kx} = x_r - x_m \quad (1)$$

$$e_{ky} = y_r - y_m \quad (2)$$

where (x_m, y_m) and (x_r, y_r) are coordinates of the centre of mass and centre of rigidity, respectively. The

following equations are used to determine the coordinates:

$$x_r = \frac{\sum K_{yi} x_i}{\sum K_{yi}} \quad (3)$$

$$y_r = \frac{\sum K_{xi} y_i}{\sum K_{xi}} \quad (4)$$

where k_{xi} and k_{yi} are the lateral stiffnesses of floor 'i' along the global X and Y directions. The torsional radius (r_k) are given in below equations

$$r_{kx} = \sqrt{\frac{\sum (K_{xi}.(y_i - y_r)^2) + (K_{yi}.(x_i - x_r)^2)}{\sum K_{yi}}} \quad (5)$$

$$r_{ky} = \sqrt{\frac{\sum (K_{xi}.(y_i - y_r)^2) + (K_{yi}.(x_i - x_r)^2)}{\sum K_{xi}}} \quad (6)$$

The mass radius of gyration of a particular floor is given by

$$r_m = \sqrt{\frac{\sum m_i {d_i}^2}{(m_i)}} \quad (7)$$

where m_i is the lumped mass at the radial distance d_i from centre of mass. The torsional angle is obtained from below equations [51].

$$\theta = \tan^{-1} {}^{\alpha}/_{0.01H} * R \quad (8)$$

where θ is the angle of the inclination, α is the blast load angle, R is the range and H is the height of each floor. The torsional stiffness is given by

$$K_\theta = K_x * \frac{B^2}{2} + K_y * \frac{D^2}{2} \quad (9)$$

where K_θ is the torsional stiffness, while K_x, K_y is the stiffness along X and Y directions, B and D are the length along X and Y directions, respectively.

3. MULTI-MODE ADAPTIVE PUSHOVER ANALYSIS

In this section, the blast load response on the RC moment-resisting frames is calculated by using a multi-mode adaptive displacement-based pushover analysis procedure. Figure 1 represents the flowchart of the multi-mode adaptive pushover analysis.

The following equations are used for the nonlinear analysis of the frame:

$$\widehat{D_n} = \exp\left[\frac{\sum_{i=1}^{N} \ln D_i}{N}\right] \quad (10)$$

where D_i is the absolute peak deformation, and N is the number of the blast wave.

$$u_{rnt} = \emptyset_{nr} \Gamma_n \widehat{D_n} \quad (11)$$

Figure 1 shows the algorithm of multi-mode adaptive pushover analysis. The multi-mode adaptive pushover analysis consumes less time, gives more accurate results compared with other methods of pushover analysis.

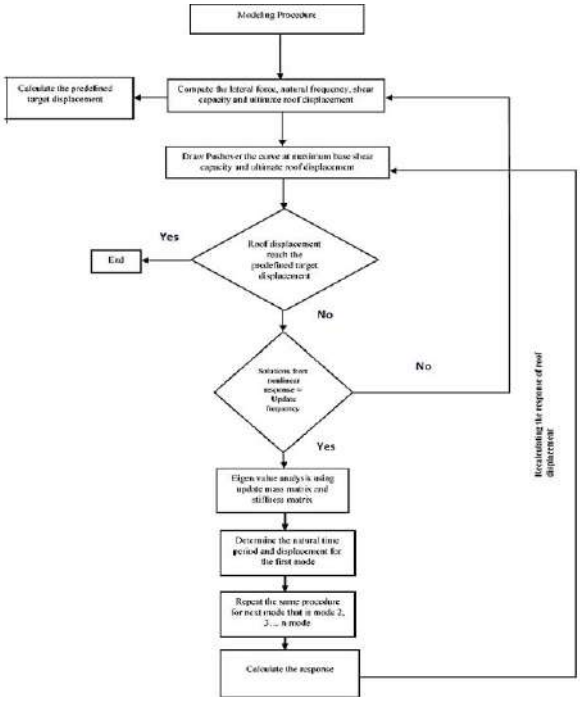

Figure 1. Flowchart of the proposed multi-mode adaptative based pushover analysis

The following steps explain the detailed procedure of the proposed MADP.

– The nonlinear inelastic mathematical model is developed which incorporates the stiffness, mass, and damping matrices.

– Calculate the natural frequencies, mode shapes, lateral force distribution, and perform nonlinear static pushover analysis.

– Determine the base shear and roof displacement for *n*th mode and draw the pushover analysis curve.

– Calculate the target roof displacement. If the roof displacement is equal to the target roof displacement, then the process will end otherwise the properties will be modified and the procedure will be repeated.

– Calculate the response for the structural system for the first mode.

– Repeat the same procedure for the other modes.

4. NUMERICAL MODEL

The RC-MRFs with three different stories are considered in the study. The load acting on the structural frame is a nonlinear dynamic load that is blast load. The load acting on the frame occurs within a millisecond and the magnitude is much larger compared to earthquake loading.

Figure 2 shows the configurations of the used RC-MRFs in the current study. The 4 storey frame has a bay width of 9.14m, while the remaining frames have a bay

width of 6.10m. Table 1 shows the physical properties of the models including the fundamental periods' range, dead load, live load, and compressive strength of the concrete used in beams and columns. Table 2 shows the natural periods of all models in different modes. Table 3 shows the dynamic properties of the investigated frames.

Figure 2 shows the RC-MRFs exposed to blast load are considered in the study. The figure shows the blast load acting at a distance range from the frame.

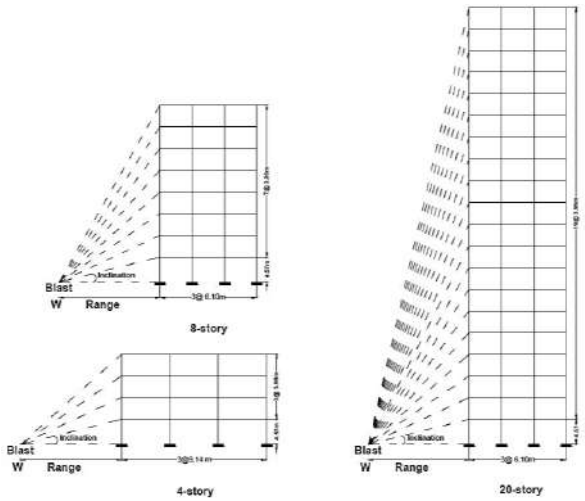

Figure 2. 2-D presentation of the RC-MRFs exposed to blast loading considered in this study

TABLE 1. Physical properties of the models

Sl No	Parameter	Magnitude
1	Dead Load	8.38 kN/m^2
2	Live load	2.40 kN/m^2
3	Compressive strength of the beams	34.5 MPa
4	Compressive strength of the columns	46 MPa

TABLE 2. Characteristics of the analyzed frames[45]

Sl No	Frame (Storey)	Height (m)	Width (m)	Periods (s)		
				I mode	II mode	III mode
1	4	12	9.14	0.64	0.20	0.20
2	8	24	6.10	1.34	0.45	0.25
3	20	60	6.10	1.71	0.64	0.38

TABLE 3. Dynamic properties of the frames

Sl No	Parameter	Value
1	Damping ratio	5%
2	Stiffness	15.11 kN/m
3	Damping	7.38 ×10^{-2}kN-s/m

5. BLAST LOADINGS

The blast load acting on structures has a short period. Table 4 shows the blast load parameters used in this study. The blast load is calculated using Equations (12)-(17).

$$P_s = \frac{670}{Z^3} + 100 \text{ kPa} \quad (P_s > 1000\text{kPa}) \tag{12}$$

$$P_s = \frac{97.5}{Z} + \frac{145.5}{Z^2} + \frac{585}{Z^3} + 1.9 \text{ kPa} \quad (10 < P_s < 1000 \text{ kPa}) \tag{13}$$

where P_s is the maximum static overpressure of the blast load and Z is the scaled distance, which is calculated as:

$$Z = \frac{R}{W^{1/3}} \tag{14}$$

where W denotes the TNT weight. The time variation of the blast load can be determined using the following equations:

$$P(t) = P_o + P_s\left(1 - \frac{t}{T_s}\right)\exp\left(-\gamma \frac{t}{T_s}\right) \tag{15}$$

$$\gamma = Z^2 - 3.7Z + 4.2 \tag{16}$$

$$T_s = W^{1/3} 10^{\left[-2.75 + 0.27 \log R/W^{1/3}\right]} \tag{17}$$

where P_o is the ambient pressure and T_s is the positive time duration of the blast load.

6. RESULTS AND DISCUSSIONS

The considered low rise, mid-rise, and high-rise structural frames are analyzed to determine the accuracy and efficiency of the proposed MADP procedure. The blast load acting on the frame has been the main input of the structural analysis. The analyses were carried out by considering three mode shapes, using modal pushover analysis, nonlinear response history analysis, and multi-mode adaptative pushover analysis. The analyses were carried out in the MATLAB [55] platform.

For seismic performance evaluation of structures, probabilistic approaches are more common [56, 57]; however, for blast loading, a deterministic approach is mainly used. The target displacement for the 4, 8, and 20 storey frames have been obtained as 11.82cm, 16.45cm, and 23.22cm, respectively. The accuracy of the roof displacement was calculated by using MADP analysis.

TABLE 4. Blast load parameter

Sl No	Parameter	Magnitude
1	Weight (W)	1000 TNT(Trinitrotoluene)*
2	Range (R)	100m
3	Scaled Distance (Z)	10 m/kg$^{1/3}$
4	Peak pressure (P_s)	100.67 kPa

* TNT generates blast energy of about 4680 joules per gram (J /g)

6. 1. 4-Story Frame Figure 3 shows the storey drift of the four-storey frame with different analysis approaches. The maximum drift occurs on the first floor and the minimum drift occurs on the second floor by MADP. The MADP will have a higher value on the 3rd floor and the remaining floors will have lower values. Figure 4 shows the pushover curve with three different mode shapes. The maximum base shear with roof displacement occurs at Mode I and the minimum occurs at Mode III. The maximum base shear is 1kN and roof displacement is 50 cm and the minimum base shear is 800 N and roof displacement is 4 cm.

Figure 5 shows the blast load acting on the four-storey frame model. The maximum load acting on the first floor has been 12 kPa at 0.03 sec and the maximum load acting on the fourth floor has been 6kPa at 0.04 sec. Figure 6 shows the mode shape of the four-storey frame.

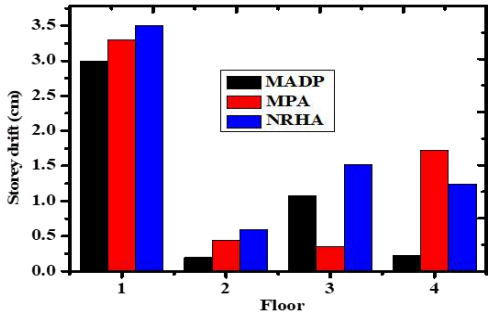

Figure 3. Story drift of 4 story frame

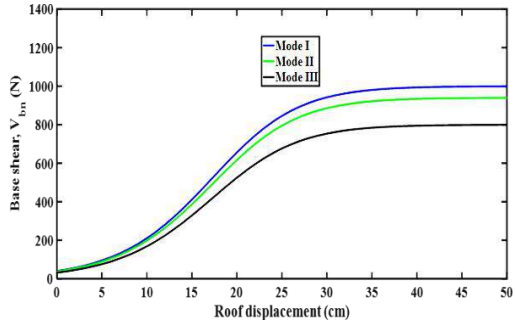

Figure 4. Pushover curve 4 story frame

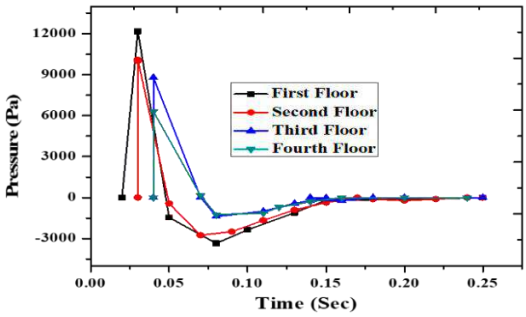

Figure 5. Load acting on 4 story frames exposed to blast load

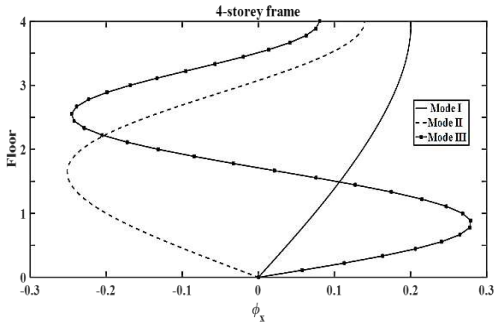

Figure 6. Mode shape of 4 story frame

6. 2. 8-Story Frame Figure 7 shows the storey drift ratio of the eight-story frame with different pushover analyses approaches, while the maximum storey drift ratio is 4, 3 and 0.5 by MPA, NRHA and MADP methods, respectively. The maximum storey drift occurs at fourth floor and minimum storey drift ratio occurs at first floor by various methods, respectively. The NRHA and MADAP show similar results, whereas the MPA has the maximum error.

Figure 8 shows the displacement of different floors with different analysis approaches. The maximum displacement occurs on the seventh floor with a value of 0.3m using modal pushover analysis and the minimum displacement occurs on the first floor of 0.068m using MADP analysis. Figure 9 shows the lateral force distribution of the floors in different modes. The maximum lateral force occurs in the third mode and the minimum lateral force occurs in the first mode. The maximum and minimum lateral forces have been 80 kN and 20 kN, respectively.

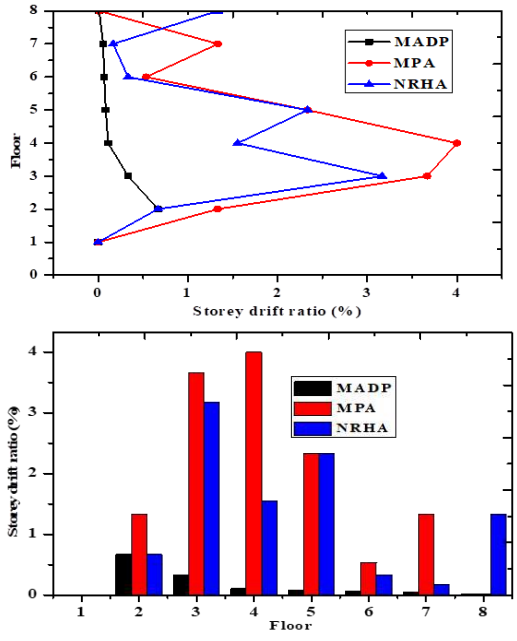

Figure 7. Story drift ratio of 8 story frame

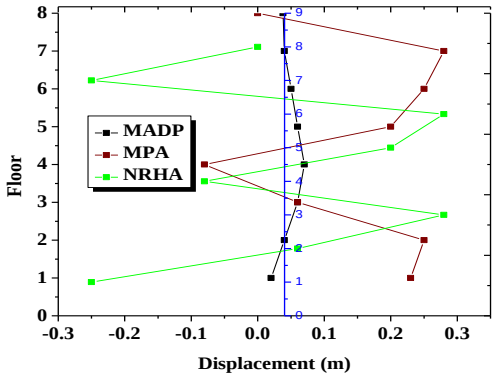

Figure 8. Displacement of 8 story frame

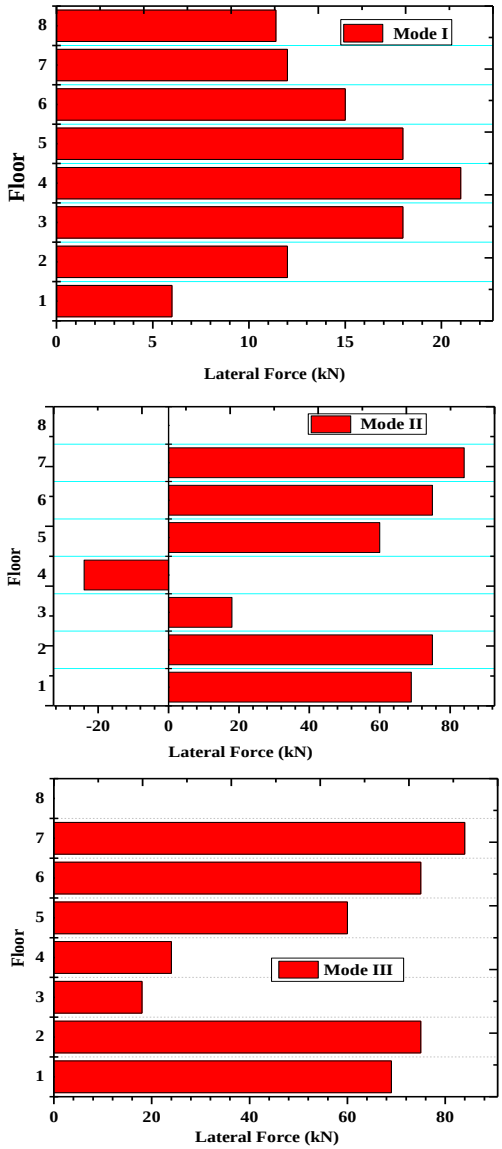

Figure 9. Lateral Force of 8 story frame

6. 3. 20-Story Frame The investigated high-rise model is a 20 storey frame. The effect of torsion and inclination of blast loading have been considered in this model. Figure 10 shows the variations of the inclination angle and torsion angle on the investigated model. It is shown in Equation (8). The maximum inclination of the blast load has been 60degree and the torsion angle was 0.010 radian. Figure 11 shows the mode shapes of the twenty storey frame.

Figure 12 shows the base shear of roof displacement of the twenty storey frame along X direction. The maximum base shear has been 2050 N in mode I and the minimum base shear has been 1600 N in mode III. Figure 13 shows the displacement of the floor level along X direction with different analysis approaches. The nonlinear responses analysis will provide maximum value compared with other methods. The variations of the displacement along the floor are presented. The MADP and MPA show small errors compared to the MADP method. The maximum displacement was 0.4m in the second floor using nonlinear response history analysis. The minimum displacement has been 0.07m using MADP. Figure 14 shows the storey drift ratio of second to fourth floors. The minimum storey drift ratio occurs at 14 to 18 floors.

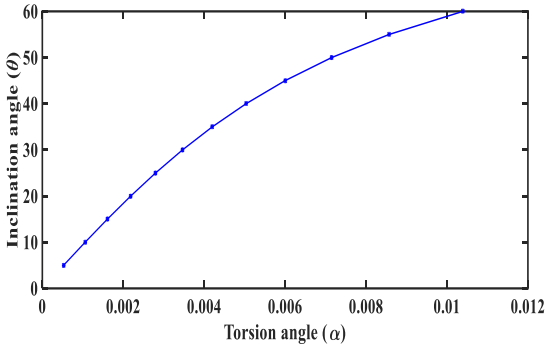

Figure 10. Relationship between inclination angle and torsion angle

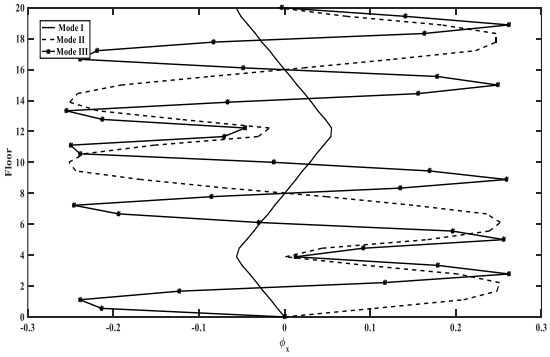

Figure 11. Mode shape of the 20 storey frame

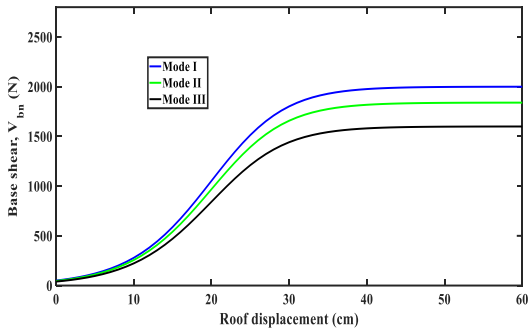

Figure 12. Base shear of the 20 storey frame along X direction

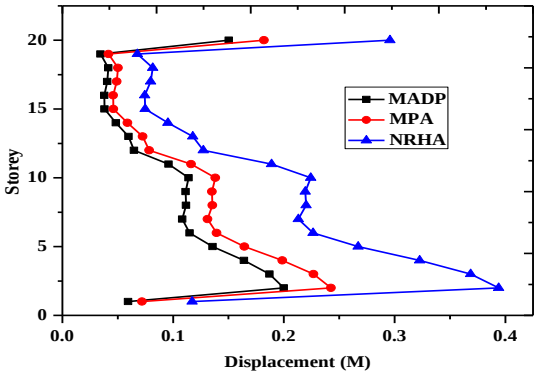

Figure 13. Displacement of the 20 storey frame along X direction

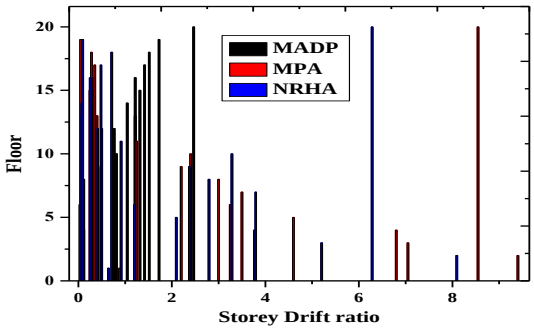

Figure 14. Storey drift ratio of the 20 storey frame along *Y* direction

Figure 15 shows the torsional moment of the fifteenth floor. The maximum torsional moment has been 1kNm at 2m.s. Figure 16 shows the torsion of the twenty-story floor with different analysis approaches. The maximum torsion occurs at 20th floor of 0.0007 rad using MADP analysis. Table 7 shows the percentage of the error of the different frames with different analyses approaches. The maximum error occurs in 20 storey model using nonlinear response history analysis and the minimum error occurs at 4 storey frame using modal pushover analysis.

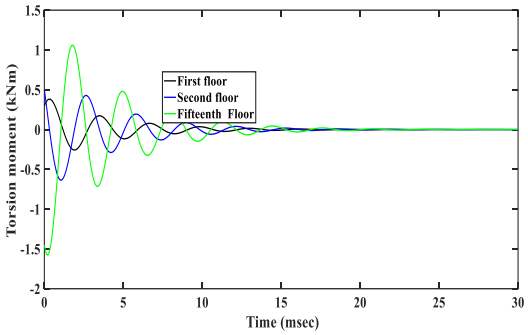

Figure 15. Torsional moment

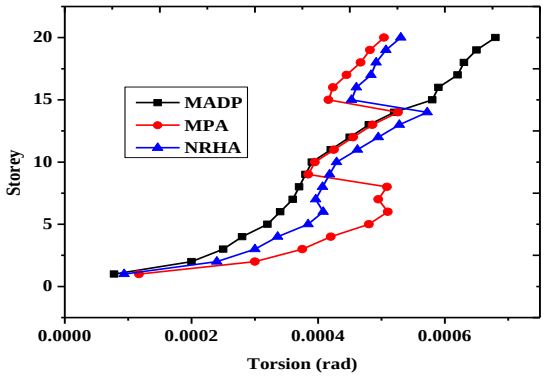

Figure 16. Torsion effect in different floors

TABLE 7. Percentage of the error of different approaches and in terms of drift ratio compared to the proposed MADP approach

Sl No	Frame	MPA	NRHA
1	4-storey	10%	25%
2	8-storey	14%	22%
4	20-storey	22%	28%

7. CONCLUSIONS

The current study investigates blast load acting on 4-, 8- and 20- storey frame models. The structural responses were determined using a proposed multi-mode adaptative pushover analysis. Three different mode shapes were considered in the simulation. For 20 storey structure (high-rise model), the torsional effect has been considered as well. The monitored responses were displacement, storey drift, storey drift ratio, base shear, and torsional effect. The main verdicts could be summarised as follows based on the calculated results:

- For 4 storey frame structure, storey drift error will be 15% and 8% for NRHA and MPA, respectively compared to MADP.

-The maximum pressure occurs at lower stories and minimum pressure occurs at higher stories for the

structure frame exposed to blast load.
-The base shear will be inversely proportional to mode shapes.
-In 8 storey model, the maximum storey drift ratio occurs at third, fourth, and fifth floors, respectively. The remaining floors had the minimum storey drift ratios.
-For an 8 storey frame structure, displacement error will be 8% and 14% for NRHA and MPA, respectively compared to MADP.
-For a high-rise structure (20 storey model) the influence of torsion with respect to variation of torsional angle and blast load angle were also considered in the study.
-Torsional moment and blast load along both *X* and *Y* directions have been the input parameters of the high-rise model exposed to blast load.

8. REFERENCES

1. Barros, R. C., and Almeida, R., "Pushover analysis of asymmetric three-dimensional building frames", ***Journal of Civil Engineering and Management***, Vol. 11, No. 1, (2005), 3–12. doi:10.1080/13923730.2005.9636327
2. Hamidia, M., Filiatrault, A., and Aref, A., "Simplified seismic sidesway collapse analysis of frame buildings", ***Earthquake Engineering & Structural Dynamics***, Vol. 43, No. 3, (2014), 429–448. doi:10.1002/eqe.2353
3. Kim, S., and D'Amore, E., "Push-over analysis procedure in earthquake engineering", ***Earthquake Spectra***, Vol. 15, No. 3, (1999), 417–434. doi:10.1193/1.1586051
4. Krawinkler, H., and Seneviratna, G. D. P. K., "Pros and cons of a pushover analysis of seismic performance evaluation", ***Engineering Structures***, Vol. 20, Nos. 4–6, (1998), 452–464. doi:10.1016/S0141-0296(97)00092-8
5. Ozturk, B., Eren Sahin, H., and Yildiz, C., "Seismic Performance Assessment of Industrial Structures in Turkey Using The Fragility Curves ", In 15th World Conference on Earthquake Engineering, Lisbon, Portugal, (2012), 1–7, 1–7
6. D'Ambrisi, A., De Stefano, M., and Tanganelli, M., "Use of pushover analysis for predicting seismic response of irregular buildings: A case study", ***Journal of Earthquake Engineering***, Vol. 13, No. 8, (2009), 1089–1100. doi:10.1080/13632460902898308
7. MacRae, G. A., "P-Δ Effects on Single-Degree-of-Freedom Structures in Earthquakes:", ***Earthquake Spectra***, Vol. 10, No. 3, (1994), 539–568. doi:10.1193/1.1585788
8. Bernal, D., "Instability of buildings during seismic response", ***Engineering Structures***, Vol. 20, Nos. 4–6, (1998), 496–502. doi:10.1016/S0141-0296(97)00037-0
9. Ibarra, L., "Collapse assessment of deteriorating SDOF systems", In Proceeding 12th European Conference on Earthquake Engineering, (2002), 9–13, 9–13
10. Williamson, E. B., " Evaluation of Damage and P -Δ Effects for Systems Under Earthquake Excitation ", ***Journal of Structural Engineering***, Vol. 129, No. 8, (2003), 1036–1046. doi:10.1061/(asce)0733-9445(2003)129:8(1036)
11. Miranda, E., and Akkar, S. D., "Dynamic Instability of Simple Structural Systems", ***Journal of Structural Engineering***, Vol. 129, No. 12, (2003), 1722–1726. doi:10.1061/(ASCE)0733-9445(2003)129:12(1722)
12. Ibarra, L., and Krawinkler, H., "Variance of collapse capacity of SDOF systems under earthquake excitations", ***Earthquake Engineering & Structural Dynamics***, Vol. 40, No. 12, (2011), 1299–1314. doi:10.1002/EQE.1089
13. Brozovič, M., and Dolšek, M., "Envelope-based pushover analysis procedure for the approximate seismic response analysis of buildings", ***Earthquake Engineering & Structural Dynamics***, Vol. 43, No. 1, (2014), 77–96. doi:10.1002/eqe.2333
14. Hasan, R., Xu, L., and Grierson, D. E., "Push-over analysis for performance-based seismic design", ***Computers and Structures***, Vol. 80, No. 31, (2002), 2483–2493. doi:10.1016/S0045-7949(02)00212-2
15. Manafpour, A. R., and Jalilkhani, M., "A Rapid Analysis Procedure for Estimating the Seismic Collapse Capacity of Moment Resisting Frames", ***Journal of Earthquake Engineering***, (2019). doi:10.1080/13632469.2019.1583144
16. Rahmani, A. Y., Bourahla, N., Bento, R., and Badaoui, M., "Adaptive upper-bound pushover analysis for high-rise moment steel frames", ***Structures***, Vol. 20, (2019), 912–923. doi:10.1016/j.istruc.2019.07.006
17. Carlos, J., Estimating Seismic Demands for Performance-Based Engineering of Buildings, Theses and Dissertations, UC Berkeley UC Berkeley Electronic. Retrieved from https://escholarship.org/uc/item/9fp377cr
18. Sullivan, T. J., Saborio-Romano, D., O'Reilly, G. J., Welch, D. P., and Landi, L., "Simplified Pushover Analysis of Moment Resisting Frame Structures", ***Journal of Earthquake Engineering***, (2018). doi:10.1080/13632469.2018.1528911
19. Hall, J. F., "On the descending branch of the pushover curve for multistory buildings", ***Earthquake Engineering & Structural Dynamics***, Vol. 47, No. 3, (2018), 772–783. doi:10.1002/eqe.2990
20. Zhang, Q. W., Megawati, K., Huang, L. P., and Pan, T. C., "Evaluating the Efficiency of Current Nonlinear Static Pushover Procedures on Estimating Torsion Effect for Asymmetric High-Rise Buildings", ***Vulnerability, Uncertainty, and Risk***, (2011), 881–888. doi:10.1061/41170(400)107
21. Hassan, W. M., and Reyes, J. C., "Assessment of modal pushover analysis for mid-rise concrete buildings with and without viscous dampers", ***Journal of Building Engineering***, Vol. 29, (2020), 101103. doi:10.1016/j.jobe.2019.101103
22. Chopra, A., and Goel, R., (, January 1)A Modal Pushover Analysis Procedure to Estimate Seismic Demands for Buildings: Theory and Preliminary Evaluation, Pacific Earthquake Engineering Research Center, Report PEER No. 2001/03, Retrieved from https://digitalcommons.calpoly.edu/cenv_fac/55
23. Chopra, A. K., and Goel, R. K., "A modal pushover analysis procedure for estimating seismic demands for buildings", ***Earthquake Engineering and Structural Dynamics***, Vol. 31, No. 3, (2002), 561–582. doi:10.1002/eqe.144
24. Goel, R. K., and Chopra, A. K., "Evaluation of Modal and FEMA Pushover Analyses: SAC Buildings", ***Earthquake Spectra***, Vol. 20, No. 1, (2004), 225–254. doi:10.1193/1.1646390
25. Goel, R. K., and Chopra, A. K.,. "Role of higher-"mode" pushover analyses in seismic analysis of buildings", ***Earthquake Spectra***, Vol. 21, No. 4, (2005), 1027–1041, 1027–1041. doi:10.1193/1.2085189
26. Bobadilla, H., and Chopra, A. K., "Modal pushover analysis for seismic evaluation of reinforced concrete special moment resisting frame buildings". Earthquake Engineering Research Center, University of California, (2007).
27. Bobadilla, H., and Chopra, A. K., "Evaluation of the MPA Procedure for Estimating Seismic Demands: RC-SMRF Buildings", ***Earthquake Spectra***, Vol. 24, No. 4, (2008), 827–845. doi:10.1193/1.2945295
28. Humar, J. L., Dynamics of Structures. Prentice-Hall, Englewood Cliffs, New Jersey, 1990.
29. Chopra, A. K., Dynamics of Structures. Prentice-Hall of India, NewDelhi, 1996.

30. Clough, R. W., Penzien, J., Dynamics of Structures. McGraw-Hill, New York, 1993.
31. Biggs, J. M., Introduction to Structural Dynamics. McGraw Hill Education, 2004.
32. Connor, J. J., Introduction to Structural Motion Control. CRC Publications, 2000.
33. Connor, J. J., Flame, S. L., Structural Motion Engineering. Springer, 2004."
34. Chopra, A. K., Goel, R. K., and Chintanapakdee, C., "Evaluation of a Modified MPA Procedure Assuming Higher Modes as Elastic to Estimate Seismic Demands", ***Earthquake Spectra***, Vol. 20, No. 3, (2004), 757–778. doi:10.1193/1.1775237
35. Faal, H. N., and Poursha, M., "Applicability of the N2, extended N2 and modal pushover analysis methods for the seismic evaluation of base-isolated building frames with lead rubber bearings (LRBs)", ***Soil Dynamics and Earthquake Engineering***, Vol. 98, (2017), 84–100. doi:10.1016/j.soildyn.2017.03.036
36. Poursha, M., Khoshnoudian, F., and Moghadam, A. S., "A consecutive modal pushover procedure for estimating the seismic demands of tall buildings", ***Engineering Structures***, Vol. 31, No. 2, (2009), 591–599. doi:10.1016/j.engstruct.2008.10.009
37. Kalkan, E., and Chopra, A. K., "Evaluation of Modal Pushover–Based Scaling of One Component of Ground Motion: Tall Buildings", ***Earthquake Spectra***, Vol. 28, No. 4, (2012), 1469–1493. doi:10.1193/1.4000091
38. Pan, X., Zheng, Z., and Wang, Z., "Estimation of floor response spectra using modified modal pushover analysis", ***Soil Dynamics and Earthquake Engineering***, Vol. 92, (2017), 472–487. doi:10.1016/j.soildyn.2016.10.024
39. Reyes, J. C., and Chopra, A. K., "Three-dimensional modal pushover analysis of buildings subjected to two components of ground motion, including its evaluation for tall buildings", ***Earthquake Engineering and Structural Dynamics***, Vol. 40, No. 7, (2011), 789–806. doi:10.1002/eqe.1060
40. Reyes, J. C., and Chopra, A. K., "Evaluation of three-dimensional modal pushover analysis for unsymmetric-plan buildings subjected to two components of ground motion", ***Earthquake Engineering & Structural Dynamics***, Vol. 40, No. 13, (2011), 1475–1494. doi:10.1002/eqe.1100
41. Reyes, J. C., Riaño, A. C., Kalkan, E., and Arango, C. M., "Extending modal pushover-based scaling procedure for nonlinear response history analysis of multi-story unsymmetric-plan buildings", ***Engineering Structures***, Vol. 88, (2015), 125–137. doi:10.1016/j.engstruct.2015.01.041
42. Tehrani, M. H., and Khoshnoudian, F., "Extended consecutive modal pushover procedure for estimating seismic responses of one-way asymmetric plan tall buildings considering soil-structure interaction", ***Earthquake Engineering and Engineering Vibration***, Vol. 13, No. 3, (2014), 487–507. doi:10.1007/s11803-014-0257-6
43. Jalilkhani, M., Ghasemi, S. H., and Danesh, M., "A multi-mode adaptive pushover analysis procedure for estimating the seismic demands of RC moment-resisting frames", ***Engineering Structures***, Vol. 213, (2020), 110528. doi:10.1016/j.engstruct.2020.110528
44. Saedi Daryan, A., Soleimani, S., and Ketabdari, H., "A modal nonlinear static analysis method for assessment of structures under blast loading", ***Journal of Vibration and Control***, Vol. 24, No. 16, (2018), 3631–3640. doi:10.1177/1077546317708517
45. Saedi-Daryan, A., Soleimani, S., and Hasanzadeh, M., "Extension of the Modal Pushover Analysis to Assess Structures Exposed to Blast Load", ***Journal of Engineering Mechanics***, Vol. 144, No. 3, (2018), 04018006. doi:10.1061/(asce)em.1943-7889.0001417
46. Kalkan, E., and Kunnath, S. K., "Adaptive Modal Combination Procedure for Nonlinear Static Analysis of Building Structures", ***Journal of Structural Engineering***, Vol. 132, No. 11, (2006), 1721–1731. doi:10.1061/(asce)0733-9445(2006)132:11(1721)
47. Antoniou, S., and Pinho, R., "Development and verification of a displacement-based adaptive pushover procedure", ***Journal of Earthquake Engineering***, Vol. 8, No. 5, (2004), 643–661. doi:10.1142/S136324690400150X
48. Gupta, B., and Kunnath, S. K., "Adaptive Spectra-Based Pushover Procedure for Seismic Evaluation of Structures", ***Earthquake Spectra***, Vol. 16, No. 2, (2000), 367–391. doi:10.1193/1.1586117
49. Papanikolaou, V. K., and Elnashai, A. S., "Evaluation of conventional and adaptive pushover analysis I: Methodology", ***Journal of Earthquake Engineering***, Vol. 9, No. 6, (2005), 923–941. doi:10.1142/S1363246905002420
50. Shakeri, K., Shayanfar, M. A., and Kabeyasawa, T., "A story shear-based adaptive pushover procedure for estimating seismic demands of buildings", ***Engineering Structures***, Vol. 32, No. 1, (2010), 174–183. doi:10.1016/j.engstruct.2009.09.004
51. Bhasker, R., and Menon, A., "Torsional irregularity indices for the seismic demand assessment of RC moment resisting frame buildings", ***Structures***, Vol. 26, (2020), 888–900. doi:10.1016/j.istruc.2020.05.018
52. Wang, Y. Bin, Liu, H. T., and Zhang, Z. Y., "Rotation spring: Rotation symmetric compression-torsion conversion structure with high space utilization", ***Composite Structures***, Vol. 245, (2020), 112341. doi:10.1016/j.compstruct.2020.112341
53. Amini, M. A., and Poursha, M., "Adaptive Force-Based Multimode Pushover Analysis for Seismic Evaluation of Midrise Buildings", ***Journal of Structural Engineering***, Vol. 144, No. 8, (2018), 04018093. doi:10.1061/(asce)st.1943-541x.0002070
54. "Chintanapakdee,C. Evaluations of the model pushover analysis procedure using vertical regular and irregular generic frames, PhD Dissertation, University of California at Berkeley; (2002).
55. MathWorks, Inc., MATLAB: The language of technical computing. Desktop tools and development environment, version 14, (2005).
56. Shojaeifar, H., Maleki, A., and Lotfollahi-Yaghin, M. A., "Performance evaluation of curved-TADAS damper on seismic response of moment resisting steel frame", ***International Journal of Engineering, Transactions A: Basics***, Vol. 33, No. 1, (2020), 55–67. doi:10.5829/ije.2020.33.01a.07
57. Menasri, Y., Nouaouria, M. S., and Brahimi, M., "Probabilistic Approach to the Seismic Vulnerability of Reinforced Concrete Frame Structures by the Development of Analytical Fragility Curves P A P E R I N F O", ***International Journal of Engineering, International Journal of Engineering, Transactions A: Basics***, Vol. 30, No. 7, (2017), 945–954. doi:10.5829/ije.2017.30.07a.03

Persian Abstract

چکیده

در این مطالعه رویکرد تحلیل استاتیکی غیرخطی به روزشونده با در نظر گرفت اثر مودهای بالاتر جهت بررسی اثر انفجار بر قاب های خمشی بتن مسلح مورد ارزیابی قرار گرفته است. نوآوری مطالعه حاضر در ترکیب اثر مودهای بالاتر و تحلیل استاتیکی غیرخطی به روزشونده بوده که تابحال برای ارزیابی اثر بار انفجار بر سازه‌ها مورد استفاده قرار نگرفته است. به منظور بررسی کارایی روش پیشنهادی، سه سازه بتن مسلح ٤، ٨ و ٢٠ طبقه در این مطالعه مورد بررسی قرار گرفته‌اند. جهت مقایسه بهتر، علاوه بر رویکرد پیشنهادی، روش تحلیل استاتیکی غیرخطی به روزشونده متداول و همچنین تحلیل غیرخطی تاریخچه زمانی نیز بر روی مدل‌ها اعمال گردیده است. بدین منظور پارامترهای اثرگذار متعددی از جمله بارگذاری جانبی، جابجایی طبقات، دریفت طبقات، نسبت دریفت طبقات و ... مدنظر بوده است. در تمامی مدل‌های سازه‌ای مورد بررسی اثر ۳ مود ارتعاشی اول در فرآیند تحلیل در نظر گرفته شده، در حالیکه برای مدل ۲۰ طبقه اثر پیچش در پاسخ سازه نیز لحاظ گردیده است. نتایج این تحقیق بیانگر دقت کافی و عملکرد مطلوب روش پیشنهادی به منظور تخمین پاسخ سازه‌ها تحت بارگذاری انفجار می‌باشد.

International Journal of Engineering

Journal Homepage: www.ije.ir

Services Composition in Multi-cloud Environments using the Skyline Service Algorithm

M. Heidari, S. Emadi*

Department of Computer Engineering, Yazd Branch, Islamic Azad University, Yazd, Iran

PAPER INFO

Paper history:
Received 08 June 2019
Received in revised form 22 September 2020
Accepted 20 November 2020

Keywords:
Skyline Service
Dominant Relationship
Web Service
Service Composition
Multi-cloud Environments

ABSTRACT

The rapid growth of cloud environments has led to the expansion of resources that offer a variety of services. The opertions of the services are usually very simple and may not satisfy the complex needs of the user, hence there is a need for a combination of these services that can fulfill the user's requirements. Most of the service composition methods in cloud environments assume that the involved services came from one cloud, and this is unrealistic because other clouds may provide more relevant services. The challenges in composition services distributed in multi-cloud environments include increased cost and a reduction in its speed due to the increasing number of services, providers, and clouds; so, in order to overcome these challenges, the number of providers and participating clouds must be reduced. This study used the Skyline service algorithm to compose services in multi-cloud environments, which examined all the clouds during the service composition process. The proposed method can provide an applicable composition service to the user with the lowest communication cost by considering the number of clouds and by using fewer providers. The Skyline algorithm involves two steps. In the first one, the best composition in a cloud environment is selected among all the possible providers by considering the number of providers and the communication time. In the second step, the Skyline algorithm is used to create all the possible compositions in a multi-cloud environment. Parameters such as fewer clouds and shorter communication times between the clouds are selected. The results show that the proposed method can find the composition with the least number of clouds, the lowest cost, and has the lowest calculation time. It can be said that the Skyline makes it possible to select a suitable composition of user-requested services in a multi-cloud environment.

***doi**: 10.5829/ije.2021.34.01a.07*

1. INTRODUCTION

Web service is a modular and self-described application that is published based on a set of standards such as SOAP, WSDL, and UDDI [1-2]. When a web service is limited to simple features, a set of separated web services must be combined to create a value-added one [3-4]. Service composition problems can be resolved by selecting a set of web services in such a way that their combination meets the functional and non-functional requirements of the user [5]. With the advent and rapid development of cloud computing, more clouds can carry out the existing tasks in the cloud with different functions, and this cloud environment is a natural choice for providing various types of resources as a service. To meet the user's needs, cloud-based systems [6-7] are usually designed by calling up several providers. The service composition in cloud environments allows for the integration of various cloud resources into a set of integrated services for providing cloud-based solutions that meet certain qualitative criteria [8]. Most of the service composition methods that have been proposed for cloud computing consider all the composite services in one cloud, rather than searching services from the various available clouds [9]. Organizations often distribute their services using cloud providers to ensure the availability and quality of the provided services, and also to reduce the risk of data loss [10]. In addition, service composition

*Corresponding Author Institutional Email: emadi@iauyazd.ac.ir (S. Emadi)

Please cite this article as: M. Heidari, S. Emadi, Services Composition in Multi-cloud Environments using the Skyline Service Algorithm , International Journal of Engineering, Transactions A: Basics Vol. 34, No. 01, (2021) 56-65

in multi-cloud environments poses many issues such as the cost of communications within the cloud, increased fiscal costs, and security issues. Hence, challenging tasks include reducing the number of participating clouds and the number of providers due to the limitations of the services. Therefore, the current study seeks to find the best possible service composition in cloud environments using the Skyline service algorithm, which uses both a smaller number of providers and clouds to reduce financial costs.

The Skyline algorithm is based on the concept of Pareto dominance [11]. It has been used to solve research problems such as web service selection, query processing over uncertain data [12-14], effective processing of advanced queries [15], and indexing of time series data. The use of the Skyline algorithm in the proposed method creates all the possible compositions of the providers in a multi-cloud environment. The best composition in a cloud environment is selected by considering the number of providers and the communication time. Parameters such as fewer clouds and a shorter computation time between the clouds are also considered in selecting the most suitable cloud composition.

The innovation of this paper includes modeling the multi-cloud environment using the Skyline in two steps. First, the providers and services were modeled based on user requests. Secondly, the clouds are modeled based on the providers and services selected in the previous step. Then, we introduce the algorithms for the extraction of the candidate services, providers, and clouds based on the Skyline rules.

The rest of this paper is organized as follows. In Section 2, the works related to service composition will be discussed using the Skyline service. In Section 3, the algorithm and the concepts of the Skyline service are expressed. Then the proposed method is outlined is Section 4. Section 5 presents the results and evaluation, and the last section is devoted to conclusion and suggestions.

2. RELATED WORKS

Most of the existing approaches to service composition in cloud environments consider all the services in the composition from a single cloud. However, certain algorithms have also been proposed to address this issue. In Section 2.1, other methods will be examined, and in Section 2.2, service composition using the Skyline algorithm will be discussed.

2. 1. Methods Provided Using Multi-cloud Algorithms Zou et al. used a tree structure to model a multi-cloud environment (MCB). Then, with the MCB tree search, the minimum request set was created. Accordingly, they proposed three algorithms for selecting the optimal cloud composition. In the first algorithm, they considered all clouds as inputs and evaluated all the possible solutions. This method determined the sequence of the service composition at the time of execution, but with the use of a large number of clouds. The second algorithm recursively defined a service composition in all the cloud compositions. The last algorithm provided an optimal cloud computing approach using an approximate method. However, it was time-consuming and may not be a good cloud computing approach because it used the composition of clouds that utilize service spaces and could impose on some compositions [16]. Gutierrez-Garcia et al. proposed an agent-based multi-cloud service composition approach by using a semi-recursive conventional protocol; however, it has the limitations of agent-based distribution [17]. Jatoth et al. proposed a quality of service (QoS) cloud service composition based on both the modified invasive weed optimization algorithm and an Adaptive Genotype Evolution based Genetic Algorithm (AGEGA) [18-19]. Gavala et al. proposed a QoS aware cloud service composition based on an Eagle Strategy with Whale Optimization Algorithm (ESWOA). However, in these three approaches, they considered multiple QoS parameters for service composition in only one cloud [20]. Yu et al. presented a Greedy-WSC algorithm and an ant colony optimization based algorithm, namely ACO-WSC, to select the service composition in cloud environments with a minimal number of clouds. The Greedy-WSC algorithm selects clouds that offer more services, and the ACO-WSC algorithm is used to combine selected clouds. Their results showed that the ant colony optimization method could efficiently find effective cloud composition with the minimum number of clouds. The disadvantage of this model was its lack of considering semantic information in the composition of web services, especially in a dynamic and distributed environment [21]. Kurdy et al. suggested a composite optimization (COM2) algorithm for cloud services that ensures the selection of clouds with the maximum number of services, which increases the likelihood of completing a service request at a minimum cost. The results of their experiments showed that COM2 was successfully able to compete with previous algorithms in the field of service composition, but it did not consider the interconnecting costs of the clouds [22]. Mezni et al. used formal concept analysis (FCA) and fuzzy formal concept analysis (FFCA) for service composition in a cloud-based environment. The FCA is based on the concept of a network, a powerful tool for classifying cloud information and services. Initially, a cloud computing model was created as a set of formal concepts; then, it extracted and combined the candidate clouds from the formal concepts. Finally, the optimal cloud composition was selected, and the multi-cloud service composition (MCSC) became a classical service

composition problem. In addition to considering the number of clouds in the composition, it also takes into account the cost between the clouds. The tests showed the effectiveness and ability of the FCA-based method to find and group cloud compositions with a minimum number of clouds, the lowest communication cost, and the lowest time to service selection in the nearest cloud or in the same cloud [23-24].

2. 2. Methods Provided Using the Skyline Algorithm Yu and Bouguettaya suggested an algorithm that used the dominant relationship between service providers to find a set of the best possible service composition for Skyline services [11]. Instead of examining all the possible composition of services, this algorithm significantly reduces the search space and proposes a low-up computing framework that enables the Skyline algorithm to scale well with a number of services. In their research, three algorithms, namely OPA, DPA and BUA, were developed to select a set of the best possible composition services. The DPA used a parent table and a broad network to achieve enhancement and route ability. The BUA used a powerful low-up computing framework with a linear composite strategy, which improved the performance and the scalability.

Wu et al. provided an algorithm for the composition of services based on service quality. In this way, when a new service comes, the previous service is deleted, and the quality of service is changed. This algorithm reduces the number of selected services through Skyline and chooses the best service using the service quality [25].

In another study, Zhang et al. used the Skyline guaranteed query processing method to build mashup cloud applications and employed similarity tests to achieve an optimal Skyline. Cloud mashup is a composition of several services with a shared data set and integrated functions. This method was used to optimize the composition of web services in large-scale cloud-based mashup applications from the Map-Reduce. Since the choice of Skyline service and hybrid processes were very timely, especially when the data space of the services was very large, a block-based blocking was proposed to shorten the process. After testing 100,000 real websites worldwide in 10 dimensions, it was found that the Map-Reduce based block-removal method was 3.25 times faster than the angular segmentation algorithm, and 1.4 times faster than the network method [26-27].

Liu et al. proposed a dynamic Skyline service selection tool to reduce redundancy. In this method, the process of choosing a service was divided into two stages: the service selection stage and the implementation phase of the selected services. The selection stage used the offline method to calculate the Skyline, and was responsible for updating the Skyline service. Therefore, the offline process never affected the performance of the phases of the service selection. The implementation phase was responsible for selecting the optimal composition of the services, which matched the QoS user limitations. The results showed that this method selected the most appropriate services [28].

Moradi and Emadi presented an algorithm for service composition using the Skyline service in parallel. In this way, the choice of services was based on the quality of service; the use of parallelization techniques had a significant impact on reducing the response time and increasing the speed of the composition of services, as well as reducing the computations [29].

However, most traditional service composition methods regard service composition in a single cloud and consider a balance between the QoS parameters. In this paper, we present an algorithm based on Skyline service, which focuses on reducing the number of clouds and providers.

3. THE SKYLINE SERVICE ALGORITHM

The existing approaches in multi-cloud service composition only reduce the number of clouds. This research, like [23], considers modeling the relationship between the providers and the clouds in the selection of optimal clouds, as well as the composition of services by the Skyline service algorithm. The Skyline service algorithm has been used to extract the optimal composition of the providers and clouds. Also, combined services can have sequential, parallel, loop, or conditional structures. In this research, only the sequential structure for combining services and their implementation is considered.

Definition 1: A multi-cloud environment is a set in which $C= \{C_1,C_2,...,C_N\}$ where C_i is a cloud and $P=\{P_1,P_2,\ldots,P_N\}$ where P_i is a provider that is hosted by the clouds. A provider also offers a set of services. Every provider may belong to more than one cloud, and every service also may belong to more than one provider.

The multi-cloud service composition problem is given a set of clouds that hosts the services offered by a number of providers. The Skyline service algorithm is designed to select the minimal sub-set of clouds and providers, while reducing the cost of communication between the providers and clouds.

Skyline was originally introduced in the database domain [30]. Given a set of S points in a D-dimensional space, the points in the Skyline are not dominated by any other place in the search space [31].

Definition 2 (Dominance Service and Skyline service): In service composition, dominance services are better in all parameters of service quality compared to other services. For example, $SA= \{S_1, S_2, S_5\}$ is a set of services that provides task A with QoS= {3, 4, 2}in time and $SB= \{S_2, S_4\}$ that provides task B with QoS= {4, 5}

in time. The Skyline service for SA= S_5 and for SB=S_2 are not dominated by other services, and it is the best candidate service [28, 32- 33].

The Skyline was introduced for the first time to create a web service and to evaluate its effectiveness [30]. In the service composition, the dominant service is the services that are better than others in all aspects of service quality. To this end, some researchers have proposed different methods for determining the dominant relationship to determine the Skyline service [34-35].

Therefore, if a service is part of Skyline, it is expected to offer better parameters than other services [36]. In the above example for SA and SB, the composition of Skyline services is {S5, S2}, in which a set of services are dominated by none of the services in the other composition [11] as {S_1, S_2}, {S_1, S_4}, {S_2, S_2}, {S_2, S_4}, {S_5, S_2}, and {S_5, S_4}.

One of the algorithms offered by the Skyline service, which is used in this investigation, is a dual progressive algorithm [11] for making composition possible. The root, that is, the parent node, is constructed first, and then the next nodes are constructed**.** The rule to create each node is that the selected services available in composition are different only in one service with its child nodes. For example, the root node in Figure 1 is a_1, b_1, c_1, and its child nodes include (a_1, b_2, c_1), (a_1, b_1, c_2), and (a_2, b_1, c_1). The lattice expansion determines only the sequence of counts between the nodes, and proves that each node is considered after its ancestors, but for nodes that do not have parent-child relationships, an appropriate order must be guaranteed. Since it may have a score of (a_1, b_2, c_1) less than (a_1, b_1, c_3), it should be counted in advance. In order to achieve the progressive counting of the base, the lattice expansion (T) with a heap (H) is used. The lattice expansion ensures that the parent node is counted before the child node. On the other hand, the heap determines the counting of the nodes that do not have a parent-child relationship. The commencement of the manufacturing process starts from the first level. At each step of the count, the lattice expansion is extracted from the heap with the lowest cost and is compared with the existing Skyline. Ultimately, the considered composition is placed in Skyline if it is not lost or eliminated. The progressive algorithm of a node can be generated several times from generating other parent nodes, which creates a replication problem. As shown in Figure 1, the top number of each node shows its parent number. For example, the node (a_3, b_2, c_2) is placed three times in the heap because it has three parents, and each time they develop (a_3, b_2, c_2), they are generated and placed in H. The multiplication of the node has many computational problems since many nodes are processed several times. The same node can be located in Skyline more than once, which causes a false Skyline [9].

The parent table [11] provides a suitable solution for solving a node problem with the least computation. Instead of considering all the ancestors, the parent table only stores information about the number of parents for a given node. The basic rule is that a node can be put in a heap only when all its parents are already processed. The parent table stores the number of parents in each node. Each time the node is compared to another node, the number of parents is reduced by one unit, and the table is updated with new values; eventually, every node in its value reaches zero in the heap. This operation ensures that all the nodes of the child are placed in the heap before the parent nodes [11].

In the next step, the best service in the lattice should be selected taking into account the dominant relationship. Then, the Button-Up Algorithm [11] strategy is to use linear compositions while doing comparisons to select the best composition. A linear composition is to compare the results of the two nodes with the next node, and achieving the best possible composition [11, 29]. Button-Up Algorithm carries out optimization and QoS calculations with positive traits inherited from dual progressive algorithm.

4. DETECTING A MULTI-CLOUD ENVIRONMENT USING THE SKYLINE SERVICE ALGORITHM

In this research, the Magnetic Cluster Expansion (MCE) is modeled as a set of lattice expansion, as shown in Figure 2. Each cloud is described as a lattice expansion created to group the providers based on the services they provide, and another lattice expansion has been created to express the relationships between the desirable providers and their hosting clouds.

Since a provider may belong to more than one cloud, so with respect to the given N clouds, the information about the services and their providers is modeled in the N lattice expansion, where each one represents the environment of a cloud. First, a number of the preferred composition of the providers are selected as equal to the

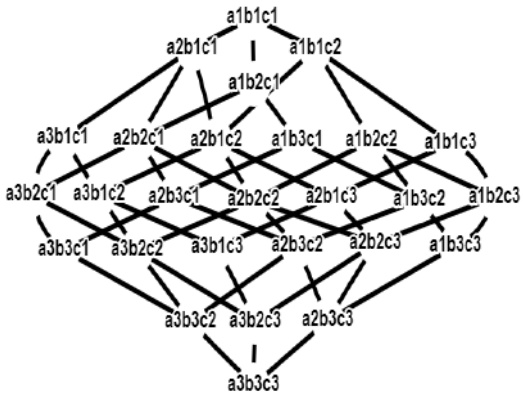

Figure 1. Lattice Expansion

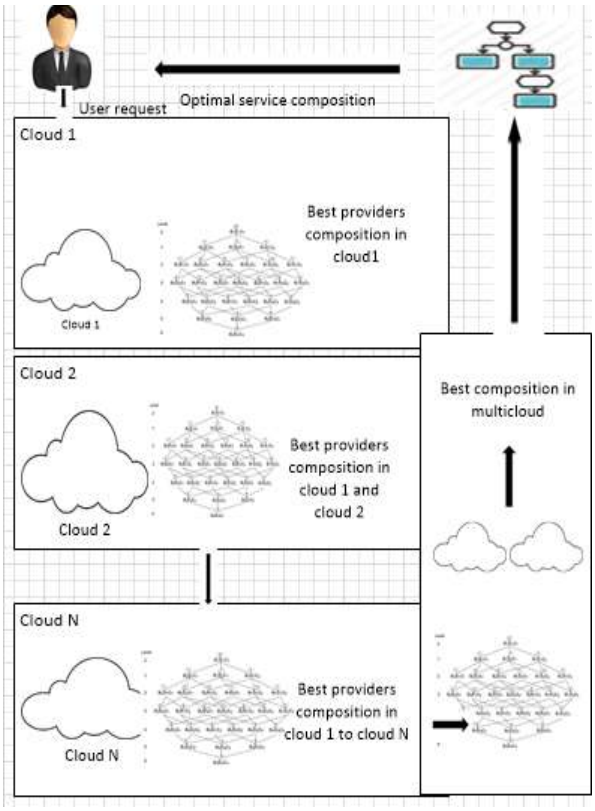

Figure 2. The proposed method

number of the available clouds. After comparing and choosing the most suitable composition, a multi-cloud spreading lattice expansion is built, and the optimal composition of the clouds is selected from this lattice expansion.

An example of a multi-cloud environment is shown in Table 1. Thirty services with various QoS functions and capabilities are provided by five providers on three clouds. For example, Cloud C_1 hosts three providers, which altogether provide 13 services. Some providers may deploy their services in multiple clouds (e.g., P_2, P_5).

Based on the example above that shows a cloud environment with three clouds, a lattice is expanded for each cloud, and for a multi-cloud environment, a distributed lattice is modeled. Table 2 describes the relationships between the providers and their host clouds, and Table 3 describes the relationships between the providers and their services in Cloud 1.

This research seeks to find a composition of clouds and providers that hosts the best service and to reduce the

TABLE 1. An example of multi-cloud environment

Clouds	**C_1**			**C_2**		**C_3**		
Providers	P_1	P_2	P_3	P_4	P_5	P_1	P_5	P_2
Services	5	4	4	2	3	5	4	3

TABLE 2. An example of relationships between the clouds and providers in a multi-cloud environment

MCE	**C_1**	**C_2**	**C_3**	**C_4**	**C_5**
P_1	0	0	1	0	1
P_2	0	1	1	0	0
P_3	0	0	1	1	0
P_4	1	1	0	0	0

TABLE 3. An example of relationships between the providers and their services in Cloud 1

$Cloud_1$	**P_1**	**P_2**	**P_3**	**P_4**
S_1	0	5	7	9
S_2	5	0	4	6
S_3	7	4	0	3
S_4	9	6	3	0

cost of communication between the services that come from different clouds. For this purpose, two algorithms are proposed to select a multi-cloud composition that uses the minimum number of providers and clouds. The steps are briefly summarized below:

Step 1- Extracting the optimal composition of providers: In this step, the best composition of providers is extracted in each of the clouds. By comparing the compositions obtained from all the clouds, the optimal composition that meets the user's request is selected and then used as input to determine the optimal cloud composition.

Step 2 - Extracting the optimal composition of the cloud: At this point, the lattice expansion, which shows the relationship between the providers and their host clouds, is used to obtain the optimal composition of clouds according to the providers selected in Step 1. The random composition of the clouds, which hosts the optimal composition of the providers, is selected as the root of the lattice expansion; the lattice expansion is thus complete and is selected based on the dominant relationship of the optimal composition of the clouds.

The following sections give more details about each of the above steps.

4. 1. Extracting the Optimal Composition of Providers This step uses the Skyline service algorithm to extract the optimal composition of providers in each cloud. In selecting the optimal composition, none of the existing approaches take into account the number of providers and the cost of communication between the providers. To determine the cost of communication between two providers, each cloud environment uses the information shown in Table 4. In this study, the matrix values are simple, representing the time of communication between two providers (in milliseconds).

TABLE 4. Matrix of communication cost between providers in cloud1

	P_1	P_2	P_3	P_4
P_1	0	5	7	9
P_2	5	0	4	6
P_3	7	4	0	3
P_4	9	6	3	0

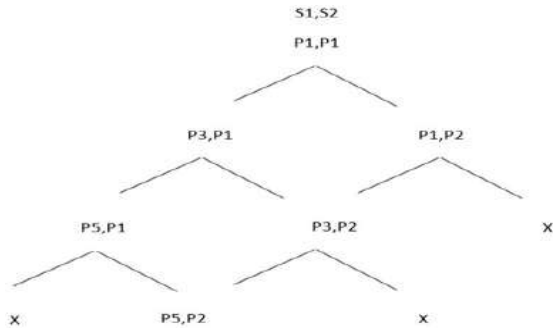

Figure 3. An example of lattice expansion of providers

This algorithm considers the user requested services to determine the appropriate composition; Sr is considered as an input to create a lattice expansion in each cloud. For creating a lattice expansion in each cloud (Algorithm 3), the root node is created based on a possible composition of providers (line 4 in Algorithm 1), which satisfies the user's requested services. For example, if a user requests S_1, S_2 services (Figure 3), the above algorithm will be considered as the root in Cloud 1 of the P_1, P_1 composition that delivers the services that are being provided; then, the child nodes are constructed.

Rule 1: The child node is a node that differs in the composition of providers with the parent node only in one provider.

So, the child nodes of the above example will be (P_3, P_1) and (P_1, P_2); after determining each node, the cost of each node is calculated according to Equation (1).

$$Si \coloneqq \alpha * Ni + \beta \sum_{j=1}^{|E|} cost\ j \quad (1)$$

where E is the set of edges that show the communication between the providers in a composition, cost j denotes the cost of communication between the providers Px and Py in the j relationship link, and Ni is the number of existing providers in the i-th composition. Also, α and β are numeric values representing the number of providers and the communication costs of the providers, respectively. To avoid the presence of providers in dispersed areas and encourage the lowest cost of communication between providers as the most important goal, the amount of α should be smaller than β. Having created the lattice expansion starting from the root node, the root node first appears in the heap and is selected as the Skyline. After removing the root node, its children are added to the heap if all their fathers are examined, and so the cost of each composition is compared with the cost of the composition in the Skyline; then, if the composition is found to be optimal, the Skyline is updated. Hence, the best composition is selected by comparing the cost of the composition. Thereafter, the second cloud's lattice expansion will be created and the optimal composition will be compared with that of the first cloud, and the best composition will be selected. The output of this algorithm is the optimal composition of providers.

4. 2. Extracting the Optimal Composition of Clouds

The composition obtained from the algorithm in the previous section is the input of this algorithm. The goal of this stage in a cloud-based environment is to classify the clouds that together provide the equired services. By evaluating all possible compositions, the optimal cloud composition is determined, from which the appropriate services are delivered to the user. Here, to determine the cost of the relationship between the two clouds, the matrix values in Table 5 are simple values that represent the time between the clouds (in milliseconds).

To determine the optimal composition of clouds, the optimal composition of providers from the previous step is considered as input to determine the root of the lattice expansion, and thus the lattice expansion is completed (Algorithm 3). When constructing cloud compositions, the cost of each compound is calculated in accordance with Equation (1). The only difference is that E is the number of edges representing the connections between the clouds in the composition, and j shows the cost of communication between the two clouds, C_x and C_y, on the j_{th} communication link. Ni is the number of clouds in the i_{th} composition. The total cost of the composition is calculated by taking into account the total communication costs in the cloud composition according to Equation (1). In this algorithm, α and β are also numerical values representing important factors such as the number of clouds and the cost of cloud communications, respectively. Thus, α should be smaller than β to avoid the presence of clouds in dispersed areas and to encourage the lowest cost of communication between the clouds, which is considered as the most important goal. For example, if the optimal composition obtained from the previous step of composition (P_3, P_1) is used, the algorithm takes into account in the multi-cloud environment of (C_3, C_3) compound that hosts the providers in the optimal composition; then, the child nodes are constructed, which are shown in Figure 4.

Rule 2: In creating each child node, the composition is different from that of the provider only with the parent node. So the child nodes of the above example will be (C_4, C_3) and (C_3, C_5).

5. EXPERIMENTAL RESULTS

This section provides details of the experiments conducted to evaluate the performance of the proposed method. The Java programming language has been used in this approach, and the development environment is NetBeans IDE 8.2.

In this study, Java classes have been used to randomly generate some experimental data sets, including a set of services and relationships between the clouds, providers, and services provided by each provider, as well as α, 0.3, and β, 0.7.

The experiments are conducted in environments with a number of different clouds (between 5 and 100) and services ranging from 1 to 20; since the creation of a multi-cloud environment is a coincidence, the test of each environment is repeated 50 times. The user's request in all the test cases consists of three services.

5. 1. Estimating the Computation Time

In these experiments, as in similar methods, a concept called density has been considered to determine the impact on the total execution time when the providers are hosted in several clouds; the total execution time is between 20 and 40%, and the number of clouds is between 5 and 100. The composition time results are shown in Figure 5.

TABLE 5. Matrix of communication cost between clouds

	C_1	C_2	C_3	C_4
C_1	0	6	8	10
C_2	6	0	9	12
C_3	8	9	0	4
C_4	10	12	4	0

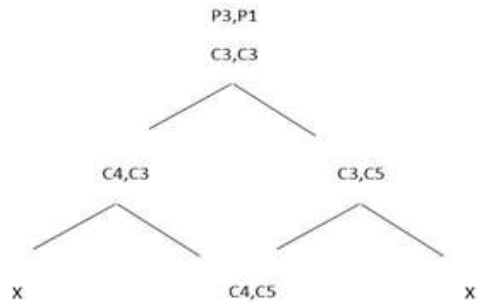

Figure 4. Example lattice expansion of clouds

Algorithm 1: Extracting optimal composition of providers

Input: A user request Sr
Output: Best provider composition
1: **Begin**
2: Best provider composition=0;
3: **for each** cloud Ci do
4: Creating expansion lattice based on Sr (Algorithm 3)
5: Best=RootNode; H=RootNode;
6: **While**(! H.isEmpty())
7: Remove the top node from H;
8: **if** n is dominated by Best
9: Best=n;
10: **end if**
11: CN=expand(n,T);
12: **for** all node ni in CN
13: P(ni) --;
14: **if**(P(ni)==0)
15: H.add(ni);
16: **end if**
17: **end for**
18: **end while**
19: **if** Best is dominated by Best provider composition
20: Best provider composition=Best;
21**: end for**
22: **return** Best provider composition;
23: **End**

Algorithm 2: Extracting optimal composition of clouds

Input: Best provider composition
Output: Best cloud composition
1: **Begin**
2: Creating expansion lattice based on
Best provider composition(Algorithm 3)
3: Best=RootNode; H=RootNode;
4: **While**(! H.isEmpty())
5: Remove the top node from H;
6: **if** n is dominated by Best
7: Best=n;
8: **end if**
9: CN=expand(n,T);
10: **for** all node ni in CN
11: P(ni) --;
12: **if**(P(ni)==0)
13: H.add(ni);
14: **end if**
15: **end for**
16: **end while**
17: **return** Best cloud composition;
18: **End**

Algorithm 3: Creating Expansion Lattice for providers (or clouds)

Input: A provider(cloud) composition that provide user request (or Best provider composition)
Output: Expansion Lattice
1: **Begin**
2: **for each** a provider(cloud) composition
3: int num=number of user request (or Best provider composition)
4: **While** (num!=0)
5: change node that number is num based provider(cloud) that is provide same service(provider)
6: num**--;**
7: **end while**
8: **end each**
9: **return** Expansion Lattice;
10: **End**

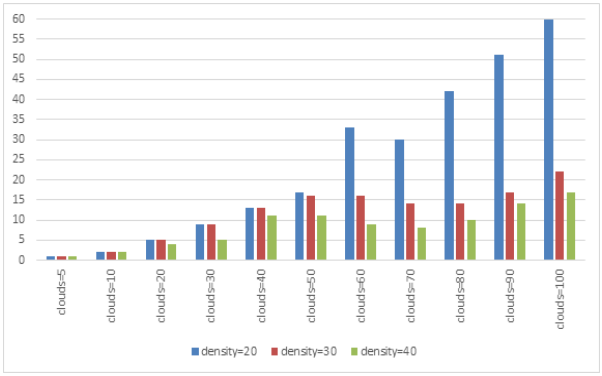

Figure 5. Results of the computation time

According to this figure, the computation time at a density of 40 is lower than the other two densities, and especially with a higher number of clouds, this difference is more evident. In general, this algorithm has a low computational time for the cloud environment with a different number of clouds. Also, the execution time is slightly high when a provider is not hosted on several clouds.

5. 2. Estimating the Cost and Number of Clouds in the Selected Composition Figure 6 shows that the size of the optimal composition and composition costs are not affected by the changes in density and the number of clouds. The experimental results show that the Skyline-based approach always produces a favorable cloud composition even in a large-scale cloud-based environment, and even when each provider is hosting a small number of clouds.

5. 3. Comparison of Cloud Communication Costs In this section, the performance and quality of the proposed solution are compared with the Mezni method [23]. These two methods are compared in a multi-cloudenvironment with 100 clouds and three user-requested services. MCE1 is a cloud environment with a density of 20, MCE2 has a density of 30, and MCE3 is 40.

The overall cost for each cloud compilation generated by the FCA and the Skyline was calculated using defined equation. The results for the FCA are shown in Figure 7, but the value of the Skyline is fixed to be 0.3. It is clear from Figure 7 that for all the MCE settings, the best cost was obtained by Skyline. It also shows that the proposed method always achieves the best cloud composition with the lowest cost.

5. 4. Comparisons of Run-time Given the time required to find the optimal cloud composition, the run times in Figure 8 show that Skyline is better than FCA for the three MCE experiments. That is, by changing the density, the proposed algorithm is faster in terms of computational time. This is explained by the dual progressive algorithm, Heap memory and parent table in Skyline algorithm. Also, using a bottom-up algorithm and the linear composition strategy, we can find the optimal combination in the lattice, without needing to run through the whole multi-cloud lattice.

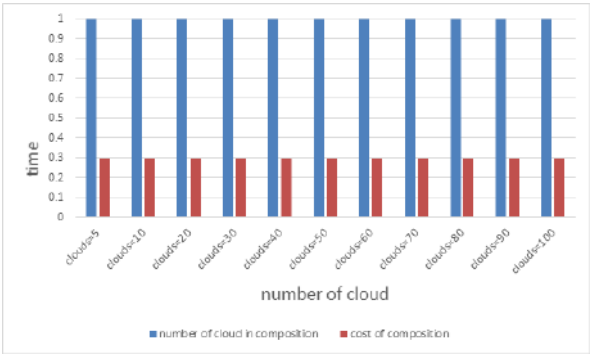

Figure 6. Estimating the cost and number of clouds in composition

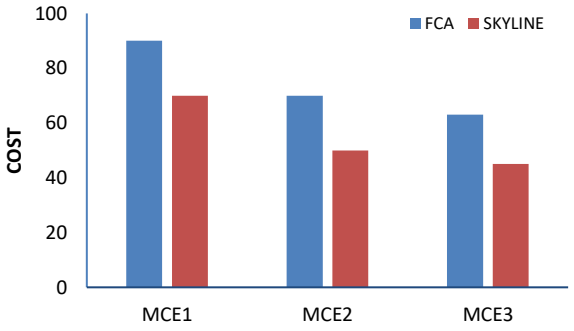

Figure 7. Estimating the cost and number of clouds for FCA and Skyline

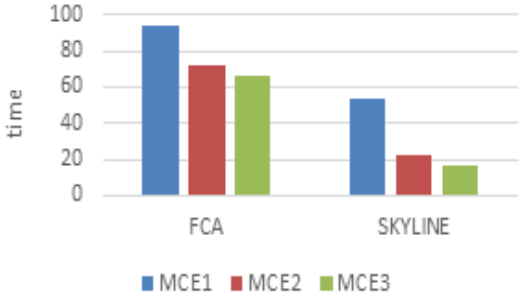

Figure 8. Run time in FCA and Skyline

6. CONCLUSIONS

With the advent of virtual resource sharing, cloud platforms have created a new paradigm that provides more efficient and convenient services. As stated previously, most of the service composition methods in cloud environments assume that the involved services come from one cloud. This study investigated the use of the Skyline service algorithm to compose services in multi-cloud environments, which examines all the clouds during the service compilation process. Since this algorithm provides the creation of all the possible combinations, the proposed method allows the selection of the optimal composition of user-requested services in a cloud-based environment. In the proposed method, the criteria for choosing the best composition in a cloud environment are fewer providers and a shorter communication time between the providers. Hence, the best composition in a cloud environment is the one that includes these criteria. Overall, the following results have been obtained:

1. The use of the Skyline algorithm makes it possible to review all the possible composition of services offered by providers in a cloud-based environment.

2. The proposed Skyline algorithm always finds the optimal cloud compositions.

3. The proposed algorithm improves the accuracy of the optimal composition and reduces the time of computation.

Also, this study focuses on the sequential structure of a service composition. This is why the total cost of communication between the clouds is calculated based on the order of the services executed as the sum of the communication costs of the provider's composition and the cloud. The sequential structure is one of the four main structures of a service composition in the YAWL model [4], and it is a topic of interest for future studies on other structures.

7. REFERENCES

1. Curbera, F., Duftler, M., Khalaf, R., Nagy, W., Mukhi, N., & Weerawarana, S., "Unraveling the Web Services Web: an Introduction to SOAP, WSDL, and UDDI", ***IEEE Internet Computing***, Vol. 6, No. 2, (2002), 86-93. DOI: 10.1109/4236.991449
2. Guinard, D., Trifa, V., Karnouskos, S., Spiess, P., & Savio, D., "Interacting with the SOA-based Internet of Things: Discovery, Query, Selection, and on-demand Provisioning of Web Services", ***IEEE Transactions on Services Computing***, Vol. 3, No. 3, (2010), 223-235. DOI: 10.1109/TSC.2010.3
3. Du, Y., Hu, H., Song, W., Ding, J., & Lü, J., "Efficient Computing Composite Service Skyline with QoS Correlations", In 2015 IEEE International Conference on Services Computing, (2015), 41-48. DOI: 10.1109/SCC.2015.16
4. Gabrel, V., Manouvrier, M., & Murat, C., "Web Services Composition: Complexity and Models", ***Discrete Applied Mathematics***, Vol. 196, (2015), 100-114. DOI: 10.1016/j.dam.2014.10.020
5. Cui, L., Kumara, S., & Lee, D., "Scenario Analysis of Web Service Composition based on Multi- Criteria Mathematical Goal Programming", ***Service Science***, Vol. 3, No. 4, (2011), 280-303. DOI: 10.1287/serv.3.4.280
6. Bypour, H., Farhadi, M., & Mortazavi, R., "An Efficient Secret Sharing-based Storage System for Cloud-based Internet of Things", ***International Journal of Engineering,*** Vol. 32, No. 8, (2019), 1117-1125. DOI: 10.5829/ije.2019.32.08b.07
7. Jeyanthi, N., Shabeeb, H., Durai, M. S., & Thandeeswaran, R., "Reputation based Service for Cloud User Environment", ***International Journal of Engineering, Transactions B: Applications***, Vol. 27, No. 8, (2014), 1179-1184. DOI: 10.5829/idosi.ije.2014.27.08b.03
8. Jula, A., Sundararajan, E., & Othman, Z., "Cloud Computing Service Composition: A Systematic Literature Review", ***Expert Systems with Applications***, Vol. 41, No. 8, (2014), 3809-3824. DOI: 10.1016/j.eswa.2013.12.017
9. Microsoft Communication & Media Industries, "Multi-Cloud Service Delivery end-to-end Management," Ref.architecture, 2013. https://cloudblogs.microsoft.c om/industry-blog/industry/uncategorized/multi-cloud- service-delivery-and-end-to-end-management-reference- architecture/
10. Venkat, M., 2016. Enterprise cloud strategy: Governance IBM. https://www.ibm.com/blogs/cloud-computing/2016/11/03/enterprise-governance-multi-cloud/
11. Yu, Q., & Bouguettaya, A., "Efficient Service Skyline Computation for Composite Service Selection", ***IEEE Transactions on Knowledge and Data Engineering***, Vol. 5, No. 4, (2013), 776-789. DOI: 10.1109/TKDE.2011.268
12. Belkasmi, D., Hadjali, A., & Azzoune, H., "On Fuzzy Approaches for Enlarging Skyline Query Results", ***Applied Soft Computing***, Vol. 74, (2019), 51-65. DOI: 10.1016/j.asoc.2018.10.013
13. Elmi, S., & Min, J. K., "Spatial Skyline Queries over Incomplete Data for Smart Cities", ***Journal of Systems Architecture***, Vol. 90, (2018), 1-14. DOI: 10.1016/j.sysarc.2018.08.005
14. Lim, J., Li, H., Bok, K., & Yoo, J., "A Continuous Reverse Skyline Query Processing Method in Moving Objects Environments", ***Data & Knowledge Engineering***, Vol. 104, (2016), 45-58. DOI: 10.1016/j.datak.2015.05.003
15. Yang, Z., Li, K., Zhou, X., Mei, J., & Gao, Y., "Top k Probabilistic Skyline Queries on Uncertain Data", ***Neurocomputing***, Vol. 317, (2018), 1-14. DOI: 10.1016/j.neucom.2018.03.052
16. Zou, G., Chen, Y., Yang, Y., Huang, R., & Xu,Y., "AI Planning and Combinatorial Optimization for Web Service Composition in Cloud Computing", In Proccedding of the International Conference on Cloud Computing and Virtualization, (2010), 1-8. DOI: 10.5176/978-981-08-5837-7_166
17. Gutierrez-Garcia, J. O., & Sim, K. M., "Agent-based Cloud Service Composition", ***Applied Intelligence***, Vol. 38, No. 3, (2013), 436-464. DOI: 10.1007/s10489-012-0380-x
18. Jatoth, C., Gangadharan, G.R., & Buyya, R., "Optimal Fitness Aware Cloud Service Composition using an Adaptive Genotypes Evolution based Genetic Algorithm", ***Future Generation Computer Systems***, Vol. 94, (2019), 185-198. DOI: 10.1016/j.future.2018.11.022
19. Jatoth, C., Gangadharan, G. R., & Fiore, U., "Optimal Fitness Aware Cloud Service Composition using Modified Invasive Weed Optimization", ***Swarm and Evolutionary Computation***, Vol. 44, (2019), 1073-1091. DOI: 10.1016/j.swevo.2018.11.001

20. Gavvala, S. K., Jatoth, C., Gangadharan, G. R., & Buyya, R., "QoS-Aware Cloud Service Composition using Eagle Strategy", ***Future Generation Computer Systems***, Vol. 90, (2019), 273-290. DOI: 10.1016/j.future.2018.07.062
21. Yu, Q., Chen, L., & Li, B., "Ant Colony Optimization Applied to Web Service Compositions in Cloud Computing", ***Computers & Electrical Engineering***, Vol. 41, (2015), 18-27. DOI: 10.1016/j.compeleceng.2014.12.004
22. Kurdi, H., Al-Anazi, A., Campbell, C., & Al Faries, A., "A Combinatorial Optimization Algorithm for Multiple Cloud Service Composition", ***Computers & Electrical Engineering***, Vol. 42, (2015), 107-113. DOI: 10.1016/j.compeleceng.2014.11.002
23. Mezni, H., & Sellami, M., "Multi-Cloud Service Composition using Formal Concept Analysis", ***Journal of Systems and Software***, Vol. 134, (2017), 138-152. DOI: 10.1016/j.jss.2017.08.016
24. Mezni, H., & Abdeljaoued, T., "A Cloud Services Recommendation System based on Fuzzy Formal Concept Analysis", ***Data & Knowledge Engineering***, Vol. 116, (2018), 100-123. DOI: 10.1016/j.datak.2018.05.008
25. Wu, J., Chen, L., & Liang, T., "Selecting Dynamic Skyline Services for QoS-based Service Composition", ***Applied Mathematics & Information Sciences***, Vol. 8, No. 5, (2014), 2579. DOI: DOI: 10.1145/1772690.1772693
26. Zhang, F., Hwang, K., Khan, S., & Malluhi, Q., "Skyline Discovery and Composition of Inter-Cloud Mashup Services", ***IEEE Transactions on Services Computing***, Vol. 9, No. 1, (2016), 72-83. DOI: 10.1109/TSC.2015.2449302
27. Zhang, J., Jiang, X., Ku, W. S., & Qin, X., "Efficient Parallel Skyline Evaluation using Mapreduce", ***IEEE Transactions on Parallel and Distributed Systems***, Vol. 27, No. 7, (2016), 1996-2009. DOI: 10.1109/TPDS.2015.2472016
28. Liu, Y., Yang, R., & Zhang, S., "Service Selection Method based on Skyline in Cloud Environment", ***International Journal of Performability Engineering***, Vol. 13, No. 7, (2017). DOI: 10.23940/ijpe.17.07.p5.10391047
29. Moradi, M., & Emadi, S., "Reducing the Calculations of Quality-Aware Web Services Composition Based on Parallel Skyline Service", ***International Journal of Advanced Computer Science and Applications***, Vol. 7, No. 7, (2016). DOI: 10.14569/IJACSA.2016.070744
30. Borzsony, S., Kossmann, D., & Stocker, K., "The skyline Operator", In Proceedings 17th IEEE International Conference on Data Engineering, (2001), 421- 430. DOI: 10.1109/ICDE.2001.914855
31. Papadias, D., Tao, Y., Fu, G., & Seeger, B., "Progressive skyline Computation in Database Systems", ***ACM Transactions on Database Systems***, Vol. 30, No. 1, (2005), 41-82. DOI: 10.1145/1061318.1061320
32. Wang, Y., Song, Y., & Liang, M., "A Skyline-based Efficient Web Service Selection Method Supporting Frequent Requests", In 2016 IEEE 20th International Conference on Computer Supported Cooperative Work in Design (CSCWD), (2016), 328-333. DOI: 10.1109/CSCWD.2016.7566009
33. Fariss, M., Asaidi, H., & Bellouki, M., "Comparative Study of Skyline Algorithms for Selecting Web Services based on QoS", Procedia Computer Science 127, (2018), 408-415. DOI: 10.1016/j.procs.2018.01.138
34. Alrifai, M., Skoutas, D., & Risse, T., "Selecting Skyline Services for QoS-based Web Service Composition", In Proceedings of the 19th International Conference on World Wide Web, (2010), 11-20. DOI: 10.1145/1772690.1772693
35. Benouaret, K., Benslimane, D., & Hadjali, A., "Ws-Sky: An Efficient and Flexible Framework for QoS-aware Web Service Selection", In IEEE Ninth International Conference on Services Computing, (2012), 146-153. DOI: 10.1109/SCC.2012.83
36. Fekih, H., Mtibaa, S., & Bouamama, S., "Local-Consistency Web Services Composition Approach based on Harmony Search", Procedia Computer Science 112, (2017), 1102-1111. DOI: 10.1016/j.procs.2017.08.135

Persian Abstract

چکیده

رشد سریع بهره‌برداری از محیط‌های ابری موجب ارائه‌ی انواع مختلف منابع به عنوان سرویس در این محیط شده است. از آن‌جا که عملکرد یک سرویس معمولاً بسیار ساده است و پاسخگوی نیاز پیچیده‌ی کاربر نیست، نیاز به ترکیب این سرویسها که قادر به ارضا نیازهای کاربران باشد، ضروری است. بیشتر روشهای ترکیب سرویس در محیط های چند ابری فرض می کنند که سرویس‌های شرکت‌کننده در ترکیب در یک ابر هستند که این رویکرد غیر واقعی است زیرا ممکن است ابرهای دیگر سرویس‌های مناسب‌تری را ارائه دهند. در ترکیب سرویس‌های توزیع شده در محیط‌های چند ابری، یک کار چالش‌برانگیز دیگر کاهش هزینه‌های مالی با کاهش تعداد ارائه‌دهندگان و ابرهای شرکت‌کننده در ترکیب و کاهش هزینه‌ی ارتباطات بین ارائه‌دهندگان و ابرها است. برای رفع این چالش باید تعداد فراهم کنندگان سرویسها در ابرها در فرایند ترکیب کاهش یابد. این تحقیق از الگوریتم Skyline Service برای ترکیب سرویس‌ها در محیط‌های چند ابری استفاده می کند تا تمام ابرها در فرایند ترکیب سرویس بررسی شوند. روش پیشنهادی می تواند یک سرویس ترکیبی قابل استفاده برای کاربر ارائه کند که پارامترهایی همچون کمترین تعداد ارائه‌دهنده و ابر را درنظر می گیرد. الگوریتم Skyline Service در دو مرحله استفاده می شود. در مرحله اول، بهترین ترکیب سرویس در یک ابر از میان تمام فراهم کنندگان با درنظرگرفتن تعداد فراهم کنندگان و زمان ارتباطی انتخاب می شود. در مرحله دوم، الگوریتم Skyline Service برای ایجاد تمام ترکیبات ممکن در محیط چند ابری استفاده می شود. پارامترهایی مثل تعداد ابر کمتر و زمان ارتباطی کمتر بین ابرها در این مرحله اعمال می شود. نتایج نشان می دهد که روش پیشنهادی می تواند ترکیبی با حداقل تعداد ابرها، کمترین هزینه و کمترین زمان محاسباتی را پیدا کند. در نهایت می توان گفت که Skyline Service یک ترکیب مناسب از سرویسهای درخواستی کاربر را در یک محیط چند ابری انتخاب می کند.

International Journal of Engineering

Journal Homepage: www.ije.ir

Effect of Segregation on Opinion Formation in Scale-free Social Networks: An Agent-based Approach

A. Mansouri*[a], F. Taghiyareh[b]

[a] *ICT Research Institute, Tehran, Iran*
[b] *Department of Electrical and Computer Engineering, University of Tehran, Tehran, Iran*

PAPER INFO

Paper history:
Received 09 May 2020
Received in revised form 14 September 2020
Accepted 30 October 2020

Keywords:
Opinion Formation
Social Networks
Social Impact Model
Segregation
Agent-Based Modeling

ABSTRACT

We consider the effect of segregation on opinion formation in social networks with and without influential leaders in scale-free random networks, which is found in many social and natural phenomena. We have used agent-based modeling and simulation, focusing on the social impact model of opinion formation. Two simulation scenarios of this opinion formation model have been considered: (1) the original scenario which randomly assigns persuasion strengths to the agents, and (2) a centrality-based scenario, which assigns persuasion strengths proportional to the agents' centralities. In the latter scenario, hubs are considered more influential leaders who are more connected to others and have higher persuasion strengths than others. The simulation results show a correlation between segregation and change of population opinion in the original model, but no correlation between both variables in the centrality-based scenario. The results lead us to conclude that with strong influential leaders in society, the effect of segregation in opinion formation is neglectable.

***doi**: 10.5829/ije.2021.34.01a.08*

1. INTRODUCTION[1]

Opinion formation is a social contagion [1] or collective behavior process [2], describing how opinions forms in society due to the members' communication. Opinion formation is essential in studying consumer behavior, organizational behavior, predicting election results, and many others. Many studies have been conducted on opinion dynamics. Some studies have shown public opinion formation through online social networks, the largest infrastructure for social interactions [3], in general topics and discussions [4, 5] as well as in many social movements and national referendums, e.g., the Arab Spring of 2011 [6], the US presidential 2016 election [7], and the Brexit referendum [8].

In opinion formation studies, a common approach is to model social opinions by a binary value to reflect two different opinions, e.g., approval and disapproval in a referendum like Brexit [8]. The social impact model of opinion formation [2] is a binary opinion model, based on the social impact theory in psychology [9], describing how every individual's opinion is affected by social impacts from agreed and disagreed individuals. A noise parameter is also considered in this model as the non-deterministic part, reflecting the non-deterministic behavior of individuals.

The segregation phenomenon, defined as "the degree to which two or more groups live separately from one another" [10], affects opinion formation [11, 12]. Segregation happens in social networks due to network structure. Segregation happens in social networks due to network structure. In the social impact model of opinion formation, with a scale-free random network and randomly assigned attributes to the individuals, the more segregated opinion group dominates, the less segregated opinion group on average. Therefore, with the same population size and individual characteristics of both opinion groups, segregation is an overall influential factor for opinion formation because a more segregated opinion group attracts some individuals from

*Corresponding Author Institutional Email: amansuri@itrc.ac.ir (A. Mansouri)

Please cite this article as: A. Mansouri, F. Taghiyareh, Effect of Segregation on Opinion Formation in Scale-free Social Networks: An Agent-Based Approach, International Journal of Engineering, Transactions A: Basics Vol. 34, No. 01, (2021) 66-74

the other group and becomes the majority opinion group of society in equilibrium [13, 14].

The concept of leadership is also notable in opinion formation. The existence of influential leaders with high persuasion strengths and a lot of connectivities with other individuals in a society may have lots of effects on opinion dynamics and opinion formation. Some studies have shown the role of troll factories and bot networks with high connectivities to lead the public opinions in election campaigns even by spreading fake news [7, 8, 15].

In this research, we consider the effect of segregation in the social impact model of opinion formation using an agent-based modeling approach. To understand the role of segregation in the social impact model, we compare the results of two scenarios of the model: the original scenario in which persuasion strengths of the agents are randomly assigned; and a centrality-based scenario in which according to some social psychology studies the strength of persuasion of individuals is proportional to their centralities in the network. Among the various centrality measures, we have used the agents' node degrees, the simplest and the most commonly used centrality measure.

The rest of this paper is organized as follows. Section 2 summarizes the background of this study. In section 3, we explain the methodology. Section 4 presents the results. In section 5, we analyze and compare the results, and Section 6 concludes this study.

2. BACKGROUND

2. 1. The Social Impact Model of Opinion Formation Opinion formation describes how opinions about a specific topic evolve among individuals who interact with each other [16]. Many opinion formation models have been introduced in recent decades, mainly as agent-based models, in which agents represent individuals in society.

The social impact model of opinion formation [2] is based on the social impact theory in psychology formulated by Bibb Latané [9]. According to this theory, the impacts on individuals are exerted by the real, implied, or imagined presence or actions of one or more people or even groups. The impact of source agents on a subject agent depends on three factors: the (spatial, closeness, time, or abstraction) distance of the source agents from the subject agent, the source agents' strength of persuasion, and the number of source agents.

The social impact model is a discrete opinion model. Every agent takes an opinion from the conventionally binary values '-1' or '+1'. The binary opinion values could be interpreted as the agents' stances about a specific topic in two stances, for example, 'for'/ 'against' or 'agree'/ 'disagree'.

In the simplest version of the social impact model [17], we have N agents in the model with opinions $o_i=\pm1$ for i=1,2,.., N. In every time step, the impact on agent i is calculated as Equation (1), in which, p_j denotes persuasiveness strength of agent j, the strength of the agent j to persuade agent i with opponent opinion to change its opinion. Similarly, s_j denotes the supportiveness strength of agent j, the strength of the agent j to convince agent i with the same opinion to keep its current opinion. The parameter d_{ij} denotes the distance between the agents i and j, and α determines how fast the impact increase between agents i and j by decreasing their distance.

$$I_i = \left[\sum_{j=1}^{N} \frac{p_j}{d_{ij}^{\alpha}}(1-o_i o_j)\right] - \left[\sum_{j=1}^{N} \frac{s_j}{d_{ij}^{\alpha}}(1+o_i o_j)\right] \quad (1)$$

Since opinions are from the binary value set ±1, the summations of Equation (1) calculate the impact of the agents to change and keep the current opinion of agent j. The former summation calculates the change impact, and the latter summation calculates the keep impact.

The opinion dynamics is expressed by Equation (2), which predicts the opinion of agent i in the next time step using its current opinion (o_i), the social impact on it (I_i), and a random field representing all sources other than social impact affecting the opinion of agent i denoted by h_i. The sign function of Equation (2) maps negative values to -1 and positive values to +1.

$$o_i(t+1) = -sign\left[o_i(t)I_i(t) + h_i\right] \quad (2)$$

2. 2. Segregation in Social Networks Segregation is a consequence of homophily in real-life social networks. Homophily is the tendency of similar individuals to bounded with each other, which can be related to one or more features, and affects the network structure [18]. Some examples of common features include gender, race, age, and education level. Therefore, links are more likely to form between similar individuals in a common community [19] than between dissimilar individuals, and the segregation phenomenon happens. Segregation is defined as the degree to which two or more groups are separated from one another [10]. Segregation could be used in many aspects of social networks, including individuals' opinions. In [20], for example, segregated opinions about US presidential elections have been detected using data collected from Twitter.

To measure the degree of segregation in a social network, various indexes have been introduced, including the segregation matrix index (SMI) [10, 21]. SMI originally assumes two segregated sub-networks, while could be generalized for more sub-networks. Suppose an undirected network of N nodes, with m_{11} links in sub-network 1 and m_{22} links in sub-network 2.

SMI assigns a number to each segregated sub-network. To calculate SMI, the densities of links in both sub-networks are calculated using Equations (3) and (4),

$$d_{11} = m_{11} / m_{11+}, \quad (3)$$

$$d_{22} = m_{22} / m_{22+}, \quad (4)$$

in which, m_{11+} and m_{22+} denote the number of all possible links in sub-networks 1 and 2, respectively, calculated as Equation (5) and Equation (6), assuming sub-networks 1 and 2 consists of n_1 and n_2 nodes, respectively:

$$m_{11+} = n_1(n_1 - 1)/2, \quad (5)$$

$$m_{22+} = n_2(n_2 - 1)/2. \quad (6)$$

Then, the density of between-group links is calculated as Equation (7):

$$d_{12} = m_{12} / m_{12+} \quad (7)$$

in which, m_{12+}, the number of all possible links between both sub-networks, is calculated as Equation (8):

$$m_{12+} = n_1 n_2. \quad (8)$$

In the next step, SMI for both sub-networks is calculated by Equation (9) and Equation (10) which are normalized to a quantity between -1 and +1. The sub-network with higher SMI is more segregated.

$$S_1 = (d_{11} - d_{12})/(d_{11} + d_{12}) \quad (9)$$

$$S_2 = (d_{22} - d_{12})/(d_{22} + d_{12}) \quad (10)$$

2. 3. Opinion Leadership in Social Networks Opinion leaders are individuals who exert personal influence on other people in certain situations [22] and have a significant role in opinion formation.

From the social-psychological viewpoint, the influence of an opinion leader on the others is related to three factors: (1) who one is: the personification of certain values by the opinion leader's figure; (2) what one knows: the competence or knowledge related to the leaders; and (3) whom one knows: the strategic location in the social network [23]. One's influence on group opinions depends on how well-connected one is in the social network that determines communication [24]. Noelle-Neumann proposed a 10 item 'personality strength' scale to measure to what extent people perceive self-confidence in leading and influencing others, and according to a survey with 270 samples accomplished by Weimann and colleagues, network centrality was compared to the 10-item personal strength rating and a correlation of +0.54 was found between the individual's number of communication links and the personality strength measures, and they claimed this correlation was even higher when relating the personality strength to the number of communication links within the individual's clique or group [25]. Another study on a fandom newsgroup in USENET [26], shown a direct correlation between the number of posts with the influential ability. Some studies use the term *evangelists* for well-connected opinion leaders in online social networks to express their influence on society's opinion formation [27, 28]. Some studies have also revealed a correlation between opinion leadership and leaders' centrality in the network using an agent-based modeling approach [12-14, 25].

Therefore, from the social structure point of view, leaders are the more influential people who are well-connected to other nodes, often called 'hubs' [29, 30]. Although the correlation between influence and network centrality has been explained in the literature, less attention has been paid to the role of opinion leaders in the context of opinion formation on social networks.

3. METHODOLOGY

We have used an agent-based modeling approach [31], which has widely been used in opinion formation models [32, 33]. To study the effect of segregation on opinion formation, we considered a noise-free social impact model; thus, we supposed h_i=0 in Equation (2), the equation for opinion dynamics. More details of our method are described in the following subsections.

3. 1. Equilibrium Phases In the noise-free social impact model, after some time steps of the simulation, one of the following equilibrium phases or states may occur [12] and terminate the simulation run:

- Frozen phase: No change is observed in the agents' opinions advancing the time step.
- Orderly fluctuated phase: At least one agent changes its opinion every other time steps, i.e., after some time steps, there are agents whose opinions are the same as their opinions in two time steps ago (and other agents' opinions are the same as the previous time step).

Figure 1 shows how an orderly fluctuated phase may occur. Possible opinions are shown in black and white. The agents' persuasiveness and supportiveness strengths assumed to be the same, and d_{ij} between every agent pairs, i, and j, are supposed to be equal. Applying the social impact model rules cause the circular agents to change their opinions, regularly in every time step, while the rectangular agents do not change their opinions.

3. 2. The Network Topology The structure of the social network of interacting agents affects opinion

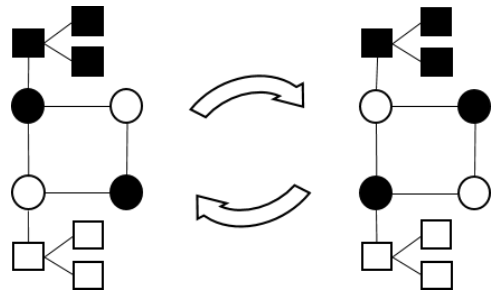

Figure 1. An orderly fluctuated phase example in the social impact model: the agents' p_j and s_j are the same; d_{ij}s are equal; the circular agents regularly change their opinions (black and white)

dynamics. Heavy-tailed distributions occur in complex systems, including social networks, and can help in data interpretation [34]. Although the universality of scale-freeness in social networks is controversial, it is common to claim that most of these networks are scale-free in the real-world [35].

In this research, we used the Barabási-Albert algorithm [36] to generate random scale-free networks of agents' connections. This algorithm starts from m_0 nodes, and using a preferential attachment mechanism adds every new node with m_1 edges that links the new node to previously added nodes with probability proportional to the nodes' degrees. The generated network is a scale-free network with power-law node degree distribution. We assumed m=2 and m_0=2 to generate random networks using this algorithm. Scale-free networks generated by this algorithm have a large number of small loops, which in turn cause many segregated nodes and groups [37].

3. 3. Two Assignment Scenarios We regarded two scenarios: the original scenario and the centrality-based scenario. In the original scenario, the persuasiveness and supportiveness strengths were assigned using a random variable from the uniform distribution Uniform(0, 100). In the centrality-based scenario, we considered the correlation between opinion leadership and the centrality of the agents in the network (as discussed in section 2). Therefore, persuasiveness and supportiveness strengths, p_i' and s_i' respectively, are assigned directly proportional to the node degrees according to Equation (11):

$$p_i' = s_i' = \left(d(i)/\Delta\right)\times 100, \quad (11)$$

where $d(i)$ denotes node degree of agent i and Δ denotes the maximum node degree in the network.

3. 4. Pseudo-Code of the Model Figure 2 shows the pseudo-code for the simulation algorithm. We assumed 1000 agents (line 1). For every agent i, p_i and s_i are assigned according to the simulation "*scenario"* (line 8), which is either "original" or "centrality-based" as mentioned before. It is also assumed that $1/(d_{ij})^{\alpha}$=1.

The 'for' loop at line 16 implements a one time step of the model. The simulation time steps continue by the 'while' loop of line 11 until a 'frozen' or 'orderly fluctuated' phase occurs. During this 'while' loop, values of ΔS and $\Delta\beta$ are calculated. ΔS indicates the difference of SMIs of both opinion groups, calculated as:

$$\Delta S = S_{-1} - S_{+1}, \quad (12)$$

in which, S_{-1} and S_{+1} denote SMI values of '-1' and '+1' opinion groups, respectively. $\Delta\beta$ indicates the difference between the percentage of '-1' opinion group before and after each time step, calculated as:

$$\Delta\beta = \beta_{next} - \beta_{current}, \quad (13)$$

in which β_{next} and $\beta_{current}$ denote the percentage of '-1' opinion group in the next time step and the current time step, respectively.

Every iteration of the 'for' loop of line 2 runs one replication of simulation. In every simulation replication, a new random seed is assigned to generate a various random numbers sequence. After 30 replications of simulation, implemented by for loop at line 2, the scatter plot for ΔS and $\Delta\beta$ variables is drawn, and the Pearson correlation coefficient is calculated in line 40.

4. RESULTS

To study the correlation between segregation and opinion formation in both mentioned scenarios of the social impact model of opinion formation, the original and the centrality-based scenarios, the simulation algorithm (Figure 2) has been run for both scenarios. The outputs of the simulation runs are presented in this section.

4. 1. The Original Social Impact Model Each simulation replication continues until an equilibrium phase, frozen or orderly fluctuated phase; therefore, every time step becomes one data sample for considering the correlation. Figure 3 shows β values, the percentage of '-1' opinion group, at every time step until an equilibrium phase for simulation of the original model.

As Figure 3 shows, simulation replications start from initial β=50%. The number of total time step samples shown in the figure is 304; therefore, the mean value of time steps until an equilibrium phase for 30 simulation replications is 10.13. The standard deviation is 2.15, minimum and maximum number of time steps are 7 and 12, respectively.

Algorithm 1: Pseudocode for the simulation.

```
N=1000 [Number of agents]
for i from 1 to 30 do [simulation replications]
    initialize rand_seed to a new seed value [to generate new random number sequence]
    B_A = Create_barabasi-albert for N nodes with m0 = m = 2
    create N agents and randomly assign each agent to one node of B_A
    randomly assign -1 opinion to 50 percent of the agents and assign +1 opinion to other agents
    for each agent Ai do
        generate and assign pi and si according to the Scenario [original or centrality-based]
    end For
    frozen_or_orderly_fluctuated = false
    while not frozen_or_orderly_fluctuated do
        S-1 = SMI(B_A, -1) [Segregated Matrix Index of -1 group]
        S+1 = SMI(B_A, +1) [Segregated Matrix Index of +1 group]
        ΔS = S-1 - S+1
        β1 = current_β()
        for every agent Ai do
            Ai_con = the agents connected to Ai according to B_A [assume Ai connects to Ai itself too]
            Ii_pers = Ii_sup = 0 [initialize sum of persuading and supporting impacts]
            for every Aj in Ai_con do
                if Aj's opinion = Ai's opinion then
                    Ii_sup = Ii_sup + sj [sum of supportive impacts]
                else
                    Ii_pers = Ii_pers + pj [sum of persuading impacts]
                end if
                Ii = 2*Ii_pers - 2*Ii_sup [Equation (1)]
                if Ii > 0 then [noise is supposed zero, decision based on Ii]
                    Ai's next opinion = -1 * Ai's opinion [change for the next time step] [Equation (2)]
                end if
            end for [every Aj in Ai_con]
        end for [every agent Ai]
        for every agent Ai do
            Ai's opinion = Ai's next opinion
        end for [every agent Ai]
        β2 = current_β()
        Δβ = β2 - β1
        save point (ΔS, Δβ)
        frozen_or_orderly_fluctuated = check_frozen_orderly_fluctuated()
    end while [not frozen_or_orderly_fluctuated]
end for
draw scatter plot for points (ΔS, Δβ) and calculate correlation
```

Figure 2. Pseudo-code for the simulation algorithm

As discussed for the pseudo-code of the simulation, for every time step depicted in Figure 3, a pair of ΔS and $\Delta\beta$ variables is calculated. The scatter plot of these pairs is shown in Figure 4, which shows a positive correlation between ΔS and $\Delta\beta$. The calculated Pearson correlation coefficient is equal to 0.728 (p-value < 0.01), indicating a strong positive correlation between ΔS and $\Delta\beta$. Both normality and homoscedasticity test have been passed. We used the D'Agostino-Pearson method and Levene method for the normality and homoscedasticity tests, respectively. The straight line on the scatter plot has been fitted using the least-square method.

4. 2. The Centrality-Based Social Impact Model

Very similar to the original model, the diagrams for the centrality-based model have been generated. Similar to Figure 3, Figure 5 shows β values in percent of the '-1' opinion group at every time step until an equilibrium phase for simulation of the centrality-based scenario. Again simulation replications start from initial β=50%. The total number of time step samples shown in the figure is 267, the mean value of time steps until an equilibrium phase is 8.90, the standard deviation is 2.04, minimum and maximum number of time steps are 5 and 13, respectively.

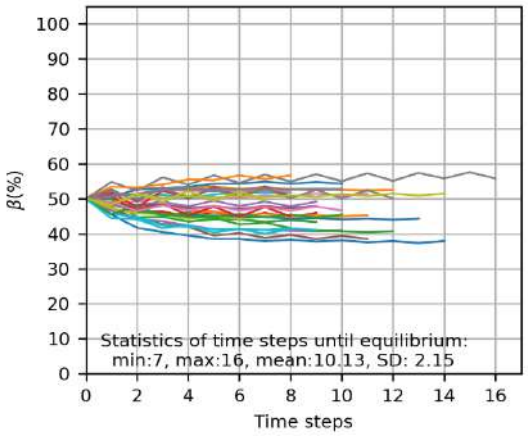

Figure 3. Percentage of the '-1' opinion group (β) for simulation replications until a frozen or orderly fluctuated equilibrium phase in the original scenario

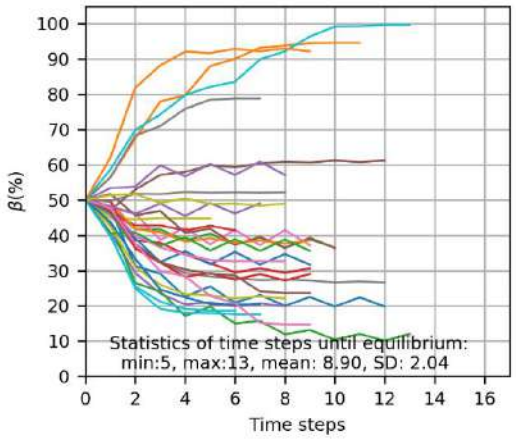

Figure 5. Percentage of the '-1' opinion group (β) for simulation replications until a frozen or orderly fluctuated equilibrium phase in the centrality-based scenario

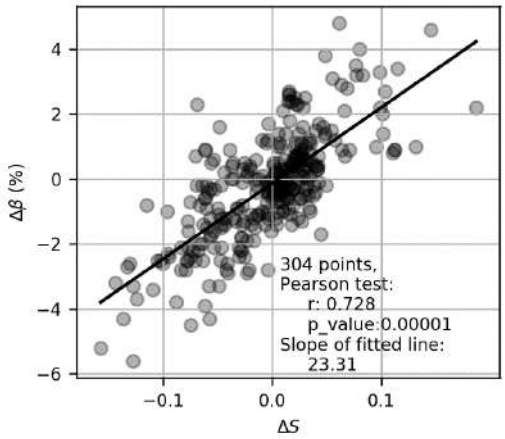

Figure 4. Scatter plot of "difference of the segregation of two opinion groups (ΔS)" and "difference of percentage of '-1' opinion group after one time step ($\Delta\beta$)"in the original scenario

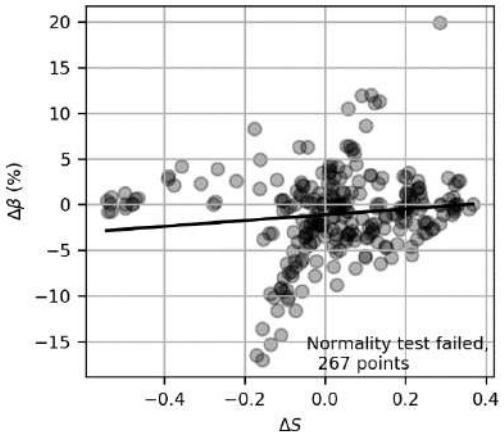

Figure 6. Scatter plot of "difference of the segregation of two opinion groups (ΔS)" and "difference of percentage of '-1' opinion group after one time step (Δβ)"in the centrality-based scenario

Similar to Figure 4 for the original social impact model, Figure 6 shows the scatter plot of pairs of ΔS and $\Delta\beta$ variables. Unlike the original model, none of the normality and homoscedasticity tests, which are the conditions for calculating the Pearson correlation coefficient, have been passed; therefore, there is no correlation between ΔS and $\Delta\beta$ in this scenario.

5. DISCUSSION

The scatter plots presented in the previous section reveal the association between segregation and change of the agents' opinions. As these plots show, there is a strong correlation between segregation and opinion change in the original scenario, and there is no correlation between these parameters in the centrality-based scenario.

In the scatter plot of Figure 4 for the original model, when ΔS=0, which means both opinion groups have the same SMI, none of both groups dominate the other group; therefore, the number of members of both opinion groups does not change much. Thus, β remains the same as the previous time step, $\Delta\beta$=0, and the fitted line passes roughly through (0,0). A positive value for ΔS means that the group with opinion '-1' is more segregated than the group with opinion '+1'.

As Figure 4 shows, the opinion '-1' becomes more dominant, and some agents from the other group ('+1' opinion group) change their opinion to '-1'. Hence, β increases and result in a $\Delta\beta$>0. With similar reasoning, ΔS<0 results in a $\Delta\beta$<0, as the figure shows. The calculated Pearson correlation coefficient, r=0.728, reveals a strong correlation between the independent variable ΔS and the dependent variable $\Delta\beta$.

In the centrality-based scenario, as Figure 6 shows, there is no correlation between ΔS and $\Delta\beta$. In this scenario, since persuasiveness and supportiveness strengths are proportional to the agents' centrality, there are some powerful leaders in society. As explained in section 2, these well-connected agents with high power of leadership could be called evangelists. The few evangelists affect many non-leader (or follower) agents; therefore, many segregated groups are affected by these evangelists. Thus, the segregation phenomenon does not play a significant role in this scenario, as Figure 6 implies, and many segregations are broken.

As comparing Figure 3 and Figure 5 reveals, the trend of β in both scenarios are entirely different. In the original scenario of the model, the diversity of opinion population changes is much less than the centrality-based scenario. It happens due to the various assignments for p_i and s_i in both scenarios. I_i could be regarded as a linear combination of two random variables p_j and s_j. In the original scenario, p_j and s_j have the uniform distribution Uniform(0, 100), but in the centrality-based scenario, corresponding variables have power-law distribution according to the node degree distribution in the Barabási-Albert network, $P(k)\sim k^{-\gamma}$ with $\gamma=2.9\pm0.1$ [36]. Since for $\gamma\leq3$, the variance of the power-law distribution is theoretically infinite and empirically very greater than the variance of Uniform(0,100), which is equal to $100^2/12$, the variance of the linear combination random variable, I_i, is very greater and cause more diversity of β in the centrality-based scenario advancing the time steps, as comparing the Figure 3 and Figure 5 shows. More details about this comparis

on are discussed in [12].

6. CONCLUSION

The segregation phenomenon and leadership power play essential roles in the social impact model of opinion formation. The results from simulations in this research implies that when powerful leaders exist in a social network, segregation has less impact on opinion formation, and the leadership power of influential well-connected leaders influences the opinion of society; therefore, the final combination of opinion groups' populations may differ much from the starting one due to these few influential well-connected leaders' existences.

On the other hand, without powerful leaders in a network, segregation strongly affects opinion formation in such a way that with a strong correlation, the more segregated opinion group is less affected by the other group and more affects the other opinion group. In this case, society's opinion may change, but the diversity of change is not so much compared to the case with powerful leaders.

According to the social impact model, influential leaders with strategic points in the network and high influential strengths connect many other individuals and try to persuade them. However, the opposite opinion segregated group(s) resist the leaders' influential strength. If the influential power dominates the segregation resistance, leaders could achieve the major opinion of the society; otherwise, segregated opposite opinion group(s) persist their own opinion. Other convinced people may emerge as opinion leaders during a successful opinion spreading by the leaders, causing a collective behavior breaking many segregated groups until the majority opinion forms.

The conclusions mentioned above could justify that influential well-connected leaders have essential roles to lead society in many social movements. Without these leaders, the segregation phenomenon determines society's opinion formation, which has less effect on society's opinion. In many social decisions, some groups try to form their own desired opinion in society and try to have an opinion leadership role, sometimes using troll and bot networks.

Our conclusion is according to the real world from a sociological viewpoint. Some studies have emphasized the leaders' structural positions in the network, the central points in the network terminology. For example, as discussed in [38], in social movements, social structural conduciveness is necessary (but not sufficient) for social movement mobilization; leaders create the impetus for movements, and structural conditions affect the emergence and effectiveness of leaders. In the online networks, this process may happen at a much faster rate and a larger scale [39, 40]. Furthermore, in some cases, bots and trolls influence public opinions, and the main leaders of the opinions are not clear for the public, such as the suspected influence of Russia in Brexit [8] and the 2016 U.S. presidential election [41].

On the other hand, highly segregated groups may resist to opinion change persuasions. The political science literature has confirmed the observation of geographical segregation and partisan alignment, that people tend to segregate themselves into their own political worlds, blocking out discordant voices and surrounding themselves with reassuring news and companions [39].

In this research, we relaxed the noise parameter of the social impact model of opinion formation. However, this parameter is very important and depends upon other parameters, including environment variables and individuals' behaviors in the opinion dynamics process. Further studies could also consider the effects of the noise parameter.

Although this study shows the correlation between segregation and distribution of persuasion strength of the agents in scale-free networks, further studies need to be carried out to understand this correlation in other

common network topologies for modeling social networks and using various probability distributions for persuasion strengths of the agents.

According to the results of this research, we concluded a positive correlation between segregation and forming the majority opinion in society using an agent-based simulation approach. However, similar to many other computational social science studies, this conclusion could be more considered by social psychologists using other tools and approaches.

7. REFERENCES

1. Iacopini, I., Petri, G., Barrat, A. and Latora, V., "Simplicial models of social contagion", ***Nature Communications***, Vol. 10, No. 1, (2019), 1-9, doi: 10.1038/s41467-019-10431-6.
2. Hołyst, J.A., Kacperski, K. and Schweitzer, F., "Social impact models of opinion dynamics", ***Annual Reviews of Computational physics***, Vol. 9, (2001), 253-273, doi: 10.1142/9789812811578_0005.
3. Mohammadi, A., and Hamidi, H., "Analysis and evaluation of privacy protection behavior and information disclosure concerns in online social networks", ***International Journal of Engineering, Transaction B: Applications***, Vol. 31, No. 8, (2018), 1234-1239, doi: 10.5829/ije.2018.31.08b.11.
4. Mansouri, A., Taghiyareh, F. and Hatami, J., "Post-based prediction of users' opinions employing the social impact model improved by emotion", ***International Journal of Web Research***, Vol. 1, No. 2, (2018), 34-42, doi: 10.22133/IJWR.2018.91425.
5. Srividya, K., Mariyababu, K. and A. M. Sowjanya, "Mining interesting aspects of a product using aspect-based opinion mining from product reviews (research note)", ***International Journal of Engineering, Transaction B: Applications***, Vol. 30, No. 11, (2017), 1707-1713, doi: 10.5829/ije.2017.30.11b.11.
6. Howard, P.N., Duffy, A., Freelon, D., Hussain, M.M., Mari, W. and Maziad, M. *Opening closed regimes: What was the role of social media during the Arab spring?* Project on Information Technology and Political Islam 2011; available at SSRN: https://ssrn.com/abstract=2595096, doi: 10.2139/ssrn.2595096.
7. Allcott, H. and Gentzkow, M., "Social media and fake news in the 2016 election", ***Journal of Economic Perspectives***, Vol. 31, No. 2, (2017), 211-236, doi: 10.1257/jep.31.2.211.
8. Narayanan, V., Howard, P.N., Kollanyi, B. and Elswah, M., "Russian involvement and junk news during brexit" (2017), Retrieved from comprop.oii.ox.ac.uk/wp-content/uploads/sites/93/2017/12/Russia-and-Brexit-v27. pdf on the 2nd of November 2020.
9. Latané, B., "The psychology of social impact", ***American Psychologist***, Vol. 36, No. 4, (1981), 343-356, doi: 10.1037/0003-066X.36.4.343.
10. Bojanowski, M. and Corten, R., "Measuring segregation in social networks", ***Social Networks***, Vol. 39, (2014), 14-32, doi: 10.1016/j.socnet.2014.04.001.
11. Feliciani, T., Flache, A. and Tolsma, J., "How, when and where can spatial segregation induce opinion polarization? Two competing models", Vol. 20, No. 2, (2017), 6, doi: 10.18564/jasss.3419.
12. Mansouri, A. and Taghiyareh, F., "Phase transition in the social impact model of opinion formation in scale-free networks: The social power effect", ***Journal of Artificial Societies and Social Simulation***, Vol. 23, No. 2, (2020), 3, doi: 10.18564/jasss.4232.
13. Mansouri, A. and Taghiyareh, F., "Correlation of segregation and social networks' majority opinion in the social impact model", in 6th International Conference on Web Research (ICWR), IEEE, 66-71, (2020), doi: 10.1109/ICWR49608.2020.9122279.
14. Mansouri, A. and Taghiyareh, F., "Effect of segregation on the dynamics of noise-free social impact model of opinion formation through agent-based modeling", ***International Journal of Web Research***, Vol. 2, No. 2, (2019), 36-44, doi: 10.22133/IJWR.2020.226249.1054.
15. Ndlela, M.N., Social media algorithms, bots and elections in africa, in Social media and elections in africa, volume 1. 2020, Springer.13-37, doi: 10.1007/978-3-030-30553-6_2.
16. Zhan, M., Liang, H., Kou, G., Dong, Y. and Yu, S., "Impact of social network structures on uncertain opinion formation", ***IEEE Transactions on Computational Social Systems***, Vol. 6, No. 4, (2019), 670-679, doi: 10.1109/TCSS.2019.2916918.
17. Castellano, C., Fortunato, S. and Loreto, V., "Statistical physics of social dynamics", ***Reviews of Modern Physics***, Vol. 81, No. 2, (2009), 591, doi: 10.1103/RevModPhys.81.591.
18. Murase, Y., Jo, H.-H., Török, J., Kertész, J. and Kaski, K., "Structural transition in social networks: The role of homophily", ***Scientific Reports***, Vol. 9, No. 1, (2019), 1-8, doi: 10.1038/s41598-019-40990-z.
19. Salehi, S. M. M. and Pouyan, A. A., "Detecting overlapping communities in social networks using deep learning", ***International Journal of Engineering, Transaction C: Aspects***, Vol. 33, No. 3, (2020), 366-376, doi: 10.5829/IJE.2020.33.03C.01.
20. ElTayeby, O., Molnar, P. and George, R., "Measuring the influence of mass media on opinion segregation through Twitter", ***Procedia Computer Science***, Vol. 36, (2014), 152-159, doi: 10.1016/j.procs.2014.09.062.
21. Fershtman, M., "Cohesive group detection in a social network by the segregation matrix index", ***Social Networks***, Vol. 19, No. 3, (1997), 193-207, doi: 10.1016/S0378-8733(96)00295-X.
22. Rogers, E.M. and Cartano, D.G., "Methods of measuring opinion leadership", ***Public Opinion Quarterly***, Vol. 26, No. 3, (1962), 435-441, doi: 10.1086/267118.
23. Katz, E., "The two-step flow of communication: An up-to-date report on a hypothesis", ***Public Opinion Quarterly***, Vol. 21, No. 1, (1957), 61-78, doi: 10.1086/266687.
24. DeMarzo, P.M., Vayanos, D. and Zwiebel, J., "Persuasion bias, social influence, and unidimensional opinions", ***The Quarterly Journal of Economics***, Vol. 118, No. 3, (2003), 909-968, doi: 10.1162/00335530360698469.
25. Weimann, G., Tustin, D.H., Van Vuuren, D. and Joubert, J., "Looking for opinion leaders: Traditional vs. Modern measures in traditional societies", ***International Journal of Public Opinion Research***, Vol. 19, No. 2, (2007), 173-190, doi: 10.1093/ijpor/edm005.
26. Baym, N.K., Tune in, log on: Soaps, fandom, and online community. Thousand Oaks, CA: Sage, Vol. 3, 2000.
27. Riquelme, F., Gonzalez-Cantergiani, P., Hans, D., Villarroel, R. and Munoz, R., "Identifying opinion leaders on social networks through milestones definition", ***IEEE Access***, Vol. 7, (2019), 75670-75677, doi: 10.1109/ACCESS.2019.2922155.
28. Cha, M., Benevenuto, F., Haddadi, H. and Gummadi, K., "The world of connections and information flow in Twitter", ***IEEE Transactions on Systems, Man, and Cybernetics-Part A: Systems and Humans***, Vol. 42, No. 4, (2012), 991-998, doi: 10.1109/TSMCA.2012.2183359.
29. Hinz, O., Skiera, B., Barrot, C. and Becker, J.U., "Seeding strategies for viral marketing: An empirical comparison", ***Journal of Marketing***, Vol. 75, No. 6, (2011), 55-71, doi: 10.1509/jm.10.0088.

30. Iyengar, R., Van den Bulte, C. and Valente, T.W., "Opinion leadership and social contagion in new product diffusion", ***Marketing Science***, Vol. 30, No. 2, (2011), 195-212, doi: 10.1287/mksc.1100.0566.

31. Chattoe-Brown, E., "Why sociology should use agent-based modelling", ***Sociological Research Online***, Vol. 18, No. 3, (2013), 1-11, doi: 10.5153/sro.3055.

32. Bianchi, F. and Squazzoni, F., "Agent-based models in sociology", ***Wiley Interdisciplinary Reviews: Computational Statistics***, Vol. 7, No. 4, (2015), 284-306, doi: 10.1002/wics.1356.

33. Hauke, J., Lorscheid, I. and Meyer, M., "Recent development of social simulation as reflected in jasss between 2008 and 2014: A citation and co-citation analysis", ***Journal of Artificial Societies and Social Simulation***, Vol. 20, No. 1, (2017), doi: 10.18564/jasss.3238.

34. Stumpf, M.P. and Porter, M.A., "Critical truths about power laws", ***Science***, Vol. 335, No. 6069, (2012), 665-666, doi: 10.1126/science.1216142.

35. Broido, A.D. and Clauset, A., "Scale-free networks are rare", ***Nature Communications***, Vol. 10, No. 1, (2019), 1-10, doi: 10.1038/s41467-019-08746-5.

36. Barabási, A.-L. and Albert, R., "Emergence of scaling in random networks", ***Science***, Vol. 286, No. 5439, (1999), 509-512, doi: 10.1126/science.286.5439.509.

37. Bianconi, G. and Marsili, M., "Number of cliques in random scale-free network ensembles", ***Physica D: Nonlinear Phenomena***, Vol. 224, No. 1-2, (2006), 1-6, doi: 10.1016/j.physd.2006.09.013.

38. Morris, A.D. and Staggenborg, S., "Leadership in social movements", ***The Blackwell companion to social movements***, 171-196, Malden, MA: Blackwell, 2004.

39. Gao, J., Schoenebeck, G. and Yu, F.-Y., "The volatility of weak ties: Co-evolution of selection and influence in social networks", in Proceedings of the 18th International Conference on Autonomous Agents and MultiAgent Systems, 619-627, (2019).

40. Bakshy, E., Messing, S. and Adamic, L.A., "Exposure to ideologically diverse news and opinion on Facebook", ***Science***, Vol. 348, No. 6239, (2015), 1130-1132, doi: 10.1126/science.aaa1160.

41. Luceri, L., Giordano, S. and Ferrara, E., "Detecting troll behavior via inverse reinforcement learning: A case study of Russian trolls in the 2016 us election", in Proceedings of the International AAAI Conference on Web and Social Media, (2020), 417-427.

Persian Abstract

چکیده

در این مقاله تأثیر پدیدهٔ جداشدگی در شبکه‌های اجتماعی بر شکل‌گیری عقیده در دو حالت بررسی شده است، در یک حالت بدون وجود رهبران بانفوذ و در حالت دیگر با وجود رهبران بانفوذ در جامعه. شبکه تعامل افراد، شبکه تصادفی بی‌مقیاس در نظر گرفته شده است که در بسیاری از پدیده‌های طبیعی یافت می‌شود. در این پژوهش از رویکرد مدل‌سازی مبتنی بر عامل استفاده شد و مدل تأثیر اجتماعی، مبنای پویایی شکل‌گیری عقیده قرار گرفت. دو سناریوی شبیه‌سازی مبتنی بر عامل اجرا شد، یکی مبتنی بر مدل اولیهٔ تأثیر اجتماعی که در آن، قدرت متقاعدکنندگی افراد یا عامل‌ها به صورت تصادفی به آنها تخصیص می‌یابد، و دیگری سناریوی مبتنی بر مرکزیت که قدرت متقاعدکنندگی افراد یا عامل‌ها متناسب با مرکزیت آنها در شبکهٔ تعامل آنها است و بنابر این، گره‌هایی که مرکزیت بیشتری دارند، قدرت متقاعدکنندگی زیادی نیز دارند و رهبران بانفوذتر در جامعه هستند. نتایج شبیه‌سازی‌ها نشان می‌دهد که یک همبستگی قوی بین میزان جداشدگیِ گروه عقیده و افزایش جمعیت گروه عقیده در مدل اولیه وجود دارد، اما در مدل مبتنی بر مرکزیت، همبستگی بین این دو وجود ندارد. بر اساس این نتایج می‌توان دریافت که وقتی رهبران با قدرت متقاعدکنندگی زیاد و ارتباطات زیاد در جامعه وجود دارند، تأثیر جداشدگی در ممانعت از شکل‌گیری عقیدهٔ جامعه به سمت عقیدهٔ رهبرانِ بانفوذ، قابل چشم‌پوشی است.

International Journal of Engineering

Journal Homepage: www.ije.ir

Epileptic Electroencephalogram Classification using Relative Wavelet Sub-band Energy and Wavelet Entropy

S. Hadiyoso*[a], I. D. Irawati[a], A. Rizal[b]

[a] *School of Applied Science, Telkom University, Bandung, Indonesia*
[b] *School of Electrical Engineering, Telkom University, Bandung, Indonesia*

PAPER INFO

Paper history:
Received 21 September 2020
Received in revised form 03 November 2020
Accepted 28 November 2020

Keywords:
Epilepsy
Electroencephalogram
Entropy
Wavelet Energy

ABSTRACT

Epilepsy is one of the common neurological disorders which can cause unprovoked seizures. Currently, diagnosis and evaluation are carried out using electroencephalogram (EEG) signal analysis, which is performed visually by clinicians. Since EEG signals tend to be random and non-stationary, the visual inspection often provides misrepresentation of results. Numerous studies have been proposed computer-based analysis for epileptic EEG classification; however, there is still a gap to improve detection accuracy with a small number of features. Therefore, in this study, we proposed an automatic detection protocol for epileptic EEG classification. The proposed methods are relative wavelet energy and wavelet entropy for feature extraction and combined with the classifier method for automatic detection. In this study, three classes of EEG consisted of pre-ictal, ictal, and interictal were used as test data and also evaluate the proposed method. EEG signals were decomposed using wavelet transform into five conventional sub-bands, including gamma, beta, alpha, theta, and delta. The relative energy and entropy were then calculated in each of these bands as a feature set. These methods are chosen with consider of low-cost computing. We tested the performance of our feature extraction method using Support Vector Machine (SVM), both linear and non-linear kernels. From the simulation, the highest accuracy was 80-96.7% for ictal vs. pre-ictal, ictal vs. inter-ictal, pre-ictal vs. inter-ictal, and ictal vs. non-ictal. Finally, this work was expected to help clinicians in the detection of epilepsy onset based on EEG signals.

***doi**: 10.5829/ije.2021.34.01a.09*

NOMENCLATURE

Ψ	Basis wavelet	w	Normal vector length
a	Scale	T	Trade-off parameter
b	Shift	ε_i	Set of slack variables
t	Time	a_i, b_i	Training set

1. INTRODUCTION[1]

Epilepsy is one of the most common neurological disorders. Patients may suffer seizures due to abnormal or excessive of electrical brain activity [1]. Currently, neurologists conduct the diagnosis and evaluation of epilepsy patients based on analysis of EEG signals by visual inspection [2]. This process takes a long time and allows many error detections [3]. EEG signals show dynamic changes in nerve activity concerning seizures in the brain [4]. Nowadays, computer based-methods have been developed to detect and analyze epilepsy based on EEG signal so that it is more effective and accurate.

EEG signals are processed to obtain features that can represent information characteristics to be classified [5, 6]. According to literature [7], EEG signal classification can be performed by processing the signals in the time domain, frequency domain, time-frequency domain, and many others using nonlinear techniques. Researchers developed a wavelet method for extracting features on EEG signals based on energy and entropy of the signal [8]. Faust et al. [4] stated that wavelet transforms produce

*Corresponding Author Institutional Email: sugondo@telkomuniversity.ac.id (S. Hadiyoso)

Please cite this article as: S. Hadiyoso, I. D. Irawati, A. Rizal, Epileptic Electroencephalogram Classification using Relative Wavelet Sub-band Energy and Wavelet Entropy, International Journal of Engineering, Transactions A: Basics Vol. 34, No. 01, (2021) 75-81

detailed information of EEG signal to detect and predict seizures. Wavelet transform has better representation than other signal processing methods. Wavelet energy describes energy information at different frequencies in the EEG signal that is adjusted to the needs of the analysis [9]. Entropy shows an index that illustrates brain wave disorder. Wavelet entropy can analyze EEG signals with very dynamic features [10]. Daubechies discrete wavelet transform and wavelet harmonic used to characterize and analyze epileptiform [11]. Wavelet analysis of EEG signals may produced accurate features to analyze different brain rhythm, even on a low scale. The other study by Lee et al. [12] combined wavelet transforms, phase-space reconstruction, and Euclidean distance to classify the normal EEG and epileptic seizures on the EEG signal. This method produced 24 features, and a minimum of four features with the highest accuracy was selected for classification using fuzzy logic. Guo et al. [9] explored relative wavelet energy for representing the EEG signal and classifying it using artificial neural networks. In our previous work, we examined the classification of seizure patterns on the EEG signal using SVM. We divided four classifications scenarios, which are three based on seizure and normal conditions from feature extractions combination consisting of Hjorth Descriptor, Independent Component Analysis (ICA), and Mel Frequency Cepstral Coefficients (MFCC) [13].

Based on previous research, we proposed a new method for seizure detection in epilepsy patients based on the relative wavelet energy and wavelet entropy from the EEG signal. In this study, a combination of wavelet methods for feature extraction and SVM for classification were conducted. Wavelet transform segmented the EEG signals into five bands consisting of gamma, beta, alpha, theta, and delta. Relative wavelet energy and entropy are then calculated for these bands as feature sets. Finally, we evaluate the performance of the proposed feature extraction method using support vector machine.

The rest of this paper is organized as follows. Section 2 illustrates the EEG dataset collection and methods that support the findings of this study. The performance evaluation and discussion are shown in section 3. The conclusion and future works are drawn in section 4.

2. MATERIAL and METHOD

2. 1. EEG Dataset In this study, the epilepsy EEG dataset, which was used for simulations, was taken from the Hauz Khas Neurology and Sleep Center, India. It is available on the https://www.researchgate.net/publication/308719109_EEG_Epilepsy_Datasets. The EEG was taken from 10 epilepsy patients in the department and recorded using Grass Telefactor Comet AS40 with 200 Hz sampling frequency. The 10-20 system placement standard was applied to 16 scalp electrodes. The EEG signal was pre-processed with a band-pass filter (0.5 Hz and 70 Hz) to reject large amounts of noise.

Furthermore, the EEG dataset was segmented into pre-ictal, ictal, and inter-ictal. Each stage contained 50 segments of the EEG signal with a duration of 5.12 seconds. Our proposed method was tested in several classification schemes included: ictal vs. pre-ictal, ictal vs. inter-ictal, pre-ictal vs. inter-ictal, and ictal vs. non-ictal.

2. 2. Proposed Method Figure 1 presents a proposed method for epileptic EEG classification. First, the EEG signal which consists of ictal, pre-ictal, and inter-ictal is segmented into delta, theta, alpha, beta, and gamma bands using Wavelet transform. The relative energy and entropy are then measured for each band. Finally, a performance evaluation was carried out using a support vector machine with various kernels. The following sub-sections describe the details of the proposed method.

2. 2. 1 Band Segmentation Using Wavelet Transform Wavelet transform (WT), or then called wavelet decomposition, is generally a frequency decomposition of sub-band signals where the components are produced by decreasing the hierarchical decomposition. Wavelet-based transformation methods has been widely used over the past decades [14]. Implementation of wavelet transform can be done by passing the high-frequency signal or high pass filter and low frequency or lowpass filter [15, 16]. This method is suitable for representing EEG signals that have characteristics, high frequency in a short period, and low frequency in a long period. Wavelet extracts features that can be used for analyzing the diverse transient case in the signal, as in the EEG signal. Wavelet transform has been commonly used for EEG analysis, as reported in studies [17-19], where WT produces high performance in signal characterization.

In the family of wavelet, the mother wavelet is the set of basis functions which is expressed in Equation (1) below.

$$\Psi_{a,b}(t) = \frac{1}{\sqrt{a}} \Psi\left(\frac{t-b}{a}\right) \quad (1)$$

where Ψ is basis or mother wavelet, $a, b \epsilon \Re, a \neq 0$ is the scale parameter, and b is the shift parameter, while t is the time.

In its function for signal segmentation or decomposition, WT is often used as a filter bank (consists of low pass and high pass filter) [20]. In this research, we use wavelet decomposition to obtain the delta, theta, alpha, beta, and gamma bands. Since the sampling frequency is 200 Hz, 5-level decomposition was applied to obtain these bands with Daubechies-2 (DB2) as the

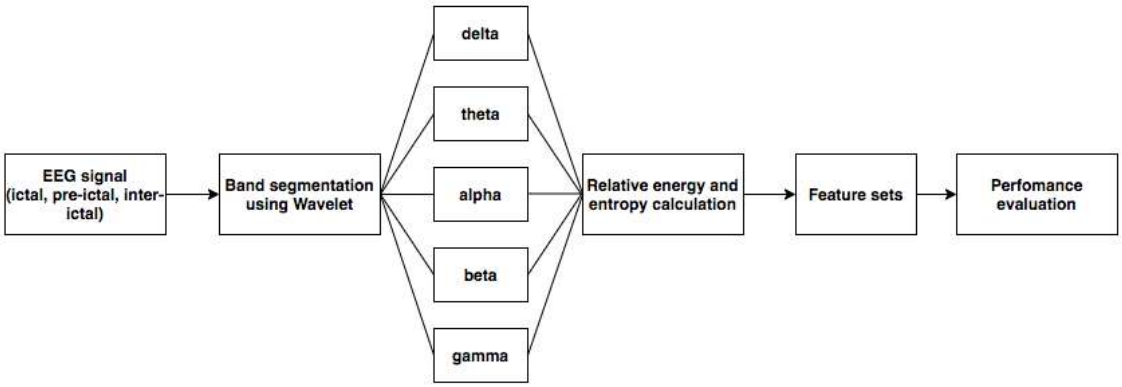

Figure 1. Proposed method for epileptic EEG classification

basis wavelet function. Sub-band D2 correspondence with gamma, D3 correspondence with beta, D4 correspondence with alpha, D5 correspondence with theta, and A5 correspondence with delta. The relative energy in each band is then measured as a function of normalization with the total energy of all bands. Shannon entropy is also calculated on all bands as a representation of the randomness or uncertainty of the signal. The scheme of the WT method can be seen in Figure 2.

2. 2. 2 Classification with Support Vector Machine (SVM) Support vector machine (SVM) is one method that is commonly used for classification problems in biomedical signal processing [21-24]. SVM is a supervised learning method. Initially, SVM was used to classify two groups and then developed to solve multi-class classification problems. In addition, SVM is also able to overcome the problem of linear and non-linear classification. SVM is used to find optimal hyperplane functions by maximizing the distance between classes [25]. Hyperplane can be determined by calculating the hyperplane's margin and measuring its maximum point. The closest pattern is called a support vector. The hyperplane in SVM is illustrated, as shown in Figure 3.

In this study, linear SVM and non-linear SVM are used to validate the proposed method. The function of linear SVM is expressed in Equation (2).

$$\min {}^{1}/_{2}\,\|\vec{w}\|^2 + T\sum_{i=1}^{k}\varepsilon_i \quad (2)$$

Where w is normal vector length, T is the trade-off parameter between training set errors and class separation. Whereas ε_i is the set of slack variables. The aim of this function is to find the minimum distance between two hyperplanes ($2\|\vec{w}\|$) by minimizing $\|\vec{w}\|$.

Since the boundary line have variations by applying other kernels, therefore non-linear SVM kernels including quadratic and cubic SVM also simulated to find the best performance in classification. This function is obtained by Equation (3).

$$k(a_i, b_i) = (a_i, b_i + 1)^d \quad (3)$$

where (a_i, b_i) is training set, meanwhile for quadratic function the $d = 2$, and for cubic function, the $d = 3$.

3. RESULTS AND DISCUSSION

Figure 4 shows the results of the Wavelet transform which generates the five conventional EEG bands,

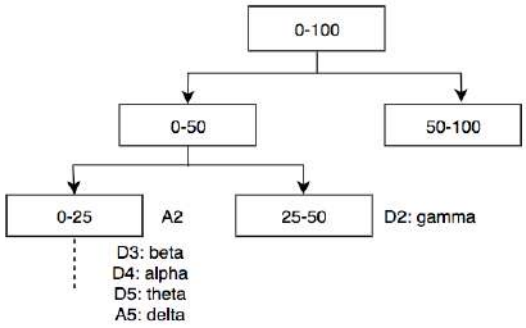

Figure 2. Wavelet decomposition and correspondence with the EEG sub-band

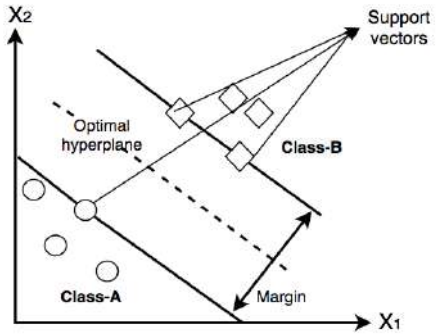

Figure 3. Hyperplane as a separator between classes [26]

including delta, theta, alpha, beta, and gamma. Then the relative energy and entropy are measured for each band. The average values of the relative energy and entropy of each EEG stage are shown in Figures 5 and 6. The relative energy in the delta and theta bands in the ictal stage tends to be higher compared to the non-ictal stage. This indicates a slowing of the EEG wave in the ictal stage. Pre-ictal and inter-ictal stages show that the relative energy in the alpha, beta, and gamma bands is higher than the ictal stage. Meanwhile, the entropy value in the ictal stage is the lowest in all EEG bands compared to the non-ictal stage.

Since entropy is related to the degree of complexity of the dynamic system, the ictal stage has the lowest signal complexity compared with other conditions. These results were confirmed by Weng et al. [27], that the ictal EEG decreased the complexity of the signal with the entropy value of the pre-ictal stage higher than the ictal stage. The parameters which are measured in this study provide discriminant features between groups of epileptic EEG signals. We also confirmed by conducting a significance test using the analysis of variance (ANOVA). In this study, features with statistically significant differences if they have a p-value <0.05 and if it generates a p-value <0.01, it has a higher degree of significant difference. The results of the significance tests for each classification problem are presented in Table 1. From these results, we highlight that in all ictal vs. non-ictal stage scenarios, there are differences with high significance (p <0.01), which is almost generated by all features. Meanwhile, in the case of inter-ictal vs. pre-ictal, there were six features that did not have high significance, two of which had p <0.05. This indicates that these two stages have several similar signal properties, which may be more difficult to classify. Next is the performance validation of the proposed method using SVM. In this study, the number of features which is used as a predictor is 10 features from the measurement of the relative energy and entropy of each EEG band.

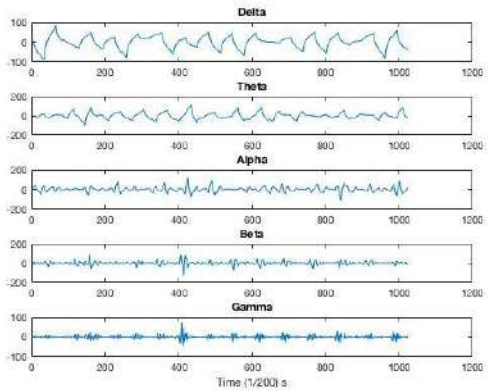

Figure 4. The results of decomposition using wavelet transform in the ictal stage

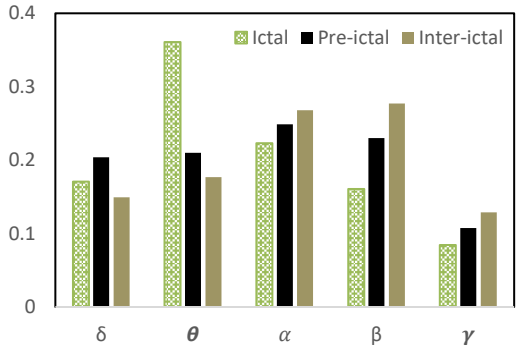

Figure 5. The average of the relative energy of the ictal, inter-ictal, and pre-ictal stages

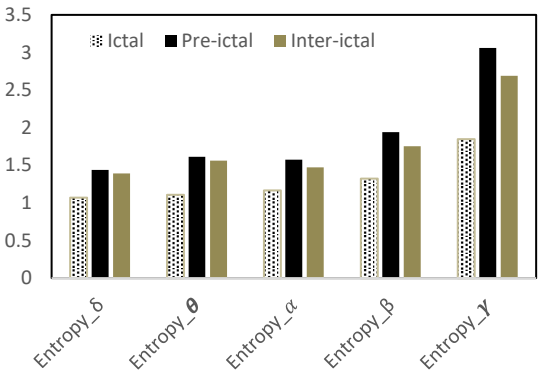

Figure 6. The average of entropy of the ictal, inter-ictal, and pre-ictal stage

TABLE 1. p-value for each classification scenarios

Feature	Ictal vs inter-ictal	Ictal vs pre-ictal	Inter-ictal vs pre-ictal	Ictal vs Inter-ictal vs pre-ictal
RGP	5.15E-09**	6.97E-03**	3.89E-03**	1.65E-07**
RBP	9.00E-18**	3.09E-05**	1.66E-03**	3.55E-13**
RAP	1.05E-05**	2.45E-02*	O.0971	2.76E-04**
RTP	1.14E-23**	4.95E-12**	0.0649	3.70E-21**
RDP	0.0812	0.117	1.08E-02*	1.37E-02*
EG	1.42E-26**	2.02E-24**	1.43E-04**	5.87E-31**
EB	2.88E-18**	2.38E-17**	6.35E-03**	4.89E-20**
EA	4.02E-18**	1.57E-16**	2.93E-02*	7.81E-20**
ET	2.88E-19**	2.33E-14**	0.435	4.80E-18**
ED	1.18E-14**	5.20E-11**	0.358	3.81E-14**

RGP = Relative gamma power; RBP = Relative beta power; RAP = Relative alpha power; RTP = Relative theta power; RDP = Relative delta power; EG = Entropy gamma; EB = Entropy beta; EA = Entropy alpha; ET = Entropy theta; ED = Entropy delta
* p-value < 0.05
** p-value < 0.01

Since SVM is a supervised learning method, a cross-validation algorithm is needed to split the training and test data. The use of this algorithm also aims to avoid overfitting. 10-fold cross-validation with SVM is used to evaluate the performance of the proposed method in the four classification problems, as explained in the sub-section above. The test results for each scenario are presented in Table 2. In the case of classification between ictal and pre-ictal the highest accuracy is 95%, with sensitivity and specificity of 94 and 96%, respectively. For ictal vs. inter-ictal cases, the highest accuracy, which is achieved, is 96%. In this case, 100% specificity was obtained, which means that the system is able to detect all inter-ictal stages without miss classification. Meanwhile, in the ictal vs non-ictal (pre-ictal and inter-ictal) stage classification, the proposed method generates an accuracy of 96.7 with 99% specificity in detecting non-ictal onset. This scenario shows that the proposed method is able to detect ictal and non-ictal onset with high accuracy and has a consistent performance when applied to ictal vs. pre-ictal or ictal vs. inter-ictal classification problems. The simulation results in this scenario are expected to be used to predict the onset of seizures. In the pre-ictal vs. inter-ictal classification problem, the system is able to produce the highest accuracy of 80% and a sensitivity of 90%. This result is quite good, considering both of the onsets have similar characteristics. Where the two conditions are the onset before the occurrence of seizures at different intervals, from the simulations conducted using different SVM kernels, it can be concluded that the quadratic kernel has the best performance, providing the highest accuracy for the three test scenarios.

The evaluation of the proposed method was also carried out by comparing it with previous studies that used the same dataset. In the ictal vs. pre-ictal scenario,

TABLE 2. The classification results for each scenario

Scenario	SVM	Accuracy (%)	Sensitivity	Specificity
Ictal vs Pre-ictal	Linear	94	92	96
	Quadratic	95	92	96
	Qubic	95	94	96
Ictal vs Inter-ictal	Linear	94	88	100
	Quadratic	95	90	100
	Qubic	96	92	100
Pre-ictal vs Inter-ictal	Linear	78	88	68
	Quadratic	80	90	70
	Qubic	76	86	66
Ictal vs Non-ictal	Linear	96.7	92	99
	Quadratic	96.7	92	99
	Qubic	95.3	90	98

TABLE 3. The system performance comparison

Study by	Method	Class	Acc. (%)
Sharma, et. al [28]	minimally mean squared frequency localized (MMSFL)-optimal orthogonal wavelet filter bank (OWFB)	ictal vs. pre-ictal	90
		pre-ictal vs. inter-ictal	NA
		inter-ictal vs. ictal	100
Gupta, et. al [29]	Discrete cosine transform (DCT), Hurst Exponent	ictal vs. pre-ictal	79.7
		pre-ictal vs. inter-ictal	74.6
		inter-ictal vs. ictal	96.5
Proposed study	**Relative Wavelet Energy (RWE) and Wavelet Entropy**	ictal vs. pre-ictal	**95**
		pre-ictal vs. inter-ictal	**80**
		inter-ictal vs. ictal	96

the proposed method outperforms the study by Sharma et al. [28] and Gupta et al. [29] where the accuracy was 90 and 79.7%, respectively. In the pre-ictal vs. inter-ictal scenario, the proposed method also outperforms the study by Gupta et al. [29], yielding an accuracy of 74.6%. This is a good result and should notably since the two stages have similar characteristics. Meanwhile, the ictal vs. inter-ictal scenario has lower performance than the study by Sharma et al. [28] and Gupta et al. [29]; however, the gap is relatively low. A brief summary of the comparisons with previous studies is presented in Table 3.

4. CONCLUSION

This paper presents a method for epileptic EEG detection using relative wavelet energy and wavelet entropy. Wavelet transform was used to generate conventional EEG bands consisting of the delta, theta, alpha, beta, and gamma. Then relative energy and entropy were measured as a feature set. From the measurement of relative power, it was known that the delta and theta band in the ictal stage was higher than in the non-ictal stage. Entropy measurements showed that the value of entropy in ictal tended to be lower than the non-ictal stage. The entropy value in pre-ictal was highest compared to other stages. This measurement was considered to be able to provide discriminant features between epileptic EEG groups. Therefore, performance evaluations were performed with SVM and cross-validation to the feature vectors, which

were generated by the proposed method. Performance evaluation was done in the four classification problems, including ictal vs. pre-ictal, ictal vs. inter-ictal, pre-ictal vs. inter-ictal, and ictal vs. non-ictal. Each scenario generates the highest accuracy of 95%, 96%, 80%, and 96.7%, respectively. In ictal vs. pre-ictal and inter-ictal vs. pre-ictal scenario, the proposed method outperformed previous studies. We notably highlighted the cases of ictal vs. non-ictal, where the proposed method produced high accuracy. It means that the proposed method was expected to be used for the prediction of onset seizures.

In future works, the results of this study will be simulated to a larger EEG epilepsy dataset. Moreover, various feature extraction and classification methods will be explored so that it becomes an opportunity to solve the more complicated case of EEG signal classification. Other classification parameters are also meaningful so that research is more challenging to be addressed.

5. REFERENCES

1. Krook-Magnuson, E. and Soltesz, I. "Beyond the hammer and the scalpel: Selective circuit control for the epilepsies." ***Nature Neuroscience***, Vol. 18, No. 3, (2015), 331-338. doi: 10.1038/nn.3943
2. Malmivuo, J. and Plonsey, R., Bioelectromagnetism - Principles and Applications of Bioelectric and Biomagnetic Fields. New York: Oxford University Press, 1995.
3. Acharya, U. R., Hagiwara, Y., Deshpande, S. N., Suren, S., Koh, J. E. W., Oh, S. L., … Lim, C. M. "Characterization of focal EEG signals: A review." ***Future Generation Computer Systems,*** Vol. 91, (2019), 290-299. doi: 10.1016/j.future.2018.08.044
4. Faust, O., Acharya, U. R., Adeli, H., and Adeli, A. "Wavelet-based EEG processing for computer-aided seizure detection and epilepsy diagnosis." ***Seizure***, Vol. 26, (2015), 56-64. doi: 10.1016/j.seizure.2015.01.012
5. Khanmohammadi, S. and Chou, C. A. "Adaptive Seizure Onset Detection Framework Using a Hybrid PCA-CSP Approach." ***IEEE Journal of Biomedical and Health Informatics,*** Vol. 22, No. 1, (2018), 154-160. doi: 10.1109/JBHI.2017.2703873.
6. Carney, P. R., Myers, S. and Geyer, J. D. "Seizure prediction: Methods." ***Epilepsy and Behavior,*** Vol. 22(SUPPL. 1), (2011), S94-S101. doi: 10.1016/j.yebeh.2011.09.001.
7. Altunay, S., Telatar, Z. and Erogul, O. "Epileptic EEG detection using the linear prediction error energy." ***Expert Systems with Applications***, Vol. 37, No. 8, (2010), 5661-5665. doi: 10.1016/j.eswa.2010.02.045.
8. Sugianela, Y., Sutino, Q. L. and Herumurti, D. "Eeg Classification for Epilepsy Based on Wavelet Packet Decomposition and Random Forest." ***Jurnal Ilmu Komputer dan Informasi,*** Vol. 11 No. 1, (2018), 27-33. doi: 10.21609/jiki.v11i1.549.
9. Guo, L., Rivero, D., Seoane, J. A., and Pazos, A. "Classification of EEG signals using relative wavelet energy and artificial neural networks", in *2009 World Summit on Genetic and Evolutionary Computation, 2009 GEC Summit - Proceedings of the 1st ACM/SIGEVO Summit on Genetic and Evolutionary Computation, GEC'09*, (2009). doi: 10.1145/1543834.1543860.
10. Sik, H. H., Gao, J., Fan, J., Wu, B. W. Y., Leung, H. K., and Hung, Y. S. "Using wavelet entropy to demonstrate how mindfulness practice increases coordination between irregular cerebral and cardiac activities." ***Journal of Visualized Experiments,*** Vol. 123, (2017), 1-10. doi: 10.3791/55455.
11. Adeli, H., Zhou, Z. and Dadmehr, N. "Analysis of EEG records in an epileptic patient using wavelet transform." ***Journal of Neuroscience Methods,*** Vol. 123, No. 1, (2003), 69-87. doi: 10.1016/S0165-0270(02)00340-0.
12. Lee, S. H., Lim, J. S., Kim, J. K., Yang, J., and Lee, Y. "Classification of normal and epileptic seizure EEG signals using wavelet transform, phase-space reconstruction, and Euclidean distance" ***Computer Methods and Programs in Biomedicine,*** Vol. 116, No. 1, (2014), 10-25. doi: 10.1016/j.cmpb.2014.04.012.
13. Dwi Saputro, I. R., Maryati, N. D., Solihati, S. R., Wijayanto, I., Hadiyoso, S., and Patmasari, R. "Seizure Type Classification on EEG Signal using Support Vector Machine." ***Journal of Physics: Conference Series,*** Vol. 1201, No. 1, (2019). doi: 10.1088/1742-6596/1201/1/012065.
14. Fereydouni, A. R., Charmin, A., Vahdati, H., and Aghdam, H. N. "Channel Estimation and Carrier Frequency Offset Compensation in Orthogonal Frequency Division Multiplexing System Using Adaptive Filters in Wavelet Transform Domain." ***International Journal of Engineering, Transactions A: Basics,*** Vol. 33, No. 7, (2020), 1231-1239. doi: 10.5829/ije.2020.33.07a.09.
15. Khoshnood, A. M., Khaksari, H., Roshanian, J., & Hasani, S. M. "Active noise cancellation using online wavelet based control system: Numerical and experimental study." ***International Journal of Engineering, Transactions A: Basics,*** Vol. 30, No. 1, (2017), 120-126. doi: 10.5829/idosi.ije.2017.30.01a.15.
16. Kehtarnavaz, N. Digital Signal Processing System Design. Academic Press, 2008.
17. Gandhi, T., Panigrahi, B. K. and Anand, S. "A comparative study of wavelet families for EEG signal classification"***Neurocomputing,*** Vol. 74, No. 17, (2011), 3051-3057. doi: 10.1016/j.neucom.2011.04.029.
18. Swami, P., Gandhi, T. K., Panigrahi, B. K., Tripathi, M., and Anand, S. "A novel robust diagnostic model to detect seizures in electroencephalography." ***Expert Systems with Applications,*** Vol. 56, (2016), 116-130. doi: 10.1016/j.eswa.2016.02.040.
19. Swami, P., Gandhi, T. K., Panigrahi, B. K., Bhatia, M., Santhosh, J., and Anand, S. "A comparative account of modelling seizure detection system using wavelet techniques." ***International Journal of Systems Science: Operations and Logistics,*** Vol. 4, No. 1, (2017), 41-52. doi: 10.1080/23302674.2015.1116637.
20. Irawati, I. D., Hadiyoso, S. and Hariyani, Y. S. "Multi-wavelet level comparison on compressive sensing for MRI image reconstruction." ***Bulletin of Electrical Engineering and Informatics,*** Vol. 9, No. 4, (2020), 1461-1467. doi: 10.11591/eei.v9i4.2347.
21. Awad, M. and Khanna, R. Support Vector Machines for Classification. Efficient Learning Machines, Berkeley, Apress, Berkeley: CA,2015
22. Hadiyoso, S., Wijayanto, I., Rizal, A., and Aulia, S. "Biometric systems based on ECG using ensemble empirical mode decomposition and variational mode decomposition." ***Journal of Applied Engineering Science,*** Vol. 18, No. 2, (2020) 181-191. doi: 10.5937/jaes18-26041.
23. Martisius, I., Damasevicius, R., Jusas, V., and Birvinskas, D. "Using higher order nonlinear operators for SVM classification of EEG data." ***Elektronika Ir Elektrotechnika,*** Vol. 3, No. 3, (2012), 99-102. doi: 10.5755/j01.eee.119.3.1373.
24. Wijayanto, I., Rizal, A. and Hadiyoso, S. "Multilevel Wavelet Packet Entropy and Support Vector Machine for Epileptic EEG Classification." *2018 4th International Conference on Science and Technology (ICST)*. Yogyakarta, (2018).
25. Zamanian, H. and Farsi, H. "A new feature extraction method to

improve emotion detection using EEG signals." ***Electronic Letters on Computer Vision and Image Analysis,*** Vol. 17, No. 1, (2018), 9-44. doi: 10.5565/rev/elcvia.1045.

26. Cortes, C. and Vapnik, V. Support-Vector Networks in Machine Learning, Boston: Kluwer Academic, 1995.
27. Weng, W. C., Jiang, G. J. A., Chang, C. F., Lu, W. Y., Lin, C. Y., Lee, W. T., and Shieh, J. S. "Complexity of multi-channel electroencephalogram signal analysis in childhood absence epilepsy." ***PLoS ONE,*** Vol. 10, No. 8, (2015), 1-14. doi: 10.1371/journal.pone.0134083.
28. Sharma, M., Bhurane, A. A. and Rajendra Acharya, U. "MMSFL-OWFB: A novel class of orthogonal wavelet filters for epileptic seizure detection." ***Knowledge-Based Systems,*** Vol. 160, (2018), 265-277. doi: 10.1016/j.knosys.2018.07.019.
29. Gupta, A., Singh, P. and Karlekar, M. "A novel signal modeling approach for classification of seizure and seizure-free EEG signals." ***IEEE Transactions on Neural Systems and Rehabilitation Engineering,*** Vol. 26, No. 5, (2018), 925-935. doi: 10.1109/TNSRE.2018.2818123.

Persian Abstract

چکیده

صرع یکی از اختلالات عصبی رایج است که می تواند باعث تشنج بدون برانگیختگی شود. در حال حاضر ، تشخیص و ارزیابی با استفاده از آنالیز سیگنال الکتروانسفالوگرام (EEG)انجام می شود که توسط پزشکان بصری انجام می شود. از آنجا که سیگنالهای EEG تصادفی و غیر ثابت هستند ، بازرسی بصری اغلب بیان نادرست نتایج است. مطالعات متعددی تجزیه و تحلیل مبتنی بر رایانه برای طبقه بندی EEG صرعی پیشنهاد شده است. با این حال ، هنوز فاصله ای برای بهبود دقت تشخیص با تعداد کمی از ویژگی ها وجود دارد. بنابراین ، در این مطالعه ، ما یک پروتکل تشخیص خودکار برای طبقه بندی EEG صرعی پیشنهاد کردیم. روش های پیشنهادی انرژی موجک نسبی و آنتروپی موجک برای استخراج ویژگی و ترکیب شده با روش طبقه بندی برای تشخیص خودکار است. در این مطالعه ، سه کلاس EEG شامل پیش اکتال ، ictal و interictal به عنوان داده های آزمون استفاده شد و همچنین روش پیشنهادی را ارزیابی کرد. سیگنال های EEG با استفاده از تبدیل موجک به پنج زیر گروه معمولی ، از جمله گاما ، بتا ، آلفا ، تتا و دلتا تجزیه شدند. سپس انرژی نسبی و آنتروپی در هر یک از این باند ها به عنوان یک مجموعه ویژگی محاسبه شد. این روش ها با در نظر گرفتن محاسبات کم هزینه انتخاب می شوند. ما عملکرد روش استخراج ویژگی خود را با استفاده از هسته های خطی و غیر خطی با استفاده از ماشین بردار پشتیبانی (SVM) آزمایش کردیم. از طریق شبیه سازی ، بالاترین دقت ۸۰-۹۶,۷٪ برای ictal در مقابل pre-ictal، ictal در مقابل inter ictal، pre ictal در مقابل inter ictal ، و ictal در مقابل غیر ictal بود. سرانجام انتظار می رفت که این کار به پزشکان در تشخیص شروع صرع بر اساس سیگنال های EEG کمک کند.

IJE TRANSACTIONS A: Basics Vol. 34, No. 01, (January 2021) 82-89

International Journal of Engineering

Journal Homepage: www.ije.ir

The Predictability of Tree-based Machine Learning Algorithms in the Big Data Context

F. Qolipour, M. Ghasemzadeh*, N. Mohammad-Karimi

Computer Engineering Department, Yazd University, Yazd, Iran

PAPER INFO

Paper history:
Received 22 August 2019
Accepted in revised form 22 October 2020

Keywords:
Stock Market
Big Data
Prediction
Machine Learning
Tree-based Algorithms
Ensemble Algorithms

ABSTRACT

This research work is concerned with the predictability of ensemble and singular tree-based machine learning algorithms during the recession and prosperity of the two companies listed in the Tehran Stock Exchange in the context of big data. In this regard, the main issue is that economic managers and the academic community require predicting models with more accuracy and reduced execution time; moreover, the prediction of the companies recession in the stock market is highly significant. Machine learning algorithms must be able to appropriately predict the stock return sign during the market downturn and boom days. Addressing the stated challenge will upgrade the quality of stock purchases and, subsequently, will increase profitability. In this article, the proposed solution relies on the utilization of tree-based machine learning algorithms in the context of big data. The proposed solution exploits the decision tree algorithm, which is a traditional and singular tree-based learning algorithm. Furthermore, two modern and ensemble tree-based learning algorithms, random forest and gradient boosted tree, has been utilized for predicting the stock return sign during recession and prosperity. The mentioned cases were implemented by applying the machine learning tools in python programming language and PYSPARK library that is used explicitly for the big data context. The utilized research data of the current study are the shares information of two companies of the Tehran Stock Exchange. The obtained results reveal that the applied ensemble learning algorithms have performed better than the singular learning algorithms. Additionally, adding 23 technical features to the initial data and subsequent applying of the PCA feature reduction method have demonstrated the best performance among other modes. In the meantime, it has been concluded that the initial data do not possess the proper resolution or generalizability, either during prosperity or recession.

***doi**: 10.5829/ije.2021.34.01a.10*

1. INTRODUCTION[1]

In recent years, machine learning methods are widely used in different areas [1,2]; also, the stock return predictability issue has been frequently investigated in financial studies, and in this regard, forecasting the stock returns for investment purposes is very imprtant [3]. Nowadays, the rapid increase in processing speed, low data storage costs, the big data availability, as well as a wide range of open-source software, have revolutionized application of machine learning techniques. However, the stated novel research field is not bound to computer science or software engineering. Currently, machine learning tools are also utilized for resolving financial issues [4].

Since large companies are more involved in economic activities and have a more transactions, they generate more massive data. As CPU speed increases, larger data packs could be analyzed; consequently, the data analyses improve the investor predictions and concurrently reduce the shareholders' uncertainties and company costs. The big data field is expanding to the modern economy context and may assist financial market participants to make more informed choices about the companies in which they intend to invest. Additionally, these data affect the price, stock value, and investment decisions of the mentioned companies [5]. Due to this, the stock return

*Corresponding Author Institutional Email: m.ghasemzadeh@yazd.ac.ir (M. Ghasemzadeh)

Please cite this article as: F. Qolipour, M. Ghasemzadeh, N. Mohammad-Karimi, The Predictability of Tree-based Machine Learning Algorithms in the Big Data Context, International Journal of Engineering, Transactions A: Basics Vol. 34, No. 01, (2021) 82-89

sign that is affected by the stock price is also influenced by them.

Capital markets include recession and prosperity. During prosperity, the stock return is positive in most companies, and vice versa. In this regard, if a company can keep its stock return positive while the market is in the state of recession, it is preferable for purchasing. Due to the mentioned reason, forecasting stock returns during the recession is highly significant. Machine learning algorithms must be able to appropriately predict stock returns in the times of market downturn and boom days. The primary motivation of conducting the present research is to study the predictability of machine learning algorithms in the boom and bust cycles of the stock market and to compare them in the context of big data. The selected data have been employed in this field for the first time. These data include 23 technical features, in addition to the 10 basic features of the Tehran stock market. In the current study, it has been sought to examine the impact of adding 23 technical features to the mentioned data in this case, in addition to the predictability of machine learning algorithms in boom and bust cycles in the big data field and its corresponding tools. Moreover, the obtained results of the original data and the new data of this field have been compared.

2. LITERATURE REVIEW

Machine learning is a scientific study that innovates various algorithms to improve its performance on a particular task gradually. Due to the remarkable ability to extract valid information from datasets and the most optimized pattern recognitions, numerous recent papers have focused on the application of machine learning techniques in financial subjects. These methods encompass basic statistical models such as logistic regression as well as artificial intelligence methods such as decision trees, support vector machines, and artificial neural networks. In contrast to traditional machine learning models, ensemble models (i.e., a combination of several models) are machine learning-based approaches in which several basic algorithms are utilized for solving a particular problem, and it has been proven that they demonstrate a higher performance in predicting financial time series in comparison to singular learning models.

In ensemble learning algorithms, bagging and boosting are among the most popular techniques in the machine learning field. Bagging (bootstrap aggregating) that has been developed by Bryman [6] is one of the most straightforward and most intuitive approaches in the ensemble, which in addition to superb performance, it also reduces the variance and prevents the occurrence of overfitting. The begging algorithm is obtained from the Bootstrap technique, which produces subsets of training data by repeating the training data set. Each subset is utilized for fitting a separate basic learner, and the final prediction results are gathered through the majority voting method. Boosting is another ensemble technique that is according to the research of Freund and Shapir [7]. In contrast to the bagging technique, this method creates various learners by applying a sequential weighting algorithm to training samples. Any sample that has not been classified by the previous learner will gain more weight in the next round of training. Consequently, unclassified training samples will usually occur in the subsequent Bootstrap sample, and the bias can be effectively reduced. The ultimate model of the Boosting algorithm is a combination of all basic learners that are weighted through their corresponding predictive performance [4]. The random forest algorithm exploits the bagging method, and the gradient boosted tree algorithm uses the boosting method.

Two types of ensemble classifiers have been organized (i.e., homogeneous and heterogeneous ensemble classifiers) through utilizing the majority voting and the bagging method by Tsai et al. [8]. In this regard, the financial ratio and macroeconomic characteristics in the Taiwan stock market have been considered to examine the performance of stock return forecasts. The result has indicated that ensemble classifiers perform more beneficial than singular classifiers from the aspect of forecast accuracy and return on investment (ROI) [8].

Similarly, a comparative study has been conducted by Ballings et al. [9] in which ensemble learning algorithms, including random forests, and the AdaBoost, have been compared to singular learning models, including neural networks, linear regression, support vector, and k-nearest neighbors algorithms. Afterward, the one-year stock price direction of European companies have been predicted. The AUC results illustrate that the random forest is the superior algorithm among the examined algorithms [9].

Random forest and XGBoost algorithms have been applied for the classification problem by Basak et al. [10]. Moreover, according to the prevailing price of the past few days, it has been predicted that stock prices would rise or fall. Eventually, experimental results have displayed that the performance of the forecasting process for different types of companies has improved in comparison to the available companies [10].

Regarding the perspective that macroeconomic indicators can solely predict the accurate one-month ahead price of major US stock indices, four ensemble models of random forest quantile regression, quantile regression neural network, bagging regression and boosting regression have been created by Wong et al. [11]. The results have demonstrated that the forecasting performances of these ensemble learning methods are superior to traditional time series models. Additionally, this study proposes a hybrid approach of long short term

memory, and then, it proves that macroeconomic features are pioneers [11].

3. MATERIALS AND METHODS

3. 1. System Model and Hypotheses The structure of a machine learning model does not necessarily require the development of an entirely novel algorithm. Customization and utilization of investigated models can also lead to improved prediction results. Even the preprocessing of information before implementing the model is also part of the study innovation. In this research, through using 10 basic features of the Tehran Stock Exchange, 23 technical features for two active companies in the stock exchange, are extracted, and the new data with 10 basic features along with the mentioned 23 technical features are generated. Afterward, the recession and prosperity of these companies are separated, and the predictability of the stock return is compared by utilizing singular, and ensemble tree-based algorithms such as decision tree and random forest ensemble algorithms and gradient boosted tree in big data space. Furthermore, it has been intended to evaluate the impact of adding 23 technical features to the initial data and exploiting the PCA feature reduction technique on the performance of these algorithms. In this regard, the general process of the study can be observed in Figure 1.

3. 2. The Proposed Method In huge markets such as the stock market, which is daily encountered with a massive amount of data and the prompt reaction of shareholders is crucial, it is highly significant to be able to select the right decisions as soon as possible.

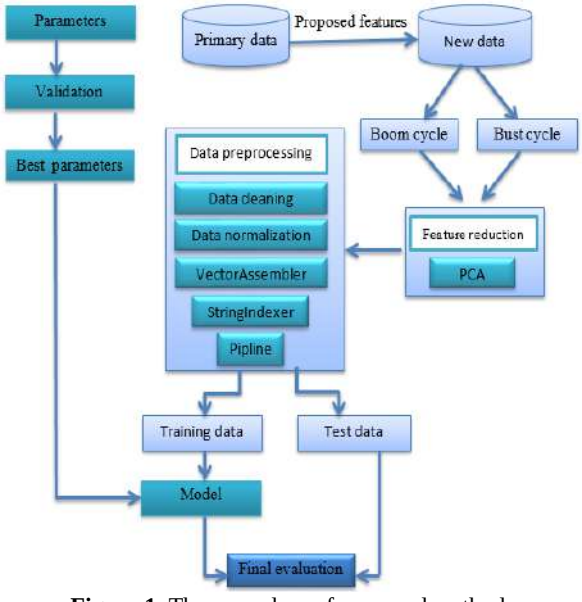

Figure 1. The procedure of proposed method

Accordingly, in forecasting the huge financial series with machine learning algorithms, achieving the minimum error rate in the minimum amount of time is critical. The initial data of this study is the stock information of two active companies in the Tehran Stock Exchange that each stock data contains ten basic features. These features include the date, initial price, highest price, lowest price, final price, volume, value, number of trades, and yesterday's stock price each day. Through technical analysis, 23 technical features were measured from the collected information of 10 basic features from companies' stocks over ten years. The new dataset is generated by extracting 23 technical features and adding to the original data along with ten basic characteristics.

Proposed features, which are based on the technical analysis are total price index, industry index, equal-weighted price index, industries index, total return, industry return, beta coefficient of industry return, beta coefficient of total index, moving average divergence convergence, three-day moving average, five-day moving average, moving average Ten-Day, 20-Day Moving Average, 30-Day Moving Average, Seven-Day Moving Average, Weighted Moving Average, Relative Strength Index, Bollinger Bands (Upper and Lower bands), First Days of Each Week, Latest Days of Stock Market, First Months of Each Year and Exchange rate index).

After collecting the suggested features, through the assistance of the total price index feature, a new feature was generated that was called the period. In this regard, it represents the market boom and bust cycles. If the stock return sign can be predicted during the recession as well as the prosperity, the great achievement will be acquired due to the particular importance that they possess recently in the capital market.

According to the period feature, the collected data have been converted into two categories of prosperity and recession periods with positive and negative signs, respectively. In addition to comparing the prosperity and recession period for each share, the impact of adding 23 technical features to the basic characteristics have been considered, as well. To achieve this aim, the performance of the decision tree, random forests, and gradient boosted tree algorithms in six created modes have been compared.

The six created modes are:

- prosperity period for each share and 10 basic features
- prosperity period for each share and new features (10 basic features + 23 technical features)
- prosperity period and feature reduction utilizing PCA feature extraction method
- recession period for each share and 10 base features
- recession period for each share and new features
- recession period and feature reduction utilizing the PCA feature extraction method.

After collecting the data and separating the boom and bust cycle (recession and prosperity period) of both companies stocks, with the assistance of the missingpy library in Python programming language and random forest technique, the missing or unassigned data values have been filled. Afterward, for the process of normalizing the data, through using the VectorAssembler function in the pyspark library, which is a designated for working with the big data, the available features were converted into a vector. Furthermore, they have given as inputs to the MimMaxScaler normalizer function; thus, a normalized vector of the features was acquired through the mentioned process.

The preprocessing step of data in the big data space relatively differs from the corresponding step in common data space. For the big data preprocessing task, after the converting of properties into a single vector property by VectorAssembler, the label property is also converted to numeric data by the StringIndexer function if it is in the string data form. Consequently, the mentioned two features are placed in a data frame by the existing Pipeline function in pyspark; moreover, they are considered as the model input.

In the field of time series prediction, by applying the machine learning algorithms after the data preprocessing step, it is necessary to convert the data into two categories: a training set and a test set. The training set is exploited for making the model, and the test set is used to validate the accuracy of the model. Of course, it is worth mentioning that the mentioned test dataset is divided into two categories of test and validation, which are used for evaluating the amount of training that has been obtained from the training data set. The evaluation outcome is solely applied to select the best training part, and after finding this part, it has been utilized for the final evaluation, which is examined with the test data. To determine the test and training set for each share, 20% of the total data have been allocated to the test set, and 80% of it has been assigned for the training set.

In financial time series, traditional cross-validation procedures such as K-fold is not utilizable due to random and unbiased selection of training data sets as well as the time dependencies in time series. As a consequence, the stages of the cross-validation method in time series are as follows:

First stage: the whole training data set has been divided into several sections. The default value of this segmentation number in the conducted implementations is three; however, after performing several experiments, the value of 10 has been selected for the segmentation number. As a result, the training samples have been separated into 10 sections, and each time, one section has been selected.

Second stage: The first two sections, which contain two-tenths of the training data, have been divided into two sections. 50% of the data (equivalent to 10% of the total training data) has been assigned for the training purpose, and the other 50% for the validation purpose and the test data.

Third stage: at this stage, one-tenth of the training data has been added at each turn, and the newly added section has been allocated to the test data, and further, the previous sections have been considered for training purposes. This process has been extended until all ten sections are validated, as displayed in Figure 1.

The classification techniques have been utilized for numerous applications in various fields of science. There are several methods for the evaluation of classification algorithms. Analysis of such criteria and their importance should be appropriately interpreted to evaluate different learning algorithms. In advance of introducing evaluation methods, it's preferable to express the fundamental and significant concept of a confusion matrix for two-class or binary classification purposes.

In the confusion matrix, four symbols are encountered: TN, FN, TP, and FP. If the sample is actually positive and is also classified as a positive sample, it is regarded that the sample has been correctly classified as positive; moreover, the "TP" symbol is assigned for it. If the corresponding sample is actually positive and is classified as negative, it is declared that the sample is conversely classified as negative, and it is displayed with the "FN" symbol. Accordingly, if the negative sample is classified as a negative sample, the sample is considered as a correctly classified negative sample; furthermore, it is represented with the "TN" symbol. Eventually, if the negative sample is classified as a positive sample, it has been considered as a misclassified positive sample and is exhibited with the "FP" symbol. As can be observed in the following, the confusion matrix is applied for the calculation of numerous standard classification criteria.

Accuracy: It is one of the most common measures for classification performance and is defined as the ratio of correctly classified samples to the total number of samples:

$$Acc = \frac{TP+TN}{TP+TN+FP+FN} \quad (1)$$

Recall: It represents the ratio of correctly classified positive samples to samples that have been actually labeled positive. This evaluation criterion is expressed as follows:

$$Recall = \frac{TP}{TP+FN} \quad (2)$$

Precision: It indicates the ratio of correctly classified positive samples to the total samples that are correctly or incorrectly classified as positive ones. This evaluation criterion is illustrated as follows:

$$Precision = \frac{TP}{TP+FP} \quad (3)$$

AUC-ROC: A perfect and superb model has an Area Under the Curve (AUC) of Receiver Operating Characteristic (ROC) close to one, which means it has adequate separability. A deficient model has an AUC close to 0, meaning it has the worst separability. Furthermore, when the AUC is 0.5, it means that the model is not able for any class separability measures.

4. EXPERIMENTS

Afterwards, the above procedure was applied to the six stated modes, and the results of three prediction algorithms were compared. Table 1 shows, that validation and testing of Pars Oil Company in the prosperity period along with the PCA feature reduction method for all three algorithms have obtained superior results in comparison to the initial and the new data with 33 features. Additionally, among the three selected algorithms, two ensemble algorithms (random forests and gradient boosted tree) have mostly acquired better results in comparison to the singular algorithm of the decision tree. Moreover, the achieved results for the test data sets in the gradient boosted tree algorithm have been better than other algorithms that demonstrate the additional generalizability of this algorithm.

In Table 2, the obtained results of the Pars Oil Company evaluation during the recession have been examined. As illustrated in this table, the PCA method leads to better results in most cases compared to the 10 basic features and the new data, which includes 33 features. However, it is crystal clear that adding 23 technical features to the initial data had positively influenced the acquired results in all three algorithms.

TABLE 1. The evaluation results of Pars Oil Company during the prosperity period

Models	**The validation results of Pars Oil Company during the prosperity period**											
	33 features				**10 basic features**				**PCA Feature reduction algorithm**			
	Au-Roc	***Precision***	***Recall***	***Accuracy***	***Au-Roc***	***Precision***	***Recall***	***Accuracy***	***Auc Roc***	***Precision***	***Recall***	***Accuracy***
DT	0.864	0.802	**0.830**	0.872	0.511	**0.505**	**0.627**	0.601	0.931	0.888	0.865	0.941
RF	0.889	**0.836**	0.804	**0.873**	0.525	0.442	0.536	**0.608**	0.944	0.888	0.865	**0.955**
GBT	**0.927**	0.803	**0.830**	0.865	**0.526**	0.460	**0.627**	0.605	**0.973**	0.888	0.865	0.953
Models	**The test results of Pars Oil Company during the prosperity period**											
	33 features				**10 basic features**				**PCA Feature reduction algorithm**			
	Au-Roc	***Precision***	***Recall***	***Accuracy***	***Au-Roc***	***Precision***	***Recall***	***Accuracy***	***Au-Roc***	***Precision***	***Recall***	***Accuracy***
DT	0.559	0.687	0.427	0.618	0.498	0.5	0349	0.502	1.0	1.0	1.0	1.0
RF	0.720	0.723	**0.533**	0.666	0.503	0.490	0.728	0.487	1.0	1.0	1.0	1.0
GBT	**0.743**	**0.776**	0.504	**0.681**	**0.526**	**0.502**	**0.980**	**0.507**	1.0	0.990	1.0	0.995

TABLE 2. The evaluation results of Pars Oil Company during the recession period

Models	**The validation results of Pars Oil Company during the recession period**											
	33 features				**10 basic features**				**PCA Feature reduction algorithm**			
	Au-Roc	***Precision***	***Recall***	***Accuracy***	***Au-Roc***	***Precision***	***Recall***	***Accuracy***	***Auc Roc***	***Precision***	***Recall***	***Accuracy***
DT	0.873	0.927	0.861	0.898	0.514	0.344	0.321	0.637	0.971	0.963	0.987	0.969
RF	**0.915**	**0.933**	0.788	0.899	0.532	0.421	0.231	**0.643**	1.0	1.0	1.0	0.996
GBT	0.914	0.923	**0.866**	**0.908**	**0.535**	**0.479**	**0.440**	0.611	1.0	1.0	1.0	0.996
Models	**The test results of Pars Oil Company during the recession period**											
	33 features				**10 basic features**				**PCA Feature reduction algorithm**			
	Au-Roc	***Precision***	***Recall***	***Accuracy***	***Au-Roc***	***Precision***	***Recall***	***Accuracy***	***Au-Roc***	***Precision***	***Recall***	***Accuracy***
DT	0.383	0.529	0.246	0.609	0.468	**0.666**	**0.547**	**0.609**	0.889	0.752	1.0	0.868
RF	**0.857**	**0.931**	**0.561**	**0.807**	0.505	0.0	0.0	0.598	**1.0**	**0.858**	**1.0**	**0.934**
GBT	0.759	0.921	0.479	0.774	**0.539**	**0.666**	0.027	0.604	1.0	0.752	1.0	0.868

Furthermore, ensemble algorithms in this period, similar to the boom period, have presented a more significant performance with respect to the singular algorithm of the decision tree, and all three algorithms have presented appropriate predictability during the boom period. The most generalizability to the new data has been observed in the random forest algorithm along with the availability of 23 technical features and the application of feature reduction technique. On the other hand, for the case of 10 basic characteristics, the decision tree results in a better performance in test data sets. Generally, both periods of the prosperity and the recession, the PCA feature reduction method has demonstrated a more significant performance for the Pars Oil Company in comparison to the two other cases. Moreover, the initial data have not represented a suitable performance, and among the applied algorithms, the ensemble algorithms had achieved more excellent results in relation to the singular algorithms.

In Table 3, the obtained results of the Shazand Petrochemical Company during the boom period have been investigated. As can be observed, in almost all of the cases, the ensemble algorithms have performed better than the singular algorithms. The performance of the feature reduction algorithm on the company's data during the prosperity period is also higher than the initial data along with 10 basic features and the 23 technical features utilization; thus, the mere initial data will not be an appropriate representative for prediction of the company's situation in the future. As the obtained values in validation and testing reveal, adding 23 technical features and subsequent feature extracting from them positively affect the performance of all three selected algorithms. The class separability and generalizability of these data in the absence of technical features and solely considering the initial data are not appropriate; while in these data, the use of technical features, as well as the ensemble algorithms, are recommended in comparison to the utilization of traditional singular algorithms.

In Table 4, the evaluation results of the Shazand Petrochemical Company during the recession have been reviews. As can be noticed, in both validation and testing, the PCA feature reduction technique has demonstrated a more significant performance compared to the other two modes, and on the other hand, 10 basic features mode did not present an appropriate performance. The stated fact means that adding 23 technical features to the corresponding data is also effective. Moreover, among the chosen algorithms, in all three cases, ensemble learning algorithms have performed better in the validation process. Furthermore, these algorithms represent proper generalizability in the test process.

The two ensemble algorithms of random forest and the gradient boosted tree approximately have similar results in all three modes, and for all four input data sets. Additionally, they have exhibited higher performance in comparison to the traditional and singular algorithm of the decision tree in most cases. Generalizability and class separability in ensemble algorithms, particularly in the new data set, including 23 technical features in addition to 10 basic features, as well as the application of the PCA feature reduction method, are superior to the singular learning methods. The predictability of algorithms during the company's recession is as accurate as its prosperity period.

TABLE 3. The evaluation results of Shazand Petrochemical Company during the prosperity period

Models	**The validation results of Pars Oil Company during the prosperity period**											
	33 features				**10 basic features**				**PCA Feature reduction algorithm**			
	Au-Roc	***Precision***	***Recall***	***Accuracy***	***Au-Roc***	***Precision***	***Recall***	***Accuracy***	***Auc Roc***	***Precision***	***Recall***	***Accuracy***
DT	0.867	0.932	0.796	0.863	0.508	0.532	0.407	0.623	0.997	0.996	1.0	0.995
RF	**0.936**	**0.939**	0.782	**0.898**	**0.573**	0.463	0.364	0.627	**1.0**	**1.0**	1.0	**1.0**
GBT	0.920	0.894	**0.862**	0.890	0.544	**0.558**	**0.573**	**0.629**	**1.0**	0.997	1.0	0.998
Models	**The test results of Pars Oil Company during the prosperity period**											
	33 features				**10 basic features**				**PCA Feature reduction algorithm**			
	Au-Roc	***Precision***	***Recall***	***Accuracy***	***Au-Roc***	***Precision***	***Recall***	***Accuracy***	***Au-Roc***	***Precision***	***Recall***	***Accuracy***
DT	0.628	**0.829**	0.323	0.626	**0.5**	0.0	0.0	**0.497**	1.0	1.0	1.0	1.0
RF	**0.773**	0.706	0.733	**0.712**	0.429	0.365	0.142	0.444	1.0	1.0	1.0	1.0
GBT	0.707	0.607	**0.885**	0.655	0.490	**0.483**	**0.695**	0.473	1.0	1.0	1.0	1.0

TABLE 4. The evaluation results of Shazand Petrochemical Company during the recession period

Models	The validation results of Shazand Petrochemical Company during the recession period											
	33 features				10 basic features				PCA Feature reduction algorithm			
	Au-Roc	*Precision*	*Recall*	*Accuracy*	*Au-Roc*	*Precision*	*Recall*	*Accuracy*	*Auc Roc*	*Precision*	*Recall*	*Accuracy*
DT	0.919	**0.885**	0.867	0.9	0.499	0.496	0.543	0.625	0.993	1.0	0.993	0.995
RF	0.934	0.877	**0.912**	0.887	0.515	0.543	0.598	**0.631**	**0.997**	1.0	0.993	0.995
GBT	**0.939**	0.883	**0.912**	**0.906**	**0.546**	**0.595**	**0.818**	0.618	0.996	1.0	**1.0**	0.995
Models	**The test results of Shazand Petrochemical Company during the recession period**											
	33 features				10 basic features				PCA Feature reduction algorithm			
	Au-Roc	*Precision*	*Recall*	*Accuracy*	*Au-Roc*	*Precision*	*Recall*	*Accuracy*	*Au-Roc*	*Precision*	*Recall*	*Accuracy*
DT	0.674	0.532	**0.506**	0.638	0.5	0.0	0.0	**0.614**	0.965	0.880	1.0	0.947
RF	**0.809**	**0.944**	0.419	**0.766**	0.517	0.4	0.024	0.609	**0.990**	**0.964**	1.0	**0.985**
GBT	0.718	0.579	0.493	0.666	**0.531**	**0.431**	**0.617**	0.538	0.957	0.880	1.0	0.947

5. CONCLUSION

The results of stock evaluations of the two active companies demonstrate that the ensemble algorithms of random forest and gradient boosted tree have better predictability in comparison to the decision tree, which is a singular tree-based algorithm, during both of the boom and bust cycles. Additionally, the AUC-ROC in these algorithms represent the fact that the ensemble algorithms create further class separability; therefore, they can accurately predict the positive and negative sign of stock return. Furthermore, adding 23 technical features to 10 basic features and subsequent creation of the new data and further feature extracting utilizing the PCA method has a significant effect in improving the performance of the algorithms. In this regard, the most excellent result has been obtained from the application of the PCA method. Moreover, the decision tree algorithm possesses a higher performance speed than the ensemble algorithms since it merely exploits one tree for the prediction procedure, and among the ensemble algorithms, the decision tree is faster in case of the current study data.

6. REFERENCES

1. Khedmati. M, Seifi. F, Azizi. M.J, "Time Series Forecasting of Bitcoin Price Based on Autoregressive Integrated Moving Average and Machine Learning Approaches", ***International Journal of Engineering, Transactions A: Basics,*** Vol. 33, No. 7, (2020), 1293-1303. DOI: 10.5829/IJE.2020.33.07A.16
2. Hemati. H.R., Ghasemzadeh. M, Meinel. C, "A Hybrid Machine Learning Method for Intrusion Detection", ***International Journal of Engineering, Transactions C: Aspects,*** Vol. 29, No. 9, (2016), 1242-1246, DOI: 10.5829/idosi.ije.2016.29.09c.09
3. Liu, J, and Kemp. A, "Forecasting the sign of U.S. oil and gas industry stock index excess returns employing macroeconomic variables", ***Energy Economics***, Vol. 81, (2019), 672-686. https://doi.org/10.1016/j.eneco.2019.04.023
4. Jiang. M, Liu. J, Zhang. L, and Liu. C, "An improved Stacking framework for stock index prediction by leveraging tree-based ensemble models and deep learning algorithms", ***Physica A-Statistical Mechanics and Its Applications***, Vol. 541, (2020) 122272. https://doi.org/10.1016/j.physa.2019.122272
5. Begenau. J, Farboodi. M, and Veldkamp. L, "Big data in finance and the growth of large firms", ***Journal of Monetary Economics***, Vol. 97, (2018), 71-87. https://doi.org/10.1016/j.jmoneco.2018.05.013
6. Breiman. L, "Bagging Predictors", ***Machine Learning Archive***, Vol. 24, No. 2, (1996), 123-140.
7. Freund. Y and Schapire. R.E, "Experiments with a New Boosting Algorithm", in Proceedings of the International Conference on Machine Learning, (1996), 148-156.
8. Tsai. C.-F, Lin. Y.-C, Yen. D.C, and Chen. Y.M, "Predicting stock returns by classifier ensembles", ***Applied Soft Computing***, Vol. 11, No. 2, (2011), 2452-2459. https://doi.org/10.1016/j.asoc.2010.10.001
9. Ballings. M, Van den Poel. D, Hespeels. N, and Gryp. R, "Evaluating multiple classifiers for stock price direction prediction", ***Expert Systems With Applications***, Vol. 42, No. 20, (2015), 7046-7056. https://doi.org/10.1016/j.eswa.2015.05.013
10. Basak. S, Kar. S, Saha. S, Khaidem. L, and Dey. S.R, "Predicting the direction of stock market prices using tree-based classifiers", ***The North American Journal of Economics and Finance***, Vol. 47, (2019), 552-567. https://doi.org/10.1016/j.najef.2018.06.013
11. Weng. B, Martinez. W.G, Tsai. Y, Li. C, Lu. L, Barth. J.R., Megahed F.M, "Macroeconomic indicators alone can predict the monthly closing price of major U.S. indices: Insights from artificial intelligence, time-series analysis and hybrid models", ***Applied Soft Computing***, Vol. 71, (2018), 685-697. https://doi.org/10.1016/j.asoc.2018.07.024

Persian Abstract

چکیده

این پژوهش در رابطه با پیش‌بینی‌پذیری الگوریتم‌های یادگیری‌ماشین گروهی و منفرد مبتنی بر درخت در دوران رکود و رونق دو شرکت حاضر در بورس تهران در بستر داده‌های حجیم است. چالش موردتوجه در این حوزه، این است که مدیران اقتصادی و جامعه علمی، همچنان به دنبال مدل‌های پیش‌بینی با دقت بیشتر و در زمان کمتر می باشند و همچنین پیش‌بینی دوران رکود شرکت‌ها در بازار بورس از اهمیت به سزایی برخوردار است. الگوریتم‌های یادگیری ماشین باید بتوانند علامت بازده سهام را در روزهای رکود بازار به‌خوبی روزهای رونق پیش‌بینی کنند. رفع چالش یادشده موجب ارتقاء کیفیت خرید سهام و به سبب آن موجب ارتقای سودآوری می‌شود. راه‌حل پیشنهادی، تکیه‌بر به‌کارگیری الگوریتم‌های یادگیری ماشین مبتنی بر درخت در بستر داده‌های حجیم دارد. در راه‌حل پیشنهادی از الگوریتم درخت تصمیم که یک الگوریتم سنتی و منفرد مبتنی بر درخت است و همچنین دو الگوریتم مدرن و گروهی مبتنی بر درخت یعنی جنگل تصادفی و درخت گرادیان تقویتی برای پیش‌بینی پذیری علامت بازده سهام در روزهای رکود و رونق، استفاده‌شده است. موارد یادشده، با به‌کارگیری ابزارهای یادگیری ماشین به زبان پایتون و در کتابخانه PYSPARK که مخصوص داده‌های حجیم است، پیاده‌سازی گردیدند. داده‌های تحقیق که در این پژوهش به کار گرفته شدند، اطلاعات مربوط به سهام دو شرکت از بورس تهران می‌باشند. نتایج نشان می‌دهند که الگوریتم‌های گروهی استفاده‌شده عملکرد بهتری نسبت به الگوریتم منفرد داشته‌اند. همچنین اضافه کردن ۲۳ ویژگی فنی به دادگان اولیه و سپس استفاده از روش کاهش ویژگی PCA بهترین عملکرد را در بین حالت‌های دیگر داشته است. این مطلب موجب پیش‌بینی با دقت بالاتری می‌گردد. دراین‌بین به این نتیجه می‌رسیم که دادگان اولیه چه در دوران رونق و چه در دوران رکود از قابلیت تفکیک‌پذیری و تعمیم‌پذیری مناسبی برخوردار نیست.

International Journal of Engineering

Journal Homepage: www.ije.ir

Employing the Empirical Mode Decomposition to Denoise the Random Telegraph Noise

A. Moshrefi, H. Aghababa*, O. Shoaei

School of Electrical and Computer Engineering, University of Tehran, Tehran, Iran

P A P E R I N F O

Paper history:
Received 06 August 2020
Received in revised form 11 October 2020
Accepted 13 November 2020

Keywords:
Electronic Devices
Empirical Mode Decompositio
Noise
Random Telegraph Noise

A B S T R A C T

Random Telegraph Noise (RTN) is a stochastic phenomenon which leads to characteristic variations in electronic devices. Finding features of this signal may result in its modeling and eventually removing the noise in the device. Measuring this signal is accompanied by some noise and therefore we require a method to improve the Signal to Noise Ratio (SNR). As a result, the extraction of an accurate RTN is a remarkable challenge. Empirical Mode Decomposition (EMD) as a fully adaptive and signal dependent method, with no dependency to the specific function, can be an appropriate solution. In this paper, we evaluate the most recent methods and compare them with our proposed approach for the artificial and actual RTN signals. The results show the higher accuracy and efficiency by about 54%, 61% and 39% improvement in SNR, Mean Square Error (MSE) and Percent Root mean square Difference (PRD) respectively for the optimized wited method. Finally, an indicator to evaluate the reliability in digital circuits is introduced.

***doi**: 10.5829/ije.2021.34.01a.11*

1. INTRODUCTION

In recent years, the noise issue has attracted the attention of semiconductor industry. This phenomenon can decrease the quality of the valuable data and negatively impact the results of analysis and modeling. There are some methods to improve the quality of measuring the noise and data. However, if the noise and data are combined together, their discrimination will be tough. In addition, we have some limitations for our instruments which cannot accurately capture the desired data. Meanwhile, providing a solution by the software analysis would be helpful to obtain the data accurately [1–3].

In the other side, as the scaling of transistor geometries towards only a few tens of nanometers continues, we find that small devices face new challenges regarding their operation reliablity. Random Telegraph Noise (RTN) is one of these challenges which happens by trapping and detrapping of the carriers in the transistor channel and it would make some variations on the drain current. RTN is one of the most important time variation sources having a prominent effect on the reliability of memories, digital and analog circuits [4, 5]. Therefore, capturing the features of RTN and its modeling is of great importance. If we can measure the RTN accurately, we can obtain an appropriate model for it. However, this measurement is usually affected by some noise and error and it calls for a method to improve the signal to noise ratio.

In this area, Karatsori et al. [6] have characterized and measured the low frequency noise in InAs MOSFET. Stampfer et al. [7] has characterized the noise produced by individual defects for MoS2 field-effect transistors. Waltl et al. [8] employed an advanced algorithm based on cumulative summation to detect the step levels in RTN. Jech et al. [9], Lai et al [10] and Ullmann et al. [11] have extracted and measured the low frequency noises in MOSFET and also they have introduced a model for the noise features. Feng et al. [12] investigated the effect of RTN on the drain current variations as a Model for the introduced FETs. Matsumoto et al. [13, 14] have evaluated the impact of RTN on the CMOS logic circuits for low supply voltages. Compagnoni et al. [15, 16], Veksler et al. [17], Ling et al. [18] have analyzed the

*Corresponding Author Institutional Email: *Aghababa@ut.ac.ir* (H. Aghababa)

Please cite this article as: A. Moshrefi, H. Aghababa, O. Shoaei, Employing the Empirical Mode Decomposition to Denoise the Random Telegraph Noise, International Journal of Engineering, Transactions A: Basics, Vol. 34, No. 1, (2021) 90-96

reliability of RRAM and Flash memory under the impact of RTN to estimate the accuracy of data loss.

Imamoto et al. [19], Forbes and Miller [20], Chen et al. [21], Ioannidis et al. [22], Pirro et al. [23] have tried to decrease the level of RTN noise by changing some parameters in the structure of MOSFET devices. Although these methods can be effective, they might be so expensive. Thus, they require the nanometer instrument technologies and they are difficult to implement. Islam et al. [24], Seo et al. [25], Kushwaha et al. [26], Tanaka et al. [27] have considered the circuit noise as a deterministic process and have introduced a model based on the oxide trap density and energy level. Gokcen and Demir [28], Mohanty et al. [29] have considered the noise as a non-stationary and stochastic process. For de-noising the drain current from the RTN, some studies have been conducted. Diaz-Fortuny et al. [30, 31] have introduced a method to remove the RTN based on the detection and comparison of trace levels between the fast and slow defects. However, this method is consuming and cannot be implemented for real-time applications. Gao et al. [32], Vaseghi [33], Petrychuk et al. [34], Higashi et al. [35], Tega et al. [32–36] have analyzed and extracted RTN using the Fast Fourier Transform (FFT) and the Short Time Fourier Transform (STFT). However, Fourier analysis cannot determine the short-time variations of signal because it can only decompose the signal to same infinitive sinus and cosine series wherein all of the time information will be removed. Du et al. [37], Principato and Ferrante [38], Hendrickson et al. [39] have employed Wavelet decomposition to separate the data and 1/f noise. They have compared the shape of mother waves and introduced the Haar function as the best Wavelet to decompose the RTN. Then they have employed the universal threshold to de-noise the RTN by the Wavelet thresholding method. However, the Wavelet transform depends on the mother wave function and is not adaptive for every type of signal. Hence, it is not considered as a useful tool. In this paper, Empiricl Mode Decomposition (EMD) method is introduced which is the basis of the adaptive orthogonal functions and can be appropriate for non-stationary signals. This method is applied to diverse RTN signals and its capability is shown in decomposing the desired and undesired data.

2. METHOD

In this section, the proposed method for RTN signal is introduced.

2. 1. Empirical Mode Decomposition In recent years, Empirical Mode Decomposition has been considered as one of the most practical and efficient approaches in signal processing area. As opposed to the Wavelet and FFT which use the specific orthogonal parametric basis, this method decomposes the signal based on the signal harmonics and is completely adaptive. Therefore, it has a strong capability to decompose non-stationary signals. This method creates some Intrinsic Mode Functions (IMFs) and a residual signal. The procedure to produce the IMFs is based on the subtraction of the baseline function from the main signal. The process continues untill the residual signal becomes constant. Baseline function is considered as the average of local extremum of the signal. The IMFs must satisfy the two following conditions:

1. The number of the extremums and zero-crossings must be equal or differ by at most one.
2. In each point, the average value of the defined envelope by the local extremums must be zero. In another word, IMFs must be symmetric functions around zero.

The algorithm can be considered as follow:

1. Find the upper and lower envelops of the signal x(t).
2. Subtract the average of envelopes (m(t)) from the signal (d(t)=x(t)-m(t)).
3. If d(t) can satisfy the two conditions of IMFs, d(t) can be saved as the first mode, otherwise re-calculate the algorithm from the 1st step for d(t).

Then, the residue signal r(t) obtained from the subtraction of the signal x(t) and the IMF_1 is considered to calculate the next modes.

To obtain the next residue, the current IMF must be subtracted from the previous residue which will be employed to obtain the mode. The summery of these relations are

$$\begin{aligned} &\mathbf{r}_1 - \mathbf{IMF}_2 = \mathbf{r}_2 \\ &\mathbf{r}_2 - \mathbf{IMF}_3 = \mathbf{r}_3 \\ &. \\ &. \\ &\mathbf{r}_{n-1} - \mathbf{IMF}_n = \mathbf{r}_n \end{aligned} \quad (1)$$

whenever the reside r_n does not have any extremum point with almost the uniform behavior, the algorithm will be finished.

Finally, the input signal x(t) can be expressed as the summation of the IMFs and a residue

$$x(t) = \sum_{i=1}^{n} IMF(i) + r(t), \quad (2)$$

where n is the number of decomposition levels and r(t) is the residual signal at the end of the algorithm [40–43]. EMD method can be summarized in Figure 1.

This method is applied to show the decomposed levels on an actual noisy RTN in Figure 2.

For the first stage, because of the adaptive decomposition of EMD, we can propose the EMD thresholding instead of the Wavelet thresholding.

Another approach is that we can employ some weights for the decomposed modes since it is clear that our desired data has not been distributed in all IMFs uniformly.

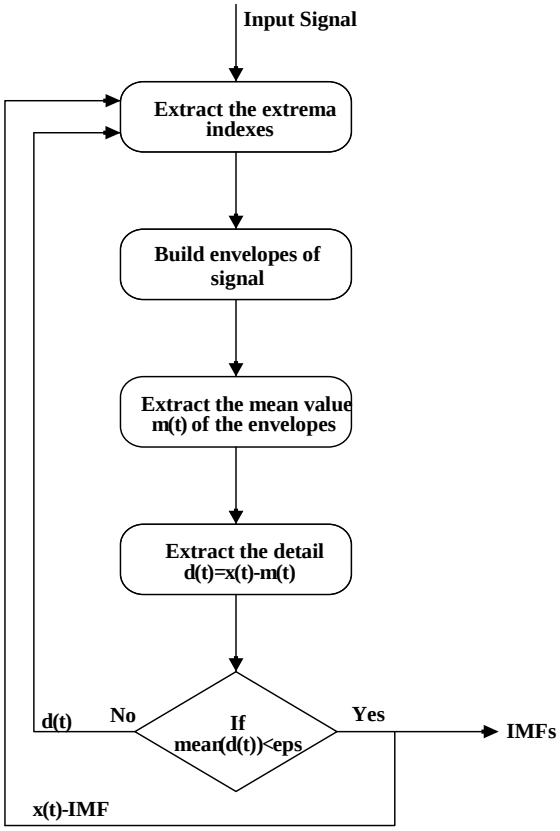

Figure 1. The EMD algorithm

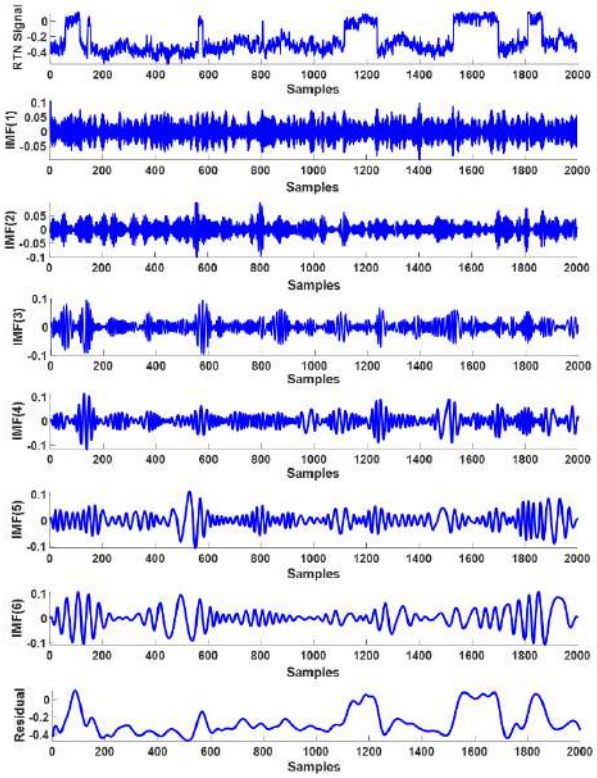

Figure 2. Employing EMD to an actual RTN in six levels

3. RESULTS

We considered two types of signals for our evaluation. Firstly, the actual signal which is extracted from an nMOSFET with Width = 0.16 μm and Length = 2 μm, which was biased by V_{GS}=2.2 V, in temperature of 50 °C based on the Measure-Stress-Measure (MSM) method and secondly, the artificial signal which is obtained from a stochastic defect modeling based on the Markov chain to simulate the RTN signal according to Grasser [44]. For the validation of our proposed methods, we applied our methods on the artificial and actual RTN signals.

For the EMD thresholding, six levels of IMFs were extracted and then the method is applied by using the Universal thresholding and soft removing. The Wavelet transform using the Haar function with six levels is used in accompany with the Universal thresholding in this method. For the weighted EMD method, we analyzed the different combinations of IMFs to see which IMF is more similar to the pure data and has higher SNR. Table 1 shows these results.

It is clear that the last IMFs are more related to the pure RTN. The results in Table 1 were obtained for noisy RTN with zero SNR. By analyzing, we understand that some IMFs have less similarity to the pure RTN and have less SNR when considered alone. However, if we add it to other IMFs, we obtain a higher SNR. Therefore, removing an IMF would not be correct and we should better consider a weight for each of the decomposed levels as below.

$$S = a*IMF_1 + b*IMF_2 + c*IMF_3 + d*IMF_4 + e*IMF_5 + f*IMF_6 + g*r \quad (3)$$

For the next stage, we employed an optimization method to reach a reasonable weights for 1000 RTN signals to reach the highest level of SNR. The input data were selected from diverse signal records with different levels of noise. The data were collected in an excel file and based on the genetic optimization algorithm with 0.8 mutation, the data were processed one by one in MATLAB software. In Table 2 the weight results are presented.

Finally, all of the mentioned methods are evaluated, and samples of this analysis have been shown for artificial and actual RTNs in Figure 3 and Figure 4 respectively.

For a better evaluation, three indicators, namely, SNR, Mean Square Error (MSE) and Percent Root mean square Difference (PRD) are calculated for the different methods.

$$\mathrm{SNR} = 10\log\left(\frac{\sum_{t=1}^{N} x^2(t)}{\sum_{t=1}^{N}\left(\tilde{x}(t)-x(t)\right)^2}\right) \quad (4)$$

$$\mathrm{MSE} = \frac{1}{N}\sum_{t=1}^{N}\left(\tilde{x}(t)-x(t)\right)^2 \quad (5)$$

TABLE 1. SNR for different combination of IMFs

IMFs	1	2	3	4	5	6	r	$\sum(1:5)$	$\sum(1:6)$	$\sum(2:r)$	$\sum(3:r)$	$\sum(4:r)$	$\sum(5:r)$	$\sum(6:r)$
SNR	1.3347	0.2310	1.6905	1.4088	2.5321	2.9312	3.7918	1.4381	1.9105	4.8923	4.2648	5.3968	5.2189	4.4283

TABLE 2. Weights for the different decomposed levels

Factor	a	b	c	d	e	f	g
Value	0.0291	0.0467	0.3277	0.2809	0.5297	0.7384	0.9271

$$PRD = 100\sqrt{\frac{\sum_{t=1}^{N}\left(\tilde{x}(t)-x(t)\right)^2}{\sum_{t=1}^{N}\left(x^2(t)\right)}} \quad (6)$$

where $x(t)$ is the clean signal and $\tilde{x}(t)$ is the de-noised signal.

The results of SNR, MSE and PRD have been reported for the mentioned method for the various SNRs in different RTNs in Tables 3, 4 and 5 respectively. The results were obtained by averaging on 50 simulations. By considering an indicator to evaluate the improvement rate of the methods, we can define

$$\text{Indicator}\,\% = \frac{\left|\sum_{i=1}^{N}\text{SNR}_{\text{EMD}} - \sum_{i=1}^{N}\text{SNR}_{\text{DWT}}\right|}{\sum_{i=1}^{N}\text{SNR}_{\text{DWT}}} * 100 \quad (7)$$

where tN is the number of the calculated SNRs. This indicator can be utilized as well for the MSE and PRD to evaluate the results.

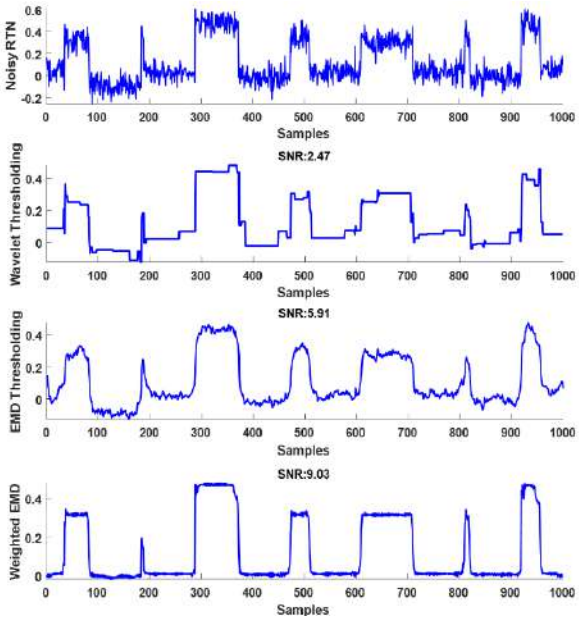

Figure 3. The results of the mentioned methods for Artificial RTN signal: a) Noisy RTN b)Wavelet thresholding c) EMD thresholding d) Weighted EMD

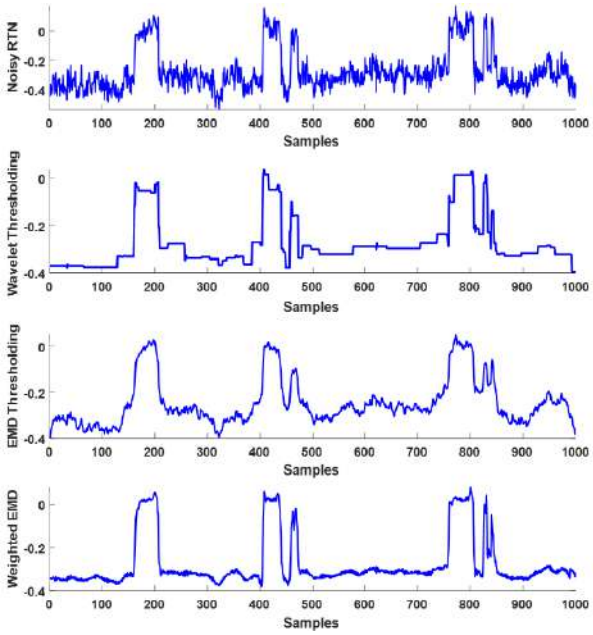

Figure 4. The results of the mentioned methods for Actual RTN signal a) Noisy RTN b)Wavelet thresholding c) EMD thresholding d) Weighted EMD

Summary of the results is shown in Figure 5. The results show 14%, 27% and 19% improvement in SNR, MSE and PRD for the EMD Thresholding, respectively. The results also show 54%, 61% and 39% improvement in SNR, MSE and PRD for the Weighted EMD, respectively.

In other side, we should consider the pros and cons of the proposed method.

TABLE 3. SNR results for the mentioned methods

Input SNR (db)	-5	0	-2.5	5	10
Method			**SNR**		
Wavelet Thresholding [39]	-2.141	2.3456	4.2704	6.8205	10.6842
EMD Thresholding	-1.034	3.0356	4.8875	7.2971	11.0345
Weighted EMD	1.629	5.1352	6.1970	8.3557	12.5159

TABLE 4. MSE results for the mentioned methods

Input SNR (db)	-5	0	-2.5	5	10
Method			**MSE**		
Wavelet Thresholding [39]	0.0281	0.0145	0.0092	0.0064	0.0043
EMD Thresholding	0.0188	0.0119	0.0073	0.0045	0.0032
Weighted EMD	0.0105	0.0061	0.0047	0.0026	0.0007

TABLE 5. PRD results for the mentioned methods

Input SNR (db)	-5	0	-2.5	5	10
Method			**PRD**		
Wavelet Thresholding [39]	98.21	70.44	56.75	42.11	36.08
EMD Thresholding	74.56	56.92	43.67	38.22	32.14
Weighted EMD	58.17	38.58	33.71	28.45	25.67

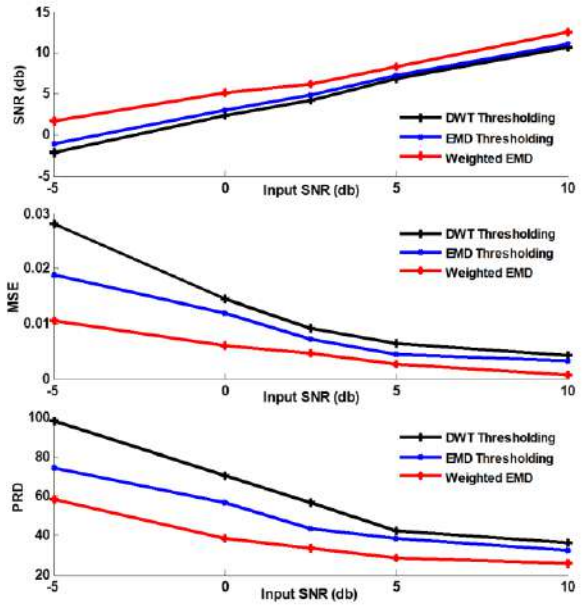

Figure 5. The results of SNR, MSE and PRD for three methods and in terms of different input SNRs

The computation time of the methods are evaluated in MATLAB by "tic toc" command and the average of the 50 runs of the algorithms is shown in Table 6. In order to obtain the computation time, we have employed a laptop with 2.2 GHz CPU clock frequency.

According to the results, Wavelet thresholding has the least computational time among the other methods, which is about 38 times faster than the weighted EMD method. However, the denoising approach is usually analyzed after recording the data as an off-line processing. Furthermore, the cost of computation in the range of around one second will not be a critical challenge and the denoising performance would be more significant than the computational time.

TABLE 6. Computation time of the mentioned methods

Method	Computation-Time (s)
Wavelet Thresholding [39]	0.023246599
EMD Thresholding	1.152699315
Weighted EMD	0.902714652

The bottle neck of the weighted EMD would be the process of finding the weights using diverse signals with different levels before denosing. It is noteworthy that the only bottle neck of this approach is finding appropriate weights.

3. 1. RTN Intensity Indicator Having de-noised the RTN signals, we can consider a criterion for finding out the energy level of RTNs to show the intensity of this phenomenon. In that regard, we can make use of the following equation.

$$I = \int_{t_0}^{t_1} s(t)dt \tag{8}$$

where I is the intensity, s(t) is the de-noised RTN signal and (t_0,t_1) is the desired interval. It is clear that de-noising would be necessary as sometimes noise might have a considerable intensity and it could potentially make an error.

This way, we can find out the quality and rate of the reliability for digital circuits. Therefore, one of the indicators to make comparison among the different circuits would be the intensity (I) of RTN and we can measure the circuits in diverse situations and capture RTNs to compare the reliability rate.

4. CONCLUSION

One of the most suitable analysis methods for RTNs as a non-stationary signal is EMD. In this paper, this tool and its application were introduced and a comparison among the existing methods was made. Firstly, we proposed the EMD thresholding method that could have a better result compared to the previous methods. Then, we analyzed the intrinsic modes for RTN and found the last modes are more similar to our desired data compared to the earlier modes. Therefore, we proposed to weight the modes in order to extract the pure RTN. The results show 14%, 27% and 19% improvement in SNR, MSE and PRD for the EMD Thresholding, respectively. Furthermore, the results also show 54%, 61% and 39% improvement in SNR, MSE and PRD for the weighted EMD, respectively.

5. ACKNOWLEDGEMENT

The authors would like to thank the Austrian Research Promotion Agency FFG, Institute for Microelectronics in TU-Wien and specially Dr. Tibor Grasser and Dr. Michael Waltl for their support in this research.

6. REFERENCES

1. Connelly, J. A., Low-Noise Electronic System Design, Guide Books, (1993), John Wiley & Sons, Inc.
2. Li, Z., Sui, N., and Wang, G., "Experimental study on vibration and noise of pure electric vehicle (PEV) drive system", International Conference on Electric Information and Control Engineering, ICEICE 2011 - Proceedings, (2011), 5914–5917. doi:10.1109/ICEICE.2011.5776874
3. Roshanian, J., Khaksari, H., Khoshnood, A. M., and Hasani, S. M., "Active Noise Cancellation using Online Wavelet Based Control System: Numerical and Experimental Study", ***International Journal of Engineering, Transactions A: Basics***, Vol. 30, No. 1, (2017), 120–126. doi:10.5829/idosi.ije.2017.30.01a.15
4. Grasser, T., Rott, K., Reisinger, H., Waltl, M., Franco, J., and Kaczer, B., "A unified perspective of RTN and BTI", ***IEEE International Reliability Physics Symposium Proceedings***, (2014), IEEE. doi:10.1109/IRPS.2014.6860643
5. Valinataj, M., "Reliability and Performance Evaluation of Fault-aware Routing Methods for Network-on-Chip Architectures", ***International Journal of Engineering, Transactions A: Basics***, Vol. 27, No. 4, (2014), 509–516. doi:10.5829/idosi.ije.2014.27.04a.01
6. Karatsori, T. A., Pastorek, M., Theodorou, C. G., Fadjie, A., Wichmann, N., Desplanque, L., Wallart, X., Bollaert, S., Dimitriadis, C. A., and Ghibaudo, G., "Static and low frequency noise characterization of ultra-thin body InAs MOSFETs", ***Solid-State Electronics***, Vol. 143, (2018), 56–61. doi:10.1016/j.sse.2017.12.001
7. Stampfer, B., Zhang, F., Illarionov, Y. Y., Knobloch, T., Wu, P., Waltl, M., Grill, A., Appenzeller, J., and Grasser, T., "Characterization of Single Defects in Ultrascaled MoS2 Field-Effect Transistors", ***ACS Nano***, Vol. 12, No. 6, (2018), 5368–5375. doi:10.1021/acsnano.8b00268
8. Waltl, M., Wagner, P. J., Reisinger, H., Rott, K., and Grasser, T., "Advanced data analysis algorithms for the time-dependent defect spectroscopy of NBTI", ***IEEE International Integrated Reliability Workshop Final Report***, (2012), 74–79, 74–79. doi:10.1109/IIRW.2012.6468924
9. Jech, M., Ullmann, B., Rzepa, G., Tyaginov, S., Grill, A., Waltl, M., Jabs, D., Jungemann, C., and Grasser, T., "Impact of Mixed Negative Bias Temperature Instability and Hot Carrier Stress on MOSFET Characteristics - Part II: Theory", ***IEEE Transactions on Electron Devices***, Vol. 66, No. 1, (2019), 241–248. doi:10.1109/TED.2018.2873421
10. Lai, Y., Li, H., Kim, D. K., Diroll, B. T., Murray, C. B., and Kagan, C. R., "Low-frequency (1/ f) noise in nanocrystal field-effect transistors", ***ACS Nano***, Vol. 8, No. 9, (2014), 9664–9672. doi:10.1021/nn504303b
11. Ullmann, B., Jech, M., Puschkarsky, K., Rott, G. A., Waltl, M., Illarionov, Y., Reisinger, H., and Grasser, T., "Impact of Mixed Negative Bias Temperature Instability and Hot Carrier Stress on MOSFET Characteristics - Part I: Experimental", ***IEEE Transactions on Electron Devices***, Vol. 66, No. 1, (2019), 232–240. doi:10.1109/TED.2018.2873419
12. Feng, W., Dou, C. M., Niwa, M., Yamada, K., and Ohmori, K., "Impact of random telegraph noise profiles on drain-current fluctuation during dynamic gate bias", ***IEEE Electron Device Letters***, Vol. 35, No. 1, (2014), 3–5. doi:10.1109/LED.2013.2288981
13. Matsumoto, T., Kobayashi, K., and Onodera, H., "Impact of random telegraph noise on CMOS logic delay uncertainty under low voltage operation", ***Technical Digest - International Electron Devices Meeting, IEDM***, (2012). doi:10.1109/IEDM.2012.6479104
14. Matsumoto, T., Kobayashi, K., and Onodera, H., "Impact of random telegraph noise on CMOS logic circuit reliability", Proceedings of the IEEE 2014 Custom Integrated Circuits Conference, CICC 2014, (2014), Institute of Electrical and Electronics Engineers Inc. doi:10.1109/CICC.2014.6945997
15. Compagnoni, C. M., Ghidotti, M., Lacaita, A. L., Spinelli, A. S., and Visconti, A., "Random telegraph noise effect on the programmed threshold-voltage distribution of flash memories", ***IEEE Electron Device Letters***, Vol. 30, No. 9, (2009), 984–986. doi:10.1109/LED.2009.2026658
16. Compagnoni, C. M., Spinelli, A. S., Beltrami, S., Bonanomi, M., and Visconti, A., "Cycling effect on the random telegraph noise instabilities of NOR and NAND flash arrays", ***IEEE Electron Device Letters***, Vol. 29, No. 8, (2008), 941–943. doi:10.1109/LED.2008.2000964
17. Veksler, D., Bersuker, G., Vandelli, L., Padovani, A., Larcher, L., Muraviev, A., Chakrabarti, B., Vogel, E., Gilmer, D. C., and Kirsch, P. D., "Random telegraph noise (RTN) in scaled RRAM devices", ***IEEE International Reliability Physics Symposium Proceedings***, (2013). doi:10.1109/IRPS.2013.6532101
18. Ling, Y. T., Wang, Z. W., Fang, Y. C., Kang, J., Wu, L. D., Yang, Y. C., Cai, Y. M., and Huang, R., "RTN impacts on RRAM-based Nonvolatile logic circuit", 2018 14th IEEE International Conference on Solid-State and Integrated Circuit Technology, ICSICT 2018 - Proceedings, (2018), Institute of Electrical and Electronics Engineers Inc. doi:10.1109/ICSICT.2018.8565665
19. Imamoto, T., Ma, Y., Muraguchi, M., and Endoh, T., "Low-frequency noise reduction in vertical MOSFETs having tunable threshold voltage fabricated with 60nm CMOS technology on 300mm wafer process", ***Japanese Journal of Applied Physics***, Vol. 54, No. 4, (2015). doi:10.7567/JJAP.54.04DC11
20. L. Forbes and D.A. Miller. Reduction of random telegraph signal (RTS) and 1/f noise in silicon MOS devices, circuits, and sensors. U.S. Patent 8,513,102, (2013).
21. Chen, X., Chen, S., Hu, Q., Zhang, S. L., Solomon, P., and Zhang, Z., "Device noise reduction for silicon nanowire field-effect-Transistor based sensors by using a schottky junction gate", ***ACS Sensors***, Vol. 4, No. 2, (2019), 427–433. doi:10.1021/acssensors.8b01394
22. Ioannidis, E. G., Leisenberger, F. P., and Enichlmair, H., "Low frequency noise investigation of n-MOSFET single cells for memory applications", ***Solid-State Electronics***, Vol. 151, (2019), 36–39. doi:10.1016/j.sse.2018.10.016
23. Pirro, L., Zimmerhackl, O., Zaka, A., Miiller-Meskamp, L., Nelluri, R., Hermann, T., Cortes-Mayol, I., Huschka, A., Otto, M., Nowak, E., Mittal, A., and Hoentschel, J., "RTN and LFN noise performance in advanced FDSOI technology", ***European Solid-State Device Research Conference***, Vols 2018-September, (2018), 254–257. doi:10.1109/ESSDERC.2018.8486917
24. Islam, A. K. M. M., Oka, M., and Onodera, H., "Measurement of temperature effect on random telegraph noise induced delay fluctuation", ***IEEE International Conference on Microelectronic Test Structures***, Vols 2018-March, (2018), 210–215, Institute of Electrical and Electronics Engineers Inc., 210–215. doi:10.1109/ICMTS.2018.8383801
25. Seo, Y., Woo, C., Lee, M., Kang, M., Jeon, J., and Shin, H., "Improving BSIM Flicker Noise Model", 2019 Electron Devices Technology and Manufacturing Conference, EDTM 2019,

(2019), 32–34. doi:10.1109/EDTM.2019.8731123

26. Kushwaha, P., Agarwal, H., Lin, Y. K., Dasgupta, A., Kao, M. Y., Lu, Y., Yue, Y., Chen, X., Wang, J., Sy, W., Yang, F., Chidambaram, P. R. C., Salahuddin, S., and Hu, C., "Characterization and Modeling of Flicker Noise in FinFETs at Advanced Technology Node", ***IEEE Electron Device Letters***, Vol. 40, No. 6, (2019), 985–988. doi:10.1109/LED.2019.2911614
27. Tanaka, C., Adachi, K., Nakayama, A., Iguchi, Y., and Yoshitomi, S., "Experimental extraction of body bias dependence of low frequency noise in sub-micron MOSFETs from subthreshold to moderate inversion regime", ***IEEE International Conference on Microelectronic Test Structures***, Vol. 2019, (2019), 162–165. doi:10.1109/ICMTS.2019.8730953
28. Gokcen, A., and Demir, M. A., "Nonstationary Low Frequency Noise in Switched MOSFET Circuits & Circuit Simulation", ***2***5th International Conference on Noise and Fluctuations (ICNF 2019), (2019).
29. Mohanty, A., Sutaria, K. B., Awano, H., Sato, T., and Cao, Y., "RTN in Scaled Transistors for On-Chip Random Seed Generation", ***IEEE Transactions on Very Large Scale Integration (VLSI) Systems***, Vol. 25, No. 8, (2017), 2248–2257. doi:10.1109/TVLSI.2017.2687762
30. Diaz-Fortuny, J., Martin-Martinez, J., Rodriguez, R., Nafria, M., Castro-Lopez, R., Roca, E., and Fernandez, F. V., "A noise and RTN-removal smart method for parameters extraction of CMOS aging compact models", 2018 Joint International EUROSOI Workshop and International Conference on Ultimate Integration on Silicon, EUROSOI-ULIS 2018, Vol. 2018, (2018), 1–4. doi:10.1109/ULIS.2018.8354740
31. Diaz-Fortuny, J., Martin-Martinez, J., Rodriguez, R., Castro-Lopez, R., Roca, E., Fernandez, F. V., and Nafria, M., "A smart noise- and RTN-removal method for parameter extraction of CMOS aging compact models", ***Solid-State Electronics***, Vol. 159, (2019), 99–105. doi:10.1016/j.sse.2019.03.045
32. Gao, L., Alibart, F., and Strukov, D. B., "Analog-input analog-weight dot-product operation with Ag/a-Si/Pt memristive devices", IEEE/IFIP International Conference on VLSI and System-on-Chip, VLSI-SoC, (2015), 88–93. doi:10.1109/VLSI-SoC.2012.7332082
33. Vaseghi, S. V., Advanced Digital Signal Processing and Noise Reduction, (2008) John Wiley & Sons.
34. Petrychuk, M., Zadorozhnyi, I., Kutovyi, Y., Karg, S., Riel, H., and Vitusevich, S., "Noise spectroscopy to study the 1D electron transport properties in InAs nanowires", ***Nanotechnology***, Vol. 30, No. 30, (2019), 305001. doi:10.1088/1361-6528/ab175e
35. Higashi, Y., Momo, N., Momose, H. S., Ohguro, T., and Matsuzawa, K., "Comprehensive understanding of random telegraph noise with", 2011 Symposium on VLSI Technology - Digest of Technical Papers, (2011), 200–201.
36. Tega, N., Miki, H., Yamaoka, M., Kume, H., Mine, T., Ishida, T., Mori, Y., Yamada, R., and Torii, K., "Impact of threshold voltage fluctuation due to random telegraph noise on scaled-down SRAM", ***IEEE International Reliability Physics Symposium Proceedings***, (2008), 541–546. doi:10.1109/RELPHY.2008.4558943
37. Du, L., Zhuang, Y., and Wu, Y., "1/fγ noise separated from white noise with wavelet denoising", ***Microelectronics Reliability***, Vol. 42, No. 2, (2002), 183–188. doi:10.1016/S0026-2714(01)00249-9
38. Principato, F., and Ferrante, G., "1 / f Noise decomposition in random telegraph signals using the wavelet transform", ***Physica A: Statistical Mechanics and Its Applications***, Vol. 380, Nos. 1–2, (2007), 75–97. doi:10.1016/j.physa.2007.02.111
39. Hendrickson, B., Widenhorn, R., and Blouke, M., "Using Wavelets to Remove Unwanted Noise from RTS Signals", ***Bulletin of the American Physical Society***, Vol. 62, No. 7, (2017).
40. Huang, N. E., "Hilbert-Huang transform and its applications", (Vol. 16), World Scientific, (2014).
41. Hari Krishna, E., Sivani, K., and Ashoka Reddy, K., "Empirical Mode Decomposition based Adaptive Filtering for Orthogonal Frequency Division Multiplexing Channel Estimation", ***International Journal of Engineering, Transactions A: Basics***, Vol. 30, No. 10, (2017), 1517–1525. doi:10.5829/ije.2017.30.10a.13
42. Seifolazadeh, A., and Edrissi, M., "determination of the rheological properties of hydroxyl terminated polybutadiene (htpb) mixtures with energetic materials and presenting empricial models", ***International Journal OF Engineering***, Vol. 18, No. 4, (2005), 413–420.
43. Wang, F., and Fang, L., "A Fault Diagnosis Method for Automaton based on Morphological Component Analysis and Ensemble Empirical Mode Decomposition", ***International Journal of Engineering, Transactions A: Basics***, Vol. 32, No. 7, (2019), 1010–1016. doi:10.5829/ije.2019.32.07a.14
44. Grasser, T., "Stochastic charge trapping in oxides: From random telegraph noise to bias temperature instabilities", ***Microelectronics Reliability***, Vol. 52, No. 1, (2012), 39–70, Pergamon, 39–70. doi:10.1016/j.microrel.2011.09.002

Persian Abstract

چکیده

نویز تلگرافی تصادفی (RTN) یکی از پدیده‌های تصادفی ناخواسته در قطعات الکترونیکی است که باعث نوسانات در مشخصه‌های مدار می‌گردد. یافتن و استخراج مشخصه های این سیگنال می‌تواند در بدست آوردن مدل مناسب به منظور جبران سازی و بهبود پارامترهای افزاره مؤثر باشد. این اندازه گیری معمولا همراه با مقادیری نویز و خطا همراه است و نیازمند روشی جهت بهبود نسبت سیگنال به نویز می باشد و بدست آوردن سیگنال RTN تمیز و دقیق از اهمیت زیادی برخوردار است. تجزیه مدهای ذاتی (EMD) به عنوان یک راهکار مناسب، کاملاً وفقی و وابسته به تغییرات سیگنال و بدون هیچگونه وابستگی به تابع خاص، می‌تواند در نظر گرفته شود. در این مقاله، روش‌های ارائه شده اخیر به همراه روش پیشنهادی برای سیگنال واقعی و مصنوعی RTN را جهت اطمینان از نتایج حاصل، ارزیابی کرده‌ایم. یافته‌های حاصل، دقت و عملکرد بالاتر روش وزن های بهینه شده را برای مقادیر نسبت سیگنال به نویزهای مختلف (SNR) و برای سیگنال‌های متنوع RTN تا ٥٤٪، ٦١٪ و ٣٩٪ به ترتیب بر اساس سه معیار SNR، MSE و PRD نشان می‌دهد. در پایان معیاری جهت بررسی و ارزیابی کیفیت و نرخ قابلیت اطمینان در مدارات دیجیتال معرفی گردیده است.

IJE TRANSACTIONS A: Basics Vol. 34, No. 01, (January 2021) 97-109

International Journal of Engineering

Journal Homepage: www.ije.ir

Novel Particle Swarm Optimization Algorithm Based on President Election: Applied to a Renewable Hybrid Power System Controller

M. Yahyazadeh*[a], M. S. Johari[a], S. H. HosseinNia[b]

[a] *Faculty of Engineering, Vali-e-Asr University of Rafsanjan, Iran*
[b] *Faculty 3mE, Departmant Precision and Microsystems Engineering, Mekelweg 2, 2628 CD DELFT, The Netherlands*

PAPER INFO

Paper history:
Received 25 August 2019
Received in revised form 30 August 2020
Accepted 03 September 2020

Keywords:
Hybrid Optimization Algorithm
Chaotic Function
Hybrid Power System
Particle Swarm Optimization Algorithm
President Election Algorithm

ABSTRACT

Particle swarm optimization has been a popular and common met heuristic algorithm from its genesis time. However, some problems such as premature convergence, weak exploration ability and great number of iterations have been accompanied with the nature of this algorithm. Therefore, in this paper we proposed a novel classification for particles to organize them in a different way. This new method which is inspired from president election is called President Election Particle Swarm Optimization (PEPSO). This algorithm is trying to choose useful particles and omit functionless ones at initial steps of algorithm besides considering the effects of all generated particles to get a directed and fast convergence. Some preparations are also done to escape from premature convergence. To validate the applicability of our proposed PEPSO, it is compared with the other met heuristic algorithm including GAPSO, Logistic PSO, Tent PSO, and PSO to estimate the parameters of the controller for a hybrid power system. Results verify that PEPSO has a better reaction in worst conditions in finding parameters of the controller.

***doi**: 10.5829/ije.2021.34.01a.12*

1. INTRODUCTION

Optimization makes an important role in many fields such as social, economic and engineering. It could help us to get more desirable results. These problems include examples such as generating an optimal duty cycle which varies with photovoltaic parameters in order to extract the maximum power, estimating the parameter of a new model of solar cells, returning the system voltages inside the permitted range (for voltage regulation of MV distribution systems), etc. As an inspiring, nature could help us to design the optimization system for complex computational problems [1-4]. Some evolutionary algorithm (which are the most successfully ones and inspired from the nature) are Genetic, Particle Swarm Optimization, Ant Colony Optimization, etc. Among the algorithms, PSO became one of the most popular methods as a solution to solve the optimization problems, due to its efficiency in complex optimization problems in various fields [5]. It can be stated that, the main advantages of the PSO algorithm are: simple concept, easy implementation, relative robustness to control parameters, and computational efficiency [6]. For the first time, PSO algorithm was introduced. In this algorithm, every particle has its own position and velocity. The particles position and velocity are updated according to each particle positions and velocity and the best particles positions and velocity in the group, to find the best solution [5]. However, besides its advantages, the algorithm has problems like getting trapped in local minima or weak convergence rate. Some efforts have been done to overcome these problems includes combining PSO with other algorithm like GA or using modified discrete algorithm of PSO [7-9]. In a study, if no achievement is resulted at the end of a certain number of steps, PSO algorithm is stopped and the final point is considered as the new beginning point. The process is repeated through repositioning until the criterion is

*Corresponding Author Institutional Email: *Yahyazadeh@vru.ac.ir* (M. Yahyazadeh)

Please cite this article as: M. Yahyazadeh, M. S. Johari, S. H. HosseinNia, Novel Particle Swarm Optimization Algorithm Based on President Election: Applied to a Renewable Hybrid Power System Controller, International Journal of Engineering, Transactions A: Basics Vol. 34, No. 01, (2021) 97-109

satisfied to decrease the locally capacity particles [10]. Particle Swarm Optimization – Grey Wolf Optimizer (PSO–GWO) method has been also used to acquire the optimal size of the different system components in order to minimize the total cost of fresh water production [11]. A modified variant, named Repository and Mutation based PSO (RMPSO) is proposed by Jana et al. [12]. In RMPSO variant, two extra repositories have been introduced and maintained. So, it is done for storing personal and global best solutions which has the same fitness values. When the dimension of the problem is scaled up, the performance of the proposed algorithm remains consistent in most of the cases in this method. In the other study, the suitability of the No Speeds and Coefficients Particle Swarm Optimization (NSC-PSO) method is investigated to solve reliability optimization problems [13]. It is done by approaching a set of test problems which comprises two known Redundancy Allocation Problem (RAP) case studies: Fault Tree optimization (FTO) and Event Tree Optimization (ETO). In another study it is suggested that the memory structure of canonical PSO is modified by introducing a multi-leader mechanism to overcome weak exploration ability and premature convergence of PSO [14]. Applying chaotic function besides a Gaussian distribution to give particles more opportunities to jump out of the local optima is also done to overcome these problems. The best advantage of chaotic sequence is their unpredictability, i.e., by their spread-spectrum characteristic, non-periodic, complex temporal behavior, and argotic properties [15]. In fact, incorporating a chaotic map for the random number generation instead of the random number generators (RNG), increases the efficiency of the Basic PSO algorithm besides introducing diversity in the solutions and is used as a compared algorithm in our paper. Therefore, using hybrid algorithm could help to combine the better characteristics of each one to achieve the best approach. For example, GAPSO has been used in constraint optimization problems [8].

According to what has expressed up to now, there are some problems with basic PSO and should be noticed to solved. Therefore, in this paper we propose a new classification for particles called president election to achieve the best solution in less iteration besides escaping from local minima. This work is done by a good and novel filtration on original particles to select the better ones for upper level of the algorithm. This new classification is introduced to give optimized particles to a kind of modified PSO algorithm to accelerate the process of election of proper particles besides avoiding weak convergence rate. In PEPSO, by an original refining, a proposed filtration is done at first. Center of gravity method is used to choose better particles at this step. In addition, by increasing the number of parties (final classifications), which is described in PEPSO algorithm, the chance to get trapped in local minima extremely reduces. So, a fast and directed convergence rate is achieved. On the other hand, because of giving best particles to the modified PSO, a better solution is achieved in less time. A modified PSO is a PSO which has been used particles from president election level and consequently avoiding functionless particles. To have a comprehensive comparison, we used a practical case i.e. hybrid power system with Fractional Order PID (FOPID) controller. The results are also shown better convergence of PEPSO in comparison with the other algorithms including GA-PSO, Logistic-PSO, Tent-PSO, and PSO.

The rest of the article is organized as follows: Section 2 describes the problem by explaining the basic PSO algorithm. The proposed method is also introduced in this section. The optimization description of the algorithm and mathematical analysis explained in section 3. Description of the hybrid power system, FOPID controller, objective function and error signal are represented in section 4. Results demonstrate and validate the effectiveness and robustness of the proposed method represented in Section 5. Sections 6 and 7 are devoted discussion and conclusions, respectively.

2. PROBLEM DESCRIPTION

To overcome problems with inspired algorithms such as Genetic or PSO, some efforts have been done in the literature [8, 11,12]. However, such systems lead to high complexity especially for multi-dimensional systems, which in turn as challenging issue, will demand to propose novel method to modify this methods. In addition, fast convergence and increasing reliability are important issues in improvement of PSO. To this respect, a new classification is proposed in this paper. All of the achievements are based on the application of hybrid power system.

2. 1. Basic PSO Algorithm PSO works with particles contains the solutions of a problem. Each particle has a position and a velocity. The evaluation is achieved by the objective function of the optimization problem. Particle position dimensions are the variables of the optimization problem. Each particle has two criterions. The criterions for updating are called *Pbest* and *Gbest* which are the best position of each particle position itself and the best position among all particles achieved, up to last iteration implemented, respectively. So, basic PSO method is based on moving the particle position to a better position to find the best solution according to the following equation:

$$v_{id}^{j+1} = z_{\max} v_{id}^{j} + b_1 \times Rnd_1 \times (p_{id}^{best,j} - p_{id}^{j}) + b_2 \times Rnd_2 \times (p_{swarm,d}^{best,j} - p_{id}^{j}), \quad (1)$$

$$p_{id}^{j+1} = p_{id}^{j} + v_{id}^{j+1}, \quad (2)$$

where b_1 and b_2 are positive constants and represent the acceleration coefficients, Rnd_1 and Rnd_2 are two random variables within [0, 1]. v_{id} is the velocity of individual i on dimension d. p_{id} is ith current position on dimension d, $p_{id}^{best,j}$ is the location of the best problem solution vector found by i, $p_{swarm,d}^{best,j}$ is the location of the best particle among all the particles in the population on dimension d in iteration j, and $z_{\max}$ is the inertia weight that warrants convergence of the PSO algorithm [1].

A maximum velocity ($v_{\max}$) for each modulus of the velocity vector of the particles is also defined to control excessive roaming of particles outside the user-defined search space. Whenever a v_{id} exceeds the defined limit, its velocity is set to $v_{\max}$.

There are some advantages with PSO algorithm and also there exist some disadvantages to work on such as: getting stuck in local optimum, population variety reduction, increasing its convergence speed problem and so on. Researchers have been trying to improve these problems with basic PSO. As an example, applying chaotic coefficient instead of random numbers is a method to improve the chance of optimal solution selection according to the following equation:

$$v_i^{j+1} = z_{\max} v_i^{j} + b_1 \times n_1 (p_i^{best,j} - p_i^{j}) + b_2 n_2 (p_{swarm}^{best,j} - x_i^{j}), \quad (3)$$

$$p_i^{j+1} = p_i^{j} + v_i^{j+1}, \quad (4)$$

where the random numbers (b_1 and b_2) is multiplied by chaotic numbers n_1 and n_2. As discussed, various approaches need an improvement. By using the new approach called PEPSO or President Election Particle Swarm Optimization, which is inspired from president election procedure, we are trying to make some improvement in iterations number in convergence to give better solution.

2. 2. President Election Algorithm Each legal age population has permission to vote their president in every country. The president is a person elected among the population. Every country consists of several provinces or states. In other classification, it consists of several parties (usually 2 parties in many countries). Every party follows its goals in every province or states. According to the fact that each candidate for president election should qualify to introduce for election and each party has at least a candidate for this vital election, an optimization algorithm with a suitable convergence could be introduced by using this model besides a modified PSO algorithm for giving it as a good direction for update. By a new classification inspired from president election, persons who are the agent of population of a country, vote to two or more candidate of parties for election to elect the best particle which denotes the president. Each person means one particle. By this novelty, a good refining is done on all particles. After giving the best particles to a modified PSO, a better solution in less time is achieved.

As shown in Figure 1, population of a country is generated at first. More population means more opportunity. Two left and right parties are marked with gray and red colors. The color of the rectangles shows the distinction between states or provinces. Finally, a person is selected to give a more optimal number. In here, by applying a filter to the whole population, about 50% of it has been removed. In this step, a center of gravity method doses the filtration. Each person´s value which has less than 50% of center of gravity´s value of the population is removed. A random distribution is applied to the remaining population, which we called legal age population in this paper, to distribute and locate at states. The number of states must be more than 2 to have at least two parties for a competition. A similar filtration like step 1 is done again for each state. Persons whose values are in the left part of the center of gravity are called left party and persons on the other side are right parties. The best person of each party in every state is one whose value is nearer to center of gravity. Parties are made by collecting best left and right party member of every state. We have 2 parties here at least. A modified PSO is applied to both parties. A modified PSO is used, because the initial particles of basic PSO is different from what has been researched in this paper. At last after finding the best particles (They are best candidates) of each party, the

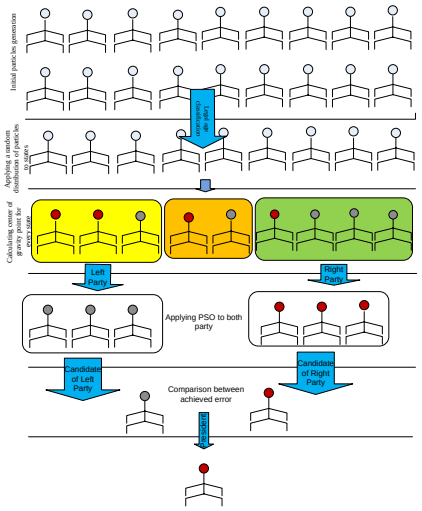

Figure 1. A graphic description of what has been done in PEPSO algorithm. Red persons represent right party members and the other color shows left party members

particle which called president here is elected by a comparison. Algorithm procedure is discussed in detail as following.

Algorithm Procedure:

Step 1. Initial particles generation:
A population is generated similar to PSO algorithm, as a greater number like a country. At this step, variables by its bounds and constants of the problem are determined. This variables and constants could be as follows:
Number of population, positions of particles and best particle, velocity of particles, number of provinces or states, variable number of the problem and its bound, maximum voted mans, inertia coefficient which has been reduced when be running the program, constants b_1 and b_2 which has been considered 1 here.

Step 2. Legal age classification from the whole population by center of gravity method is done in this step. About 50% of persons (particles) are rejected to vote according to their distance from the center of gravity point. Center of gravity point calculations are Equations (5) and (6):

Let us consider particles $p_i; i=1,...,n$, each with position m_i (value of fitness function here) that are located in space with coordinates $r_i; i=1,...,n$, the coordinate R (the position of the center of gravity mass point here) of the center of mass, which satisfy the following equation.

$$\sum_{i=1}^{n} m_i(r_i - R) = 0 \tag{5}$$

Solving the equation for R yields the following formula:

$$R = \frac{1}{M}\sum_{i=1}^{n} m_i r_i, \tag{6}$$

where M is sum of the masses (fitness function values) of all particles.

Step 3. Applying a random distribution of persons to states:

A number of states are given to program as a constant. More states give more accuracy. At first, 50% persons are distributed to number of states and called maximum voted mans (MVM). Then by a random distribution and a bound which is considered in range of $[1, MVM]$, $E=\{1,2,...,MVM\}$ the number of legal age population in each state is specified according to following equation:

$$N_P = rand_k\ (MVM);\ k=\{1,2,...,h\}, \tag{7}$$

where N_P^k is number of persons that could be vote in one state. The remaining persons are distributed to states in equal ratio as follows:

$$F_N = N_p^k + \frac{N_R}{N_S}, \tag{8}$$

where F_N, N_R, and N_S are final number of persons that could be vote, number of remaining persons and number of states, respectively.

$$F_{N_L} = MVM - \sum(F_{N-1}) \tag{9}$$

where F_{N_L} is final number of persons could vote in last remaining state and F_{N-1} is F_N except last remaining state.

Step 4. Similar to step 2 center of gravity points for every state is calculated.

Step 5. The state population is dividing into two parties. The right party is located in the right position of the center of gravity point and the left party in against position. By this classification in each state, the nearest persons of right and left position to the center of gravity point are selected as the agent of that party at that state according to Equations (10) and (11).

$$P_r < C_r < C_g, \tag{10}$$

where P_r, C_r, and C_g are fitness value of persons in right position of gravity point, fitness value of candidate of right party in each state and fitness value of center of gravity point, respectively.

$$C_g < C_l < P_l, \tag{11}$$

where C_g, C_l, and P_l are fitness value of center of gravity point , fitness value of candidate of left party in each state and fitness value of persons in left position of gravity point, respectively.

Step 6. At this step, in order to have better agents for candidates in each party, we need to modify PSO algorithm and then one is applied to each party agent to find the best candidates. A modified PSO algorithm is defined as follows:

The first and second step of using random number and locating them in the fitness function in basic PSO algorithm is omitted here. It is shown in Figure 2.

Step 7. Each candidate who has the minimum error and proper solution between two parties is elected as the president (best particle).

Step 8. End iteration criterion: If the minimum error is close to zero (or a constant which could be defined in the program) at first iteration the program will end and if not, the next iteration starts again. The end condition for best solution could be end iteration too.

3. OPTIMIZATION DESCRIPTION OF THE ALGORITHM

3. 1. Explanations and Flowcharts of the Algorithm By using this algorithm, an original refining on the whole population is done by considering

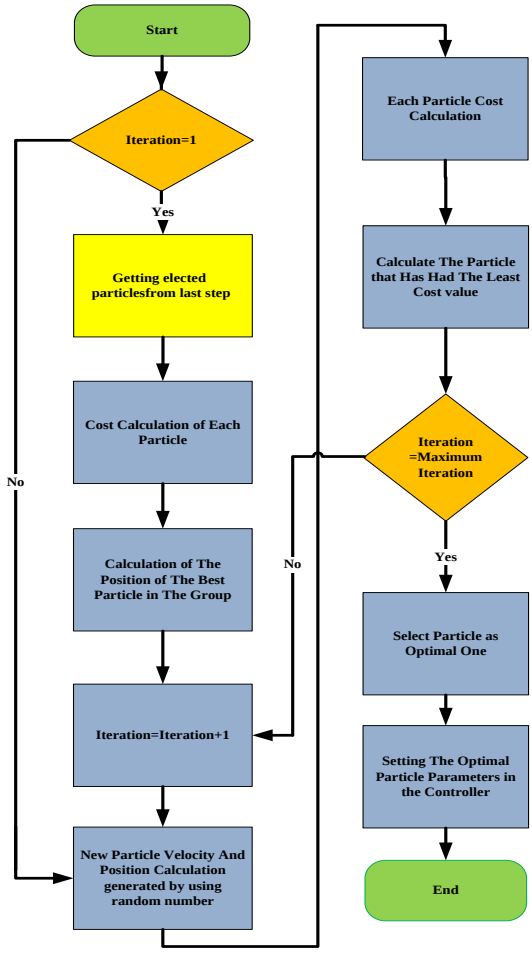

Figure 2. Diagram of modified PSO Algorithm. Yellow color block show the differences between modified and basic PSO algorithm. In PSO algorithm the particles are selected randomly. In here an elected particles are given to the next steps of basic PSO

the whole population experiences to elect the best particles for upper levels. In other word, all particles are acting as a deciding particle and vote the best particles to be candidates. The particles are called intelligent particles. This process which is done by center of gravity method in this new approach, create several search spaces which its number is in accordance with parties. So by locating the best particles to avoid functionless particles and using several search spaces in order to avoiding getting stuck in local minima or an early convergence, a better optimal point and faster convergence is achieved. Flowchart of modified PSO algorithm is shown in Figure 2 and PEPSO algorithm is shown in Figure 3. As illustrated in this figure, a considerable difference between basic PSO and this modified PSO is original refining which is done to achieve the optimal solution. This difference has been shown by yellow color box in this diagram. Since the limitation of calculation time for all particles position in basic PSO algorithm which limits the number of initial particles, the great number of population of PEPSO, with respect to a country population, is the other advantage of the approach that increases the opportunity of an optimal particle selection. In addition by the original refining, few number of best particles elect for applying into modified PSO algorithm. Due to kinds of properties of the new approach, less iteration for every test is needed. Here just to have a better comparison with the other models, the number of iterations is selected 50.

3. 2. Analysis In PSO algorithm, each particle has two criterions for updating called *Pbest* and *Gbest*. *Pbest* is the last best position of each particle position itself and *Gbest* is the best position among all particles achieved, up to last iteration implemented. All particles are updated in each iteration. As clear from its name, PEPSO are trying to choose the competent particle among all population. So by an inspiring from what has been done in president election procedure, it has been trying to find the best and proper solution for the problem (the best person as president for a country). A good

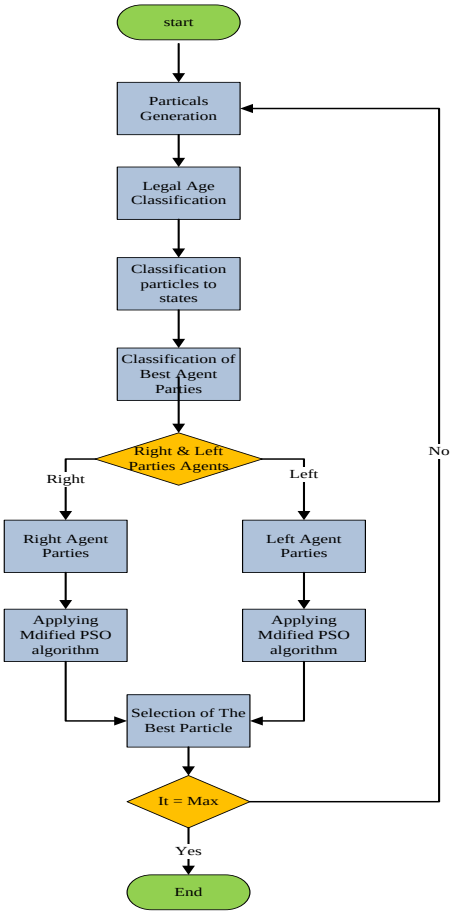

Figure 3. Diagram of President Election Particle Swarm Optimization Algorithm

selection is the final result. In PEPSO, with respect to the original refinery step which is done on primary particles (intelligence particles) the number of functionless particles has been decreasing effectively. Therefore the upper steps in PEPSO algorithm is a kind of competition and cooperation between better particles called candidate here. As shown in Figure 3, in fact PSO is a step of PEPSO algorithm which provides an iteration pass for more proper particles. The number of search space could also increased by an increase in number of parties. A multi-party mechanism (two-party here) enhances diversity of particles' search pattern to escape from local minima and increase weak convergence rate of basic PSO. So a greater chance space is created to find minima. Fast convergence by escaping from local minima is also achieved.

4. DESCRIPTION OF HYBRID POWER SYSTEM

4. 1. Hybrid Power System Due to the increasing use of fossil fuels and amount of required energy, a hybrid power system which benefited renewable energies will become a necessity. In a hybrid power system there are several energy components. Among them wind and solar renewable energy depends on weather conditions and the consuming load may at times exceed the production values. So the use of energy storage devices such as batteries, Ultra capacitors and flywheel along with other equipments at a power grid, seems to be necessary [16]. The dependence of each of the energies on seasonal weather and climate conditions and also using solar and wind energy together which are connected to a power grid, a decline in one generation could be compensated by the other. For these reasons, researchers have been interested in using the hybrid power system.

4. 2. Fractional-order Fuzzy Logic PID Controller Selecting a superior controller for this hybrid power system is also a question. Among the controllers, FOPID (Fractional Order PID) controller is getting more interested between researchers due to the design performance and flexibility of fractional calculus [17]. So according to a research on the controller of hybrid power system, a FOPID controller is selected [16]. The schematic of the hybrid power system using fractional-order fuzzy PID controller is illustrated in Figure 4.

A structure of Fractional-order fuzzy logic PID controller is shown in Figure 5. The controller parameters are $\{K_E, K_D\}$ and $\{K_{PI}, K_{PD}\}$ as an input and output scaling factor, respectively. Parameters $\{\lambda, \mu\}$ determine the fractional order differential-integrals respectively. The heart of system controller is formed of fuzzy membership functions as shown in Figure 6.

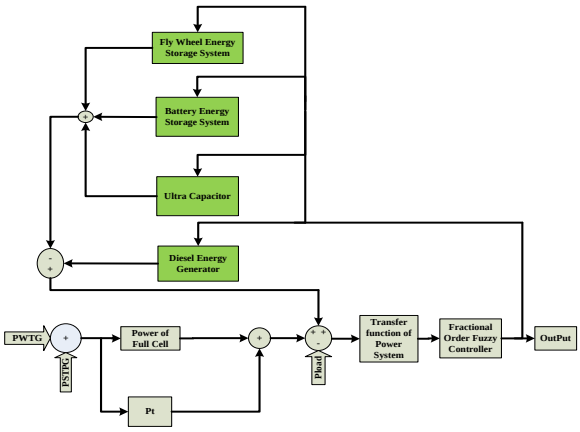

Figure 4. Schematic of hybrid power system with its components. This figure consists of 4 parts: inputs which includes power of the wind, sun and Diesel generator, saving parts which consists of battery, fly wheel and ultra capacitor, control system and output delivered to loads. Parts of input energy are given to fuel cell to run it [16]

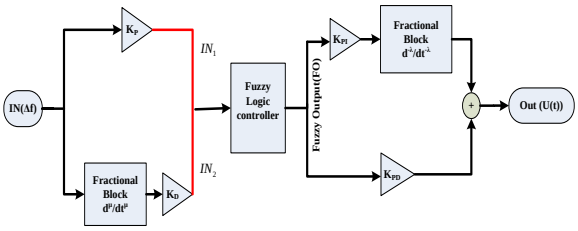

Figure 5. Schematic of the fractional-order fuzzy PID controller (The red line marks the use of a multiplexer which acts as a fuzzy switch to select one of the fuzzy inputs. Δf is input signal)

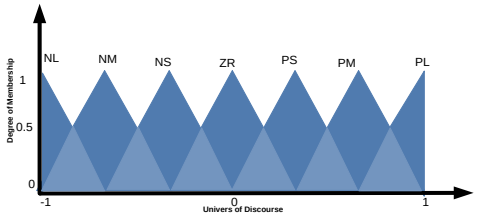

Figure 6. Membership functions of the fuzzy PID controller

Fuzzy linguistic variables NL, NM, NS, ZR, PS, PM and PL represent a negative large, negative medium, negative small, zero, positive small, positive medium and positive large respectively. The rule base considered for the fuzzy controller is depicted in Table 1 and the corresponding membership functions in Figure 6. The method used to calculate the output of the fuzzy controller has been chosen center of gravity defuzzification. Fuzzy system consists of two input variables and one output variable. In order to balance the computational complexity and at the same time having a

high degree of certainty, the number of membership functions of fuzzy control was elected seven [18]. For a simple analysis, Triangular membership functions have been used. Figure 7 shows plot surface of fuzzy controller for the control parameters.

4. 3. Objective Function and the Controller Parameters An integral performance index has been considered as the objective function for optimization in Equation (12). The simulation period is also considered $T_{Max} = 120\,s$. At this equation the weighted sum of squared frequency deviation and the deviation of controlled signal v from its expected steady state value v_{ss} are used as follows:

$$J = \int_0^{T_{sim}} \left(q_1 (\Delta f)^2 + q_2 (v - v_{ss})^2 \right) dt. \quad (12)$$

The first term represents the Integral of Squared Error (ISE) of grid frequency deviation and the second one is the Integral of Squared Deviation of Controller Output for the disturbance rejection task of the controller. The positive weight coefficients q_1 and q_2 determines the relative importance of the first and second term and considered $q_1 = q_2 = 1$ here.

4. 4. Error Signal For all the cases (generated and demand powers independent of controller structure and Δf , frequency deviation) there is a sudden jumps and stochastic component superimposed on a base value at arbitrary instants of time to show a sudden large change in the power at different time instants (40s and 80s in this case). So the steady state control signal v_{ss} changes after each switching in the load and generation and shows a proper performance of the control system. The ideal and achieved output control signal has been depicted in Figures 8 and 9, respectively [19]. Figure 8 shows the ideal signal which expected to be achieved by some controlled loads that have been given to the system. This steady state output signal which varies after each switching on generated power and consumption load is based on the following equation:

$$v_{ss}(t) = 0.81G(t) + 0.17G(t-40) + 1.12G(t-80) \quad (13)$$

$G(t)$ is a step function. Figure 9 shows the real signal which has been resulted by the controller. Error has been resulted by a subtraction between these two signals (ideal and achieved output by the controller) according to Equation (14). Figure 10 shows error signal after minimization by the controller.

$$E = I_o - A_o \quad (14)$$

which E , I_o , and A_o are error signal, ideal output of the controller, and achieved output of the controller, respectively.

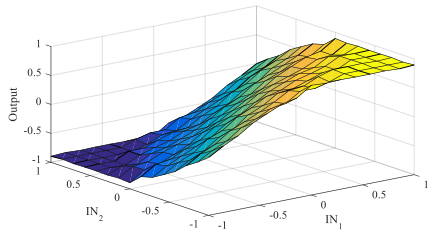

Figure 7. Fuzzy controller surface

TABLE 1. Rule base for error, fractional rate of error and FLC output

e ($d^u e/dt^u$)	NL	NS	NM	ZR	PS	PM	PL
PL	ZR	PS	PM	PL	PL	PL	PL
PM	NS	ZR	PS	PM	PL	PL	PL
PS	NM	NS	ZR	PS	PM	PL	PL
ZR	NL	NM	NS	ZR	PS	PM	PL
NM	NL	NL	NM	NS	ZR	PS	PM
NS	NL	NL	NL	NM	NS	ZR	PS
NL	NL	NL	NL	NL	NM	NS	ZR

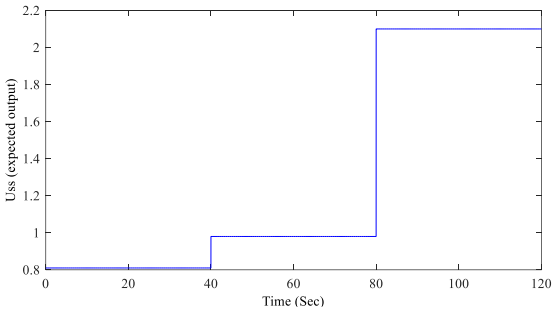

Figure 8. Desired output (reference signal). The ideal output of the controller which should varies by controlled loads that have been given to hybrid system

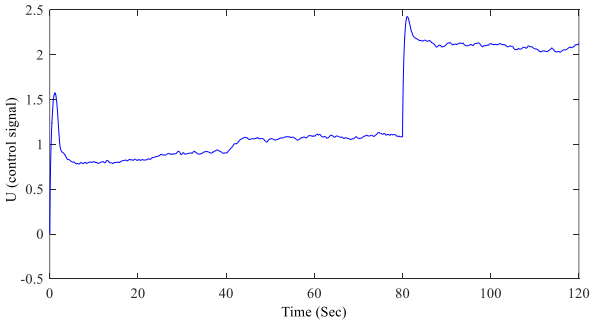

Figure 9. Real output of control signal produced by controller after optimization

5. RESULTS AND ALNALYSIS

In this section the application of PEPSO for parameter estimation of FOPID controller will be evaluated and corresponding results is presented. To validate the superior performance of PEPSO, a comparison is done with a couple of state of art algorithm including GAPSO [19], Logistic [15], Tent [17] and Basic PSO [17].

Parameters estimation and optimization of a FOPID controller of a hybrid power system have been used as the case studies of this research. These parameters estimation is done for all introduced above algorithm. The number of parameters decision (dimension in an optimization problem) is 6. For a fair comparison the number of initial particles is set to 100 for all algorithm all algorithm uses a same cost and fitness function. The compared algorithm has been run for 50 times. For all algorithm $b_1 = b_2 = 1$ and z is linearly decreased from 0.9 to 0.1. Used ranges for FOPID parameter controller of a hybrid power system have also been tabulated in Table 2.

Basic PSO was introduced by its equations. Logistic and Tent PSO are as follows:

Logistic chaotic function: This function is described by Equation (15). α and x_0 are equal to 0.4 and 0.2027, respectively.

$$x_{n+1} = \alpha x_n (1 - x_n), \tag{15}$$

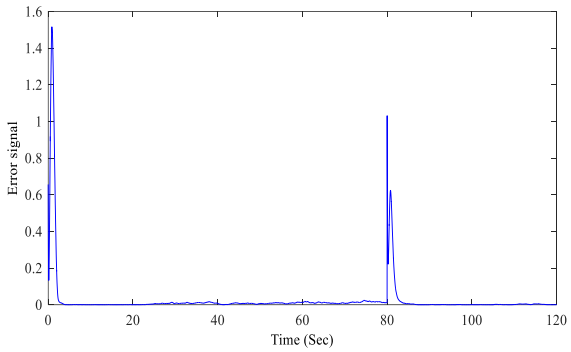

Figure 10. Output error signal after optimization

TABLE 2. Used ranges of FOPID parameters of the controller in a hybrid power system

Parameters	Lower bound	Upper bound
K_D	0	1
K_E	0	1
K_{PI}	0	40
K_{PD}	0	40
λ	0.01	0.99
μ	0.01	0.99

Tent chaotic function: This function is described by Equation (16) and resulted in a chaotic sequence in the interval $(0,1)$.

$$\begin{cases} \frac{1}{x_n} & x_n < 0.7 \\ \frac{1-x_n}{0.3} & Otherwise \end{cases}, \tag{16}$$

which are replaced in Equation (3). GAPSO algorithm is similar to Zhang et al. [19]. The objective function is also described in section (4).

Table 3 briefly compares the performance of different algorithm in control parameters. As clear from the table, the best optimum value is obtained by PEPSO. In addition since the aim of optimization system design is often to achieve an optimal value in an appropriate time, PEPSO shows an acceptable and optimum value in less iteration and time. The corresponding and desired error of Table 2 is obtained in minimum time by the PEPSO illustrated in Figure 11. As it is clear from the figure, PEPSO was achieved to a best optimal solution in all iterations. Also it was achieved the best solution in initial iterations, with a large difference in resulted value, than the others. Therefore, the result showed a better performance of this algorithm to the optimal value.

From the tabulated results in Table 4, the performance of PEPSO against the other algorithm could be observed. As it is clear from the table, PEPSO has the best performance in normal conditions of hybrid power system. The next is Logistic, Tent, PSO, and GAPSO. Equation (17) shows the calculation equation of performance ratio. In this equation k represents the algorithm. $Performance - Ratio_k$ is the performance difference percentage of the other algorithms in comparison with PEPSO.

$$Performance - Ratio_k = \frac{(ISE, ISDCO, J_{\min})_{PEPSO} - (ISE, ISDCO, J_{\min})_k}{(ISE, ISDCO, J_{\min})_{PEPSO}}, \quad k \in (GAPSO, LogisticPSO, TentPSO, PSO) \tag{17}$$

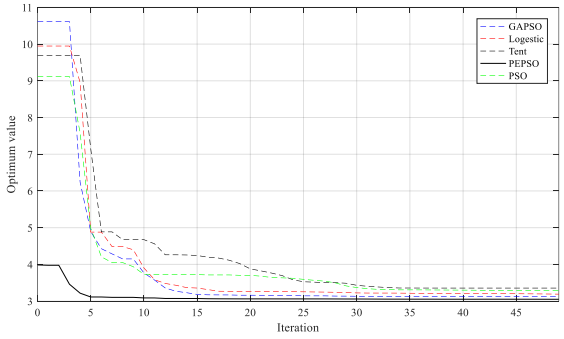

Figure 11. Optimum value achievement for 5 algorithms. This figure shows that PEPSO has been resulted to an optimal solution with significant difference than the other algorithms (GAPSO [19], Logistic [15], Tent [15], and PSO [16]) in initial iterations and the best solution

TABLE 3. Comparison of the results for 5 algorithms in the optimal solution and running time

Parameters	Lower bound	Upper bound	Parameters	Lower bound	Upper bound	Parameters	Lower bound	Upper bound
K_D	0	1	K_{PI}	0	40	λ	0.01	0.99
K_E	0	1	K_{PD}	0	40	μ	0.01	0.99

Algorithm Type	K_E	K_D	K_{PI}	K_{PD}	λ	μ	J_{min}	Iteration	Running Time
PSO	0.2312	0.0493	8.3117	3.3303	0.1372	-0.9900	3.2856	12	9016.898475
Chaotic PSO (Logistic map)	0.1906	0.1413	40.0000	14.2068	0.0100	-0.9900	3.1284	11	8935.013240
PEPSO	0.1993	0.0032	6.3430	3.2717	0.1762	-0.9713	3.0498	6	6987.518315
Chaotic PSO (Tent map)	0.2352	0.0959	12.0500	5.7828	0.0351	-0.9531	3.1895	11	7884.394049
GA-PSO	0.9023	0.0000	1.5141	0.8001	0.6528	-0.9900	3.3548	21	7018.75095

TABLE 4. Performance ratio of GAPSO, Logistic PSO, Tent PSO, PSO versus PEPSO

Algorithm	ISE	ISDCO	J	Performance decrease of ISE	Performance decrease of ISDCO	Performance decrease % of J
PEPSO	1.0195	2.0303	3.0498	-	-	-
GAPSO	1.2390	2.1158	3.3548	-21.5	-4.21	-10.00
Logistic PSO	1.0828	2.0456	3.1284	-5.84	-0.75	-2.58
Tent PSO	1.1039	2.0856	3.1895	-8.28	-2.72	-4.58
PSO	1.0258	2.2598	3.2856	-0.61	-11.30	-7.73

5. 1. Robustness Analysis In this section, we studied the parameter estimation of PEPSO and the other algorithms at the worst state of the hybrid power system. This is done by disconnecting FESS, BESS, DEG and check the controller operation. To test the robustness:

1. The corresponding performance error measures by each algorithm from nominal values against disconnecting different energy storage component of the hybrid power system are investigated in Table 5. The percentage change of ISE, ISDCO, J from its nominal value is calculated by each algorithm according to Equation (18). In this equation k represents the opened element and i represents the algorithm. $Performance-decreases_{k_i}$ shows the performance decrease of each algorithm in opened element states of the hybrid power system in comparison with normal conditions.

$$Performance-Decrease_{k_i} = \frac{(ISE, ISDCO, J_{\min})_{No\min al_i} - (ISE, ISDCO, J_{\min})_{k_i}}{(ISE, ISDCO, J_{\min})_{No\min al_i}}, \quad (18)$$

$$k \in (DEG, FESS, BESS), i \in (GAPSO, LogisticPSO, TentPSO, PSO)$$

Results represent the best performance with PEPSO. This also shows a better robustness investigation by PEPSO in comparison with the other algorithm. The next rank belongs to Tent for ISE, GAPSO for ISDCO and J. So from the viewpoint of the best achieved ISE, ISDCO and J, PEPSO outperforms all other optimization algorithm.

2. The parameter of the transfer function of the maximum power storing/producing component should be modified to consider the worst state. This component is UC [16]. So a 30 and 50% increase and decrease of the UC transfer function parameters are given to the system to test the robustness. Deviation and control signal in accordance with 30% and 50% variation in parameters of the UC transfer function are shown in Figures 12 and 13, respectively. The control signal representations which have been achieved by using different algorithms in Figures 12 and 13 show system behavior at the worst. Comparable results can be seen in Table 6. This table shows that by a 30% increase in gain and time constant, PEPSO has the best performance to achieve the minimum error. This algorithm also shows acceptable performance by a 50% increase in achieving to ISDCO (Integral of Squired Deviation of Controller Output) and total (ISDCO+ISE) error. Optimal performance of the algorithm by a 50% decrease in gain and time constant in ISE (Integral of Squired Error) is investigated from the table. In some cases, in which the other algorithm including Logistic and Tent PSO has better performance, the output error achieved by PEPSO is so close to the other optimization algorithms. Then, it could be deducted that the best total error reduction refers to PEPSO.

TABLE 5. Performance of each algorithm in error calculation when a part of the hybrid system (DEG, FESS, BESS) is opened

Algorithm	REMOVED Element	Performance measure			Performance Decrease		
		ISE	ISDCO	J	ISE	ISDCO	J
PEPSO	Nominal	1.0195	2.0303	3.0498	-	-	-
	DEG	1.1528	2.1052	3.2580	13.07	3.69	6.83
	FESS	1.2213	2.2451	3.4664	19.79	10.58	13.66
	BESS	1.1498	2.1100	3.2598	12.78	3.92	6.89
GAPSO	Nominal	1.2390	2.1158	3.3548	-	-	-
	DEG	1.4989	2.2211	3.7218	20.98	4.97	10.93
	FESS	1.6089	2.3485	3.9574	29.85	11.00	17.96
	BESS	1.5520	2.1992	3.7512	25.26	3.94	11.81
Logistic PSO	Nominal	1.0828	2.0456	3.1284	-	-	-
	DEG	1.2550	2.2675	3.5225	15.90	10.84	12.59
	FESS	1.3509	2.3715	3.6924	24.75	15.93	18.03
	BESS	1.2565	2.2783	3.5348	16.01	11.37	12.99
Tent PSO	Nominal	1.1039	2.0856	3.1895	-	-	-
	DEG	1.2695	2.3589	3.6284	15.00	13.1	13.76
	FESS	1.3307	2.4552	3.7859	20.54	17.72	18.70
	BESS	1.2915	2.3931	3.6846	16.99	14.74	15.52
PSO	Nominal	1.0258	2.2598	3.2856	-	-	-
	DEG	1.2633	2.4521	3.7154	23.15	8.51	13.08
	FESS	1.3000	2.5112	3.8112	26.73	11.12	16.00
	BESS	1.2397	2.4954	3.7351	20.85	10.42	13.68

TABLE 6. Robustness test against 30 and 50% variations of the transfer function UC parameters for different algorithm -optimal values is shown by green color

Algorithm	Parameter	30% decrease	50% decrease	30% increase	50% increase
PEPSO	ISE	1.5434	3.7594	1.0604	1.0237
	ISDCO	50.8295	243.3733	11.2241	23.9957
	Total	52.3729	247.1327	12.2845	25.0194
Chaotic PSO (Tent map)	ISE	1.5396	3.7713	1.2024	1.0265
	ISDCO	51.7938	243.365	11.3193	24.0153
	Total	53.3334	247.1363	12.5217	25.0318
Chaotic PSO (Logistic map)	ISE	1.5654	3.8831	1.4056	1.0242
	ISDCO	50.868	243.3124	11.6293	24.0210
	Total	52.4334	247.1955	13.0349	25.0452
GA-PSO	ISE	1.6989	3.7558	1.1153	1.2174
	ISDCO	52.0777	246.5943	11.2824	24.1207
	Total	53.7766	250.3501	12.3977	25.3381

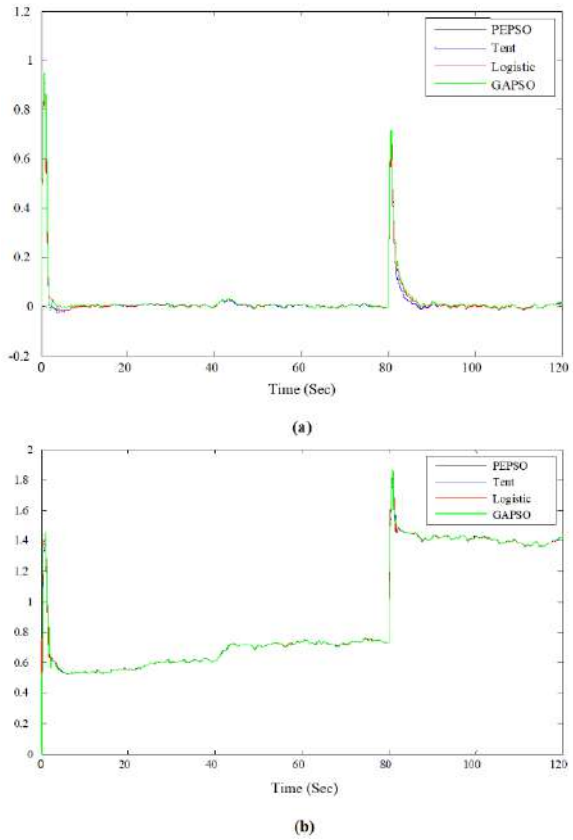

Figure 12. (a) Deviation signal generated by 30% increase in UC transfer function parameters. (b) Control signal generated by 30% increase in UC transfer function parameters

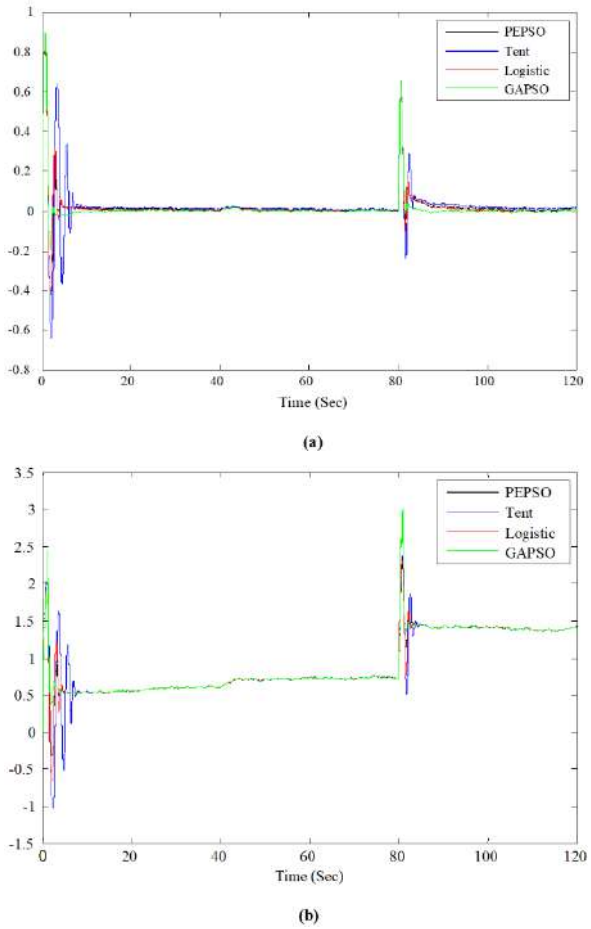

Figure 13. (a) Deviation signal generated by 50% increase in UC transfer function parameters. (b) Control signal generated by 50% increase in UC transfer function parameters

6. DISCUSSION

We used PEPSO algorithm in comparison with the other algorithm including GAPSO, Logistic PSO, Tent PSO, PSO. This is done to estimate the parameter of a FOPID controller to test the performance of PEPSO in a realistic example. Control system output and error are shown in Figures 8 and 9, respectively in section (4). PEPSO has achieved the optimal value in less iteration according to Figure 11. This is due to the refining step before applying particles to modified PSO algorithm. Robustness analysis has also been studied in section (5). This is done to show the best algorithm in parameters estimation of the controller in worst state. So, we are trying to improve convergence time by omitting functionless particles. This is done at a refinery step called President Election. But there are some challenges for every algorithm to execute. Giving intelligence to the particles for this algorithm is one of them. After researches and tests, center of gravity method had been chosen. But there may be existed another method for refinery step to improve this algorithm. Another challenge is President Election system which is different in every country. For this problem, the main common principle which exists in most countries has been selected. But every country principle could be test as an individual.

7. CONCLUSION

A new algorithm called PEPSO was proposed in this paper. It is inspired from president election procedure. After an introduction of how this algorithm works, performances of a variety of several heuristic algorithms including PSO, GAPSO, LOGISTIC PSO and TENT PSO on hybrid power systems, as a practical example, was discussed and compared with PEPSO. At first basic PSO was explained and then PEPSO introduced. After that fractional order fuzzy logic PID controller which was used as the heart of hybrid system was studied, objective function is the next part. Results was discussed and

studied at last. It has been observed that among the algorithms, PEPSO algorithm had a better convergence than the others. By using this proposed algorithm, the iterations significantly reduced which is the main feature of this algorithm. In this new approach, original refining particles on the whole population was performed. So by avoiding functionless particles and using several search spaces in order not to getting stuck in local minima and a faster convergence, a better optimal solution was resulted. To test the robustness, the parameter of the transfer function of the maximum power storing/producing component was studied. Results in this part have also shown a better performance of PEPSO among all used hybrid algorithms in this paper.

Some future works could be done to improve the algorithm or implementation on controller like using adaptive fuzzy optimal controller design by referring to fuzzy adaptive decentralized optimal control for strict feedback nonlinear large-scale systems, fuzzy adaptive output feedback optimal control design for strict-feedback nonlinear systems, and the other similar approaches. So, combining the other algorithms such as genetic with this proposed approach in optimization problem of the hybrid power systems is the testable that can be conducive for further improvements.

8. REFERENCES

1. Gao, H., Kwong, S., Yang, J., and Cao, J., "Particle swarm optimization based on intermediate disturbance strategy algorithm and its application in multi-threshold image segmentation", ***Information Sciences***, Vol. 250, (2013), 82-112. DOI: 10.1016/j.ins.2016.07.017.
2. Soufi, Y., Bechouat, M., and Kahla, S., "Fuzzy-PSO controller design for maximum powerpoint tracking in photovoltaic system", ***International Journal of Hydrogen Energy***, Vol. 42, No. 13, (2017), 8680-8688. DOI: 10.1016/j.ijhydene.2016.07.212.
3. Khanna, V., Das, B.K., Bisht, D., Vandana, and Singh, P.K., "A three diode model for industrial solar cells and estimation of solar cell parameters using PSO algorithm", ***Renewable Energy***, Vol. 78, (2019), 105-113. DOI: 10.1016/j.renene.2014.12.072.
4. Yahyazadeh, M. and Rezaeeye, H., "Optimal Placement and Sizing of Distributed Generation Using Wale Optimization Algorithm Considering Voltage Stability and Voltage Profile Improvement, Power Loss and Investment Cost Reducing", ***Iranian Journal of Science and Technology, Transactions of Electrical Engineering***, Vol. 44, (2020), 227-236. DOI: 10.1007/s40998-019-00224-4.
5. Gholami Dehbalaeea, M.R., Shaeisia, G.H., and Valizadeh M., "A Proposed Improved Hybrid Hill Climbing Algorithm with the Capability of Local Search for Solving the Nonlinear Economic Load Dispatch Problem", ***International Journal of Engineering, Transactions A: Basics***, Vol. 33, No. 4, (2020), 575-585. DOI: 10.5829/ije.2020.33.04a.09.
6. Park, J-B., Jeong, Y-W., Shin, J-R., and Lee, K.Y., "An Improved Particle Swarm Optimization for Nonconvex Economic Dispatch Problems", ***IEEE Transactions on Power Systems***, Vol. 25, NO., (2010), 156-166. DOI: 10.1109/TPWRS.2009.2030293.
7. Madoliat, R., Khanmirza, E., and Pourfard, A., "Application of PSO and Cultural Algorithms forTransient Analysis of Natural Gas Pipeline", ***Journal of Petroleum Science and Engineering***, Vol. 149, (2017), 504-514. DOI: 10.31590/ejosat.717872.
8. Akbarpour H., Karimi G., and Sadeghzadeh A., "Discrete Multi Objective Particle Swarm Optimization Algorithm for FPGA Placement (Research Note)", ***International Journal of Engineering, Transactions C: Aspects***, Vol. 28, No. 3, (2015), 410-418. DOI: 10.5829/idosi.ije.2015.28.03c.10.
9. Jam S., Shahbahrami A., and Ziyabari, S.H.S., "Parallel Implementation of Particle Swarm Optimization Variants Using Graphics Processing Unit Platform", ***International Journal of Engineering, Transactions A: Basics***, Vol. 30, No. 1, (2017), 48-56. DOI: 10.5829/idosi.ije.2017.30.01a.07.
10. Sancaktar I., Tuna B., and Ulutas M., "Inverse kinematics application on medical robot using adapted PSO method", ***Engineering Science and Technology, an International Journal,*** Vol. 21, No. 5, (2018), 1006-1010. DOI: 10.1016/j.jestch.2018.06.011.
11. Abdelshafy, A.M., Hassan, H., and Jurasz, J., "Optimal design of a grid-connected desalination plant powered by renewable energy resources using a hybrid PSO–GWO approach", ***Energy Conversion and Management***, Vol. 173, (2018), 331-347. DOI: 10.1016/j.enconman.2018.07.083.
12. Jana, B., Mitra, S., and Acharyaa, S., "Repository and Mutation based Particle Swarm Optimization (RMPSO): A new PSO variant applied to reconstruction of gene regulatory network", ***Applied Soft Computing***, Vol. 74, (2019), 330-355. DOI: 10.1016/j.asoc.2018.09.027.
13. Anescu, G. and Paul Ulmeanu, A., "A No Speeds and Coefficients PSO approach to reliability optimization problems", ***Computers & Industrial Engineering***, Vol. 120, (2018), 31-41. DOI: 10.1016/j.cie.2018.04.020.
14. Liu P. and Liu J., "Multi-leader PSO (MLPSO): A new PSO variant for solving global optimization problems", ***Applied Soft Computing***, Vol. 61, (2017), 256-263. DOI: 10.1016/j.asoc.2017.08.022.
15. Alatas B., Akin E., and Bedri Ozer A., "Chaos Embedded Particle Swarm Optimization Algorithms", ***Chaos Solitons and fractals***, Vol. 40, No. 4, (2009), 1715-1734. DOI: 10.1016/j.chaos.2007.09.063.
16. Pan I. and Das S., "Fractional Order Fuzzy Control of Hybrid Power System with Renewable Generation Using Chaotic PSO", ***ISA Transaction***, Vol. 62, (2016), 19-29. DOI: 10.1016/j.isatra.2015.03.003.
17. Monje, C.A., Chen, Y.Q., Vinagre, B.M., Xue, D., and Feliu, V., Fractional-order systems and controls: fundamental and applications, Advanced Industrial Control Series, Springer-Verlag, (2010).
18. Das, S., Pan, I., and Das, Sh., "Performance Comparison of Optimal Fractional order Hybrid Fuzzy PID Controllers For Handling Oscillatory Fractional Order Processes with Dead Time", ***ISA Transactions***, Vol. 52, No. 4, (2013), 550-566. DOI: 10.1016/j.isatra.2013.03.004.
19. Zhang, Q., Ogren, R.M., and Kong, S., "A comparative study of biodiesel engine performance optimization using enhanced hybrid PSO–GA and basic GA", ***Applied Energy***, Vol. 165, (2016), 676-684. DOI: 10.1016/j.apenergy.2015.12.044.

Persian Abstract

چکیده

بهینه سازی ازدحام ذرات از زمان پیدایش یک الگوریتم متداول محبوب و رایج بوده است. با این حال، برخی از مشکلات مانند همگرایی زودرس، توانایی کاوش ضعیف و تعداد تکرار زیاد با ماهیت این الگوریتم همراه بوده است. بنابراین، در این مقاله طبقه‌بندی جدیدی برای ذرات پیشنهاد می‌گردد تا با روشی بهتر بتوان آن‌ها را سازماندهی نمود. روش جدید که از انتخابات رئیس جمهوری الهام گرفته شده است، بهینه‌سازی ازدحام ذرات انتخابات رئیس جمهور (PEPSO) نامیده می‌شود. این الگوریتم سعی دارد ذرات مفید را انتخاب کرده و در مراحل اولیه الگوریتم، ذرات بدون عملکرد را حذف نماید و علاوه بر این، اثرات تمام ذرات تولید شده را برای دستیابی به یک همگرایی سریع در نظر می‌گیرد. برخی مقدمات نیز برای رهایی از همگرایی زودرس انجام می‌شود. بمنظور اعتبارسنجی کاربرد بهینه‌سازی ازدحام ذرات پیشنهادی، برای یافتن پارامترهای کنترل کننده برای یک سیستم قدرت ترکیبی، نتایج با الگوریتم‌های دیگر شامل GAPSO، Logistic PSO، Tent PSO و PSO مقایسه می‌شود. نتایج نشان می‌دهند که PEPSO حتی در بدترین شرایط در یافتن پارامترهای کنترل‌کننده واکنش و دقت بهتری دارد.

International Journal of Engineering

Journal Homepage: www.ije.ir

Effect of Tail Capacitor on Phase Noise in LC Cross-connected Oscillators: An Analytical Investigation

E. Ebrahimi, M. Mos'hafi, H. Firouzkouhi*

Integrated Circuits Design Laboratory, Faculty of Electrical and Robotics Engineering, Shahrood University of Technology, Shahrood, Iran

P A P E R I N F O

Paper history:
Received 24 May 2020
Received in revised form 05 November 2020
Accepted 21 November 2020

Keywords:
CMOS Cross-coupled Oscillator
Impulse-Sensitivity-Function
LC Tank
Phase Noise
Noise Filtering

A B S T R A C T

This paper investigates the effect of tail capacitance on phase noise of an LC-VCO (LC voltage-controlled-oscillator). First, the analytical relations of the phase noise for different values of tail capacitor (C_T) are derived and then for verifying them, simulation and calculated results are compared. For simplicity, three scenarios such as small, medium and large values of C_T are considered. In a case study an LC-VCO is designed in a standard 0.18µm CMOS technology, and simulation and numerical results have been presented for different values of C_T. In this case study, numerical analysis shows that for C_T =200fF (medium C_T) and C_T =10pF (large C_T), the phase noise at 1MHz offset from the 5.2GHz is -96dBc/Hz and -118dBc/Hz, respectively. According to the results, the ISF (Impulse sensitivity function) is improved by increasing the amount of C_T. Numerical values also demonstrate that excessive increase of C_T has no effect on the phase noise. While choosing bigger C_T can effectively reduce the noise contribution of the tail by bypassing the noise of tail transistor, but low impedance path generated by C_T may degrade the phase noise by reducing tank quality factor.

doi: *10.5829/ije.2021.34.01a.13*

1. INTRODUCTION

Oscillators are one of the important blocks in many applications such as RF electronics and digital systems. Since the oscillators have a non-linear behavior, it is very hard to model and analyze them. One of the most important parameters in oscillators is phase noise. The noise injected into the circuit by active and passive elements can show itself as a phase (frequency) perturbation in the desired signal which is called phase noise (or Jitter). Phase noise is one of the key parameters to determine the spectral purity of a signal generated by an oscillator. Depicted in Figure 1(a), single sideband (SSB) phase noise is defined as the ratio of the spectral power density measured at an offset frequency from the carrier (in 1Hz bandwidth) to the total power of the carrier signal and is stated as dBc/Hz. New communication circuits need low phase noise oscillators to satisfy the strict requirement of the modern communication standards. Among different type of oscillators [1], LC-VCOs attract many attentions due to their superior phase noise performance, reliable startup and ability for integration above standard CMOS technologies.

So far, several models for the prediction of phase noise were presented. Among these models, the most well-known phase noise model is Leeson's equation [2] in which the noise behavior of an oscillator is assumed linear-time-invariant (LTI). As reported in [2, 3] the verified Leeson's phase noise equation at offset frequency $\Delta\omega$ from the oscillation frequency ω_0, is expressed as Equation (1).

$$L\{\Delta\omega\} = 10\times\log\left\{\frac{2FkT}{P_s}\times\left[\left(1+\frac{\omega_0}{2Q_L\Delta\omega}\right)^2\right]\times\left(1+\frac{\Delta\omega_{1/f^3}}{|\Delta\omega|}\right)\right\} \quad (1)$$

in which k, T, P_s and Q_L are Boltzmann constant, absolute temperature, signal power and quality factor of the inductor respectively. $\Delta\omega_{1/f^3}$ is also the corner frequency and F denotes an experimental noise factor parameter. According to Figure 1(b) and (1), the plot can be divided into three regions. First region where $\Delta\omega >> \omega/2Q$ has a

*Corresponding Author Email: *Hossein.firouzkouhi@gmail.com* (H. Firouzkouhi)

Please cite this article as: E. Ebrahimi, M. Mos'hafi, H. Firouzkouhi, Effect of Tail Capacitor on Phase Noise in LC Cross-connected Oscillators: An Analytical Investigation, International Journal of Engineering, Transactions A: Basics, Vol. 34, No. 1, (2021) 110-119

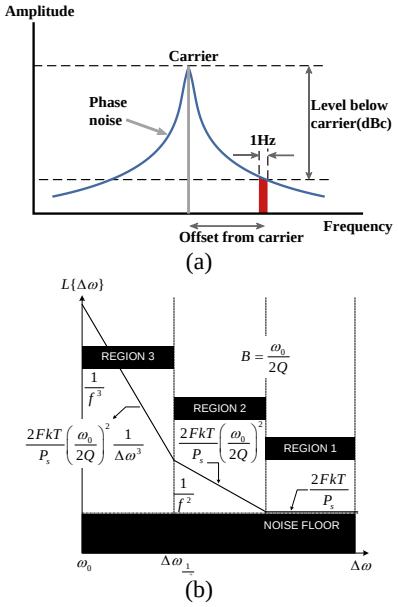

Figure 1. (a) Output spectrum of a practical oscillator and (b) different regions of phase noise vs frequency offset

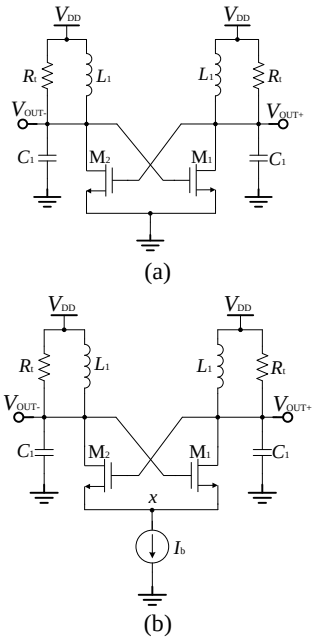

Figure 2. LC-tank oscillator (a) without current source and (b) with tail current source

flat profile and is dominated by the thermal noise. In regions two and three ($\Delta\omega << \omega / 2Q$) the white thermal noise and flicker noise make the phase noise with the slope of $1/\Delta\omega^2$ and $1/\Delta\omega^3$, respectively [4].

Alper Demir's model is one of the complex and accurate phase noise model (but almost without enough circuit intuition) [5]. In addition, the Demir's model can predict cyclostationary noise and also can present a fast simulation CADs [4].

As explained By Hajimiri et al. [3], in their phase noise model introduces a general theory of the phase noise for different kind of voltage-controlled oscillators (VCO) [4]. This model has a lower complexity with enough circuit intuition and can explain up and down conversion of noise in the close frequencies to the carrier. Another advantage of this model is that it introduces impulse-sensitivity-function (ISF) concept to consider the linear-time-variance (LTV) and cyclostationary behavior of noise in oscillators. The ISF is calculated by injecting an impulse current as the noise source of the device and measuring the phase shift (zero crossing) at the output voltage of the oscillator [6].

One of the oscillators which has the best performance in terms of phase noise amongst all CMOS VCOs is cross-connected LC-tank oscillator depicted in Figure 2 [3]. Figures 2(a) and 2(b) show two possible configurations of a cross-connected oscillator, i.e. without and with tail current source [7]. Using tail transistor is one of the ideas in the design of the cross-coupled LC-tank VCOs which was ignored in past decades. Later, it was considered more in [6, 8, 9] and discovered that it plays a prominent role in phase noise of the LC-tank VCO.

$$V_{OUT\pm} = \frac{4}{\pi} \times (R_t I_b) \quad (2)$$

While eliminating tail transistor in Figure 2(a) results in higher voltage headroom, using tail transistor in Figure 2(b) is preferred due to several reasons: first it creates a high impedance in series to the cross-connected switching transistors, reduces the loading of LC resonator and prohibits tank quality factor degradation [9]. Second, it defines the bias current I_b of the cross-connected pair and the output voltage of the oscillator as Equation (2) that results in more controllable and robust design against supply variations [6, 7, 10]. (R_t is loss of the LC-tank and I_b is the tail bias current.)

On the other hand, tail transistor can impose extra noise to the VCO and degrade the phase noise. Since the tail node (x) is a common mode node, the even harmonics especially second harmonic are usually dominant in that node. The switching cross-coupled pair, which acts as a single-balance mixer, up/down converts low frequency noise into two correlated sidebands around the fundamental frequency. It should be noted that the low-frequency noise in tail current source does not affect the phase noise directly. In fact, noise frequencies around the second harmonic is down converted close to the oscillation frequency [7, 10, 11]. It should be considered that because the level of the third and higher order harmonics is low and can be filtered by the LC-tank resonator, so the effect of the second order harmonic is dominant and significant in phase noise [6].

Filtering technique is one of the best options for eliminating the unwanted (second) harmonics caused by

tail transistor and improving the phase noise of the oscillators [7]. Therefore, several techniques for attenuating the second harmonic in LC-tank oscillators have been proposed [7–9, 12–14], but the preferred technique is usually putting a capacitor in parallel to the tail transistor to bypass the second harmonic noise to ground. The tail capacitor acts as follows: (a) it attenuates the high-frequency noise components at tail node *x*, (b) prevents the up-conversion of the low-frequency noise of tail transistor into phase noise [9], and (c) reduces voltage variation at tail node and decreases the channel length modulation [9].

While using tail in Figure 2(b) produces a high impedance path, big shunt capacitor (C_T) bypasses it and results in loading the LC tank with lower impedance. In other words, LC tank is loaded through switching transistors by a low impedance and its quality factor is degraded. So, although a shunt capacitor to the tail node results in lower harmonic distortion in the output of the oscillator, it may degrade the quality factor of the LC-tank and accordingly the phase noise caused by switching transistors [6, 9]. In next section, we will conclude that the effect of harmonics filtering by C_T is more dominant than degradation of the quality factor on the phase noise.

It is worth mentioning as reported in literature [6, 9] the effect of capacitive noise filtering on phase noise is only investigated by simulation but no analysis is presented. Further, Andreani et al. [15] used a closed-form symbolic formula for phase noise of cross-connected oscillators in the case of negligible C_T is obtained by using phase noise relation in (3) which was introduced by Hajimiri [6] and others [15].

$$L\{\Delta\omega\} = 10 \times \log_{10}\left(\sum \frac{\Gamma^2_{rms} \times \overline{i_n^2}/\Delta f}{2 \times q^2_{\max} \times \Delta\omega^2}\right) \quad (3)$$

where $\overline{i_n^2}/\Delta f$ and Γ_{rms} represent the power spectral density of the current noise source and the root-mean-square of the ISF respectively. The maximum charge at output capacitor is denoted by q_{max}. By neglecting C_T (i.e. very small tail capacitances), a phase noise closed-formula obtained from literature [6, 15] as follows:

$$L(\Delta\omega) = 10 \times \log\left[\frac{k_B T}{N^2 C^2 A^2 \Delta\omega^2 R_t} \times \left(\gamma + 1 + \frac{\eta[\Phi]}{N} \gamma g_m R_t\right)\right] \quad (4)$$

in which K_B, g_m, A and C are, respectively, the Boltzmann constant, the transconductance of each transistor, the amplitude of output voltage and total capacitance of LC tank. $\eta[\Phi]$ represents the tail current phase noise coefficient [16], N=1 for single-ended and N=2 for differential oscillators. Apparently, C_T and its effect are not presented in (4).

Recently, Razavi [16] has been presented an intuitive but very instructive discussion for the effect of tail capacitance on oscillator phase noise. It was explained that the tail capacitance bypasses the second harmonics of tail node, produces a doublet around each zero-crossing, results in up-conversion of flicker noise of cross-connected transistors and also shunts the noise of tail transistor (at $2\omega_0$) to ground.

On the other hand, along with different phase noise analyses, several researches were also devoted to the phase noise reduction of LC oscillators and different techniques have been introduced in literature. Since zero crossing points are strongly vulnerable to the noise, in literature [17] a phase noise reduction technique is presented by pushing high closed-loop gain to the non-zero-crossing points of the outputs. In order to reduce the close-in phase noise caused by the flicker noise of tail transistor, a resistive feedback is used in literature [18] and the flicker noise of the tail transistor has been suppressed. However, such a diode-connected tail transistor reduces the output impedance of tail and may degrade the quality factor of the tank. Current-switching as well as capacitive-degeneration techniques are utilized simultaneously to reduce the flicker and thermal noise of tail and cross-connected transistors [19].

In this paper the effect of different values of tail capacitor on total phase noise is analytically studied and compared with simulation results. The rest of the paper is organized as follows: the phase noise analysis in a cross-connected VCO for three scenarios of C_T are described in Section 2 and a closed-formula for each ISF is presented. Section 3 compares simulation results with numerical values obtained by derivations. Finally, conclusions are given in Section 4.

2. PHASE NOISE ANALYSIS FOR SMALL, MEDIUM AND LARGE VALUES OF TAIL CAPACITANCES

In the LC-tank oscillator shown in Figure 3(a), the differential cross-connected transistors make a negative transconductance that can eliminate the loss of the LC tank [6, 8, 9]. For an LC-tank oscillator with arbitrary phase of sinusoidal output, the output voltage can be described by Equation (5):

$$\begin{aligned} V_{OUT+}(\varphi) &= A_{TANK} \times \sin(\varphi) \\ V_{OUT-}(\varphi) &= -A_{TANK} \times \sin(\varphi) \end{aligned} \quad (5)$$

Denoting DC bias current of tail transistor by $2I_B$, the current of M_1 and M_2, and the total current of them can be written as Equations (6), (7) and (8), respectively.

$$I_1(\varphi) = \frac{\beta}{2}(A_{TANK} \times \sin(\varphi) + V_S(\varphi))^2 \quad (6)$$

$$I_2(\varphi) = \frac{\beta}{2}(-A_{TANK} \times \sin(\varphi) + V_S(\varphi))^2 \quad (7)$$

$$2I_B = I_1(\varphi) + I_2(\varphi) \quad (8)$$

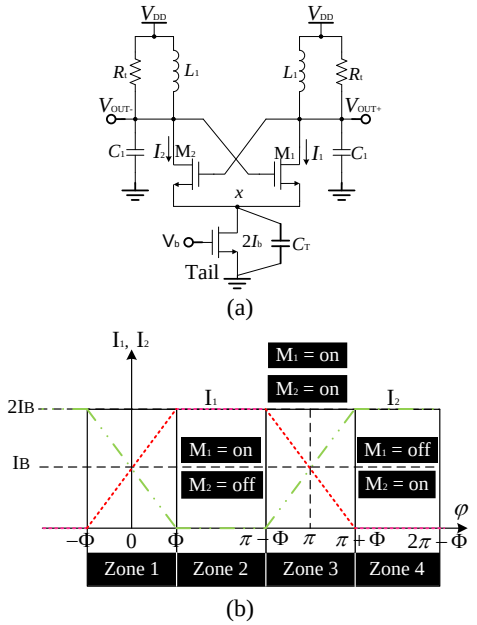

Figure 3. (a) Cross-connected LC-tank oscillator with C_T, and (b) ideal current of transistor versus φ

where $\beta = \mu C_{ox}\frac{w}{l}$, and $V_S(\varphi)$ is given by Equation (9).

$$V_S(\varphi) = \sqrt{\frac{2I_B}{\beta} - A^2_{Tank}\sin^2(\varphi)} \tag{9}$$

The current of each cross-connected transistor (i.e. I_1 and I_2) is depicted in Figure 3(b) for one period in which 2Φ is the conduction angle. By substituting Equation (9) into Equation (7) and setting the equation to zero, the half conduction angle Φ is obtained as Equation (10).

$$\Phi = \arcsin\sqrt{\frac{I_B}{\beta \times A^2_{TANK}}} \tag{10}$$

Considering (6), (7) and (9), the transconductance of M_1 and M_2 can be given by Equations (11) and (12).

$$g_{m1}(\varphi) = \beta A(\sin(\varphi) + \sqrt{2\sin^2(\Phi) - \sin^2(\varphi)}) \tag{11}$$

$$g_{m2}(\varphi) = \beta A(-\sin(\varphi) + \sqrt{2\sin^2(\Phi) - \sin^2(\varphi)}) \tag{12}$$

According to Figure 3(b) the cross-connected transistors operate in four different zones during each period. Due to switching of M_1 and M_2 the current of each transistor is usually supposed as a square waveform shown in Figure 3(b) (though the LC tank operates as a narrowband filter and generates sinusoidal output voltages). As discussed earlier, in order to reduce the noise of tail transistor, a capacitor C_T is placed between node *x* and ground. In this section, we will discuss about the effect of tail capacitive filtering by derivation of the ISF for three scenarios of C_T, *i.e. very small, medium and big* C_T.

The ISF of tank resistance R_t at nodes V_{OUT+} and V_{OUT-} (denoted by $\Gamma_{Rt,+}$, $\Gamma_{Rt,-}$) is independent of tail capacitance and has been derived Andreani and Wang [20] as Equation (13).

$$\Gamma_{Rt,+}(\varphi) = \frac{\cos(\varphi)}{N} \quad , \quad \Gamma_{Rt,-}(\varphi) = -\frac{\cos(\varphi)}{N} \tag{13}$$

2.1. Derivation of ISF When CT Is Medium In prior works, the ISF of oscillator has been calculated with the assumption of negligible C_T. In the case of non-negligible C_T, the charge of C_T cannot be discharged completely during each period. In order to model it, we define a factor α as the ratio of discharged ΔQ_d to the total charge ΔQ of C_T. The amount of charge for C_T during a period (while discharging through transistors $M_{1,2}$) is obtained by Equation (14).

$$Q_{C_T}(t) = \Delta Q \times e^{-\frac{t}{\tau}} \tag{14}$$

where τ is the time constant of tail node *x* ($\tau = C_T/g_{m1,2}$). The charge variation (ΔQ_d) of node *x* can be calculated by Equation (15).

$$\Delta Q_d = \Delta Q - Q_{C_T} = \Delta Q(1 - e^{-\frac{t}{\tau}}) \tag{15}$$

So, the factor α is obtained as follows:

$$\alpha = \frac{\Delta Q_d}{\Delta Q} = (1 - e^{-\frac{t}{\tau}}) \tag{16}$$

2. 1. 1. Calculation of Γ_{ids}

2. 1. 1. 1. Zone 2 ($\Phi < \varphi < \pi - \Phi$) In this zone M_1 is on and M_2 is off. As shown in Figure 4(a), applying $\overline{i^2_{ds1,n}}$ as an impulse current of area ΔQ charges C_1 and C_T by ΔQ and $-\Delta Q$, respectively. If we assume that C_T is not so small, the time constant of node *x* is comparable with period of oscillation and as a result C_T is not fully discharged as shown in Figure 4(a). If only $\Delta Q_d = -\alpha.\Delta Q$ is transferred from C_T to C_1 in each period, the final charge of C_1 and voltage variation at output node are as Equations (17) and (18), respectively.

$$\Delta Q_1 = \Delta Q - \alpha.\Delta Q = (1-\alpha)\Delta Q \tag{17}$$

$$\Delta V_1 = (1-\alpha)\Delta V \tag{18}$$

Also, the charge and voltage variation of C_T (i.e. tail node) can be express as Equations (19) and (20), respectively.

$$\Delta Q_T = -(1-\alpha)\Delta Q \tag{19}$$

$$\Delta V'_T = (\alpha - 1)\Delta V_T \tag{20}$$

whrere,

$$\Delta V_T = \frac{C_1}{C_T}\Delta V_1 \tag{21}$$

As seen in Equations (20) and (21), contrary to the case with negligible C_T, in this case the voltage of C_T is non-zero and can affect tank voltage through M_1 (as a common-gate configuration with gain A_{CG}). Since the voltage at C_T is amplified by $A_{CG}=g_{m1}R_t$, the total voltage change at output node is obtained as Equation (22).

$$\Delta V_1' = \Delta V_1 + A_{CG,1}\times\Delta V_T' \tag{22}$$

By substituting Equations (18), (20) and (21) into Equation (22), we have:

$$\begin{aligned}\Delta V_1' &= (1-\alpha)\Delta V + A_{CG,1}(\alpha-1)\times\frac{C_1}{C_T}\Delta V \\ &= \Delta V_1' = (1-g_{m1}.R_T\frac{C_1}{C_T})\times(1-\alpha)\Delta V\end{aligned} \tag{23}$$

As known from [16], ΔV results in $\Gamma_{Rt}=\frac{cos(\varphi)}{N}$ and thus according Equation (23) in this zone $\Gamma_{ids,1}$ can be obtained as Equation (24).

$$\Gamma_{i_{ds1}} = (1-g_{m1}R_t\frac{C_1}{C_T})(1-\alpha)\Gamma_{Rt} \tag{24}$$

2. 1. 1. 2. Zones 1 and 3 ($-\Phi<\varphi<\Phi$, $\pi-\Phi<\varphi<\pi+\Phi$) Since M_1 and M_2 are simultaneously on in this zones, the charge of $-\alpha.\Delta Q$ this time is passed from C_T through both of the transistors to capacitors C_1 and C_2, as depicted in Figure 4(b). The final charge and voltage variation of C_1 are obtained by Equations (25) and (26), respectively.

$$\Delta Q_1 = \Delta Q - \frac{g_{m1}}{g_{m1}+g_{m2}}\times\alpha\Delta Q = \frac{g_{m2}+(1-\alpha)g_{m1}}{g_{m1}+g_{m2}}\Delta Q \tag{25}$$

$$\Delta V_1 = \frac{g_{m2}+(1-\alpha)g_{m1}}{g_{m1}+g_{m2}}\Delta V \tag{26}$$

Also, the final charge and voltage variation of C_2 are given as follows:

$$\Delta Q_2 = \frac{-\alpha\times g_{m1}}{g_{m1}+g_{m2}}\Delta Q \tag{27}$$

$$\Delta V_2 = \frac{-\alpha\times g_{m2}}{g_{m1}+g_{m2}}\Delta V \tag{28}$$

Again, considering the effect of none-zero voltage of C_T on C_1 and C_2 and fully correlation of ΔV_1 with ΔV_2 [15], total voltage change at C_1 (i.e.$\Delta V_1'$) is expressed by Equation (29).

$$\begin{aligned}\Delta V_1' = \Delta V_1 + A_{CG,1}(1-\alpha)\times\Delta V_T - \\ \rightarrow \Delta V_2 - A_{CG,2}(1-\alpha)\Delta V_T\end{aligned} \tag{29}$$

By replacing Equation (21), (26) and (28) in Equation (29) we have Equation (30).

$$\begin{aligned}\Delta V_1' = \frac{g_{m2}+(1-\alpha)g_{m1}}{g_{m1}+g_{m2}}\Delta V + (g_{m1}.R_T\frac{C_1}{C_T})(\alpha-1)\Delta V - \\ \rightarrow \frac{\alpha\times g_{m2}}{g_{m1}+g_{m2}}\Delta V - (g_{m2}.R_T\frac{C_1}{C_T})(\alpha-1)\Delta V\end{aligned} \tag{30}$$

Simplifying Equation (30), Equation (31) is obtained.

$$\begin{aligned}\Delta V_1' = [(g_{m1}-g_{m2})(\alpha-1)R_T\frac{C_1}{C_T} + \\ \rightarrow \frac{(1+\alpha)\times g_{m2}+(1-\alpha)\times g_{m1}}{g_{m1}+g_{m2}}]\Delta V\end{aligned} \tag{31}$$

Finally, one can obtain $\Gamma_{i_{ds1}}$ as Equation (32).

$$\begin{aligned}\Gamma_{i_{ds}1}(\varphi) = [(g_{m1}-g_{m2})(\alpha-1)R_T\frac{C_1}{C_T} + \\ \rightarrow \frac{(1+\alpha)\times g_{m2}+(1-\alpha)\times g_{m1}}{g_{m1}+g_{m2}}]\times\Gamma_{Rt}\end{aligned} \tag{32}$$

2. 1. 1. 3. Zone 4 ($\pi+\Phi<\varphi<2\pi-\Phi$) Apparently, in this zone M_1 is off and does not contribute to the phase noise of output voltage. So, we have: $\Gamma_{ids1}(\varphi)=0$. Accordingly, the impulse sensitivity function of M_1 during a period is summarized as follows:

$$\Gamma_{i_{ds}}(\varphi) = \begin{cases} [(g_{m1}-g_{m2})(\alpha-1)R_T\frac{C_1}{C_T} + & -\Phi<\varphi<\Phi \\ \rightarrow \frac{(1+\alpha)\times g_{m2}+(1-\alpha)\times g_{m1}}{g_{m1}+g_{m2}}]\times\Gamma_{Rt}(\varphi) & \\ (1-g_{m1}R_t\frac{C_1}{C_T})(1-\alpha)\Gamma_{Rt} & \Phi<\varphi<\pi-\Phi \\ [(g_{m1}-g_{m2})(\alpha-1)R_T\frac{C_1}{C_T} + & \pi-\Phi<\varphi<\pi+\Phi \\ \rightarrow \frac{(1+\alpha)\times g_{m2}+(1-\alpha)\times g_{m1}}{g_{m1}+g_{m2}}]\times\Gamma_{Rt}(\varphi) & \\ 0 & \pi+\Phi<\varphi<2\pi-\Phi \end{cases} \tag{33}$$

It is worth mentioning that the channel current noise of M_1 and M_2 is a cyclostationary noise and can be written as Equation (34).

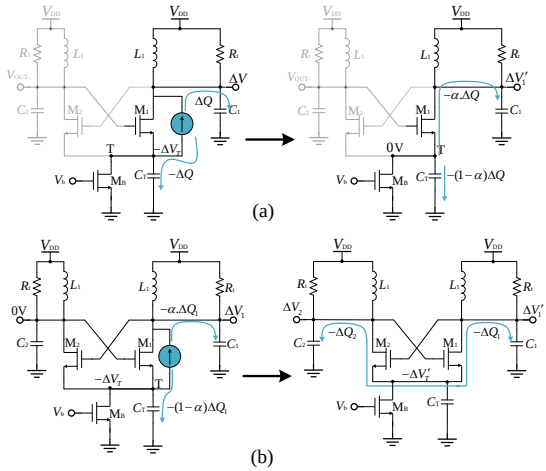

Figure 4. ISF derivation when C_T is not small, (a) only M_1 is on and (b) both transistors are on

$$\overline{i_n^2(t)} = \overline{i_n^2} \times \sigma(t), \tag{34}$$

where $\overline{i_n^2}$ is a stationary term and $\sigma(t)$ is the noise modulation factor (NMF) which can be derived easily from noise characteristic relation [3]. According to Andreani et al. [15] and using $g_{m1}(\varphi)$ in Equation (11), the channel thermal noise of M_1 can be written as (35). Comparing Equation (35) with Equation (34), the NMF is easily obtained as Equation (36).

$$\overline{i_n^2}(t) = 4KT\gamma g_{m1}(\varphi) = \\ \rightarrow 4KT\gamma\beta A_{\tan k} \times (\sin(\varphi) + \sqrt{2\sin^2(\Phi) - \sin^2(\varphi)}) \tag{35}$$

$$\sigma(t) = \sqrt{(\sin(\varphi) + \sqrt{2\sin^2(\Phi) - \sin^2(\varphi)})} \tag{36}$$

Based on Hajimiri's theorem, in the case of cyclostationary noise, effective root mean square (RMS) of ISF (i.e. $\Gamma_{ids,eff}$) should be calculated from Equation (33). Since the integral equation of $\Gamma_{ids,eff}$ has no algebraic closed-form expression, the closed-form symbolic formulas for RMS value of Equation (33) is not presented here. Instead, using numerical methods the numerical values of $\Gamma_{ids,eff}$ for required Φ are presented in the next section.

2. 1. 2. Derivation of Tail ISF (Γ_{Tail}) As depicted in Figure 5, the impulse current noise of $\overline{i}_{n,tail}^2$ charges C_T with charge area of ΔQ. It should be noted that impulse current only passes through C_T and does not charge $C_{1,2}$.

2. 1. 2. 1. Zones 1 and 3 In these zones both of the transistors are on and $\alpha \times \Delta Q$ from C_T is discharged through M_1 and M_2 to the output capacitors (C_1, C_2) that results in charge variation of ΔQ_1 and ΔQ_2 respectively.

As similar to previous section one can calculate the charge and voltage variation at outputs ($C_{1,2}$) by Equation (37) to Equation (40).

$$\Delta Q_1 = \frac{g_{m1}}{g_{m1} + g_{m2}} \times \alpha \Delta Q \tag{37}$$

$$\Delta Q_2 = \frac{g_{m2}}{g_{m1} + g_{m2}} \times \alpha \Delta Q \tag{38}$$

$$\Delta V_1 = \frac{g_{m1}}{g_{m1} + g_{m2}} \times \alpha \Delta V \tag{39}$$

$$\Delta V_2 = \frac{g_{m2}}{g_{m1} + g_{m2}} \times \alpha \Delta V \tag{40}$$

Once again, considering the correlation between outputs and effect of residual charge of C_T, the total voltage variation due to $\overline{i}_{n,tail}^2$ at capacitor C_1 can be written as:

$$\Delta V_1' = \Delta V_1 + A_{CG,1}(1-\alpha)\Delta V_T - \Delta V_2 - \\ \rightarrow A_{CG,2}(1-\alpha)\Delta V_T \tag{41}$$

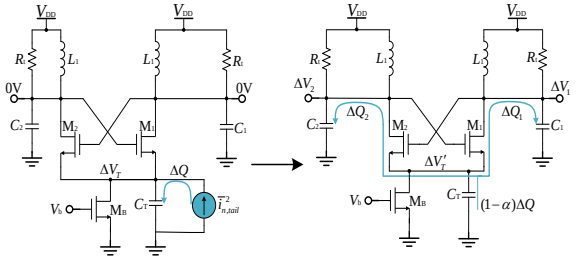

Figure 5. Circuit for calculating ISF of tail noise when C_T is not small in zones 1 and 3

Using Equations (39), (40) and (21), Equation(41) is rewritten as follows:

$$\Delta V_1' = \frac{g_{m1}}{g_{m1} + g_{m2}} \times \alpha \Delta V + g_{m1} R_T \frac{C_1}{C_T}(1-\alpha)\Delta V - \\ \rightarrow \frac{g_{m2} \times \alpha \Delta V}{g_{m1} + g_{m2}} - g_{m2} R_T \frac{C_1}{C_T}(1-\alpha)\Delta V \tag{42}$$

As a result, the impulse sensitivity function of tail can be derived as follow:

$$\Gamma_{Tail}(\varphi) = (g_{m1} - g_{m2})[\frac{\alpha}{g_{m1} + g_{m2}} + \\ \rightarrow R_T \frac{C_1}{C_T}(1-\alpha)] \times \Gamma_{Rt}(\varphi) \tag{43}$$

2. 1. 2. 2. Zone 2 In this zone M_1 is on and M_2 is off and similar to previous section $\alpha \times \Delta Q$ from C_T is discharged to C_1 and total voltage change of output voltage can be express as bellow.

$$\Delta V_1' = \Delta V_1 + A_{CG,1}(1-\alpha)\Delta V_T \\ = [\alpha + g_{m1} R_t (1-\alpha)\frac{C_1}{C_T}]\Delta V \tag{44}$$

So, the ISF of tail in this zone is given by Equation (45).

$$\Gamma_{Tail}(\varphi) = [\alpha + g_{m1} R_t (1-\alpha)\frac{C_1}{C_T}] \times \Gamma_{Rt}(\varphi) \tag{45}$$

2. 1. 2. 3. Zone 4 In this zone M_2 is on and M_1 is off, charge $\alpha \times \Delta Q$ is transferred to C_2 and results in $\alpha \times \Delta V$. Considering the residual charge on C_T, total voltage variation at C_2 is given by $\Delta V_2 = [\alpha + g_{m2} R_t (1-\alpha)\frac{C_1}{C_T}]\Delta V$. Again, with regard to the fully correlation of differential outputs, $\Delta V_1 = -\Delta V_2$ and accordingly ISF is obtained. So, the ISF of the tail in a period is given by Equation (46):

$$\Gamma_{Tail}(\varphi) = \begin{cases} (g_{m1} - g_{m2})[\frac{\alpha}{g_{m1} + g_{m2}} + R_T \frac{C_1}{C_T}(1-\alpha)] \times \Gamma_{Rt}(\varphi) & -\Phi < \varphi < \Phi \\ [\alpha + g_{m1} R_t (1-\alpha)\frac{C_1}{C_T}] \times \Gamma_{Rt}(\varphi) & \Phi < \varphi < \pi - \Phi \\ (g_{m1} - g_{m2})[\frac{\alpha}{g_{m1} + g_{m2}} + R_T \frac{C_1}{C_T}(1-\alpha)] \times \Gamma_{Rt}(\varphi) & \pi - \Phi < \varphi < \pi + \Phi \\ -[\alpha + g_{m2} R_t (1-\alpha)\frac{C_1}{C_T}] \times \Gamma_{Rt}(\varphi) & \pi + \Phi < \varphi < 2\pi - \Phi \end{cases} \tag{46}$$

2. 2. ISF Calculation When C_T Is Big In the case of big C_T, we can replace $\alpha = 0$ in Equation (33) and Equation (46). Thus, the impulse sensitivity functions of cross-connected and tail transistors are simply derived as Equations (47) and (48), respectively.

$$\Gamma_{i_{ds}}(\varphi)=\begin{cases}[1-(g_{m1}-g_{m2})R_t\dfrac{C_1}{C_T}]\times\Gamma_{Rt}(\varphi) & -\Phi<\varphi<\Phi\\ (1-g_{m1}R_t\dfrac{C_1}{C_T})\Gamma_{Rt} & \Phi<\varphi<\pi-\Phi\\ [1-(g_{m1}-g_{m2})R_t\dfrac{C_1}{C_T}]\times\Gamma_{Rt}(\varphi) & \pi-\Phi<\varphi<\pi+\Phi\\ 0 & \pi+\Phi<\varphi<2\pi-\Phi\end{cases} \quad (47)$$

$$\Gamma_{Tail}(\varphi)=\begin{cases}(g_{m1}-g_{m2})[R_t\dfrac{C_1}{C_T}]\times\Gamma_{Rt}(\varphi) & -\Phi<\varphi<\Phi\\ [g_{m1}R_t\dfrac{C_1}{C_T}]\times\Gamma_{Rt}(\varphi) & \Phi<\varphi<\pi-\Phi\\ (g_{m1}-g_{m2})[R_t\dfrac{C_1}{C_T}]\times\Gamma_{Rt}(\varphi) & \pi-\Phi<\varphi<\pi+\Phi\\ -[g_{m1}R_t\dfrac{C_1}{C_T}]\times\Gamma_{Rt}(\varphi) & \pi+\Phi<\varphi<2\pi-\Phi\end{cases} \quad (48)$$

2. 3. ISF Calculation When C_T Is Small Although the impulse sensitivity function of cross-connected and tail transistors has been derived for very small values of C_T in prior works [6, 15], just for the purpose of double checking the derivations obtained in this paper, one can substitute $\alpha = 1$ in Equations (33) and (46) and obtain Equations (49) and (50); those are exactly identical to equations obtained by Andreani et al. [15].

$$\Gamma_{i_{ds}}(\varphi)=\begin{cases}\dfrac{2g_{m2}}{g_{m1}+g_{m2}}\times\Gamma_{Rt}(\varphi) & -\Phi<\varphi<\Phi\\ 0 & \Phi<\varphi<\pi-\Phi\\ \dfrac{2g_{m2}}{g_{m1}+g_{m2}}\times\Gamma_{Rt}(\varphi) & \pi-\Phi<\varphi<\pi+\Phi\\ 0 & \pi+\Phi<\varphi<2\pi-\Phi\end{cases} \quad (49)$$

$$\Gamma_{Tail}(\varphi)=\begin{cases}\dfrac{g_{m1}-g_{m2}}{g_{m1}+g_{m2}}\times\Gamma_{Rt}(\varphi) & -\Phi<\varphi<\Phi\\ \Gamma_{Rt}(\varphi) & \Phi<\varphi<\pi-\Phi\\ \dfrac{g_{m1}-g_{m2}}{g_{m1}+g_{m2}}\times\Gamma_{Rt}(\varphi) & \pi-\Phi<\varphi<\pi+\Phi\\ -\Gamma_{Rt}(\varphi) & \pi+\Phi<\varphi<2\pi-\Phi\end{cases} \quad (50)$$

Comparing ISF obtained for non-small and small C_T from literature [6, 15] reveals that the tail capacitance can reduce phase noise contribution of tail transistor while it adds some terms to Γ_{ids} and may increase phase noise contribution of cross-connected transistors. However, more investigation is presented by numerical values of phase noise for different tail capacitance in Section 3.

3. NUMERICAL AND SIMULATION RESULTS

For more investigation, an LC-tank cross-connected oscillator has been designed and simulated with the circuit parameters shown in Table 1 in a standard 0.18µm CMOS technology. Simulation results show that this oscillator has an oscillation frequency of 5.2 GHz and the power consumption is 8.87 mW. The output voltages are also depicted in Figure 6. In this circuit the switching angle is obtained $\Phi = 50°$.

In continue, the simulated and analytical phase noise of the VCO for different values of tail capacitances are presented and the effect of different values of C_T on phase noise is discussed.

3. 1. Case 1: Non-negligible (Medium) C_T As mentioned before, the noise of cross-connected transistors is cyclostationary and RMS value of each ISF should be calculated by $\Gamma^2_{rms}=\frac{1}{T}\int\Gamma^2(\varphi)d\varphi$. Since, for a given Φ, the integrals have no closed-form expression, their numerical values for different Φ are illustrated. Figs 7(a) and (b) show $\Gamma^2_{i_{ds}-eff-RMS}$ and $\Gamma^2_{Tail-RMS}$ for different values of Φ in the case of C_T=100 fF.

To calculate total phase noise of the circuit by (3), the values of effective ISFs at desired Φ are obtained from Figures 7(a) and (b). The calculated phase noise versus offset frequency for three different tail capacitances and α is shown in Figure 8.

According to Figure 8, in the case of non-negligible tail capacitance, increasing C_T results in phase noise reduction. Also, it indicates that for a given tail capacitance, lower time constant at node *x* (i.e. higher α) is led to better phase noise.

TABLE 1. Circuit parameters for VCO

Parameter	Value
M_{tail}	16 µm/0.18 µm
$M_{1,2}$	26.8 µm/0.18 µm
L_1=L_2	1 nH
R_t	6 Ω
C_1=C_2	0.837 pf
V_{DD}	1.8 V
V_b	1 V

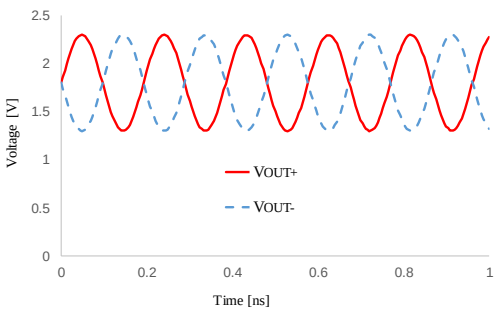

Figure 6. Output waveforms

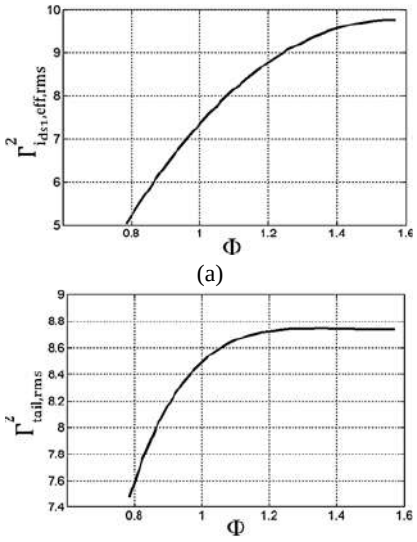

Figure 7. (a) $\Gamma^2_{i_{ds}-eff-RMS}$ and (b) $\Gamma^2_{Tail-RMS}$ vs Φ (radians) for C_T=100 fF

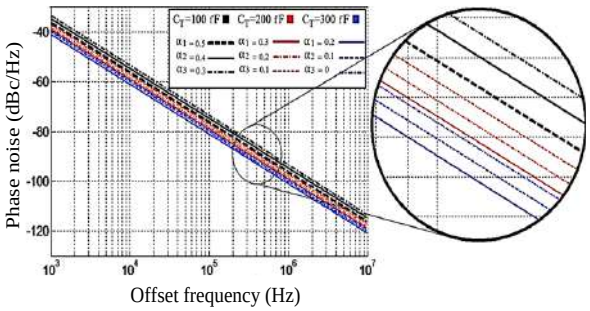

Figure 8. Calculated phase noise for different values of C_T and α when C_T is not negligible.

3. 2. Case 2: C_T Is Big In the case of big tail capacitances, the time constant of the tail node is bigger than the period of oscillation and α=0. Using Equations (39) and (40), numerical values of $\Gamma^2_{i_{ds}-eff-RMS}$ and $\Gamma^2_{Tail-RMS}$ for different values of Φ and C_T=1pF are shown in Figures 9(a) and 9(b), respectively. As expected, the effective ISF of cross-connected transistors (i.e. their noise contribution) in Figure 9 is increased (deteriorated) by increasing Φ. In contradict with Figure 7(b), effective tail ISF for big tail capacitances is decreased by increasing Φ.

Using Equation (3), total phase noise of the VCO for C_T=1pF and $\Phi = 50^\circ$ was calculated using MATLAB software and shown in Figure 10. The simulated phase noise of the oscillator (by ADS) is also depicted in Figure 10 that shows a good agreement with the numerical results.

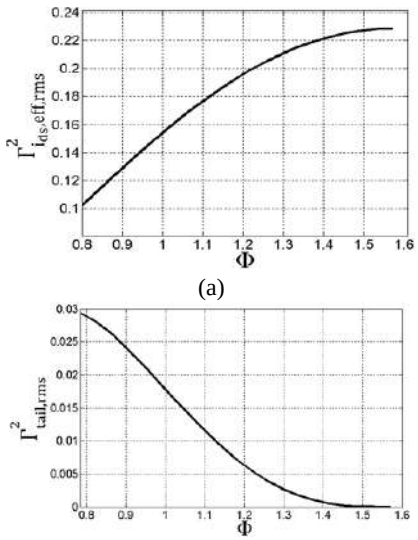

Figure 9. Effective ISF of (a) the cross-connected current and (b) tail transistors vs Φ (radian) for C_T=1pF

According to Figure 11, a bigger tail capacitance is led to a lower phase noise, though for very large C_T increase of C_T has a negligible effect on the phase noise. Therefore, for each VCO, there is an optimum value of C_T in which the tail transistor has lowest contribution to the total phase noise. For example, as shown in Figure 11 the optimum value for C_T is 10 pF and by increasing C_T the phase noise cannot be decreased anymore.

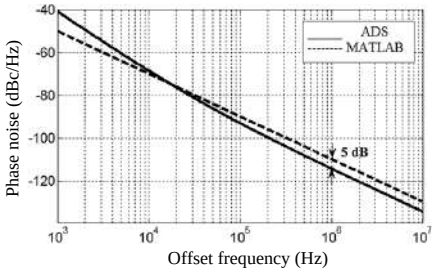

Figure 10. Simulated and calculated Phase noise for C_T=1pF

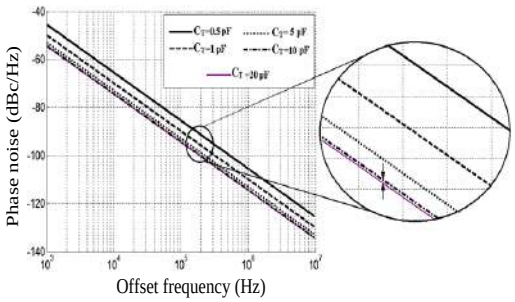

Figure 11. Calculated phase noise for different big tail capacitances

4. CONCLUSION

This paper presented an analytical study of the impact of capacitive filtering on the phase noise in an LC-tank oscillator. Considering the three scenarios for value of C_T the ISF of each transistor has been calculated and the effect of tail capacitance has been discussed. According to the analysis, tail transistor dramatically deteriorates total phase noise and the use of a parallel capacitance can effectively reduce the noise contribution of the tail. It is worth mentioning; the analysis also shows that the time constant of the tail node (x) has a very important role in the amount of noise rejection. While bigger tail capacitance is led to a more noise rejection of tail transistor, it creates a low impedance path and deteriorates the quality factor of LC tank. So, the phase noise caused by cross-connected transistors may be increased. Although the ISF of transistors is usually degraded by increasing conduction angle, our analysis reveals, in the case of large C_T, tail ISF is improved by increasing conduction angle.

5. REFERENCES

1. Chlis, I., Pepe, D., and Zito, D., "Comparative analyses of phase noise in 28 nm CMOS LC oscillator circuit topologies: Hartley, colpitts, and common-source cross-coupled differential pair", ***The Scientific World Journal***, Vol. 2014, (2014), 1–13. doi:10.1155/2014/421321
2. Leeson, D. B., "A Simple Model of Feedback Oscillator Noise Spectrum", ***Proceedings of the IEEE***, Vol. 54, No. 2, (1966), 329–330. doi:10.1109/PROC.1966.4682
3. Hajimiri, A., and Lee, T. H., "A general theory of phase noise in electrical oscillators", ***IEEE Journal of Solid-State Circuits***, Vol. 33, No. 2, (1998), 179–194. doi:10.1109/4.658619
4. Vishwasrao Shinde, S., "Review of Oscillator Phase Noise Models", Proceedings of the International MultiConference of Engineers and Computer Scientists 2014 Vol II, (2014), 1–8.
5. Demir, A., Mehrotra, A., and Roychowdhury, J., "Phase noise in oscillators: a unifying theory and numerical methods for characterization", ***IEEE Transactions on Circuits and Systems I: Fundamental Theory and Applications***, Vol. 47, No. 5, (2000), 655–674. doi:10.1109/81.847872
6. Hajimiri, A., and Lee, T. H., "Design issues in CMOS differential LC oscillators", ***IEEE Journal of Solid-State Circuits***, Vol. 34, No. 5, (1999), 717–724. doi:10.1109/4.760384
7. Hegazi, E., Sjöland, H., and Abidi, A. A., "A filtering technique to lower LC oscillator phase noise", ***IEEE Journal of Solid-State Circuits***, Vol. 36, No. 12, (2001), 1921–1930. doi:10.1109/4.972142
8. Samori, C., Lacaita, A. L., Villa, F., and Zappa, F., "Spectrum folding and phase noise in LC tuned oscillators", ***IEEE Transactions on Circuits and Systems II: Analog and Digital Signal Processing***, Vol. 45, No. 7, (1998), 781–790. doi:10.1109/82.700925
9. Andreani, P., and Sjöland, H., "Tail current noise suppression in RF CMOS VCOs", ***IEEE Journal of Solid-State Circuits***, Vol. 37, No. 3, (2002), 342–348. doi:10.1109/4.987086
10. Jafari, B., and Sheikhaei, S., "Phase noise reduction in a CMOS LC cross coupled oscillator using a novel tail current noise second harmonic filtering technique", ***Microelectronics Journal***, Vol. 65, (2017), 21–30. doi:10.1016/j.mejo.2017.05.003
11. Darabi, H., and Abidi, A. A., "Noise in RF-CMOS mixers: A simple physical model", ***IEEE Journal of Solid-State Circuits***, Vol. 35, No. 1, (2000), 15–25. doi:10.1109/4.818916
12. Grebennikov, A., "Noise Reduction in Transistor Oscillators: Part 2—Low Frequency Loading and Filtering", ***High Frequency Electronics***, (2005), 24–36
13. Ismail, A., and Abidi, A. A., "CMOS differential LC oscillator with suppressed up-converted flicker noise", Digest of Technical Papers - IEEE International Solid-State Circuits Conference, (2003). doi:10.1109/isscc.2003.1234224
14. Samori, C., Zanchi, A., Levantino, S., and Lacaita, A. L., "A fully-integrated low-power low-noise 2.6-GHz bipolar VCO for wireless applications", ***IEEE Microwave and Wireless Components Letters***, Vol. 11, No. 5, (2001), 199–201. doi:10.1109/7260.923027
15. Andreani, P., Wang, X., Vandi, L., and Fard, A., "A study of phase noise in colpitts and LC-tank CMOS oscillators", ***IEEE Journal of Solid-State Circuits***, Vol. 40, No. 5, (2005), 1107–1118. doi:10.1109/JSSC.2005.845991
16. Razavi, B., Design of CMOS Phase-Locked Loops: From Circuit Level to Architecture Level, (2020), Cambridge University Press.
17. Aghabagheri, R., Miar-Naimi, H., and Javadi, M., "A Phase Noise Reduction Technique in LC Cross-coupled Oscillators with Adjusting Transistors Operating Regions", ***International Journal of Engineering, Transactions A: Basics***, Vol. 33, No. 4, (2020), 560–566. doi:10.5829/IJE.2020.33.04A.07
18. Mazloum, J., and Sheikhaei, S., "1/ f 3 (Close-in) Phase Noise Reduction by Tail Transistor Flicker Noise Suppression Technique", ***Journal of Circuits, Systems and Computers***, Vol. 29, No. 3, (2020). doi:10.1142/S0218126620500358
19. Sun, P., "A low-power and low-phase noise capacitive-degeneration LC VCO", ***International Journal of Electronics Letters***, Vol. 4, No. 4, (2016), 466–471. doi:10.1080/21681724.2015.1082196
20. Andreani, P., and Wang, X., "On the phase-noise and phase-error performances of multiphase LC CMOS VCOs", ***IEEE Journal of Solid-State Circuits***, Vol. 39, No. 11, (2004), 1883–1893. doi:10.1109/JSSC.2004.835828

Persian Abstract

چکیده

این مقاله تأثیر خازن دنباله را روی نویز فاز اسیلاتورهای کنترل‌شده با ولتاژ (LC-VCO) تحلیل می‌کند. در ابتدا روابط عددی نویز فاز به ازای مقادیر مختلف خازن دنباله (C_T) استنتاج شده است و سپس به‌منظور تائید آن، شبیه‌سازی و نتایج عددی باهم مقایسه شده‌اند. برای ساده‌سازی روابط سه حالت کوچک، متوسط و بزرگ برای خازن دنباله در نظر گرفته شده است. در یک مطالعه موردی یک اسیلاتور کنترل‌شده با ولتاژ در فناوری ۱۸۰ نانومتر CMOS طراحی و نتایج عددی برای مقادیر مختلف خازن دنباله ارائه‌شده است. در این مقاله تحلیل‌های عددی نشان می‌دهد که برای C_T =200fF (مقدار متوسط خازن دنباله) و C_T =10pF (مقدار بزرگ خازن دنباله)، مقدار نویز فاز در آفست فرکانسی ۱ مگاهرتز از فرکانس مرکزی ۵/۲ گیگاهرتز به ترتیب برابر ۹۶ dBc/Hz- و ۱۱۸ dBc/Hz- است. بر طبق نتایج شبیه‌سازی و تحلیل‌های عددی، مقدار تابع حساسیت ضربه (ISF) با افزایش خازن دنباله بهبود می‌یابد. مقادیر عددی همچنین نشان می‌دهد که افزایش بیش‌ازحد خازن دنباله هیچ تأثیری روی نویز فاز ندارد. درحالی‌که انتخاب خازن بزرگ‌تر می‌تواند به‌طور مؤثری نویز فاز کل را با حذف نویز ترانزیستور دنباله کاهش دهد اما تأثیر مسیر امپدانس پایین ایجادشده توسط خازن دنباله نیز می‌تواند نویز فاز را با کاهش ضریب کیفیت تانک خروجی کاهش دهد.

International Journal of Engineering

Journal Homepage: www.ije.ir

Squirrel Search Optimization for Non-convex Multi-area Economic Dispatch

V. P. Sakthivel*[a], P. D. Sathya[b]

[a] Department of Electrical and Electronics Engineering, Government College of Engineering, Dharmapuri, India
[b] Department of Electronics and Communication Engineering, FEAT, Annamalai University, Chidambaram, India

PAPER INFO

Paper history:
Received 04 April 2020
Received in revised form 28 October 2020
Accepted 14 November 2020

Keywords:
Metaheuristic Approach
Multi-area Economic Load Dispatch
Multi Fuel Alternatives
Swarm Intellegence
Valve Point Impacts

ABSTRACT

Multi-area economic load dispatch (MAELD) decides the measure of power that can be fiscally generated in one area and transfered to another area. The goal of MAELD is to determine the most prudent production arrangement that could deliver the nearby power requirement without violating tie-line limits. This study presents a new swarm algorithm called as squirrel search optimization (SSO) to solve the MAELD problems. The impacts of transmission losses, prohibited operating zones, valve point loading and multi-fuel alternatives are additionally contemplated. SSO impersonates the searching conduct of flying squirrels which depends on the dynamic bouncing and skimming procedures. To demonstrate the potency of the suggested approach, it is examined on three different test systems for solving the MAELD problems. Comparative examinations are performed to analyze the adequacy of the suggested SSO approach with exchange market algorithm and different strategies revealed in the literature. The experimental results show that the proposed SSO approach is equipped for acquiring preferred quality solutions over the other existing strategies.

***doi**: 10.5829/ije.2021.34.01a.14*

NOMENCLATURE

a_{ij}, b_{ij}, c_{ij}	Cost coefficients of generator j in area i	nz, ng	Total number of POZs and generating units respectively
e_{ij}, f_{ij}	Cost coefficients of the VPL effect of generator j in area i	P_{Di}	Power demand in area i
$F_{ij}(P_{ij})$	Fuel cost of the generator j in area i	P_{dp}	predator presence probability
nf	Number of fuel alternatives	P_{ij}	Real power generation of generator j in area i
M_i	Number of participated generators in area i	$P_{i\,j,min}$, $P_{\,ij,max}$	Minimum and maximum generation j in area i
m	Index of prohibited zone	$T_{\,iz}$	Tie line power stream from area i to area z

1. INTRODUCTION

Multi-area economic load dispatch (MAELD) is a portion of economic load dispatch (ELD) which concentrates on critical issues about energy management of the modern power systems. In reality, MAELD characterizes the amount of power which can be monetarily delivered in one area and transferred to another. The principle objective of MAELD is to determine the most conservative power generation strategy which could stream the nearby power demands with no abusing tie-line limit limitations. As of late, MAELD is considered as a new part of ELD issues which are profoundly encouraging for utilizing in the power grids.

In recent years, swarm intelligence algorithms have been broadly used to solve the MAELD problem. Jayabarathi et al. [1] proposed a proficient technique for multi-area economic dispatch problems using evolutionary programming (EP) approach. The performance of the various evolutionary algorithms, for example as real-coded genetic algorithm (RCGA), particle swarm optimization (PSO), differential evolution (DE) and covariance matrix adapted evolution strategy (CMAES) on MAELD problems with Karush–Kuhn–Tucker optimality confirmations were examined by Manoharan et al. [2]. The simulation results revealed that

*Corresponding Author Institutional Email: vp.sakthivel@yahoo.com (V. P. Sakthivel)

Please cite this article as: V. P. Sakthivel, P. D. Sathya, Squirrel Search Squirrel Search Optimization for Non-convex Multi-area Economic Dispatch, International Journal of Engineering, Transactions A: Basics Vol. 34, No. 01, (2021) 120-127

the CMAES algorithm offers preferred outcomes over different algorithms considered. Sharma et al. [3] investigated and analyzed the performance of different DE strategies enhanced with time-varying mutation to solve the reserve constrained MAELD problem. Somasundaram and Jothi Swaroopan [4] introduced another computationally efficient fuzzified particle swarm optimization algorithm for solving the security-constrained MAELD of an interconnected power system. Basu proposed artificial bee colony (ABC) optimization [5], teaching learning-based optimization (TLBO) [6] and fast convergence evolutionary programming [7] for solving MAELD problem with tie-line constraints, transmission losses, multiple fuels and valve point effects. Nguyen et al. [8] developed hybrid cuckoo search algorithm to solve the MAELD problem. Ghasemi et al. [9] presented hybrid DE-PSO technique for addressing the MAELD, reserve constrained MAELD and reserve constrained multi area ecological/economic dispatch issues. Zhang et al. [10] introduced an improved grasshopper optimization algorithm to take care of the MAELD issue. The suggested approach considered the tie-line constraints including transmission losses, POZ, MFO and VPL impacts, and validated with different meta-heuristics.

A new model was proposed to examine impacts of uncertainties associated to component failures, load demand and wind power on the generation scheduling [11]. A dynamic optimization approach for optimal choice of energy carriers in thermal power plants was developed to analyse the substitution of energy carriers in short-term planning of a power plant [12]. A hybrid PSO and genetic operators was used for Pareto based optimization of solar systems [13].

Recently, a new nature-inspired algorithm named red deer algorithm (RDA) which mimicked the behaviour of Scottish red deer was developed [14]. Furthermore, the parameters and operators of RDA were made adaptive to improve the performance of this optimizer [15]. The effectiveness of improved RDA was proved on some benchmarked functions and design optimization of brushless motor. Fathollahi-Fard et al. developed a new single-solution algorithm called social engineering optimizer (SEO) which inspired the social engineering phenomena [16]. An improved SEO was developed to solve a truck scheduling problem in a cross-docking system [17]. A multi-objective SEO was applied to solve the HHC routing and scheduling problem [18] and an integrated water supply and wastewater collection network design problem [19].

From the review of the literature, many studies have neglected MFO, VPL and the intertemporal constraints. The MAELD problem with MFO and VPL effects becomes highly non-convex and challenging. It is vital to apply more effective heuristic approach to overcome the curse of dimension and improve the solution accuracy. To fill the research gap, a new approach, squirrel search optimization is employed for solving the highly non-convex MAELD problems with several operating constraints. The SSO algorithm proposed by Mohit Jain et al. [20] models the foraging activities of squirrel individuals.

The primary contributions of this paper can be summarized hereunder:

1. This paper models a more realistic formulation of the MAELD problem by considering all actual constraints and nonlinear characteristic of generating units including ramp rate limits, POZ, MFO and VPL impacts.
2. The envisaged research work considers different kinds of MAELD problems.
3. To demonstrate the supremacy of the suggested SSO approach, it has been examined on 2-area, 3-area and 4-area power systems, and compared with the state-of-the-art approaches surfaced in the literature.

2. PROBLEM FORMULATION OF MAELD PROBLEM

The goal of MAELD is to endeavor the optimal set of generation values in every zone just as shifting power between various zones so as to minimize the objective function subject to various imperatives.

The quadratic cost function of submitted generation units in all zones can be detailed as follows:

$$F_t = \sum_{i=1}^{n_g} \sum_{j=1}^{M_i} F_{ij}(P_{ij}) \tag{1}$$

$$\sum_{i=1}^{n_g} \sum_{j=1}^{M_i} (a_{ij} + b_{ij}P_{ij} + c_{ij}P_{ij}^2) \tag{2}$$

To display the impact of valve-points, a common amended sinusoid commitment is added to the quadratic function which is defined as:

$$F_t = \sum_{i=1}^{n_g} \sum_{j=1}^{M_i} a_{ij} + b_{ij}P_{ij} + c_{ij}P_{ij}^2 + \left|e_{ij} \times \sin(f_{ij} \times (P_{ij,min} - P_{ij}))\right| \tag{3}$$

Since generators are provided with multi-fuel sources, every generator ought to be defined with a few piecewise quadratic capacities superimposed sine terms mirroring the impact of fuel type changes and the generator must distinguish the most conservative fuel to consume. The MAELD problem with VPL and MFO can be modeled as:

$$F_t = \sum_{i=1}^{n_g} \sum_{j=1}^{M_i} a_{ijk} + b_{ijk}P_{ijk} + c_{ijk}P_{ijk}^2 + \left|e_{ijk} \times \sin(f_{ijk} \times (P_{ijk,min} - P_{ijk}))\right| \tag{4}$$

where k= 1, . . ., nf

The following equality and inequality constraints are addressed to solve the MAELD problem.

The total power generated from a set of committed units must fulfil the total load demand, tie line power flow and transmission losses, and is given by:

$$\sum_{j=1}^{M_i} P_{ij} = P_{Di} + P_{Li} + \sum_{z,z\neq i} T_{iz} \quad (5)$$

The real output power of thermal units ought to be in their range between minimum and maximum limits:

$$P_{ij,min} \leq P_{ij} \leq P_{ij,max} \quad (6)$$

Because of security basis, power shifted between various lines must not surpass their cutoff points. The power transfer requirement between two unique regions is characterized by

$$-T_{iz,min} \leq T_{iz} \leq T_{iz,max} \quad (7)$$

The POZs are owing to the function of steam valve or vibrations in the shaft bearings. The viable operating sectors of unit is defined by

$$\begin{matrix} P_{ij,min} \leq P_{ij} \leq P_{ij,1}^{L} \\ P_{ij,k-1}^{U} \leq P_{ij} \leq P_{ij,k}^{L} \qquad k = 2, \ldots .. nz \; P_{ij,nz}^{U} \leq \\ P_{ij} \leq P_{ij,max} \end{matrix} \quad (8)$$

3. SYNOPSIS OF SSO

The hunt procedure starts when flying squirrels begin scavenging. During fall, the squirrels look for nourishment assets by skimming from one tree to the next. At the same time, they change their area and investigate various regions of trees. As the climatic conditions are sufficiently hot, they can meet their every day vitality needs more rapidly on the eating routine of oak seeds accessible in bounty and thus they devour oak seeds quickly after discovering them. The capacity of hickory nuts will help them in keeping up their vitality prerequisites in amazingly brutal climate and decrease the expensive searching excursions and in this way increment the likelihood of endurance.

Toward the finish of winter season, flying squirrels again become dynamic. This is a monotonous procedure and proceeds till the life expectancy of a flying squirrel and structures the establishment of SSO. The SSO refreshes the places of squirrels as indicated by the ebb and flow season, the sort of squirrels and if chasers show up.

Expecting that the quantity of the populace is N, the upper and lower limits of the pursuit space are X_U and X_L. N squirrels are arbitrarily created as follows:

$$X_i = X_L + rand(1, D) \times (X_U - X_L) \quad (9)$$

where, X_i indicates the ith squirrel, (i = 1 : N); rand is an random number somewhere in the range of 0 and 1; D is the dimension of the problem.

SSO requires that there is just a single squirrel at each tree, accepting the absolute number of the squirrels is *N*, subsequently, there are *N* trees in the forests. All the *N* trees contain one hickory tree and N_a oak seed trees; the others are typical trees that have no nourishment. The hickory tree is the best nourishment asset for the squirrels and the oak seed tree comes in just short of the win. The squirrels are separated into three kinds: squirrels situated at hickory trees (W_h), squirrels situated at oak seed trees (W_a) and squirrels situated at ordinary trees (W_n).

The squirrels refresh their situations by skimming to the hickory trees or oak seed trees as follows:

$$X_i^{t+1} = \begin{cases} X_i^t + d_g G_c (X_{ai}^t - X_i^t) & if\ r_1 \geq P_{dp} \\ Random\ location & otherwise \end{cases} \quad (10)$$

$$X_i^{t+1} = \begin{cases} X_i^t + d_g G_c (X_h^t - X_i^t) & if\ r_2 \geq P_{dp} \\ Random\ location & otherwise \end{cases} \quad (11)$$

where, r_1 and r_2 are random numbers in the range of [0, 1], P_{dp} is predator presence probability, X_h is the location of squirrel individual which reached the hickory tree and *t* indicates the current iteration. G_c and d_g are gliding constant and distance respectively.

Toward the start of every generation, the SSO necessitates that the entire populace is in winter, which implies all the squirrels are refreshed by Equations (10) and (11). The squirrels are refreshed, regardless of whether the season change is decided by the following formulae.

$$S_c^t = \sqrt{\sum_{k=1}^{d} \left(X_{ai,k}^t - X_{h,k}^t\right)^2} \quad (12)$$

$$S_{min} = \frac{10e^{-6}}{(365)^{t/(t_{max}/2.5)}} \quad (13)$$

If $S_{tc} < S_{min}$, winter is finished and the season goes to summer, or else, the season is unaltered. When the season goes to summer, all the squirrels who float to W_h remain at the refreshed area, and all the squirrels who skim to W_a and do not meet with chasers, move their locations as follows:

$$X_{inew}^{t+1} = X_L + Le'vy(x) \times (X_U - X_L) \quad (14)$$

Le′vy is the arbitrary walk model whose progression complies with the Le′vy appropriation and can be determined by

$$Le'vy(x) = 0.01 \times \frac{\alpha \times r_a}{|r_b|^{\frac{1}{\beta}}} \quad (15)$$

where, r_a and r_b are two randomly distributed numbers in [0, 1], α and β are constants.

4. SUCCESSIVE PROGRESSION OF SSO FOR MAELD PROBLEM

In this section, strategy to implement the SSO approach for solving the MAELD problems has been depicted as flow diagram in Figure 1.

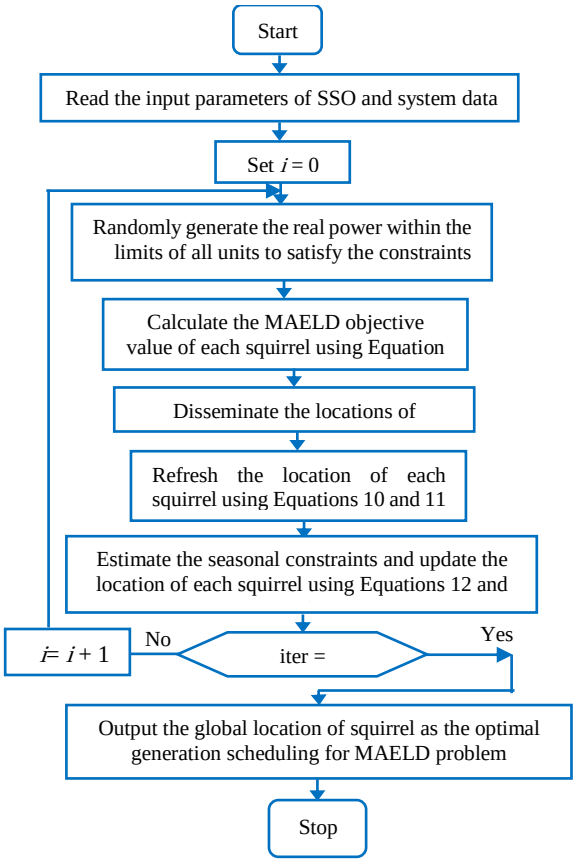

Figure 1. Flow chart of SSO approach applied in MAELD problems

5. NUMERICAL RESULTS

To assess the efficaciousness of the envisaged SSO approach in solving the MAELD, computational simulations are applied on three diverse test systems such as two-area system with 6 generating units, three-area system with 10-units and four-area system with 40 units. Furthermore, to check the adequacy of the envisaged SSO approach, the EMA approach is utilized for solving the MAELD and compared with those of recently published state-of-the-art approaches. The SSO and EMA approaches are executed using MATLAB 7.1 on an Intel core i3 processor with 4 GB RAM, and is executed for 50 free runs for all the test systems. The accompanying three case studies are contemplated.

Case study 1. MAELD with transmission line losses and POZ impacts

Case study 2. MAELD with transmission losses, VPL and MFO

Case study 3. MAELD with VPL impacts

5. 1. Parameter Tuning Taguchi method is used to tune the parameters of the suggested SSO algorithm. The parameters such as number of iterations, population size, P_{dp} and G_c are chosen as independent design variables. Each variable has three set values (level values) as given in Table 1. Then, L_9 orthogonal array is used to determine the optimal SSO parameters. Table 2 presents the tuned SSO parameters. The parameters are tuned at Run # 4 (a, b, c, d: 2, 1, 2, 3) for Case study 1, and Run # 5 (a, b, c, d: 2, 2, 3, 1) for Case studies 2 and 3 in the Taguchi array.

5. 2. Case Study 1 This case study considers a two-area test system having six generating units. The total power load is 1263 MW. The power balance, generating unit limits, tie line limitations, transmission losses and POZ are considered. In Ref. [5], the data of cost coefficients, emission coefficients and POZ are given. The power demand shared by area 1 and area 2 are 60 and 40 % of absolute load demand separately. The power stream from area 1 to area 2 is limited to 100 MW.

The generation plan and the fuel cost procured by the proposed SSO approach are tabulated in Table 3. Besides, the area 1 imports power from area 2. Figure 2 shows a comparison between the fuel costs procured by the SSO and EMA approaches, and other techniques surfaced in the literature.

In Figure 2, it is obvious that the SSO approach has obtained the minimum generation cost than the fuel costs procured by the other aforementioned approaches.

5. 3. Case Study 2 In this case, 3 areas, 10-unit test system with transmission losses, VPL and MFO is taken into consideration. Area 1, area 2 and area 3 comprise 4, 3 and 3 generating units respectively which are displayed in Figure 4. The power demand of this system is 2700 MW. The power demand shared by area1, area 2 and area 3 are 50 %, 25% and 25 % of total load

TABLE 1. Calibration of SSO

Parameters	Level 1	Level 2	Level 3
a: Number of iterations	100	200	500
b: Population size	10	20	40
c: P_{dp}	0.05	0.1	0.15
d: G_c	1.8	1.9	2

TABLE 2. Tuned parameters of SSO

Parameters	Case study 1	Case study 2	Case study 3
Number of iterations	200	200	200
Population size	10	20	20
P_{dp}	0.1	0.15	0.15
G_c	2	1.8	1.8

TABLE 3. Best dispatch solution acquired by the envisaged SSO approach for case study 1

Unit	Power generation (MW)
P1,1	500
P1,2	200
P1,3	149.9909
P2,1	204.3295
P2,2	154.6983
P2,3	67.5957
T21	82.7642
PL1	9.4267
PL2	4.1891
Generation cost ($/h)	12255.3789

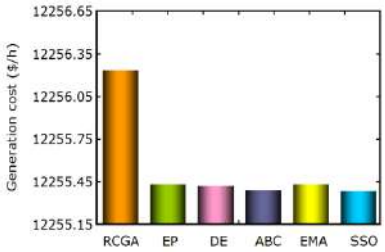

Figure 2. Comparison of generation costs procured by various approaches for Case study 1

TABLE 4. Best dispatch solution acquired by the envisaged SSO approach for case study 2

Unit	Fuel types	Power generation (MW)
$P_{1,1}$	2	225.7694
$P_{1,2}$	1	211.5842
$P_{1,3}$	2	491.3265
$P_{1,4}$	3	238.5371
$P_{2,1}$	1	252.6869
$P_{2,2}$	3	235.7538
$P_{2,3}$	1	264.7952
$P_{3,1}$	3	236.4286
$P_{3,2}$	1	330.8961
$P_{3,3}$	1	247.9518
T_{21}		17.2813
T_{31}		9.8161
T_{32}		8.6328
Generation cost ($/h)		654.4665

demand respectively. The power stream from one area to another area is restricted to 100 MW. Table 4 presents the simulation results acquired by the proposed SSO approach. It can be seen that the optimal generation cost acquired by the SSO approach is 654.4665 $/h which is the least among the compared approaches. The Area 1 imports power from areas 2 and 3, and area 3 exports power to area 2. The comparison between the results of SSO approach with those of EMA, RCGA, EP, DE and ABC approaches are illustrated in Figure 3. The results show that the proposed strategy obtains the best generation scheduling in comparison with different strategies.

5. 4. Case Study 3 A four-area with forty units' system is utilized in this case study. All the units have VPL impacts, and thus the cost functions are non-arched. The cost coefficients of this system are accessible in Ref. [5]. The system has a total load equivalent to 10500 MW. The schematic diagram of this four area test system is shown in Figure 6. Each area consists of 10 generation units. The distribution of power demand for area 1, area 2, area 3 and area 4 are 15, 40, 30 and 15 % of total load demand respectively.

The power flow from area 1 to area 3, area 2 to area 3 and area 2 to area 4 are restricted to 200 MW. The tie-line limits for area 1 to area 4, area 2 to area 4 and area 3 to area 4 is 100 MW. The optimal generation dispatch acquired by the envisaged approach is given in Table 5. The area 2 imports power from areas 1, 3 and 4; the area 1 imports power from areas 3 and 4, and area 4 exports power to area 3. In this case study, the effectiveness of the SSO approach has been compared with that of the EMA, RCGA, EP, DE and ABC approaches.

Figure 4 outlines the results of this examination. Once more, the SSO gave prevalent results than the previously mentioned approaches.

5. 5. Sensitivity Analysis The sensitivity analysis is performed for the number of food sources (N_{fs}), and the results are tabulated in Table 6. It is seen from the investigation that the expansion in number of food sources brings about upgraded precision and stability of the approach. The expanded level of N_{fs} prompts more focuses in search space around which search is engaged. Consequently, new solutions are discovered and better investigation of search space is accomplished.

5. 6. Managerial Insights The application of SSO to the MAELD problem demonstrates new managerial

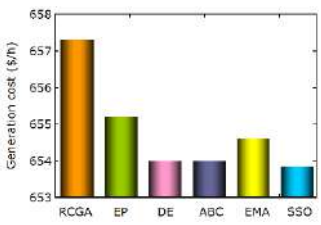

Figure 3. Comparison of generation costs procured by various approaches for Case study 2

TABLE 5. Best dispatch solution acquired by the envisaged SSO approach for case study 3

Unit	Power generation (MW)	Unit	Power generation (MW)
$P_{1,1}$	110.8909	$P_{3,1}$	523.8627
$P_{1,2}$	110.5472	$P_{3,2}$	523.558
$P_{1,3}$	97.9593	$P_{3,3}$	523.7572
$P_{1,4}$	178.5386	$P_{3,4}$	523.7537
$P_{1,5}$	88.2575	$P_{3,5}$	523.3404
$P_{1,6}$	140	$P_{3,6}$	523.5308
$P_{1,7}$	258.8407	$P_{3,7}$	10
$P_{1,8}$	284.2543	$P_{3,8}$	10
$P_{1,9}$	284.5497	$P_{3,9}$	10
$P_{1,10}$	130	$P_{3,10}$	86.4694
$P_{2,1}$	164.7045	$P_{4,1}$	190
$P_{2,2}$	168.9706	$P_{4,2}$	153.5285
$P_{2,3}$	141.9572	$P_{4,3}$	189.7943
$P_{2,4}$	393.5854	$P_{4,4}$	164.1622
$P_{2,5}$	393.8418	$P_{4,5}$	164.6892
$P_{2,6}$	470.9157	$P_{4,6}$	164.3112
$P_{2,7}$	489.7922	$P_{4,7}$	87.6541
$P_{2,8}$	489.9491	$P_{4,8}$	87.2630
$P_{2\,9}$	510.9340	$P_{4,9}$	108.1656
$P_{2,10}$	510.7577	$P_{4,10}$	512.9133
T_{12}	195.1514	T_{41}	60.5383
T_{31}	35.7749	T_{42}	90.9470
T_{32}	178.4934	T_{43}	95.9961
Generation cost ($/h)			122268.82

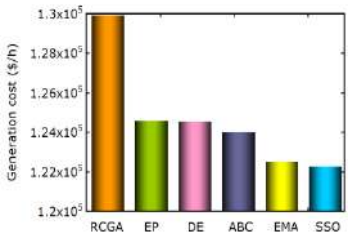

Figure 4. Comparison of generation costs procured by various approaches for Case study 3

insights. This method provides a better performance in comparison with other heuristic approaches. Examining the results obtained by the SSO and other approaches, the following points can be noticed.

Tables 1-3 provide that the minimum fuel costs accomplished by SSO approach. The fuel cost obtained are 12255.3789 $/h, 654.4665 $/h, and 122268.8214 $/h for case studies 1, 2, and 3 respectively. Those fuel costs are less when compared with the revealed results in recent literature as shown in Figures 2-4. This fact demonstrates that the SSO algorithm is capable to obtain solutions of a better quality and more stable than the other algorithms.

TABLE 6. Sensitivity analysis with different the number of food sources

Number of food sources (N_{fs}), (%)	Fuel cost ($/h)		
	Case study 1	Case study 2	Case study 3
20	12256.1364	655.2347	122292.6732
40	12255.3789	654.8431	122284.3763
60	12255.3789	654.4665	122268.8214
80	12255.3789	654.4665	122268.8214

The quality of the solutions is evaluated based on a sequence of runs. In this paper, 50 independent runs are performed for EMA and SSO approaches. For this sequence, the values of the best, average, worst and standard deviation of the generation costs are recorded. The statistical values obtained from the EMA and SSO approaches are tabulated in Table 7.

The low value of the standard deviation indicates that the SSO algorithm have the ability to reach stable solutions, when more runs are performed (50 runs). Furthermore, the SSO has a better one than the EMA strategy.

The convergence comparison of SSO and EMA approaches is shown in Figure 5. It can be observed that the SSO approach takes lesser number of cycles to unite into the global optimal solution. Figure 6 shows the average CPU time adopted by the SSO, EMA and other strategies for the case study 3. It is significant that time prerequisite is less and better than other referenced techniques. Consequently, it tends to be noted that the SSO technique is computationally productive when compared with the recently referenced strategies.

Finally, Wilcoxon rank-sum test is performed for all the case studies. the A p-value beneath 0.05 accomplished utilizing this test is estimated as plentiful proof over the null hypothesis. Figure 7 shows the p-values acquired by SSO versus EMA using Wilcoxon

TABLE 7. Comparison of results between EMA and SSO

Fuel cost	Case study 2		Case study 3	
	EMA	SSO	EMA	SSO
Best cost	654.6	654.46	122525.75	122268.82
Average cost	656.86	655.53	122854.83	122352.95
Worst cost	657.99	656.96	123148.32	122653.37
Standard deviation	0.954	0.74	35.78	20.36

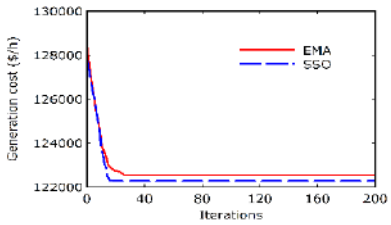

Figure 5. Convergence comparison of SSO and EMA approaches

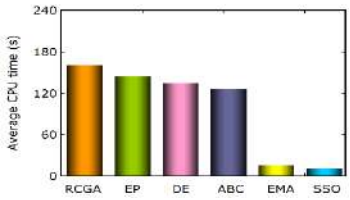

Figure 6. Comparison of average CPU time adopted by various approaches for Case study 3

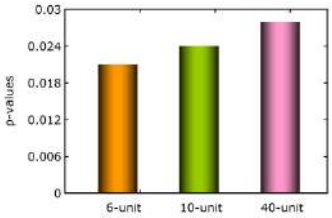

Figure 7. Comparison of Wilcoxon test results for all the Case studies

rank-sum tests. It is apparent from the figure that the p-value for each study is lower than the ideal estimation of 0.05. Consequently, the SSO approach produces statistically significant results.

6. CONCLUSION

In this paper, a new swarm insight approach, squirrel search optimization (SSO) approach is effectively bestowed to solve the MAELD problem. To assess the potency of the suggested approach, a benchmarking analysis is directed between the SSO, EMA and different heuristic approaches surfaced in the literature. Three sorts of non-smooth MAELD issues; MAELD with transmission losses and POZ (2-area with 6-unit system), MAELD with VPL impacts (4-area with 40-unit system), and MAELD with VPL and MFA impacts (3-area with 10-unit system) are addressed. The main conclusions of the paper are itemized hereunder:

- In SSO, the predator presence behaviour and a seasonal monitoring condition are incorporated to update the position of squirrel in a better way, which enhances the exploration and exploitation search abilities of the algorithm significantly. The global search ability of the algorithm is further enhanced by Levy distribution. Accordingly, the convergence behaviour and the global optimization capability of the suggested SSO approach are better than those of the other heuristic approaches in solving different MAELD problems.
- Simulation results prove that the suggested SSO approach is of prominent dominance in both solution quality and computational efficiency.

As a scope of further research, the SSO algorithm can be applied for solving more complex large-scale static and dynamic ELD problems, large-scale multi-area economic environmental dispatch, and unit commitment problems.

7. REFERENCES

1. Jayabarathi, T., Sadasivam, G., and Ramachandran, V., "Evolutionary programming based multi-area economic dispatch with tie line constraints", ***Electric Machines & Power Systems***, Vol. 28, No. 12, (2000), 1165-1176. doi: 10.1080/073135600449044.
2. Manoharan, P.S., Kannan, P.S., Baskar, S., and Iruthayarajan, M., "Evolutionary algorithm solution and KKT based optimality verification to multi-area economic dispatch", ***International Journal of Electrical Power & Energy Systems***, Vol. 31, No. 7-8, (2009), 365-73. doi: 10.1016/j.ijepes.2009.03.010.
3. Sharma, M., Manjaree, P., and Laxmi. S., "Reserve constrained multi-area economic dispatch employing differential evolution with timevarying mutation", ***International journal of Electrical Power & Energy Systems***, Vol. 33, No. 3, (2011), 753-66. doi: 10.1016/j.ijepes.2010.12.033.
4. Somasundaram P., and Jothi Swaroopan, N.M., "Fuzzified Particle Swarm Optimization Algorithm for Multi-area Security Constrained Economic Dispatch", ***Electric Power Components and Systems***, Vol. 39, No. 10, (2011), 979-990. doi: 10.1080/15325008.2011.552094.
5. Basu, M., "Artificial bee colony optimization for multi-area economic dispatch," ***International journal of Electrical Power & Energy Systems***, Vol. 49, (2013), 181-187. doi:10.1016/j.ijepes.2013.01.004.
6. Basu, M., "Teaching–learning-based optimization algorithm for multi-area economic dispatch", ***Energy***, Vol. 68, (2014), 21-28. doi: 10.1016/j.energy.2014.02.064.
7. Basu, M., "Fast Convergence Evolutionary Programming for Multi-area Economic Dispatch", ***Electric Power Components and Systems***, Vol. 45, No. 15, (2017), 1629-1637. doi: 10.1080/15325008.2017.1376234.
8. Nguyen, K.P., Dinh, N.D., and Fujita, G., "Multi-area economic dispatch using hybrid cuckoo search algorithm", In: 50th International Universities Power Engineering Conference (UPEC), Stoke on Trent, UK; (2015), 1-6. doi: 10.1109/UPEC.2015.7339777.
9. Ghasemi, M., Aghaei, J., Akbari, E., Ghavidel, S., and Li, L., "A differential evolution particle swarm optimizer for various types of multi-area economic dispatch problems," ***Energy***, Vol. 107, (2016), 182–195. doi: 10.1016/j.energy.2016.04.002.
10. Zhang, P., Ma, W., and Dong, Y., "Multi-area economic dispatching using improved grasshopper optimization algorithm", ***Evolving Systems***, (2019). doi: 10.1007/s12530-019-09320-6.

11. Valinejad, J., Oladi, Z., Barforoushi, T., and Parvania, M., "Stochastic unit commitment in the presence of demand response program under uncertainties", ***International Journal of Engineering, Transactions B: Applications***, Vol. 30, No. 8, (2017), 1134-1143. doi: 10.5829/ije.2017.30.08b.04.
12. Razzaghi, T., and Kianfar, F., "The optimal energy carriers' substitutes in thermal power plants: A fuzzy linear programming model", ***International Journal of Engineering, Transactions C: Aspects,*** Vol. 25, No. 1, (2012), 55-66. doi: 10.5829/idosi.ije.2012.25.01c.07.
13. Bagheri, A., Sadafi, M., and Safikhani, H., "Multi-objective optimization of solar thermal energy storage using hybrid of particle swarm optimization, multiple crossover and mutation operator", ***International Journal of Engineering, Transactions B: Applications,*** Vol. 24, No. 3, (2011), 367-376. doi: 10.5829/idosi.ije.2011.24.04b.07.
14. Fathollahi-Fard, A.M., Hajiaghaei-Keshteli, M., and Tavakkoli-Moghaddam, R., "Red deer algorithm (RDA): a new nature-inspired meta-heuristic," ***Soft Computing,*** Vol. 24, (2020), 14637-14665. doi: 10.1007/s00500-020-04812-z.
15. Fathollahi-Fard, A.M., Azari, M.N., and Hajiaghaei-Keshteli, M., "An improved red deer algorithm to address a direct current brushless motor design problem," ***Scientia Iranica,*** (2019). doi: 10.24200/SCI.2019.51909.2419.
16. Fathollahi-Fard, A.M., Hajiaghaei-Keshteli, M., and Tavakkoli-Moghaddam, R., "The social engineering optimizer (SEO)," ***Engineering Applications of Artificial Intelligence,*** Vol. 72, (2018), 267-293. doi:10.1016/j.engappai.2018.04.009.
17. Fathollahi-Fard, A.M., Ranjbar-Bourani, M., Cheikhrouhou, N., and Hajiaghaei-Keshteli, M., "Novel modifications of social engineering optimizer to solve a truck scheduling problem in a cross-docking system," ***Computers & Industrial Engineering,*** Vol. 137, (2019), 106103. doi: 10.1016/j.cie.2019.106103.
18. Fathollahi-Fard, A.M., Ahmadi, A., Goodarzian, F., and Cheikhrouhou, N., "A bi-objective home healthcare routing and scheduling problem considering patients' satisfaction in a fuzzy environment, ***"Applied Soft Computing Journal,*** Vol. 93, (2020), 106385. doi:10.1016/j.asoc.2020.106385.
19. Fathollahi-Fard, A.M., Ahmadi, A., and Mirzapour Al-e-Hashem, S.M.J., " Sustainable closed-loop supply chain network for an integrated water supply and wastewater collection system under uncertainty," ***Journal of Environmental Management,*** Vol. 275, (2020), 111277. doi:10.1016/j.jenvman.2020.111277.
20. Jain, M., Singh, V., and Rani, A., "A novel nature-inspired algorithm for optimization: Squirrel search algorithm", ***Swarm and Evolutionary Computation,***Vol.44, No. 2, (2019), 148-175. doi: 10.1016/j.swevo.2018.02.013.

Persian Abstract

چکیده

اعزام بار اقتصادی چند ناحیه ای (MAELD) اندازه گیری توانی را تعیین می کند که می تواند در یک منطقه به صورت مالی تولید شود و به منطقه دیگری منتقل شود. هدف MAELD تعیین محتاطانه ترین ترتیب تولید است که می تواند نیاز برق تقریباً را نقض کند و محدودیت های خط اتصال را نقض کند. این مطالعه یک الگوریتم ازدحام جدید به نام بهینه سازی جستجوی سنجاب (SSO) برای حل مشکلات MAELD ارائه می دهد. تأثیرات تلفات انتقال ، مناطق عملیاتی ممنوع ، بارگذاری نقطه سوپاپ و گزینه های چندگانه سوز علاوه بر این نیز مورد بررسی قرار می گیرد. SSO جعل هویت سنجاب های پرنده را انجام می دهد که بستگی به روشهای پرش و پرش پوستی دارد. برای نشان دادن قدرت روش پیشنهادی ، آن را در سه سیستم آزمون مختلف برای حل مشکلات MAELD بررسی شده است. معاینات مقایسه ای برای تجزیه و تحلیل کفایت روش SSO پیشنهادی با الگوریتم بازار ارز و استراتژی های مختلف نشان داده شده در ادبیات انجام می شود. نتایج تجربی نشان می دهد که روش SSO پیشنهادی برای دستیابی به راه حل های با کیفیت ترجیحی نسبت به سایر استراتژی های موجود مجهز است.

International Journal of Engineering

Journal Homepage: www.ije.ir

A Bi-level Programming Approach for Pre-positioning Emergency Warehouses

E. Saghehei[a], A. Memariani[*b], A. Bozorgi-Amiri[c]

[a] *Department of Industrial Engineering, South Tehran Branch, Islamic Azad University, Tehran, Iran*
[b] *Department of Electrical and Computer Engineering, Kharazmi University, Tehran, Iran*
[c] *School of Industrial Engineering, College of Engineering, University of Tehran, Tehran, Iran*

PAPER INFO

Paper history:
Received 20 March 2020
Received in revised form 02 September 2020
Accepted 03 September 2020

Keywords:
Relief Supply Chain
Bi-level Programming
Evolutionary Algorithm
National Emergency Warehouse
Location-allocation Problem

ABSTRACT

In some countries, regional authorities may attempt to rebalance the allocation of national facilities in benefit of their own region which, in turn, may cause disturbances in the central government's decision-making proces. Regarding the hierarchical nature of these types of decisions, classical optimization models are not effective in decision-making and the use of multi-level programming can increase the efficiency of planning. Our paper aims to address the issue of a bi-level programming model to conduct the location analysis of emergency warehouses. A three-echelon relief supply chain is considered in which the relief network involves national and regional warehouses and demand cities. The upper-level model decides on the location of national warehouses, allocating them to regional warehouses. The lower-level model determines the location of regional warehouses and allocates them to demand points. The structure of both levels is based on the median location-allocation problem. Three solution approaches are presented based on the full enumeration and two types of nested evolutionary methods (genetic and heuristic local search algorithms). For the model to be used in Iran, the efficiency of algorithms is analyzed for two sizes of problems. The obtained results show the proper functioning of the solution approaches.

***doi**: 10.5829/ije.2021.34.01a.15*

1. INTRODUCTION

Although many advances in science and technology have contributed to the increased immunity of human beings against natural disasters, numerous crises have caused various socioeconomic damages annually. As evidenced in 2015, natural disasters affected more than 90 million people with 23000 people losing their lives in 113 countries. Added to this, the damage caused by these disasters is estimated to be $ 66.5 billion [1]. Owing to both human and financial losses, interests and efforts are devoted to the development of disaster management strategies. It consists of four sequential stages: mitigation, preparedness, response, and recovery. At the preparedness stage, the aim is to decrease the operation time in the response phase [2]. Pre-positioning of emergency warehouses is one of the main tasks concerning the preparedness stage. Positioning relief supplies near the expected location of disaster is called pre-positioning [3]. These relief supplies include food, potable water, medicine, vaccines, medical equipment, tents and generators [4]. Pre-positioning is one of the appropriate strategies employed to reduce human casualties and damages to the logistics infrastructure. This strategy may develop several benefits, including an improved response time and better purchase price of supplies for relief organizations [5].

Management of the emergency warehouses network is considered the responsibility of the central government in most countries, and the design of this network is usually centralized at the upper-level of governance. Facility positioning is one of the key issues in designing a network of emergency warehouses for pre-positioning relief items. In some countries, the central government's decisions on the positioning of national resources have been ignored by regional decision-makers. Accordingly, provincial managers and parliamentarians use national facilities for their representative area regardless of

*Corresponding Author Institutional Email: memariani@khu.ac.ir (A. Memariani)

Please cite this article as: E. Saghehei, A. Memariani, A. Bozorgi-Amiri, A Bi-level Programming Approach for Pre-positioning Emergency Warehouses, International Journal of Engineering, Transactions A: Basics Vol. 34, No. 01, (2021) 128-139

planning prospects, influencing the central government's optimal decisions. Clearly, in field studies of facility positioning for managing logistics at times of disaster, the modeling approach of most previous studies was based on classical optimization techniques. The use of single-level programming to model the problem of positioning emergency warehouses in these countries is not highly efficient. Therefore, to encourage the greater participation of lower-level decision-makers in the planning process, the bi-level programming approach can be used to model the problem of pre-positioning emergency warehouses. In this paper, a bi-level optimization model is designed to apply location-allocation to national and regional warehouses. Owing to the bi-level optimization model complexity, in this paper, three innovative solution approaches are presented by full enumeration and the nested evolutionary sequential approach. The main contributions of this research can be summarized as follows:

- Introduction of a bi-level programming structure for the use of national and regional decision-makers in the field of emergency warehouse positioning
- Development of a bi-level model to locate and allocate national and regional warehouses for relief supply pre-positioning
- Design of nested evolutionary approaches and an exact method based on full enumeration to solve binary bi-level location-allocation models
- Comparison of nested genetic and heuristic algorithms with different allocation modes to solve a model with a large number of variables

The remaining of this article is organized as follows. Section 2 and 3 are dedicated to review of the literature on pre-positioning problems and the application of single-level and bi-level programming in disaster logistics. Section 4 presents the bi-level model for location-allocation. Section 5 is related to the approaches to solve the model. Section 6 is devoted to the results of solving the optimization model. The final section presents conclusions and suggestions.

2. LITERATURE REVIEW

2. 1. Single-level Emergency Warehouses Location

Many review articles are found on the application of optimization in disaster management, of which [6-8] have especially addressed the pre-positioning problem. Balcik, Bozkir and Kundakcioglu [9] reviewed and categorized the pre-positioning based on problem characteristics and the structure of optimization models. Rawls and Turnquist [10] modeled the pre-positioning problem to determine the location of the distribution center, level of relief items and assignment of distribution centers to demand points, using the stochastic mix-integer model and the Lagrangian L-shaped method (LLSM). In their next study, they developed the previous model considering the service quality constraint [11]. Bozorgi-Amiri, Jabalameli, Alinaghian and Heydari [12] presented a multi-objective optimization model for the pre-positioning problem. They used a robust optimization approach to model uncertainty. Verma and Gaukler [4] designed two models for facility positioning in the United States' Strategic National Stockpile, one being deterministic and the other stochastic. The amount of damage inflicted upon response facilities and population centers was considered a probabilistic function of distance-damage. The results indicated that the costs of facility locationing in the stochastic model were less than those in the deterministic model. Rezaei-Malek, Tavakkoli-Moghaddam, Zahiri and Bozorgi-Amiri [13] developed a stochastic model to analyze the location of warehouses and design a distribution plan. The objective functions were considered to be the response time post-disaster and operation costs at the pre-disaster phase. Mohammadi, Ghomi and Jolai [14] presented a stochastic multi-objective model for the relief supply pre-positioning problem in which the demand covering and total cost and satisfaction ratio were considered objectives. Javadian, Modares and Bozorgi-Amiri [15] formulated the relief supply chain to locate local distribution centers and central warehouses. They proposed two multi-objective evolutionary algorithms and compared them with e-constraint method based real data in Iran case study. Aslan and Çelik [16] proposed two-stage stochastic programming in which the first stage includes the emergency warehouse location and relief supply transportation planning in the second stage. Their optimization model's innovation was taking into account the probabilistic cost of repairing damaged roads.

2. 2. Bi-level Location in Disaster Logistic

Decentralized decision-making problems are typically modeled under the Stackelberg game [17]. These problems can be modeled in the form of bi-level programming. In other words, an optimization problem as the leader (upper-level) is limited by another optimization problem as the follower (lower-level) [18]. In bi-level programming, the leader sets his/her decision first, and then the follower decides to optimize his/her goals while being aware of the decision taken by the follower. Not until does it reach the equilibrium point, this process continues [19]. The general form of the bi-level programming model is formulated as follows:

$$\begin{aligned} &\min_{x\in X, y\in Y} F(x,y) \\ &s.t \\ &y \in argmin\{f(x,y): g(x,y) \le 0, y \ge 0\} \\ &y \in Y \\ &G(x,y) \le 0 \\ &x \ge 0 \end{aligned} \tag{1}$$

where $G(x,y)$ and $g(x,y)$ denote the upper and lower level constraints, respectively.

The application of bi-level location in disaster logistics is concerned with evacuation, relief distribution, facility location, and pre-positioning. Each of these problems can be divided into two phases (pre and post-disaster). As Table 1 shows, most studies have focused on evacuation, and fewer researches have investigated the effect of pre-positioning emergency warehouses. Kongsomsaksakul, Yang and Chen [20] provided a bi-level optimization model for an evacuation plan, based on a problem presented by the Stackelberg game. Planning authority and evacuees were considered to be the leader and the follower, respectively. The leader determined the number and locations of shelters, and the follower selected the target shelter and route. Hua-li, Xun-qing and Yao-feng [21] developed a location-routing problem in the urban emergency system as bi-level programming in which the objective of the upper-level was to maximize the total time satisfaction served and the lower-level was to minimize the total cost. Li, Nozick, Xu and Davidson [22] in their study developed a scenario-based bi-level model for evacuation planning. The facility planner and network user were considered as upper and lower decision-makers, respectively. The upper-level was a two-stage stochastic programming model for location and allocation. The lower-level model was concerned with the network decision-maker regarding route selection. Camacho-Vallejo, González-Rodríguez, Almaguer and González-Ramírez [23] proposed a bi-level programming model to optimize the location of distribution centers in humanitarian logistics. The government of the affected country and non-profit international organizations were considered to be the upper-level and the lower-level, respectively. The objective functions of the upper and lower level model were known to be the minimization response time and the minimization cost of sending relief items to the storage center. Gutjahr and Dzubur [24] developed a multi-

TABLE 1. A review of recent researches on bi-level location in disaster logistic

Author's	Problem	Disaster	Upper-level		Lower-level		Solving	Uncerainty
			Decision	Objective function	Decision	Objective function		
Kongsomsaksakul, Yang and Chen [20]	Evacuation	General	Shelter location	Evacuation time(↓)	Route choice	Travel Time(↓)	Nested evolutionary	-
Ng, Park and Waller [27]	Evacuation	Manmade	Shelter location	Evacuation time(↓)	Route choice	Travel Time(↓)	Nested evolutionary	-
Apivatanagul, Davidson and Nozick [28]	Evacuation	Hurricane	location-Allocation	Risk, travel time(↓)	Route choice	Travel Time(↓)	Heuristic algorithm	+
Li, Nozick, Xu and Davidson [22]	Evacuation	Hurricane	location-Allocation	Cost(↓)	Route choice	Travel Time(↓)	Heuristic algorithm	+
Hua-li, Xun-qing and Yao-feng [21]	Facility location	General	Location	Cost(↓)	Route choice	Time satisfaction(↑)	Genetic algorithm	-
Camacho-Vallejo, González-Rodríguez, Almaguer and González-Ramírez [23]	Distribution	Earthquake	Allocation	Response time(↓)	Allocation	Shipping cost(↓)	Heuristic algorithm	-
Gutjahr and Dzubur [24]	Distribution	General	Location	Costs(↓), Uncovered demand(↓)	Allocation	Wardrop equilibrium(↓)	Exact method	-
Xu, Wang, Zhang and Tu [25]	Distribution	Earthquake	Location	Weighted distance(↓)	Route choice	Transportation times(↓)	Genetic algorithm	+
Chen, Tadikamalla, Shang and Song [29]	Pre-positioning	Earthquake	location-Allocation	Response time(↓)	Allocation	Allocation fairness(↓)	Nested differential evolution	-
Safaei, Farsad and Paydar [26]	Pre-positioning	Flood	Location-Allocation	Cost(↓)	Allocation	Supply risk(↓)	Exact method	+
Haeri, Motlagh, Samani and Rezaei [30]	Pre-positioning	Earthquake	Location-Inventory	Unsatisfied demand(↓) Cost(↓)	Allocation	Transportation costs(↓)	Fuzzy goal programming	+

objective bi-level optimization model to locate distribution centers in a relief supply chain. The aid-providing organization was regarded as the leader and the beneficiaries as followers. The objectives of the leader were to minimize the total opening cost for distribution centers and total uncovered demand, and the followers' objective was to provide user equilibrium related to the leader. Xu, Wang, Zhang and Tu [25] proposed a multi-objective bi-level programming for the location-routing problem in the post-earthquake phase. The leader (Rescue Control Center) decided on the location of distribution centers, and the follower (Logistics Company) selected an optimal route to collect relief supplies from distribution centers. Road conditions were considered a source of uncertainty in this optimization model. Safaei, Farsad and Paydar [26] utilized a bi-level programming model to locate distribution centers and select suppliers. The leader's objective function was to minimize operational costs and uncoated demands, and the lower-level aimed to minimize the risk of the supplier's choice.

3. PROBLEM DESCRIPTION

In this paper, the disaster emergency network was assumed to comprise three stages (see, Figure 1). The first stage includes a set of national warehouses, the second contains regional warehouses, and the last is comprised of demand cities. Regional warehouses receive their relief supplies from national warehouses. Demand cities are serviced only from regional warehouses, and the direct shipment of goods from national warehouses to demand cities is prohibited.

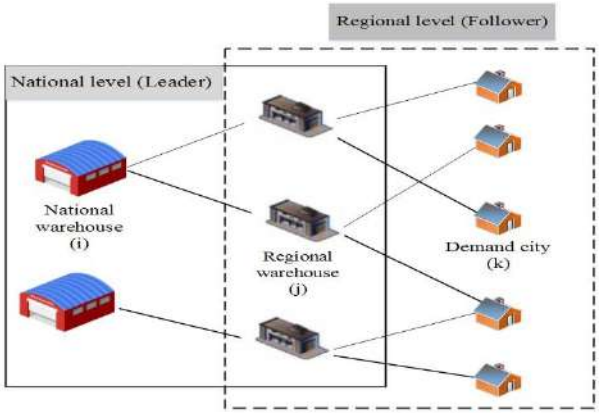

Figure 1. Bi-Level Emergency Warehouse Location-Allocation Problem (BL-EW-LAP)

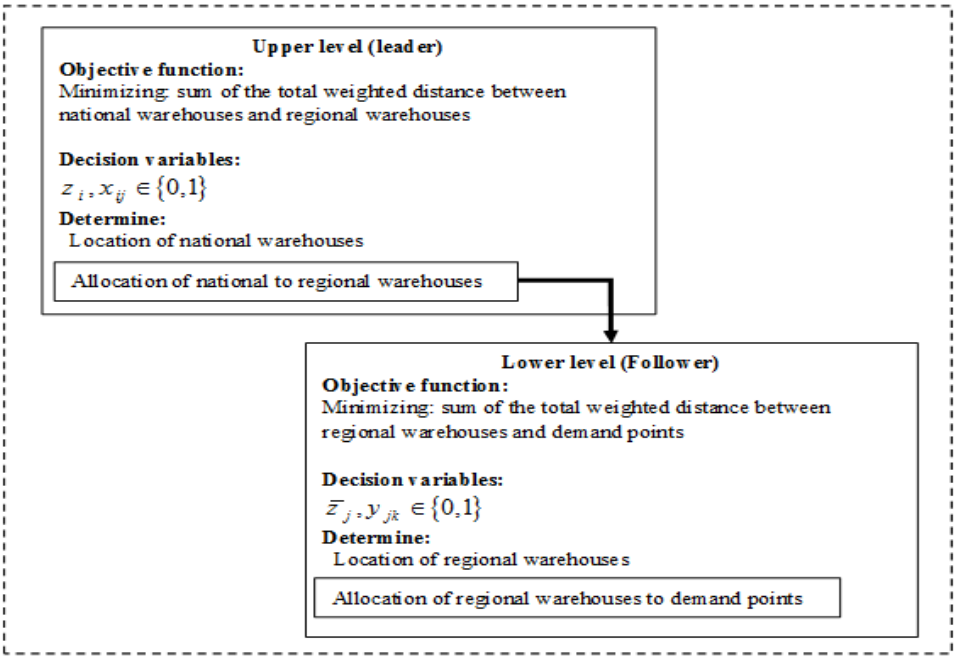

Figure 2. Framework of model for bi-level location-allocation problem

According to Figure 2. the problem has a bi-level structure for which the national top-level decision-maker is regarded as the leader and regional decision-maker as the follower. The aim of both decision-makers is to locate warehouses that completely cover all demands. The leader makes the decision on the location of national warehouses, and their assignment to regional warehouses. The case holds the same for the follower deciding on the location of regional warehouses and their assignment to demand cities. The following assumptions are considered for modeling:

- This model considers a single relief item
- The capacity of each emergency warehouse at both levels is based on the proportion of demand covered by candidate cities.
- Each demand city cannot be served by more than one regional warehouse.
- Each regional warehouse cannot be served by more than one national warehouse.
- The total capacity of all located regional warehouses must be more than the total weight of demand cities.
- The total capacity of all located national warehouses must be greater than the capacity of all regional warehouses.

There is no shipping between the same warehouses in each stage.

Indices

I set of candidate cities for national warehouses
J set of candidate cities for regional warehouses
K set of demand cities

Parameters:

urd_{ij} Road distance of national warehouse i from regional warehouse j
lrd_{jk} Road distance of regional warehouse j from demand cities k
ldw_k Demand weight associated to demand cities k
$ucap_i$ Capacity of national warehouse i
$lcap_j$ Capacity of regional warehouse j
$umax$ Number of national warehouses to establish
$lmax$ Number of regional warehouses to establish

Decision variable:

$Z_i = 1$ if a national warehouse is established at candidate city i, and 0 otherwise.
$X_{ij} = 1$ if regional warehouse j is allocated to national warehouse i, and 0 otherwise.
$\bar{Z}_j = 1$ if a regional warehouse is established at candidate city j, and 0 otherwise.
$Y_{jk} = 1$ if demand point k is allocated to regional warehouse j and 0 otherwise.
udw_j Demand weight associated to each regional warehouse j $\left(udw_j = \sum_{k=1}^{k} ldw_k * Y_{jk}\right)$

BL-EW-LAP Model:

Upper-level model (ULM)

$$min \quad \sum_{i=1}^{n}\sum_{j=1}^{m} udw_j urd_{ij} X_{ij} \tag{2}$$

$$Subject\ to: \ \sum_{i=1}^{n} Z_i = umax \tag{3}$$

$$\sum_{i=1}^{n} X_{ij} = 1 \qquad \forall j \tag{4}$$

$$\sum_{j=1}^{m} udw_j X_{ij} \le ucap_i Z_i \qquad \forall i \tag{5}$$

$$\sum_{k=1}^{k} ldw_k Y_{jk} = \sum_{i=1}^{n} udw_j X_{ij} \quad \forall j \tag{6}$$

$$Z_i\ , X_{ij} \in \{0,1\} \tag{7}$$

Lower-level model (LLM)

$$Min \ \ \sum_{j=1}^{m}\sum_{k=1}^{k} ldw_k lrd_{jk} Y_{jk} \tag{8}$$

$$Subject\ to: \ \sum_{j=1}^{m} \bar{Z}_j = lmax \tag{9}$$

$$\sum_{j=1}^{m} Y_{jk} = 1 \quad \forall k \tag{10}$$

$$\sum_{k=1}^{k} ldw_k Y_{jk} \le lcap_i \bar{Z}_j \qquad \forall j \tag{11}$$

$$\sum_{k=1}^{k} ldw_k Y_{jk} = \left(\sum_{i=1}^{n} udw_j X_{ij}\right)\bar{Z}_j \qquad \forall j \tag{12}$$

$$\bar{Z}_j\ , Y_{jk} \in \{0,1\} \tag{13}$$

Equations (2)-(7) refer to the upper-level model (ULM), whereas Equations (8)-(13) represent the lower-level model (LLM). Equations (7) and (13) set binary conditions for the decision variables of both levels. The objective function of the upper-level is to minimize the total weighed distance between national and regional warehouses. Equation (3) ensures that the maximum number of national warehouses that can be established on the candidate sites is equal to $(umax)$. From equation (4), it is guaranteed that each regional warehouse j is likely to be allocated to national warehouse i. Equation (5) is to ensure that the regional warehouse allocated to the national warehouse will not exceed the capacity. Equation (6) is a balance constraint for each regional warehouse. In other words, the amount of demand weights of cities allocated to a regional warehouse should be equal to the value allocated from the national warehouse. Similar to that of the upper-level, the objective function of the lower-level model minimizes the total weighed distance between regional warehouses and demand cities (Equation (8)). The interpretation of Equations (9)-(12) is similar to that of Equations (3)-(6). In fact, in Equation (12), udw_j is equal to $\sum_k ldw_k * Y_{jk}$; therefore, udw_j becomes a decision variable. Consequently, the equation will be non-linear. To linearize Equation (12), we utilize A_{jk} as an auxiliary variable and introduce the following sub-situations:

$$\sum_{k=1}^{k} ldw_k Y_{jk} = \sum_{i=1}^{n}\sum_{k=1}^{k} ldw_k A_{jk} X_{ij} \quad \forall j \tag{14}$$

$$A_{jk} \le Y_{jk} \quad \forall j,k \tag{15}$$

$$A_{jk} \le \bar{Z}_j \quad \forall j,k \tag{16}$$

$$A_{jk} \ge Y_{jk} + \bar{Z}_j - 1 \quad \forall j,k \tag{17}$$

$$A_{jk} \in \{0,1\} \tag{18}$$

4. SOLUTION ALGORITHMS

Several approaches have been proposed to classify algorithms for bi-level optimization problems that can be generally divided into two groups; classical and evolutionary approaches [31]. For bi-level programming to be a strong NP-hard problem [32], utilization of evolutionary algorithms for this type of problems is well-suited. Applications of evolutionary algorithms for bi-level programming can be divided into four groups: i) Single level transformation, ii) Nested, iii) Multi-objective, iv) Co-evolutionary [33]. Genetic algorithm is one of the most effective evolutionary algorithms frequently used for bi-level optimization problems. In [34-37], the genetic algorithm is utilized in the nested evolutionary sequential approach. Different types of evolutionary algorithms have also been used to solve facility location bi-level programming models. Huang and Liu [38] developed an interactive evolutionary framework for mixed integer bi-level programming in the location-allocation problem. They employed genetic algorithm for the lower-level model and enumeration vertex method for the upper-level model. Chen, Tadikamalla, Shang and Song [29] developed an improved differential evolution algorithm (IDE) to solve a binary bi-level model for the emergency warehouse location-allocation problem. The computational results of IDE were compared with the results of conventional differential evolution algorithms.

As Table 2 shows, there have been three approaches developed to tackle the BL-EW-LAP. The first approach, named Full Enumeration and Exact Algorithm (FE-EA), is based on explicit complete enumeration methods. The general structure of the second and third approaches is based on the Nested Evolutionary Approach (NEA). These approaches have been named Nested Genetic and Exact Solution (NG-ES) and Nested Heuristic Local Search and Exact Solution (NHLS-ES), for which the genetic algorithm and the heuristic local search algorithm have been proposed to solve ULM. In both approaches, the LLM has been solved by the exact algorithm. In this study, GAMS was used with branch-bound algorithm as an exact algorithm in the proposed approaches.

TABLE 2. The solution approaches for BL-EW-LAP

Name of Algorithm	Type of approach	Upper-level solution	Lower-level solution
FE-EA	Full enumeration	Exact algorithm	Exact algorithm
NG-ES	Nested evolutionary	Genetic algorithm	Exact algorithm
NHLS-ES	nested evolutionary	Heuristic local search	Exact algorithm

4. 1. Full Enumeration and Exact Algorithm (FE-EA) According to Figure 3, in the first step, the FE-EA algorithm identifies all the allocation modes of national warehouses to regional warehouses (X_{ij}). In the second and third steps, (X_{ij}) are sent to the LLM and the optimal solutions of the LLM $(\bar{Z}_j^*, Y_{jk}^*)$ are calculated by the exact algorithm. In steps 4 and 5, (Y_{jk}^*) as a parameter are sent to the ULM and the optimal solutions of the ULM (Z_i^*, X_{ij}^*) are calculated for all cases through the exact algorithm. Finally, the best solution of the ULM is determined to be the optimal solution for the bi-level problem.

4. 2. NEA for the BL-EW-LAP Model In this approach, in the first step, an initial solution $(Z_i, X_{ij}, \bar{Z}_j, Y_{jk})$ is generated for the bi-level model. In the next step, X_{ij} is sent as a parameter for LLM. In the sequel, through the exact algorithm, optimal solutions of the LLM $(\bar{Z}_j^*, Y_{jk}^*)$ are calculated. In the next step, the values $(\bar{Z}_j^*, Y_{jk}^*)$ are transferred to ULM and replaced with the previous solutions. Then, the evaluation phase is performed. In this framework, the genetic algorithm and the heuristic local search algorithm are proposed separately. In the initial solution phase, $(Z_i, \bar{Z}_j)$ are generated randomly, and (X_{ij}, Y_{jk}) are calculated through the two heuristic allocation algorithms (Demand algorithm or Average distance algorithm), presented in [39]. In both heuristic allocation algorithms, assignment of facilities is based on the nearest distances. The difference between heuristic methods is the sorting criteria of nodes and their priority determination in the assignment. In the demand algorithm (DE), regional warehouses and demand cities with higher demand weights (udw_j, ldw_k) are of higher priorities. In Average distance algorithm (AD), regional warehouses with the highest average distance to national warehouses and demand cities with the highest average distance to the regional warehouses are of higher priorities. Since allocation processes at upper and lower levels are performed through two allocation methods, in the NEA framework, four algorithms can be separately used to solve the model for each approach.

4. 3. Nested Genetic-Exact Solution (NG-ES) Generally, this algorithm consists of two phases; the initial solution generation and the evaluation phase.

1: **Construct** all allocation modes of the ULM (X_{ij})
2: **Let** X_{ij} be as a parameters into the LLM
3: **Calculate** $\bar{Z}_j^*, Y_{jk}^*$ by an exact algorithm
4: **Let** Y_{jk}^* be as a parameters into the ULM
5: **Calculate** $Z_i^*, X_{ij}^*, OF_{ULM}^*$ for each Y_{jk}^* by an exact algorithm
6: **Find** Min$\{OF_{ULM}^*\}$

Figure 3. Pseudo-code of FE-EA algorithm

Figure 13 presents the Pseudo code of NG-ES. In the initial solution phase, an initial population (POP_0) is generated. As Figure 4 shows, the structure of the chromosome is composed of two parts, the first one assigned to locating the national warehouse and the second dedicated to locating the regional warehouse. The length of the array for both parts is equal to the maximum number of warehouses, which can be placed at national and regional levels($umax, lmax$). A solution is made by unique integers between 1 and m for part 1 and unique integers between 1 and n for part 2. In this phase, demand cities are allocated to regional warehouses, and (Y_{jk}) is calculated by one of the heuristic allocation algorithms. In the next step, the weight associated to each regional warehouse (udw_j) is calculated using equation ($\sum_k ldwY_{jk}$). Again, through the heuristic allocation algorithm, regional warehouses are allocated to the national warehouse, and (X_{ij}) is calculated. Next, (X_{ij}) is sent to LLM as the parameter. In the next step, LLM is solved using the exact algorithm. Afterward, the optimal solution of LLM (Y_{jk}^*) is sent for ULM. Regarding (Y_{jk}^*), (X_{ij}) is modified and replaced with the previous solution.

In the evaluation phase of the algorithm, crossover and mutation operators were applied to the existing solutions. A two-point crossover operator was designed according to Figure 4. In the crossover operation, one of the two parts of the chromosome is randomly selected with the same chance (probability of selection = 0.5), and the two-point crossover operator is applied to that part. If each chromosome part contains a duplicate index indicating an infeasible solution, it will be modified as observed in Figure 5. Similar to the crossover operator, the mutation operation selects one part of the chromosome randomly with the same chance. Afterward, one cell is randomly selected and replaced with an index not existing in the parent. Therefore, the mutation operator produces an offspring from one parent chromosome.

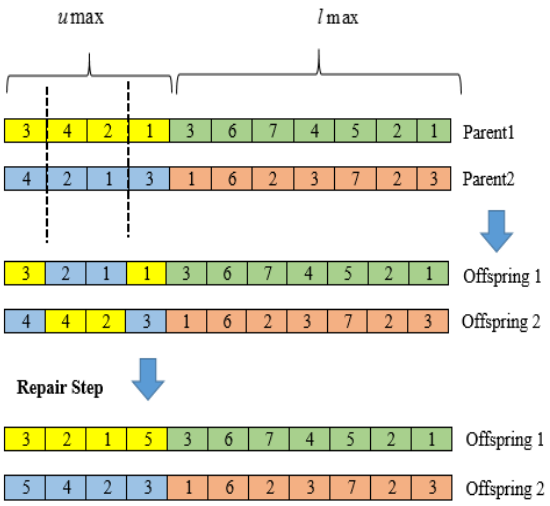

Figure 4. Two-point crossover operator

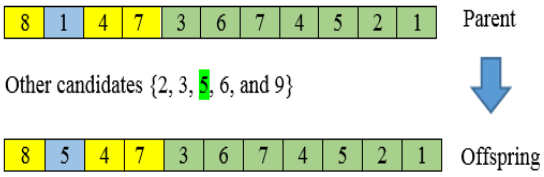

Figure 5. Mutation operator

4. 4. Nested Heuristic Local Search-Exact Solution (NHLS-ES) The general structure of NHLS-ES is similar to that of NG-ES. Figure 12 presents the Pseudo code of the NHLS-ES algorithm. The initial solution generation is the same as the NG-ES algorithm. The evaluation phase uses the mutation operator to generate a neighborhood solution. Mutation operator selects one part of the chromosome randomly. The probability of the selection for the first and second parts of the chromosome is calculated based on formulas (19) and (20), respectively. Figure shows the neighbor search operator.

$$p_{first} = u\max/(u\max + l\max) \quad (19)$$

$$p_{second} = l\max/(u\max + l\max) \quad (20)$$

The mutation operator is sequentially three-point, two-point, and one-point. In each iteration of the mutation process, if it is better than the best solution, the objective value of a new solution is considered the best solution. At each stage of mutation, the Sub-Iter is specified as the number of internal repetitions. If in that number of repetitions, the objective value is not improved, the type of mutation is changed from three-point to two-point and eventually from two-point to one-point. Generally, unless the best answer improves the number of iterations ($MaxCon$), the algorithm stops.

5. RESULTS

5. 1. Case Study The model parameters were adjusted based on the Iran case study. Nine large cities and all centers of provinces in Iran (31 provinces) were selected as national and regional warehouses candidates, respectively. Furthermore, 118 cities with more than 150000 people were considered demand cities. According to formula (21), (udw_k) is calculated based on the earthquake risk (ER) and the population of the city (PO). Population statistic was extracted from the

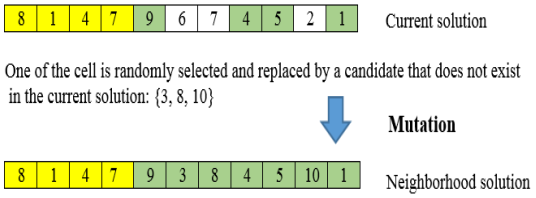

Figure 6. Neighbor search operator

Statistical Center of Iran website based on the Population and Housing Census (2016). The Iranian Code of Practice for Seismic Resistant Resign of Building, Standard No.2800 was used to calculate the earthquake risk of the cities (ER).

$$udw_k = ER_k * PO_k \quad (21)$$

In this paper, to calculate the distances matrix between nodes (urd_{ij}, lrd_{jk}), road distance was obtained from the Google Maps Platform and Distance Matrix API service. A code was written in Python programming language to determine the distance matrix of nodes (urd_{ij}, lrd_{jk}).

5. 2. Computational Results The small size problem was solved by FE-EA, and the optimal location and allocation were reported. When the lower-level problem was solved to optimality, the performance assessment of the bi-level problem was conducted using the upper-level objective [33]. Table 3 reports the numerical results obtained by NG-ES and NLS-ES algorithms for the upper-level. As Table 3 show, two algorithms from NG-ES and one from NLS-ES were obtained as the optimal solution.

Owing to the inefficiency of FE-EA in large-size problems, it is only solved by NHLS-S and NG-ES. Tables 4 and 5 report the best and the average values for all algorithms. The minimum value of the leader's objective function is related to NG-ES with the DE-AD code. This algorithm uses the DE and AD algorithm to allocate facilities at upper and lower levels, respectively. As Figures 7 and 8 show, based on the best and average value, NG-ES (DE-AD) outperforms other algorithms and is selected as the appropriate algorithm for BL-EW-LAP. According to Figure 9, all types of NG-ES algorithm have better performance than NHLS-ES for standard deviation. In addition, NHLS-ES is converged much faster than NG-ES is (Figure 10). Since BL-EW-LAP is a strategic and long-term problem, CPU time is not considered the important criterion to select an appropriate algorithm.

Figure 11 illustrates the behavior of the objective functions and the effect of the leader's response on the follower for different solutions. The leader is monotonically decreasing, while the follower has some fluctuation. Table 6 depicts the effect of parameters $(umax, lmax)$ change on the value of the objective function. With the increasing number of national warehouses, the objective function of both levels is reduced, but the increase in the number of regional warehouses does not affect the objective function of the leader and follower models.

TABLE 3. Results of all algorithm for the upper-level in the small size problem

NHLS-ES	NG-ES	Algorithm code
912589320.2	912589320.2	DE-DE
946221123	912589320.2	DE-AD
946221123	946221123	AD-DE
946221123	1101597134	AD-AD

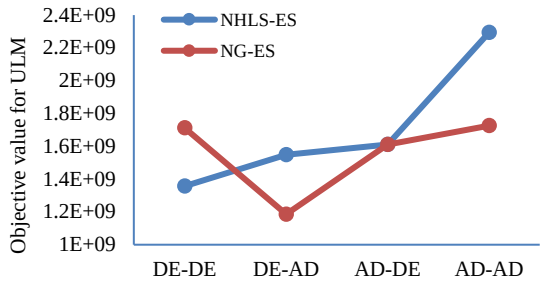

Figure 7. Best solution (NG-ES,NHLS-ES)

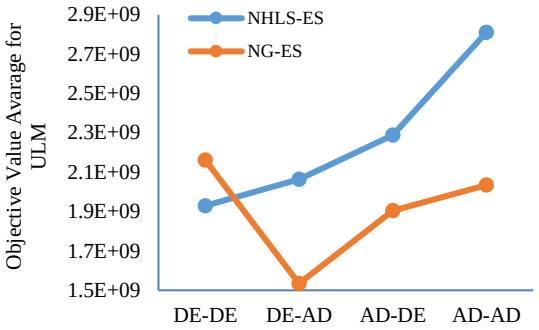

Figure 8. Average of solutions (NG-ES,NHLS-ES)

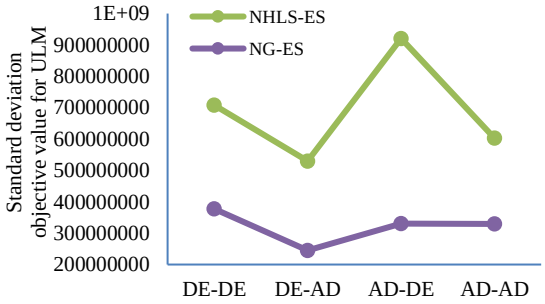

Figure 9. Standard deviation of solutions (NG-ES,NHLS-ES)

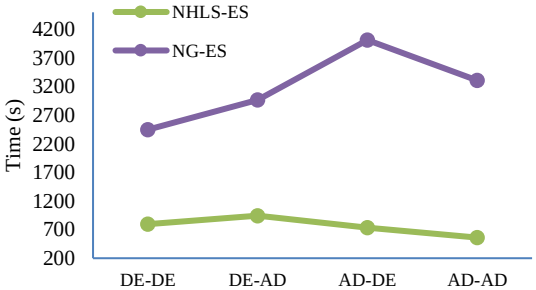

Figure 10. CPU time of Algorithms (NG-ES,NHLS-ES)

TABLE 4. Results of NHLS-ES algorithm for the large size problem

Algorithm code	Average of leader solutions	Best solution Leader	Best solution follower	Standard deviation	CPU time
DE-DE	1929385300	1356849145	19240511260	708256048.8	797.2
DE-AD	2062886677	1548416948	12505727872	529921735	943.8
AD-DE	2287684536	1610141001	16760613398	920550513	736.8
AD-AD	2810441087	2293225935	15642906833	602752285.6	560.3

TABLE 5. Results of NG-ES algorithm for the large size problem

Algorithm code	Average of leader solutions	Best solution Leader	Best solution follower	Standard deviation	CPU time
DE-DE	2161814222	1186002289	15220205195	377314775	2448
DE-AD	1665766868	2135123991	12515807758	449096980	2821
AD-DE	1904908088	1610141001	13067224449	330637134	4015
AD-AD	2033692902	1725735466	16780294548	329650646	3307

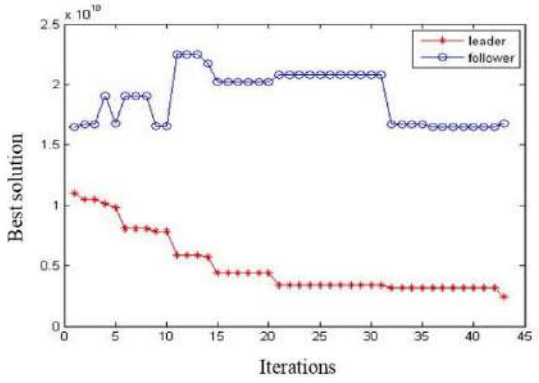

Figure 11. The variations of objective functions

TABLE 6. Impact of change $(umax, lmax)$ on objective functions

$umax$	$lmax$	Leader objective function	Follower objective function
2	3	912589320.2	2913096362
2	4	912589320.2	2913096362
2	5	912589320.2	2913096362
3	4	768888241.7	2709942156
3	5	768888241.7	2709942156

6. CONCLUSION

In this paper, a new bi-level programming model was designed for location-allocation emergency warehouses in the pre-positioning relief supply problem. In this model, the leader makes a decision on the location and allocation of national warehouses by predicting the location of regional warehouses and allocating them to demand cities. The application of this type of modeling suits countries where the design of the relief network is decentralized. The contribution of our problem in the pre-positioning literature is to model the location-allocation emergency warehouses problem in the framework of bi-level optimization. This model can also be used in the decentralized business supply chain. One requirement of logistic planning in disaster management is a limitation in the dispatch time of relief items from national warehouses to regional warehouses and the regional warehouse to service demand points. Accordingly, as a future suggestion, some constraints can be considered on the response time or coverage radius for national and regional warehouses. This helps the optimization model to become more realistic. Furthermore, there is more than one decision-maker at national and regional levels, leading to the design of multi-leader and multi-follower bi-level models. This kind of problem has more complexity than single leader/follower bi-level programming, especially for discrete problems. Another modeling suggestions is to consider various objective functions for upper-level and lower-level models. Furthermore, this problem can be modeled in the context of critical facility location.

Based on the comparison of NG-ES and NHLS-ES, it can be concluded that the developed algorithms compute the solution of the acceptable accuracy with a reasonable amount of time for a real problem. The NG-ES approach exhibited better results in this paper in terms of the standard deviation of solutions. The genetic algorithm exploits the well observed solutions, and it increases the intensification of the algorithm. NG-ES (DE-AD) outperformed all the sub-groups of NG-ES and NHLS-ES with the best, average and standard deviation of solutions for models with many variables. The main reasons behind the superiority of NG-ES (DE-AD) over three other nested genetic algorithms are concerned with the allocation method. The solution generation of all modes of NG-ES and NHLS-ES is a bottom-up approach (lower-level model to upper-level model), meaning that to calculate (X_{ij}), (Y_{jk}) must be calculated first. In certain cases, the generation of good solutions for the follower

may exclude the generation of good solutions for the leader. This mechanism reduced the exploration of the search space (diversification), influencing its performance considerably. The development of nested evolutionary with different initial solution mechanisms and an exact method to solve these large size problems precisely can be a suggestion for further research.

7. REFRENCES

1. CRED, *Disaster data: A balanced perspective*. 2015.http://reliefweb.int/report/world/cred-crunch-newsletter-issue-no-41-february-2016-disaster-data-balanced-perspective.
2. Gharib, Z., Bozorgi-Amiri, A., Tavakkoli-Moghaddam, R. and Najafi, E., "A cluster-based emergency vehicle routing problem in disaster with reliability", ***Scientia Iranica,Transaction E, Industrial Engineering***, Vol. 25, No. 4, (2018), 2312-2330, DOI: 10.24200/SCI.2017.4450.
3. Akkihal, A.R., "Inventory pre-positioning for humanitarian operations", Massachusetts Institute of Technology, Doctoral dissertation, (2006),
4. Verma, A. and Gaukler, G.M., "Pre-positioning disaster response facilities at safe locations: An evaluation of deterministic and stochastic modeling approaches", ***Computers & Operations Research***, Vol. 62, (2015), 197-209, DOI: 10.1016/j.cor.2014.10.006.
5. Rawls, C.G. and Turnquist, M.A., "Pre-positioning and dynamic delivery planning for short-term response following a natural disaster", ***Socio-Economic Planning Sciences***, Vol. 46, No. 1, (2012), 46-54, DOI: 10.1016/j.seps.2011.10.002.
6. Caunhye, A.M., Nie, X. and Pokharel, S., "Optimization models in emergency logistics: A literature review", ***Socio-Economic Planning Sciences***, Vol. 46, No. 1, (2012), 4-13, DOI: 10.1016/j.seps.2011.04.004.
7. Anaya-Arenas, A.M., Renaud, J. and Ruiz, A., "Relief distribution networks: A systematic review", ***Annals of Operations Research***, Vol. 223, No. 1, (2014), 53-79, DOI: 10.1007/s10479-014-1581-y.
8. Hoyos, M.C., Morales, R.S. and Akhavan-Tabatabaei, R., "Or models with stochastic components in disaster operations management: A literature survey", ***Computers & Industrial Engineering***, Vol. 82, (2015), 183-197, DOI: 10.1016/j.cie.2014.11.025.
9. Balcik, B., Bozkir, C.D.C. and Kundakcioglu, O.E., "A literature review on inventory management in humanitarian supply chains", ***Surveys in Operations Research management Science***, Vol. 21, No. 2, (2016), 101-116, DOI: 10.1016/j.sorms.2016.10.002.
10. Rawls, C.G. and Turnquist, M.A., "Pre-positioning of emergency supplies for disaster response", ***Transportation research part B: Methodological***, Vol. 44, No. 4, (2010), 521-534, DOI: 10.1016/j.trb.2009.08.003.
11. Rawls, C.G. and Turnquist, M.A., "Pre-positioning planning for emergency response with service quality constraints", ***OR Spectrum***, Vol. 33, No. 3, (2011), 481-498, DOI: 10.1007/s00291-011-0248-1.
12. Bozorgi-Amiri, A., Jabalameli, M.S., Alinaghian, M. and Heydari, M., "A modified particle swarm optimization for disaster relief logistics under uncertain environment", ***The International Journal of Advanced Manufacturing Technology***, Vol. 60, No. 1-4, (2012), 357-371, DOI: 10.1007/s00170-011-3596-8.
13. Rezaei-Malek, M., Tavakkoli-Moghaddam, R., Zahiri, B. and Bozorgi-Amiri, A., "An interactive approach for designing a robust disaster relief logistics network with perishable commodities", ***Computers & Industrial Engineering***, Vol. 94, (2016), 201-215, DOI: 10.1016/j.cie.2016.01.014.
14. Mohammadi, R., Ghomi, S.F. and Jolai, F., "Prepositioning emergency earthquake response supplies: A new multi-objective particle swarm optimization algorithm", ***Applied Mathematical Modelling***, Vol. 40, No. 9, (2016), 5183-5199, DOI: 10.1016/j.apm.2015.10.022.
15. Javadian, N., Modares, S. and Bozorgi-Amiri, A., "A bi-objective stochastic optimization model for humanitarian relief chain by using evolutionary algorithms", ***International Journal of Engineering, Transaction A: Basics***, Vol. 30, No. 10, (2017), 1526-1537.
16. Aslan, E. and Çelik, M., "Pre-positioning of relief items under road/facility vulnerability with concurrent restoration and relief transportation", ***IISE Transactions***, Vol. 51, No. 8, (2019), 847-868, DOI: 10.1080/24725854.2018.1540900.
17. Simaan, M. and Cruz Jr, J.B., "On the stackelberg strategy in nonzero-sum games", ***Journal of Optimization Theory and Applications***, Vol. 11, No. 5, (1973), 533-555.
18. Sakawa, M. and Nishizaki, I., "Cooperative and noncooperative multi-level programming, Springer Science & Business Media, Vol. 48, (2009).
19. Bracken, J. and McGill, J.T., "Mathematical programs with optimization problems in the constraints", ***Operations Research***, Vol. 21, No. 1, (1973), 37-44.
20. Kongsomsaksakul, S., Yang, C. and Chen, A., "Shelter location-allocation model for flood evacuation planning", ***Journal of the Eastern Asia Society for Transportation Studies***, Vol. 6, (2005), 4237-4252, DOI: 10.11175/easts.6.4237.
21. Hua-li, S., Xun-qing, W. and Yao-feng, X., A bi-level programming model for a multi-facility location-routing problem in urban emergency system, in Engineering education and management. 2012, Springer.75-80.
22. Li, A.C., Nozick, L., Xu, N. and Davidson, R., "Shelter location and transportation planning under hurricane conditions", ***Transportation Research Part E: Logistics and Transportation Review***, Vol. 48, No. 4, (2012), 715-729, DOI: 10.1016/j.tre.2011.12.004.
23. Camacho-Vallejo, J.-F., González-Rodríguez, E., Almaguer, F.-J. and González-Ramírez, R.G., "A bi-level optimization model for aid distribution after the occurrence of a disaster", ***Journal of Cleaner Production***, Vol. 105, (2015), 134-145, DOI: 10.1016/j.jclepro.2014.09.069.
24. Gutjahr, W.J. and Dzubur, N., "Bi-objective bilevel optimization of distribution center locations considering user equilibria", ***Transportation Research Part E: Logistics and Transportation Review***, Vol. 85, (2016), 1-22, DOI: 10.1016/j.tre.2015.11.001.
25. Xu, J., Wang, Z., Zhang, M. and Tu, Y., "A new model for a 72-h post-earthquake emergency logistics location-routing problem under a random fuzzy environment", ***Transportation Letters***, Vol. 8, No. 5, (2016), 270-285, DOI: 10.1080/19427867.2015.1126064.
26. Safaei, A.S., Farsad, S. and Paydar, M.M., "Robust bi-level optimization of relief logistics operations", ***Applied Mathematical Modelling***, Vol. 56, (2018), 359-380, DOI: 10.1016/j.apm.2017.12.003.
27. Ng, M., Park, J. and Waller, S.T., "A hybrid bilevel model for the optimal shelter assignment in emergency evacuations", ***Computer-Aided Civil and Infrastructure Engineering***, Vol. 25, No. 8, (2010), 547-556, DOI: 10.1111/j.1467-8667.2010.00669.x.
28. Apivatanagul, P., Davidson, R.A. and Nozick, L.K., "Bi-level optimization for risk-based regional hurricane evacuation planning", ***Natural hazards***, Vol. 60, No. 2, (2012), 567-588, DOI: 10.1007/s11069-011-0029-9.
29. Chen, Y.-x., Tadikamalla, P.R., Shang, J. and Song, Y., "Supply allocation: Bi-level programming and differential evolution

algorithm for natural disaster relief", ***Cluster Computing***, Vol., (2017), 1-15, DOI: 10.1007/s10586-017-1366-6.

30. Haeri, A., Motlagh, S.-M.H., Samani, M.R.G. and Rezaei, M.S., "A bi-level programming approach for improving relief logistics operations: A real case in kermanshah earthquake", ***Computers & Industrial Engineering***, (2020), 106532, DOI: 10.1016/j.cie.2020.106532.
31. Sinha, A., Malo, P. and Deb, K., "A review on bilevel optimization: From classical to evolutionary approaches and applications", ***IEEE Transactions on Evolutionary Computation***, Vol. 22, No. 2, (2017), 276-295, DOI: 10.1109/TEVC.2017.2712906.
32. Hansen, P., Jaumard, B., Savard, G. and Computing, S., "New branch-and-bound rules for linear bilevel programming", ***SIAM Journal on Scientific***, Vol. 13, No. 5, (1992), 1194-1217.
33. Talbi, E.-G., A taxonomy of metaheuristics for bi-level optimization, in Metaheuristics for bi-level optimization. 2013, Springer.1-39.
34. Shepherd, S. and Sumalee, A., "A genetic algorithm based approach to optimal toll level and location problems", ***Networks and Spatial Economics***, Vol. 4, No. 2, (2004), 161-179, DOI: 10.1023/B:NETS.0000027771.13826.3a.
35. Wang, G.-m., Wang, X.-j., Wan, Z.-p. and Jia, S.-h., "An adaptive genetic algorithm for solving bilevel linear programming problem", ***Applied Mathematics and Mechanics***, Vol. 28, No. 12, (2007), 1605-1612, DOI: 10.1007/s10483-007-1207-1.
36. Zuo, Z., Kanamori, R., Miwa, T. and Morikawa, T., "A study of both optimal locations and toll levels road pricing using genetic algorithm", ***Journal of the Eastern Asia Society for Transportation Studies***, Vol. 8, (2010), 145-156, DOI: 10.11175/easts.8.145.
37. Parvasi, S.P., Mahmoodjanloo, M. and Setak, M., "A bi-level school bus routing problem with bus stops selection and possibility of demand outsourcing", ***Applied Soft Computing***

Vol. 61, No., (2017), 222-238, DOI: 10.1016/j.asoc.2017.08.018.

38. Huang, B. and Liu, N., "Bilevel programming approach to optimizing a logistic distribution network with balancing requirements", ***Transportation Research Record***, Vol. 1894, No. 1, (2004), 188-197, DOI: 10.3141/1894-20.
39. Saranwong, S. and Likasiri, C., "Product distribution via a bi-level programming approach: Algorithms and a case study in municipal waste system", ***Expert Systems with Applications***, Vol. 44, (2016), 78-91, DOI: 10.1016/j.eswa.2015.08.053.

8. Appendix: Pseudo Code of Solution Algorithms

1: **Input**
2: **Let** $Sub-iter$ be internal loop iteration
3: **Let** $Lmax$ be number of local search method
4: **Let** CON be a counter that initially set to 0
5: **Let** $MaxCON$ be the maximum number of trials that the algorithm is not improved improve the solution*/
6: **Generate** an initial solution/*integer string* /
7: **For** all chromosomes
8: **Calculate** Y_{jk} by the allocation heuristic algorithm
9: **Calculate** $udw_j = \sum_k ldw_j Y_{jk}$
10: **Calculate** X_{ij} by the allocation heuristic algorithm
11: **Let** X_{ij} be as a parameters into the LLM
12: **Calculate**, Y_{jk}^* by an exact algorithm
13: **Let** Y_{jk}^* be as a parameters into the ULM
14: **Update** udw_j and calculate X_{ij} by the allocation heuristic algorithm based on chromosome
15: L=1
16: Best Solution = Current Solution
17: **While** $Con < MaxCon$
18: iter =1
19: **Repeat**
20: **Create** new neighborhood by mutation method
21: **Calculate** new neighborhood objective function
22: **If** $F_{New} \leq F_{Best}$
23: Current solution = new neighborhood
24: Iter=iter+1
25: **Until** (iter ≤ Sub-iter)
26: **If** current solution < Best Solution
27: Best Solution = current solution
28: L=L
29: Con=0
30: Else
31: L=L+1
32: **If** L>Imax
33: L=1
34: Con=Con+1
35: End
36: **Output** best solution found

Figure 12. Pseudo-code of NHLS-ES

1. **Input**
2. **Let** p_c be the percentage of Crossovers population
3. **Let** p_m be the percentage of Mutation population
4. **Let** $npop$ be the size of population
5. **Let** spr be the percentage of Selection pressure rate
6. **Let** CON be a counter that initially set to 0
7. **Let** $MaxCON$ the maximum number of trials that the algorithm is not improved
8. Selection method of parent /*Roulette wheel selection*/

Initial Solution generation

9. **Generate** an initial population of chromosomes (pop_0) /*integer string*/
10. **For** all chromosomes
11. **Calculate** Y_{jk} by the allocation heuristic algorithm
12. **Calculate** $udw_j = \sum_k ldw_j Y_{jk}$
13. **Calculate** X_{ij} by the allocation heuristic algorithm
14. **Let** X_{ij} be as a parameters into the LLM
15. **Calculate** Y_{jk}^* by an exact algorithm
16. **Let** Y_{jk} be as a parameters into the ULM
17. **Update** udw_j and calculate X_{ij} by the allocation heuristic algorithm

Evaluation phase:

18. **While** $CON < MaxCON$
19. $n_c = npop * p_c$ / * number of chromosomes that will be generated by crossover*/
20. $i = 1$;
21. **While** $i \leq n_c/2$
22. Select two chromosomes as parents based on Roulette wheel selection
23. Generate two offspring chromosomes by crossover operator
24. $n_m = npop * p_m$; / * number of chromosome that will be mutated*/
25. $j = 1$;
26. **While** $j \leq n_m$
27. Select a random chromosome
28. Mutate chromosome
29. **For** each new chromosome
30. Repeat 10 to 17 steps
31. Calculate OF_{ULM} of each new chromosome
32. **Merge and sort population**

Update stop condition

33. If the best solution not improve
34. $CON = CON + 1$
35. Else
36. $CON = 0$
37. **End**
38. **Output** best solution

Figure 13. Pseudo-code of NG-ES

Persian Abstract

چکیده

در برخ کشورها مدیران منطقه ای تلاش می کنند تسهیلات ملی را به نفع مناطق خود تخصیص دهند که این موضوع باعث اختلال در نظام تصمیم گیری دولت مرکزی می شود. با توجه به ساختار سلسله مراتبی این نوع تصمیم گیری ها، استفاده از مدلهای بهینه سازی کلاسیک از کارایی مناسبی در تصمیم گیری برخوردار نمی باشد و استفاده از رویکردهای بهینه سازی چند سطحی می تواند باعث افزایش اثربخشی برنامه ها شود. مقاله ما با هدف بکارگیری رویکرد برنامه ریزی دوسطحی در مساله مکانیابی انبارهای اضطراری بحران انجام شده است. یک زنجیره تامین امدادی سه لایه ای شامل انبارهای ملی، منطقه ای و نقاط تقاضا به عنوان شبکه امداد رسانی در نظر گرفته شده است. مدل سطح بالا در خصوص مکان یابی انبارهای ملی و تخصیص آنها به انبارهای منطقه ای تصمیم گیری میکند. مدل سطح پایین نیز مکان انبارهای منطقه ای و تخصیص آنها به نقاط تقاضا را مشخص میکند. ساختار هر دو مدل براساس مساله مکان یابی-تخصیص میانه تنظیم شده است. سه روش براساس رویکرد حل براساس شمارش کامل و دو الگوریتم تکاملی تودرتو (الگوریتم ژنتیک و جستجو همسایگی) ارائه شده است. مدل در ایران استفاده شده است و اثربخشی الگوریتمها برای دو سایز مساله تحلیل شده است. نتایج بدست آمده نشان دهنده عملکرد مناسب رویکردهای حل می باشد.

International Journal of Engineering

Journal Homepage: www.ije.ir

Comparative Performance of Machine Learning Ensemble Algorithms for Forecasting Cryptocurrency Prices

V. Derbentsev[a], V. Babenko*[b], K. Khrustalev[c], H. Obruch[d], S. Khrustalova[c]

[a] *Informatics and Systemology Department, Institute Information Technologies in Economics, Kyiv National Economic University named after Vadim Hetman, Kyiv, Ukraine*

[b] *International E-commerce and Hotel & Restaurant Business Department, V. N. Karazin Kharkiv National University, Kharkiv, Ukraine*

[c] *Department of Computer-Integrated Technologies, Automation and Mechatronics, Kharkiv National University of Radio Electronics, Kharkiv, Ukraine*

[d] *Department of Economics and Management of Industrial and Commercial Business, Ukrainian State University of Railway Transport, Ukraine*

PAPER INFO

Paper history:
Received 06 July 2020
Received in revised form 13 August 2020
Accepted 03 September 2020

Keywords:
Cryptocurrencies Time Series
Short-term Forecasting
Machine Learning
Random Forest
Gradient Boosting

ABSTRACT

This paper discusses the problems of short-term forecasting of cryptocurrency time series using a supervised machine learning (ML) approach. For this goal, we applied two of the most powerful ensemble methods including Random Forests (RF) and Stochastic Gradient Boosting Machine (SGBM). As the dataset was collected from daily close prices of three of the most capitalized coins: Bitcoin (BTC), Ethereum (ETH) and Ripple (XRP), and as features we used past price information and technical indicators (moving average). To check the effectiveness of these models we made an out-of-sample forecast for selected time series by using the one step ahead technique. The accuracy rate of the forecasted prices by using RF and GBM were calculated. The results verify the applicability of the ML ensembles approach for the forecasting of cryptocurrency prices. The out of sample accuracy of short-term prediction daily close prices obtained by the SGBM and RF in terms of Mean Absolut Percentage Error (MAPE) for the three most capitalized cryptocurrencies (BTC, ETH, and XRP) were within 0.92-2.61 %.

***doi**: 10.5829/ije.2021.34.01a.16*

1. INTRODUCTION[1]

Cryptocurrencies are one of the popular modern financial assets. Despite the fact that in the last decade, since the appearance of the first cryptocurrency namely Bitcoin, their exchange rates and market capitalization have undergone several dramatic ups and downs. The total market capitalization of cryptocurrencies amounted to $ 15.6 billion at the beginning of 2017; at the beginning of 2020 it was about $ 230 billion, and the maximum market cap had reached almost a trillion dollars ($ 860 billion) in the middle of 2018 [1].

The role and position of cryptocurrencies in the global financial market is a controversial and debatable topic [2-4]. Significant fluctuations in their prices and legal uncertainty of the transactions performed with them in most countries causes significant uncertainty and, as a result, high investment risk of these assets.

A vast majority of economists and researchers inclined to believe that cryptocurrencies are speculative financial assets, intended primarily for short-term investments horizon (see, for example [2-6]). That's why for decision-making in the cryptocurrency market it would be necessary to develop adequate forecasting tools.

It should be noted, that cryptocurrency time series are characterized by high volatility, non-Gaussian distributions, heavy tails and the presence of abnormal and extreme events [7-8]. At the same time, the key drivers which determine the price of cryptocoins are still poorly understood and identified [4-6].

*Corresponding Author Institutional Email: vitalinababenko@karazin.ua (V. Babenko)

Please cite this article as: V. Derbentsev, V. Babenko, K. Khrustalev, H. Obruch, S. Khrustalova, Comparative Performance of Machine Learning Ensemble Algorithms for Forecasting Cryptocurrency Prices, International Journal of Engineering, Transactions A: Basics Vol. 34, No. 01, (2021) 140-148

Therefore classical approaches based on statistical frameworks, time-series and econometric models, which were efficiently used for modeling and forecasting traditional assets (fiat currencies, commodity prices, securities value, etc.), in the case of cryptocurrencies have proven to be ineffective.

Thus, the main purpose of our research is exploring and comparing the efficiency of Machine Learning (ML) ensembles-based approaches, such as Random Forest (RF) and Gradient Boosting Machine (GBM) on the problem of short-term forecasting of cryptocurrency prices.

2. LITERATURE REVIEW

Recently, ML methods and algorithms, which have shown significant effectiveness in many areas of complex systems research (biomedicine, neurorobotics, image and voice analysis, pattern recognition, machine translation, etc.) [9-12], have been applied to financial time series analysis [13-16].

The most common ML algorithms in financial forecasting are Artificial Neural Networks (ANNs) of various architectures [16-20], and Support Vector Machines (SVM) [20-23].

These approaches have proven to be effective for the forecasting of financial assets [19-24] and cryptocurrencies [18, 23, 25-28].

Several studies [18, 26, 28] presented the results of predicting cryptocurrency exchange rates by using ARIMA (as baseline) and different ML approaches. Summarizing their results allows us to conclude that ML algorithms outperform time series models in predicting both cryptocurrency prices (or returns) and their volatility.

There is a number of research papers (see, for example, Makridakis et al., [13]; Bontempi et al., [14]; Persio and Honchar, [15]), which presented results stating that ANN outperformed other ML methods at forecasting cryptocurrencies prices.

However, Hitam and Ismail [27] compared forecasting performance of different ML algorithms by using cryptocurrency time series (prices). They tested ANNs, SVM and Boosted NN for top-six cryptocoins and conducted that SVM has better predictive accuracy (in terms of Mean Absolut Percentage Error, MAPE) than others.

Mallqui and Fernandes [28] examined Bitcoin price direction and daily exchange rate predictions using ANN and SVM. Regarding obtained results, the SVM presented the best performance for both price trend change (classification problem, accuracy 59.45%) and exchange rate predictions (regression problem, MAPE within 1.52-1.58%).

During the last few years the main attention of researchers has been focused on the application of Deep Learning (DL) approaches in the field of financial forecasting, including cryptocurrencies [18, 29-33].

Sezer et al. [29] recently prepared a detailed overview devoted to applying DL techniques for forecasting financial time series.

McNally [18] focused on predicting Bitcoin trends (classification problem) by using Recurrent Neural Network (RNN) and Long Short Term Memory (LSTM). He used only past prices and several technical indicators such as the simple moving average for prediction. The accuracy that he obtained for predicting changes in the direction of the Bitcoin trend was within 51-52% for both of the methods.

Kumar and Rath [22] compared the forecasting ability of LSTM and Multi-Layer perceptron (MLP) for predicting the direction of price changes in Etherium. They used daily, hourly, and minute data and concluded that LSTM requires significantly more training time; despite this it did not significantly outperform MLP.

In the study of Yao et al. [31], devoted DL forecasting cryptocurrency prices, was used extended dataset, which included lagged prices value, market cap, trading volume, circulating and maximum supply. According to their results the prediction accuracy has been significantly increased when a wider dataset is used.

Chen et al. [32] developed two stage forecasting strategy. On the first stage they used ANN and RF for feature selection of several economic and technological factors, and on the second stage they made predictions on the Bitcoin exchange rate by using LSTM. As to their results, LSTM had better forecasting performance than ARIMA and SVM. Moreover, incorporating economic and technological factors as additional predictors increases prediction accuracy.

It should be noted that if we are solving the complex problem of regression (forecasting) or classification, it often happens that none of the models provides the desired quality and accuracy. In this cases, we can build an ensemble of individual models (algorithms) in which the errors of each other are mutually compensated.

This idea is based on another powerful class of ML approaches of designing ensembles C&RT: Random Forest (RF) [34-35] and Gradient Boosting Machine (GBM) [36-37], which used bagging (RF) and boosting (GBM) technique. Both RF and GBM are powerful methods that can efficiently capture complex nonlinear patterns in data.

But much less attention has been paid to these algorithms in the field of financial time series analysis. Thus, Varghade and Patel [21] tested RF and SVM to forecast stock market index S&P CNX NIFTY. They noted that the Decision Trees model outperforms the SVR, although RF at times is found to overfit the data.

Kumar and Thenmozh [22] explored set of classification models for predicting direction of index

S&P CNX NIFTY. Their empirical results suggest that both the SVM and RF outperforms the other classification methods (NN, Linear Discriminant Analysis, Logit), in terms of predicting the direction of the stock market movement, but at the same time SVM it turned out to be more accurate.

Recently appeared several papers devoted to applying ensembles approaches for forecasting cryptocurrency prices [38-40]. Borges and Neves [38] tested four ML algorithms for price trend predicting: LR, RF, SVM and GBM. All learning algorithms outperform the Buy and Hold investment strategy in cryptomarket. The best result was obtained by ensembles voting (accuracy 59.3%).

Chenet et al. [39] applied a set of learning models including RF, XGBoost, Quadratic Discriminant Analysis, SVM and LSTM for Bitcoin 5-minute interval and daily prices. The authors used a large dataset including technological, market and trading, socio-media and fundamental factors. A somewhat unexpected result was that for daily prices, better results were obtained by using statistical methods (average accuracy 65%) as compared to ML methods (average accuracy 55.3%). Among ML models the SVM was the best performing, with an accuracy of 65.3%.

Sun et al. [40] developed a novel method of the price prediction trend of cryptocurrency market (42 coins) by using modification of GBM (LightGBM). The authors, besides past prices, also included several macroeconomic factors: Dow Jones index, S&P 500 index, WTI crude oil price index and others which affect the price fluctuation of cryptocurrency market. They tested different time period (2-days, 2-weeks, 2-month) and the best performance has been received for two week forecasting time horizon: accuracy whiting 0.52 (RF) to 0.61 (SVM, LightGBM).

For instance of rewired papers [38-40], which examined the prediction of price trend changes (classification problem), we focused on forecasting exchange rates (prices) by using RF and GBM (regression problem). Moreover, we used the stochastic GBM (SGBM), which has some advantages such as less learning time, less used memory and higher accuracy.

3. METHODOLOGY

3. 1. Supervised Machine Learning Approach

In our study we will apply supervised machine learning technique to forecast cryptocurrency time series. Consider a sample of pairs of features $\mathbf{x}=\left(x_1, x_2,..., x_p,..., x_M\right)$ (lagged daily prices $y_{i-1}, y_{i-2},..., y_{i-p}$, $i>p$ and several technical indicators $x_{p+1},..., x_M$), and the target variable (price on the next day) y : $\left(\mathbf{x}_i, y_i\right)_{i=1,2,...,n}$ length *n*.

We believe that between the target and features there is an unknown functional dependence f, which can be parameterized by an approximation function:

$$y \approx \hat{f}(\mathbf{x}) = f(\mathbf{x}, \theta). \tag{1}$$

Let $L(y, f)$ be the loss function, which characterizes the deviations between the actual and predicted values of target variable. Thus, our task is to minimize the loss function in the sense of mathematical expectation on the available dataset:

$$\begin{aligned}\hat{f}(\mathbf{x}) &= \arg\min_{f(\mathbf{x})} L\left(y, \hat{f}(\mathbf{x})\right) = \\ &= \arg\min_{f(\mathbf{x})} \mathrm{E}_{xy} L(y, f(\mathbf{x}, \theta)) = f(\mathbf{x}, \theta)\end{aligned} \tag{2}$$

For solving (2) we have to optimize $L(\cdot)$ using parameters θ

$$\begin{aligned}\hat{\theta} &= \arg\min_{\theta} \mathrm{E}_{xy} L(y, f(\mathbf{x}, \theta)) = \\ &= \mathrm{E}_x\left[\mathrm{E}_y\left(L(y, f(\mathbf{x}, \theta)) | \mathbf{x}\right)\right].\end{aligned} \tag{3}$$

In this context we can approximate the empirical loss function for *N* steps using:

$$L_\theta(\hat{\theta}) = \sum_{i=1}^{N} L\left(y_i, f\left(\mathbf{x}_i, \hat{\theta}\right)\right), \tag{4}$$

$$\hat{\theta} = \sum_{i=1}^{N} \hat{\theta}_i . \tag{5}$$

There are a lot of numerical technics to minimize loss function $L_\theta(\hat{\theta})$. The efficient approach is the gradient descent method, according to which we need to calculate gradient of loss function on each step $t=1,2,...,N$:

$$\nabla L_\theta(\theta) = \left[\frac{\partial L(y, f(\mathbf{x}, \theta))}{\partial \theta}\right]_{\theta=\hat{\theta}}. \tag{6}$$

It should be mentioned that when we employ an ML method it is necessary to solve the problem of Bias-Variance trade-off.

This is the problem of simultaneously minimizing two sources of error that prevent supervised learning algorithms from generalizing beyond their training set [9]:

- The *bias* is an error from erroneous assumptions in the learning algorithm, high bias can cause an algorithm to miss the relevant relations between features and target outputs (underfitting);
- The *variance* is an error from sensitivity to small fluctuations in the training set, high variance can cause overfitting, i.e., modeling the random noise in the training data, rather than the intended outputs.

Therefore, when adjusting the model parameters, we have to find a compromise between the forecast error caused by its *bias* and the unstable parameter values (high variance).

Consider the quadratic loss function:

$$L(y, f(\mathbf{x},\theta)) = \frac{1}{2}\sum_{i=1}^{l}(y_i - f(\mathbf{x}_i,\theta))^2. \quad (7)$$

Then the mean square forecast error *PE* can be represented in the form of sum of three terms:

$$PE = \mathrm{E}_{xy}\left[(y_i - f(\mathbf{x}_i,\theta))^2\right] = \mathrm{Bias}^2(\hat{f}) + \mathrm{Var}(\hat{f}) + \sigma^2 \quad (8)$$

The first component characterizes the bias of the training method, that is, the deviation of the average response of the trained algorithm from the response of the ideal algorithm. The second component characterizes variance, i.e., the scatter of the responses of trained algorithms compared to the average response.

The third component characterizes the noise in the data and is equal to the error of the ideal algorithm; therefore, it is impossible to construct an algorithm having a lower standard error.

Our main goal is to make a one-step-ahead forecast cryptocurrencies price based on available data set, their past values and compare predictive ability of different ML algorithms for solving this task. Thereby we investigat the ML methods including Random Forest (RF) and Gradient Boosting Machine (GBM). These ensemble ar methods based on using a set of "weak learning" algorithms, in general Decision Trees (C&RT). Despite the fact that each of them has low accuracy (both for classification and regression), we can get enough strength by combining the base week learners into ensembles model, which allows to achieve a better forecasting performance. This is because an ensemble technique helps reduce bias and / or variance described above (8).

3. 2. Random Forest RF proposed by Leo Breiman and colleagues [34, 35] is one of the most powerful ML approach. It is based on bagging technique that uses compositions of basic algorithms. Training data set is divided into many random subsets with replacement (bootstrap samples) and each of base classifier is trained on its own sub-set. The final classifier $a_N(\mathbf{x},\theta)$ is built as the average of the basic algorithms $h_i(\mathbf{x})$ (for regression):

$$a_N(\mathbf{x},\theta) = \frac{1}{N}\sum_{i=1}^{N} h_i(\mathbf{x},\theta), \quad (9)$$

where *N* represents the number observations (samples) in training set $(\mathbf{x}_i, y_i)_{i=1,2,\ldots,N}$.

Unlike boosting, which will be described in the next section, all elementary classifiers used in bagging are trained independently. The idea is that the classifiers do not correct each other's mistakes, but compensate them by voting. Basic classifiers must be independent (uncorrelated), so they can be classifiers based on different groups of methods (for example, linear regression, decision trees, neural networks and so on) or trained on independent data sets. In the second case, we can use the same basis algorithm.

Thus bagging efficiency is achieved by training the basic algorithms in different sub-sets obtained by bootstrap. Also in RF the feature used for branching in the certain node is not selected from all possible features set, but only from their random subset of size m. Moreover they are selected randomly, typically with replacement, that's why the same feature can appear several times, even in one branch. The number of features for training each tree is recommended to choose as $m \approx \frac{M}{3}$ (for regression task), where *M* is the total number of features.

The base models alone are not very accurate, but their ensemble allows significantly improves the quality of the prediction.

RF uses fully grown decision trees. It tackles the error reduction task by reducing variance. The trees are made uncorrelated to maximize the reduction in variance, but the algorithm cannot reduce bias (which is slightly higher than the bias of an individual tree in the forest).

It should be noted that RF are used in deep trees because basic algorithms require low bias; the spread is eliminated by averaging the responses of various trees.

3. 3. Gradient Boosting Machine Over the past two decades boosting has remained one of the most popular ML methods along with NN and SVM. Boosting, in contrast to bagging, does not use simple voting but a weighted one. The major attractions of boosting are that it is easy to design computationally efficient weak learners. A very popular type of weak learner is a shallow decision tree: a decision tree with a small depth limit.

In following, Friedman [36, 37] will cover the basic steps of GBM. By analogy with RF (see expression (9)) we will build a weighted sum of N basic algorithms

$$a_N(\mathbf{x}) = \frac{1}{N}\gamma_N\sum_{i=0}^{N} h_i(\mathbf{x},\theta) \quad (10)$$

and the initial algorithm $h_0(\mathbf{x},\theta)$ can be defined, for example, in the following form:

$$h_0(\mathbf{x},\theta) = \frac{1}{l}\sum_{i=1}^{l} y_i, \quad (11)$$

where l is the number of samples in training set ($l < n$, as a rule $l \approx 0.7 \div 0.8n$).

Assume we have already built ensemble $a_{N-1}(\mathbf{x},\theta)$ of $N-1$ classifiers on the $N-1$ step. Then we select the next basic algorithm $h_N(\mathbf{x})$ in such a way that the error given by (13) can be reduced as much as possible:

$$\sum_{i=1}^{l}[L(y_i, a_{N-1}(\mathbf{x}_i,\theta)+\gamma_N h_N(\mathbf{x}_i,\theta))]\rightarrow \min_{\gamma_N, h_N}. \quad (12)$$

If we choose $h_N(\mathbf{x}_i.\theta)$ in the following form

$$h_N(\mathbf{x},\theta)=\arg\min_{h(\mathbf{x},\theta)}\sum_{i=1}^{l}(h(x_i,\theta)-s_i)^2, \quad (13)$$

and put the deviation s_i equal to the anti-gradient of the loss function $L(\cdot)$

$$s_i=-\frac{\partial L(\cdot)}{\partial z}\Big|_{z=a_{N-1}(x_i)} \quad (14)$$

we will take one step of the gradient descent, which is being implemented by moving towards the fastest reduction of the loss function. Thus, we perform gradient descent in the l-dimensional space of algorithm predictions on the objects of the training set.

As soon as a new basic algorithm is found, it is possible to select its coefficient γ_N by analogy with the gradient descent:

$$\gamma_N=\arg\min_{\gamma}\sum_{i=1}^{l}L(y_i, a_{N-1}(\mathbf{x}_i,\theta)+\gamma_N h_N(\mathbf{x}_i,\theta)) \quad (15)$$

Note that unlike the RF, GBM is prone to retraining, which leads to increase errors on the test sample and on out of sample data. Because of this, as a rule, shallow decision trees are used in boosting. These trees have a large bias, but are not inclined to overfitting.

One more of the effective ways to solve this problem is to reduce the step: instead of moving to the optimal point in the direction of the anti-gradient, a shortened step is taken by

$$a_N(\mathbf{x},\theta)=a_{N-1}(\mathbf{x},\theta)+\lambda(\gamma_N h_N(\mathbf{x})), \quad (16)$$

where $\lambda\in[0,1]$ is the learning rate.

It should be noted that both of the above described ensembles approaches (RF and GBM) have their own advantages and disadvantages. Boosting works better on large training samples. It can properly reproduce the boundaries of classes with complex shape. Bagging is preferable for short training sets, it also allows efficient parallelization of calculations, while boosting is performed strictly sequentially.

GBM is based on weak learners (high bias, low variance). In terms of decision trees, weak learners are shallow trees, sometimes even as small as decision stumps (trees with two leaves).

The main advantage of boosting is that it reduces both variance and bias in forecasting, nonetheless the reduction of the forecast error is still carried out mainly due to the reduction in bias. That's why the bias correction leads to a greater risk of overfitting. It can be argued that in financial applications, RF based on bagging is usually preferable to boosting. Bagging solves the overfitting problem, while boosting solves the underfitting one.

4. DATASET

To limit our analysis to the most popular crypticurrencies, we use the daily close prices and trading volumes of the three most capitalized coins: Bitcoin (BTC), Ethereum (ETH) and Ripple (XRP). Our initial dataset covers the period from 01/01/2015 to 31/12/2019 for BTC and XRP (1826 observations), and from 07/08/2015 to 31/12/2019 for ETH (1608 observations) according to the Yahoo Finance [41]. Figure 1 shows the daily closing prices for the selected coins.

For training the models, fitting and tuning their parameters, the dataset was divided into training and test subsets in ratio of 80 and 20%. Moreover, the last 92 observations (from 01/10/2019 to 31/12/2019) were reserved for validation which was performed by out-of-sample one-step ahead forecast BTC, ETH, and XRP prices.

5. EMPIRICAL RESULTS

5. 1. Feature Selection Since we focus on ML approach of forecasting cryptocurrencies data, the main purpose of our paper is to get the most accurate one-step ahead forecast of daily prices, based on their past values and several other factors.

According to some empirical studies devoted forecasting cryptocurrencies prices [9, 42, 43], there is a

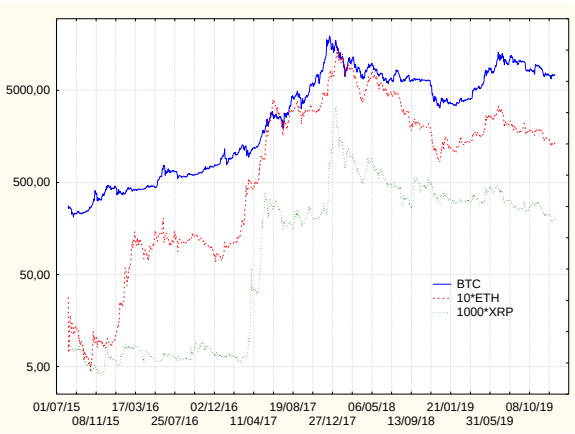

Figure 1. Daily closing prices for BTH, ETH, and XRP ($ USD) from 07/08/15 to 31/12/19 (log-scale)

seasonal lag which is a multiple of 7 if we use daily observations. In our opinion, this is due to the fact that cryptocurrencies (unlike traditional financial assets, for which a lag of 5 is often observed) are traded 24/7. The results of our correlation analysis also showed the existence of statistically significant lags, multiples of 7, for selected coins.

Therefore, we used the previous values of daily prices for the last four weeks as predictors (lagged daily prices $y_{i-1}, y_{i-2}, ..., y_{i-28}$). To take into account the changing trends, we used moving average prices of different orders: "fast" – 3,5,7 days, and "slow" – 21, 28 and 35 days.

In addition, we also included in the dataset two exogenous variables: daily trading volumes and the growth rates of daily trading volume with a lag of one day. Thus, the final dataset contains 36 features.

5. 2. Hyper-parameters Tuning It should be noted that hyper-parameters tuning is an important and sophisticated step of the model design. First of all, it is necessary to choose the functional form of the loss function given by Equation (5). To cover the main purpose of our study, the quadratic loss (8) was selected, which generally used for solving the regression problem,.

For both of the methods (RF, and GBM), the data is randomly partinioned into training and testing sets. A GBM modification that uses such a partition is called Stochastic GBM (SGBM) [37], which we applied in this study. The training sample is used to fit the models by adding simple trees to ensembles. Testing set is used to validate their performance. For regression tasks, validation is usually measured as the average error. We selected 30% of the dataset as test cases for both the approaches.

Since the RF is not inclined to overfitting, one can choose a large number of trees for the ensemble. We designed RF model with 500 trees. At the same time, in order for the model to be able to describe complex nonlinear patterns in data, it is necessary to use complex trees. So we have chosen a maximum of 15 levels.

Other important parameter for RF is the number of features to consider at each split. As noted in Section 3.2 for regression task it is recommended to choose this value as $m \approx \frac{M}{3}$, where M is the total number of features. We tested different RF models with value m between 8 and 12.

As a stop condition for the number of trees in SGBM (boosting steps) we took the number of trees at which the error on the test stops decreasing. This is necessary in order to avoid the overfitting. For boosting, unlike the RF, the simple trees are usually used. That's why we fitted maximum number of levels in trees and number of terminal nodes by the criteria of lowest average squared error on both training and test samples.

The final values of hyper-parameters setting are reported in Table 1.

An important parameter for GBM is the learning rate (shrinkage). Regularization by shrinkage consists of modifying the update rule (16) by tuning λ. We selected this value on the grid search according to minimum prediction error on the test set.

The natural logarithm is derived from all features for stabilizing the variance. This is special case of Box-Cox transform.

5. 3. Forecasting Performance The short-term forecasts were made for the selected coins using the absolute values of prices. The target variable is the prediction value of close prices for each cryptocurrencies in the next time period (day) although we used daily observation. Both SGBM and RF models were trained with the same set of features.

For testing efficiency of both approaches, we carried out prediction prices of the selected coins on the hold out last 91 observations by using one-step ahead forecasting technique. The final results are shown in Figures 2-4.

Analysis of the graphs allows us to conclude that both of the ensemble approaches generlally well approximate cryptocurrencies time series dynamics, but one can see a certain delay in the model graphs in comparison to the real data.

For comparing prediction performance of different ensembles (SGBM, and RF) we applied Mean Absolute Percentage Error (MAPE) and Root Mean Square Error (RMSE). Table 2 shows summary of the estimation accuracy for our models using these metrics.

Thus, we can conclude that both methods have the same order of accuracy for the out-of-sample dataset prediction, although boosting is somewhat more

TABLE 1. Final hyper-parameters setting

Parameters	RF	GBM
Loss-function	quadratic	quadratic
Training / test subsamples proportion, %	70/30	70/30
Random subsample rate	0.7	0.7
Number of trees in ensemble	500	250
Maximum number of levels in trees	15	4
Maximum number of features to consider at each split	12	-
Maximum number of terminal nodes in trees	150	15
Minimum samples in child nodes	5	-
Learning rate (shrinkage)		0.1

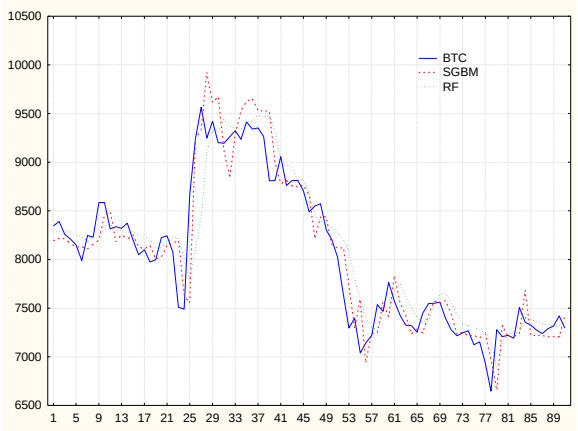

Figure 2. Out of sample prediction of BTC prices

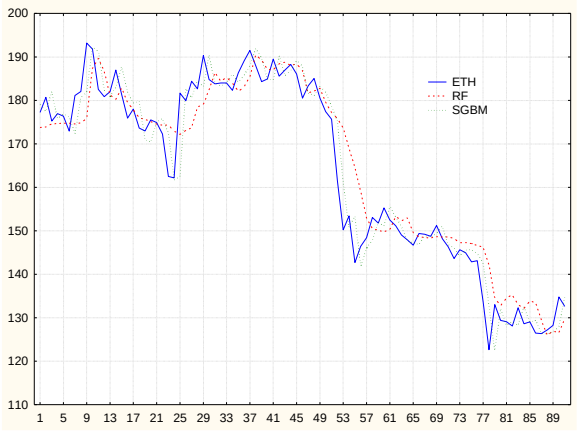

Figure 3. Out of sample prediction of ETH prices

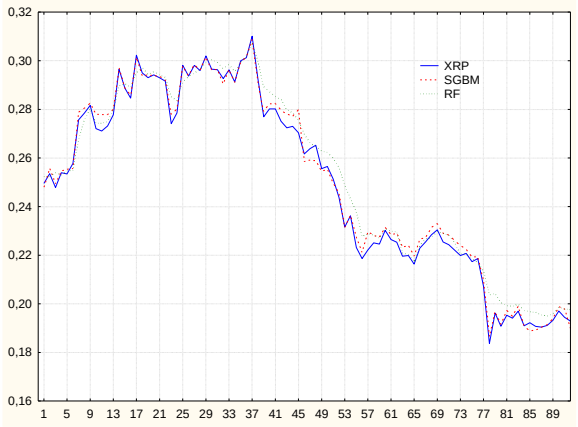

Figure 4. Out of sample prediction XRP prices

accurate. The best prediction performance is produced by SGBM for XRP– 0.92 %, and the best obtained result by RF is 1.84% for XRP.

Our results are comparable in MAPE accuracy metrics with the other research. In [28], the authors obtained prediction error for Bitcion close prices (MAPE) within 1-2% by using SVM and ANN.

TABLE 2. Out-of-sample accuracy forecasting performance results

	SGBM		RF	
	MAPE, %	RMSE	MAPE, %	RMSE
BTC	**2.31**	**263.34**	2.61	305.95
ETH	3.02	5.02	**2.26**	**6.72**
XRP	**0.92**	**0.0029**	1.84	0.0057

6. CONCLUSION AND DISCUSSION

Our research has shown the efficiency of using ML ensemble-based approaches for predicting cryptocurrency time series. According to our results, the out of sample accuracy of short-term forecasting daily prices obtained by SGBM and RF in terms of MAPE for three of the most capitalized cryptocurrencies (BTC, ETH, and XRP) was within 0.92-2.61 %.

By designing models, we explored different sets of features. Our base dataset contained only past values of the target variable with 14, 21 and 28 lag depth. In this case a larger dataset provided better training of the SGBM and RF, and gave more efficient results. The inclusion of additional features into the model , in particular technical indicators (moving averages), and trading volumes, led to an increased accuracy (MAPE) both on in- and out of samples on average from 1 to 3%.

In our opinion, forecasting accuracy can be improved by including additional features, for example, open, max, min and average prices, fundamental variables, different indicators and oscillators, such as Price rate-of-change, Relative strength index, and so on.

Future research should extend by investigating the predictive power of both features described above and others additional features. In the conclusion, we note that the proposed methodology by the development of combined ensemble of C&RT with other powerful ML models, such as NN and SVM is a promising approach to forecasting not only time series of cryptocurrencies, but also other financial time series. Moreover, it seems promising to us to use DL approaches for feature selection.

7. REFERENCES

1. Coinmarketcap, *Crypto-Currency Market Capitalizations*. https://coinmarketcap.com/ currencies. Accessed: 15 May 2020.
2. Krugman P., *Bits and Barbarism*. http://www.nytimes.com/2013/12/23/opinion/krugmanbits-and-barbarism.html. Accessed: 15 May 2020.
3. CNBC, *Top Economists Stiglitz, Roubini and Rogoff Renew Bitcoin Doom Scenarios*. https://www.cnbc.com/2018/07/09/nobel-prize-winning-economist-joseph-stiglitz-criticizes-bitcoin.html. Accessed: 15 May 2020.

4. Selmi, R., Tiwari, A., Hammoudeh, S., "Efficiency or speculation? A dynamic analysis of the Bitcoin market", ***Economic Bulletin***, Vol. 38, No. 4, (2018), 2037-2046. https://econpapers.repec.org/RePEc:ebl:ecbull:eb-18-00395. Accessed: 15 May 2020.
5. Cheah, E., Fry, J.,"Speculative bubbles in Bitcoin markets? An empirical investigation into the fundamental value of bitcoin", ***Economic Letters***, Vol., No. 130, (2015), 32-36. doi: 10.1016/j.econlet.2015.02.029
6. Ciaian, P., Rajcaniova, M., and Kancs, A., "The economics of BitCoin price formation", ***Applied Economics,*** Vol. 48, No. 19, (2016), 1799-1815. doi: 10.1080/00036846.2015.1109038
7. Catania L., Grassi, S., "Modelling Crypto-Currencies Financial Time-Series", ***CEIS Research Paper***, Vol. 15, No. 8, (2017), 1-39. https://ideas.repec.org/p/rtv/ceisrp/417.html. Accessed: 15 May 2020.
8. Soloviev, V., Belinskij, A., "Complex Systems Theory and Crashes of Cryptocurrency Market", ***Communications in Computer and Information Science***, Vol. 1007, (2019) 276-297. https://link.springer.com/chapter/10.1007/978-3-030-13929-2_14.
9. Flach, P.: *Machine Learning: The Art and Science of Algorithms that Make Sense of Data*. Cambridge University Press. Cambridge, UK, (2012).
10. Sheikhi, S., Kheirabadi, M. T., Bazzazi, A. "An Effective Model for SMS spam Detection using Content-based features and Averaged Neural network", ***International Journal of Engineering , Transactions B: Applications***, Vol. 33, No. 2, (2020), 221-228. doi: 10.5829/IJE.2020.33.02B.06
11. Kumar, S., Sahoo, G. A., "Random Forest Classifier based on Genetic Algorithm for Cardiovascular Diseases Diagnosis", ***International Journal of Engineering, Transactions B: Applications***, Vol. 30, No. 11, (2017), 1723-1729. doi: 10.5829/ije.2017.30.11b.13
12. Patil, S., Phalle, V., "Fault Detection of Anti-friction Bearing using Ensemble Machine Learning Methods", ***International Journal of Engineering, Transactions B: Applications,*** Vol. 31, No. 11, (2018), 1972-1981. doi: 10.5829/ije.2018.31.11b.22
13. Makridakis, S., Spiliotis, E., Assimakopoulos, V., "Statistical and Machine Learning forecasting methods", ***Plos one***, March 27, (2018), 1-26. doi: 10.1371/journal.pone.0194889
14. Bontempi, G., Taieb, S., Borgne, Y., "Machine Learning Strategies for Time Series Forecasting", European Business Intelligence Summer School eBISS 2012, 62-77. Springer-Verlag. Berlin Heidelberg, (2013). doi: 10.1007/978-3-642-36318-4_3
15. Persio, L., Honchar, O., "Multitask machine learning for financial forecasting", ***International Journal of Circuits Systems and Signal Processing***, Vol. 12, (2018), 444-451.
16. Kourentzes, N., Barrow, D.K., Crone, S,F., "Neural network ensemble operators for time series forecasting", ***Expert Systems with Applications,*** Vol. 41, No. 9, (2014), 4235-4244. doi:10.1016/j.eswa.2013.12.011
17. Liu W, Wang Z, Liu X, Zeng N, Liu Y, Alsaadi FE., "A survey of deep neural network architectures and their applications" ***Neurocomputing***, Vol. 234 (C), (2017), 11-26. doi:10.1016/j.neucom.2016.12.038.
18. McNally, S., Roche, J., Caton, S. "Predicting the price of bitcoin using machine learning", in: 2018 26th Euromicro Int. Conf. Parallel, Distrib. Network-Based Process., IEEE, (2018), 339-343. doi: 10.1109/PDP2018.2018.00060
19. Hamid SA, Habib A., "Financial Forecasting with Neural Networks", ***Academy of Accounting and Financial Studies Journal,.*** Vol. 18, No. 4, (2014), 37-55. https://www.abacademies.org/articles/aafsjvol1842014.pdf. Accessed: 15 May 2020.
20. Boyacioglu, M., Baykan, O.K., "Predicting direction of stock price index movement using artificial neural networks and support vector machines: The sample of the Istanbul Stock Exchange", ***Expert Systems with Applications***, Vol. 38, No. 5, (2011), 5311-5319. doi: 10.1016/j.eswa.2010.10.027
21. Varghade, P., Patel, R, "Comparison of SVR and Decision Trees for Financial Series Prediction", ***International Journal on Advanced Computer Theory and Engineering***, Vol. 1, No. 1, (2012), 101-105.
22. Kumar, M., "Forecasting Stock Index Movement: A Comparison of Support Vector Machines and Random Forest", ***SSRN Working Paper,*** (2006). doi: 10.2139/ssrn.876544
23. Peng, Y., Henrique, P., Albuquerque, M., "The best of two worlds: Forecasting high frequency volatility for cryptocurrencies and traditional currencies with Support Vector Regression", ***Expert Systems with Applications,*** Vol. 97, (2018), 177-192. doi: 10.1016/j.eswa.2017.12.004
24. Ahmed NK, Atiya AF, Gayar NE, El-Shishiny H., "An Empirical Comparison of Machine Learning Models for Time Series Forecasting", ***Econometric Reviews***, Vol. 29, No. 5-6, (2010), 594-621. doi:10.1080/ 07474938.2010.481556
25. Akyildirim, E., Goncuy, A., Sensoy, A., Prediction of Cryptocurrency Returns using Machine Learning, (2018). https://arxiv.org/pdf/1805.08550.pdf. Accessed 15 May 2020.
26. Amjad, M., Shah, D., "Trading Bitcoin and Online Time Series Prediction", ***NIPS 2016: Time Series Workshop***., (2016). http://proceedings.mlr.press/v55/amjad16.pdf (2016). Accessed 15 May 2020.
27. Hitam, N. A., Ismail, A. R., "Comparative Performance of Machine Learning Algorithms for Cryptocurrency Forecasting", (2018). https://www.researchgate.net/ publication/327415267. Accessed 15 May 2020.
28. Mallqui, D., Fernandes, R. "Predicting the direction, maximum, minimum and closing prices of daily Bitcoin exchange rate using machine learning techniques", ***Applied Soft Computing Journal***, Vol. 75, (2019), 596-606. doi: 10.1016/j.asoc.2018.11.03
29. Sezer, O.B., Mehmet Ugur Gudelek, M.U., Ozbayoglu, A.M. "Financial Time Series Forecasting with Deep Learning : A systematic literature review: 2005–2019", ***Applied Soft Computing Journal***, Vol. 90, (2020), 106-181. doi: 10.1016/j.asoc.2020.106181
30. Kumar, D., Rath, S.K. "Predicting the Trends of Price for Ethereum Using Deep Learning Techniques", in: Artificial Intelligence and Evolutionary Computations in Engineering Systems, Springer, 2020, 103-114. doi: 10.1007/978-981-15-0199-9_9
31. Yao, Y., Yi, J., and Zhai, S., "Predictive Analysis of Cryptocurrency Price Using Deep Learnin", ***International Journal of Engineering & Technology***, Vol. 7, No. 3, 27, (2018), 258-264. doi: 10.14419/ijet.v7i3.27.17889
32. Chen, W., Xu, H., Jia, L., Gao, Y. "Machine learning model for Bitcoin exchange rate prediction using economic and technology determinants", ***International Journal of Forecasting***, (2020), (article in press). doi: 10.1016/j.ijforecast.2020.02.008
33. Saxena, A., Sukumar, T., "Predicting bitcoin price using LSTM and compare its predictability with ARIMA model", ***International Journal of Pure and Applied Mathematics,*** Vol. 119, No. 17, (2018), 2591-2600. https://acadpubl.eu/hub/2018-119-17/3/214.pdf. Accessed: 15 May 2020.
34. Breiman, L., Friedman, H., Olshen, R. A., & Stone, C. J., *Classification and Regression Trees*. Belmont, NJ. Wadsworth International Group, (1984).

35. Breiman, L., "Random Forests", ***Machine Learning***, Vol. 45, (2001), 5-32. doi: 10.1023/A:1010933404324

36. Friedman, Jerome H., "Greedy Function Approximation. A Gradient Boosting Machine", ***Annals of Statistics***, Vol. 29, No. 5, (2001), 1189-232. doi: 10.2307/2699986

37. Friedman, Jerome H., "Stochastic Gradient Boosting", ***Computational Statistics and Data Analysis***, Vol. 38, No. 4, (1999), 367-378. doi: 10.1016/S0167-9473(01)00065-2

38. Borges, T.A., Neves, R.N. "Ensemble of Machine Learning Algorithms for Cryptocurrency Investment with Different Data Resampling Methods", ***Applied Soft Computing Journal*** , Vol. 90, (2020), 106-187. doi: 10.1016/j.asoc.2020.106187

39. Chen, Z., Li, C., Sun, W. Bitcoin Price Prediction Using Machine Learning: An Approach to Sample Dimension Engineering, ***Journal of Computational and Applied Mathematics***, Vol. 365, (2020), 112395. doi: 10.1016/j.cam.2019.112395

40. Sun, X., Liu, M., Sima, Z. "A novel cryptocurrency price trend forecasting model based on LightGBM", ***Finance Research Letters***, Vol. 32, (2020), 101084. doi: doi.org/10.1016/j.frl.2018.12.032

41. Yahoo Finance. https://finance.yahoo.com. Accessed: 15 May 2020.

42. Guryanova, L., Yatsenko, R., Dubrovina, N., Babenko, V. "Machine Learning Methods and Models, Predictive Analytics and Applications". Machine Learning Methods and Models, Predictive Analytics and Applications 2020: Proceedings of the Workshop on the XII International Scientific Practical Conference Modern problems of social and economic systems modelling (MPSESM-W 2020), Kharkiv, Ukraine, June 25, 2020, Vol-2649, (2020), 1-5. URL: http://ceur-ws.org/Vol-2649/

43. Alessandretti, L., ElBahrawy, A., Aiello, L., Baronchelli, A., "Anticipating Cryptocurrency Prices Using Machine Learning", ***Hindawi Complexity,*** (2018) doi: 10.1155/2018/8983590

Persian Abstract

چکیده

در این مقاله مشکلات پیش بینی کوتاه مدت سری زمانی ارز رمزنگاری شده با استفاده از یک رویکرد یادگیری ماشین تحت نظارت ML بحث شده است. برای این منظور ، ما از دو روش قدرتمندترین گروه از جمله جنگل های تصادفی (RF) و دستگاه تقویت گرادیان تصادفی SGBM استفاده کردیم. همانطور که مجموعه داده از قیمت بسته شده روزانه سه سکه با بیشترین سرمایه جمع آوری می شود: بیت کوین BTC، اتریوم ETH و ریپل XRP، و به عنوان ویژگی هایی از اطلاعات قیمت گذشته و شاخص های فنی (میانگین متحرک) استفاده کردیم. برای بررسی اثربخشی این مدل ها ، ما با استفاده از تکنیک یک قدم جلوتر پیش بینی خارج از نمونه برای سری های زمانی انتخاب شده را انجام دادیم. میزان دقت قیمت پیش بینی شده با استفاده از RF و GBM محاسبه شد. نتایج به کارگیری رویکرد گروه های ML برای پیش بینی قیمت ارزهای رمزنگاری شده را تأیید می کند. صحت خارج از نمونه پیش بینی کوتاه مدت قیمت های روزانه بسته شده توسط SGBM و RF از نظر میانگین درصد مطلق خطا (MAPE) برای سه ارز رمزپایه (BTC، ETH و XRP) در محدوده ۰,۹۲–۲,۶۱٪ بود.

International Journal of Engineering

Journal Homepage: www.ije.ir

Provision of an Optimal Strategy to Forecast the Prices Set by the Electricity Market in the Competitive Iranian Energy Market in Fall

S. M. Kavoosi Davoodi[a], S. E. Najafi*[a], F. Hosseinzadeh Lotfi[b], H. Mohammadiyan[c]

[a] *Department of Industrial Engineering, Science and Research Branch, Islamic Azad university, Tehran, Iran*
[b] *Department of Mathematics, Science and Research Branch, Islamic Azad university, Tehran, Iran*
[c] *Department of Industrial Engineering, Mazandaran University of Science and Technology Branch, Babol, Iran*

PAPER INFO

Paper history:
Received 10 August 2020
Received in revised form 16 October 2020
Accepted 30 october 2020

Keywords:
Combined Network
Iranian Electricity Market
Multilayer Perceptron Neural Network
Price Forecasting
Self-organizing Map Network

ABSTRACT

Given the complexities of the electricity market, various factors, such as uncertainties, the ways upon which the markets are set, how the debts are settled, the market structure and regulations, production prices, constraints governing the units and networks, etc. are influential in determining the optimal pricing strategies. Various methods and models have been presented to resolve the pricing issue in the competitive electricity industry. The most prominent of which include pricing methods are based on the prediction of competitors' behavior; also pricing methods based on the forecasts of market price, methods based on the game theory and lastly, pricing methods based on the intelligent algorithms. Therefore, this study was conducted to provide an optimal strategy in order to forecast the electricity market price set in the competitive Iranian electricity market (based on the data collected). In this paper, the proposed method uses a compound network based on the neural networks. The analyzed data include the amount of the consumed energy as well as temperature (if applicable) and the price set for the past days and weeks. The self-organizing map (SOM) network was used for the input clustering based on the similar days. A number of multilayer perceptron (MLP) neural networks were used to combine the extracted data consisting of the energy levels, the price set, and temperature (if possible). The results showed improvements in the performance of the smart systems based on the neural networks in predicting the electricity prices.

doi: *10.5829/ije.2021.34.01a.17*

1. INTRODUCTION

Since the industrial revolution, energy has become a key factor in everyday life. Fossil fuels have become the most primary energy production in the world [1]. However, with the population growth and technological development, the current world is facing two vital problems, environmental pollution, and energy resource shortages [2]. One way to overcome problems is to improve efficiency and reduce emission [3]. The other way is to develop alternate energy resources [2]. Most recent research paid attention to renewable resources for their properties of environmental-friendly and sustainability. The most competitive renewables include water, wind, photovoltaic energy, and biofuel. Many of them have been proved to be advanced in addressing energy and environmental issues [4, 5]. Today, electrical energy became an essential element of human life as one of the most favorable types of energy. In order to supply this energy, vast and extensive power systems have emerged in various countries. The management and control of such systems was initially the responsibility of governments or quasi-public institutions, and if assigned to the private sector, would have a vertically integrated management structure. Most of the previous theories presented about power systems were based on the idea that electricity is a public service sector with intrinsic monopolistic properties. Many renewable sources have been applied to the electricity market. In the last few years, electricity market prices decreased a lot due to the close-to-zero marginal costs from renewable energies [6]. Therefore, the electricity market participants are

*Corresponding Author Email: *Najafi1515@yahoo.com* (S. E. Najafi)

Please cite this article as: S. M. Kavoosi Davoodi, S. E. Najafi, F. Hosseinzadeh Lotfi, H. Mohammadiyan, Provision of an Optimal Strategy to Forecast the Prices Set by the Electricity Market in the Competitive Iranian Energy Market in Fall, International Journal of Engineering, Transactions A: Basics, Vol. 34, No. 1, (2021) 149-161

seeking ways to be more competitive in the market. Many companies have adopted new electricity price plans [7], for example, time-of-use electricity price plans. These plans charge higher rates when demand is high, and lower rates when demand is low. This encourages customers to wisely decide their electricity usages and reduce on-peak energy usages [8]. This situation makes not only the producers but also the customers pursue more precise forecasts of the electricity market prices than ever. However, electricity price usually has complex features, such as highly volatile behavior and non-linearity, which makes it rather difficult to build a precise forecasting model [9, 10].

Accurate electricity price forecasting may help electricity market participants to formulate reasonable competition strategies. Specifically, power producer scan use the forecasting results to optimize unit output, while power consumers can use the results to optimize purchase portfolio [11]. However, the complex features of electricity prices such as periodicity and high volatility make the forecasting pretty difficult [12].

In recent years, a lot of models have been proposed for electricity price forecasting [13, 14]. In general, the commonly used models can be classified into two primary categories: soft computing models [15, 16] and time-series models [17, 18].

The amount of information available to participants in the market is a fundamental issue in selecting the type of method used to resolve the pricing issue. Since the competitors in the electricity market do not adopt a specific predictable procedure because of the market's competitive nature; thus, producers' behavior in pricing strategy regulation is not logical and the assumption of profit maximization is not rational to predict competitors' behavior. Thus, the application of the game theory and smart algorithms is not appropriate due to the restrictive hypothesis in problem modelling, such as predicting competitor power plant costs and the rationality of their behavior in setting pricing strategies.

Recently, interests regarding algorithms used to control forecasting issues are referred to as artificial neural networks (ANNs). The interesting feature of neural networks is their ability to utilize price properties which in general, either cannot be determined or entail arduous computations for their synthesis. The development of computer technology has enabled vast competencies to combine methods in one place and at one time. A number of papers published in the forecasting field often implement the neural networks method.

In spite of the achievements reported in the field of forecasting, the price forecast issue remains problematic. As an example, there is no general forecaster that can be employed to forecast prices in any geographic region, the reason being that factors that affect prices differ in terms of area and region e.g. if load is considered as one of the influential factors on pricing, it is clear that the system load varies in each geographic region, and the consumption level in one area cannot be considered as the system load for other areas.

The development of statistical methods necessitates significant time and costs to achieve normal operation while the use of a neural network requires a short time period to configure. Herein, the Genetic Algorithm, another section of artificial intelligence, plays an integral role in optimizing game engineering functions. One of the issues of using neural networks is the lack of a solution and specific relationship to determine the number of layers or neurons of the hidden layers, since the determination of the aforementioned parameters depends on experience and cannot be determined definitively. However, the use of the Genetic Algorithm to determine neurons is an efficient, expeditious, and reliable method that may be achieved by integrating it with the neural network to a hybrid network, which significantly enhances forecast accuracy [19].

With the emergence of competitive electricity markets around the world, the issue of optimal pricing strategy has been raised. Electricity vendors in the world's prominent electricity market often have various options for generating revenue at any given time, with various technical and non-technical constraints. Thus, vendors in the electricity market are continuously faced with an optimization issue to make optimal decisions. Since 2003, Iran's electricity market was incepted amidst the reconstruction of Iran's infrastructure. Currently, the market is active only on the production section. Amidst the strengthening of Article 44 of the Iranian Constitution and the transfer of power plants to the private sector, the pricing strategy issue in the electricity market has become more prominent. In Iran, the fear of losing out has always led to pricing being set with high caution. Also, the study of pricing history pertaining to power plants across the country indicates that most vendors have difficulties in selecting the optimal strategies in fuel constraint conditions [20].

The purpose of this research is to answer the following question:

What is the optimal strategy for predicting the price of electricity in a competitive electrical energy market within the framework of the laws and regulations of the Iranian electricity market?

In this regard, in the present research, the following hypotheses will be used to explain the utilized approaches:

Among the types of power plants, only the thermal power plant is examined. In determining the optimal

pricing strategy, the prediction of the next day load is considered definitive.

However, to demonstrate load variances in the results, sensitivity analysis is conducted for load variations. The electricity market, as with all other markets, will be a demand-driven market. As with the real electricity market, the supply suggestion function in this market will be linear and ascending relative to the production level, and the demand function will also be linear but descending relative to the demand level.

To determine the optimal price strategy, the DC load distribution is used in the market pricing model. For instance, Panapakidis and Dagoumas [21] used artificial neural networks (ANNs) model for electricity price forecasting in Southern Italy. Sandhu et al. [22] employed the neural networks to forecast Ontario electricity prices. To better capture the characteristics of electricity prices, a combination of ANN models and other models is often presented. For instance, Ortiz et al. [23] proposed a combined model based on artificial neural networks. Keles et al. [24] develop a model based on ANNs and optimal parameter model. Singh et al. [25] presented a combined model with generalized neuron model and wavelet transform. Itaba and Mori [26] utilized the general radial basis function network and fuzzy clustering. Wang et al. [10] develop a hybrid model combined with ANNs and decomposition technique. It should be noted that although the ANNs model can describe the nonlinear characteristics of electricity price series, it cannot well deal with the linear fitting problem [27]. To describe the linear features of electricity prices, the time series model is often applied, which is considered as one of the most effective techniques [28]. Traditional time series models, such as autoregressive integrated moving average (ARIMA), autoregressive and moving average (ARMA) and generalized autoregressive conditional heteroscedasticity (GARCH), have been frequently applied to forecast electricity prices. Besides, Diongue et al. [29] and Girish [30] proposed some new time series models such as GIGARCH and autoregressive-GARCH. To better capture the features of electricity prices, some other models have been combined with time series models [9, 31]. Since electricity price series is composed by linear and nonlinear components, the integrated models that have linear and nonlinear fitting capabilities can improve the forecasting accuracy [32, 33]. For this reason, the empirical mode decomposition (EMD) approach has been used for electricity price decomposition by some researchers [34, 35].

A study conducted entitled "assessing the methods of forecasting the price of electricity in the energy market" where they stated that: today, decision making for market participants to increase profitability is highly complicated [36].

Another study conducted entitled "Simultaneous forecasting of price and demand in a smart electricity distribution network". In this paper, a forecast framework is proposed that provides dynamic forecasts for electricity price and demand [37].

A conducted study titled "Short-term forecast of electricity prices using time-fuzzy neural networks" where it was stated: in the restructured environment, one of the most vital issues in the planning of independent operators and vendors is the forecasting of electricity prices [38].

Other study conducted by Shayeghi and Ghasemi on daily electricity price forecast using an enhanced neural network based on wavelet transform and the chaotic gravitational search algorithm [39].

Meng et al. predicted a model for energy consumption in residential building in rural areas of Chongqing [40]. Recently, a new hybrid artificial neural networks and fuzzy regression model for time series forecasting has been proposed [41]. Artificial neural network (ANN), as the main approach in the field of Artificial Intelligence (AI), has attracted much interest over the past decade for its ability to forecast financial performance [42]. A system dynamics approach is used to capture the long-run behavior of electricity markets and to characterize the evolution of the electricity prices and the demand [43]. Khedmati et al. [44] proposed time series forecasting of bitcoin price based on autoregressive integrated moving average and machine learning approaches.

2. RESEARCH METHODOLOGY

Since the forecast in this study takes place in Iran, which has specific climate conditions, thus it was attempted to utilize a new combination of the parameters and to categorize the data into various classes with higher accuracy. Parameters, such as the past load price, temperature and humidity were considered in each category with a novel combination of these traits. Data categorization methods and precise selection of the parameters are discussed further.

In this project, information on the consumed electricity load price for time duration 2014-2017 in Mazandaran province was used, as well as considering the temperature during this period. Upon the data collection stage, data were analyzed and dynamically identified in order to categorize the data into smaller groups based on their common characteristics and to create a separate model for each group. Numerous studies have emphasized that

various pricing activities cannot be presented by one model.

In this vein, initially, the consumed loads during the defined period were forecasted with no favorable results without considering the specific data categorization. Given the substantial changes in the electricity consumption amidst season changes, categorization should first be conducted based on the seasons. Hence, they were are categorized into four groups, i.e., spring, summer, fall ,and winter. Although, it should be noted that the forecasts in all the seasons with the exception of summer were accurately conducted by the current systems and human expertise.

Various days of the week have their own curves, even though it has been claimed that the curves of mid-week consumed loads (for Iran, from sunday to wednesday) were similar. For the holidays, different consumed load curves were used. Moreover, the consumed load curves on days before and after the holidays differ from the normal days of the week. However, in the real world, it is not possible to manually conduct such categorization. Therefore, in this paper, a categorization method is presented to schedule these cases.

The holidays are among the other factors influencing the consumption price curve. Since, there are two types of holidays in Iran, i.e., religious and national holidays, both should be taken into consideration. In this project, forecasts of the religious and national holidays were conducted separately. Although, it should be noted that according to the comparisons of the consumed load price from 2009 to 2012, the consumed load in Iran and experts' opinions indicated no need for the forecasts for some of the holidays since, the consumed loads on these days were similar to that of the previous years. For example, the consumed loads on 2nd April and day of Ashura were the same as the previous year.

2. 1. Hybrid Neural Network Artificial neural networks (ANNs) are suitable tools for modeling and forecasting the data. Various types of neural networks have been introduced, each with a specific application. One of the main and beneficial capabilities of the neural networks is their function on the vast quantities of variables as well as on the complex systems. Despite the simplicity of utilizing the neural networks, there are also drawbacks, such as setting the parameters of the network architecture and placing the network in local optimizations and extension of the learning process time period. In this regard, various solutions have been proposed to resolve each issue; one of the most favorable of which is the combination of these networks. The combination of the neural networks varies in different applications. The use of a non-monitored neural network to cluster the similar data, and in the next stage, to train the supervised networks using the similar samples in one cluster is one of the most valuable functions of this type of network . Another use of the hybrid networks is that the inputs are of different ranges entailing the lack of appropriate network training and the negligence of a number of traits. In this regard, the traits that are of different nature are trained with different networks, and ultimately these types of networks are combined.

The hybrid networks are used to forecast the price of the consumed load due to the existence of several effective factors. Due to the lack of access to all of these factors, two of the most valuable features i.e., temperature and cost of the previously consumed loads are used. These two parameters are highly influential on one another but at the same time, are extremely different in nature. The most important reasons for this include:

1) Temperature difference of a few degrees may multiply the consumed load price by a few hundred. Therefore, the slightest temperature changes in the network should be accurately modelled.
2) The range of temperature changes is within 5-30°C if the consumption load is between 200-1500 MW in the province under assessment.
3) The effect of temperature variation in different hours of the day exhibits a different trend. As an example, a temperature change of two degrees between 13-15 hours shows a significantly greater effect on the consumption compared to a two -degree change in the early hours of the day.
4) Temperature changes in various seasons do not exhibit the same effect. For example, a one -degree temperature change in the summer exhibits a different change compared to the same change in winter.
5) Temperature changes within temperature ranges are also significant. For example, a temperature variation of two degrees within a temperature range of less than 20 degrees may not exhibit much effect on the load consumption but a temperature variation of one degree at temperatures over 24 degrees will exhibit a significant effect on the consumption load.

As previously mentioned, these parameters are of completely different nature in terms of the size but are highly influential on one another. For this reason, two different networks were used in this project for these two parameters.

2. 2. Clustering It should be determined that to which cluster the data belong, and this process is repeated as long as the representatives of the clusters no further change. Clustering is different from the classification. In

the classification, the input samples are labeled; however, they are not labeled in the clustering. In fact, clustering methods make the identical data to be identified and implicitly labeled. Actually, prior to the data classification operation, a sample clustering process can be performed and then, the centers of the resulting clusters can be specified. Afterwards, a label can be assigned to the cluster centers, and the classification operation can then be performed for the new input samples.

In the recent years, many methods including k-means, fuzzy k-means, neural network-based clustering, such as self-organizing map (SOM)-based clustering, and othershave been proposed for the clustering.

2. 3. Self-organizing Map Neural Network The SOM neural network is an unsupervised network used for clustering the data. On each application to an input, this algorithm maps its self-organizing Kohonen feature with respect to the neurons from a one or two -dimensional net type neuron. This net type network of the neurons is organized by the input samples ultimately approximating the distribution of the network inputs in a discrete environment. This network is consisted of two layers; the first layer is the input layer where the input samples are inserted and through which they are applied to the network neurons. The second layer includes the output neurons. In a normal state, each neuron has only one binary output possessing a value of one or zero. If the neuron in question wins the competition over the resources, its output will acquire the value of one and the remaining neurons will have zero outputs. The neuron that its weight has the most resemblance to the input sample is considered the winning neuron for a specific input. In this case, its output will acquire the value of one and the output of the remaining neurons will be zero. The weight vector of the winning neuron is corrected along with its neighboring neurons. This correction causes the progression of the neurons' weights towards the recent input, whilst the weights of the other neurons will remain unchanged.

This is one of the most important parameters for detecting the number of clusters (the number of similar days for this project). For this purpose, the k-mean and Fisher's hybrid algorithm were used in this project.

2. 4. Genetic Algorithm The genetic algorithm (GA) is a programming technique that uses the genetic evolution as a problem -solving model. Its input is the problem to be solved and the solutions are coded according to a pattern called the fitness function evaluating each possible solution, most of which are randomly selected [45].

The GA, as a search technique is used in the computer science to determine the optimal solution and address the search issues [46]. These algorithms are a type of evolutionary algorithms inspired by the branches of biological sciences, such as heredity, mutation, saltation (biology), natural selection, and composition.

Evolution starts from a completely random set of entities and is repeated in the subsequent generations. In each generation, the most suitable ones are selected instead of the best. Three criteria are typically used as the stopping criterion:

1. Runtime Of The Algorithm
2. Number Of The Generations
3. Convergence Error Criteria

The most prominent applications of the GA include the hydrological routing of runoff in a dry river network, assistance in resolving the multi-criteria decision issues, multi-objective optimization in the water resources management, optimization and loading of the electricity distribution networks, etc.

2. 5. Selection of the Input Parameters and Variables Based on the prior assessments, the time and temperature variables were selected as two factors influencing on the price and the previously consumed loads. Among the climate variables, only the temperature variable is used since, most of other climate factors are included in this variable. Given the fact that the temperature has a significant influence on the consumption trend, namely in the northern region of the country and since, the forecasts are on an hourly basis apparently, using the temperature parameter on an hourly basis or closer time intervals will entail the improved operation. It is important to consider the previous number of days and weeks in terms of the consumed load price and temperature. According to the studies and opinions of the experts in the field of electricity distribution, the use of load and temperature at various hours of the previous days and weeks is highly effective (although it can be equivalent to the hours of the forecasted day). In this project, data of the preceding two days and two equivalent days of the previous weeks were used. In addition, the information on hourly temperature of the forecasted day was also used. Other utilized useful information included the load price and temperature of the preceding hour. Since, the information on the preceding 24 hours of the forecasted day was available thus, the data pertaining to the previous hours were used as the input in order to forecast those of the next hours [47].

2. 6. Proposed Method forecasting the short-term load price is a vital factor in the future planning of

the power systems and electricity market management . In the recent years, various methods have been presented to improve the performance of such systems due to the significance of this issue. In this paper, a modern method is presented to forecast the short term hourly electrical energy costs based on the hybrid neural networks. In this method, influential parameters playing a key role in the accuracy of these types of systems are identified and the most prominent ones are selected. Due to the varying electrical price fluctuations amidst different days and seasons, these parameters do not adhere to a common pattern. In this regard, the data are divided into the classes that are close in nature in order to improve the forecasts. Since, detection of the similar successive days during the week is one of the effective forecast parameters , data pertaining to the various seasons are analyzed separately. In the proposed method, initially, similar days are placed in the close clusters using the SOM network. In the next stage, the price and temperature parameters of the similar days are trained separately in two MLP neural networks due to their difference in the nature and range of changes. Finally, the two networks are merged with another MLP network. In the proposed hybrid network, the evolutionary search method was used to assign a suitable initial weight in order to train the neural network. Due to the changes in the price data, the price of the previous hour has a significant effect on forecasting the current state. Thus, in the proposed method, the forecasted data of the preceding hour were used as one of the inputs for the next stage.

Figure 1 shows an overview of the proposed method. In the proposed method, the trained dataset was initially allocated to the SOM neural network. In this stage, the number of clusters was determined using the k-means and Fisher's criterion hybrid method. This number varied for each hour of the day. Thus, network training for 24 hours was conducted separately and in succession. In the proposed structure, upon specifying the number of clusters, it should be determined that each sample entering to the network from the trained dataset belongs to which cluster and in the next stage, the associated MLP network is setup based on the selected cluster. Essentially, each MLP network is trained with the dataset pertaining to its relevant cluster. Finally, for the test dataset, the sample distance from the clusters is initially determined along with its relevant cluster. Then, the test sample is evaluated using the MLP network associated with the cluster.

In the proposed method, each cluster does not only use one MLP network, but a combination of MLPs is utilized. The input dataset is divided into two categories i.e., load price and temperature which are of extremely different nature and their effects vary significantly according to the range of changes. In the proposed method, two separate

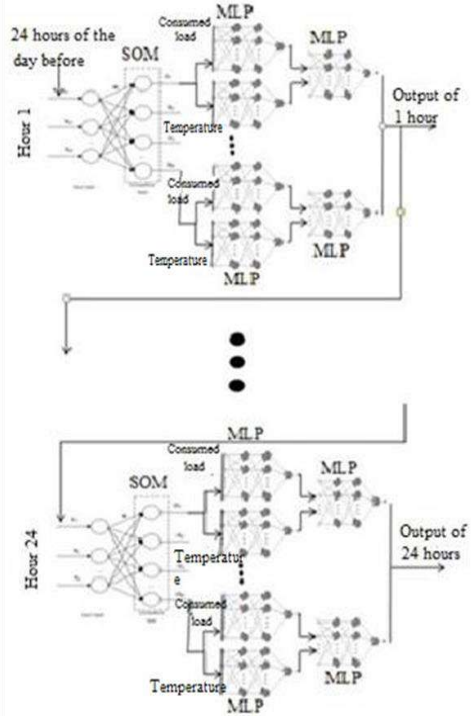

Figure 1. An overview of the hybrid network to forecast the load price of the next 24 hours

networks are used for the temperature and load. Finally, the outputs from these networks are merged with other MLPs and the forecast is achieved. In the proposed method, the output for each hour is used as the input for the next hour. In the process of training the perceptron neural network, a GA is used to obtain the initial weights in order to raise the accuracy of the price forecasting.

Data analysis was done using the MATLAB software. In this paper, evaluation criteria, such as the mean absolute error (MAE), mean absolute percentage error (MAPE), and R^2 were used. The MAE refers to the difference between the predicted value and the real value, which is shown by Equation (1).

$$\text{MAE} = \frac{1}{n}\sum_{i=1}^{n}|y_i - \hat{y}_i| \quad (1)$$

The MAPE is calculated using the Equation (2):

$$\text{MAPE} = \frac{1}{n}\sum_{i=1}^{n}\left|\frac{\hat{y}_i - y_i}{\hat{y}_i}\right| \times 100 \quad (2)$$

The R^2 criterion statistically measures how close the data are to the fitted regression line. R^2 is also called as the coefficient of determination for detection coefficient. The definition of the coefficient of determination (R^2) is relatively simple:" the coefficient of determination (R^2) indicates the percentage of variations in a dependent

variable determined by the independent variable" or in other words, the coefficient of determination indicates "to what extent the variations in the dependent variable are influenced by the independent variable and the rest of the changes of the dependent variable are related to other factors". The coefficient of determination is always between 0.0-100%. Zero percentage indicates that the model does not describe the response data variability around its mean, and 100% indicates that the model describes all the response data variability around its mean [48]. Equation (3) is used to calculate this coefficient.

$$R2 = 1 - \frac{SS_{res}}{SS_{tot}} \quad (3)$$

In Equation (4), SS_{res} and SS_{tot} are derived as:

$$SStot = \sum_i (y_i - \bar{y})^2 \quad (4)$$

In the above equations, $\bar{y}$ is the mean of the main data derived by $\bar{y} = \sum_i y_i$.

3. RESULTS

Table 1 presents the network structure related to the temperature for different seasons. In this table, forecasts for each year were conducted separately.

It is noteworthy that the values associated with the number of neurons, number of hidden layers, and threshold of the validated set were also calculated. In this regard, Figure 2 shows a sample of the results obtained for the summer for these parameters. As shown in Figure 2(a), the optimal number of neurons is equal to 5. According to Figures 2(b) and 2(c), the number of hidden layers and the threshold are equal to 0.1. All the results for subsequent tests were achieved using the validated data.

The parameters used for estimation of the neural network based on the validated data, (a) number of the neurons, (b) number of the hidden layers, and (c) threshold. A structure similar to Table 1 was used to design a price-related network. In the proposed structure, the number of price traits is one less than the input structure presented in Table 1, which is related to the forecasted hour. In this network, the forecast of the preceding stage is used for the load of the preceding hour (with the exception of 1 a.m.). Essentially, the forecast for the current hour is the input for the next hour. Table 2 shows the MLP neural network structure used for combination of the previous two MLP networks.

In this research, separate tests were designed for each season to analyze the consumed loads in each season separately. Although, it should be noted that the fundamental issue for this type of data concerns the summer season, which should be considered despite the favorable results achieved for all the seasons. The training results and test data for the consumed load in fall were presented. Moreover, a comparison was made between the proposed hybrid method and the MLP method.

Initially, the number of clusters was determined through the k-means clustering method and Fisher's criterion. Figure 3 shows the results of a specific hour in fall. Evidently, the number of clusters for this specific hour was equal to 4. Essentially, a network was considered for the temperature and price for each cluster.

TABLE 1. MLP network configuration parameters for load and temperature inputs

Number of input neurons	11	2 temperature trait of previous weeks 2 temperature trait of the previous days 2 load trait of the previous weeks 2 load trait of the previous days 1 temperature trait of the preceding hour 1 load trait of the preceding hour 1 temperature trait of the forecasted hour
Number of trained samples		46 samples for each hour
Number of validated samples		10 samples for each hour
Number of test samples		23 samples for each hour
Number of hidden layers		1
Number of neurons in the hidden layers		5
Error back propagation algorithm	Learning rate	0.05
	Maximum number of repetitions	100
	Error threshold to stop learning	0.1
	Slope of activation function	1
	value of β in $f(x) = \tanh(\beta x)$	
Genetic Algorithm	Initial population	200
	Number of generations	10
	Size of each chromosome	30
	Selection function	@selectiontournament
	Termination function	@crossoversinglepoint
	Mutation function	@mutationgaussian

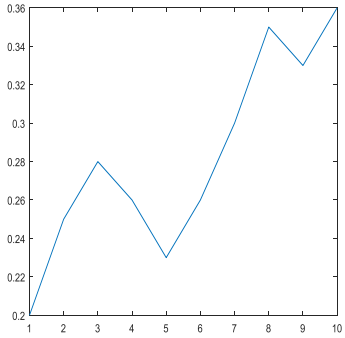
(a): horizontal: number of neurons, errors

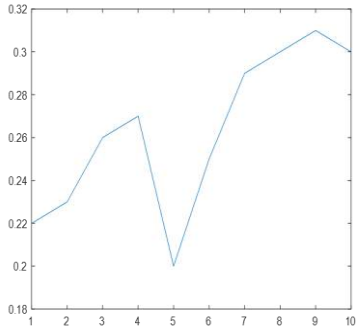
(b): horizontal: number of hidden layers,

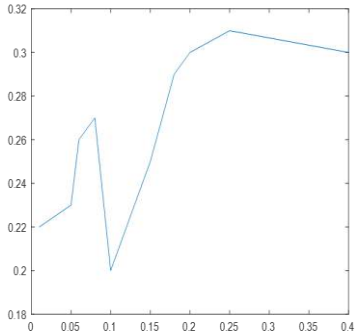
(c): horizontal: threshold vertical: error

Figure 2. Errors vs number of neurons, number of hidden layers and threshold

TABLE 2. Multi-layer perceptron neural network configuration parameters to combine networks

Number of input neurons	2	1 output trait related to the MLP network with load price input 1 output trait related to the MLP network with temperature input
Number of trained samples		46 samples for each hour
Number of validated samples		10 samples for each hour
Number of test samples		23 samples for each hour
Number of hidden layers		1
Number of neurons in the hidden layer		3
Error back propagation algorithm	Learning rate	0.05
	Maximum number of repetitions	100
	Error threshold to stop learning	0.1
	Slope of activation function value of β in $f(x) = \tanh(\beta x)$	1
Genetic Algorithm	Size of initial population	200
	Number of generations	10
	Size of each chromosome	9
	Selection function	@selectiontournament
	Termination function	@crossoversinglepoint
	Mutation function	@mutationgaussian

In the next step, the GA was used to calculate the initial weights, the results of which are shown in 10 iterations in Figure 4.

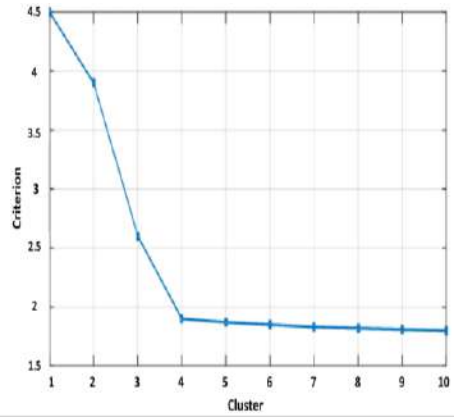

Figure (3). The rate of change in Fisher's criterion in regard to the number of clusters in the load set pertaining to fall

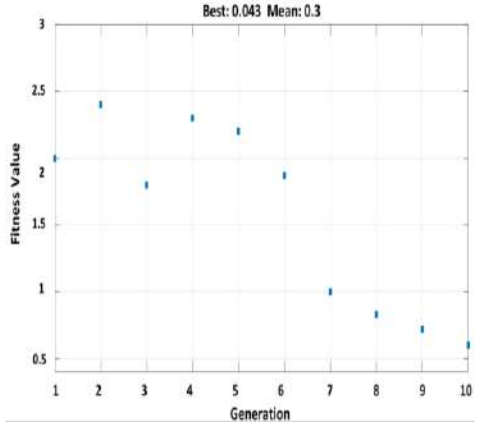

Figure 4. The achieved fitness value using the Genetic Algorithm in 10 repetitions

Figures 5 and 6 show the results obtained for the training and test datasets in fall. Clearly, the results achieved for summer and fall using the proposed method were superior to those obtained using the MLP -based method. Overall, the hybrid MLP and SOM method exhibited the superior results. Table 3 shows a comparison between the results obtained from the MLP network in various seasons and those obtained using the proposed method.

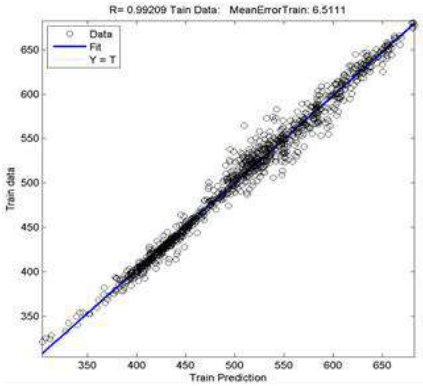

(a) MLP network

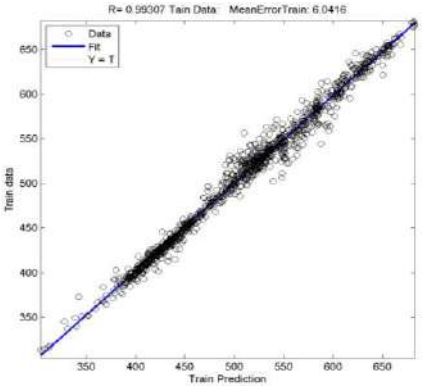

(b) MLP-SOM hybrid network

Figure 5. Results achieved in the training stage for fall

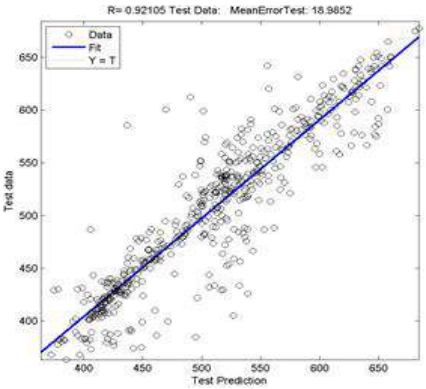

(a) MLP network

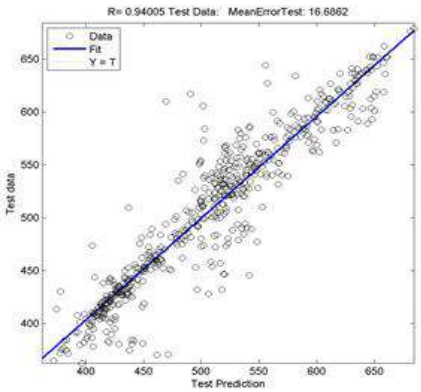

(b) MLP-SOM hybrid network

Figure 6. Results from the test stage for fall

TABLE 3. Comparison between the load forecasts achieved using the simple MLP method and those obtained from the MLP-SOM hybrid method

Year	Season	Method	R
2016	Spring	MLP	90.57%
		Proposed method	93.4%
	Summer	MLP	85.2%
		Proposed method	91.28%
	Fall	MLP	92.10%
		Proposed method	94%
	Winter	MLP	94.49%
		Proposed method	95.72%
2017	Spring	MLP	91.32%
		Proposed method	94.02%
	Summer	MLP	87.70%
		Proposed method	92.89%
	Fall	MLP	90.17%
		Proposed method	93.45%
	Winter	MLP	93.65%
		Proposed method	94.36%

Figures 7, 8 and 9 show samples of the achieved results. Figure 7 shows proposed system output in month 8 of 2017. Figure 8 shows the proposed system output in month 10 of 2016. Figure 9 shows the proposed system output in month 4 of 2015. Figure 10 shows the chart of real and forecasted price changes of 365 days in 2015. Figure 11 shows the results achieved by the proposed method for various seasons of 2016.

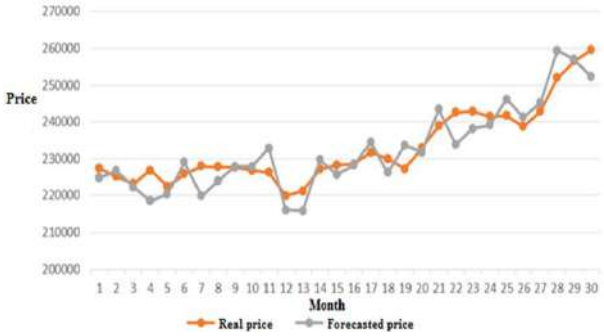

Figure 7. Chart of price changes in Iran October 2017

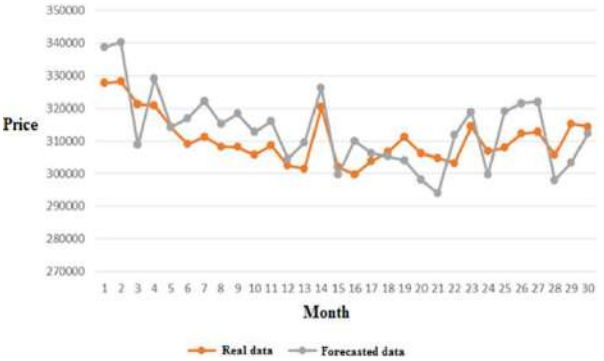

Figure 8. Chart of price changes in Iran December 2016

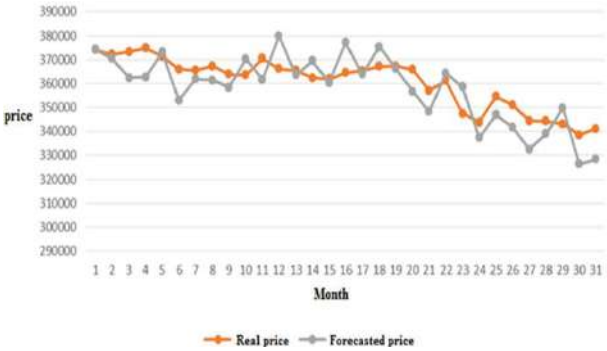

Figure 9. Chart of price changes in Iran June 2015

Figure 10. Chart of price changes for 365 days in 2016

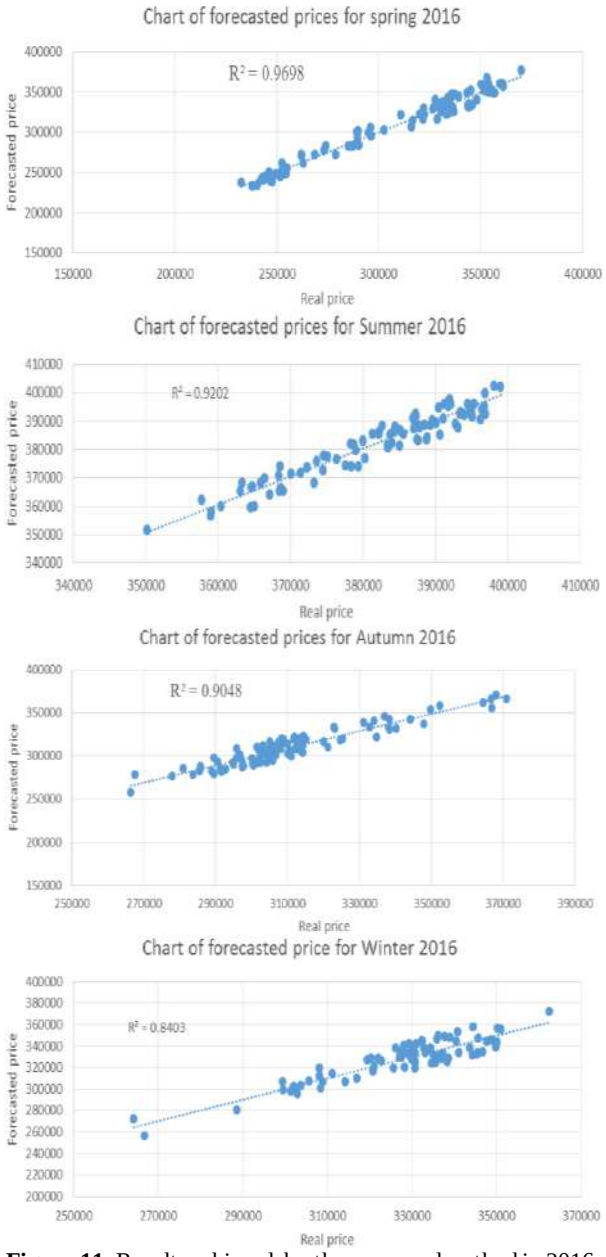

Figure 11. Results achieved by the proposed method in 2016

4. CONCLUSION

The provision of a smart system to forecast the price of electricity can entail an integral contribution to the competitive market in the dependent industry and country. In this regard, herein, a solution was presented based on the neural networks. Results showed an improved performance of such systems. Nevertheless, efforts can be made for further improving these systems. In this section,

the suggestions are presented that may aid the researchers and enthusiasts in this field based on the experiences attained in this study.

1) Data should be extracted in addition to the energy and temperature data
2) A fuzzy system should be applied to extract the rules governing the market of such energy. Essentially, there are rules and regulations for the complex forecast systems, such as energy, which are typically extracted based on the experiences, e.g., the effect of stock changes in the stock market or political changes in a country severely influencing the precision of forecasting. To this end, it is possible to acquire and analyze these changes using a fuzzy system.

In the proposed method, as well as in the implementation phases of the project, there were some limitations which upon elimination will appease many of the issues pertaining to the price forecasting systems. Some of the limitations of this paper and relevant applications are as follows.

Since, the load and temperature-related information is not available in many regions on an hourly basis, the design of a comprehensive system to gather hourly temperature and load information may be significantly effective in improving such applications. For example, herein, the temperature information was used for Iran.

The availability of price and load-related information pertaining to the numerous years may be vital in designing a comprehensive system and statistical analysis of the information, but regrettably for Iran, only the information related to 5 years i.e., from 2011 to 2016 was available.

Upon considerable inquiries, the information was extracted for the Mazandaran province in Iran. Unfortunately, such information is not archived in many of Iran's provinces and thus, it cannot be studied comprehensively.

Numerous factors, such as political and economic events have a significant effect on the energy prices. Unfortunately, there was no comprehensive information on the important events in Iran to be used in this investigation. If such information is available, it could result in improvements in the proposed method.

5. REFERENCES

1. Lin, L., Cunshan, Z., Vittayapadung, S., Xiangqian, S., and Mingdong, D., "Opportunities and challenges for biodiesel fuel", ***Applied Energy***, Vol. 88, No. 4, (2011), 1020–1031. doi:10.1016/j.apenergy.2010.09.029
2. Dhinesh, B., Maria Ambrose Raj, Y., Kalaiselvan, C., and KrishnaMoorthy, R., "A numerical and experimental assessment of a coated diesel engine powered by high-performance nano biofuel", ***Energy Conversion and Management***, Vol. 171, (2018), 815–824. doi:10.1016/j.enconman.2018.06.039
3. Vigneswaran, R., Annamalai, K., Dhinesh, B., and Krishnamoorthy, R., "Experimental investigation of unmodified diesel engine performance, combustion and emission with multipurpose additive along with water-in-diesel emulsion fuel", ***Energy Conversion and Management***, Vol. 172, (2018), 370–380. doi:10.1016/j.enconman.2018.07.039
4. Dhinesh, B., and Annamalai, M., "A study on performance, combustion and emission behaviour of diesel engine powered by novel nano nerium oleander biofuel", ***Journal of Cleaner Production***, Vol. 196, (2018), 74–83. doi:10.1016/j.jclepro.2018.06.002
5. Nomura, N., Inaba, A., Tonooka, Y., and Akai, M., "Life-cycle emission of oxidic gases from power-generation systems", ***Applied Energy***, Vol. 68, No. 2, (2001), 215–227. doi:10.1016/S0306-2619(00)00046-5
6. Sánchez de la Nieta, A., González, V., and Contreras, J., "Portfolio Decision of Short-Term Electricity Forecasted Prices through Stochastic Programming", ***Energies***, Vol. 9, No. 12, (2016), 1069. doi:10.3390/en9121069
7. Najafi, A., Falaghi, H., Contreras, J., and Ramezani, M., "Medium-term energy hub management subject to electricity price and wind uncertainty", ***Applied Energy***, Vol. 168, (2016), 418–433. doi:10.1016/j.apenergy.2016.01.074
8. Yang, P., Tang, G., and Nehorai, A., "A game-theoretic approach for optimal time-of-use electricity pricing", ***IEEE Transactions on Power Systems***, Vol. 28, No. 2, (2013), 884–892. doi:10.1109/TPWRS.2012.2207134
9. Yang, Z., Ce, L., and Lian, L., "Electricity price forecasting by a hybrid model, combining wavelet transform, ARMA and kernel-based extreme learning machine methods", ***Applied Energy***, Vol. 190, (2017), 291–305. doi:10.1016/j.apenergy.2016.12.130
10. Wang, D., Luo, H., Grunder, O., Lin, Y., and Guo, H., "Multi-step ahead electricity price forecasting using a hybrid model based on two-layer decomposition technique and BP neural network optimized by firefly algorithm", ***Applied Energy***, Vol. 190, (2017), 390–407. doi:10.1016/j.apenergy.2016.12.134
11. Abedinia, O., Amjady, N., Shafie-Khah, M., and Catalão, J. P. S., "Electricity price forecast using Combinatorial Neural Network trained by a new stochastic search method", ***Energy Conversion and Management***, Vol. 105, (2015), 642–654. doi:10.1016/j.enconman.2015.08.025
12. Lago, J., De Ridder, F., Vrancx, P., and De Schutter, B., "Forecasting day-ahead electricity prices in Europe: The importance of considering market integration", ***Applied Energy***, Vol. 211, (2018), 890–903. doi:10.1016/j.apenergy.2017.11.098
13. Weron, R., (, October 1)"Electricity price forecasting: A review of the state-of-the-art with a look into the future", ***International Journal of Forecasting***, Vol. 30, No. 4, (2014), 1030–1081, Elsevier B.V., 1030–1081. doi:10.1016/j.ijforecast.2014.08.008
14. Lago, J., De Ridder, F., and De Schutter, B., "Forecasting spot electricity prices: Deep learning approaches and empirical comparison of traditional algorithms", ***Applied Energy***, Vol. 221, (2018), 386–405. doi:10.1016/j.apenergy.2018.02.069
15. Wang, J., Liu, F., Song, Y., and Zhao, J., "A novel model: Dynamic choice artificial neural network (DCANN) for an electricity price forecasting system", ***Applied Soft Computing Journal***, Vol. 48, (2016), 281–297. doi:10.1016/j.asoc.2016.07.011
16. Bento, P. M. R., Pombo, J. A. N., Calado, M. R. A., and Mariano, S. J. P. S., "A bat optimized neural network and wavelet transform

approach for short-term price forecasting", ***Applied Energy***, Vol. 210, (2018), 88–97. doi:10.1016/j.apenergy.2017.10.058

17. Ghasemi, A., Shayeghi, H., Moradzadeh, M., and Nooshyar, M., "A novel hybrid algorithm for electricity price and load forecasting in smart grids with demand-side management", ***Applied Energy***, Vol. 177, (2016), 40–59. doi:10.1016/j.apenergy.2016.05.083
18. Mirakyan, A., Meyer-Renschhausen, M., and Koch, A., "Composite forecasting approach, application for next-day electricity price forecasting", ***Energy Economics***, Vol. 66, (2017), 228–237. doi:10.1016/j.eneco.2017.06.020
19. Tian, L., and Noore, A., "Short-term load forecasting using optimized neural network with genetic algorithm", In International Conference on Probabilistic Methods Applied to Power Systems, (2005). https://ieeexplore.ieee.org/abstract/document/1378676
20. Ansari, M., and Amoli, M. T., "Optimal pricing strategy in Iran's electricity market using probabilistic supply curve model", 28th International Electricity Conference, (2013). [In Persion]. http://psc-ir.com/cd/2013/papers/2404.pdf
21. Panapakidis, I. P., and Dagoumas, A. S., "Day-ahead electricity price forecasting via the application of artificial neural network based models", ***Applied Energy***, Vol. 172, (2016), 132–151. doi:10.1016/j.apenergy.2016.03.089
22. Sandhu, H. S., Fang, L., and Guan, L., "Forecasting day-ahead price spikes for the Ontario electricity market", ***Electric Power Systems Research***, Vol. 141, (2016), 450–459. doi:10.1016/j.epsr.2016.08.005
23. Ortiz, M., Ukar, O., Azevedo, F., and Múgica, A., "Price forecasting and validation in the Spanish electricity market using forecasts as input data", ***International Journal of Electrical Power and Energy Systems***, Vol. 77, (2016), 123–127. doi:10.1016/j.ijepes.2015.11.004
24. Keles, D., Scelle, J., Paraschiv, F., and Fichtner, W., "Extended forecast methods for day-ahead electricity spot prices applying artificial neural networks", ***Applied Energy***, Vol. 162, (2016), 218–230. doi:10.1016/j.apenergy.2015.09.087
25. Singh, N., Mohanty, S. R., and Dev Shukla, R., "Short term electricity price forecast based on environmentally adapted generalized neuron", ***Energy***, Vol. 125, (2017), 127–139. doi:10.1016/j.energy.2017.02.094
26. Itaba, S., and Mori, H., "A Fuzzy-Preconditioned GRBFN Model for Electricity Price Forecasting", ***Procedia Computer Science***, Vol. 114, (2017), 441–448. doi:10.1016/j.procs.2017.09.010
27. Tang, L., Yu, L., He, K., "A novel data-characteristic-driven modeling methodology for nuclear energy consumption forecasting". ***Applied Energy***; Vol. 128, 1–14 (2014). https://doi.org/10.1016/j.apenergy.2014.04.021
28. Chai, J., Zhang, Z. Y., Wang, S. Y., Lai, K. K., and Liu, J., "Aviation fuel demand development in China", ***Energy Economics***, Vol. 46, (2014), 224–235. doi:10.1016/j.eneco.2014.09.007
29. Diongue, A. K., Guégan, D., and Vignal, B., "Forecasting electricity spot market prices with a k-factor GIGARCH process", ***Applied Energy***, Vol. 86, No. 4, (2009), 505–510. doi:10.1016/j.apenergy.2008.07.005
30. Girish, G. P., "Spot electricity price forecasting in Indian electricity market using autoregressive-GARCH models", ***Energy Strategy Reviews***, Vols 11–12, (2016), 52–57. doi:10.1016/j.esr.2016.06.005
31. Zhang, J., and Tan, Z., "Day-ahead electricity price forecasting using WT, CLSSVM and EGARCH model", ***International Journal of Electrical Power and Energy Systems***, Vol. 45, No. 1, (2013), 362–368. doi:10.1016/j.ijepes.2012.09.007
32. Yan, X., and Chowdhury, N. A., "Mid-term electricity market clearing price forecasting: A hybrid LSSVM and ARMAX approach", ***International Journal of Electrical Power and Energy Systems***, Vol. 53, No. 1, (2013), 20–26. doi:10.1016/j.ijepes.2013.04.006
33. Zhu, B., Chevallier, J., Zhu, B., and Chevallier, J., "Carbon Price Forecasting with a Hybrid ARIMA and Least Squares Support Vector Machines Methodology", ***Pricing and Forecasting Carbon Markets***, (2017), 87–107. doi:10.1007/978-3-319-57618-3_6
34. He, K., Yu, L., and Tang, L., "Electricity price forecasting with a BED (Bivariate EMD Denoising) methodology", ***Energy***, Vol. 91, (2015), 601–609. doi:10.1016/j.energy.2015.08.021
35. Qiu, X., Suganthan, P. N., and Amaratunga, G. A. J., "Short-term Electricity Price Forecasting with Empirical Mode Decomposition based Ensemble Kernel Machines", ***Procedia Computer Science***, Vol. 108, (2017), 1308–1317. doi:10.1016/j.procs.2017.05.055
36. Mirzayian Dezfuli, I., and Nikukar, J., "Assessment of electricity price forecast methods in the energy market", 4th International Science and Engineering Conference, (2017). [In Persion]. https://www.civilica.com/Paper-ICESCON04-ICESCON04_148.html
37. Vahidi, A., and Tofighi, M. H., "Simultaneous forecast of price and demand in a smart electricity distribution network", 2nd International Conference on Modern Scientific Research in Computer Science and Engineering, (2017). [In Persion]. https://www.civilica.com/Paper-COMCONF02-COMCONF02_222.html
38. Nasiri Ghusheh Bolagh, M., "Short-term electricity price forecast using times series in a neural fuzzy method" 3rd Regional Control, Electronics and Artificial Intelligence Conference, (2016). [In Persion]. https://www.civilica.com/Paper-CEAI03-CEAI03_006.html
39. Shayeghi, H., and Ghasemi, A., "Daily electricity price forecast using an enhanced neural network based on wavelet transform and gravitational search chaotic method, ", ***Journal of Electrical Engineering, Tabriz University***, (2016). [In Persion]. https://www.civilica.com/Paper-JR_TJEE-JR_TJEE-45-4_010.html
40. Meng, L., Hossain, M. U., Farzana, S., and Thengolose, A. L., "Estimation and Prediction of Residential Building Energy Consumption in Rural Areas of Chongqing", ***International Journal of Engineering, Transactions C: Aspects***, Vol. 26, No. 9, (2013), 955–962. doi:10.5829/idosi.ije.2013.26.09c.03
41. Neshat, N., "An Approach of Artificial Neural Networks Modeling Based on Fuzzy Regression for Forecasting Purposes", ***International Journal of Engineering, Transactions B: Applications***, Vol. 28, No. 11, (2015), 1651–1655. doi:10.5829/idosi.ije.2015.28.11b.13
42. Ahmadi, E., Abooie, M. H., Jasemi, M., and Mehrjardi, Y. Z., "A Nonlinear Autoregressive Model with Exogenous Variables Neural Network for Stock Market Timing: The Candlestick Technical Analysis", ***International Journal of Engineering, Transactions C: Aspects***, Vol. 29, No. 12, (2016), 1717–1725. doi:10.5829/idosi.ije.2016.29.12c.10
43. Neshat, N., Amin-Naseri, M. R., and Ganjavi, H. S., "A Game Theoretic Approach for Sustainable Power Systems Planning in Transition", ***International Journal of Engineering, Transactions C: Aspects***, Vol. 30, No. 3, (2017), 394–403. doi:10.5829/idosi.ije.2017.30.03c.09
44. Khedmati, M., Seifi, F., and Azizi, M. J., "Time series forecasting

of bitcoin price based on autoregressive integrated moving average and machine learning approaches", ***International Journal of Engineering, Transactions A: Basics***, Vol. 33, No. 7, (2020), 1293–1303. doi:10.5829/ije.2020.33.07a.16

45. Kavoosi Davoodi, S. M., Najafi, S. E., Hosseinzadeh Lotfi, F., and Mohammadiyan bisheh, H., "An accurate analysis of the parameters affecting consumption and price fluctuations of Electricity in the Iranian market during Summer", ***Scientia Iranica***, (2020). doi:10.24200/sci.2020.52550.2771
46. Bagheri, F., Ziaratban, M., and Tarokh, M. J., "Predicting Behaviors of Insurance Costumers by Using the Genetic Algorithm", ***Journal of Mathematics and Computer Science***, Vol. 14, (2014), 54–70
47. Kohani, S., and Zong, P., "A Genetic Algorithm for Designing Triplet LEO Satellite Constellation with Three Adjacent Satellites", ***International Journal of Aeronautical and Space Sciences***, Vol. 20, No. 2, (2019), 537–552. doi:10.1007/s42405-019-00149-6
48. Purohit, I., and Purohit, P., "Inter-comparability of solar radiation databases in Indian context", ***Renewable and Sustainable Energy Reviews***, Vol. 50, (2015), 735–747, Elsevier Ltd, 735–747. doi:10.1016/j.rser.2015.05.020

Persian Abstract

چکیده

با توجه به پیچیدگی‌های موجود در بازار برق عوامل بسیاری از جمله عدم قطعیت‌های موجود، نحوه بسته شدن بازار، نحوه تسویه حساب، ساختار و قوانین بازار، هزینه تولید، قیود حاکم بر واحدها و شبکه و ... در تعیین استراتژی بهینه قیمت‌دهی موثر است. تاکنون روش‌ها و مدل‌های مختلفی برای حل مسأله قیمت‌دهی در فضای رقابتی صنعت برق ارائه شده که مهمترین آنها شامل روش‌های قیمت‌دهی مبتنی بر پیش‌بینی رفتار رقبا، روش‌های قیمت‌دهی مبتنی بر پیش‌بینی قیمت بازار، روش‌های مبتنی بر تئوری بازی و بالاخره روش‌های قیمت‌دهی بر مبنای الگوریتم‌های هوشمند می‌باشد. هدف این پژوهش ارائه استراتژی بهینه جهت پیش‌بینی قیمت تسویه بازار انرژی الکتریکی در بازار رقابتی برق ایران (بر اساس داده‌ها در فصل پاییز) است. در روش پیشنهادی مقاله حاضر از شبکه ترکیبی بر پایه شبکه‌های عصبی استفاده شده است. در داده‌های مورد تحلیل میزان انرژی مصرفی و همچنین دما (در صورت امکان) و قیمت در روزهای گذشته و هفته گذشته استفاده شده است. در روش پیشنهادی از شبکه ترکیبی از SOM برای خوشه‌بندی ورودی بر اساس روزهای مشابه استفاده شده است. از چند شبکه عصبی MLP برای ترکیب داده‌های استخراجی از میزان انرژی، قیمت گذشته و دما (در صورت امکان) استفاده شده است. نتایج نشان‌دهنده بهبود عملکرد سیستم‌های هوشمند متنی بر شبکه‌های عصبی در پیش‌بینی قیمت برق بود.

IJE TRANSACTIONS A: Applications Vol. 34, No. 01, (January 2021) 162-170

International Journal of Engineering

Journal Homepage: www.ije.ir

Reactive Scheduling Addressing Unexpected Disturbance in Cellular Manufacturing Systems

V. Rahimi, J. Arkat*, H. Farughi

Department of Industrial Engineering, University of Kurdistan, Sanandaj, Iran

P A P E R I N F O

Paper history:
Received 04 July 2020
Received in revised form 22 July 2020
Accepted 03 September 2020

Keywords:
Reactive Scheduling
Cellular Manufacturing System
Resistance to Change
Arrival of New Jobs

A B S T R A C T

Most production environments face random, unexpected events such as machine failure, uncertain processing times, the arrival of new jobs, and cancellation of jobs. For the reduction of the undesirable side effects of an unexpected disruption, the initial schedule needs to be reformed partially or entirely. In this paper, a mathematical model is presented to address the integrated cell formation and cellular rescheduling problems in a cellular manufacturing system. As a reactive model, the model is developed to handle the arrival of a new job as a disturbance to the system. Based on the principle of resistance to change, the reactive model seeks a new solution with the minimum difference from the initial solution. This is realized through a simultaneous minimization of the total completion time and the number of displaced machines. For the investigation of the performance of the proposed model, some numerical examples are solved using the GAMS software. The results demonstrate the ability of the reactive model to obtain solutions resistant to unexpected changes.

***doi**: 10.5829/ije.2021.34.01a.18*

NOMENCLATURE

Sets and Indices			
$\boldsymbol{M}$	Set of machine types ($m \in \{1, 2, \dots, M\}$)	TE_p	Intercellular transportation time for part p
$\boldsymbol{P}$	Set of parts in the initial plan ($p \in \{1, 2, \dots, P\}$)	F_{kp}	Completion time of the k^{th} operation of part p in the initial plan
$\boldsymbol{P'}$	Set of parts in the reactive plan ($p' \in \{1, 2, \dots, P'\}$)	X_{kpmjc}	A binary parameter that takes value 1 if, in the initial plan, the k^{th} operation of part p is processed on the j^{th} duplication of machine type m in cell c, and takes value 0 otherwise
$\boldsymbol{MS}_m$	Set of duplications of machine type m ($j, j' \in \{1, 2, \dots, MS_m\}$)	D	The occurrence time of the disturbance (the unexpected arrival of a new job)
$\boldsymbol{C}$	Set of cells ($c, c' \in \{1, 2, \dots, C_{max}\}$)	Y_{mjc}	A binary parameter that takes value 1 if, in the initial plan, the j^{th} duplication of machine type m is allocated to cell c, and takes value 0 otherwise
$\boldsymbol{K}_p$	Operation sequence of part p ($k, k' \in \{1, 2, \dots, K_p\}$)	YY'_c	A binary variable that takes value 1 if cell c is formed after the disturbance, and takes value 0 otherwise
$\boldsymbol{M}_{kp}$	Set of alterative machine types for the k^{th} operation of part p	$Z'_{kpk'p'mj}$	A binary variable that takes value 1 if the k^{th} operation of part p is processed after the disturbance before the k'^{th} operation of part p' on the j^{th} duplication of machine type m, and takes value 0 otherwise
		v_{kp}	A binary parameter that takes value 1 if the starting time of processing the k^{th} operation of part p in the initial plan is before the occurrence of the disturbance, and takes value 0 otherwise
Parameters		**Decision Variables**	
C_{min}	Minimum number of cells that should be formed	F'_{kp}	Completion time of the k^{th} operation of part p (after the disturbance)
C_{max}	Maximum number of cells that should be formed	X'_{kpmjc}	A binary variable that takes value 1 if the k^{th} operation of part p is processed after the disturbance on the j^{th} duplication of machine type m in cell c, and takes value 0 otherwise
BL	Minimum number of machines in each cell	Y'_{mjc}	A binary variable that takes value 1 if the j^{th} duplication of machine type m is allocated after the disturbance to cell c, and takes value 0 otherwise
BU	Maximum number of machines in each cell	YY'_c	A binary variable that takes value 1 if cell c is formed after the disturbance, and takes value 0 otherwise
L	A large positive number	$Z'_{kpk'p'mj}$	A binary variable that takes value 1 if the k^{th} operation of part p is processed after the disturbance before the k'^{th} operation of part p' on the j^{th} duplication of machine type m, and takes value 0 otherwise
T_{kpm}	Processing time of operation k of part p on a machine of type m	Fy_{kp}	A binary variable that takes value 1 if the completion time of the k^{th} operation of part p in the reactive plan changes concerning that in the initial plan, and takes value 0 otherwise

* Corresponding Author's Email: *j.arkat@uok.ac.ir* (J. Arkat)

Please cite this article as: V. Rahimi, J. Arkat, H. Farughi, Reactive Scheduling Addressing Unexpected Disturbance in Cellular Manufacturing Systems, International Journal of Engineering, Transactions A: Applications Vol. 34, No. 01, (2021) 162-170

1. INTRODUCTION

Scheduling is a decision problem that plays a crucial role in manufacturing and service systems. In today's competitive environment, it seems inevitable to have a scheduling process and an efficient operation sequence, a necessity for survival in the commercial space. For example, companies are required to adhere to the pre-promised delivery times, and failure to comply with them can lead to loss of significant profit. They should also plan their jobs so that they can utilize the available resources most properly. Scheduling addresses resource allocation over specific time frames and is aimed at optimizing one or more specified variables. Many researchers often assume that manufacturing systems operate in static environments in which no unexpected events occur. However, many manufacturing systems are in dynamic and random conditions, and at any moment, they may encounter unexpected events such as machine failure, the arrival of new jobs into the system, cancellation of jobs, delay in the arrival or shortage of materials, and change in the job priority. This leads to the non-optimality and infeasibility of the initial schedule. In order to address unexpected disruptions in a manufacturing system, an appropriate approach must be adopted. A framework of strategies for rescheduling manufacturing systems has been presented by Vieira et al. [1]. Wojakowski and Warzolek [2] presented a classification of scheduling problems under production uncertainty. Scheduling can provide better coordination in manufacturing systems to increase efficiency and reduce operating costs. Ideally, the manufacturing system should follow the schedule as far as possible; however, unexpected events can change the status of the system and affect its performance.

In general, there are three approaches for addressing random disturbances, as listed below. (1) Proactive approach. This approach attempts to provide a schedule that minimizes the negative effects of disturbances, which will occur in the future by predicting the occurrence of unexpected events and incorporating them into the initial schedule. (2) Reactive schedule. This approach first provides the initial schedule regardless of the effects of unexpected disturbances, and as soon as unexpected events occur, it modifies the initial schedule given the reactive measures that need to be taken. In general, these reactions are divided into two categories. One involves reactions that seek to modify and improve the initial schedule and the other concerns reactions that attempt to provide a completely new schedule. A dispatching rule is a reactive model that schedules jobs based on a predefined criterion. Rescheduling is another reactive approach, which modifies the initial schedule in order to adapt the status of the system to the disturbance that has occurred. Most conducted studies have generated the modified schedule based only on workshop performance criteria. When operators process jobs based on an initial schedule, the other parts of the system, such as the inventory control, are also planned based on the initial schedule. The modified schedule may be completely different from the initial one. Hence, since the other activities of the system have been planned according to the initial schedule, it has a significant effect on the activities of the other departments, which leads to infeasibility or non-optimality in the system. For this reason, the corrective measures must be taken such that minimal changes are required in the system while workshop criteria are considered. (3) Proactive-reactive approach. This approach is a combination of the above two and consists of two stages. At the first stage, it provides an initial schedule, like the proactive approach. At the second stage, which is the reactive stage, a new schedule is presented as soon as an unexpected event occurs.

The pace of change in customer needs has increased, and in such a competitive environment, manufacturers are forced to produce a wide variety of products in different volumes. Under such conditions, manufacturing systems should, on the one hand, have high flexibility to produce a wide range of products, as in a job shop system, and, on the other hand, produce high volumes of products over short periods, as in a flow shop system. Group technology (GT) and its relevant manufacturing systems are an accepted solution to the problem of semi-mass production of various products. Cellular manufacturing system (CMS), the most well-known application of group technology, attempts to identify manufacturing similarities of parts, based on which part families are formed and produced using relatively independent production units called machine cells. Some of the important benefits of CMSs are that they can simplify and reduce material transportation, reduce material flow in manufacturing, reduce setup and production time and costs, improve production control, and increase flexibility. The process of CMS design consists of four main steps: (1) cell formation (CF) (e.g., Sakhaii et al. [3] and Soolaki and Arkat [4]), (2) cellular layout (e.g., Arkat et al. [5] and Rahimi et al. [6]), (3) cellular scheduling (Arkat and Ghahve [7]), and (4) resource assignment (e.g., Mehdizadeh and Rahimi [8] and Bagheri et al. [9]).

A comprehensive review of published articles in the field of the CMS scheduling problem has been presented by Feng et al. [10]. Given the unexpected disruptions in production systems, which lead to the reduction of system efficiency, an appropriate approach should be adopted to address these disruptions in CMSs. Rahmani and Ramezanian [11] have presented a comprehensive literature review in the field of dealing with random disturbances in scheduling problems. In the area of CMSs, few studies have examined addressing unexpected disturbances, most of which have presented a knowledge-based approach. Olumolade [12] proposed a

reactive approach to solve the CMS scheduling problem when machine failure occurs. They assumed that the CMS did not include additive machines. Weckman [13] presented a framework for reactive scheduling in the cellular manufacturing environment using the notions of neural networks, genetic algorithms, and simulation in such a way that the neural network was used to generate the initial solution to the genetic algorithm. The solution obtained by the genetic algorithm was applied to the simulation model for the specification of the efficiency of the scheduling based on the performance criteria. Li and Murata [14] presented a mixed-integer programming model for the reactive scheduling problem for waiting jobs in a CMS against occurrences of machine failure. They proposed a hybrid binary particle swarm optimization algorithm and simulated annealing algorithm for solving the problem. When the initial schedule changes, the workforce resists against the change directly or indirectly. In other words, after each disruption, the operators and internal parts of the system prefer to process jobs based on the initial schedule and to process new ones at the end. Therefore, they resist any changes in the initial plan. The research conducted in this area by Caruth et al. [15], Giangreco, and Pecci [16], and Rahmani and Ramezanian [11] shows that worker dissatisfaction and resistance to change may increase processing time.

The implementation benefits of CMSs include reduction of setup times, reduction of material transportation, reduction of the work-in-process inventory, better production efficiency, and higher-quality, shorter response times to the customer requirements. Of course, it is worth noting that the benefits of implementing a CMS for a company arise when the implemented CMS is based on the results of solving models that properly consider all the features of the system. Most of the CMSs considered in previous studies postulate an initial set of jobs to be processed in the manufacturing system, while a new, unexpected job may arrive in the manufacturing system during the program execution for which there is no predetermined plan. The purpose of this research is to investigate how to handle the arrivals of new, unexpected jobs in the CMS, events that lead to changes in the system parameters, and, consequently, non-optimality of the optimal solution found for normal conditions. For specification of how to address unwanted changes in input parameters, a reactive model is presented for the conditions that hold after the occurrence of a disturbance. The primary purpose of the model is to determine how to change the decisions (concerning cell formation and cell scheduling) so that the system is encountered with the slightest consequences in terms of costs and time. In order to consider the cost and time consequences, the reactive planning approach is formulated in such a way that the decision variables in the initial plan are considered as the parameters of the reactive model. Moreover, the notion of resistance to change (RTC) in the reactive scheduling problem, which has received little attention, is introduced.

2. PROBLEM STATEMENT AND MATHEMATICAL MODEL

In this section, a cellular manufacturing system is investigated, where there is the feasibility of processing non-sequential operations of parts on identical machines. These parts are referred to as reentrant parts. It is also possible to process some of the operations of the parts using several alternative machines. Here, the number of formed cells is unknown a prior and considered as a decision variable. Each machine has several identical copies, and each part has a number of alternative process routings. The number of machines in each cell and the number of cells each have a known minimum and maximum. Intercellular transportation time is assumed to be constant, and processing times include setup times. With an initial plan outlining machine grouping and part process routings, as well as the cellular scheduling, the goal is to make appropriate changes to address the situation where a part is added as a new order. Since a new, unexpected job may arrive in the system during the execution of the initial plan, we present a modified model to provide a new plan considering the original workshop criterion and the stability criterion. The proposed mathematical model seeks to present a plan which is not only minimizes the main criterion of the workshop (total completion time of parts) but also makes the slightest changes as compared to the initial plan. For this purpose, the notion of resistance to change is used, which increases in processing time. We apply the RTC concept creatively by combining it with the concept of system stability.

For this purpose, the set of parts in the plan on the arrival of a new job is indicated by $\boldsymbol{P}'$. The following sets of parameters and decision variables are also introduced.

The mathematical model of the problem is as follows:

$$min \sum_{p\epsilon \boldsymbol{P}'} F'_{K_p,p} \tag{1}$$

$$min \sum_{m\epsilon \boldsymbol{M}} \sum_{j\epsilon \boldsymbol{MS}_m} \sum_{c\epsilon \boldsymbol{C}} \left| Y'_{mjc} - Y_{mjc} \right| \tag{2}$$

$s.t.$

$$F'_{kp} \geq F_{kp} - M * (1 - v_{kp}) \qquad \forall p\epsilon \boldsymbol{P}, k\epsilon \boldsymbol{K}_p \tag{3}$$

$$F'_{kp} \leq F_{kp} + M * (1 - v_{kp}) \qquad \forall p\epsilon \boldsymbol{P}, k\epsilon \boldsymbol{K}_p \tag{4}$$

$$\sum_{c\epsilon \boldsymbol{C}} Y'_{mjc} \leq 1 \qquad \forall m\epsilon \boldsymbol{M}, j\epsilon \boldsymbol{MS}_m \tag{5}$$

$$\sum_{c\epsilon \boldsymbol{C}}\sum_{m\epsilon \boldsymbol{M}_{kp}}\sum_{j\epsilon \boldsymbol{MS}_m} X'_{kpmjc} = 1 - \nu_{kp} \quad \forall p\epsilon \boldsymbol{P'}, k\epsilon \boldsymbol{K}_p \tag{6}$$

$$X'_{kpmjc} \le Y'_{mjc} \quad \forall m\epsilon \boldsymbol{M}, c\epsilon \boldsymbol{C}, p\epsilon \boldsymbol{P}, k\epsilon \boldsymbol{K}_p, j\epsilon \boldsymbol{MS}_m \tag{7}$$

$$BL\ .YY'_c \le \sum_{m\epsilon \boldsymbol{M}}\sum_{j\epsilon \boldsymbol{MS}_m} Y'_{mjc} \le BU\ .\ YY'_c \quad \forall c\epsilon \boldsymbol{C} \tag{8}$$

$$YY'_c \ge\ YY'_{c+1} \qquad \forall c\epsilon \boldsymbol{C} - \{C_{max}\} \tag{9}$$

$$\sum_{c\epsilon \boldsymbol{C}} YY'_c \ge C_{min} \tag{10}$$

$$t_{p,k,k+1} = \frac{TE_p}{2}\cdot\sum_{c\epsilon \boldsymbol{C}}\Big|\sum_{m\epsilon \boldsymbol{M}_{k+1,p}}\sum_{j\epsilon \boldsymbol{MS}_m}\big(X'_{k+1,pmjc}\cdot(1-\nu_{k+1,p}) + X_{k+1,pmjc}\cdot\nu_{k+1,p}\big) - \sum_{m\epsilon \boldsymbol{M}_{k,p}}\sum_{j\epsilon \boldsymbol{MS}_m}\big(X'_{kpmjc}\cdot(1-\nu_{kp}) + X_{kpmjc}\cdot\nu_{kp}\big)\Big| \quad \forall p\epsilon \boldsymbol{P}, k\epsilon \boldsymbol{K}_p - \{K_p\} \tag{11}$$

$$F'_{1p} \ge \sum_{c\epsilon \boldsymbol{C}}\sum_{m\epsilon \boldsymbol{M}_{1p}}\sum_{j\epsilon \boldsymbol{MS}_m} T_{1pm}\cdot\big(X_{1pmjc}\cdot\nu_{1p}\big) + T'_{kpm}\cdot\Big(X'_{1pmjc}\cdot(1-\nu_{1p})\Big) \quad \forall p\epsilon \boldsymbol{P'} \tag{12}$$

$$F'_{k+1,p} \ge F'_{kp} + \sum_{c\epsilon \boldsymbol{C}}\sum_{m\epsilon \boldsymbol{M}_{k+1,p}}\sum_{j\epsilon \boldsymbol{MS}_m} T_{k+1,pm}\cdot\big(X_{k+1,pmjc}\cdot\nu_{k+1,p}\big) + T'_{k+1,pm}\cdot\Big(X'_{k+1,pmjc}\cdot(1-\nu_{k+1,p})\Big) + t_{p,k,k+1} \quad \forall p\epsilon \boldsymbol{P'}, k\epsilon \boldsymbol{K}_p - \{K_p\} \tag{13}$$

$$Z'_{kpk'p'mj} + Z'_{k'p'kpmj} = \sum_{c\epsilon \boldsymbol{C}}\big(X'_{kpmjc}\cdot(1-\nu_{kp}) + X_{kpmjc}\cdot\nu_{kp}\big).\big(X'_{k'p'mjc}\cdot(1-\nu_{k'p'}) + X_{k'p'mjc}\cdot\nu_{k'p'}\big) \quad \forall p,p'\epsilon \boldsymbol{P'}, k\epsilon \boldsymbol{K}_p, k'\epsilon \boldsymbol{K}_{p'}, p = p'\ and\ k = k'\ are\ incompatible;\ \forall j\epsilon \boldsymbol{MS}_m, m\epsilon \boldsymbol{M}_{kp} \cap \boldsymbol{M}_{k'p'}, c\epsilon \boldsymbol{C} \tag{14}$$

$$F'_{kp} - F'_{k'p'} + L\cdot\big(1 - Z'_{k'p'kpmj}\big) \ge T_{kpm}\cdot\nu_{kp} + T'_{kpm}\cdot(1-\nu_{kp}) \quad \forall p,p'\epsilon \boldsymbol{P'}, k\epsilon \boldsymbol{K}_p, k'\epsilon \boldsymbol{K}_{p'}, p = p'\ and\ k = k'\ are\ incompatible;\ \forall j\epsilon \boldsymbol{MS}_m, m\epsilon \boldsymbol{M}_{kp} \cap \boldsymbol{M}_{k'p'}, c\epsilon \boldsymbol{C} \tag{15}$$

$$F'_{kp} + L\cdot\nu_{kp} \ge D + \sum_{c\epsilon \boldsymbol{C}}\sum_{m\epsilon \boldsymbol{M}_{kp}}\sum_{j\epsilon \boldsymbol{MS}_m} T'_{kpm}\cdot X'_{kpmjc}\ , \quad \forall p\epsilon \boldsymbol{P'}, k\epsilon \boldsymbol{K}_p \tag{16}$$

$$\big|F'_{kp} - F_{kp}\big| \le L\ .Fy_{kp} \qquad \forall p\epsilon \boldsymbol{P'}, k\epsilon \boldsymbol{K}_p \tag{17}$$

$$T'_{kpm} = T_{kpm} + \alpha.\,Fy_{kp}\ .T_{kpm} \quad \forall p\epsilon \boldsymbol{P'}, k\epsilon \boldsymbol{K}_p, m\epsilon \boldsymbol{M}_{kp} \tag{18}$$

$$Y'_{mjc}, X'_{kpmjc}, Z'_{kpk'p'mj}, YY'_c, Fy_{kp}\epsilon\{0,1\} \tag{19}$$

The objective function (1) minimizes the total completion time of parts. The objective function (2) minimizes the total number of displacement machines in the reactive plan as compared to that in the initial plan. Constraints (3) and (4) show that the completion times of operations, the processing of which has started before the occurrence of the disturbance, do not change in the reactive plan. Constraint (5) indicates that each machine should be allocated maximally to one cell. Constraint (6) guarantees that if the processing of each operation of a part has not started before the disturbance, it will be processed on one machine in a specific cell. Constraint (7) ensures that operations assigned to a specific cell are processed on machines allocated to that cell. Constraint (8) set the number of machines in each cell. Constraint (9) indicates that cells are formed sequentially according to their numbers; *i.e.*, cell 1 is first formed, cell 2 is formed next, and the following cells are formed in the same order if needed. Constraint (10) applies the lower bound of the number of formed cells. Equation (11) calculates the transportation time between k^{th} and $(k+1)^{th}$ operations of part p. Constraint (12) guarantees that the completion time of the first operation of part p is as large as its processing time. Constraint (13) indicates the precedence relationships among the operations of each part. Constraint (14) defines the precedence relation between operations of two different parts or two different operations of the same part on a machine. Constraint (15) guarantees that maximally one part is processed on each machine at a time. Constraint (16) shows that the completion time of operation, the processing of which has not started, is at least as large as its processing time as well as the disturbance time. The pair of Constraints (17) and (18) are considered to calculate the processing times of operations of parts after the disturbance. This means that if the completion time of each part changes with respect to that in the initial plan, its processing time will increase. Constraint (19) shows the range of the decision variables.

The mathematical model presented is nonlinear. It has been reformulated as a linear model in order to solve the problem with exact methods.

3. COMPUTATIONAL RESULTS

For validation and verification of the proposed model, two numerical examples are presented. These problems are solved using the GAMS software on a PC with an Intel Core i5 processor 1.6 GHz and a 6-GB RAM. In the following, the numerical examples are presented first. Then, we assume that we have an initial plan for the presented examples that are used at the presented mathematical model. Finally, it is assumed that a new job arrives during the execution of the initial plan, and the presented model is used to present the reactive plan for addressing the disturbance. Given that the model of the reactive plan is bi-objective, we use the normalized weighted sum method in this paper, and in order to

present one of the solutions, we select the same weight for the objective functions.

Numerical example 1

The first example includes seven parts and six machine types, and the upper and lower bounds are 2 and 3, respectively. Machine type 5 has two duplications, and the other types have only one. Other data for this example is shown in Table 1.

Table 1 shows the information concerning the operation sequence of parts, processing times on alternative machines, and intercellular transportation times of parts for the first example. Also, Table 2 illustrates the optimal solution for the initial plan, which its information is presented in Table 3.

Now, we assume that a new job arrives in the system for processing during the execution of the presented plan. We refer to this part as part 8. We assume that the new part includes four operations on machines 4, 6, 3, and 2 with processing times 5, 9, 8, and 12, respectively, and that the intercellular transportation time is 9. We modify the initial schedule using the model presented for the reactive plan. Given that the disturbance time is also important in the presentation of the reactive plan, we examine the reactive plan at different disturbance times (the arrival time of a new job D). Below, we first examine the reactive plan concerning $D = 13$. Based on the solution to the reactive model, the results shown in Tables 2 and 3 are updated as Tables 4 and 5.

Based on the results obtained from the sensitivity analysis of the values of the arrival time of new jobs (D), as shown in Table 6, the higher the arrival time of a new job at the initial times, the higher the required computational time. On the other hand, it is observed that the values of the objective functions change as does the arrival time of a new job, and this change can also be due to the initial plan changes in terms of the starting time, the formed cells, or both.

TABLE 1. Production data for the first numerical example

Part	Machine type m (T_{kpm})					TE_p
	$k=1$	$k=2$	$k=3$	$k=4$	$k=5$	
1	1(8)	4(12)	5(3)	3(7), 5(14)	2(5), 4(15)	6
2	3(6), 5(4)	4(12), 6(10)	5(5)			9
3	3(8)	2(4)	6(7)	3(5)		12
4	2(2)	3(4)	6(14)			5
5	1(2), 2(3)	4(5), 6(6)				11
6	1(3)	3(5), 5(3)				8
7	4(3)	5(5)	1(7)	5(6)	4(4), 6(7)	10

TABLE 2. The initial plan for the first numerical example

Cell	Machine Type	Part						
		2	3	4	1	5	6	7
1	2		2	1	5			
	3		1,4	2	4			
	5	1,3			3			
	6	2	3	3				
2	1				1	1	1	3
	4				2	2		1,5
	5*						2	2,4

* This represents the second copy of machine type

TABLE 3. Operations starting and completion times for the initial plan of the first numerical example

Part	Starting time and Completion time of part operations F_{kp}				
	$k=1$	$k=2$	$k=3$	$k=4$	$k=5$
1	5,13	13,25	31,34	34,41	41,46
2	0,4	4,14	14,19		
3	0,8	8,12	14,21	21,26	
4	0,2	8,12	21,35		
5	0,2	3,8			
6	2,5	5,8			
7	0,3	8,13	13,20	20,26	26,30

TABLE 4. Results concerning the reactive plan for the first numerical example

Cell	Machine Type	Part							
		2	3	4	8	1	5	6	7
1	2		2**	1**	4	5			
	3		1**, 4	2**	3	4			
	5	1**, 3				3			
	6	2**	3	3	2				
2	1					1**	1**	1**	3
	4				1	2	2**		1**, 5
	5*							2**	2**, 4

** This represents the operations of parts that their processing has been started before arriving new job

TABLE 5. Operations starting and completion times for the reactive plan for the first example

Part	Starting time and Completion time of part operations F_{kp}				
	$k=1$	$k=2$	$k=3$	$k=4$	$k=5$
1	5,13	13,25	31,34	34,41	41,46
2	0,4	4,14	14,19		
3	0,8	8,12	14,21	21,26	
4	0,2	8,12	21,35		
5	0,2	3,8			
6	2,5	5,8			
7	0,3	8,13	13,20	20,26	30,34.06
8	25,30	39,48	48,56	56,68	

TABLE 6. Sensitivity analysis on the arrival time of the new job

D	Z1	Z2	Time
5	236	0	0.464
10	239.645	0	0.519
15	244.06	0	0.291
20	244.06	0	0.306
25	231.225	4	0.16

Numerical example 2

The second numerical example includes 10 part types and 8 machine types, and the upper and lower bounds are 3 and 4, respectively (*i.e.*, $P=10, M=8, C_{min}=3$ *and* $C_{max}=4$). The machine types 5 and 6 have two duplications (*i.e.*, $MS_5=MS_6=2$), and the other types of machines have only one duplication. The information generated on this problem is shown in Table 7. Besides, $BL=2, BU=5$. (The numerical example has been taken from Feng et al. [10].)

Table 7 shows the information concerning the operation sequence of parts, processing times on alternative machines, and intercellular transportation times of parts for the second numerical example.

The information in Table 8 shows that three cells have been formed. The machines 2, 3, 6, 7, and 8 have been assigned to cell 1, machines 1 and 4, and the second copy of machine 5 have been assigned to cell 2, and machines 5 and the second copy of machine 6 have been assigned to cell 3. Moreover, for operations that can be processed with more than one machine type, one of the machines is selected for processing. For example, both machine types 3 and 5 can process the first operation of part 3, and, based on the results, the first copy of machine 5, which has been assigned to cell 3, is selected for processing. Many parts are processed without intercellular movements and in single cells totally, while other parts are processed in two or more cells, where the intercellular transportation time of the part is needed. For example, the fourth operation of part 2 is processed in cell 1 on machine type 6, while its fifth operation is processed on machine type 5 in cell 3. In this case, the intercellular transportation time of part 2 between cells 1 and 3 is needed. The information in Table 9 specifies the starting and completion times of the parts. For example, the first operation of part 1 is started on machine 1 in cell 2 at time 3, and it is completed at time 11, given the time required for processing the operation.

TABLE 7. Production data for the second numerical example

Part	Machine type (T_{kpm})					TE_p
	$k=1$	$k=2$	$k=3$	$k=4$	$k=5$	
1	1(8)	4(12)	5(3)	3(7), 5(14)	4(15), 8(5)	6
2	3(5)	8(10)	3(4)	6(7)	5(6)	9
3	3(6), 5(4)	6(10), 8(12)	5(5)			12
4	2(2)	7(4)	6(14)			5
5	4(15)	1(5)	5(6)			11
6	3(8)	8(4)	6(7)	3(5)	5(10), 7(5)	8
7	6(8), 8(10)	2(11)	7(5)			10
8	1(2), 2(3)	6(6), 8(5)				12
9	1(3)	3(5), 5(3)				11
10	4(3)	5(5)	1(7)	5(6)	6(7), 8(4)	10

TABLE 8. The initial plan for the second numerical example

Cell	Machine Type	Part									
		2	4	6	7	8	1	5	9	10	3
	2		1		2	1					
	3	1,3		1,4			4				
1	6	4	3	3	1						
	7		2	5	3						
	8	2		2		2	5			5	
	1						1	2	1	3	
2	4						2	1		1	
	5*						3	3	2	2,4	
3	5	5									1,3
	6*										2

* This represents the second copy of machine type

TABLE 9. Operations starting and completion times for the initial plan of the second numerical example

Part	Starting time and Completion time of part operations F_{kp}				
	$k=1$	$k=2$	$k=3$	$k=4$	$k=5$
1	3,11	18,30	30,33	39,46	46,51
2	0,5	8,18	18,22	31,38	38,44
3	0,4	4,14	14,19		
4	3,5	5,9	9,23		
5	3,18	18,23	24,30		
6	5,13	18,22	23,30	30,35	35,40
7	0,8	8,19	19,24		
8	0,3	3,8			
9	0,3	3,6			
10	0,3	6,11	11,18	18,24	34,38

Now, we assume that a new job arrives in the system for processing during the execution of the presented plan. We refer to this part as part 11. We assume that the new part includes four operations on machines 5, 8, 4, and 3 with processing times 10, 4, 8, and 13, respectively, and that the intercellular transportation time is 9. Below, we examine the reactive plan concerning $D = 13$. Based on the solution to the reactive planning model, the results obtained in Tables 8 and 9 are updated, as shown in Tables 10 and 11.

TABLE 10. Results concerning the reactive plan for the second numerical example

Cell	Machine Type	Part										
		4	7	8	5	9	10	1	2	3	6	11
1	2	1*	2*	1*								
	7	2*	3								5	
2	1				2	1*	3*	1*				
	5**				3	2*	2*,4					
	6	3*	1*				5					
3	3							4	1*,3		1*,4	4
	4				1*		1*	2				3
	5							3	5	1*,3		1
	6*								4	2*	3	
	8			2*				5	2*		2	2

** This represents the second copy of machine type

* This represents the operations of parts that their processing has been started before arriving new job

TABLE 11. Results concerning the starting and completion times of the part operations for the reactive plan for the second numerical example

Part	Starting time and Completion time of part operations F'_{kp}				
	$k=1$	$k=2$	$k=3$	$k=4$	$k=5$
1	3,11	18,30	30,33	37,44	44,49
2	0,5	8,18	27,31	32,39	39,45
3	0,4	4,14	14,19		
4	3,5	5,9	9,23		
5	3,18	18,23	24,30		
6	5,13	21,25	25,32	32,37	45,50
7	0,8	8,19	19,24		
8	0,3	3,8			
9	0,3	3,6			
10	0,3	6,11	11,18	18,24	24,31
11	19,29	29,33	36,44	44,57	

Through a comparison of the results obtained for the reactive plan with those for the initial plan, it is observed that some changes have occurred in cell formation and selection of alternative machines for the numerical example. As observed, machine 6 is displaced from cell 1 into cell 2, machines 3 and 8 from cell 1 into cell 3, and machine 4 from cell 2 into cell 3. The fifth operation of part 10 is processed on the other alternative machine, *i.e.*, machine 6, in cell 2 rather than on machine 8. The new job arriving into the system has also been assigned to a machine for processing. Moreover, it is observed through a comparison of Tables 9 and 11 that jobs are processed according to the initial plan, and the processing of the operations of parts is started earlier or later in some cases. Furthermore, the job having arrived newly in the system starts its processing at time 19 on machine 5 in cell 3, and its following operations are started at times 29, 36.345, and 44.345 on machines 8, 4, and 3, respectively.

4. CONCLUSION AND SUGGESTIONS FOR FUTURE RESEARCH

Since manufacturing systems operate in dynamic, uncertain conditions, unexpected events often take place in these systems. The occurrence of unexpected events in manufacturing environments may lead to the infeasibility and non-optimality of the initial plan. In order to overcome unexpected disturbances, the initial schedule needs some modifications. In this paper, we considered a cellular manufacturing system, including many design features, the objective of which is to minimize the total completion time of parts. First, we assume that we have

an initial plan in the cellular manufacturing system. Then, we presented a mathematical model in order to react to new arrivals of jobs into the system. The presented reactive model has been designed such that it considers both the classical scheduling criterion (total completion time of parts) and two new criteria (stability in the system and resistance to changes). In the presented mathematical model, machines are allocated to manufacturing cells, processing routes are selected for parts, and the sequence of operations are processed on machines in such a way that the total completion time of parts is minimized as the first objective function. The total number of replacements of machines in the reactive plan is minimized as compared to that in the initial plan as the second objective function. For validation of the proposed model, some numerical examples were generated and solved using the GAMS software. The results of the numerical examples show that the reactive plan is sensitive to the disturbance time, and the closer this time to that at the beginning of the plan, the greater the computational time. Moreover, changes in the occurrence time of disturbance change the values of the objective function and the optimal solution. Finally, suggestions for future studies are made below.

- Given that machine failure and unavailability is another unexpected disturbance in the manufacturing system, it can provide an appropriate area of research to present a reactive planning model in addressing unexpected failures of machines in cellular manufacturing systems.
- Given the importance of the operator assignment problem in cellular manufacturing systems, it can provide an appropriate topic for continuing the present study to investigate the new model (initial planning model and reactive planning model) by considering the operator assignment problem.
- Given the importance of production planning in manufacturing systems and its dependence on the cell formation problem, it can provide an appropriate research area to integrate it with the problem under review in this paper.
- The arrival of a new job into a cellular manufacturing system as an unexpected disturbance was investigated in this paper. The reverse may also take place, where a customer cancels one or more jobs, the operation of which has not been started. It can be another future research area to investigate this state.

5. REFERENCES

1. Vieira, G.E., Herrmann, J.W. and Lin, E., "Rescheduling manufacturing systems: A framework of strategies, policies, and methods", ***Journal of Scheduling***, Vol. 6, No. 1, (2003), 39-62. https://doi.org/10.1023/A:1022235519958
2. Wojakowski, P. and Warżołek, D., "The classification of scheduling problems under production uncertainty", Vol. 4, (2014).
3. Sakhaii, M., Tavakkoli-Moghaddam, R. and Vatani, B., "A robust model for a dynamic cellular manufacturing system with production planning", ***International Journal of Engineering***, Vol. 27, No. 4, (2014), 587-598. DOI: 10.5829/idosi.ije.2014.27.04a.09
4. Soolaki, M. and Arkat, J., "Incorporating dynamic cellular manufacturing into strategic supply chain design", ***The International Journal of Advanced Manufacturing Technology***, Vol. 95, No. 5-8, (2018), 2429-2447. https://doi.org/10.1016/j.asoc.2016.12.039
5. Arkat, J., Farahani, M.H. and Ahmadizar, F., "Multi-objective genetic algorithm for cell formation problem considering cellular layout and operations scheduling", ***International Journal of Computer Integrated Manufacturing***, Vol. 25, No. 7, (2012), 625-635. https://doi.org/10.1080/0951192X.2012.665182
6. Rahimi, V., Arkat, J. and Farughi, H., "A vibration damping optimization algorithm for the integrated problem of cell formation, cellular scheduling, and intercellular layout", ***Computers & Industrial Engineering***, (2020), 106439. https://doi.org/10.1016/j.cie.2020.106439
7. Arkat, J. and Ghahve, H., "Scheduling of virtual manufacturing cells with outsourcing allowed", ***International Journal of Computer Integrated Manufacturing***, Vol. 27, No. 12, (2014), 1079-1089. https://doi.org/10.1016/j.cie.2020.106439
8. Mehdizadeh, E. and Rahimi, V., "An integrated mathematical model for solving dynamic cell formation problem considering operator assignment and inter/intra cell layouts", ***Applied Soft Computing***, Vol. 42, (2016), 325-341. https://doi.org/10.1016/j.asoc.2016.01.012
9. Bagheri, F., Safaei, A.S., Kermanshahi, M. and Paydar, M.M., "Robust design of dynamic cell formation problem considering the workers interest", ***International Journal of Engineering***, Vol. 32, No. 12, (2019), 1790-1797. DOI: 10.5829/IJE.2019.32.12C.12
10. Feng, H., Xia, T., Da, W., Xi, L. and Pan, E., "Concurrent design of cell formation and scheduling with consideration of duplicate machines and alternative process routings", ***Journal of Intelligent Manufacturing***, Vol. 30, No. 1, (2019), 275-289. https://doi.org/10.1007/s10845-016-1245-7
11. Rahmani, D. and Ramezanian, R., "A stable reactive approach in dynamic flexible flow shop scheduling with unexpected disruptions: A case study", ***Computers & Industrial Engineering***, Vol. 98, (2016), 360-372. https://doi.org/10.1016/j.cie.2016.06.018
12. Olumolade, M., "Reactive scheduling system for cellular manufacturing with failure-prone machines", ***International Journal of Computer Integrated Manufacturing***, Vol. 9, No. 2, (1996), 131-144. https://doi.org/10.1080/095119296131742
13. Weckman, G.R., "A framework for reactive scheduling in a cellular manufacturing environment", Vol., No.
14. Li, W.-L. and Murata, T., "Particle swarm optimization method for rescheduling of job processing against machine breakdowns for nondisruptive cell manufacturing system", in 2012 6th International Conference on New Trends in Information Science, Service Science and Data Mining (ISSDM2012), IEEE. (2012), 523-528.
15. Caruth, D., Middlebrook, B. and Rachel, F., "Overcoming resistance to change", ***SAM Advanced Management Journal***, Vol. 50, No. 3, (1985), 23-27.
16. Giangreco, A. and Peccei, R., "The nature and antecedents of middle manager resistance to change: Evidence from an italian context", ***The International Journal of Human Resource Management***, Vol. 16, No. 10, (2005), 1812-1829. https://doi.org/10.1080/09585190500298404

Persian Abstract

چکیده

اغلب محیط های تولیدی با حوادث تصادفی و غیرمنتظره مانند خرابی ماشین، زمان های پردازش غیرقطعی، ورود کارهای جدید و از دستور کار خارج شدن کارها مواجه هستند. به منظور کاهش اثر اختلالات غیرمنتظره، زمان بندی اولیه نیازمند اصلاحاتی است. در این مقاله، یک مدل ریاضی عدد صحیح مختلط ارائه می‌شود تا مسائل تشکیل سلول و زمان‌بندی مجدد را در یک سیستم تولید سلولی در نظر بگیرد. در مدل ریاضی ارائه شده، فرض می‌شود کاری جدید جهت پردازش به عنوان یک اختلال وارد سیستم می‌شود. براساس اصول مقاومت در برابر تغییر، مدل واکنشی، راه‌حل جدیدی با کمینه تغییرات از جواب اولیه را جستجو می‌کند. به منظور برخورد با این اختلال، یک مدل واکنشی جدید ارائه می‌شود. مدل واکنشی ارائه شده به‌گونه‌ای عمل می‌کند که به صورت همزمان معیار کلاسیک زمان‌بندی (مجموع زمان‌های تکمیل قطعات) و تعداد جابجایی‌های ماشین‌ها را کمینه کند. به منظور اعتبارسنجی مدل پیشنهاد شده، تعدادی مثال عددی به کمک نرم‌افزار GMAS حل می‌شوند. نتایج، توانایی مدل واکنشی را در دستیابی به راه‌حل های مقاوم در برابر تغییرات غیرمنتظره نشان می‌دهد.

International Journal of Engineering

Journal Homepage: www.ije.ir

Assessment the Cost-effectiveness of Information Support for the Business Processes of a Virtual Machine-building Enterprise in the Framework of Industry 4.0

V. Babenko*[a], O. Demyanenko[b], V. Lyba[c], O. Feoktystova[d]

[a] *International E-commerce and Hotel & Restaurant Business Department, V. N. Karazin Kharkiv National University, Kharkiv, Ukraine*
[b] *Department of Finance, National Aerospace University "Kharkiv Aviation Institute", Kharkiv, Ukraine*
[c] *Department of Economics, Marketing and International Economic Relations, National Aerospace University "Kharkiv Aviation Institute", Kharkiv, Ukraine*
[d] *Department of Management, National Aerospace University "Kharkiv Aviation Institute", Kharkiv, Ukraine*

PAPER INFO

Paper history:
Received 06 July 2020
Received in revised form 13 August 2020
Accepted 03 September 2020

Keywords:
Industry 4.0
Virtual Machine-building Enterprise
Multi-nomenclature Production
Cost-effectiveness
Product Life Cycle

ABSTRACT

The features of the organization information support for business processes on the typical virtual machine-building enterprise (VME) with a multi-nomenclature nature of production in the framework of Industrial 4.0 were considered. It has been established that in accordance with the concept of Industry 4.0, namely with the individualization of production and consumption, a modern virtual machine-building enterprise must adapt to the production of goods in small batches, moreover in a large assortment and with frequent change of nomenclature in a wide range. It is shown that under these conditions, the effectiveness of the implementation of production processes directly depends on the effectiveness of information support at all stages of the product life cycle (PLC). A methodology is proposed for evaluating the effectiveness of information support for PLC processes in the conditions of multi-nomenclature production of a virtual engineering enterprise. The methodological basic concepts are web-mining and multi-agent technology. A comparative analysis of the activities of a typical VME was carried out, which showed that the introduction of information support tools increased the efficiency of VME business processes.

***doi**: 10.5829/ije.2021.34.01a.19*

NOMENCLATURE

PLC	Product Life Cycle	TVME	Typical VME
VME	Virtual Machine-building Enterprises		

1. INTRODUCTION

The development of the internet, information and communication technologies, sustainable communication channels, cloud technologies and digital platforms has led to the emergence of open information systems and global industrial networks that go beyond the boundaries of an individual enterprise and interact with each other. Such systems and networks have a transformative effect on all sectors of the modern economy and business and transfer industrial automation to a new, fourth stage of industrialization. Industry 4.0-transition to a fully automated digital production, controlled by intelligent systems in real time in constant interaction with the external environment, going beyond the boundaries of one enterprise, with the prospect of combining things and services into a global industrial network [1, 2]. Many developed countries and business giants are active participants in the fourth industrial revolution: state programs, commercial associations and nonprofit organizations are created with the goal of removing barriers to the creation of Industry 4.0.

The basis of Industry 4.0: interoperability, virtualization, decentralization and real-time operation. Cyberphysical systems, cloud computing and big data

*Corresponding Author Institutional Email: *vitalinababenko@karazin.ua* (V. Babenko)

Please cite this article as: V. Babenko, O. Demyanenko, V. Lyba, O. Feoktystova, Assessment the Cost-effectiveness of Information Support for the Business Processes of a Virtual Machine-building Enterprise in the Framework of Industry 4.0, International Journal of Engineering, Transactions A: Basics Vol. 34, No. 01, (2021) 171-176

technologies, the internet of things are becoming increasingly popular in business, along with vertical and horizontal integration, virtualization and digitalization of the entire process of creating a value added chain [3].

Industry 4.0, thanks to the flexibility and adaptability provided by cyberphysical systems, will help to implement mass production on individual orders, which will reduce the price of products. The classical methods of organizing production suggested that only large batches of goods could be produced by the flow method. Thanks to the new principles of organizing production processes, it becomes possible to produce single products in an industrial way. Today, there is a steady trend towards a transition from tight centralized management of production processes to a decentralized model for collecting, processing information and making decisions. Moreover, the level of autonomy is constantly growing. Ultimately, such a system becomes an active component capable of independently managing its production process [4].

Industry 4.0 has led to the emergence of a new type of production, such as virtual, which does not have a fixed organizational and territorial structure, and in which the process of creating information for software-controlled technological equipment and the manufacture of the product itself can be distributed in time and space between many enterprises [5]. The most intensively indicated type of production is developing in the field of mechanical engineering, by acquiring the form of virtual machine-building enterprises (VME) [6, 7]. The key element determining the effectiveness of the VME functioning is a special information environment, implemented on the basis of a special applied information technology.

At the moment, in the publications of foreign and domestic authors, issues related to the justification of the economic efficiency of the creation and operation of VME have not been considered. The main reasons for this research gap is that the technology for creating, deploying and supporting the operation of VME in other countries lies in the field of private business and constitutes elements of know-how. In Ukraine, however, there is practically no experience in organizing such enterprises and, therefore, publications devoted to the problems associated with justifying the economic efficiency of creating and functioning of VME.

The main advantage of VME, which is the almost complete absence of fixed assets, also creates vulnerability for enterprises of this type, since a failure in information communications between subcontractors disrupts the coordination of the entire production process, which entails significant financial losses, up to the financial collapse of VME. Thus, the problem of ensuring the financial efficiency of VME basically boils down to the problem of ensuring the efficiency of information support for business processes in such enterprises.

The aim of the article is to set out the concept of organizing information support for business processes at the VME as typical production facilities within the framework of Industry 4.0, as well as to assess the cost-effectiveness of its implementation at the VME.

2. MATERIALS AND METHODS

VME lifecycle management methodology includes conceptual and methodological parts.

The VME concept is based on the following principles: a virtual enterprise searches for new partners with resources, knowledge and abilities corresponding to market needs for joint organization and implementation of this activity [8, 9].

Methodological support of VME lifecycle management involves the choice of a paradigm for creating the appropriate software, and within the framework of the chosen paradigm - the development of methods that ensure the creation and support of a VME unified and information space.

Thus, the most important characteristic of a virtual organization is a flexible, adaptive, dynamic network structure. Since such an information space does not exist in the real physical world, but is created through the information integration of the resources of partners (subcontractors). The information of VME activities was carried out within the framework of a concept that covers key aspects of the activity of such an enterprise, namely, planning production volumes, based on an analysis of the market situation, as well as the organization of production, by making an informed choice of subcontractors. Based on the features of VME described above, the methodological part of the methodology should be based on the agent-based programming paradigm [10], as the most appropriate to the specifics of VME. Within this paradigm, two methods have been developed: the method of information support of business processes of VME and the method of forming coordinating decisions by agents when choosing subcontractors for manufacturing products at the VME.

The method of information support of business processes of VME is based on the use of multiple agents in the form of one-page web resources. The generalized description of the method includes five stages, three of which are implemented when creating a multi-agent web-oriented environment, and the fourth and fifth - in the process of its functioning:

1. Development of an online store for the sale of VME products.
2. Development of the main site of the VME with the implementation of the functions of informing users about: the structure of the VME, additional characteristics of the products, the system of discounts, service.

3. Development of a set of reflexive agents in the form of doorway sites, the number of which coincides with the range of products manufactured by VME. In addition to information about a particular type of product, the agent carries information about the VME.
4. Formation of a plan for the production of VME products based on market analysis (this stage is implemented directly in the process of functioning of a multi-agent web-oriented environment).
5. Formation of a community of agents whose mission is to select subcontractors for the implementation of the plan for the production of VME products formed at the previous stage.

The fifth stage of the method of VME business processes informational support is the most critical for ensuring the effective functioning of the VME, since here the greatest number of production risks arise.

Formulate a formal model of the process of selecting subcontractors G when ordering S, taking into account input information about conditions, terms and quality:

$$G_S = \left\langle A_S, D_S, C_D, T_A, E_D, P_E, A^T, A^D, C^D, D^E, E^P \right\rangle, \quad (1)$$

where T_A – many requirements regarding the subcontractor selection process; A_S – the set of all technological operations of filling S; D_S – a set of units (operations), which includes order S; C_D – subcontractors for performing operations from the plurality D_S; P_E – set of parameters of the operation D_S elements E_D; A^T, A^D – mapping, are set by the technological operations of order manufacturing; C^D – mapping is determined by the database; E_D – set of elements that are included in the transaction; D^E, E^P – are in the design documentation for the manufacture of the order (device).

Thus, based on the foregoing, describe the method of forming coordinating decisions by agents when choosing subcontractors for manufacturing products at the VME:

1. For each operation of selecting a subcontractor G_S for manufacturing order S select (using the mapping K_H - the result of the first recognizer in the created system) signs of potential conflicts $H^K : K_H \subseteq H_D$ and form a conflicting set of operations from A_S.
2. Determine the type of each potential collision. Form two subsets - signs of resolvable K_H^+ and insoluble K_H^- collisions in an automated mode. For insoluble collisions, execute a request to the user to form possible coordinating decisions.
3. For each resolvable collision, from K_H^+ determine the participating subcontractors (a subset $D_S = f^{-1}(K_H^+)$ as the full prototype of the signs of resolvable collisions).
4. By analyzing the subcontractors (suitable for performing the necessary operations– C^D) determine the previous subcontractors C_D participating in such an operation involved in the conflict and the corresponding recognizer.
5. Form the necessary restrictions O_T for the requirements of the execution of the order from A_S.
6. To verify the real existence of a collision by completing a request to the appropriate recognizer (determine the truth) $P^O(O_i) = P_j$).
7. In the event of a conflict (if $P^O(O_i) \neq P_j$) determine the method for resolving it using the existing apr`iority knowledge base for resolving typical conflicts.
8. Form a coordinating decision (from O_T) for each conflict identified and fill out a draft output form for the user.

3. RESULTS AND DISCUSSION

To verify the effectiveness of implementing the research results, it is necessary to analyze the financial activities of a typical VME (TVME) to determine the results of implementation supportive information of business processes [11-13] for the last three years of the activity of a typical VME - RSA "Vector" (hereinafter referred to as TVME). Moreover, the analysis is based on comparing the results of the activities of TVME without the introduction (2017, 2018) with the implementation (2019) of the described information support tools.

First of all, we will conduct an assessment of business activity [14]. It is aimed to analyze the results and effectiveness of the current main production activities of TVME. The value of the analysis of business activity lies in the formation of an economically sound assessment of the effectiveness and intensity of use of the organization's resources, as well as in identifying reserves for their increase. Reflect the main indicators of the enterprise in Table 1.

Analyzing Table 1, we can conclude that TVME operates at the expense of borrowed funds of customers. In 2019, the cost of production decreased, which should have reflected in revenue from sales and, accordingly, net profit in the negative direction, but with a decrease in the cost of production by 939 thousand c.u. net profit increased by 6.5 thousand c.u. The average headcount of TVME personnel is noticeably allocated - 4 people, which is associated with the virtual form of organization of such an enterprise.

To calculate the total liquidity ratio, it is necessary to summarize all the assets of the enterprise with weighting factors, depending on the speed of their

TABLE 1. Main technical and economic indicators of TVME

No	Indicator, thousand c.u.	2017	2018	2019
1	Income (revenue) from product sales	1605.3	1373.1	1394.1
2	Cost of sales	1104.8	1201.1	1107.2
3	Net profit	1.0	8.8	15.3
4	Equity	11.8	11.8	11.8
5	Current responsibility	694.7	262.9	357.7
6	Fixed assets	148.0	151.9	153.2
7	Current assets	580.9	261.1	353.7
8	Average number of personnel	2	4	4

feasibility, and assess liabilities by the maturity of obligations. Next, we calculated the total liquidity ratio of TVME taking into account the breakdown of assets into groups. At the final stage of applying the methodology, profitability ratios were calculated. Summary calculations are shown in Table 2.

Based on the data in Table 2, construct graphs that display the visibility of the results (Figures 1-4).

Turnover ratios bear a positive trend, as there is an increase in the indicator. This is due to the fact that the periods for which the full production cycle takes place became longer, and consequently, the profit increased.

It is necessary to track the ratio of the turnover of receivables and payables for the analyzed period (Figure 2).

TABLE 2. Summary performance indicators of TVME for 2017-2019 years

Name of indicator	2017	2018	2019	Rate of increase (Δ)
Asset turnover ratio	2.00	2.40	3.03	0.63
Current assets turnover ratio	2.26	3.26	4.53	1.27
Accounts receivable turnover ratio	5.76	7.23	15.78	8.55
Accounts payable turnover ratio	2.66	3.06	4.5	1.44
Inventory turnover ratio	3.04	4.87	3.85	1.02
Equity turnover ratio	38.9	34.93	27.15	-7.78
Accounts payable to total assets ratio	0.82	0.64	0.71	0.07
Total liquidity ratio	0.26	0.28	0.008	-0.272
Production profitability ratio	2.20	3.32	2.75	0.57
Return on sales ratio	0.00062	0.0064	0.01	0.0036
Direct cost margin	0.09	0.73	1.38	0.65

From Figure 2 it is seen that the accounts payable turnover ratio has a higher growth rate than the receivable turnover ratio. Those TVME manages to repay the borrowed funds for the production of the order faster than it receives funds for the purchased goods.

TVME profitability indicators for 2017-2019 in graphical form are shown in Figure 3.

Let us analyze the main indicators that directly affect the profit of the enterprise - the coefficient of profitability of direct costs, the coefficient of profitability of production. Figure 3 shows that the gross cost of TVME significantly decreased, which led to an increase in profit. An increase in the profitability ratio of production indicates an increase in the profitability of production due to the continuous improvement of the means of information support of business processes at TVME.

Figure 4 shows the main performance indicators of TVME. This figure illustrates the change in the coefficient of profitability of sales and the coefficient of total liquidity of the enterprise for 2017 - 2019. The overall liquidity ratio for a virtual manufacturing enterprise is very heterogeneous, because manufacturing enterprises are characterized by a direct relationship between the liquidity ratio and the financial stability of the enterprise. In our case, the liquidity ratio has the opposite value, since TVME exists at the expense of borrowed funds of customers without having fixed assets and stocks in stock.

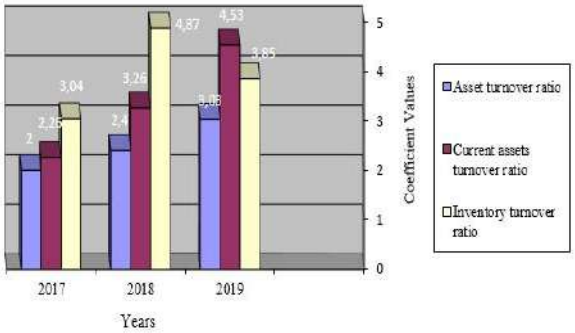

Figure 1. Turnover of TVME assets for 2017-2019 years

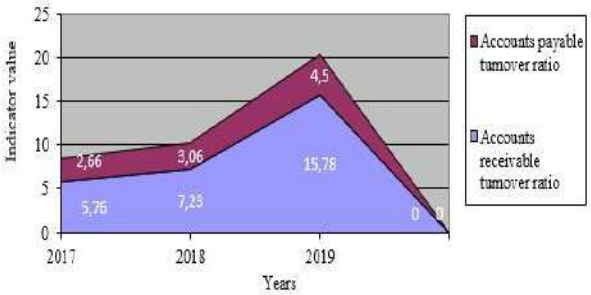

Figure 2. The ratio of the turnover of receivables and payables TVME for 2017-2019 years

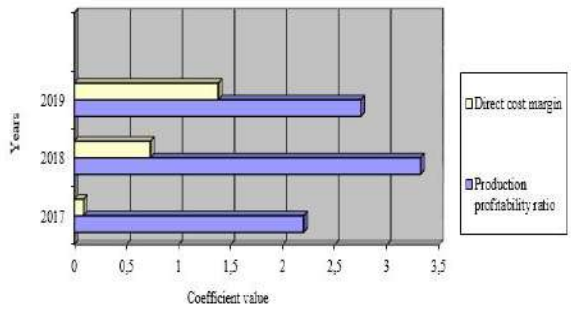

Figure 3. TVME profitability indicators for 2017–2019 years

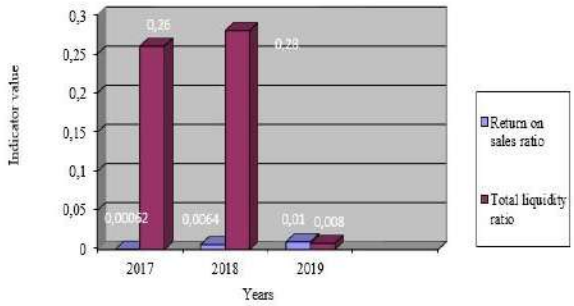

Figure 4. The main performance indicators of TVME for 2017-2019 years

4. CONCLUSION

It is shown that in the conditions of Industry 4.0, VMEs are one of the main types of production facilities. The concept of information of VME activity is presented, which covers two most important stages - technical and economic planning and technical preparation of production. The methodological basic concepts are web-mining and multi-agent technology. A comparative analysis of the activities of a typical VME was carried out, which showed that the introduction of information support tools increased the efficiency of VME business processes.

The main significance of the results obtained is that their application in practice makes it possible, on the one hand, to expand the capabilities of top managers of traditional manufacturing engineering enterprises to diversify order fulfilment by selecting subcontractors, and, on the other hand, to automate the lifecycle management process of existing VMEs.

5. REFERENCES

1. Hoffmann, R., "Investment Opportunities in Industry 4.0 – Industrial Revolution «Made in Germany»", (2016). https://www.ecovis.com/focus-china/investmentopportunities-industry-4–0/
2. "Industry 4.0: Smart manufacturing for the future", (2014). http://www.academia.edu/21125581/SMART_MANUFACTURING_FOR_THE_FUTURE_INDUSTRIE_4.0_Future_Markets
3. "Industry 4.0: How to navigate digitization of the manufacturing sector", McKinsey&Company, Report, (2015), https://www.mckinsey.com/business-functions/operations/ourinsights/industry-four-point-o-how-to-navigae-thedigitization-of-the-manufacturing-sector
4. Matyushenko, I., Danova, M., Feoktystova, O. and Melnyk, R., "Formation of teams of performers of projects at innovative enterprises within the framework of the «Industry 4.0» concept", ***International Journal of Supply Chain Management,*** Vol. 8, No. 4, (2019), 962-969.
5. Babenko, V., "Enterprise innovation management in industry 4.0: modeling aspects", in Tromp, J.G. and etc. (Eds.) Emerging Extended Reality Technologies For Industry 4.0, (2020), 141-163, (Chapter 9), doi:10.1002/9781119654674.ch9
6. Pavlenko, V., Shostak, I., Sobchak, A., Morozova, O. and Danova, M. "The Concept of Virtual Manufacturing Enterprise Operation as a Green Complex System", In: Kharchenko, V., Kondratenko Y., Kacprzyk J. (eds) Green IT Engineering: Components, Networks and Systems Implementation. Studies in Systems, Decision and Control, Springer, Cham, vol 105, (2017), 265-285, https://doi.org/10.1007/978-3-319-55595-9_13
7. Shamsuzzoha, A., Abels, S. and Helo, P. "Adaptive Virtual Enterprise Process Management - Perspective of Cloud-based Data Storage", ***15th International Conference on Enterprise Information Systems***, Angers, France, Vol. 1, (2013), 88-94, https://doi.org/10.5220/0004394900880094
8. Coroiu, A. M., "E-Commerce and Intelligent Agents in Virtual Enterprises", ***Advanced Materials Research***, Vol. 1036, (2014), 1055-1059, https://doi.org/10.4028/www.scientific.net/amr.1036.1055
9. Sobchak, A., Shostak, E., Tseplyaeva, T., Popova, O., Firsova, A., "Designing an approach to building the teams of high technological projects performers at virtual instrumentmaking enterprises", ***Eastern-European Journal of Enterprise Technologies***, No. 3/2 (81), (2016), 47-54, doi:10.15587/1729-4061.2016.71493
10. Shostak, I., Kapitan, R., Volobuyeva, L. and Danova, M., "Ontological Approach to the Construction of Multi-Agent Systems for the Maintenance Supporting Processes of Production Equipment," ***International Scientific-Practical Conference Problems of Infocommunications. Science and Technology (PIC S&T)***, Kharkiv, Ukraine, (2018), 209-214, https://doi.org/10.1109/INFOCOMMST.2018.8631896.
11. Bakanov, M. I., "Teoriya ekonomicheskogo analiza (Economic analysis theory)", Finansy i statistika, Moscow, (2011).
12. Doroudyan, M. H., Owlia, M. S., Sadeghib, H., Amiri, A., "Monitoring Financial Processes with ARMA-GARCH Model Based on Shewhart Control Chart (Case Study: Tehran Stock Exchange)", ***International Journal of Engineering, Transactions B: Applications***, Vol. 30, No. 2, (2017), 270-280, https://doi.org/10.5829/idosi.ije.2017.30.02b.14
13. Kameli, A., Javadian, N. and Daghbandan, A. "Multi-period and Multi-objective Stock Selection Optimization Model Based on Fuzzy Interval Approach", ***International Journal of Engineering, Transactions C: Aspects***, Vol. 32, No. 9, (2019), 1306-1311, https://doi.org/10.5829/ije.2019.32.09c.11.
14. Babenko, V., Perevozova, I., Mandych, O., Kvyatko, T., Maliy, O. and Mykolenko, I. "World informatization in conditions of international globalization: Factors of influence", ***Global Journal of Environmental Science and Management***, Vol. 5, (2019), 172-179, https://doi.org/10.22034/gjesm.2019.05.SI.1

Persian Abstract

چکیده

ویژگیهای پشتیبانی اطلاعات سازمان برای فرآیندهای تجاری در شرکت ماشین سازی مجازی معمولی (VME) با ماهیت تولید چند نامی در چارچوب Industrial 4.0 در نظر گرفته شد. مشخص شده است که مطابق با مفهوم صنعت ٤,٠ ، یعنی با خصوصی سازی تولید و مصرف ، یک شرکت ماشین سازی مجازی مدرن باید با تولید کالا در دسته های کوچک ، علاوه بر این در یک مجموعه بزرگ و با تغییرات مکرر ، سازگار شود. از نامگذاری در طیف گسترده ای. نشان داده شده است که تحت این شرایط ، اثربخشی اجرای فرآیندهای تولید مستقیماً به تأثیر پشتیبانی اطلاعات در تمام مراحل چرخه عمر محصول (PLC)بستگی دارد. یک روش برای ارزیابی اثربخشی پشتیبانی اطلاعات برای فرآیندهای PLC در شرایط تولید چند نامی یک شرکت مهندسی مجازی پیشنهاد شده است. مفاهیم اساسی روش شناختی ، وب کاوی و فناوری چند عاملی است. تجزیه و تحلیل مقایسه ای از فعالیت های یک VME معمولی انجام شد ، که نشان داد معرفی ابزارهای پشتیبانی اطلاعات باعث افزایش کارایی فرآیندهای تجاری VME می شود.

International Journal of Engineering

Journal Homepage: www.ije.ir

Synthesis and Characterization of Photocatalytic Activity of Hematite/ Cobalt Oxide/ Graphite Nanocomposites

F. Mansouri, Z. Khakpour*, A. Maghsoudipour

Ceramic Department, Materials and Energy Research Center, Tehran, Iran

P A P E R I N F O

Paper history:
Received 20 June 2020
Received in revised form 13 September 2020
Accepted 29 October 2020

Keywords:
Synthesis
Photo Catalyst
Hydrogen
Methylene Blue
Photoactivity

A B S T R A C T

In this study, at first step nanopowder particles of α-Fe_2O_3 (Hematite) and Co_3O_4 were synthesized separately thorough simple chemical method from an aqueous solution of iron (III) nitrate nonahydrate ($Fe(NO_3)_3.9H_2O$) and cobalt (II) nitrate hexahydrate ($Co(NO_3)_2.6H_2O$) as precursors. After that, three composites from synthesized nanopowders of Fe_2O_3 with 8, 16 and 24 wt.% of Co_3O_4 were prepared. Graphite nanopowder was added to one composition of samples in weight percentages of 1.17 and 2.35. The composition and morphology of the composites were investigated by XRD and FE-SEM, respectively. FE-SEM analysis showed that the morphology of the powders and composites were all spherical in nanoscale. The photocatalytic activity of the composites was examined by measuring the photo-degradation of the aqueous solution of methylene blue under simulated solar light. To determine the photo catalytic activity, the degradation of methylene blue (MB) in the absence of light (dark test) was taken as well. Results showed that addition of Co_3O_4 to Fe_2O_3 decrease the activity of photo-catalytic process while nano-graphite enhanced photo-catalytic process by upward of ~2 % with respect to the composite without graphite nanoparticles. Stoichiometric calculations showed that the amount of hydrogen produced by water by the composite of Fe_2O_3-16% Co_3O_4-2.35% Graphite nanoparticles was 27 μmol H_2/h.g under solar light irradiation.

***doi**: 10.5829/ije.2021.34.01a.20*

1. INTRODUCTION

Today's political, economic and economic crises, such as limiting the viability of fossil fuel reserves, environmental concerns, population congestion, economic growth, and consumption coefficient, are all world-wide issues that push researcher to finding new solutions [1]. In an age where we are all concerned about the side effects of fossil fuels, such as global warming, pollutants spreading, and the termination of these fuels, hydrogen can be taken into consideration[1-3]. There are four ways to produce hydrogen gas from different sources: hydrogen gas from natural gas, oil, coal and water electrolysis, sharing 48, 30, 18 and 4% of Hydrogen production respectively [4]. When hydrogen is produced from hydrocarbons such as fossil or bio-fuels, trapping CO_2 and isolating it are among the requirements of production program. Hydrogen produced from water, on the other hand, does not pose a challenge of conversion point, whereas it does require energy from an external source[5]. If this energy comes from a renewable energy source such as solar energy, hydrogen could be potential option of green energy and supplying energy to any device from laptops to submarines [2, 3]. Photo catalytic of water is one of the inexpensive and clean methods for producing hydrogen gas [4]. Hematite (α-Fe_2O_3) posses some of essential features such as an ideal band gap of 2.2 eV with broad visible light absorption up to 590 nm which enable it to absorb 40% of the wavelengths. It also has excellent stability under aqueous operating conditions and a valence band positioned sufficiently low for oxidizing that made hematite as one of the most attractive materials for photo-electrochemical (PEC) water splitting [6, 7]. However, relatively low efficiency (12.9%), low electron mobility, lower potential conduction band than needed for hydrogen

*Corresponding Author Institutional Email: *z-khakpour@merc.ac.ir* (Z. Khakpour)

Please cite this article as: F. Mansouri, Z. Khakpour. A. Maghsoudipour, Synthesis and Characterization of Photocatalytic Activity of Hematite/ Cobalt Oxide/ Graphite Nanocomposites, International Journal of Engineering, Transactions A: Basics Vol. 34, No. 01, (2021) 177-183

reduction and high rate of recombination of electrons/ holes are classified as major limitations [7, 8]. To overcome these disadvantages application of nanotechnology has provided improvement by producing nanoparticle catalysts and morphological modification in order to minimize the charge collection distance while maintaining good light absorption. For instance, H. Wender et al reported that synthesis hematite nano-rings altered the edge of the bandage in a way to increase hydrogen gas production from an aqueous solution [9]. Other ways are doping strategy and making composite with other semiconductor materials or metals that modify the function of the photo-catalyst. Ch. Liu et. al in 2017 reported that hematite/carbon composite improves photo-catalytic performance of hematite [10]. They claimed that 120 mg photo-catalytic powder could produce 6.667 μmol H_2/hg. Therefore, it is of great interest to study the photoelectric properties of α-Fe_2O_3 nanostructures in combination with other materials to make composite for their promising application in photo-catalysis or photoelectric conversion device. For instance, in of TiO_2/$BiVO_4$ composite, $BiVO_4$ nanoparticles promoted absorption and production of electrons, TiO_2 is key role to convert electron to water [11]. In another endeavor using nanoparticles of Gold and TiO_2 composite reduced the probability of electron-holes recombination [12]. A number of other n-type semiconductors, such as TiO_2 [12, 13], ZnO [13] and Co_3O_4 [14, 15] have been studied as photo anode materials for water splitting however, all requirements have not yet been accomplished by that compounds. These materials are good candidates for making composite by hematite. Perry et al. Reported that Co_3O_4 nanoparticles produce 2000 μmol H_2/hg from water: ethanol (1:20) solution under light radiation [16, 17].

In this study, we synthesize hematite and Co_3O_4 nanoparticles in order to prepare composition of hematite/Co_3O_4. In order to promote electron transfer mechanism and improve the performance of photo-catalytic properties Graphite is added to hematite. The photo activity performance of hematite in composition with cobalt oxide and graphite in form of Co_3O_4/Fe_2O_3 nano-composite and Co_3O_4/Fe_2O_3 /G (FCG) nano-composites are studied for the first time and result have been discussed.

2. MATERIALS AND METHODS

2. 1. Material Synthesis To prepare a Fe_2O_3-Co_3O_4 nanocomposite at first step α-Fe_2O_3 (Hematite) and Co_3O_4 nanopowders were separately synthesized by the chemical route. (Fe $(NO_3)_3.9H_2O$) (99.9%, Merck), (Co $(NO_3)_2.6H_2O$) (99.9%, Merck), $(NH_4)_2C_2O_4$ (99.9 Merck) and ethanol C_2H_5OH (99.5 % Merck) were used as the starting materials. Distilled water was used as a solvent. For synthesis of α-Fe2O3 (Hematite), Fe $(NO_3)_3.9H_2O$ was dissolved in distilled water with stirring at room temperature. After a while, ethanol solution was added dropwise to the stirring mixture at room temperature. The pH value was defined according to the experimental conditions given in reference [18]. The resulting dark dispersion was continuously stirred for 1 h at room temperature and then temperature was raised to 80 ℃ and maintained until yielding a black powder. The black powder was calcined in a furnace at 500 °C for 3 h to obtain a complete crystalline nano-powder. The synthesis procedure of Co_3O_4 included dissolving Co $(NO_3)_2.6H_2O$ (99.9% of Merck) in 100 ml of distilled water and di-ammonium oxalate $(NH_4)_2C_2O_4$ (99.99 Merck) separately as well. Ammonium oxalate solution was immediately poured into the cobalt nitrate solution at room temperature that led to precipitation of pink cobalt oxalate with the chemical formula of CoC_2O_4. During the precipitation process, the solution is stirred continuously until completion. At this stage, cobalt oxalate is conformed completely, and stirrer is turned off to deplete the sedimentary sediment and the waste solution. After drying, the sediment was transferred into an electric furnace for calcination where it was kept at 500 ℃ for 3 hours resulting in Co_3O_4 black powder [19].

2. 2. Preparation of Composite Catalysts Composite catalysts were prepared in different weight ratios of Co_3O_4/ Fe_2O_3, thermal operation was performed for 1 hour at 700 ℃ and the products were labeled FCx (x= 8, 16, 24 wt. %) corresponding to the weight ratio of the Co_3O_4/Fe_2O_3 nanocomposites. The Co_3O_4/Fe_2O_3 /G (FCG) nano-composites were prepared by adding Graphite nanopowder to Co_3O_4/Fe_2O_3 in weight values of 1.17 and 2.35% wt% of graphite to determine the effect of graphite addition on photoactivity. After adding graphite, the resulting composite was heated for one hour at 700 ℃ in an electric furnace.

2. 3. Characterization The prepared nanopowders and composites samples were characterized with X-ray powder diffractometer (XRD). The XRD used was Philips X-Ray Diffract meter with Cu Kα radiation source (λ = 1.54274).The morphology of samples was characterized by Field emission scanning electron microscopy (FESEM) Vega Tescan. Synthesized powders were ultrasonically dispersed into ethanol and the suspensions were then spread on the surface of aluminum foil to prepare sample for FESEM. Gold coating was performed before observation for better conductivity.

The UV–Vis diffused reflectance spectra (DRS) were taken using a Perkin Elmer, Model Lambda 25.

2. 3. Photocatalytic Activity Test The prepared composites were used to degrade Methylene Blue (MB) under a 55 W xenon lamp, and its photocatalytic

performance was studied through comparison with P25. Photocatalytic samples of 10 mg were added to 100 mL of a 10^{-5} Molar of MB solution and magnetically stirred for 0.5 h in the dark to obtain the adsorption–desorption balance, and the xenon lamp was then turned on. A 5 mL sample of the solution was taken out every 20 min and centrifuged at a high speed; then, it was tested using a UV-vis spectrophotometer in 664 nm, with distilled water as a contrast. The concentration of MB was calculated according to Lambert–Beer's law. The concentration of MB can be determined from the intensity of the color peak (664 nm) of solution. A standard calibration curve was constructed in the working range of 1.8–3.1 ppm (Figure 1).

The measurements were carried out over the wavelength range of 400–1000 nm. The concentration of MB was calculated according to Lambert–Beer's law by using Equation (1) that indicates relation between UV absorption and MB concentration:

$$C = 5.3968\ A - 0.564 \quad (1)$$

where C (ppm) is MB concentration and A is the absorption value obtained in UV-Vis measurements.

3. RESULTS AND DISCUSION

The crystal structure of the synthesized catalysts α-Fe_2O_3 nanoparticles and Co_3CO_4 nanoparticles were examined via XRD measurement and the data is shown in Figure 2. The observed pattern after heat treatment at 500 ℃ of the collected products exhibited all the expected peaks from the α-Fe_2O_3 structure (a) and Co_3CO_4 (b) without any detectable peaks from impurities and other phases. Powder X-ray diffraction (XRD) data can be indexed to the characteristic peaks of hematite (JCPDS 33-06 64) and Cobalt Oxide (JCPDS 01-076-1802).

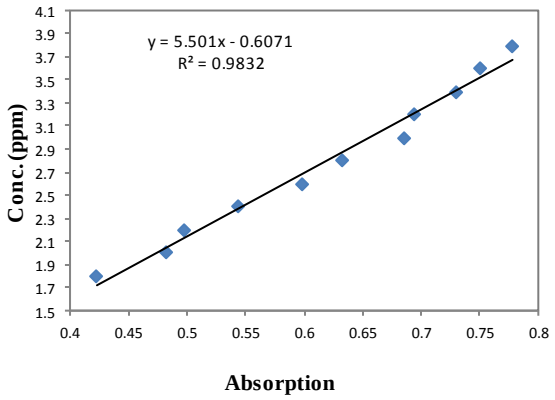

Figure 1. UV–Vis spectroscopy calibration curve for MB concentration

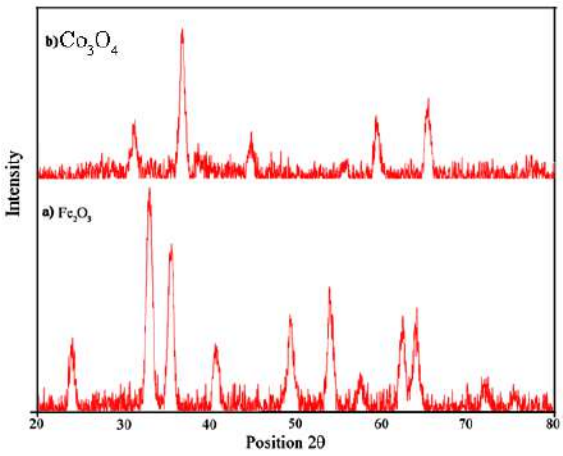

Figure 2. XRD patterns of the synthesized a) Hematite and b) Co_3O_4 powder after calcinations at 500℃

Morphologies of the synthesized α-Fe_2O_3 and Co_3O_4 nanoparticles were characterized using scanning electron microscopy. The SEM images of the samples are shown in Figure 3. It can be seen that the synthesized Co_3O_4 nanopowder catalysts have very homogenous morphologies, regular dispersion and with nearly spherical shapes varying in size from approximately 30 to 50 nm. A closer look, specifically on α-Fe_2O_3, allows to see that these particles consist of significantly smaller sphere –like grains with the size around 40-60 nm confirming that the synthesized nano-sized α-Fe_2O_3 particles have formed these soft agglomerations.

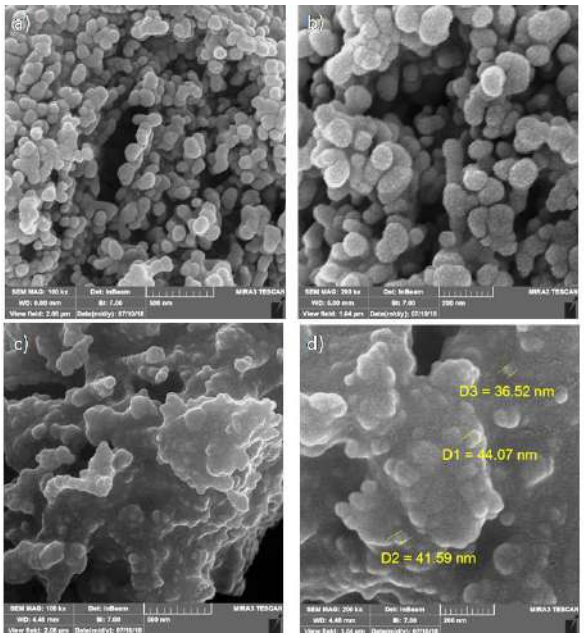

Figure 3. SEM images of the synthesized Co_3O_4 (a, b) and α-Fe_2O_3 (c. d) nanoparticles after calcinations at 500℃

Composites of powder were prepared with heat treatment specified amounts of each of the powders after mechanically mixed together. All heat treatments were performed at a temperature of 700 ℃. Figure 4 shows XRD pattern of Fe_2O_3/Co_3O_4/Graphite (FC3G2) composite (2.35 wt.% Graphite was added to FC3: 84 $Fe_2O_3/16Co_3O_4$ (wt.%)). It shows that the composite comprises of all three compounds of Fe_2O_3, Co_3O_4, and Graphite.

The three different compounds of synthesized hematite nanopowder, 84 $Fe_2O_3/16Co_3O_4$ (wt.%) composite and Fe_2O_3/Co_3O_4/Graphite (FC3G2) composite (2.35 wt.% Graphite added to FC3) were characterized by UV-visible absorption spectra to compare their optical absorption properties. Results are shown in Figure 5. The spectra show changes in the behavior of absorbance wavelengths when cobalt oxide and graphite were added to hematite powder and formed composites. Accordingly, it can be concluded that the absorbance of ultraviolet waves (wavelengths 190 to 200 nm) in FC3G2 composite is about 7.36% more than that of hematite; nevertheless, in visible ranges (between 400 and 700 nm) hematite absorbs about 30% more lights compared to FC3G2 composite. By adding cobalt oxide to hematite, the absorption peak is shifted to the left (indicated by green color in Figure 5), indicating an increase in the energy of band gap. With the addition of graphite to the two based composite of Fe_2O_3/Co_3O_4, the absorption edge has increased (blue curve), which means that graphite has no effect on the energy band gap and has only increased the absorption of ultraviolet waves.

The photocatalytic activity was examined by a colorant decomposition test using MB, which is very stable chemical dye under normal conditions. In general, absorption spectra can be used to measure the concentration changes of MB in extremely dilute aqueous solution. The MB displays an absorption peak at the wavelength of about 664 nm. Time-dependent photo-degradation of MB is shown in Figure 6. In all curves in

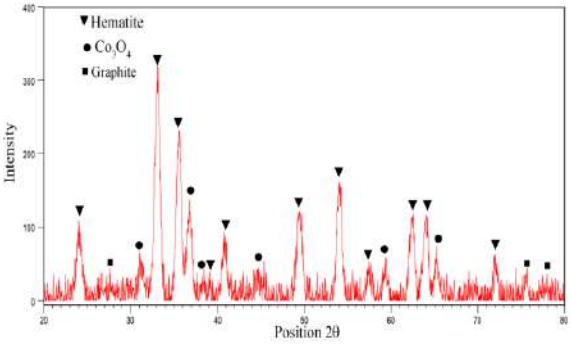

Figure 4. XRD patterns of the Fe_2O_3/Co_3O_4/Graphite (FC3G2) composite powder after heat treatment at 700℃

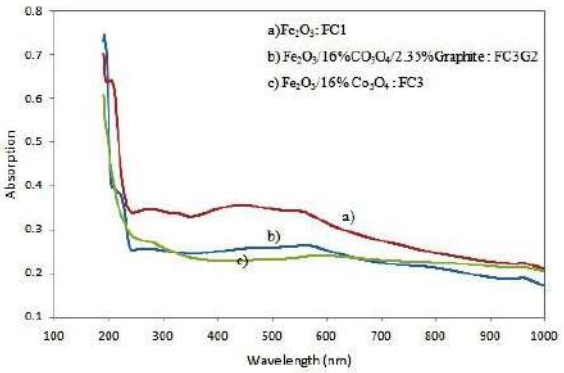

Figure 5. UV-visible absorbance spectrum

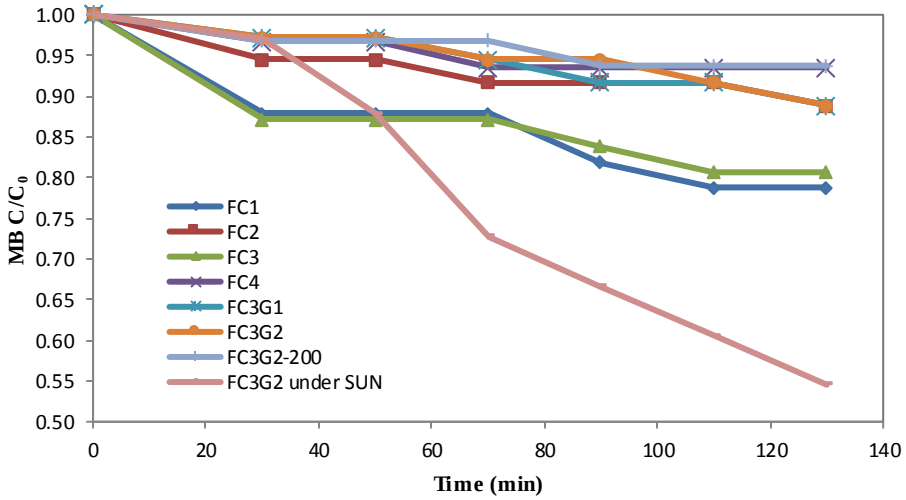

Figure 6. Changes in MB concentration photocatalytic degradation in the presence of different compounds of catalysts nanopowders: Pure Fe_2O_3 (FC1), Composites of Fe_2O_3/Co_3O_4 (FC2, FC3 and FC4), Composite Fe_2O_3/Co_3O_4/Graphite (FC3G2)

the first 30 minutes, decreasing in methylene blue concentration will be due to surface absorption of the powder since the test was performed in absolute darkness for 30 min. after which radiation was started up to 130 min that exhibited the photocatalytic activity of the catalysts powder. It is illustrated that MB decomposes in the presence of pure hematite and in composite samples of Fe_2O_3/Co_3O_4 with 8, 16 and 24 wt.% of Co_3O_4. The results of the dark tests showed that increasing Co_3O_4 did not follow a fixed pattern for surface adsorption of methylene blue molecules. Methylene blue is a cationic dye that is widely used in the textile industry [20]. The surface charge of hematite particles is negative [21], while the surface charge of Co_3O_4 particles is positive + 41[22]. Therefore, raising the amount of Co_3O_4 leads to decrease of the absorption of methylene blue molecules on the surface of the composite powder. According to those results, the distribution of hematite and Co_3O_4 particles is expected to be such that the hematite particles surrounded the cobalt oxide particles, in which case the effect of adding cobalt oxide to the absorption or excretion of methylene blue molecules is reduced because there are fewer interfaces between cobalt oxide particles and methylene blue molecules. For instance, in the FC3 composite containing 16% cobalt oxide, Co_3O_4 particles are more surrounded by hematite than in the FC4 composite with 24 wt.% cobalt oxide. According to the results shown in Figure 6, the highest amount of adsorbent in dark belongs to FC3 and the lowest surface absorbance is for FC2 containing 8% cobalt. Moreover, according to Fabrizio Creazzo et al. [22], if the FCC network of Co_3O_4 cuts from the side of (110), one side of the disconnected network will have a negative charge, while the other side will have a positive charge [22]. Based on this, it can be predicted that in the composition containing 16% cobalt oxide, the levels of sections with negative charge of cobalt oxide had a higher level of common with methylene blue solution, which caused more absorption of methylene blue molecules and in the composition containing 8% cobalt oxide had a more positively cross-sectional area with the methylene blue solution.

The results reveal that the introduction of Graphite improves the photocatalytic activity by reducing the surface absorbance. This can conclude that Graphite as a conductive material reduces the recombination of electrons and holes that leads to improving photoactivity. It is seen from Figure 6 that in FC3G2 samples with 2.35 wt.% Graphite, the photo activity increased by 1.89% compared to FC3 sample without Graphite.

The photo activity of nano-composite FC3G2 in the two concentrations of 100 ppm and 200 of catalysts were compared and result is shown in Figure 6. The photo activity of nano-composite in concentration of 100 ppm showed better result. The decrease in photo activity by increasing the amount of photocatalytic powder is due to raising the population of particles that leads to more collision between particles, then decreasing the active surface for absorbing electromagnetic waves. The photocatalytic activity of catalysts reduces about 2% by increasing the amount of photocatalytic powder to 200 ppm.

Figure 7 shows an overview of the performance of all synthesized nano-composites. The highest rate of photo activity is related to hematite nanoparticles (FC1), and among the composites, the best photocatalytic performance belongs to the FC3G2 composite with 2.35 wt.% Graphite. On the other hand, the lowest amount of photo activity is related to FC4 composite, which contains the highest amount of cobalt oxide. Therefore, adding cobalt oxide to the composite has not yielded to desired results.

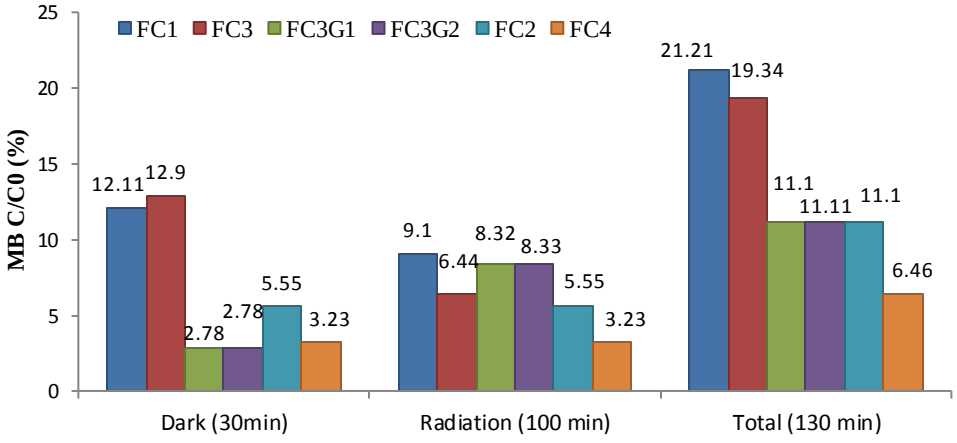

Figure7. Comparing photocatalytic activity in the presence of different compounds of catalysts nanopowders

The photo activity of nano-composite FC3G2 was examined under sunlight. The results of this experiment show that the photo activity of the nano-composite under irradiation of the solar light is about 4.5 times higher than that of the photo activity in the xenon 55 W lamp that caused degradation of about 55% of methylene blue. The higher removal efficiency of methylene blue over FC3G2 composite compared to all experiments done under radiation of xenon 55 W lamp is probably due to increase in dye adsorption on the photocatalyst surface under solar light which will react with active species in the photo catalysis process.

Calculations show that this photocatalytic nano-composit powder can produce 5.7 µmol H2 per hour in a 1 liter of water under radiation of xenon 55 W. However, this same composite produced 27 µmol H2 per hour under solar light irradiation. The results indicated that the removal efficiency of photo activity could be enhanced effectively in FC3G2 composite under solar light irradiation; that phenomenon has been reported by S Lub et al. [23].

4. CONCLUSION

Nano-hematite and nano-cobalt oxide were successfully synthesized by simple chemical method without using a surfactant or templates. The synthesis process employs low-cost raw materials and yields a phase-pure, polycrystalline product. Compositing strategy in order to promote photocatalytic properties of hematite was studied. According to the UV-vis experiment graphite improves the photocatalytic activity of hematite. However, adding Co_3O_4 to hematite transports the edge of the adsorbent to lower wavelengths, which means that the band gap has increased. The photocatalytic activities of the nano-hematite were determined by investigating the degradation of MB upon irradiation of UV lamp and solar light in the presence of the hematite and other composites. Of the various compounds synthesized, hematite nanoparticles were found to have the best photocatalytic performance during the degradation of MB, however among the composites, FC3G2 composite (containing 2.35% graphite and 16% cobalt oxide) had the best photocatalytic performance. Photocatalytic activity of FC3G2 composite under solar light was higher than that of UV irradiation. Photocatalytic activity of FC3G2 composite under solar light was higher than that of UV irradiation.

5. REFERENCES

1. Lee, J.S., "Photocatalytic water splitting under visible light with particulate semiconductor catalysts", ***Catalysis Surveys from Asia***, Vol. 9, (2005), 217-227. DOI: 10.1007/s10563-005-9157-0.
2. Maeda, K. and Domen, K., "New non-oxide photocatalysts designed for overall water splitting under visible light", ***The Journal of Physical Chemistry C***, Vol. 111, No. 22, (2007), 7851-7861. DOI: 10.1021/jp070911w.
3. Osterloh, F.E., "Inorganic materials as catalysts for photochemical splitting of water", ***Chemistry of Materials***, Vol. 20, No. 1, (2008), 35-54. DOI: 10.1021/cm7024203.
4. Mangold, K.-M., "Introduction to hydrogen technology.By roman j. Press, k. S. V. Santhanam, massoud j. Miri, alla v. Bailey, and gerald a. Takacs", ***ChemSusChem***, Vol. 2, No. 8, (2009), 781-781. DOI: 10.1002/cssc.200900109.
5. Dutta, S., "A review on production, storage of hydrogen and its utilization as an energy resource", ***Journal of Industrial and Engineering Chemistry***, Vol. 20, (2014), 1148–1156. DOI: 10.1016/j.jiec.2013.07.037.
6. Maeda, K., Xiong, A., Yoshinaga, T., Ikeda, T., Sakamoto, N., Hisatomi, T., Takashima, M., Lu, D., Kanehara, M., Setoyama, T., Teranishi, T. and Domen, K., "Photocatalytic overall water splitting promoted by two different cocatalysts for hydrogen and oxygen evolution under visible light", ***Angewandte Chemie International Edition***, Vol. 49, No. 24, (2010), 4096-4099. DOI: 10.1002/anie.201001259.
7. Liu, S., Kokot, S. and Will, G., "Photochemistry and chemometrics—an overview", ***Journal of Photochemistry and Photobiology C: Photochemistry Reviews***, Vol. 10, No. 4, (2009), 159-172. https://doi.org/10.1016/j.jphotochemrev.2010.01.001.
8. Chen, Y.H. and Lin, C.C., "Effect of nano-hematite morphology on photocatalytic activity", ***Physics and Chemistry of Minerals***, Vol. 41, No. 10, (2014), 727-736. 10.1007/s00269-014-0686-9.
9. Wender, H., Gonçalves, R.V., Dias, C.S.B., Zapata, M.J.M., Zagonel, L.F., Mendonça, E.C., Teixeira, S.R. and Garcia, F., "Photocatalytic hydrogen production of $CO(OH)_2$ nanoparticle-coated α-Fe_2O_3 nanorings", ***Nanoscale***, Vol. 5, No. 19, (2013), 9310-9316. DOI: 10.1039/C3NR02195E.
10. Liu, C.a., Fu, Y., Xia, Y., Zhu, C., Hu, L., Zhang, K., Wu, H., Huang, H., Liu, Y., Xie, T., Zhong, J. and Kang, Z., "Cascaded photo-potential in a carbon dot-hematite system driving overall water splitting under visible light", ***Nanoscale***, Vol. 10, No. 5, (2018), 2454-2460. DOI: 10.1039/C7NR08000J.
11. Zhu, Y., Wan, T., Wen, X., Chu, D. and Jiang, Y., "Tunable type i and ii heterojunction of coox nanoparticles confined in g-c3n4 nanotubes for photocatalytic hydrogen production", ***Applied Catalysis B: Environmental***, Vol. 244, (2019), 814-822. https://doi.org/10.1016/j.apcatb.2018.12.015.
12. Nahar, S., Zain, M., Kadhum, A., Abu Hasan, H. and Hasan, M.R., "Advances in photocatalytic CO_2 reduction with water: A review", ***Materials***, Vol. 10, (2017), 629. DOI: 10.3390/ma10060629.
13. Miao, R., Luo, Z., Zhong, W., Chen, S.-Y., Jiang, T., Dutta, B., Nasr, Y., Zhang, Y. and Suib, S., "Mesoporous TiO_2 modified with carbon quantum dots as a high-performance visible light photocatalyst", ***Applied Catalysis B: Environmental***, Vol. 189, (2016), 26-38. DOI: 10.1016/j.apcatb.2016.01.070.
14. Moro, F., Yu Tang, S.V., Tuna, F. and Lester, E., "Magnetic properties of cobalt oxide nanoparticles synthesised by a continuous hydrothermal method", ***Journal of Magnetism and Magnetic Materials***, Vol. 348, (2013), 1-7. https://doi.org/10.1016/j.jmmm.2013.07.064.
15. Mohamed, R.M., McKinney, D.L. and Sigmund, W.M., "Enhanced nanocatalysts", ***Materials Science and Engineering: R: Reports***, Vol. 73, No. 1, (2012), 1-13. https://doi.org/10.1016/j.mser.2011.09.001.

16. Mangrulkar, P.A., Joshi, M.M., Tijare, S.N., Polshettiwar, V., Labhsetwar, N.K. and Rayalu, S.S., "Nano cobalt oxides for photocatalytic hydrogen production", ***International Journal of Hydrogen Energy***, Vol. 37, No. 13, (2012), 10462-10466. https://doi.org/10.1016/j.ijhydene.2012.01.112.
17. Moniz, S.J.A., Shevlin, S.A., Martin, D.J., Guo, Z.-X. and Tang, J., "Visible-light driven heterojunction photocatalysts for water splitting – a critical review", ***Energy & Environmental Science***, Vol. 8, No. 3, (2015), 731-759. DOI: 10.1039/C4EE03271C.
18. Farahmandjou, M. and soflaee, f., "Low temperature synthesis of α- Fe_2O_3 nano-rods using simple chemical route", ***Journal of Nanostructures***, Vol. 2, (2015), 413. DOI: 10.7508/jns.2014.04.002.
19. Manteghi, F., Kazemi, S.H., Peyvandipour, M. and Asghari, A., "Preparation and application of cobalt oxide nanostructures as electrode materials for electrochemical supercapacitors", ***RSC Advances***, Vol. 5, No. 93, (2015), 76458-76463. DOI: 10.1039/C5RA09060A.
20. Liu, L., Zhang, B., Zhang, Y., He, Y., Huang, L., Tan, S. and Cai, X., "Simultaneous removal of cationic and anionic dyes from environmental water using montmorillonite-pillared graphene oxide", ***Journal of Chemical & Engineering Data***, Vol. 60, No. 5, (2015), 1270-1278. DOI: 10.1021/je5009312.
21. Mustafa, S., Tasleem, S. and Naeem, A., "Surface charge properties of Fe_2O_3 in aqueous and alcoholic mixed solvents", ***Journal of Colloid and Interface Science***, Vol. 275, No. 2, (2004), 523-529. https://doi.org/10.1016/j.jcis.2004.02.089.
22. Creazzo, F., Galimberti, D.R., Pezzotti, S. and Gaigeot, M.-P., "Dft-md of the (110)-CO_3O_4 cobalt oxide semiconductor in contact with liquid water, preliminary chemical and physical insights into the electrochemical environment", ***The Journal of Chemical Physics***, Vol. 150, No. 4, (2019), 041721. DOI: 10.1063/1.5053729.
23. Lubis, S., Sheilatina and Murisna, "Synthesis, characterization and photocatalytic activity of α- Fe_2O_3/bentonite composite prepared by mechanical milling", ***Journal of Physics: Conference Series***, Vol. 1116, (2018), 042016. DOI: 10.1088/1742-6596/1116/4/042016.

Persian Abstract

چکیده

در این مطالعه، در مرحله‌ی اول ذرات نانوپودر α-Fe_2O_3 (هماتیت) و Co_3O_4 به طور جداگانه با استفاده از روش شیمیایی ساده محلول آبی از نیترات آهن و نیترات کبالت از پیش‌ماده‌های اولیه $Fe(NO_3)_3.9H_2O$ و هگزاهیدرات $Co(NO_3)_2.6H_2O$ سنتز شدند. پس از آن، سه کامپوزیت از نانوپودرهای سنتز شده به ترتیب با افزودن ۸، ۱۶ و ۲۴ درصد وزنی Co_3O_4 به Fe_2O_3 تهیه شدند. نانوپودر گرافیت نیز به یک ترکیب از نمونه‌های ذکر شده به میزان ۱,۱۷ و ۲,۳۵ درصد وزنی اضافه شد. ترکیب فازی و ساختاری و مورفولوژی کامپوزیت‌ها به‌ترتیب توسط XRD و FE-SEM بررسی شدند. تحلیل FE-SEM نشان داد که مورفولوژی پودرها و کامپوزیت‌ها همه در مقیاس نانو و کروی شکل هستند. فعالیت فوتوکاتالیستی کامپوزیت‌ها با اندازه گیری تخریب محلول آبی متیلن بلو تحت تابش نور خورشید شبیه‌سازی شده بررسی شد. برای تعیین فعالیت فوتوکاتالیستی، تخریب آبی متیلن (MB) در غیاب نور (آزمایش تاریک) نیز گرفته شد. نتایج نشان داد که افزودن Co_3O_4 به Fe_2O_3 باعث کاهش فعالیت فرآیند فوتوکاتالیستی می‌شود، در حالی که نانو گرافیت فرآیند فوتوکاتالیستی را به میزان ~ ۲٪ نسبت به کامپوزیت بدون نانوذرات گرافیت افزایش می‌دهد. محاسبات استوکیومتری نشان داد که مقدار هیدروژن تولید شده توسط آب توسط نانوذرات کامپوزیت Fe_2O_3 /Co_3O_4/Graphite در برابر تابش نور خورشید برابر با ۲۷ $\mu mol\ H_2/h.g$ است.

International Journal of Engineering

Journal Homepage: www.ije.ir

Optimization of Thermal Decomposition Conditions of Bone to Achieve the Highest Percentage of Crystalline Phase in Bone Char using Gene Expression Programming and Artificial Neural Network

F. Fatahi, G. R. Khayati*

Department of Materials Science and Engineering, Shahid Bahonar University of Kerman, Kerman, Iran

P A P E R I N F O

Paper history:
Received 04 August 2020
Received in revised form 20 October 2020
Accepted 29 October 2020

Keywords:
Artificial Neural Networks
Bone Char
Gene Expression Programming
Modeling
Pyrolysis Conditions

A B S T R A C T

Bone char (BC) is one of the most common adsorbent with extensive applications in the removal of pollutions. The adsorption capability of BC is proportional to the crystalline index, i.e, the atomic ratio of Ca/P. This study is an attempt to model the crystalline index of BC that by thermal decomposition of natural bone using artificial neural network (ANN) and genetic expression programming (GEP). In this regard, 100 various experimental data used to construct the ANN and GEP models, separately. Through the data collection step, heating rate, the type of precursor, calcination temperature, and residence time selected as the inputs for the preset output as Ca/P ratio. The results reveal that the minimum amount of Ca/P ratio are at the heating rate 10 °C/min, HNO_3 1.6 M as activation agent, calcination temperature 1000 °C, and residence time 2 h. R squared indices is used to compare the performance of extracted models. Finally, the best ANN uses to investigate the effect of each practical variable by sensitivity analysis and revealed that the residence time is the most effective parameter on the crystalline index while acid activation is of secondary importance.

doi: *10.5829/ije.2021.34.01a.21*

1. INTRODUCTION

Due to the increasing growth of various industries and industrial products around the world, challenges about the severe damages to the environment are increasing. Therefore, to reduce the environmental degradations, it is necessary to reduce the amount of waste by consideration of a logical and cost-effective solution. Solid waste, e.g., animal waste, are a potential source of renewable materials. Thermal conversion of solid waste into char has been widely studied as a promising solution for waste disposal. During this conversion, a valuable by-product is produced that can be used in many fields of industrial production to reduce the environmental damages [1, 2]. Bone char (BC) is a black, porous, granular substance that prepared by heating of animal bones. It is one of the most common sorbents with unique characteristics including eco-friend, accessible, cheap, and excellent regenerating specification. Adsorption of pollution is one of the most common applications of BC, e.g., water treatment process, in the industry. It traditionally uses as discoloration agent in the sugar industry [3, 4]. Adsorption of F, Cd, Zn, Ni, Cu and As from aqueous solution with low cost are the other applications of BC. Therefore, finding a solution to produce and control the characteristics of BC is of great importance [5, 6]. There is a significant dependency between the compositions of BC to its preparation methods. There are 50-80 wt.% hydroxyapatite, 10-16 wt.% $CaCO_3$, and 7-10 wt.% carbon in the chemical composition of BC. Incomplete combustion of natural bones with controlled oxygen is the main approach for the preparation of BC. Table 1 illustrates the physical and chemical properties and application of BC that have been prepared by different methods. There is a strong dependency between the crystallinity index of BC (i.e., the ratio of Ca/P) on its

*Corresponding Author Institutional Email: *khayati@uk.ac.ir* (G. R. Khayati)

Please cite this article as: F. Fatahi, G. R. Khayati, Optimization of Thermal Decomposition Conditions of Bone to Achieve the Highest Percentage of Crystalline Phase in Bone Char using Gene Expression Programming and Artificial Neural Network, International Journal of Engineering, Transactions A: Basics, Vol. 34, No. 1, (2021) 184-194

capacity as an adsorbent agent [7]. In this regard, optimization of the amount of Ca/P ratio plays a key role for design and preparation of BC with a better adsorption performance. P and Ca are the main constituents of bone. The other constituents with lower contents are Na, C, Mg, and O. In general, stoichiometric amount of Ca/P ratio in bone is 1.67 [8, 9]. However, based on Table 1, the Ca/P ratio is completely variable and the charring of animal bones is the main preparation method of BC. Some advantages including low production and activation process caused the evolution of charring of animal bones as a promising approach for the preparation of BC. Unfortunately, this process suffers from the comprehensive investigation on the analysis of complicated interaction between the practical variables including pre-process or activation of bones by acidic solutions, calcination temperature, heating rate, and residence time. To the best of our knowledge, several methods have been used to produce BC. However, no research has been done to model the crystalline index of BC based on practical variables, so far. Hence, illustration of reliable models based on experimental data is strongly proposed to enhance the performance of BC. This study aims at constructing new predictive models based on gen expression programming (GEP) and artificial neural network (ANN), for determination of the Ca/P ratio as a function of practical variables. To construct these models, 100 reliable trails were done for the preparation of BC. The data are used to train and test GEP and ANN models. The calcination temperature changed between 400 °C to 1000 °C, the residence time is considered in the range of 1 to 4 h, and the heating rate changed from 5 to 12 °C/min. The performance of both models are compared to each other. Finally, the effect of each practical variable is investigated by sensitivity analysis.

2. MATERIALS AND METHODS

The thigh bone of cow is used as a precursor to prepare the bone char. As a first step, selected thigh bone washed for 2 h in boiling deionized water to wipe out meat and fat residues and left 24 h to dry. Then, the dried bones are crashed (with the particle size lower than 1 mm) and uses as mother sample for the preparation of BC.

2. 1. Specimen Preparation A CVD furnace equipped with the ceramic holder is used through the calcination step. At first, the origin bones sample divide into 100 parts. 60 parts directly heated to prepare BC. The remained 40 parts pre-processed by the addition of 490 mL of HNO_3 (with various concentrations including 0.49, 1.1, 1.6 M) to 50 gr of crashed bones in Erlenmeyer flask on a hot plate at the temperature of 80 °C. The prepared solution is mixed for 24 h. Then, the solution is cleared, and the pre-processed samples locate in a porcelain capsule. Finally, the prepared BC sample stored in a micro tubes for further analysis. As shown in Table 2, the BC samples that directly used identified by 1 and the pre-processed bones with 0.49, 1.1, and 1.6 M HNO_3 solutions are identified by 2, 3, and 4, respectively. BC samples synthesized under the special conditions of pyrolysis including the calcination temperature (400-1000 °C), heating rate (5-12 °C/min), residence time (1-4 h) and argon gas (400 mL/min). EDX analysis is utilized to investigate the weight percentages of Ca and P elements to calculate the crystalline index (Table 2).

TABLE 1. Chemical composition of BC as a function of preparation condition and its applications

Ref.	Total Ca (wt.%)	Total P (wt.%)	Total C (wt.%)	Hydroxyapatite (%)	Application of BC
[10]	-	-	9-11	70-76	Adsorption of toxic ions
[11]	-	-	11.0	76	Adsorption of fluoride
[12]	-	13.4	12.5	-	Filtrations of P
[13]	28	15.2	13	-	Filtrations of P
[14]	-	15	6.3	85	Adsorption of fluoride
[15]	39	20	-	80	Water treatment
[16]	30.7	14	-	69	Filtrations of P
[17]	27.1	12.7	18.0	-	Used as P-fixing soil influenced by root-mycorrhiza-bio char interactions
[18]	18.5	14.9	11.2	-	Improvement the phosphorus-cadmium-interaction
[17]	33.7	15.3	8.2	-	Used as P-fixing soil
[19]	23.9	15.7	-	89	Adsorption of Cr (III) from water solution
[20]	24.2	11.5	3.8	-	Absorption the methylene blue
[21]	23.8	13	10.4	56	Improvement of the transformations of P in plant-based structure
[22]	-	-	10.0	80-90	Enhancement of photocatalytic performance by ZnO/BC composites

TABLE 2. Summary of the experimental design used to the synthesis of BC

No.	Inputs				Output
	Precursor [a]	Calcination temperature (°C)	Heating rate (°C/min)	Residence time (h)	Ca/P Ratio
1	3	1000	7	1	1.31
2	4	400	5	1	1.27
3	3	700	5	4	1.45
4	3	400	12	3	1.41
5	2	1000	5	3	1.72
6	2	400	7	4	1.92
7	4	700	7	3	1.03
8	2	700	12	1	1.69
9	1	900	10	2	2.02
10	3	800	10	2	1.30
11	1	500	7	2	2.30
12	1	600	10	3	2.14
13	1	800	5	1	2.24
14	3	500	10	1	1.46
15	4	600	7	4	1.05
16	3	900	12	3	1.17
17	2	600	5	2	1.93
18	2	500	10	4	1.79
19	2	800	7	3	1.75
20	4	500	12	2	0.99
21	4	900	5	1	1.03
22	1	800	12	4	1.97
23	4	700	10	2	0.96
24	2	600	12	1	1.74
25	1	500	5	3	2.34
26	1	400	10	1	2.28
27	1	1000	12	2	1.92
28	1	900	7	4	2.07
29	4	800	10	3	0.89
30	3	400	5	2	1.63
31	2	1000	10	4	1.55
32	3	600	5	4	1.50
33	2	900	7	2	1.73
34	1	700	7	1	2.23
35	3	600	7	1	1.50
36	4	1000	7	2	0.91
37	4	900	10	1	0.88
38	2	800	12	2	1.63
39	4	500	12	4	0.95
40	1	400	12	3	2.18
41	1	700	5	4	2.22
42	2	500	5	3	1.95
43	3	700	10	3	1.33
44	2	400	10	4	1.83
45	3	800	7	4	1.35

46	3	900	12	4	1.15
47	4	600	10	3	0.99
48	3	1000	10	1	1.22
49	4	800	5	1	1.08
50	2	700	12	1	1.69
51	2	900	5	3	1.76
52	4	400	7	2	1.19
53	1	600	12	2	2.11
54	3	500	7	1	1.55
55	1	1000	7	3	2.04
56	3	700	5	2	1.49
57	1	1000	5	4	2.08
58	3	1000	12	3	1.12
59	2	500	10	2	1.83
60	3	900	5	2	1.40
61	4	500	5	3	1.18
62	2	600	7	3	1.85
63	2	800	12	1	1.65
64	4	400	12	4	1.00
65	1	900	10	1	2.04
66	3	800	10	4	1.26
67	2	400	5	1	2.04
68	2	700	10	4	1.69
69	4	600	5	4	1.11
70	4	1000	10	2	0.82
71	4	900	7	3	0.93
72	1	400	10	3	2.24
73	1	500	7	4	2.26
74	1	800	5	2	2.22
75	1	600	12	1	2.13
76	3	400	7	2	1.58
77	4	700	12	3	0.88
78	3	500	12	1	1.40
79	4	800	7	1	1.02
80	2	1000	5	1	1.76
81	2	900	12	4	1.54
82	2	700	7	2	1.82
83	3	600	10	2	1.39
84	3	800	7	3	1.37
85	1	700	12	2	2.06
86	1	700	7	1	2.23
87	4	600	12	2	0.95
88	3	1000	12	3	1.12
89	4	400	10	1	1.12
90	2	500	10	3	1.81
91	1	900	5	3	2.15
92	1	600	10	4	2.12
93	4	500	5	4	1.16

94	2	1000	7	2	1.68
95	3	400	7	4	1.53
96	1	800	5	2	2.22
97	3	700	5	3	1.47
98	3	900	12	2	1.19
99	3	600	5	1	1.56
100	4	1000	12	4	0.92

[a] Number of 1, 2, 3, and 4 refer to the sample that uses as-cleaned bone, initial bone sample modified with 0.4, 1.1, and 1.6 M of HNO_3, respectively.

3. METHODOLOGY

3. 1. 1. Genetic Expression Programming (GEP)

GEP is the hybrid version of genetic algorithm (GA) and genetic programming (GP) to enhance the performance of each one [23-27]. The main elements of GEP are terminal set, fitness function, and termination condition. GEP different from GP in the way of the solution representation condition. The creation of a fixed length of character strings to show the solution as a computer model in a tree-like structure is the administered approach in GEP. These trees named expression trees (ETs) [24, 25, 28]. The operation of GEP element is performed at chromosome level and leads to the simplification in the creation of genetic diversity. Multigenics is another characteristic of GEP. Accordingly, it provides a higher capability for the solution of more complex problems. GEP elements take the value of independent input data and can convert or process them [29]. $\pm,\times.\sqrt{a,b,c}$ are typical GEP operations where a, b and c are the function sets of elements. $\pm$, $\times$ *and* $\sqrt{}$ are the terminal nodes. Karva notation or K-expression used this notation to illustrate the proposed model [23]. Besides the expression-trees, K-expression can report the proposed model in GEP. The root of ET is the first position in K-expression [27, 30]. The transformation of ET starts from the root and readsthrough the string one by one. The size of the corresponding ETs as a function of the complexity of process changes within the GEP process. As a general law, the length of each expression must be equal or less than the length of genes. Validation of the randomly selected genome is performed by the head-tail methods. Head and tail are the main components of the gene. The former composed of the function and terminal symbols, while the latter only concluding terminal symbols [28]. Selection and copy of individuals through the GEP employed the roulette wheel strategy. The validation of the population is determined by various operators, including rotation, crossover, and mutation. It is necessary to note that, rotating the sub-parts of the genome respect to the randomly chosen point was performed by rotation operators. Validation of proposed GEP models is carried out by the employment of statistical indicator, including the mean square error (MSE; Equation (1)), correlation coefficients (Equation (2)) [31] and mean absolute percentage error (MAPE; Equation (3)).

$$MSE = \frac{1}{n}\sum_{i=1}^{n}\left(t_i - o_i\right) \quad (1)$$

$$R^2 = 1 - \left(\frac{\sum_{i=1}^{n}(t_i - o_i)^2}{\sum_{i=1}^{n} o_i}\right) \quad (2)$$

$$MAPE = \frac{1}{n}\left(\sum_{i=1}^{n}\left|\frac{t_i - o_i}{t_i}\right|\right)\times 100 \quad (3)$$

where, o, t and n are the predicted value, the actual value and the total number of data, respectively. GEP model has higher accuracy, when MSE and MAPE are closer to zero, and R^2 closer to 1. Figure 1 shows the flowchart in GEP and, Figure 2 illustrates the chromosome with two genes and its decoding in GEP.

3. 1. 2. Evaluation of the Existing Models

Table 2 shows the collected experimental dataset including 100 samples. 70 samples are used in training step and 30 in testing step through the construction of GEP models. The practical parameters include the type of precursor (activated or non-activated by HNO_3), calcination temperature (°C), residence time (h), and

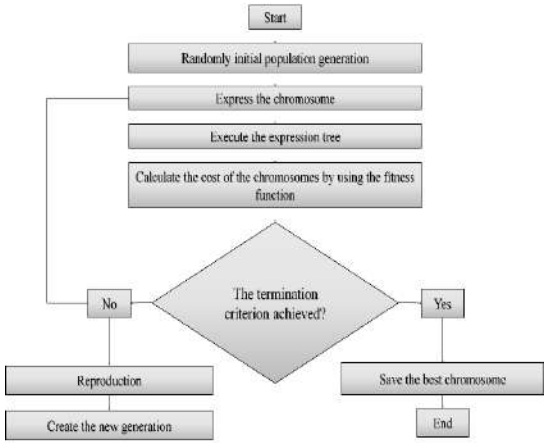

Figure 1. Flowchart of GEP

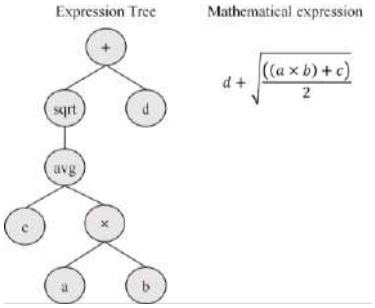

Figure 2. Representation of the typical chromosome with two genes and its decoding in GEP

heating rate (°C/min) selected as inputs. Ca/P ratio (crystalline index) is considered as the output. For GEP-based formulas, fitness (f_i), from a single program, is measured by Equation (4):

$$f_i = \sum_{i=1}^{C_t}\left(M - \left|C_{ij} - T_i\right|\right) \quad (4)$$

where, C_{ij} is the value returned by the individual chromosome, T_j the target value for the fitness case j, and (i) for fitness case and M the range of selection j. The benefit of this fitness functions is that the system can discover the optimal solution. In other words, to construct the chromosomes, fundamental functions (e.g., ln, 3Rt, x^2) and basic arithmetic operators (e.g., -, *, /, +) are chosen. Parameters of the training of GEP models are shown in Table 3.

3. 1. 3. GEP Model Results GEP proposes a distinct mathematical model for the prediction of target value. Figure 3 showed the expression-trees of the most appropriate GEP model in which d0, d1, d2 and d3 in the order represented the type of precursor, calcination temperature, heating rate and residence time. Equation (5) gives the prediction of the Ca/P ratio obtained from GEP expression tree. In Equation (5), Tp, Ct, Hr, Rt represent the type of precursor, calcination temperature, heating rate and residence time, respectively.

TABLE 3. Illustration of parameters applied in GEP models

Parameters	Setting
Function set	+, -, *, /, ln, x^2, 3Rt, Atan, Tanh, Avg2, lnv, NOT
Chromosomes	25
Head size	6
Number of genes	5
Linking function	Addition
Fitness function error type	RRSE
Mutation rate	0.002
Inversion rate	0.004
One-point recombination rate	0

$$y = A\tan\left[\mathrm{Tanh}(Tp) - A\tan(2Ct) + \frac{41.31-(Tp)}{Rt}\right] + \left[\mathrm{Tanh}\left(\frac{(Tp)^2}{19.48}\right) + A\tan\left(\frac{(Hr)\times(Tp)^2}{2}\right)\right] + \mathrm{Tanh}\left[\frac{12.86}{Hr} + \frac{1}{A\tan(Tp)} + 0.3(Tp)\right] + 24.69 \quad (5)$$

The comparison of empirical and predicted values by GEP models for Ca/P in training phase is depicted as regression plots in Figure 4.

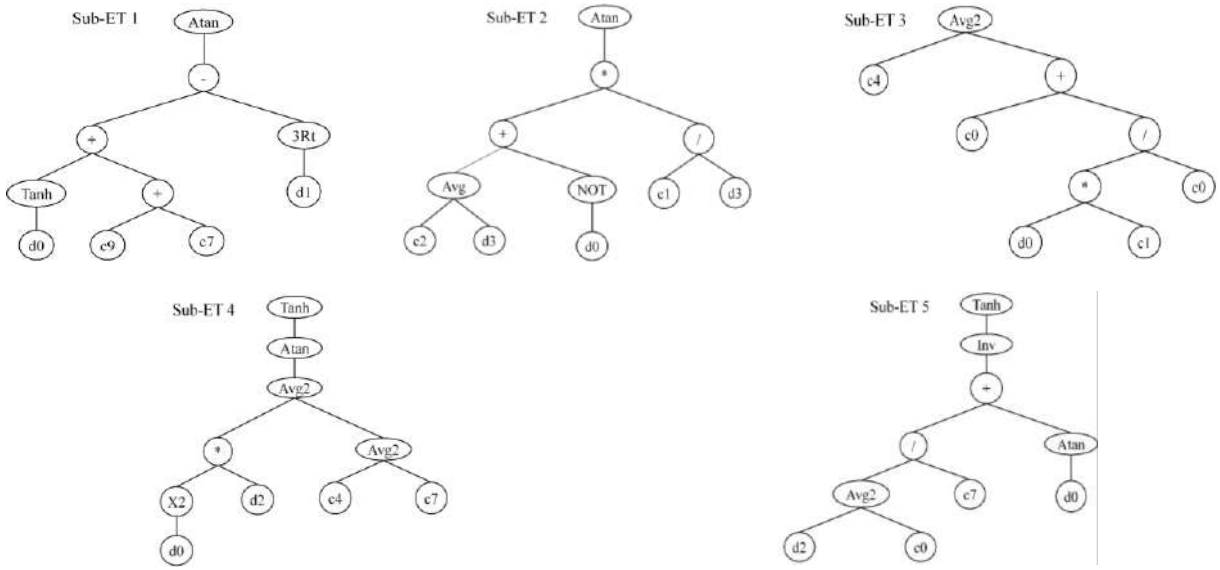

Figure 3. Expression-trees of most appropriate GEP model (d0: the type of precursor, d1: calcination temperature, d2: heating rate and d3: residence time)

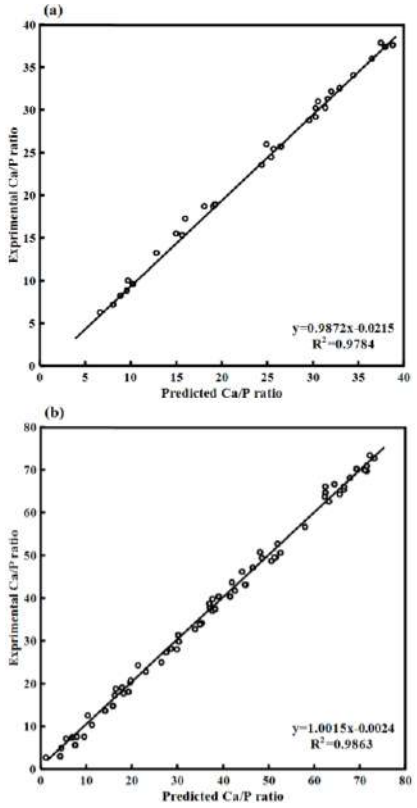

Figure 4. Illustration of (a) testing and (b) training regression in GEP model

3. 2. 1. Artificial Neural Network (ANN)

Artificial neural network (ANN) is a powerful technique to model the data with complicated interaction between the input/output parameters. The unique characteristics of neural networks caused to the evolution of this approach as a good alternative to determine the nonlinear dependency and extensively used in the processing of materials, e.g. simulation of the behavior of complex materials [32]. As shown in Figure 5, an ANN structure is generally separated into three sections: the input layer, the hidden layer, and the output layer. The nodes or neurons are connected by weights, which is similar to the intensity of the bioelectric transfer between node cells in a real neural network. Trained results can be summarized in terms of weight and bias [33]. The number of neurons in the output and input layers are equal to the output and input parameters, while the hidden layer is more than one layer and the number of neurons in each layer is tolerated. Network structure adjustment plays a key role in improving network performance [34].

$$N_{in} - \left[N_1 - N_2 - \ldots - N_h \right] h - N_{out} \quad (6)$$

where, N_{out} and N_{in} refer to the number of output and input variables, respectively. Subscript h shows the number of hidden layers, and N_h, N_1, N_2 and are the number of neurons in any hidden layer.

The network receives data from the input layer, decomposes data into hidden layers, and next outputs through the output layer. In each output layer and hidden layer, neurons consider the output of the neurons in the previous layer as their new input. Data using the weight bias and transfer subordinate in the neuron to obtain the output as shown in Equation (7).

$$X_i^{(n)} = f\left[\Sigma W_{ij}^{(n)} X_i^{(n-1)} + b_j^{(n)} \right] \quad (7)$$

where, X_j^n is the output of a node j in the n_{th} layer, W_{ji}^n the weight from the node, i in (n-1) the layer to node j in the n_{th} layer, and b_j (n) the bias of a node j in the n_{th} layer [35].

During the training phase, the network will set up hundreds of data cycles with data, weight, and bias until it reaches the correct error level or is maximized [36]. The simulation of weight and bias can be obtained as Equation (8):

$$W_{ij}^{(n)}(k) = W_{ij}^{(n)}(k-1) - \alpha \frac{\partial E}{\partial b_j^{(n)}} \quad (8)$$

In Equation (8), α illustrates the learning rate, and k refers to the repetition [37]. Figure 6 represents the schematic representation of the connection between the output and input resultant of a neuron.

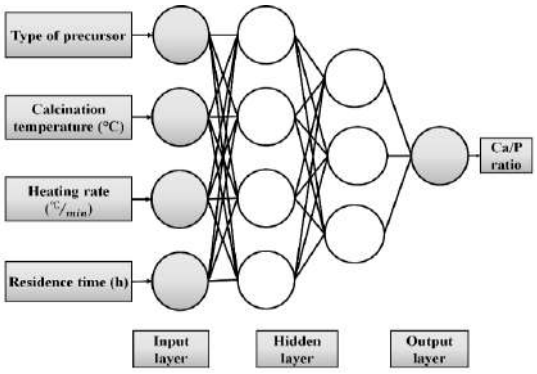

Figure 5. The schematic structure of an artificial neural network with input, output, and testing parameters

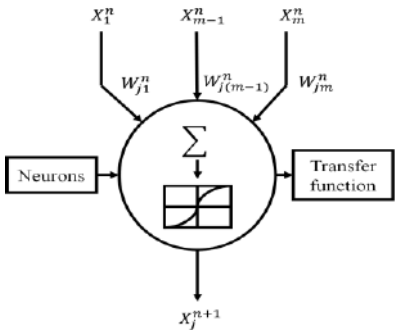

Figure 6. Schematic explanation of the connection between the output and input resultant of a neuron

3. 2. 2. Implementation In general, sufficient practical data is required to create an efficient neural network. Architecture, training strategy, transfer commutable, and other elements of the neural network must attentively determine and refined to be optimized. Therefore, a well-trained neural network can be used to analyze the new input data.

An ANN performance assessment coming back to step 2 if the implementation is not satisfactory, uses the trained network to simulate or predict the process parameters in operational database area. In summary, ANN including the collection and application of practical information, network training and configuration, an ANN performance assessment, coming back to step 2 in the case that the implementation is not satisfactory and use of trained network to simulate or predict the process parameters.

3. 2. 3. Evaluation of the Existing Models In present study, 70 experiments were utilized for training, and 30 for testing of ANN models through the prediction of Ca/P ratio. The inputs and output are the same as GEP modeling.

3. 2. 4. ANN Model Results Figure 7 represents the linear regression plots of appropriate model through training of neural network.

4. RESULTS AND DISCUSSION

Based on the experimental data and EDX analysis, it is found that by decreasing Ca/P ratio, the crystalline index is increased in the BC sample. Comparison of empirical and predicted values by GEP and ANN models for the Ca/P ratio are shown in Figures 4 and 7, respectively. Accordingly, the best constructed model by GEP has MSE =0.0015 and R^2 = 0.9784 in testing and MSE =0.008 and R^2 = 0.9863 in training. While, the best ANN model has MSE =1.81 and R^2 = 0.9897 in testing and MSE =0.9800 and R^2 = 0.9989 in training. Since the error indices in both models are less than 3 % [24], R^2 was used as a criterion and model ANN was selected for further analysis.

4. 1. Sensitivity Analysis of the ANN Model To determine the effective parameters in the pyrolysis condition on the Ca/P ratio, sensitivity analysis has been used by employment of ANN model. In this analysis, a step-by-step approach to ANN is performed by changing each of the input parameters once at a constant speed. In this study, various constants are obtained at 2, 6, and 10%. For each input parameter, the output percentage is changed due to the variation in the input parameter. The sensitivity of each input parameter is calculated using Equation (9).

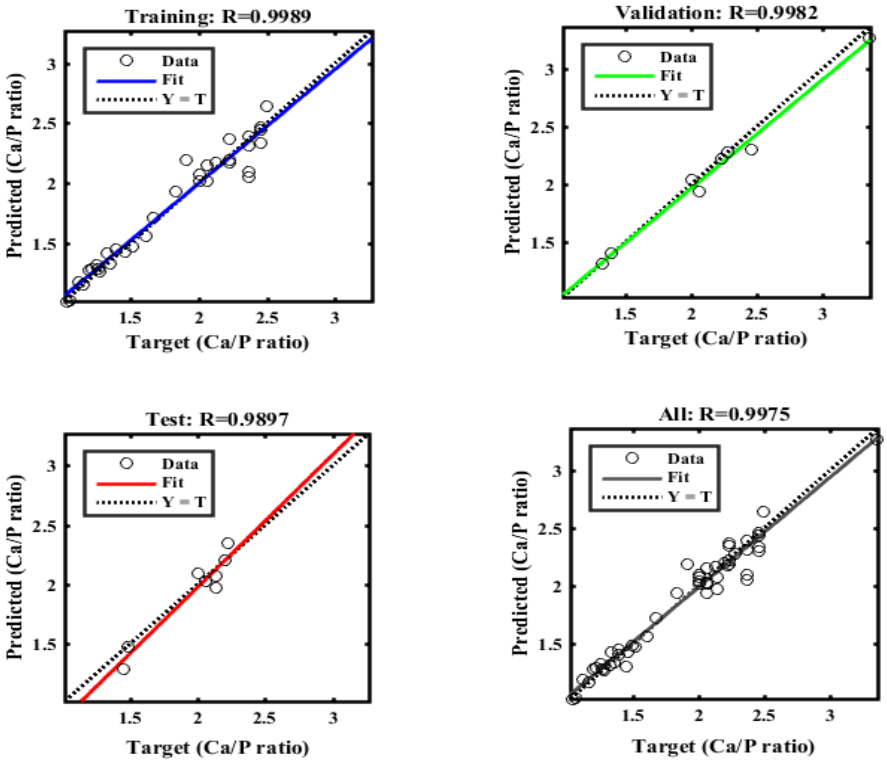

Figure 7. Regression plots of the trained neural network model that shows the linear regression factor for training, testing, validation, and all the data set

$$S_i(\%) = \frac{1}{N}\sum_{j=1}^{N}\left|\frac{\%\ Change\ in\ output}{\%\ Change\ in\ input}\right|_j \times 100 \qquad (9)$$

where, S_i (%) represented the sensitivity of an input parameter, and N is refers to the number of data set used to test the network. Figure 8 shows the results of sensitivity analysis. It shows that residence time is the most effective parameters in the Ca/P ratio, while precursor type has a relatively smaller effect on it. Furthermore, it shows that any increase in residence time increases the Ca/P ratio and decrease the crystalline index. The results of GEP and ANN are relatively similar to the empirical results, and confirm the conclusive role of residence time and type of precursor on Ca/P ratio. Since the reaction happens through calcination, the effect of residence time is considered along with the type of precursor on the values of the Ca/P ratio, which is shown in the 3D surface plot in Figure 9 (a). This surface is plotted for calcination temperature of 700 °C, and 10 °C/min heating rate. To better understand the 3D surface, the contour plot is depicted in Figure 9 (b). The shaded region shows the extrapolation area of the model, which can be used for other conditions of pyrolysis. This, along with the unshaded region confirmed the above explanation.

4. 2. Confirmation Test To ensure the accuracy of the proposed model by ANN, a confirmation test is done. In this regard, the BC sample is prepared using un-activated crushed bone at the temperature of 700 °C, 10°C/min heating rate and 2 h residence time. As shown in Table 4, the predicted value of Ca/P ratio in the ANN model is 2.52, while based on EDX analysis the actual value of this ratio is 2.55. This consistency indicates the high accuracy of GEP model. Figure 10 shows the EDX spectrum of this sample.

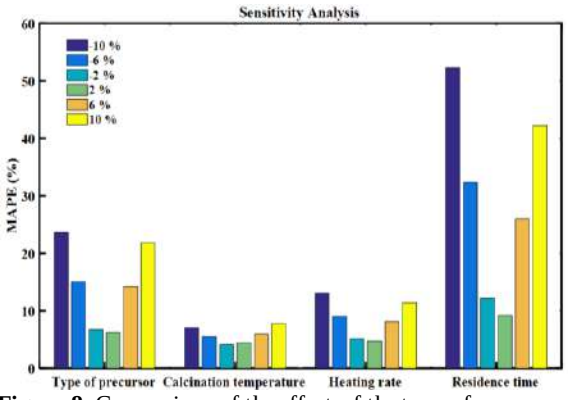

Figure 8. Comparison of the effect of the type of precursor, calcination temperature, heating rate, residence time on Ca/P ratio using sensitivity analysis

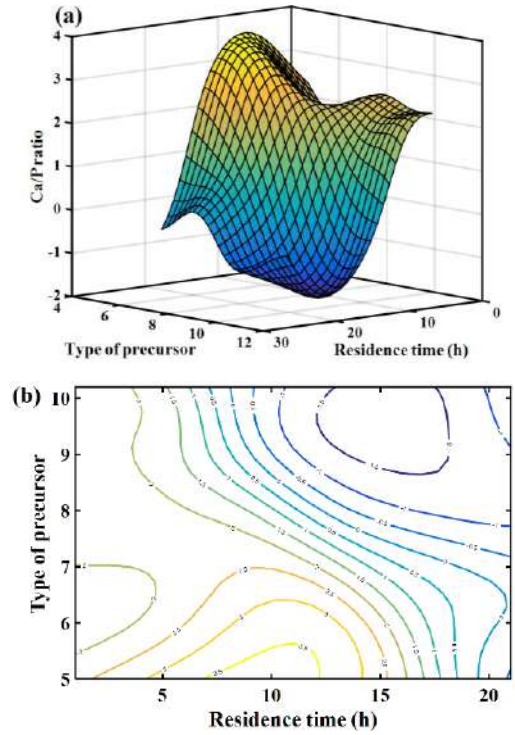

Figure 9. (a) 3D surface plot of Ca/P ratio that predicts by ANN model in calcination temperature of 700°C and heating rate 10°C/min; (b) the contour plot of the 3D surface; the shaded area shows the extrapolation region of ANN model.

TABLE 4. EDX spectrum of the validation test (un-activated crushed bone that heated at 10°C/min heating rate to 700°C, and residence time 2 h)

O	48.96
Na	0.92
Mg	0.42
P	13.78
S	0.74
Ca	35.17

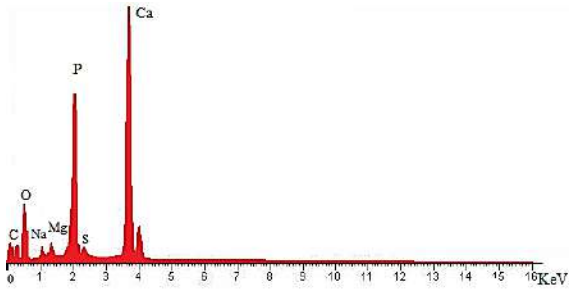

Figure 10. EDX Spectrum of prepared BC using un-activated crushed bone that heated at heating rate 10°C/min to 700°C, and residence time 2 h

5. CONCLUSION

In this study, various pyrolysis conditions used to produce BC. ANN and GEP techniques are employed to model the Ca/P ratio based on the practical conditions. In summary:

1: BC is prepared from crushed bone as precursor in the form of as-cleaned and activated by HNO_3 in pyrolysis technique;

2: Data collection is done using the design of experiment by consideration of heating rate, the type of precursor, calcination temperature, and residence time as practical parameters;

3: The Ca/P ratio selects as criteria for the estimation of the crystalline index of BC;

4. The excellent ability of ANN and GEP techniques are proved to model the Ca/P ratio based on pyrolysis conditions;

5. By consideration of R squared, ANN has the higher accuracy with respect to GEP to model the Ca/P ratio;

6. Validation of results is done using confirmation test;

7. Sensitivity analysis of proposed ANN model revealed that the residence time and the type of precursor in regular are the most effective parameters on Ca/P ratio.

7. REFRENCES

1. Alkurdi, S.S., Al-Juboori, R.A., Bundschuh, J., Bowtell, L. and McKnight, S., "Effect of pyrolysis conditions on bone char characterization and its ability for arsenic and fluoride removal", ***Environmental Pollution***, Vol. 262, (2020), 114221. https://doi.org/10.1016/j.envpol.2020.114221
2. Leinweber, P., Hagemann, P., Kebelmann, L., Kebelmann, K. and Morshedizad, M., Bone char as a novel phosphorus fertilizer, In Phosphorus recovery and recycling. 2019, Springer. 419-432. https://doi.org/10.1007/978-981-10-8031-9_29
3. Dotto, G.L., Salau, N.P.G., Piccin, J.S., Cadaval, T.R.S.A. and de Pinto, L.A.A., Adsorption kinetics in liquid phase: Modeling for discontinuous and continuous systems, In Adsorption processes for water treatment and purification. 2017, Springer. 53-76.
4. de Melo, N.H., de Oliveira Ferreira, M.E., Neto, E.M.S., Martins, P.R. and Ostroski, I.C., "Evaluation of the adsorption process using activated bone char functionalized with magnetite nanoparticles", ***Environmental Nanotechnology, Monitoring & Management***, Vol. 10, (2018), 427-434. https://doi.org/10.1016/j.enmm.2018.10.005
5. Wang, M., Liu, Y., Yao, Y., Han, L. and Liu, X., "Comparative evaluation of bone chars derived from bovine parts: Physicochemical properties and copper sorption behavior", ***Science of The Total Environment***, Vol. 700, (2020), 134470. https://doi.org/10.1016/j.scitotenv.2019.134470
6. Dalvand, H., Khayati, G.R., Darezereshki, E. and Irannejad, A., "A facile fabrication of nio nanoparticles from spent ni–cd batteries", ***Materials Letters***, Vol. 130, (2014), 54-56. https://doi.org/10.1016/j.matlet.2014.05.057
7. Medellin-Castillo, N.A., Padilla-Ortega, E., Tovar-García, L.D., Leyva-Ramos, R., Ocampo-Pérez, R., Carrasco-Marín, F. and Berber-Mendoza, M.S.J.A., "Removal of fluoride from aqueous solution using acid and thermally treated bone char", ***Adsorption***, Vol. 22, No. 7, (2016), 951-961. https://doi.org/10.1007/s10450-016-9802-0
8. Zhao, J., Zhao, J., Chen, J., Wang, X., Han, Z. and Li, Y., "Rietveld refinement of hydroxyapatite, tricalcium phosphate and biphasic materials prepared by solution combustion method", ***Ceramics International***, Vol. 40, No. 2, (2014), 3379-3388. https://doi.org/10.1016/j.ceramint.2013.09.094
9. Levinskas, G.J. and Neuman, W.F., "The solubility of bone mineral. I. Solubility studies of synthetic hydroxylapatite", ***The Journal of Physical Chemistry***, Vol. 59, No. 2, (1955), 164-168. https://doi.org/10.1021/j150524a017
10. Cheung, C.W., Chan, C.K., Porter, J.F. and McKay, G., "Combined diffusion model for the sorption of cadmium, copper, and zinc ions onto bone char", ***Environmental Science & Technology***, Vol. 35, No. 7, (2001), 1511-1522. https://doi.org/10.1021/es0012725
11. Medellin-Castillo, N.A., Leyva-Ramos, R., Ocampo-Perez, R., Garcia de la Cruz, R.F., Aragon-Pina, A., Martinez-Rosales, J.M., Guerrero-Coronado, R.M. and Fuentes-Rubio, L., "Adsorption of fluoride from water solution on bone char", ***Industrial & Engineering Chemistry Research***, Vol. 46, No. 26, (2007), 9205-9212. https://doi.org/10.1021/ie070023n
12. Warren, G., Robinson, J. and Someus, E., "Dissolution of phosphorus from animal bone char in 12 soils", ***Nutrient Cycling in Agroecosystems***, Vol. 84, No. 2, (2009), 167-178. https://doi.org/10.1007/s10705-008-9235-6
13. Siebers, N. and Leinweber, P., "Bone char: A clean and renewable phosphorus fertilizer with cadmium immobilization capability", ***Journal of Environmental Quality***, Vol. 42, No. 2, (2013), 405-411. https://doi.org/10.2134/jeq2012.0363
14. Medellin-Castillo, N., Leyva-Ramos, R., Padilla-Ortega, E., Perez, R.O., Flores-Cano, J. and Berber-Mendoza, M., "Adsorption capacity of bone char for removing fluoride from water solution. Role of hydroxyapatite content, adsorption mechanism and competing anions", ***Journal of industrial and Engineering Chemistry***, Vol. 20, No. 6, (2014), 4014-4021. https://doi.org/10.1016/j.jiec.2013.12.105
15. Rojas-Mayorga, C.K., Silvestre-Albero, J., Aguayo-Villarreal, I.A., Mendoza-Castillo, D.I. and Bonilla-Petriciolet, A., "A new synthesis route for bone chars using co2 atmosphere and their application as fluoride adsorbents", ***Microporous and Mesoporous Materials***, Vol. 209, (2015), 38-44. https://doi.org/10.1016/j.micromeso.2014.09.002
16. Zwetsloot, M.J., Lehmann, J. and Solomon, D., "Recycling slaughterhouse waste into fertilizer: How do pyrolysis temperature and biomass additions affect phosphorus availability and chemistry?", ***Journal of the Science of Food and Agriculture***, Vol. 95, No. 2, (2015), 281-288. https://doi.org/10.1002/jsfa.6716
17. Zwetsloot, M.J., Lehmann, J., Bauerle, T., Vanek, S., Hestrin, R. and Nigussie, A., "Phosphorus availability from bone char in a p-fixing soil influenced by root-mycorrhizae-biochar interactions", ***Plant and Soil***, Vol. 408, No. 1-2, (2016), 95-105. https://doi.org/10.1007/s11104-016-2905-2
18. Morshedizad, M., Zimmer, D. and Leinweber, P., "Effect of bone chars on phosphorus-cadmium-interactions as evaluated by three extraction procedures", ***Journal of Plant Nutrition and Soil Science***, Vol. 179, No. 3, (2016), 388-398. https://doi.org/10.1002/jpln.201500604
19. Flores-Cano, J.V., Leyva-Ramos, R., Carrasco-Marin, F., Aragón-Piña, A., Salazar-Rabago, J.J. and Leyva-Ramos, S., "Adsorption mechanism of chromium (iii) from water solution on bone char: Effect of operating conditions", ***Adsorption***, Vol. 22, No. 3, (2016), 297-308. https://doi.org/10.1007/s10450-016-9771-3

20. Iriarte-Velasco, U., Sierra, I., Zudaire, L. and Ayastuy, J.L., "Preparation of a porous biochar from the acid activation of pork bones", ***Food and Bioproducts Processing***, Vol. 98, No., (2016), 341-353. https://doi.org/10.1016/j.fbp.2016.03.003

21. Robinson, J.S., Baumann, K., Hu, Y., Hagemann, P., Kebelmann, L. and Leinweber, P., "Phosphorus transformations in plant-based and bio-waste materials induced by pyrolysis", ***Ambio***, Vol. 47, No. 1, (2018), 73-82. https://doi.org/10.1007/s13280-017-0990-y

22. Jia, P., Tan, H., Liu, K. and Gao, W., "Synthesis and photocatalytic performance of zno/bone char composite", ***Materials***, Vol. 11, No. 10, (2018), 1981. https://doi.org/10.3390/ma11101981

23. Koza, J.R. and Koza, J.R., "Genetic programming: on the programming of computers by means of natural selection" (Vol. 1), MIT press, 1992.

24. de Castilho, V.C., El Debs, M.K. and do Carmo Nicoletti, M., "Using a modified genetic algorithm to minimize the production costs for slabs of precast prestressed concrete joists", ***Engineering Applications of Artificial Intelligence***, Vol. 20, No. 4, (2007), 519-530. https://doi.org/10.1016/j.engappai.2006.09.003

25. Ferreira, C., "Gene expression programming: A new adaptive algorithm for solving problems", ***Complex Systems***, Vol. 13, No. 2, (2001), 87-129. arXiv:cs/0102027

26. Cheng, M.-Y., Firdausi, P.M. and Prayogo, D.J.E.A.o.A.I., "High-performance concrete compressive strength prediction using genetic weighted pyramid operation tree (gwpot)", ***Engineering Applications of Artificial Intelligence***, Vol. 29, No., (2014), 104-113. https://doi.org/10.1016/j.engappai.2013.11.014

27. Ferreira, C., "Gene expression programming: Mathematical modeling by an artificial intelligence, Springer, Vol. 21, (2006).

28. Ong, C.S., Huang, J.J. and Tzeng, G.H., "Building credit scoring models using genetic programming". ***Expert Systems with Applications***, Vol. 29, No. 1, (2005), 41-47. https://doi.org/10.1016/j.eswa.2005.01.003

29. Mollahasani, A., Alavi, A.H., Gandomi, A.H.J.C. and Geotechnics, "Empirical modeling of plate load test moduli of soil via gene expression programming", Vol. 38, No. 2, (2011), 281-286. https://doi.org/10.1016/j.compgeo.2010.11.008

30. Hosseini, M., Khayati, G.R., Mahdavi, M. and Danesh-Manesh, H., "Modeling and optimization of roll-bonding parameters for bond strength of ti/cu/ti clad composites by artificial neural networks and genetic algorithm", ***International Journal of Engineering, Transactions C: Aspects***, Vol. 30, No. 12, (2017), 1885-1893. https://doi.org/10.5829/ije.2017.30.12c.10

31. Si, H.Z., Wang, T., Zhang, K.J., De Hu, Z., Fan, B.T.J.B. and Chemistry, M., "Qsar study of 1, 4-dihydropyridine calcium channel antagonists based on gene expression programming", ***Bioorganic & Medicinal Chemistry***, Vol. 14, No. 14, (2006), 4834-4841. https://doi.org/10.1016/j.bmc.2006.03.019

32. Guessasma, S., Montavon, G. and Coddet, C., "Neural computation to predict in-flight particle characteristic dependences from processing parameters in the aps process", ***Journal of Thermal Spray Technology***, Vol. 13, No. 4, (2004), 570-585. https://doi.org/10.1361/10599630419391

33. Austin, N., Kumar, P.S. and Kanthavelkumaran, N.,, "Artificial neural network involved in the action of optimum mixed refrigerant (domestic refrigerator)", ***International Journal of Engineering-Transactions A: Basics***, Vol., No., (2013), 1235-1242. https://doi.org/10.5829/idosi.ije.2013.26.10a.13

34. Pradeep, J., Srinivasan, E. and Himavathi, S., "Neural network based recognition system integrating feature extraction and classification for english handwritten", ***International Journal of Engineering, Transactions B: Applications***, Vol. 25, No. 2, (2012), 99-106. https://doi.org/10.5829/idosi.ije.2012.25.02b.03

35. Khanmohammadi, S., "Neural network modelling of optimal robot movement using branch and bound tree", ***International Journal of Engineering***, Vol. 7, No. 2, (1994), 95-110. Retrieved from: http://www.ije.ir/article_71101_2db276aad3a417e1836645f7e4b24984.pdf

36. Mahdavi, M. and Khayati, G.R., "Artificial neural network based prediction hardness of al2024-multiwall carbon nanotube composite prepared by mechanical alloying", ***International Journal of Engineering, Transactions C: Aspects***, Vol. 29, No. 12, (2016), 1726-1733. https://doi.org/10.5829/idosi.ije.2016.29.12c.11

37. Neshat, E. and Saray, R.K., "An optimized chemical kinetic mechanism for hcci combustion of prfs using multi-zone model and genetic algorithm", ***Energy Conversion and Management***, Vol. 92, No., (2015), 172-183. https://doi.org/10.1016/j.enconman.2014.11.057

Persian Abstract

چکیده

زغال استخوان یکی از رایج‌ترین انواع جاذب با کاربردهای گسترده برای از بین بردن آلودگی‌ها می‌باشد. توانایی جذب این ماده به شاخص کریستالی آن وابسته‌است، که از طریق نسبت Ca/P معین می‌شود. در این تحقیق تلاش شد که شاخص کریستالی زغال استخوان از طریق مدل‌سازی شرایط تجزیه‌ی حرارتی این ماده توسط شبکه‌ی عصبی‌مصنوعی و برنامه‌ریزی بیان ژنتیکی انجام‌شود. به همین منظور ۱۰۰ داده‌ی تجربی متفاوت به صورت جداگانه برای ساخت مدل‌های شبکه‌ی عصبی مصنوعی و برنامه‌نویسی بیان ژنتیک مورد استفاده قرارگرفت. در مرحله‌ی جمع‌آوری داده‌های تجربی، آهنگ گرمایش، نوع فعال‌ساز، دمای کلسیناسیون و مدت زمان نگه‌داری نمونه‌ها به عنوان داده‌های ورودی، و نسبت Ca/P به عنوان خروجی تعیین‌شد. نتایج نشان‌داد که با آهنگ گرمایش ۱۰درجه‌ی سانتی‌گراد بردقیقه، دمای کلسیناسیون ۱۰۰۰ درجه‌ی سانتی‌گراد و مدت زمان نگه‌داری ۲ ساعت باعث دست‌یابی به کمترین میزان نسبت Ca/P خواهدشد. از شاخص ضریب تعیین برای مقایسه‌ی عملکرد مدل های استخراج شده از شبکه‌ی عصبی مصنوعی و برنامه نویسی بیان ژنتیکی استفاده‌شد. در نهایت، بهترین مدل شبکه‌ی عصبی مصنوعی برای تحقیق در مورد تاثیر هر یک از متغیرهای عملی بر روی شاخص کریستالی از طریق آنالیز حساسیت استفاده‌شد. مشخص‌شد که زمان نگه‌داری نمونه موثرترین پارامتر در تعیین شاخص کریستالی ماده است، در حالی که نوع فعال ساز اهمیت کمتری دارد.

International Journal of Engineering

Journal Homepage: www.ije.ir

Dynamic Response Analysis of a High Glide Ratio Parachute System

M. A. Ghapanvary*, M. Nosratollahi, J. Karimi

Department of Aerospace Engineering ,Malek-Ashtar University of Technology, Tehran, Iran

P A P E R I N F O

Paper history:
Received 19 September 2019
Received in revised form 10 September 2020
Accepted 14 October 2020

Keywords:
Multi-body System
Dynamic Response
Anhedral Angle
Gliding Path

A B S T R A C T

This paper is concerned with the dynamic stability study of a gliding parachute-payload system along its gliding path. To scrutinize the respective dynamic response characteristics after releasing from high altitude, a modified multi-body model is developed. In the stability analysis procedure, the yawing motion of the payload is considered in system dynamics, which in turn creates a state-dependent matrix in the stability analysis and makes the linearization algorithm more cumbersome. To solve the problem, a unified Jacobian-based symbolic differentiation algorithm is implemented and the dynamics is linearized about various operating points along gliding segment of a typical planned trajectory. Based on results, the system has short period and phugoid modes in longitudinal channel just like an aircraft. In addition to dutch roll mode, the system has a low frequency coupled roll-spiral mode in lateral-directional channel which is a result of effective canopy anhedral angle. It is shown, the coupled mode can be decomposed into two distinct roll and spiral modes for small anhedral angles. Based on results, as the parachute descends, both the period and damping ratio for the short period mode were increased by 18 and 30%, respectively. For the phugoid mode the period of oscillations is decreased by 20% and the damping ratio, almost remains constant. For the lateral-directional channel,. As the parachute descends, the dutch roll mode is destabilized whereas the other modes are stabilized. Furthermore, from a practical point of view, lengthening the suspension lines stabilizes the coupled roll-spiral mode whereas destabilizes the other modes.

***doi**: 10.5829/ije.2021.34.01a.22*

NOMENCLATURE

S_C	Canopy reference area (m^2)	**Greek Symbols**	
$[f_O]^G, [m_O]^G$	Constraint force and mpment vector acting on the confluence point (N, N.m)	ϕ_G, θ_G, ψ_G	Paylod Euler angles (deg)
I_G^G, I_P^P	Mass moment of inertia tensors for the gliding parachute and payload ($kg.m^2$)	μ	Canopy Rigging Angle (deg)
m^{G+A}, m^P	Mass of parachute and included air mass, mass of the payload (kg)	**Subscripts**	
s_{PO}, S_{PO}	Canopy reference area (m^2)	C, G, E, P	Canopy, gliding parachute, earth, payload frames

1. INTRODUCTION

Basically, a high glide ratio cargo delivery parachute is deployed from high altitude to attain a large stand-off distance and so may experience different trim conditions through the gliding segment of their trajectory. Parachute system can be perturbed from its trim condition, in presence of a disturbance. In this situation, when the parachute system returns to its initial trim point, it is called an asymptotically stable system. As, it achieves a new trim condition; it is called a marginally or neutrally stable and otherwise it is called an unstable system. Up to now, several researches were carried out about the dynamics and stability analysis of different systems such as torsional micro-actuators [1], axis gimbal system [2]. Also, many studies are devoted to investigate the control of the system vibration and oscillatory platforms. In this respect, the stability of the

*Corresponding Author Institutional Email: *ma.ghapanvary@isrc.ac.ir* (M. A. Ghapanvary)

Please cite this article as: M. A. Ghapanvary, M. Nosratollahi, J. Karimi, Dynamic Response Analysis of a High Glide Ratio Parachute System, International Journal of Engineering, Transactions A: Basics Vol. 34, No. 01, (2021) 195-201

system was provided with a fuzzy controller [3]. Oscillatory transporting Platform was used to sieving extremely wet earth mass [4]. The vibration of a system was controlled using tuned mass dampers [5]. Meanwhile, due to the highly coupled dynamics and complex behavior of the parachute and payload system, its stability has not been extensively discussed, as yet. However, in some studies, the stability analysis of the system was evaluated for a simplified model at sea level. The parachute stability characteristics were considered as a function of the inertia properties of the payload and obtained that the damping ratio and period were increased as related inertia increased [6]. The center of gravity and lift coefficient limits for a parachute were analyzed and various conditions and expressions for forward and backward center of gravity limits were given in literature [7]. The effects of scale and wing loading on a parachute using a linearized model for aerodynamic coefficients were studied in literature [8]. The lateral mode of parachute with a simplified model for a personnel-type parachute was modeled but the effect of apparent mass and inertia were not considered in the analysis [9].

The apparent mass force and moment coefficients were proposed by Lissaman and Brown [10]. Also, it was reported that canopies with wing loading less than 5kg/m^2 suffered from adverse effects of apparent mass during motion. It has been reported by Lingard [11], that by increasing the line length may destabilize the parachute whereas increasing the altitude had a stabilizing effect for the parachute. Also was concluded that increasing the aspect ratio resulted in increasing the static stability. The stable trim points were extracted using bifurcation analysis [12]. The main disadvantage of this method is stringent dependency of analysis to initial conditions. Moreover, several researches have been performed to model the behavior and dynamic response of the parachute systems. These works are summarized to model the parachute dynamics with different degrees of freedom and to study the system dynamics behavior. Usually, low-fidelity models with a reduced order were used to design the guidance, navigation and control (GNC) system. In this respect, a model with 4-DOF was presented which consist of planar dynamics with capability to roll and yaw [13]. Some models with 6-DOF were introduced in literature [14,15] that considered the parachute and payload system as a single rigid body system. Another 6-DOF model was presented in which the longitudinal mode was controlled by changing canopy incidence [16]. Turn response to asymmetric deflections and response to the gust was simulated using an 8-DOF model [17]. Another 8-DOF model was developed by Redelinghuys [18] for parachute with a suspended Unmanned Aerial Vehicle (UAV) and so the additional analytical constraints were added to the equations of motion. Other 8-DOF model with payload pitching and yawing motion was presented in which the constraint forces and moments were analytically solved during solving equations of motion. A comparison between 7-DOF and 8-DOF models was carried out and it is shown that a 7-DOF can describe the parachute dynamics when payload was connected in four points. Therefore, in case of a four-point connection of parachute to the payload, the payload yawing motion can disturb the overall system's response. Specially, when speaking about the lateral-directional responses, separation of the parachute and payload into one connection point leads to rolling, pitching and yawing motion with respect to the canopy which needs to a 9-DOF model. In this respect, different 9-DOF models were developed. It was assumed that there was only asymmetric TE deflection which was used to control the parachute in lateral-directional channel and the longitudinal channel was controlled by varying the canopy incidence angle [19]. Therefore, the symmetric brake deflection is replaced with canopy incidence angle in equations of motion. Mooij et al. [20] presented method similar to the approach proposed by Slegers and Castello [21], the equations of motion were solved simultaneously with constraint forces and moments, whereas in analytical dynamics required artificial constraint stabilization to satisfy the constraint at the confluence point [22]. The parachute systems had two modes of short period and phugoid in longitudinal channels and roll, duch roll and spiral modes in lateral-directional channel. In recent studies, using a 6-DOF linearized model discussed in litrature [23, 24], a dynamic stability study was carried out for a powered low anhedral canopy parachute. The eigenvalues of longitudinal and lateral-directional channels were obtained whereas the trim points were extracted through a static 4-DOF model of straight trimmed flight in which the effect of relative pitching motion of the payload on the dynamic modes was considered.

Clearly, achieving a large gliding distance necessitates releasing the gliding platform from a high altitude which in turn results in a wide variation of air density. This changes the parachute velocity from release to the impact points. Moreover, the apparent mass and inertia terms and so the dynamic response will change due to this variation. Evidently, in order to design of a gliding parachute, it is necessary to take the stability characteristics into account. Therefore, since the flight condition is varying, it is important to investigate the trend of the dynamic stability over the flight envelope.

On the other hand, as a significant design variable for gliding parachutes, the anhedral angle can affect the dynamic response as well as the gliding capability. The effective values of this design variable may result in different lateral-directional dynamics. Therefore, this paper is inspired by these problems to study each mode of system dynamics at different operating points along the gliding flight path. In other wods, the effect of

variation of altitude and the anhedral angle, which is the most important control parameter in lateral channel, on each dynamic mode of the system is scrutinized. This issue was ambiguously discussed in aforementioned studies. Herein, the yawing motion of the payload is considered in system dynamics creates a state-dependent matrix in dynamic equations which has not been considered for the parachute-payload system as yet. So, due to the complexity of the linearization of the airdrop system, the stability analysis procedure is difficult and time-consuming. This paper presents a unified jacobian-based symbolic differentiation algorithm that the system of equations is linearized by means of the algorithm.

2. PARACHUTE MODEL DESCRIPTION

For a parachute system model, when parachute and payload are considered as separate bodies, components of constraint forces and moments will be appeared. Hence, the rotational motion of the payload in space can be expressed as a combination of parachute rotational motion in space and a relative yawing motion. So, to avoid prolonging the paper with repetitive relationships, a model is used and modified for longitudinal trailing edge control surface instead of incidence angle, as longitudinal control input.

The schematic of the high glide ratio parachute-payload system is shown in Figure 1. Based on the figure, there are 4 different reference frames for deriving equations of motion. These frames are attached to the canopy, gliding parachute (includes the canopy and suspension lines), payload and earth as an inertial reference frame.

By rearranging the translational, rotational and kinematic constraint equations, the complete set of equations of motion which describes the parachute-payload dynamics is summarized in a nonlinear state-space form as below:

$$M\dot{X} = F \tag{1}$$

In which the respective matrices are as follows :

$$\begin{bmatrix} m^{G+A}+[J_M]^G & -m^{G+A}[S_{GO}]^G+[J_M]^G & 0_{3\times3} & 0_{3\times1} & 0_{3\times1} & -I_{3\times3} & 0_{3\times2} \\ m^P[T]^{PG} & -m^P[S_{PO}]^P[T]^{PG} & 0_{3\times3} & -[S_{PO}]^P & 0_{3\times1} & [T]^{PG} & 0_{3\times2} \\ [S_{MG}]^G[J_M]^G & [I_G^G]^G+[J_M]^G-[S_{MG}]^G[J_M]^G & 0_{3\times3} & 0_{3\times1} & 0_{3\times1} & -[S_{OG}]^G & 0 \\ 0_{3\times3} & [I_P^P]^P & 0_{3\times3} & [I_P^P]^P & 0_{3\times1} & [S_{GP}]^P & [T]^{PG} \\ 0_{3\times3} & 0_{3\times3} & I_{3\times3} & 0_{3\times1} & 0_{3\times1} & 0_{3\times3} & 0_{3\times2} \\ 0_{1\times3} & 0_{1\times3} & 0_{1\times3} & 0 & 1 & 0_{1\times3} & 0_{1\times2} \end{bmatrix} \begin{bmatrix} \dot{V}_O^E \\ \dot{\omega}^{GE} \\ \dot{\phi}_G \\ \dot{\theta}_G \\ \dot{\psi}_G \\ \dot{r}_P \\ \dot{\psi}_P \\ F_O \\ M_{Ox} \\ M_{Oy} \end{bmatrix} = \begin{bmatrix} F_1 \\ F_2 \\ F_3 \\ F_4 \\ F_5 \\ F_6 \end{bmatrix} \tag{2}$$

in which the right hand side expression for the force and moments can be expressed as:

$$\begin{aligned}
F_1 &= -m^{GA}[\Omega^{GE}]^G[V_O^E]^G - m^{GA}[\Omega^{GE}]^G[\Omega^{GE}]^G[s_{GO}]^G - [\Omega^{GE}]^G[J_M]^G[V_O^E]^G + \dots \\
&\quad [\Omega^{GE}]^G[J_M]^G[S_{MO}]^G[\omega^{GE}]^G - [\Omega^{GE}]^G[J_M]^G[T]^{GL}[V_A^E]^L + m^G[T]^{GL}[0\ 0\ g]^T + [f_{aero_G}]^G \\
F_2 &= -m^P[T]^{PG}[\Omega^{GE}]^G[V_O^E]^G - m^P[\Omega^{GE}]^G[\Omega^{GE}]^G[S_{Po}]^P + m^P[S_{Po}]^P[\Omega^{PG}]^P[T]^{PG}[\omega^{GE}]^G + \dots \\
&\quad m^P[T]^{PG}[T]^{GL}[0\ 0\ g]^T + [f_{aero_P}]^P \\
F_3 &= -[\Omega^{GE}]^G[I_G^G]^G[\omega^{GE}]^G - [\Omega^{GE}]^G[J_M]^G[\omega^{GE}]^G - [S_{MG}]^G[\Omega^{GE}]^G[J_M]^G[V_O^E]^G + \dots \\
&\quad [S_{MG}]^G[\Omega^{GE}]^G[J_M]^G[S_{MO}]^G[\omega^{GE}]^G + [S_{MG}]^G[\Omega^{GE}]^G[J_M]^G[T]^{GL}[V_A^E]^L + \dots \\
&\quad [S_{GC}]^G[f_{aero_G}]^G + [m_{aero_{C/4}}]^G + [0\ 0\ m_{OZ}{}^P]^T + [S_{LG}]^G[f_{aero_{Lines}}]^G \\
F_4 &= -[\Omega^{PE}]^P[I_P{}^P]^P[\omega^{PE}]^P - [T]^{PG}[0\ 0\ m_{OZ}{}^P]^T + [I_P{}^P]^P[\Omega^{PG}]^P[T]^{PG}[\omega^{GE}]^G \\
F_5 &= [1\ \sin\phi_G\tan\theta_G\ \cos\phi_G\tan\theta_G \mid 0\ \cos\phi_G\ -\sin\phi_G \mid 0\ \sin\phi_G/\cos\theta_G\ \cos\phi_G/\cos\theta_G][\omega^{GE}]^G \\
F_6 &= r_P - r_G
\end{aligned} \tag{3}$$

Using lyapunov indirect method herein, local response characteristics are obtained for the decoupled dynamics with varying trim points. Since the state matrix is state dependent, the conventional differentiation is not applicable. For this purpose, the state matrix is inverted and taken to the right hand side of the equation. Then the Jacobian operator is applied to linearize the unified symbolic expression. Finally, by expressing the equations of motion in a compact form (2), the nonlinear system can be written in a matrix form as below:

$$\begin{aligned}
&M\dot{x} = f(\bar{x},\bar{u}) \\
&\bar{x} = [u_o, v_o, w_o, p_G, q_G, r_G, \phi_G, \theta_G, \psi_G, r_P, \psi_P] \\
&\bar{u} = [\delta s, \delta u]
\end{aligned} \tag{4}$$

Herein, the system dynamics should be linearized about an operating point including system states and control inputs. The inputs of the system dynamics are symmetric and asymmetric trailing edge deflections during a steady gliding flight. Therefore, equilibrium points vector can be assigned as follows:

$$\bar{X}_{eq} = [u_0, 0, w_0, 0, 0, 0, 0, \theta_0, 0, 0, 0], \ \bar{U}_{eq} = [0, 0] \tag{5}$$

Based on lyapunov linearization method, a nonlinear system has a behavior similar to its linear model in small motion intervals [20]. In order to study the effect of each input on system response, it is necessary to omit the other inputs, thus the control inputs are set to be zero. So, the parachute system which has relatively slow dynamics, can be linearized about its operating points as an invariant system as follows:

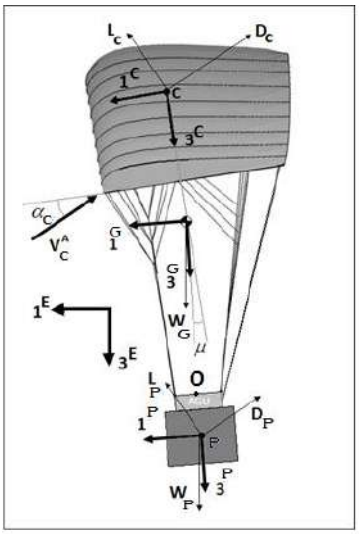

Figure 1. High glide ratio parachute-payload system

$$\Delta\dot{x} = A\Delta x + B\Delta u$$
$$A = \frac{\partial(M^{-1}f)}{\partial x}_{(x=x_0,u=u_0)} \quad (6)$$
$$B = \frac{\partial(M^{-1}f)}{\partial x}_{(x=x_0,u=u_0)}$$

It should be noted that, since the matrix M is state dependent and a function of the payload relative yawing angle, the inverse of matrix M should be considered in calculating the Jacobian matrix in linearization procedure. In this respect, the diagram of the dynamic stability analysis procedure of parachute-payload assembly is shown in Figure 2.

As shown in Table 1, to compare the present algorithm with a practical case, the methodology is used to determinte ALEX PADS modes. As a desireable matching and ignorable errors, the algorithm is verified and consequently is applicable for all parachute models.

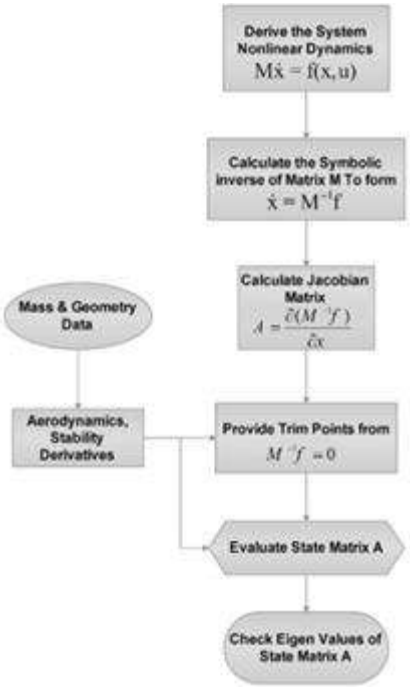

Figure 2. Novel algorithm flowchart for dynamic stability analysis of multi-body parachute-payload system

TABLE 1. Estimation of Alex dynamic modes [26]

Dynamic Mode	Period (s)	Estimated period (s)	Damping Ratio	Estimated Damping Ratio
Short period	1.1	1.2	0.58	0.5
Phugoid	8.4	8.3	0.4	0.36
Dutch Roll	1.8	1.87	0.19	0.2
Roll-Spiral	6.7	7.06	0.47	0.5

Now, a high penetrating GPDAS platform with a maximum 1000 kg rigged cargo, the dynamic response can be studied. The platform can achieve a desired stand-off distance of more than 30km. The parachute specifications are listed in Table 2.

3. RESULTS AND DISCUSSION

In order to investigate the dynamic behavior of the present parachute, two cases were considered in which several trim points are obtained for different altitudes along the gliding path, for a fix payload mass and different anhedral angles. The extracted trim points along the gliding path are given in Table 3. As can be seen in the table, from the maximum operational altitude to minimum level, the velocity decreases gradually whereas the pitch angle remains constant for a fix rigging scheme.

The root loci for the longitudinal channel modes are illustrated in Figure 3. The arrows show the direction of increasing in altitude from the sea level to its maximum value. Based on results, as the parachute descends, both the period and damping ratio for the short period mode are increased by 18 and 30%, respectively. For the phugoid mode the period of oscillations is decreased by more than 20% whereas it's damping ratio, almost remains constant. Overally, the systems stability level in longitudinal channel is improved during the parachute descend. In other words, applying brakes at high altitudes to control the glide ratio may deteriorate the system longitudinal stability particularly in faster mode.

TABLE 2. Parachute specification

Parameter	Value
Chord (m)	5.5
Span (m)	16.5
Rigging angle (deg)	2
Parachute mass (kg)	32
Number of main Lines	40
Line diameter (mm)	0.003
Line Length to span ratio	0.85
Payload Dimensions (m)	1*1*1

TABLE 3. Trim points along the gliding path

h (m)	Uc (m/s)	Wc (m/s)
0	15.49	2.61
2500	17.54	2.95
5000	20	3.37
7500	23	3.87
9000	25.14	4.23

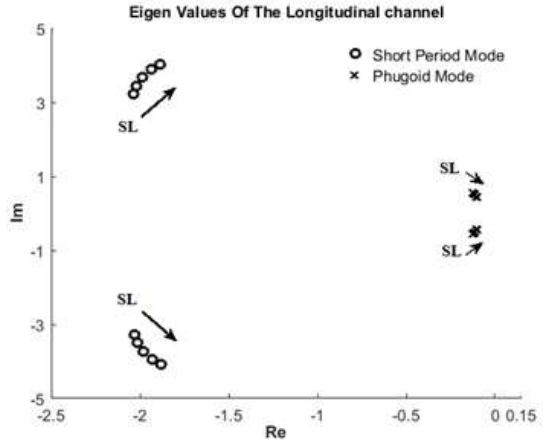

Figure 3. Root locus of the longitudinal modes

On the other hand, the root loci for the lateral-directional modes are provided as shown in Figure 4. Based on results, the lateral-directional modes include a pair of complex conjugate root which characterizes the dutch roll mode and another pair of complex conjugate root which introduces a coupled roll-spiral mode. The arrows show the direction of increasing in altitude from the minimum to its maximum value.

For arced circular canopies, increasing the anhedral angle will decrease the line length which leads to a small rolling moment. Hence, the resultant rolling and yawing moments produce a coupled roll-spiral mode in which roll and spiral modes are combined together. The vlaues of line length and trim points evaluated at lowest altitude, are given in Table 4.

Based on the above results, when the line length increases, the damping of the coupled roll spiral mode tends to 1 and so the combined mode decomposes into two real eigenvalues which represent the conventional roll and spiral modes. The root loci of the longitudinal and lateral-directional channels are shown in Figures 5 and 6, respectively. Based on results, in longitudinal channel, variation of the suspension line length has a significant effect on phugoid damping whereas the short period damping changes slightly.

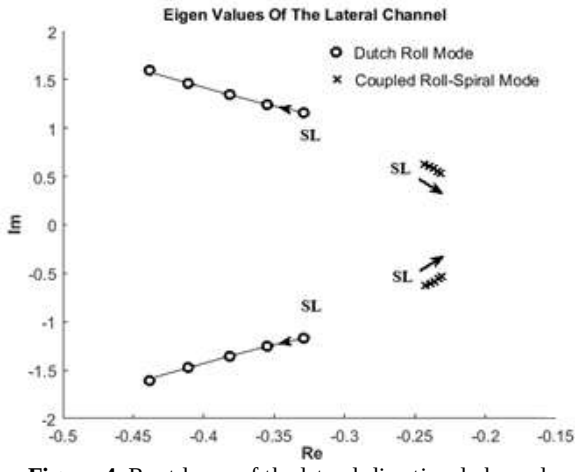

Figure 4. Root locus of the lateral-directional channel

TABLE 4. Anhedral angles and respective trim points

Anhedral Angle (deg)	$\frac{R_{Lines}}{b}$	Uc (m/s)	Wc (m/s)	θ(deg)
32.70	0.6	15.5	3.18	-4.30
15.0	1	15.36	2.54	-4.13
9.74	1.5	14.99	2.49	-3.89
7.24	2	14.76	2.51	-3.82
5.76	2.5	14.58	2.54	-3.80

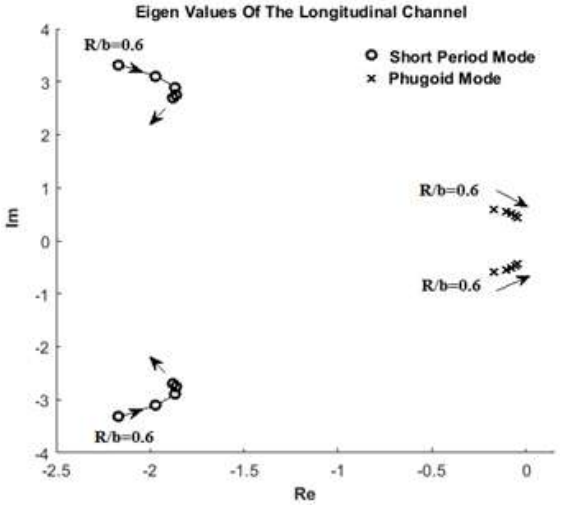

Figure 5. Root locus of the longitudinal modes for different anhedral angles

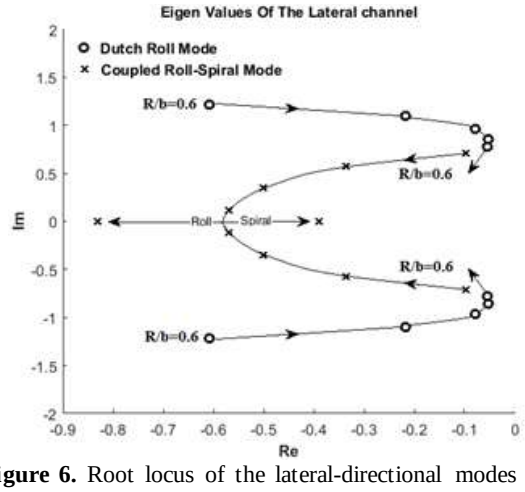

Figure 6. Root locus of the lateral-directional modes for different anhedral angles

Also, for the lateral-directional channel, both the dutch roll and coupled roll-spiral modes change considerably. In fact, the values of the line to span ratio from 1.5 to 2 are not practical but show how the root loci move in s-plane. In all channels the period of the dynamic modes is directly proportional to the suspension line length. In other words, the higher the line length is, the higher the period of all modes becomes. Hence, for the practical values of the line length, except the coupled roll-spiral mode in the lateral-directional channel, increasing the line length will decrease the levels of stability in the other modes, i.e. short period, phugoid and dutch roll.

4. CONCLUSION

In order to realize the gliding parachute dynamic behavior over the gliding envelope, using a multi-body model, the dynamic stability of a large gliding parachute-payload assembly was studied. The eigenvalues for different trim points along the gliding segment were obtained for decoupled longitudinal and lateral-directional channels.

Unlike the conventional flying vehicle modes, the roll and spiral modes of the present gliding parachute were coupled to each other that arose from effective anhedral angle of the canopy. The coupled roll-spiral mode has a higher damping ratio as compared to the lightly damped dutch roll mode. The dynamic stability analysis showed that, as the parachute glided from the maximum operational altitude to the sea level, the system stability level in longitudinal channel was improved. In this respect, the period and damping ratio of the short period mode were increased. For the phugoid mode, the period was decreased whereas its damping ratio almost remained constant. For the coupled roll-spiral mode, both the period and the damping ratio of oscillations were slightly decreased. As the parachute descended, among the dynamic modes, the dutch roll mode along the gliding path was destabilized. Therefore, as a worst case for evaluating the level of stability of the system modes particularly in conceptual design phase, it is recommended to perform the systems dynamic stability analysis at maximum operational altitude for the short period mode and at minimum altitude for the dutch roll mode. On the other hand, the eigenvalues were extracted for different line length to analyze the effect of the anhedral angle on system dynamics, especially in coupled mode. Based on results, in longitudinal channel, changing the suspension line length had a significant effect on phugoid damping whereas the short period damping was slightly changed. Also, for the lateral-directional channel, both the dutch roll and coupled roll-spiral modes were considerably changed. In all channels, the period of the dynamic modes was directly proportional to the suspension line length. So, the higher the line length was, the higher the period of all modes became. Based on results, as the parachute descends, both the period and damping ratio for the short period mode were increased by 18 and 30%, respectively. For the phugoid mode the period of oscillations was decreased by more than 20% whereas it's damping ratio, almost remained constant. Generally, the system stability level in longitudinal channel was improved during the parachute descend.

In all channels the period of the dynamic modes was directly proportional to the suspension line length. Hence, for the practical values, except the coupled roll-spiral mode of the lateral-directional channel, increasing the line length decreased the levels of stability for the other modes. In addition, increasing the line to span ratio by twice herein, resulted in separation of the roll and spiral modes from each other. So the suspension line length which represented the canopy anhedral angle, was the main responsible for the mentioned coupled roll-spiral mode. For the practical values of the suspension line length, only the coupled roll-spiral mode showed improving in the system stability with lengthening the lines whereas the other modes were destabilized. Also, the linearized symbolic model was verified by comparing the results with an available parachute data, with a negligible error in prediction of the dynamic modes. Therefore, the model could be used during design cycle and was applicable to all gliding parachutes

5. REFERENCES

1. Abbasnejad B., Shabani R., Rezazadeh G., Stability Analysis in Parametrically Excited Electrostatic Torsional Micro-actuators, International ***Journal of Engineering, Transactions C: Aspects***, Vol. 27, No. 3, (2014) 487-498. DOI: 10.5829/idosi.ije.2014.27.03c.17.
2. Pirzadeh M., Toloei A. R., Vali A. R., 'Effects of Flight Dynamics on Performance of One Axis Gimbal System, Considering Disturbance Torques', ***International Journal of Engineering, Transactions B: Applications***, Vol. 28, No. 8, (2015) 1108-1116. DOI : 10.5829/idosi.ije.2015.28.08b.01.
3. Berdnikov V., Lokhin V.,'Synthesis of Guaranteed Stability Regions of a Nonstationary Nonlinear System with a Fuzzy Controller', ***Civil Engineering Journal***, Vol. 5, No. 1, (2019), DOI: 10.28991/cej-2019-03091229.
4. Mihajlović G., Živković M.,' Sieving Extremely Wet Earth Mass by Means of Oscillatory Transporting Platform', ***Emerging Science Journal***, Vol. 4, No. 3 (2020) 172-182. DOI: 10.28991/esj-2020-01221
5. Rahimi F., Aghayari R., Samali B.,'Application of Tuned Mass Dampers for Structural Vibration Control: A State-of-the-art Review', ***Civil Engineering Journal***, Vol. 6, No. 8, (2020), 1622-1651. DOI: 10.28991/cej-2020-03091571
6. Hailiang M., Zizeng Q.,'9-DOF Simulation of Controllable Parachute System for Gliding and Stability', ***Journal of National University of Defense Technology***, Vol. 16, No. 2, (1994), 49–54.

7. Iosilevskii G (1995) Center of Gravity and Minimal Lift Coefficient Limits of a Gliding Parachute. ***Journal of Aircraft***, Vol. 32, No. 6, 1297-1302. DOI: 10.2514/3.46878
8. Brown, G. J., 'Parachute Steady Turn Response to Control Input', Aerospace Design Conference, Irvine, CA, USA, (1993). DOI: 10.2514/6.1993-1241
9. Crimi P (1990) Lateral Stability of Gliding Parachutes. ***Journal of Guidance, Control and Dynamics,*** Vol. 13, No. 6, 1060-1063. DOI: 10.2514/3.20579
10. Lissaman, P, Brown G, "Apparent Mass Effects on Parachute Dynamics. Aerospace Design Conference", Irvine, California, USA. (1993), DOI : 10.2514/6.1993-1236
11. Lingard J. S., 'Ram-air Parachute Design'.13th AIAA Aerodynamic Decelerator Systems Technology Conference; Clearwater Beach, Florida, USA, (1995).
12. Prakash O., Daftary A., Ananthkrishnan A., 'Bifurcation Analysis of Parachute-Payload System Flight Dynamics', AIAA Atmospheric Flight Mechanics Conference and Exhibit; San Francisco, California, USA, (2005). DOI: 10.2514/6.2005-5806
13. Jann, T Advanced Features for Autonomous Parachute Guidance, Navigation and Control. 18th AIAA Aerodynamic Decelerator Systems Technology Conference and Seminar; Munich, Germany, (2005). DOI: 10.2514/6.2005-1642
14. Barrows T Apparent Mass of Parachutes with Spanwise Camber. ***Journal of Aircraft***, Vol. 39, No. 3, (2002), 445-451. DOI: 10.2514/2.2949
15. Zhang Z, Zhao Z, Fu Y., 'Dynamics analysis and simulation of six-DOF parafoil system', ***Cluster Computing***, Vol. 22, No. 5, (2018), 1-12. DOI: 10.1007/s10586-018-1720-3
16. Slegers N., Beyer E., Costello M., 'Use of Variable Incidence Angle for Glide Slope Control of Autonomous Parachute'. ***Journal of Guidance, Control, and Dynamics***, Vol. 31, No. 3, (2008), 585-596. DOI: 10.2514/1.32099
17. Müller S, Wagner O, Sachs G. 'A High-Fidelity Nonlinear Multibody Simulation Model for Parachute Systems,, 17th AIAA Aerodynamic Decelerator Systems Technology Conference and Seminar; Monterey, California, (2003). DOI: 10.2514/6.2003-2120
18. Redelinghuys C.,'A Flight Simulation Algorithm for a Parachute Suspending an Air Vehicle', ***Journal of Guidance, Control, and Dynamics***, Vol. 30, No. 3, (2007), 791-803. DOI: 10.2514/1.25074
19. Slegers N Effects of Canopy-Payload Relative Motion on Control of Autonomous Parachute. ***Journal of Guidance, Control, and Dynamics***, Vol. 33, No. 1, (2010), 116-125. DOI: 10.2514/1.44564
20. Mooij E, Wijnands Q, Schat, B.,'9-DOF Parachute/Payload Simulator Development and Validation', AIAA Modeling and Simulation Technologies Conference and Exhibit; Austin, Texas, USA, (2003). DOI: 10.2514/6.2003-5459
21. Slegers N., Castello M.,' spects of Control for a Parachute and Payload System', ***Journal of Guidance, Control and Dynamics***, Vol. 26, No. 6, (2003), 898-905. DOI: 10.2514/2.6933
22. Strickert G., Jann T., 'Determination of the Relative Motion Between Parachute Canopy and Load Using Advanced Video-Image Processing Techniques', 15th Aerodynamic Decelerator Systems Technology Conference; Toulouse, France, (1999), DOI: 10.2514/6.1999-1754
23. Yang H., Song L., Chen W., 'Research on parachute stability using a rapid estimate model', ***Chinese Journal of Aeronautics***, Vol. 30, No. 5, (2017), 1670-1680. DOI: 10.1016/j.cja.2017.06.003
24. Gorman C. M., Slegers N. J., 'Comparison and Analysis of Multi-body Parafoil Models With Varying Degrees of Freedom', 21th AIAA Aerodynamic Decelerator Systems Technology Conference and Seminar, Dublin, Ireland, (2011). DOI: 10.2514/6.2003-5611
25. Slotine J J., Lee W., Applied nonlinear control. New Jersey: Prentice-Hall Inc, (1991).
26. O. A. Yakimenko, 'Precision Aerial Delivery Systems: Modeling, Dynamics, and Control. Progress in astronautics and aeronautics', American Institute of Aeronautics and Astronautics, Inc. Volume 248. Virginia:, (2015).

Persian Abstract

چکیده

این مقاله به مطالعه پایداری دینامیکی سیستم چتر سرشی- محموله در طول مسیر پرواز سرش آن پرداخته است. بدین منظور و برای بررسی دقیق مشخصه‌های پاسخ دینامیکی مربوطه، پس از رهایش از ارتفاع بالا یک مدل دوجسمی بهبودیافته توسعه داده شده است. در فرآیند تحلیل پایداری، حرکت نوسانی سمتی محموله در دینامیک سیستم لحاظ گردیده است، که به نوبه خود موجب ایجاد یک ماتریس ضرایب وابسته به حالت گردیده و الگوریتم خطی سازی را مشکل می‌سازد. برای حل مسئله، یک الگوریتم مشتق‌گیری سمبلیک یکپارچه مبتنی بر ژاکوبین پیاده سازی شده و دینامیک سیستم در نقاط کاری مختلف در طول بخش سرش از مسیر طرح‌ریزی شده، خطی گردیده است. بر اساس نتایج ، سیستم چتر سرشی دقیقاً همانند هواپیما در کانال طولی دارای مودهای پریود کوتاه مدت و فیوگوید است. در کانال عرضی-سمتی، علاوه بر مود داچ رول سیستم دارای یک مود غلت و مارپیچ کوپل شده با فرکانس پایین است که منتج از زاویه آنهدرال بالای چتر است. نتایج نشان می‌دهد که در کانال عرضی-سمتی، مود کوپل شده برای زاویه های آنهدرال کوچک به دو مود متمایز غلت و مارپیچ تجزیه می‌شود. همچنین بر اساس نتایج، با نزول چتر ، دوره تناوب و نسبت میرایی برای مود پریود کوتاه ، به ترتیب ۱۸ و ۳۰ درصد افزایش می یابد. برای مود فیوگوید، دوره نوسانات ۲۰٪ کاهش یافته در حالیکه نسبت میرایی تقریباً ثابت خواهد بود. به عبارتی دیگر، با نزول چتر ، پایداری مود داچ رول کاهش می‌یابد، در حالی که مودهای دیگر پایدارتر می‌شوند. علاوه بر این، از نقطه نظر عملی، ازدیاد طول طنابهای تعلیق، پایداری مود کوپل غلت و مارپیچ را افزایش داده در حالی که پایداری مودهای دیگر کاهش خواهد یافت.

International Journal of Engineering

Journal Homepage: www.ije.ir

Numerical Study on Vibration Attenuation of Cylinder using Active Rotary Oscillating Controller

A. H. Rabiee*

School of Mechanical Engineering, Arak University of Technology, Arak, Iran

P A P E R I N F O

Paper history:
Received 24 May 2019
Received in revised form 28 October 2020
Accepted 29 October 2020

Keywords:
Vortex-induced Vibration
Galloping
Square-section Cylinder
Active Rotary Oscillation

A B S T R A C T

The present article is an attempt at utilizing a feedback control system based on cylinder rotary oscillations in order to attenuate the two-degree-of-freedom vibrations of an elastically-supported square-section cylinder in presence of flow. The control system benefits from the cylinder rotational oscillations about its axis that acts according to lift coefficient feedback signal of the cylinder. Based on the performed numerical simulations, it becomes clear that the active control system has successfully mitigated the two-degree-of-freedom vibrations of square cylinder both in the lock-in region and galloping zone. For a Reynolds number of Re = 90 located in the lock-in region, the active rotary oscillating (ARO) controller has achieved a 98% reduction in the cylinder transverse vibration amplitude, while the corresponding value for the in-line vibration is 88%. Moreover, for a Reynolds number of Re = 250 in the galloping zone, the ARO controller has successfully attenuated the cylinder transverse vibration amplitude by 72%, while the same value for the in-line vibration is 70%. One also observes that the ARO controller decreases the amplitude of lift and drag coefficients in the lock-in region by, respectively, 95% and 94%. In contrast, the corresponding percentages for the cylinder in the galloping zone are 24% and 39%, respectively.

doi: *10.5829/ije.2021.34.01a.23*

1. INTRODUCTION

Fluid-solid interaction has been a subject of interest for engineers due its enormous importance in the design of marine risers and platforms, submarine transport pipelines, cooling systems in power plants especially nuclear plants, heat exchangers and suspending bridges [1-3]. Vortex-induced vibrations (VIV) are a subset of flow-induced vibrations (FIV) in which frequency synchronization between vortex shedding frequency and structural natural frequency generates high-amplitude self-excited vibrations. In addition to VIV, galloping is considered to be a type of FIV happening for cylinders of the non-circular cross section such as square cylinders [4, 5]. Galloping is defined as the self-excited instabilities that result in high-amplitude and low-frequency oscillations in Reynolds number ranges higher that VIV [6, 7]. In the galloping zone, the transverse motion of structure generates aerodynamic forces which in turn increase oscillations. Right after the flow velocity exceeds the critical value related to galloping, the vibration amplitude continuously rises with increasing flow velocity. High-amplitude vibrations related to VIV and galloping can bring about fatigue failure. Consequently, reduction of such instabilities using passive and active control strategies is of critical importance [8-10].

A plethora of passive methods have been utilized for FIV reduction. Passive methods are not dependent on external energy sources and are usually easier to implement compared with active control strategies [11, 12]. However, passive control methods are effective only in certain working conditions. In fact, to effectively reduce FIV, one needs to determine the physical properties of passive control systems beforehand. After that, changing these physical characteristics is either too difficult or impossible as the structural and environmental conditions would be changed. Active control approaches, unlike passive methods, alters the structure-flow system behavior by the direct application

*Corresponding Author Institutional Email: *rabiee@arakut.ac.ir* (A. H. Rabiee)

Please cite this article as: A. H. Rabiee, Numerical Study on Vibration Attenuation of Cylinder using Active Rotary Oscillating Controller, Transactions A: Basics Vol. 34, No. 01, (2021) 202-211

of energy to the system using actuators. Common examples of active control include acoustic excitation and rotating the cylinders, as well as suction and blowing [13-16]. Benefitting from constant rotation and/or oscillating rotation of cylinder is one of the most effective methods for controlling the oscillating forces exerted on a stationary cylinder as well as the vibration of an elastically-supported cylinder. This has been the center of attention of numerous researchers.

There have been several studies concerning flexibility mounted cylinders with cross-over vibrations; while relatively little research has been done on rotational oscillating or rotary cylinders. Dimotakis and Tokumaru [17] were probably the first researchers to investigate the open-loop strategy for flow behind an oscillating non-vibrating cylinder. They demonstrated that the strength of vortices could be severely decreased, along with noticeable suppression of drag coefficient. The drag suppression demonstrated by Dimotakis and Tokumaru [17] were confirmed by 2D flow calculations by He et al. [18]. Ray and Christofides [19] investigated the effect of a rotating control cylinder on the reduction of drag force exerted on a long cylinder using an open-loop control approach. Nazarinia et al. [20] investigated the flow around a cylinder subjected to forced translational and rotational oscillations, both numerically and experimentally, guiding them for a detailed understanding of flow control and wake structure. Lu et al. [21] used an active feedback control method to significantly suppress the lift force of a flow excited rotary oscillating circular cylinder. Leontini and Thompson [22] investigated externally applied rotary oscillations to control the flow behind a cylinder, which can only vibrate in the cross-over direction. They display that applied rotational oscillation can significantly increase the amplitude of cross-over vibration, which is beneficial for power generation. Du and Sun [23] used an active control approach in which applied torsional vibrations are used to suppress cross-over cylinder displacement. The FIV magnitudes in the "synchronization" region were significantly reduced by changing the vortex shedding frequency to the rotational oscillation frequency. Wong et al. [24] offered an experimental study of the dynamic behavior and vertical structure of a circular cylinder that rotates harmoniously and experiences flow-induced transverse vibrations. Hasheminejad et al. [13] adopted active control approach to reduce the 1D-VIV a circular cylinder at using external torsional vibrations.

Numerous methods have been proposed with regard to the reduction of vibrations caused by vortex-shedding of circular cylinders. On the contrary, few studies have been carried out on square-section cylinders. Owing to their sharp corners, these cylinders display a completely different behavior from circular cylinders [25, 26]. Minewitsch et al. [27] benefited from a finite element method (FEM) to study the interaction between the wake and streamwise oscillations of cylinders at Re = 200. Yang et al. [28] conducted numerical investigations based on FEM for rectangular-section cylinders oscillating in the cross-over direction. They found out that the vortex-shedding mechanisms of circular and rectangular cylinders are completely different. Singh et al. [29] considered the forced cross-over oscillations of square cylinders at different frequency ratios. Sen and Mittal [30] numerically evaluated the free vibration of a square cylinder able to oscillate in the transverse and streamwise directions in the Reynolds number range of 60–600. For a zero structural damping and a mass of ratio of 10, they noticed that the lock-in region starts from Re = 87, while galloping begins from Re = 175. Zhao et al. [31] studied the effect of flow-approaching angle on the two-degree-of-freedom (2-DoF) vibrations of a square cylinder with the mass ratio of 3 at Re = 100. In another study, Sen and Mittal [25] examined the 2-DoF vibrations of square cylinders for various mass ratios. They observed that the transverse vibrations of square cylinders in the galloping region increase at mass ratios higher than 5. Zhao [32] investigated the effect of aspect ratio, defined as the ratio of cylinder dimension in the transverse direction to the dimension in the streamwise direction, on the 1-DoF and 2-DoF vibrations of square and rectangular cylinders with a mass ratio of 10 at Re = 200.

A number of methods have been proposed with regard to the reduction of vibrations caused by vortex-shedding of circular cylinders. On the contrary, few studies have been carried out on square-section cylinders. Venkatraman and Narayanan [33] conducted a study on the active control of vibrations due to the vortex-shedding of a circular cylinder as well as the galloping of a square prism. They modeled the oscillating cylinder as a 1-DoF linear oscillator, on which the fluid effect was considered as an external disturbance. By applying a sinusoidal wave on piezoelectric ceramic actuators installed on a square cylinder, Cheng et al. [34] concurrently controlled the flow and structural vibrations. Dai et al. [35] investigated the effectiveness of time-delay control systems to reduce the high amplitude of an elastically-supported square cylinder. They demonstrated that time-delay controller can postpone the beginning of galloping vibrations. Using numerical simulations, Wu et al. [36] investigated the effect of twist angle on the vibration attenuation of a square cylinder that freely vibrated in the transverse direction. They showed that the twist of cylinder surface alters the separation point of vortex shedding which in turn changes the frequency of vortex shedding, hence the reduction in vibrations.

The above literature review shows that although extensive studies have been performed in the field of controlling the VIV of circular cylinders, few researches

have been conducted on the effect of employed techniques for square cylinders. Accordingly, this article considers the subject of active control of square cylinder based on the rotational oscillations of the cylinder as one of the best approaches for FIV mitigation that has successfully been applied for circular cylinders.

The rest of the article is as follows: section 2.1 presents the equations of flow and oscillator, followed by a summary of the solution technique of fluid-structure interaction in section 2.2. The mechanism of active rotary oscillating (ARO) controller is presented in section 2.3 and the validation of current study is delineated in section 2.4. In addition, section 3 demonstrates the results and discussions related to the ARO controller via several figures. Finally, the most important findings are outlined in section 4.

2. NUMERICAL APPROACH

2. 1. Equations of Flow and Oscillator The numerical analysis starts by utilizing the two-dimensional (2D) incompressible equations of Navier-Stokes (NS) for flow simulation which are concisely expressed as:

$$\frac{\partial \mathbf{u}}{\partial t} = -(\mathbf{u}.\nabla).\mathbf{u} - \nabla p + \frac{1}{\mathrm{Re}}\nabla^2\mathbf{u}, \qquad \nabla.\mathbf{u} = 0, \tag{1}$$

where $\mathbf{u}=(u_x/U, u_y/U)$ is the non-dimensional vector of flow velocity in which U represents the free flow velocity, p is the pressure, ρ is the density of fluid in question, and Re signifies the Reynolds number.

By submerging a rigid body in fluid, the vacillating torques and forces initiate the motion of body. In this article, the 2-DoF vibration of an elastically-supported rigid square-section cylinder is studied that is under the action of external rotary oscillations applied through the feedback control system. The schematic of problem is shown in Figure 1. Furthermore, the nondimensional 2-DoF motion equation developed for the cylinder is written as:

$$\frac{\partial^2 Q_i}{\partial t^2} + 4\pi\zeta\frac{\partial Q_i}{\partial t} + 4\pi^2 Q_i = \frac{V_r^2 C_i}{2m^*}, \tag{2}$$

where $Q_1 = X$ and $Q_2 = Y$ represent the nondimensional values of square cylinder motion amplitude along x and y directions, respectively. They are expressed as $Q_i = q_i / D$ in which q_i is the real displacement value and D signifies the side length of the studied cylinder. Also, $\zeta = c/\left(2\sqrt{km}\right)$ is the damping ratio quantity in which damping and stiffness coefficients are defined by c and k, respectively, $V_r = U / f_n D$ depicts the reduced speed

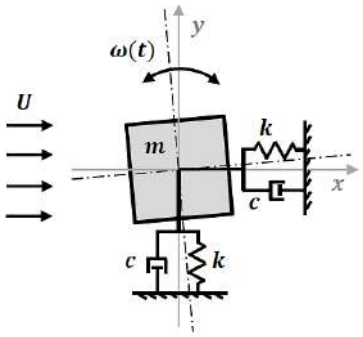

Figure 1. Schematic of flow-induced vibration on square-section cylinder

in which f_n is the structural natural frequency, $C_1 = C_D$ and $C_2 = C_L$. Finally, $m^* = m/m_d$ represents the mass ratio in which m and m_d are the mass of, respectively, cylinder and displaced fluid.

2. 2. Description of Fluid/Structure Solvers A brief introduction of the employed fluid/structure solvers and their most important properties are provided here. Aided by the computational fluid dynamics software package, ANSYS Fluent, along with a UDF otherwise known as user-defined function, Equation (1) is solved based on a time iteration approach. The computational domain of the cylinder is considered to be a rectangle. The distance between the cylinder center and the pair of domain upstream and downstream boundaries is shown by (L_u, L_d) as depicted in Figure 2. The dimension of the lateral boundary is displayed by *H*. In addition, the block ratio is defined as $B = D/H$. By considering a blockage ratio of 0.05, the finite volume mesh in question is displayed in Figure 3. The triangle meshes are deformed at each time step using the moving-deforming mesh function while the vibration and rotation of the cylinder inside the studied domain take place. The UDF written in C programming language decides what movement should be made in the central region. At the same time, unstructured meshes are rearranged in the external zone. The flow is considered as laminar unsteady for simulation purposes. An implicit pressure-based solver of first order is in charge of computing hydrodynamic loadings based on existing continuity and momentum relations. Other assumptions include non-slip boundary conditions on cylinder surface, free-stream velocity at the inflow, stress-free condition at the downstream boundary, zero cross-flow velocity and zero stress components on upper and lower boundaries. Furthermore, the UDF calculates the movement of the sprung cylinder according to the applied hydrodynamic forces. Fluent receives transverse and in-line velocities through the macro. In addition, surface boundary

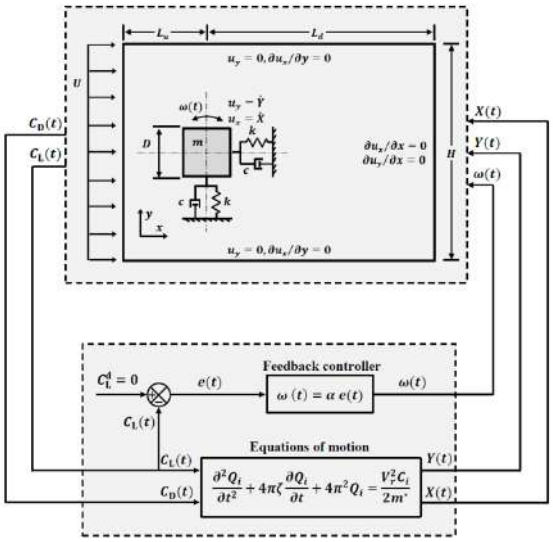

Figure 2. Block diagram of active rotary oscillating controller

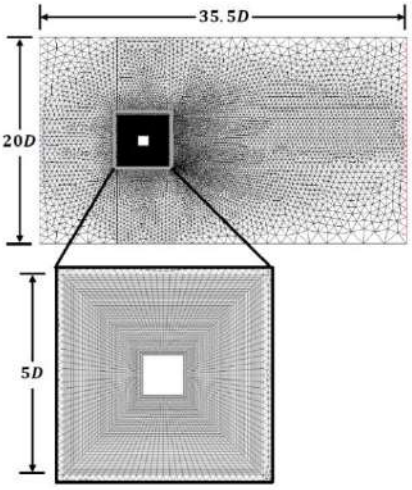

Figure 3. Utilized computational domain

condition $(\dot{x}_{n+1}, \dot{y}_{n+1}) = (u_x, u_y)$ is used to repeatedly determine various quantities including surface flow velocity, mesh arrangement and cylinder location. Refs. [37, 38] provide a more detailed explanation of flow-structure interaction.

2. 3. Active Rotary Oscillating Controller To restrain in-line and transverse movements in the current FIV arrangement, feedback control approaches are suitable choices in conjunction with the rotary oscillations of the cylinder. To this aim, one may choose the lift coefficient $C_L(t)$ as the feedback signal from which the data on the flow-field close to the cylinder including the vortex shedding frequency are obtainable. Hence, the description of the proportional closed-loop controller can be written as:

$$\omega(t) = \alpha\, e(t), \tag{3}$$

where $\omega(t)$ represents the nondimensional angular velocity of the cylinder in question, $\alpha > 0$ signifies the proportional gain of the controller. Also, $e(t)$ is described as:

$$e(t) = C_L^d(t) - C_L(t), \tag{4}$$

where $C_L^d(t)$ is the desired quantity of lift coefficient. The present study assumes a zero value for $C_L^d(t)$, thus the control output is found to be:

$$\omega(t) = -\alpha\, C_L(t). \tag{5}$$

One should note that he minus sign in Equation (5) shows that the direction of obtained lift coefficient $C_L(t)$ is opposite to the imposed rotary oscillations $\omega(t)$. The overall arrangement of the control system is shown in Figure 2.

2. 4. Validation The input parameters for validating the performed numerical simulations are as follows: $m^* = 10, \xi = 0, B = 0.05; F_N = f_N D/U \quad = 14.39/\mathrm{Re}$. These values are used to obtain the changes in the peak amplitude of transverse oscillation for a 2-DoF sprung square-section cylinder with respect to different Reynolds numbers at a fixed blockage ratio of 0.05. As shown in Figure 4, a good agreement exists between the results of this study and those of Sen and Mittal [25], the latter of which is based on a special finite element analysis.

3. NUMERICAL RESULTS

To investigate the performance of ARO controller for the considered square cylinder with regard to the 2-DoF VIV and galloping, the parameters of the validation section are used [25]. In addition, the Reynolds numbers for the

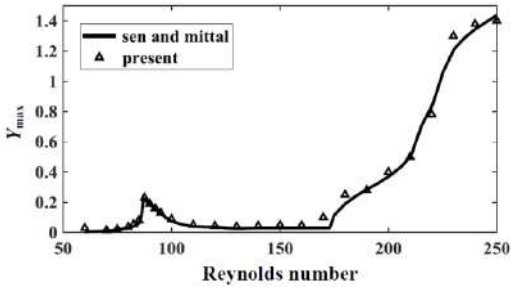

Figure 4. Variation of cylinder transverse displacement amplitude with Reynolds number

lock-in and galloping regions are taken as Re = 90 and Re = 250, respectively. For a blockage ratio of 0.05, the computational domain with $H = 20D$ is displayed in Figure 3 in which the center square section containing 7000 grid cells is located in a larger domain of 20000 grid cells.

First, the effect of control parameter value (α) on the transverse vibration amplitude of the square-section cylinder is investigated. For brevity, only the final results are reported here. The active rotary oscillating controller has a successful performance in the attenuation of cylinder transverse oscillations for a wide range of control parameters. As the control parameter increases, the maximum transverse displacement amplitude of cylinder first decreases and then rises. The maximum amount of reduction in cylinder transverse vibrations is achieved at Re = 90 with the control parameter $\alpha = 1.5$.

The time evolution response of the non-dimensional cross-flow and streamwise displacements of the cylinder for both controlled and uncontrolled cases can be seen in Figure 5 at the critical Reynolds number of 90 that is located in the lock-in region when the control parameter is $\alpha = 1.5$. One notices the sinusoidal response of cross-flow displacement whose frequency of oscillation is close to the vortex shedding frequency. On the other hand, the frequency of oscillation for the in-line displacement is twice as much. The ARO controller decreases the cross-flow vibration magnitude by up to 98%. The corresponding value for streamwise vibrations is 88%.

As discussed earlier, due to the different nature of galloping from VIV, it is good practice to separately study the effect of the active controller on the galloping of the square cylinder. A wide range of parameters are studied at Re = 250 in the galloping zone. It is noticed that $\alpha = 1$ yields the highest amount of reduction in the galloping of the square cylinder. The time evolution response of the non-dimensional cross-flow and streamwise displacements of the cylinder for both controlled and uncontrolled cases can be seen in Figure 6 at Re = 250 that is located in the galloping zone when the control parameter is $\alpha = 1$. The amount of reduction in cross-flow vibration by the active controller is 72%. The corresponding value for the attenuation of streamwise oscillation is 70%.

Comparing Figures 5 and 6 show that the uncontrolled response of the cylinder, especially for in-line oscillations in the galloping zone has significantly increased with respect to the lock-in region. Moreover, the amount of reduction in the vibration of the square cylinder in the lock-in region is more than the galloping zone. Next, to find the main reason behind the reduction of square cylinder vibrations by cylinder rotary oscillations in addition to the difference between the vibration reduction capability in the lock-in region and galloping zone, the values of force coefficients and vortex shedding frequency are inspected. The calculated values of controlled and uncontrolled lift and drag coefficients at Re = 90 (lock-in region) for $\alpha = 1.5$ as in the time evolution responses are shown in Figure 7. The computed magnitudes of lift and drag coefficients are decreased by as much as 95% and 94% using the ARO controller. This shows the capability of active rotary oscillating controller in decreasing the amplitude of lift and drag coefficients exerted on the square cylinder

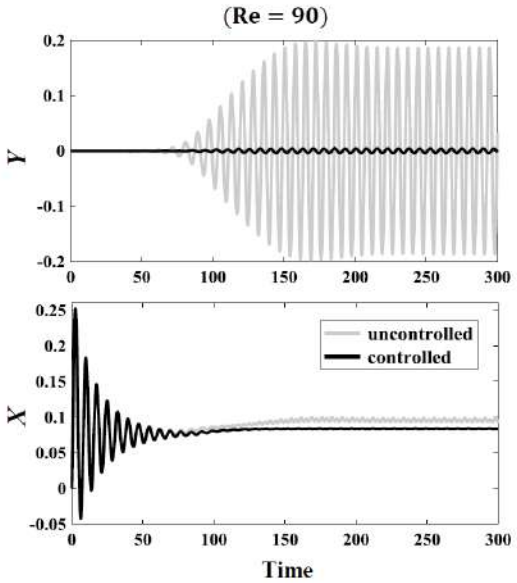

Figure 5. The time evolution of the non-dimensional cross-flow and streamwise displacements for controlled and uncontrolled cases at Re = 90

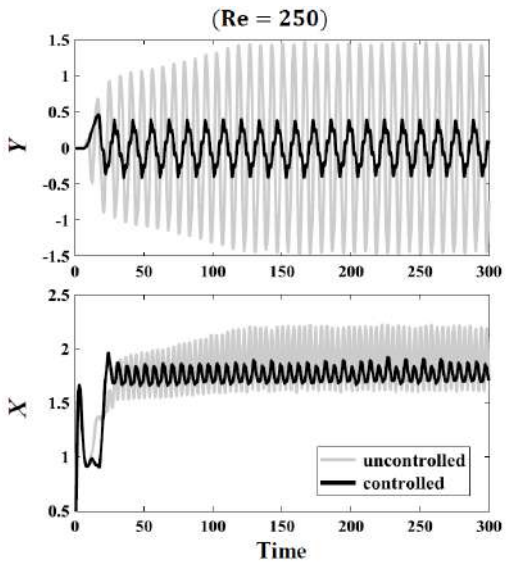

Figure 6. The time evolution of the non-dimensional cross-flow and streamwise displacements for controlled and uncontrolled cases at Re = 250

in the lock-in region. This in turn significantly reduces the transverse and in-line oscillations of the cylinder. The calculated values of controlled and uncontrolled lift and drag coefficient at Re = 250 (galloping zone) for $\alpha = 1$ as in the time evolution responses are shown in Figure 8.

The computed magnitudes of lift and drag coefficients are decreased by 24 and 39% using the ARO controller. As observed, the amount of reduction in the lift and drag coefficients of galloping zone are much less than the lock-in region. In addition, the regular and periodic oscillations of the controlled lift and drag coefficients related to the lock-in region have turned perturbatory. It is in fact concluded that the reduction mechanism of in-line and transverse vibrations for the lock-in region and galloping zone are different from each other.

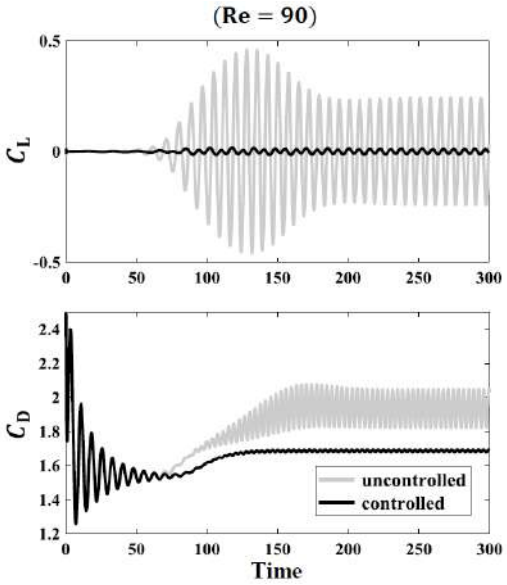

Figure 7. The time evolution of the lift and drag coefficients for controlled and uncontrolled cases at Re = 90

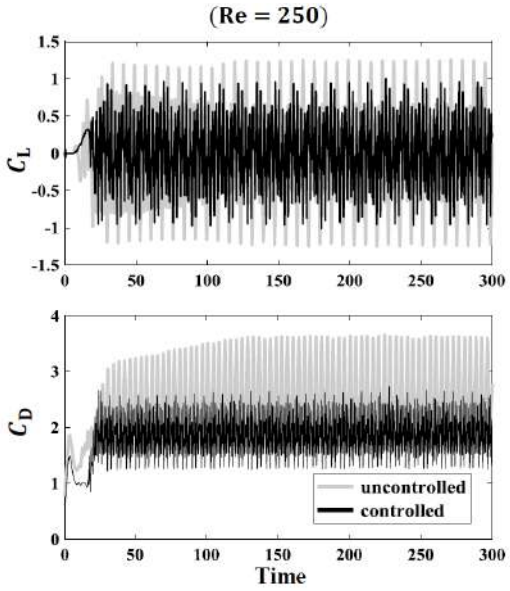

Figure 8. The time evolution of the lift and drag coefficients for controlled and uncontrolled cases at Re = 250

For a more detailed evaluation, the power spectral densities corresponding to the active rotary oscillating controller as well as the uncontrolled cylinder are provided in Figure 9 for Re = 90 and Re = 250. The normalized vortex shedding frequency of the uncontrolled cylinder in this case ($f/f_n = 1$) at the Reynolds number of 90 is a sign of structural resonance, i.e. the vortex shedding frequency becomes equal to the natural frequency of structure. Using forced rotational oscillations of the cylinder, the feedback control system has successfully shifted down the normalized vortex shedding frequency from $f/f_n = 1$ to $f/f_n = 0.9$. Hence, frequency synchronization is disturbed and consequently, the energy transfer from flow to cylinder by the increase in the variations of lift coefficient has decreased significantly. These results in a reduction of cylinder transverse oscillations by 98%. On the other hand, at Re = 250 in the galloping zone, the normalized vortex shedding frequency is equal to $f/f_n = 0.87$. In this case, in which frequency synchronization has not occurred, the active controller has shifted down the vortex shedding frequency from $f/f_n = 0.87$ to $f/f_n = 0.55$.

Therefore, it is concluded that the main reason behind a reduction of 72% in the cross-flow oscillations of the cylinder in the galloping zone is the disturbance of surrounding flow and the weakening of flow-structure coupling and not the de-synchronization-type action. This explains why the reduction percentages of lift

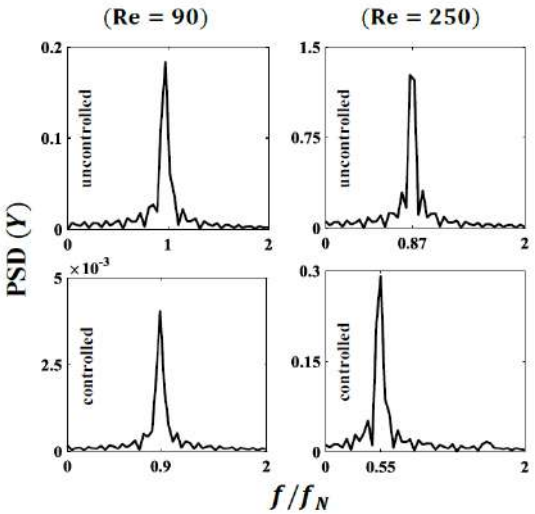

Figure 9. Power spectral density of cross-flow cylinder displacement for uncontrolled and controlled cases

coefficient and transverse vibrations of the cylinder are different in the lock-in region and galloping zone.

Figure 10 shows the time history of the relative error of controlled cylinders at Re = 90 and 250. As observed, the relative error in both the lock-in and galloping zones are small, although the performance of ARO controller in reducing the transverse oscillation of the cylinder in the lock-in region (Re = 90) is better than that in the galloping zone (Re = 250).

At this stage, to show the efficacy and robustness of ARO controller against possible structural uncertainties, the mass and stiffness of the cylinder are changed and numerical simulations are repeated with the same designed controller based on the nominal model. In this regard, Figures 11 and 12 show the time history of the transverse displacement of the square cylinder for ±20% variations in the cylinder mass and stiffness at Re = 90 and 250, respectively. As observed, the ARO controller, despite being developed according to the nominal model, has maintained its proper performance in spite of significant structural uncertainties.

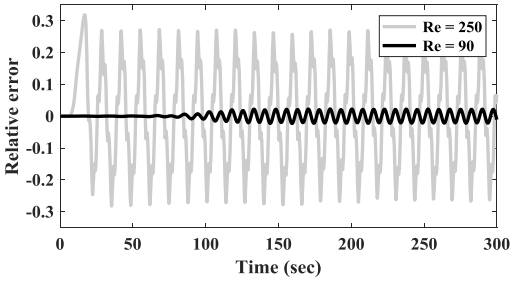

Figure 10. The time evolution of the relative error for controlled cases at Re = 90 and 250

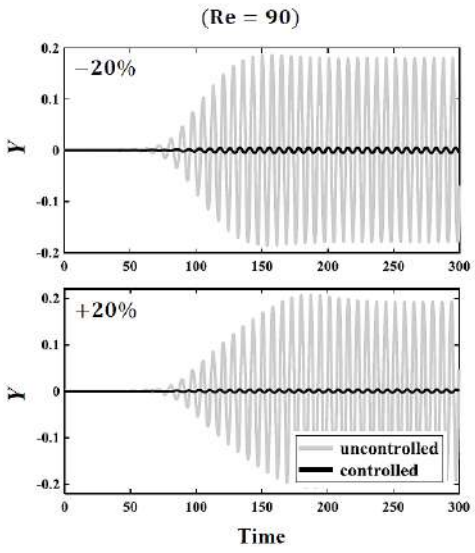

Figure 11. The robustenss of ARO controller with respect to ±20% perturbation in (m, k) at Re = 90

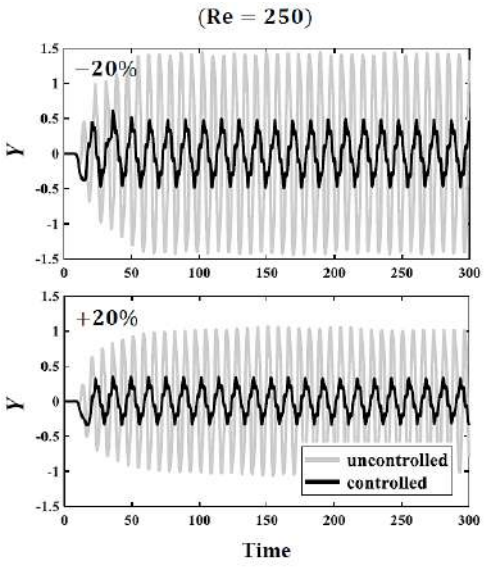

Figure 12. The robustenss of ARO controller with respect to ±20% perturbation in (m, k) at Re = 250

Finally, the correlations between the presented results are summarized as follows. The disturbance of frequency synchronization for the cylinder in the lock-in region reduces the lift coefficient, which in turn reduces the transverse oscillations of the cylinder. As a result, the main reason for the reduction of cylinder oscillations in the lock-in region is the disturbance of frequency synchronization. Regarding the cylinder in the galloping zone, the rotary oscillation disrupts the flow around the cylinder and weakens the fluid-structure coupling. This, and not the disturbance of frequency synchronization, is the main reason for the decrease in the transverse oscillations of the cylinder in the galloping zone. Reducing the lift coefficient as well as the transverse oscillations results in a relatively more smooth flow around the cylinder. Furthermore, as the equations of motion of the cylinder are coupled due to the flow, the drag coefficient on the cylinder also decreases. Accordingly, a decrease in streamwise oscillations owing to the reduction in the transverse oscillations of the cylinder can be observed in both the lock-in and galloping zones.

4. CONCLUSIONS

A closed-loop active control strategy was implemented to attenuate the two-degree-of-freedom vibrations of a square-section cylinder freely oscillating in the transverse and in-line directions in the lock-in and galloping regions. The control system benefited from the cylinder rotary oscillations about its axis which was based on the feedback signal from cylinder lift coefficient. Due to the difference between VIV and

galloping mechanisms, the effectiveness of control strategy was separately studied in both regions. VIV occurs when the vortex-shedding frequency equals the oscillator natural frequency. Galloping is specific to non-circular cylinders and causes high-amplitude, low-frequency oscillations in a range of Reynolds numbers greater than that of VIV. As soon as the flow velocity surpasses a critical value associated with galloping, the amplitude of vibrations continuously rises with increasing flow velocity. High-amplitude oscillations as a result of VIV and galloping can lead to catastrophic failures of structures. Thus, attenuating such instabilities is of utmost importance.

The main observations of the present study are discussed in what follows. The maximum percentage of reduction in cylinder transverse vibration was achieved in the lock-in region (Re = 90) for a control parameter value of $\alpha = 1.5$. At this Reynolds number, the ARO controller successfully reduced the amplitude of transverse and in-line vibrations of the cylinder by 98 and 88%, respectively. In addition, the reduction in the lift and drag coefficients in this region was equal to 95 and 94%, respectively. Moreover, the maximum amount of reduction percentage in cylinder transverse amplitude in the galloping zone (Re = 250) was realized using the control parameter $\alpha = 1$. At this Reynolds number, the ARO controller successfully decreased the amplitude of cylinder transverse vibration by 72%, while the corresponding value for the in-line vibration was 70%. Furthermore, the reduction in the lift and drag coefficients in this zone was, respectively, 24 and 39%. The normalized vortex shedding frequency for the uncontrolled square cylinder in the lock-in region was $f/f_n = 1$, indicating the synchronization of vortex shedding frequency with the natural frequency of structure. Here, the utilized control system successfully shifted down the vortex shedding frequency to $f/f_n = 0.9$. On the other hand, for a square cylinder in the galloping zone, the normalized vortex shedding frequency was equal to $f/f_n = 0.87$ that was further reduced to $f/f_n = 0.55$ with the aid of control system. Thus, it can be concluded that the main reason behind the reduction in the cylinder transverse vibration in the galloping zone is the disturbance of flow around the cylinder and weakening of structure-flow coupling and not the de-synchronization-type action. This describes the difference of lift coefficient and transverse vibrations of cylinder in the lock-in and galloping regions.

5. REFERENCES

1. Williamson, C., and Govardhan, R., "A brief review of recent results in vortex-induced vibrations", ***Journal of Wind Engineering and Industrial Aerodynamics***, Vol. 96, No. 6-7, (2008), 713-735. DOI: 10.1016/j.jweia.2007.06.019
2. Azizi, K., "Computational Fluid Dynamic-Two Fluid Model Study of Gas-Solid Heat Transfer in a Riser with Various Inclination Angles", ***International Journal of Engineering, Transaction A: Basics***, Vol. 30, No. 4, (2017), 464-472. DOI: 10.5829/idosi.ije.2017.30.04a.02
3. Rabiee, A. H., and Farahani, S. D., "Effect of synthetic jet on VIV and heat transfer behavior of heated sprung circular cylinder embedded in a channel", ***International Communications in Heat and Mass Transfer***, Vol. 119, (2020), 104977. DOI: 10.1016/j.icheatmasstransfer.2020.104977
4. Joly, A., Etienne, S., and Pelletier, D., "Galloping of square cylinders in cross-flow at low Reynolds numbers", ***Journal of Fluids and Structures***, Vol. 28, (2012), 232-243. DOI: 10.1016/j.jfluidstructs.2011.12.004
5. Sedaaghi, M. H., "Experimental investigation of the effect of splitter plate angle on the under-scouring of submarine pipeline due to steady current and clear water condition", ***International Journal of Engineering, Transactions C: Aspects***, Vol. 28, No. 3, (2015), 368-377. DOI: 10.5829/idosi.ije.2015.28.03c.05
6. Rabiee, A. H., "Galloping and VIV control of square-section cylinder utilizing direct opposing smart control force", ***Journal of Theoretical and Applied Vibration and Acoustics***, Vol. 5, No. 1, (2019), 69-84. DOI: 10.22064/TAVA.2019.113251.1144
7. Rabiee, A. H., and Farahani, S., "A comprehensive study of heat transfer characteristic and two-dimensional FIV for heated square-section cylinder with different damping ratios", ***International Communications in Heat and Mass Transfer***, Vol. 116, (2020), 104680. DOI: 10.1016/j.icheatmasstransfer.2020.104680
8. Rabiee, A. H., "Regenerative semi-active vortex-induced vibration control of elastic circular cylinder considering the effects of capacitance value and control parameters", ***Journal of Mechanical Science and Technology***, Vol. 32, No. 12, (2018), 5583-5595. DOI: 10.1007/s12206-018-1104-x
9. Rabiee, A. H., and Esmaeili, M., "Simultaneous vortex-and wake-induced vibration suppression of tandem-arranged circular cylinders using active feedback control system", ***Journal of Sound and Vibration***, Vol. 469, (2020), 115131. DOI: 10.1016/j.jsv.2019.115131
10. Hasheminejad, S. M., Rabiee, A. H., and Markazi, A., "Dual-Functional Electromagnetic Energy Harvesting and Vortex-Induced Vibration Control of an Elastically Mounted Circular Cylinder", ***Journal of Engineering Mechanics***, Vol. 144, No. 3, (2017), 04017184. DOI: 10.1061/(ASCE)EM.1943-7889.0001411
11. Kumar, R. A., Sohn, C.-H., and Gowda, B. H., "Passive control of vortex-induced vibrations: an overview", ***Recent Patents on Mechanical Engineering***, Vol. 1, No. 1, (2008), 1-11. DOI: 10.2174/1874477X10801010001
12. Golafshani, A., and Gholizad, A., "Passive vibration control for fatigue damage mitigation in steel jacket platforms", ***International Journal of Engineering, Transactions A: Basics***, Vol. 21, No. 4, (2008), 313-324.
13. Hasheminejad, S. M., Rabiee, A. H., and Bahrami, H., "Active closed-loop vortex-induced vibration control of an elastically mounted circular cylinder at low Reynolds number using feedback rotary oscillations", ***Acta Mechanica***, Vol. 229, No. 1, (2018), 231-250. DOI: 10.1007/s00707-017-1960-y
14. Muralidharan, K., Muddada, S., and Patnaik, B., "Numerical simulation of vortex induced vibrations and its control by suction and blowing", ***Applied Mathematical Modelling***, Vol. 37, No. 1-2, (2013), 284-307. DOI: 10.1016/j.apm.2012.02.028
15. Abbaspour, M., and Jahanmiri, M., "Experimental investigation of drag reduction on ahmed model using a combination of active flow control methods", ***International Journal of Engineering, Transactions A: Basics***, Vol. 24, No. 4, (2011), 403-410. DOI: 10.5829/idosi.ije.2011.24.04a.09

16. Rabiee, A. H., "Two-degree-of-freedom flow-induced vibration suppression of a circular cylinder via externally forced rotational oscillations: comparison of active open-loop and closed-loop control systems", ***Journal of the Brazilian Society of Mechanical Sciences and Engineering***, Vol. 42, No. 9, (2020), 1-15. DOI: 10.1007/s40430-020-02562-5

17. Dimotakis, P., and Tokumaru, P., Rotary oscillation control of a cylinder wake, Proceeding of 2nd Shear Flow Conference, 1-12, 1991.

18. He, J.-W., Glowinski, R., Metcalfe, R., Nordlander, A., and Periaux, J., "Active control and drag optimization for flow past a circular cylinder: I. Oscillatory cylinder rotation", ***Journal of Computational Physics***, Vol. 163, No. 1, (2000), 83-117. DOI: 10.1006/jcph.2000.6556

19. Ray, P., and Christofides, P. D., "Control of flow over a cylinder using rotational oscillations", ***Computers & Chemical Engineering***, Vol. 29, No. 4, (2005), 877-885. DOI: 10.1016/j.compchemeng.2004.09.014

20. Nazarinia, M., Jacono, D. L., Thompson, M. C., and Sheridan, J., "Flow over a cylinder subjected to combined translational and rotational oscillations", ***Journal of Fluids and Structures***, Vol. 32, (2012), 135-145. DOI: 10.1016/j.jfluidstructs.2011.05.005

21. Lu, L., Qin, J.-M., Teng, B., and Li, Y.-C., "Numerical investigations of lift suppression by feedback rotary oscillation of circular cylinder at low Reynolds number", ***Physics of Fluids***, Vol. 23, No. 3, (2011), 033601. DOI: 10.1063/1.3560379

22. Leontini, J., and Thompson, M., Active control of flow-induced vibration from bluff-body wakes: the response of an elastically-mounted cylinder to rotational forcing, Proceeding of 18th Australasian fluid mechanics conference, Launceston, Australia: Citeseer, pp. 1-4, 2012.

23. Du, L., and Sun, X., "Suppression of vortex-induced vibration using the rotary oscillation of a cylinder", ***Physics of Fluids***, Vol. 27, No. 2, (2015), 023603. DOI: 10.1063/1.4913353

24. Wong, K., Zhao, J., Jacono, D. L., Thompson, M., and Sheridan, J., "Experimental investigation of flow-induced vibration of a sinusoidally rotating circular cylinder", ***Journal of Fluid Mechanics***, Vol. 848, (2018), 430-466. DOI: 10.1017/jfm.2018.379

25. Sen, S., and Mittal, S., "Effect of mass ratio on free vibrations of a square cylinder at low Reynolds numbers", ***Journal of Fluids and Structures***, Vol. 54, (2015), 661-678. DOI: 10.1016/j.jfluidstructs.2015.01.006

26. Zhao, M., Cheng, L., and Zhou, T., "Numerical simulation of vortex-induced vibration of a square cylinder at a low Reynolds number", ***Physics of Fluids***, Vol. 25, No. 2, (2013), 023603. DOI: 10.1063/1.4792351

27. Minewitsch, S., Franke, R., and Rodi, W., "Numerical investigation of laminar vortex-shedding flow past a square cylinder oscillating in line with the mean flow", ***Journal of Fluids and Structures***, Vol. 8, No. 8, (1994), 787-802. DOI: 10.1016/S0889-9746(94)90280-1

28. Yang, S.-J., Chang, T.-R., and Fu, W.-S., "Numerical simulation of flow structures around an oscillating rectangular cylinder in a channel flow", ***Computational Mechanics***, Vol. 35, No. 5, (2005), 342-351. DOI: 10.1007/s00466-004-0621-x

29. Singh, A., De, A., Carpenter, V., Eswaran, V., and Muralidhar, K., "Flow past a transversely oscillating square cylinder in free stream at low Reynolds numbers", ***International Journal for Numerical Methods in Fluids***, Vol. 61, No. 6, (2009), 658-682. DOI: 10.1002/fld.1979

30. Sen, S., and Mittal, S., "Free vibration of a square cylinder at low Reynolds numbers", ***Journal of Fluids and Structures***, Vol. 27, No. 5, (2011), 875-884. DOI: 10.1016/j.jfluidstructs.2011.03.006

31. Zhao, J., Leontini, J. S., Jacono, D. L., and Sheridan, J., "Fluid–structure interaction of a square cylinder at different angles of attack", ***Journal of Fluid Mechanics***, Vol. 747, (2014), 688-721. DOI: 10.1017/jfm.2014.167

32. Zhao, M., "Flow-induced vibrations of square and rectangular cylinders at low Reynolds number", ***Fluid Dynamics Research***, Vol. 47, No. 2, (2015), 025502. DOI: 10.1088/0169-5983/47/2/025502

33. Venkatraman, K., and Narayanan, S., "Active control of flow-induced vibration", ***Journal of Sound and Vibration***, Vol. 162, No. 1, (1993), 43-55. DOI: 10.1006/jsvi.1993.1101

34. Cheng, L., Zhou, Y., and Zhang, M., "Perturbed interaction between vortex shedding and induced vibration", ***Journal of fluids and Structures***, Vol. 17, No. 7, (2003), 887-901. DOI: 10.1016/S0889-9746(03)00042-2

35. Dai, H., Abdelkefi, A., Wang, L., and Liu, W., "Control of cross-flow-induced vibrations of square cylinders using linear and nonlinear delayed feedbacks", ***Nonlinear Dynamics***, Vol. 78, No. 2, (2014), 907-919. DOI: 10.1007/s11071-014-1485-z

36. Wu, C.-H., Ma, S., Kang, C.-W., Lim, T.-B. A., Jaiman, R. K., Weymouth, G., and Tutty, O., "Suppression of vortex-induced vibration of a square cylinder via continuous twisting at moderate Reynolds numbers", ***Journal of Wind Engineering and Industrial Aerodynamics***, Vol. 177, (2018), 136-154. DOI: 10.1016/j.jweia.2018.03.030

37. Hasheminejad, S. M., Rabiee, A. H., Jarrahi, M., and Markazi, A., "Active vortex-induced vibration control of a circular cylinder at low Reynolds numbers using an adaptive fuzzy sliding mode controller", ***Journal of Fluids and Structures***, Vol. 50, (2014), 49-65. DOI: 10.1016/j.jfluidstructs.2014.06.011

38. Hasheminejad, S. M., Rabiee, A. H., and Jarrahi, M., "Semi-active vortex induced vibration control of an elastic elliptical cylinder with energy regeneration capability", ***International Journal of Structural Stability and Dynamics***, (2017), 1750107. DOI: 10.1142/S0219455417501073

Persian Abstract

چکیده

در این مقاله یک سیستم کنترل پس‌خور بر مبنای نوسانات چرخشی استوانه به منظور کاهش ارتعاشات دو درجه‌ی آزادی یک لوله با مقطع مربع در معرض جریان قرار گرفته بر روی بستر الاستیک به کار گرفته شده است. سیستم کنترل از نوسانات چرخشی استوانه حول محورش که بر مبنای فیدبک پس‌خور ضریب لیفت استوانه عمل می کند، بهره می‌گیرد. با توجه به شبیه سازی های عددی انجام شده مشخص می شود که سیستم کنترل فعال در کاهش نوسانات دو درجه آزادی استوانه مربعی هم در ناحیه‌ی قفل شدگی فرکانسی، و هم در ناحیه‌ی گالوپینگ موفق عمل کرده است. برای عدد رینولدز Re=90 واقع در ناحیه‌ی قفل شدگی فرکانسی، کنترلر فعال موفق شده است به مقدار ۹۸٪ دامنه ارتعاشات عرضی استوانه را کاهش دهد، در حالی که مقدار مشابه برای دامنه‌ی ارتعاشات طولی استوانه برابر با ۸۸٪ می‌باشد. همچنین برای عدد رینولدز Re=250 واقع در ناحیه‌ی گالوپینگ، کنترلر فعال موفق شده است دامنه‌ی ارتعاشات عرضی استوانه را به میزان ۷۲٪ کاهش دهد، در حالی که مقدار مشابه برای دامنه‌ی ارتعاشات طولی استوانه برابر با ۷۰٪ می‌باشد. همچنین، مشاهده می‌شود که کنترلر ARO موفق شده است دامنه‌ی ضرایب لیفت و درگ استوانه در ناحیه قفل شدگی را به ترتیب به میزان ۹۵ و ۹٤٪ کاهش دهد، درحالی که درصدهای مشابه برای استوانه در ناحیه‌ی گالوپینگ به ترتیب برابر با ۲٤ و ۳۹٪ می‌باشند

International Journal of Engineering

Journal Homepage: www.ije.ir

Gear Fault Detection using Machine Learning Techniques- A Simulation-driven Approach

V. C. Handikherkar*, V. M. Phalle

Department of Mechanical Engineering, Veermata Jijabai Technological Institute (VJTI), Mumbai, India

P A P E R I N F O

Paper history:
Received 12 August 2020
Received in revised form 18 September 2020
Accepted 30 October 2020

Keywords:
Machine Learning
Simulated Data
Vibration Analysis
Gear Fault Diagnosis
Condition Monitoring

A B S T R A C T

Machine Learning (ML) based condition monitoring and fault detection of industrial equipment is the current scenario for maintenance in the era of Industry-4.0. The application of ML techniques for automatic fault detection minimizes the unexpected breakdown of the system. However, these techniques heavily rely on the historical data of equipment for its training which limits its widespread application in industry. As the historical data is not available for each industrial machine and generating the data experimentally for each fault condition is not viable. Therefore, this challenge is addressed for gear application with tooth defect. In this paper, ML algorithms are trained using simulated vibration data of the gearbox and tested with the experimental data. Simulated data is generated for the gearbox with different operating and fault conditions. A gearbox dynamic model is utilized to generate simulated vibration data for normal and faulty gear condition. A pink noise is added to simulated data to improve the exactness to the actual field data. Further, these simulated-data are processed using Empirical Mode Decomposition and Discrete Wavelet Transform, and features are extracted. These features are then fed to the training of different well-established ML techniques such as Support Vector Machine, Random Forest and Multi-Layer Perceptron. To validate this approach, trained ML algorithms are tested using experimental data. The results show more than 87% accuracy with all three algorithms. The performance of the trained model is evaluated using precision, recall and ROC curve. These metric show the affirmative results for the applicability of this approach in gear fault detection.

***doi**: 10.5829/ije.2021.34.01a.24*

NOMENCLATURE

$I_m / I_b / I_1 / I_2$	Mass moment of inertia of rotor/load/pinion/gear	c_p / c_g	Torsional damping of flexible coupling Input/Output
M_1 / M_2	Input/Output torque from Motor/Load	k_1 / k_2	Vertical Radial stiffness of bearing Input/Output
m_1 / m_2	Mass of pinion/gear	c_1 / c_2	Vertical Radial viscous damping coefficient of bearing Input/Output
R_{b1} / R_{b2}	Base circle of pinion/gear	y_1 / y_2	Linear displacement of Pinion/Gear in the y-direction
k_p / k_g	Torsional stiffness of flexible coupling Input/Output	$\theta_m / \theta_b / \theta_1 / \theta_2$	Angular displacement of motor/load/pinion/gear

1. INTRODUCTION

Rotating machinery are the most essential systems of the industrial machinery. Gearboxes are the most widely used sub-systems of the rotating machinery that are vulnerable to failure and system breakdown. As they operate under harsh operating conditions, which may develop fault on gears. Also, continuous operation under these conditions causes gear to degrade and leads to the failure. Failure of gear causes the transmission system breakdown, production and economic loss.

Different maintenance strategies such as breakdown or unplanned, preventive or scheduled and Condition Based Maintenance (CBM) are employed to ensure the satisfactory operation of rotating machinery over its useful life. Earlier was the breakdown or unplanned

*Corresponding Author Email: *vishwadeepch@gmail.com* (V. C. Handikherkar)

Please cite this article as: V. C. Handikherkar, V. M. Phalle, Gear Fault Detection using Machine Learning Techniques- A Simulation-driven Approach, International Journal of Engineering, Transactions A: Basics Vol. 34, No. 01, (2021) 212-223

maintenance in which maintenance is carried out only at the breakdown; preventive or scheduled maintenance was carried out at predefined intervals, and CBM was carried out based on the information on the condition of machine [1]. Out of this CBM strategy gained popularity in the industry as it avoids unnecessary maintenance. In current Fourth Industrial Revolution (i.e. Industry 4.0) for industry equipment maintenance, machine learning based condition monitoring system are being developed for automatic fault diagnosis [2]. Machine learning has been applied not only in industry equipment maintenance but also in different fields such as roadways maintenance [3], predicting student grades [4] etc.

Vibration analysis is a most widely used condition monitoring technique for gear fault daignosis. In literature two approaches have been used for the gear fault diagnosis, one is data driven approach and other is physical model based approach. The data-driven approach purely rely on the historical or in-service data of gearbox to predict the faults in gear, and physical model based approach makes use of physics based models to create a virtual system to mimic the vibration characteristics of gearbox under different operating conditions [5]. Subsequent section discusses the literature on these two approaches.

Several researchers have used Machine Learning (ML) techniques for developing automatic fault detection of industrial machinery based on the data driven approach. Recently, Lei et al. [6] presented a review of different ML techniques employed for machine fault diagnosis. To develop a fault diagnosis technique based on the data driven approach using the ML techniques, require a historical data of in-service equipment or experimental data to train the ML algorithms. ML techniques like Support Vector Machine (SVM), k-Nearest Neighbour (kNN), Artificial Neural Network (ANN) Ensemble techniques etc. [6] have been employed for the bearing and gear fault diagnosis. Samanta [7] used this approach for the binary classification (i.e. healthy and faulty) of gear using SVM and ANN. In this input features were selected and optimized using the genetic algorithm, SVM resulted in better classifier over the ANN. Similarly, Samanta et al. [8] used three different ANN classifiers such as Multi-Layer Perceptron (MLP), Radial Basis Function Network and Probabilistic Neural Network for the bearing fault classification. Using genetic algorithm and Probabilistic Neural Network a test accuracy of 100% was obtained. Further, the effectiveness of pre-processing of data using Discrete Wavelet Transform (DWT) on the classification by SVM and ANN was studied by Tyagi and Panigrahi [9], and results show that pre-processing improves the performance of both the classifiers and that SVM outperforms ANN. Discrete wavelet transform and multi-layer perceptron was used by Sanz et al. [10] to determine the gear condition status and the model is able to predict 1% decrease in the mesh stiffness. Shen et al. [11] used a transductive SVM for gear fault classification for data having more numbers of unlabeled data than labelled data; in this features were extracted using Empirical Mode Decomposition (EMD). Shao et al. [12] also utilized an EMD technique with higher-order cumulant method for gear fault classification and developed a virtual system for gear damage detection. Li et al. [13] proposed a bearing fault detection method using Improved Iterative Windowed Interpolation Discrete Fourier Transform technique. For the combined gear and bearing fault detection Dhamande and Chaudhari [14] proposed that, features extracted using continuous and discrete wavelet transform have been more prominent in detecting the combined fault than time and frequency domain features. A highest accuracy of 90% and 97% for training and testing respectively was obtained using the SVM. Attaran et al. [15] developed bearing fault detection technique based on kurtogram in time-frequency domain using ANN. A 100% training accuracy was noted for ANN. Bajric et al. [16] used features extracted using the discrete wavelet transform and time synchronous averaging method for a wind turbine gearbox fault detection. Researchers have also utilized ensemble techniques such as Random Forest (RF) for the fault classification. Han and Jiang [17] used RF classifier for the bearing fault classification; in this the variational mode decomposition and autoregressive model parameters have been employed for the fault feature extraction. Cerrada et al. [18] utilized RF classifier for the gear fault classification and used a genetic algorithm to select the best features and a best precision value of 0.9781 was obtained. Patil and Phalle [19] have used Random Forest, Gradient Boosting Classifier and Extra Tree classifier ensemble techniques for the bearing fault classification, in this features were ranked using decision tree and randomized lasso feature ranking technique and fed to these classifiers. Results showed that the features, ranked using DT technique, when fed to the classifier provided better accuracy compared to randomized lasso with fewer features and execution time. A highest accuracy of 98.21% was recored using DT ranking technique. In literature cited above fault diagnosis system was developed based on the data driven approach and utilized an experimental test rig to generate the training dataset for the training of ML algorithms.

In physical model based approach, dynamic model is used to mimic the actual operating conditions of the gearbox, and vibration response of gearbox under different conditions can be studied theoretically. Numerous dynamic models of the gearbox have been developed by researchers to study the vibration characteristics of the gearbox under healthy and faulty gear conditions. Liang et al. [5] presented a review of different gearbox fault dynamic models developed. The vibrations in gears are caused due to fluctuation in

applied load, speed and Time-Varying Mesh Stiffness (TVMS), transmission errors etc. When faulty tooth engages the TVMS changes, due to this change in vibration response is observed. Therefore, the calculation of the TVMS for normal and faulty gear condition is essential. Researchers have developed different analytical methods such as potential energy, square waveform and finite element method for calculating the TVMS [5]. For obtaining the vibration response different models have been developed. Bartelmus [20] developed a dynamic model having 8-Degrees of Freedom (DoF) incorporating torsional and lateral motion and friction. Howard et al. [21] developed a 16-DoF model to study the effect of crack on gear tooth and friction between the tooth in contact on the vibration response. Abouel-seoud et al. [22] developed a model for wind turbine gearbox having twelve DoF to study the vibration response of gearbox under three faults like crack, spall and tooth breakage. A single-stage spur gearbox model incorporating the gyroscopic effect was developed by Mohammed et al. [23]. Literature cited above discusses the use of physical model based approach in gear fault diagnosis and the study is limited to calculating TVMS, obtaining the vibration response under different fault conditions and identifing the most sensitive condition indicators. The vibration response obtained using dynamic model is not having any noise, but in actual practice vibration response is masked with the environmental noise and determining the fault in such noisy data using the condition indicators is not possible.

It is clear that for the application of the data driven approach historical data is required for training of ML algorithm and in physical model based method study is limited to calculating TVMS, obtaining vibration response under different fault conditions and determining sensitive condition indicators. But these condition indicators does not perform well in case of actual vibration data.

Most of the studies reported in the literature for fault diagnosis of mechanical components using ML techniques have been utilizing a data-driven approach. The dependence of this approach on historical data from in-service equipment or data from the experimental test setup to train the ML algorithm restricted its full spread implementation in industrial machinery fault diagnosis. As in-service data for the equipment is not available and generating data using experimental test rig is not viable. Also, the cost associated with creating the data for each fault and at different operating conditions is very high; and model trained using these data are often valid for the condition and machine for which the data is collected. Also, training of ML algorithms are dependent on the diversity of data i.e. data at different operating conditions, more diverse data better is training. But generating this kind of diverse data experimentally is not feasible. Therefore, an alternative approach is required to overcome this limitation of the data driven approach and generate the diverse data with minimum cost.

The present paper addresses the limitation of the data-driven approach by employing a dynamic model of gearbox to generate the training dataset that includes the extensive variety of operating and fault conditions, for the training of ML algorithm. The data is generated by simulating the actual conditions of the gearbox therfore this approach is called as a simulation driven approach. In this a single-stage spur gearbox dynamic model is employed to generate simulated vibration acceleration data for different gear conditions (normal and faulty) at different loads and speeds. ODE15s solver function in Matlab is used to solve the equations of motion to obtain the simulated vibration response. Pink noise is added to simulated data to improve its exactness to the actual field data. These data are then processed using the DWT and EMD signal processing techniques, and features are extracted to create a training dataset. Various extensively used ML algorithms like SVM, MLP and RF are trained using this simulated training data set and tested using the experimental data.

2. METHODOLOGY

Figure 1 shows the schematic of the methodology of the simulation-driven approach adopted for gear fault detection. The simulation-driven gear fault diagnosis approach proposed in this work involves obtaining vibration acceleration data for normal and faulty gear conditions at different loads and speeds using the six DoF gear dynamic model. Pink noise is added to obtained simulated vibration data to improve the exactness

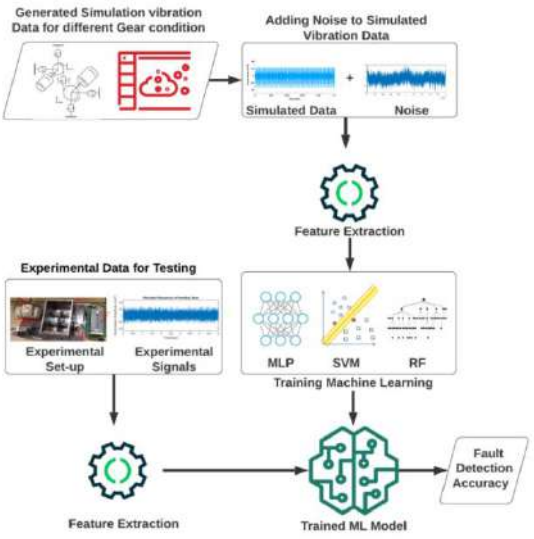

Figure 1. Schematic for Simulation Driven Fault Detection Methodology

towards the actual vibration data. Discrete Wavelet Transform (DWT) and Empirical Mode Decomposition (EMD) are used to process these vibration signals, and then statistical features are extracted. Using these features training data set is prepared and fed for the training of ML algorithms such as SVM, MLP and RF. To test this simulation-driven approach experimental data is collected from the experimental test rig. This experimental data is processed similarly as simulated data and features are extracted to prepare the testing data. Also, the theoretical background of signal processing and ML techniques used in this study are presented in this section.

2. 1. Discrete Wavelet Transform (DWT) DWT is an effective tool for signal and image processing in a wide range of research as well as in industrial applications [14,16]. The wavelet transform gives both frequency and time domain information about the signal. The continuous wavelet transform of signal *x(t)* is

$$W_{\psi}(\tau,s)=\int_{-\infty}^{+\infty} x(t)\psi^{*}_{\tau,s}(t)dt \quad (1)$$

where $\psi^{*}_{\psi\tau,s(t)}$ is a conjugate of $\psi_{\tau,s}(t)$, that is the scaled and shifted version of the transforming function, called a mother wavelet which is defined as:

$$\psi_{\tau,s}(t)=\frac{1}{\sqrt{s}}\psi\left(\frac{t-\tau}{s}\right) \quad (2)$$

The transformed signal is a function of translation (τ) and scale (*s*) parameters. Other wavelet functions can be derived using the mother wavelet. Scale and translation correspond to frequency band and time information respectively in the transform domain. The DWT is derived from the discretization of $W_{\psi}(\tau,s)$ given by

$$DWT(j,k)=\frac{1}{\sqrt{2^{j}}}\int_{-\infty}^{\infty} x(t)\psi\left(\frac{t-2^{j}k}{2^{j}}\right)dt \quad (3)$$

Vector A and D are obtained by passing the signal x through low and high pass filters. approximate and detailed coefficients are obtained by downsampling these vectors. By repeating the process of decomposition using the approximate coefficients, different levels of DWT coefficients can be obtained.

Researchers have used different mother wavelet functions and levels of decomposition in bearing and gear fault diagnosis. In this study, db5 is used as a mother wavelet function and 3rd level decomposition for gear fault diagnosis.

2. 2. Empirical Mode Decomposion (EMD) EMD is an effective adaptive signal processing technique. Finite numbers of intrinsic mode functions (IMF) can be obtained by decomposing complicated data [24, 25]. A number of extrema and zero crossings are same for linear or non-linear mode. The procedure for obtaining these IMF's from a given signal is as follows.

Firstly, all the local extrema are determined, and a cubic spline curve is employed to connect all the local maxima to obtain the upper envelop and all local minima to obtain the lower envelop. The entire signal should be enclosed by these upper and lower envelops. A mean of upper and lower envelop is m_1 and the difference between the *x(t)* and m_1 gives the first component h_1

$$x(t)-m_1=h_1 \quad (4)$$

If h_1 is an IMF, then h_1 is the first component of *x(t)*. If h_1 is not an IMF, the above procedure is repeated considering h_1 as original signal

$$h_1-m_{11}=h_{11} \quad (5)$$

After sifting for *k* times, h_{1k} becomes an IMF, that is

$$h_{1(k-1)}-m_{1k}=h_{1k}=c_1 \quad (6)$$

c_1 *is the* first IMF component obtained from the original. Separating c_1 from *x(t)*, We get

$$r_1=x(t)-c_1 \quad (7)$$

Now, r_1 is considered as the original signal and the process described above is repeated *n* time to obtain *n*-IMFs of signal *x(t)*.

$$x(t)=\sum_{j=1}^{n} c_j+r_n \quad (8)$$

The above procedure is repeated till r_n becomes a monotonic function from which no more IMFs can be drawn out.

Thus, decomposition of the signal results into *n*-empirical modes and a residue r_n. Where r_n is the mean trend of *x(t)*. The IMFs contain different frequency bands and the components of frequency included in each frequency band are different, and they change with the variation of signal *x(t)*, r_n represents the central tendency of signal *x(t)*.

2. 3. Machine Learning Techniques In the present work Support Vector Machine, Multi-Layer Perceptron and Random Forest, widely used and popular ML techniques are utilized for the gear fault classification.

2. 3. 1. Support Vector Machine (SVM) SVM is a supervised ML technique employed for the classification and regression in the small sample dataset. In SVM classifier, data is separated by a decision boundary known as the hyperplane such that the margin of separation between two classes is maximized and points that decide the margin are called as support vectors as shown in Figure 2.

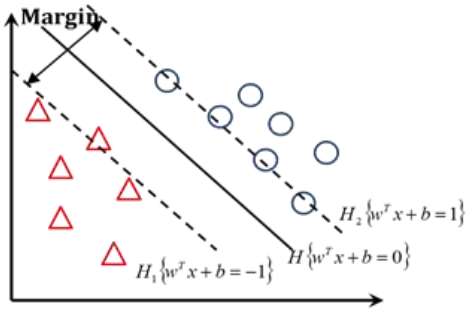

Figure 2. Hyperplane classifying two classes

This is done by minimizing the quadratic function under linear inequality constraints. Consider a training sample set *{(xi, yi) }; i=1* to *N*, where *N* is the total number of samples. It is to determine the separation plane with the smallest generalization error. The labels associated with the two classes, i.e. triangle and circle class are $y_i = -1$ and $y_i = +1$ respectively. Slack variables are considered $\xi_i \geq 0$ for non-separable data. The hyperplane *f(x) = 0* that separates the given data can be obtained as a solution to the following optimization problem [4].

$$\text{Minimize } \frac{1}{2}\|w\|^2 + C\sum_{i=1}^{N}\xi_i \text{ Subject to } \begin{cases} y_i\left(w^T x_i + b\right) \geq 1-\xi_i \\ \xi_i \geq 0, i=1,2,\ldots N \end{cases} \quad (9)$$

where, *C* is a constant representing error penalty

2. 3. 2. Multi-Layer Perceptron (MLP) **MLP** is a type of Back Propagation Artificial Neural Network which includes an input layer, output layer and two or more weighted perceptron (hidden layers) [8]. The targets of each layer are characterized by a function, and subsequently, the targets of preceding layers are served as inputs to the succeeding layer. Each layer consists of a specific number of neurons which carry information to neurons of subsequent layers.

For example, consider a training set (X_i^j, Y_i^j) with *N* features and *M* samples where *i=1, 2, 3,…M* and *j= 1, 2, 3,…N*. The first layer will consist of *N* neurons with each j^{th} neuron containing *M* samples of j^{th} feature. Neurons in subsequent layers are also fixed accordingly (with an additional node neuron), but the last layer will have only one neuron for regression model and for the classification problem number of neurons will be equal to a number of classes. The parameter which controls the mapping of information from one layer to another, say $\emptyset_j$ is multiplied with training samples X_i^j and the resultant matrix multiplication is fed as a parameter to the function. For example, a neuron a_1 of the second layer is represented as:

$$a_1 = f\left(\phi_1^T, X_j^1\right) \quad (10)$$

where, f is the sigmoid function.
Hence, the prediction is given by a_L. To minimize the loss function, this is followed by back-propagation method wherein another parameter say ∂ is computed for each layer with the help of gradient descent. The values of ∂ are computed from the last layer to the first layer and are updated by means of gradient descent. Also, for the last layer:

$$\partial_L = (a_L - y) \quad (11)$$

where, *y* is the target.
The following layers are given by:

$$\partial_{L-1} = \left[\phi_{L-1}\right]^T * \partial_L * \left[(a_{L-1}) * (1-a_{L-1})\right] \quad (12)$$

where, $\left[(a_{L-1}) * (1-a_{L-1})\right]$ is the differentiated term of the sigmoid function. Hereafter, the product of two ∂ and *a* are computed to add over each iteration to get the gradient which will minimize the loss function. This process is done with regularization.
Hence the 'accumulator' i.e. $\frac{d(L(a_L, y))}{dy}$ (i.e. the derivative of loss function) is given by:

$$D_{ij} = \frac{1}{M}\left(\Delta_{ij}^{(L)}\right) + \alpha * \phi_{ij}^{(L)} \quad (13)$$

where, α is the regularization parameter and M is the number of samples.
Also, initially $\Delta_{ij}^{(L)} = 0$ and it is updated as follows:

$$\Delta^{(L)} = \Delta^{(L)} + \partial_{L-1} * \left[a_L\right]^T \quad (14)$$

The accumulator i.e. D is added over each step to minimize the loss function and get better value of prediction i.e. a_L.

2. 3. 3. Random Forest (RF) is a polpular ensemble machine learning technique, in which many decision trees are built on bootstrapped sample same as bagging from training dataset and to get the output prediction, prediction from each tree is averaged in case of regression and majority voting in case of classification. RF is better than a single decision tree and reduces the over-fitting by averaging. High variance and low bias of decision trees make it unstable. RF consists of bootstrap aggregating (bagging) with a randomized selection of features at each split. A bootstrap aggregating algorithm improves the stability and accuracy of an individual predictive model [18,19].

Consider *A*, number of trees generated by the random forest. Using bootstrap sampling, select the subset from

the training dataset. For each subset grow tree $\{t_1(x), t_2(x),\ldots..,t_A(x)\}$ where $x \in \{x_1, x_2, \ldots, x_n\}$. x is an n-dimensional feature vector, and this feature vector is prepared by randomly selecting n features from a total of N features. Using the Gini impurity (I_g) pick a node e out of those n variables for the best split point.

$$I_{G(p)} = 1 - \sum_{a=1}^{b} R_a^2 \quad (15)$$

where, a is the number of classes (a=1, 2, 3, …., b) and R_a is the fraction of instances tagged with class a. Then split the node into two daughter nodes and repeat the above procedure for growing A number of trees. Y_1, Y_2,….Y_k is the output of these trees, where $k \in \{1, 2, \ldots, A\}$ is the prediction for a classified object by the k^{th} tree, and a collection of all individuals make a final classification decision.

3. SIMULATION DRIVEN APPROACH

In the present work, a model developed by Bartelmus [20] is used to obtain the vibration response. The model includes both torsional and lateral motions. In this gearbox, the casing is assumed as rigid so as vibration propagates linearly along the casing. Figure 3 depicts the model used in this work.

In this model the system is rotated by a motor and a load torque is applied at the output. M_1 and M_2 are the motor and load torque, respectively. Flexible couplings are used to connect the motor shaft and input shaft on which pinion is mounted, and load shaft and shaft on which gear is mounted. Shafts containing pinion and gear are mounted on bearings, and these bearings are mounted on the rigid casing. A model consists of two parameters stiffness and damping and includes both linear and rotational (lateral and torsional) equations of motion. Equations (16)-(23) represent the equations of motion for the system shown in Figure 3. x - direction vibration response is a free response (Equations (16) and (17)). When the system is stable response in this direction will disappear; therefore, vibration in y - direction is considered here to get the response of healthy and faulty gears. Single fault on a single pinion tooth is considered for obtaining vibration response for faulty gear condition. Vibration response of faulty gears includes responses of gearbox having faults such as spalled, cracked and chipped gear tooth. Firstly, TVMS of normal and faulty conditions is calculated using the potential energy method presented in [26-28]. The value of calculated TVMS which act as an internal excitation, is considered while obtaining the vibration response.

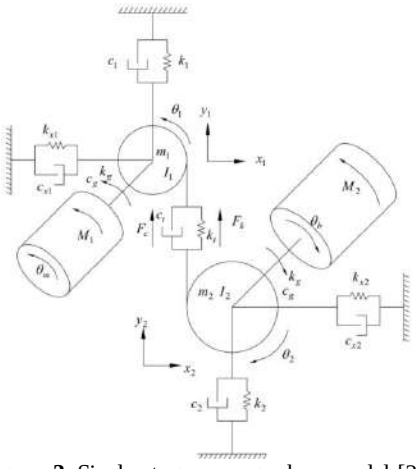

Figure 3. Single-stage spur gearbox model [20]

$$m_1\ddot{x}_1 = -k_{x1}x_1 - c_{x1}\dot{x}_1 \quad (16)$$

$$m_2\ddot{x}_2 = -k_{x2}x_2 - c_{x2}\dot{x}_2 \quad (17)$$

$$m_1\ddot{y}_1 + c_1\dot{y}_1 + k_1y_1 = -F_k - F_c \quad (18)$$

$$m_2\ddot{y}_2 + c_2\dot{y}_2 + k_2y_2 = F_k + F_c \quad (19)$$

$$I_1\ddot{\theta}_1 = k_p(\theta_m - \theta_1) + c_p(\dot{\theta}_m - \dot{\theta}_1) - R_{b1}(F_k + F_c) \quad (20)$$

$$I_2\ddot{\theta}_2 = R_{b2}(F_k + F_c) - k_g(\theta_2 - \theta_b) - c_g(\dot{\theta}_2 - \dot{\theta}_b) \quad (21)$$

$$I_m\ddot{\theta}_m = M_1 - k_p(\theta_m - \theta_1) - c_p(\dot{\theta}_m - \dot{\theta}_1) \quad (22)$$

$$I_b\ddot{\theta}_b = -M_2 + k_g(\theta_2 - \theta_b) + c_g(\dot{\theta}_2 - \dot{\theta}_b) \quad (23)$$

$$F_k = k_t(R_{b1}\theta_1 - R_{b2}\theta_2 + y_1 - y_2) \quad (24)$$

$$F_c = c_t(R_{b1}\dot{\theta}_1 - R_{b2}\dot{\theta}_2 + \dot{y}_1 - \dot{y}_2) \quad (25)$$

The gear parameters utilized in this model to obtain the simulated vibration data are given in Table 1. Figure 4 (a-b) shows the sample of TVMS obtained for normal and faulty gear conditions respectively for one rotation of pinion. The equations of motion (Equations (18)-(23)) are solved simultaneously using ODE15s solver function in Matlab to obtain the vibration response. The vibration response is obtained for different load and speed conditions. Figure 5 (a-b) shows the vibration response obtained at 1800rpm for normal and faulty gear condition, respectively for 0.1 s.

To increase the exactness of simulated vibration signals with the actual field data noise is added to the simulated response. A pink noise (1/f power spectrum) is added, as pink noise is present everywhere in nature, electronics, machinery, and numerous other fields [29]. Chen et al. [30] used this pink noise power spectrum to generate the bearing signals. Randomly this noise is

TABLE 1. Gear parameters for simulated data

Gear Parameter	Value
Number of teeth on Pinion/Gear	$N_p = 19$, $N_g = 48$
Pressure angle	20^0
Diametral Pitch	$P = 0.2032\ m^{-1}$
Width of Teeth	$L = 0.16\ m$
Contact ratio	$C_r = 1.6456$
Young's Modulus	$E = 2.068 \times 10^{11}\ Pa$
Poisson's Ratio	$\upsilon = 0.3$
Mass of the Pinion/Gear	$m_p = 0.96\ kg$, $m_g = 2.88\ kg$
Mass moment of inertia of the Pinion/Gear	$I_p = 4.3659 \times 10^{-4}\ kgm^2$ $I_g = 8.3602 \times 10^{-4}\ kgm^2$
Mass moment of inertia of the motor/Load	$I_m = 0.0021\ kgm^2$ $I_b = 0.0105\ kgm^2$
Tortional stiffness of the coupling	$k_p = k_g = 4.4 \times 10^4\ Nm/rad$
Damping coefficient of the coupling	$c_p = c_g = 5.0 \times 10^5\ Nm/rad$
Radial stiffness of the bearing	$k_1 = k_2 = 6.56 \times 10^7\ N/m$
Damping coefficient of the bearing	$c_1 = c_2 = 1.8 \times 10^5\ Ns/m$
Base circle radius of Pinion/Gear	$R_{b1} = 0.02834\ m$, $R_{b2} = 0.0716\ m$

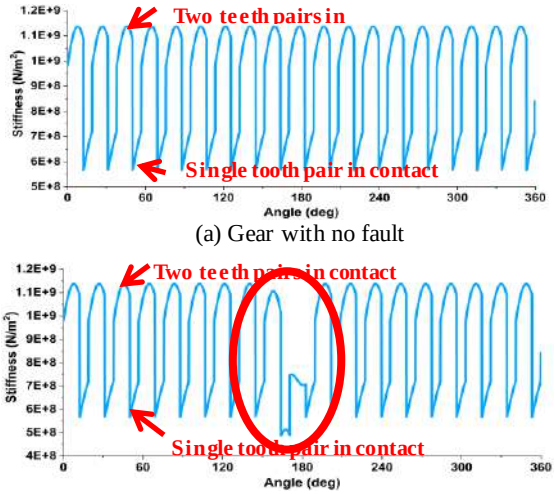

(a) Gear with no fault

(b) Gear with fault

Figure 4. Time Varying Mesh Stiffness (TVMS)

added to simulated vibration signals so that S/N ratio can range from 1 to 30.

4. EXPERIMENTAL TEST RIG

To validate the simulation-driven approach ML algorithms trained using the simulated training data is to be tested using the experimental data. For the broader

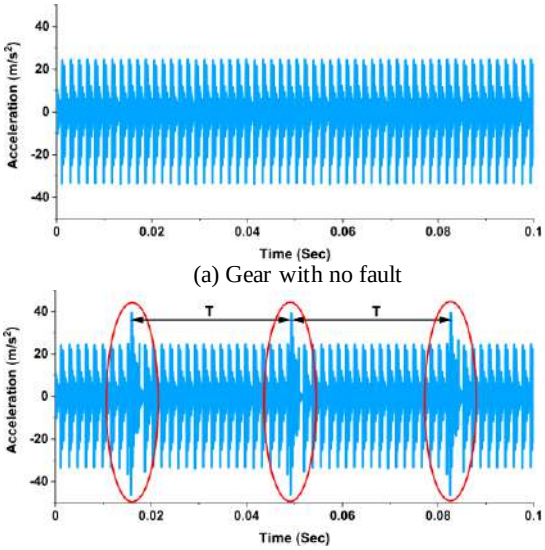

(a) Gear with no fault

(b) Gear with fault

Figure 5. Simulated Vibration Response at 1800rpm

applicability of this approach in gear fault detection, gearbox test rig having different gear geometric parameters than the one used to obtain the simulated data is to be employed for generating the testing/validation data. Figure 6 shows the gearboxexperimental setup used to collect the validation data. Validation data for normal and faulty conditions are collected at different load and speed conditions. The gear test rig has spur gear having full depth involute profile and has 25 and 61 number of teeth on pinion and gear respectively and 20^0 pressure angle, 4 mm module, 20 mm width. An electric motor drives the pinion, and a load is applied at the driven end using the magnetic brake. Tri-axial accelerometer mounted on the gearbox is connected to the OROS data acquisition system to collect the vibration data. Validation or testing data contains an equal number of samples of normal and faulty gear condition.

5. FEATURE ETRACTION AND SELECTION

Numerous features have been proposed in the literature for gear fault diagnosis using time domain, frequency

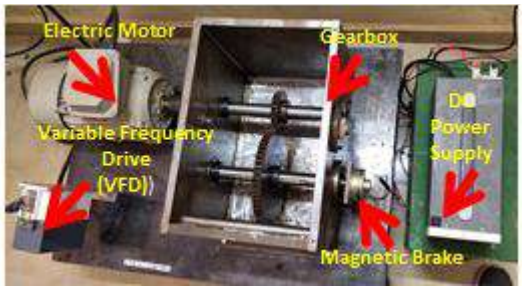

Figure 6. Gearbox experimental test rig

domain, wavelet decomposition and Empirical Mode Decomposition etc. In the present work, wavelet decomposition and EMD are used to process vibration signals. A signal is decomposed in 3 levels using the db5 mother wavelet function, and also the signal is processed using EMD to obtain the IMFs. Statistical features Skewness, Kurtosis, Root Mean Square (RMS) Crest Factor, Shape Factor, Impulse Factor and Clearance Factor are extracted from all three decomposition levels of wavelet and IMF's of EMD. Equations (26)-(32) presents the mathematical expression for calculating these features.

In literature different methods of feature reduction are available such as Principal Component Analysis (PCA), Factor Analysis (FA), Independent component analysis (ICA), High correlation between two columns. These methods were utilized for feature reduction but application of first three methods i.e. PCA, FA and ICA didn't yield satisfactory results. As PCA is a widely used feature reduction technique, results obtained using this is presented here.

5. 1. Principal Component Aanalysis (PCA) PCA is a feature dimensionality reduction technique which is used for the compression and classification of the data. The dimensionality of data set is reduced by finding the new variables that are smaller than the original data set and retain most of the information. These new variables are called as the principal components which are uncorrelated.

In this paper for feature reduction high correlation between two columns method is adopted. In which correlation between the extracted features is determined. Features having high correlation coefficient are linearly dependent and have the same effect as the dependent variable. Therefore, one of the two features having high correlation coefficients is removed. The remaining features are then fed one by one to ML algorithms and a trial and error approach is adopted to select the features giving best results. Table 2 presents a list of selected features. The extracted features from both simulated and experimental data are normalized to the zero mean and to a range of ±1 to prepare training and testing data set.

$$\boldsymbol{Skewness}(\boldsymbol{SK_a}) = \frac{\sum_{n=1}^{N}(a(n)-\mu_a)^3}{(N-1)\sigma_a{}^3} \quad (26)$$

$$\boldsymbol{Kurtosis}(\boldsymbol{K_a}) = \frac{\sum_{n=1}^{N}(a(n)-\mu_a)^4}{(N-1)\sigma_a{}^4} \quad (27)$$

$$\boldsymbol{Root\ Mean\ Square}(\boldsymbol{a_{rms}}) = \sqrt{\frac{\sum_{n=1}^{N}(a(n))^2}{N-1}} \quad (28)$$

$$\boldsymbol{Crest\ Factor} = \frac{a_p}{a_{rms}} \quad (29)$$

$$\boldsymbol{Shape\ Factor}\ (\boldsymbol{SF_a}) = \frac{a_{rms}}{\frac{1}{N}\sum_{n=1}^{N}|a(n)|} \quad (30)$$

TABLE 2. Selected Extracted Features

Feature Extraction Method	Features
Wavelet Transform	1st level Detailed Coefficients - Crest Factor
	3rd Level Detailed Coefficients – Skewness
	3rd Level Approximation Coefficients - Crest Factor
Empirical Mode Decomposition	IMF2 – RMS
	IMF4 – RMS, Shape Factor, Kurtosis
	IMF6 – Clearance Factor, Impulse Factor, Kurtosis
	IMF7 – Kurtosis
	IMF8 – Shape Factor

$$\boldsymbol{Impulse\ Factor}(\boldsymbol{IF_a}) = \frac{a_p}{\frac{1}{N}\sum_{n=1}^{N}|a(n)|} \quad (31)$$

$$\boldsymbol{Clearance\ Factor}(\boldsymbol{CLF_a}) = \frac{a_p}{\left(\frac{1}{N}\sum_{n=1}^{N}\sqrt{|a(n)|}\right)^2} \quad (32)$$

6. RESULTS AND DISCUSSION

A simulated vibration data is obtained for different load and speed conditions, as described in section 3. While getting the vibration data single fault is considered on a single pinion tooth. Figure 4(a-b) shows the TVMS for the healthy and faulty gear, respectively, for the one pinion revolution. The contact ratio of gear is around 1.6, i.e. for 60% of duration two pairs of teeth are in contact and hence the increase in TVMS in this region. Figure 4(a) shows the TVMS for the healthy gear, which shows a similar pattern for all the tooth engagements. However, for the faulty case (Figure 4(b)), when faulty tooth engages decrease in the TVMS is observed for the duration of engagement of faulty tooth. The faulty tooth contact region is highlighted in Figure 4(b). This change in the TVMS affects the vibration response of the gear. This variation in vibration response of normal and faulty gear is clearly shown in Figure 5(a-b), respectively. In Figure 5(b) the part of the vibration response whenever faulty tooth engages is highlighted. As the fault is considered on the pinion, for every pinion rotation this faulty tooth will come in contact and hence the change in vibration response. *T* in Figure 5(b) represents the time period for one pinion rotation. To improve the exactness of the simulated data towards the actual data noise is added. These signals are then processed using the DWT and EMD, and total 84 statistical features are extracted from all levels of decomposition of DWT and IMF's of EMD. To reduce the dimensionality of the dataset

Principal Component Analysis (PCA) was employed, and ML algorithms were tested for a different number of principal components, and its classification accuracies were obtained. Figure 7 shows the testing accuracy obtained for all three ML techniques for a different number of principal components. This figure indicates that accuracy obtained using PCA for a different number of components was between 65 and 78% for all three classifiers. These accuracy values obtained using PCA were not satisfactory. Therefore, to reduce the dimensionality of the dataset, a different method is utilized. In this, a correlation among the extracted features is determined. One of the two features having high correlation coefficients is removed as features having high correlation coefficient are linearly dependent and have the same effect as the dependent variable. Remaining features are then fed one by one to train the ML algorithm and features giving best results are selected. Table 2 presents a list of selected features.

The ML algorithms are trained using these selected features, and ten cross-validation accuracy is obtained. The ML algorithm's parameter tuning is done based on simulated data and a grid search algorithm. For the wider applicability of the simulation-driven approach, ML algorithms trained using simulated data is validated by experimental data generated using the gearbox test rig having different gear geometric parameters than the one used to create the simulated data. The classifier accuracy is a metric utilized in this study for the evaluation of the classification algorithm. Figure 8 shows training and testing accuracies obtained for SVM, MLP and RF machine learning algorithms.

Training accuracy of more than 90% and testing accuracy of more than 87% is obtained for all the three classifiers. The highest training and testing accuracy of 95 and 90% is obtained using the RF classifier. The values of accuracies for all three classifiers imply the applicability of the simulation-driven approach for gear fault detection. The performance of the proposed simulation-driven approach is compared with the existing data-driven approach. ML algorithms are trained and tested using experimental data in the data-driven

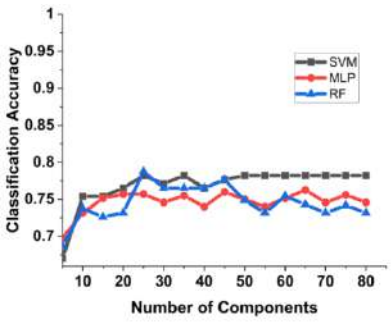

Figure 7. Testing Accuracy of ML algorithms for different principal components

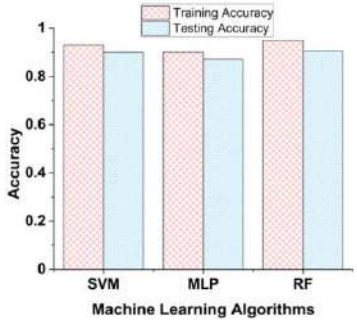

Figure 8. Accuracies by using Simulation Driven Approach

approach. Figure 9 shows the accuracies obtained using the data-driven approach. The accuracies obtained for all the three classifiers using data-driven and simulation-driven approach are comparable, and there is very little difference in their accuracies. Therefore, the simulation-driven approach can be applied for the gear fault classification when actual historical data is not available.

Classifier accuracy is considered as a metric for the evaluation of the ML algorithm. However, for the complete performance evaluation of the classification algorithm precision and recall are also evaluated. Precision is the ratio of correctly classified positive cases to the total number of positively classified cases and recall is the ratio of correctly classified positive cases and the total number of actual positive cases. Figure 10 shows the values of precision and recall for each classifier. For all the three classifiers precision and recall values are more than 87%. The higher values of precision mean the less number of instances are classified as faulty when it is normal, that is fewer chances of false alarms for the maintenance and avoid undue maintenance task. The higher value of recall increases the chances of positive alarms as lesser instances are classified as normal when it is faulty, to carry out the maintenance task when it is actually required. All the three classifiers show the considerable values of precision and recall (Figure 10), which increases the confidence in the simulation-driven approach presented in this paper for gear fault detection. Precision and recall values for the RF classifier are slightly higher than the other classifiers.

Another metric used for the evaluation of the binary classification is the Area under the receiver operating characteristic curve (AUC). The curve of true positive rate Vs false positive rate at different classification threshold values is known as the Receiver Operating Characteristic curve abbreviated as ROC. Figure 11 depicts the ROC curve for the three classifiers. The AUC values are 0.97, 0.92 and 0.98 for SVM, MLP and RF, respectively. A higher value of AUC means that classifier is confident that randomly selected positive instance is positive than the randomly selected negative instances as positive. The ROC curve (Figure 11) and the AUC values obtained for three classifiers shows the agreement with

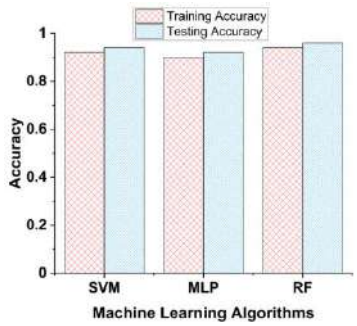

Figure 9. Accuracies by using Data Driven Approach

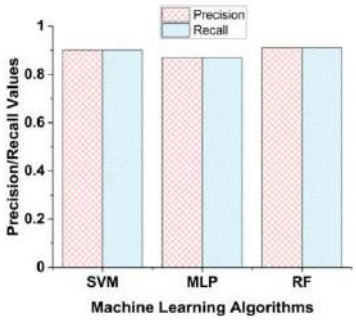

Figure 10. Precision and Recall for SVM, MLP and RF

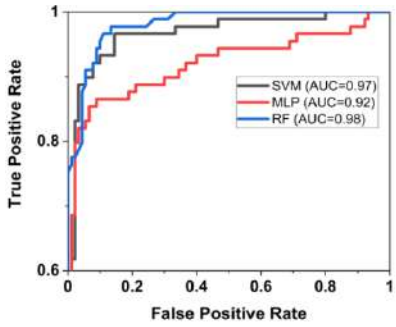

Figure 11. ROC curve for SVM, MLP and RF classifiers

the applicability of the simulation-driven approach for the gear fault classification.

7. CONCLUSION

Condition monitoring and fault diagnosis of the gearbox using the machine learning techniques utilize the data-driven approach, but the requirement of in-service/experimental data for the training of ML algorithm has prevented its widespread application in the industry. Also, for the better training of ML algorithm high diverse data is required. The present paper implements a simulation-driven approach for the spur gear fault detection and validates this approach using the experimental data. Simulated vibration response is generated using a gearbox dynamic model to produce the extensive variety of data of at different operating and fault condition. Firstly, TVMS is calculated for normal and faulty gear condition. TVMS is reduced when faulty gear tooth engages, and this results in the change in vibration response. ODE15s solver function in Matlab is employed to solve the equations of motion to obtain the simulated vibration response. This simulated vibration data is not having any noise, but in actual practical application the signal is masked with environmental noise. Therefore, a pink noise is added to improve the exactness of the simulated vibration signals to the actual vibration signals. Pink noise is added because it is present everywhere in nature, electronics, machinery, and numerous other fields. These signals are then processed using the EMD and DWT signal processing techniques. Features are extracted from simulated data and fed for the training of ML algorithm. For the wider applicability of the simulation-driven approach, ML algorithm trained using the simulated data is validated by using experimental data collected from a test rig having different gear parameters. The results show that the simulation-driven approach gives the considerable training and testing accuracy for all the three classifiers. This approach is then compared with the existing data driven approach and the results obtained are comparable. However, the performance of the this approach can be improved by considering the dynamic model with high degrees of freedom and considering more effect such as friction, gyroscopic effect etc. In the present era of Industry 4.0 the proposed method has the potential to improve the machine learning based condition monitoring of the gearbox using simulated data. However, the simulated data cannot replace the experimental data, but it can serve as a starting point for the gear fault diagnosis when no historical data is available. The implementation of this approach will help in monitoring the condition of the gearbox from the day of installation.

8. REFERENCES

1. Salameh, J. P., Cauet, S., Etien, E., Sakout, A., & Rambault, L., "Gearbox condition monitoring in wind turbines: A review", ***Mechanical Systems and Signal Processing***, Vol. 111, (2018), 251-264. DOI: 10.1016/j.ymssp.2018.03.052
2. Wang, K., "Intelligent predictive maintenance (IPdM) system–Industry 4.0 scenario", ***WIT Transactions on Engineering Sciences***, Vol. 113, (2016), 259-268. DOI: 10.2495/IWAMA150301
3. Karimzadeh, A., & Shoghli, O., "Predictive Analytics for Roadway Maintenance: A Review of Current Models, Challenges, and Opportunities", ***Civil Engineering Journal***, Vol. 6, No. 3, (2020), 602-625. DOI: 10.28991/cej-2020-03091495
4. Damuluri, S., Islam, K., Ahmadi, P., & Qureshi, N. S., "Analyzing Navigational Data and Predicting Student Grades Using Support Vector Machine", ***Emerging Science Journal***, Vol. 4, No. 4, (2020), 243-252. DOI: 10.28991/esj-2020-01227

5. Liang X, Zuo MJ, Feng Z., "Dynamic modeling of gearbox faults: A review", ***Mechanical Systems and Signal Processing***, Vol. 98, (2018), 852-876. DOI: 10.1016/j.ymssp.2017.05.024
6. Lei Y, Yang B, Jiang X, Jia F, Li N, Nandi AK., "Applications of machine learning to machine fault diagnosis: A review and roadmap", ***Mechanical Systems and Signal Processing***, Vol. 138, (2020), 106587. DOI: 10.1016/j.ymssp.2019.106587
7. Samanta, B., "Gear fault detection using artificial neural networks and support vector machines with genetic algorithms", *Mechanical systems and signal processing*, Vol. 18, No. 3, (2004), 625-644. DOI: 10.1016/S0888-3270(03)00020-7
8. Samanta B, Al-Balushi KR, Al-Araimi SA., "Artificial neural networks and genetic algorithm for bearing fault detection", ***Soft Computing***, Vol. 10, No. 3, (2006), 264-271. DOI: 10.1007/s00500-005-0481-0
9. Tyagi, S., Panigrahi, S. K., "A DWT and SVM based method for rolling element bearing fault diagnosis and its comparison with Artificial Neural Networks", ***Journal of Applied and Computational Mechanics***, Vol. 3, No. 1, (2017), 80-91. DOI: 10.22055/JACM.2017.21576.1108
10. Sanz J, Perera R, Huerta C., "Gear dynamics monitoring using discrete wavelet transformation and multi-layer perceptron neural networks", ***Applied Soft Computing***, Vol. 12, No. 9, (2012), 2867-2878. DOI: 10.1016/j.asoc.2012.04.003
11. Shen Z, Chen X, Zhang X, He Z., "A novel intelligent gear fault diagnosis model based on EMD and multi-class TSVM", ***Measurement***, Vol. 45, No. 1, (2012), 30-40. DOI: 10.1016/j.measurement.2011.10.008
12. Shao R, Hu W, Huan X, Chen L., "Multi-damage feature extraction and diagnosis of a gear system based on higher order cumulant and empirical mode decomposition", ***Journal of Vibration and Control***, Vol. 21, No. 4, (2015), 736-754. DOI: 10.1177/1077546313482342
13. Li, X., Han, L., Xu, H., Yang, Y. and Xiao, H., "Rolling Bearing Fault Analysis by Interpolating Windowed DFT Algorithm", ***International Journal of Engineering, Transactions A: Basics***, Vol. 32, No. 1, (2019), 121-126. DOI: 10.5829/ije.2019.32.01a.16
14. Dhamande LS, Chaudhari MB., "Compound gear-bearing fault feature extraction using statistical features based on time-frequency method", ***Measurement***, Vol. 125, (2018), 63-77. DOI: 10.1016/j.measurement.2018.04.059
15. Attaran, B., Ghanbarzadeh, A. and Moradi, S., "A Novel Intelligent Fault Diagnosis Approach for Critical Rotating Machinery in the Time-frequency Domain", ***International Journal of Engineering, Transactions A: Basics***, Vol. 33, No. 4, (2020), 668-675. DOI: 10.5829/IJE.2020.33.04A.18
16. Bajric R, Zuber N, Skrimpas GA, Mijatovic N., "Feature extraction using discrete wavelet transform for gear fault diagnosis of wind turbine gearbox", Shock and Vibration, (2016), DOI: 10.1155/2016/6748469
17. Han T, Jiang D., "Rolling bearing fault diagnostic method based on VMD-AR model and random forest classifier", ***Shock and Vibration***, (2016), DOI: 10.1155/2016/5132046
18. Cerrada M, Zurita G, Cabrera D, Sánchez RV, Artés M, Li C., "Fault diagnosis in spur gears based on genetic algorithm and random forest", ***Mechanical Systems and Signal Processing***, Vol. 70-71, (2016), 87-103. DOI: 10.1016/j.ymssp.2015.08.030
19. Patil S, Phalle V., "Fault Detection of Anti-friction Bearing using Ensemble Machine Learning Methods", ***International Journal of Engineering, Transactions B: Applications***, Vol. 31, No. 11, (2018), 1972-1981. DOI: 10.5829/ije.2018.31.11b.22
20. Bartelmus W., "Mathematical modelling and computer simulations as an aid to gearbox diagnostics", ***Mechanical Systems and Signal Processing***, Vol. 15, No. 5, (2001), 855-871. DOI: 10.1006/mssp.2001.1411
21. Howard I, Jia S, Wang J., "The dynamic modelling of a spur gear in mesh including friction and a crack", ***Mechanical Systems and Signal Processing***, Vol. 15, No. 5, (2001), 831-853. DOI: 10.1006/mssp.2001.1414
22. Abouel-seoud SA, Dyab ES, Elmorsy MS., "Influence of tooth pitting and cracking on gear meshing stiffness and dynamic response of wind turbine gearbox", ***International Journal of. Science and Advanced. Technology***, Vol. 2, No. 3, (2012), 151-165. DOI:
23. Mohammed, O. D., Rantatalo, M., & Aidanpää, J. O., "Dynamic modelling of a one-stage spur gear system and vibration-based tooth crack detection analysis", ***Mechanical Systems and Signal Processing***, Vol. 54-55, (2015), 293-305. DOI: 10.1016/j.ymssp.2014.09.001
24. Parey A, El Badaoui M, Guillet F, Tandon N., "Dynamic modelling of spur gear pair and application of empirical mode decomposition-based statistical analysis for early detection of localized tooth defect", ***Journal of Sound and vibration***, Vol. 294, No. 3, (2006), 547-561. DOI: 10.1016/j.jsv.2005.11.021
25. He Q, Li P, Kong F., "Rolling bearing localized defect evaluation by multiscale signature via empirical mode decomposition", ***Journal of Vibration and Acoustics***, Vol. 134. No. 6, (2012). DOI: 10.1115/1.4006754
26. Handikherkar V.C., Phalle V.M., "Vibration Analysis Based Spalling Defect Severity Assessment of Spur Gearbox Using a Dynamic Model", ***Developments and Novel Approaches in Nonlinear Solid Body Mechanics***, Vol. 130, (2020), 363-375. DOI: 10.1007/978-3-030-50460-1_20
27. Wu S, Zuo MJ, Parey A., "Simulation of spur gear dynamics and estimation of fault growth", ***Journal of Sound and Vibration***, Vol. 317, No. (3-5), (2008), 608-624. DOI: 10.1016/j.jsv.2008.03.038
28. Chaari F, Baccar W, Abbes MS, Haddar M., "Effect of spalling or tooth breakage on gearmesh stiffness and dynamic response of a one-stage spur gear transmission", ***European Journal of Mechanics-A/Solids***, Vol. 27, No. 4, (2008), 691-705. DOI: 10.1016/j.euromechsol.2007.11.005
29. Bak, P., Tang, C., & Wiesenfeld, K., "Self-organized criticality: An explanation of the 1/f noise", ***Physical Review Letters***, Vol. 59, No. 4, (1987), 381. DOI: 10.1103/PhysRevLett.59.381
30. Chen, B., Yan, Z., & Chen, W., "Defect detection for wheel-bearings with time-spectral kurtosis and entropy", ***Entropy***, Vol. 16, No. 1, (2014), 607-626. DOI: 10.3390/e16010607

Persian Abstract

چکیده

نظارت بر شرایط مبتنی بر یادگیری ماشین (ML) و تشخیص عیب تجهیزات صنعتی سناریوی فعلی برای نگهداری در دوره Industry-4.0 است. استفاده از تکنیک های ML برای تشخیص خودکار عیب ، خرابی غیرمنتظره سیستم را به حداقل می رساند. با این حال ، این تکنیک ها به شدت به داده های تاریخی تجهیزات برای آموزش آن متکی هستند که کاربرد گسترده آن را در صنعت محدود می کند. از آنجا که داده های تاریخی برای هر ماشین صنعتی در دسترس نیست و تولید داده ها به صورت آزمایشی برای هر شرایط خطا قابل استفاده نیست. بنابراین ، این چالش برای استفاده از چرخ دنده با نقص دندان حل می شود. در این مقاله ، الگوریتم های ML با استفاده از داده های ارتعاش شبیه سازی شده گیربکس آموزش داده شده و با داده های تجربی آزمایش می شوند. داده های شبیه سازی شده برای گیربکس با شرایط کارکرد و خطای مختلف تولید می شود. از یک مدل دینامیکی گیربکس برای تولید داده های ارتعاش شبیه سازی شده برای شرایط دنده نرمال و معیوب استفاده شده است. یک نویز صورتی به داده های شبیه سازی شده اضافه می شود تا دقت داده های درست را بهبود بخشد. علاوه بر این ، این داده های شبیه سازی شده با استفاده از تجزیه حالت تجربی و تغییر شکل موجک گسسته پردازش می شوند و ویژگی ها استخراج می شوند. این ویژگی ها سپس به آموزش تکنیک های مختلف ML کاملاً ثابت مانند ماشین بردار پشتیبان ، جنگل تصادفی و پرسپترون چندلایه منتقل می شود. برای تأیید این روش ، الگوریتم های ML آموزش دیده با استفاده از داده های تجربی آزمایش می شوند. نتایج بیش از ۸۷٪ دقت با هر سه الگوریتم را نشان می دهد. عملکرد مدل آموزش دیده با استفاده از منحنی دقت ، فراخوان و ROC ارزیابی می شود. این معیارها نتایج مثبتی را برای کاربرد این روش در تشخیص عیب دنده نشان می دهد.

International Journal of Engineering

Journal Homepage: www.ije.ir

Magnetohydrodynamic (MHD) Flow in a Channel Including a Rotating Cylinder

F. Mobadersani*, S. Bahjat

Department of Renewable Energy, Faculty of Mechanical Engineering, Urmia University of Technology, Urmia, Iran

P A P E R I N F O

Paper history:
Received 02 July 2019
Received in revised form 16 October 2020
Accepted 29 October 2020

Keywords:
Nanofluid
Heat Transfer
Magnetohydrodynamics
Finite Element
Rotational Cylinder

A B S T R A C T

Heat transfer analysis in channels and enclosures has significant attention nowadays. In the present work, fluid flow and heat transfer of a vertical channel consisting of a rotating cylinder utilizing nanofluid have been studied, numerically. Uniform magnetic field has been applied to the fluid field. Different cylinder rotation directions, Hartmann number and rotational velocity of cylinder configurations have been considered. The results indicate that by increasing the Hartmann number, for low values of non-dimensional angular velocity the average Nusselt number increases. In addition, in higher Hartmann numbers, the average Nusselt number does not change remarkably with non-dimensional angular velocity. Furthermore, studying lift and drag coefficients demonstrate that in a constant Hartmann number, the highest drag coefficient takes place in maximum cylinder angular velocity. Additionally, almost uniform distribution of drag coefficient can be seen in higher Hartmann numbers. The numerical results have been compared with the previously reported results. This comparison illustrates excellent agreement between them.

***doi**: 10.5829/ije.2021.34.01a.25*

1. INTRODUCTION

Poor thermal characteristics of working fluids such as water, ethylene glycol, and oil are the main obstacle of the convectional heat transfer. In order to assess high thermal conductivity, the idea of adding metallic and non-metallic particles to common fluids was already existed. Because of the low development of technology in the past, they added coarse particles with average diameters of the millimeter and micrometer to base fluids to improve their thermal characteristics. Adding coarse particles to the convectional fluids causes to increase pressure drop, gravitic sedimentation, clog the entrance of channels and pipes and erosion of the walls. One of the innovative ways to overcome these problems is adding the metallic – nonmetallic nanoscale particles to the base fluids and make nanofluids. Nanofluids are combinations of nanoparticles with a maximum volume fraction of 5% added to the base fluids. Additionally, the average diameters of those particles are lesser than 100nm. Furthermore, the general types of nanoparticles which used in nanofluids are oxides of metallic and metallic particles such as alumina, Cu, CuO, magnetite and organic particles such as carbon nanotubes. In addition to high stability of nano size particles in base fluid, using nanofluids leads to increase thermal conductivity of fluid significantly [1-6]. Many researchers have investigated the influences of adding those particles on applications such as drug targeting, heat exchangers, power plants and etc. Gravndyan et al. [7] have investigated the effects of ribs mounted on channel surface utilizing Ti_2O/water nanofluid. They reported in all values of Reynolds number and ribs aspects ratios, increasing volume fraction of nanoparticle raise the average Nusselt number. In another study, Ahmadi et al. [8] reported, despite pressure drop increases, augmenting nanoparticles volume concentration has positive impacts on thermal conductivity. Thermal conductivity increase with temperature increment is reported in Bahiraei and Mashaei investigation [9]. They reported that by utilizing small nanoparticle, effects of temperature on thermal conductivity increase. Ho et al. [10] experimentally investigated the effects of nanoparticle volume fraction on heat transfer efficiency in a microchannel. The results

*Corresponding Author Institutional Email: *f.mobadersani@mee.uut.ac.ir* (F. Mobadersani)

Please cite this article as: F. Mobadersani, S. Bahjat C. Y., Magnetohydrodynamic (MHD) Flow in a Channel Including a Rotating Cylinder , International Journal of Engineering, Transactions A: Basics Vol. 34, No. 01, (2021) 224-233

indicate that in a special Reynolds number by raising nanoparticle volume fraction, the average Nusselt number enhances. In addition, they obtained 53% increment in average Nusselt at Re=1641 and volume fraction of 1% in comparison with the pure water. Additionally, Heydari and Kermani [11] studied effects of blocks attached to the bottom wall of the channel utilizing nanofluid. Their results show that in all values of Reynolds number and volume fractions of nanoparticles, augmenting numbers of blocks enhances top wall average Nusselt number. Khanafer et al. [12] presented a numerical simulation of nanofluid inside a cavity for various Grashof numbers. They reported increases in volume fraction of nanoparticles at any Grashof number enhances the average Nusselt number, although intensity of increasing is severe in higher Grashof numbers. Santra et al. [13] studied the influences of Reynolds number and volume fraction of nanoparticles on the flow and heat transfer in two parallel plates utilizing nanofluid as Newtonian and non-Newtonian fluid. Their results show that the enhancement of the average Nusselt number due to increasing volume fraction in consideration of non-Newtonian fluid is higher than Newtonian fluid. Roslan et al. [14] numerically investigated square enclosure with a inner rotating cylinder utilizing different types of the nanoparticles. They reported Ag particles shows better efficiency in convection heat transfer with comparison to Ti_2O, Cu and Al_2O_3. In addition, their results illustrate cylinder rotation in any direction in case of R=0.2, (dimensionless radius of the cylinder) has negative impacts on the average Nusselt number.

Hydrodynamical study of electrical conductive liquids under the influence of magnetic field is called Magnetohydrodynamics. In the other word, MHD is the investigation of the flow-structure by applying a uniform magnetic field and considering effects of Lorentz force. Lorentz force is the magnetic force which rises from the electrical conductivity of fluids and acts as a braking force. MHD flows has a wide range of industrial applications such as crystal growth, metal casting, polymer industry, and liquid metal cooling blankets for fusion reactors[15-19]. Aminossadati et al. [20] reported by applying a uniform magnetic field, horizontal velocity profile along centerline of the channel decrease whereas at the vicinity of the walls increase. As well as, they indicated that raising Hartmann number augments the convective heat transfer. Heydari et al. [21] numerically investigated the effects of nanoparticles concentration and effects of Lorentz force in the horizontal channel. Their results demonstrate that exerting magnetic field leads to reduce temperature layer thickness and consequently accelerate heat removal from the surface. Additionally, they reported raising nanoparticles volume fraction enhances the temperature layer thickness. Selimefendigil and Oztop [22] studied numerically mixed convection lid-driven enclosure with a inner rotating cylinder. Their results show that existing magnetic field has negative impacts on convective heat transfer. Furthermore, augmenting Richardson number results in average Nusselt number enhancement. Hosseini et al. [23] reported, the uniform magnetic field affects the velocity profile and forces it to be uniform. On the other hand, the magnetic field increases velocity gradient near the walls which results in convective heat transfer improvement. Oztop et al. [24] numerically investigated the effects of Grashof and Hartmann numbers in lid-driven cavity. Their results indicate that at any Grashof number, the existence of a magnetic field causes convective heat transfer decrement. Aminfar et al. [25] numerically investigated the effects of magnetic fields in straight duct utilizing ferrofluid by considering both FHD and MHD approach. They concluded that by increasing the strength of Lorentz force, the velocity profile becomes flat and velocity gradient near the walls enhances. Consequently, the Nusselt number and friction coefficient rise due to increasing the strength of Lorentz force. Ma et al. [26] investigated flow in channel with the extended surface under the influence of a uniform magnetic field utilizing hybrid nanoparticles. They observed that Lorentz force strongly affects the structure of flow and weaken the strength of the recirculation zones. Besides, augmenting the magnetic field results in better convection heat transfer. Mahmoudi et al. [27] concluded that applying a uniform magnetic field leads to reduction in convection heat transfer. Additionally, in all values of Hartmann and Rayleigh numbers, by raising volume fraction of nanoparticles the average Nusselt number enhances.

To the best of our knowledge, there is no prior study on the MHD flow in the vertical channel with an inner rotating cylinder utilizing nanofluid. The goal of our study is to investigate the effects of magnetic field and cylinder rotation on convective heat transfer.

2. MATHEMATICAL FORMULATION

Schematic view of the study domain is represented in Figure 1. Consider two parallel vertical plates with wide H and length L=3.5H that Cu-H_2O nanofluid flows through it. A rotating cylinder has been considered between the plates. The left wall of the channel is assumed to be adiabatic, while the right wall maintained at constant higher temperature T_h. No-slip boundary conditions are imposed on the left and right walls. Nanofluid with temperature of T_{in} (T_h>T_{in}) and velocity, V_{in} , flows through the domain. An adiabatic cylinder with a diameter of d=0.4H is placed in the channel with the coordinance (0.5H, 0.5L) and rotates at constant angular velocity ω .Uniform horizontal magnetic field applies to the channel. In addition, the gravitational

acceleration acts in the opposite y-direction. The geometry is assumed to be long enough to ignore end effects at the z-direction and can be considered as 2D dimensions. Ultrafine nanoparticles are assumed to have uniform shape and size. In addition, fluid phase and nanoparticles are assumed to be in thermal equilibrium with no-slip velocity between them. Thermophysical properties of the water and nanoparticles are taken to be constant except for density which changes linearly with Boussinesq approximation. The thermophysical properties of water and nanoparticles are shown in Table 1. According to the above assumptions, the continuity, momentum, and energy equations for the laminar, Newtonian fluid, incompressible and steady state flow by considering Boussinesq approximation with negligible viscous dissipation and Joule heating can be written as:

$$\frac{\partial u}{\partial x}+\frac{\partial v}{\partial y}=0 \tag{1}$$

$$u\frac{\partial u}{\partial x}+v\frac{\partial u}{\partial y}=-\frac{1}{\rho_{nf}}\frac{\partial p}{\partial x}+\nu_{nf}\left(\frac{\partial^2 u}{\partial x^2}+\frac{\partial^2 u}{\partial y^2}\right) \tag{2}$$

$$u\frac{\partial v}{\partial x}+v\frac{\partial v}{\partial y}=-\frac{1}{\rho_{nf}}\frac{\partial p}{\partial y}+\nu_{nf}\left(\frac{\partial^2 v}{\partial x^2}+\frac{\partial^2 v}{\partial y^2}\right) -\frac{\sigma_{nf}B^2}{\rho_{nf}}v+\beta_{nf}g(T-T_{in}) \tag{3}$$

$$u\frac{\partial T}{\partial x}+v\frac{\partial T}{\partial y}=\alpha_{nf}\left(\frac{\partial^2 T}{\partial x^2}+\frac{\partial^2 T}{\partial y^2}\right) \tag{4}$$

Density and the specific heat capacity and the thermal expansion of the nanofluid are defined, respectively as [28-30]:

$$\rho_{nf}=(1-\phi_p)\rho_{bf}+\phi_p\rho_p \tag{5}$$

$$(\rho c_p)_{nf}=(1-\phi_p)(\rho c_p)_{bf}+\phi_p(\rho c_p)_p \tag{6}$$

$$(\rho\beta)_{nf}=(1-\phi_p)(\rho\beta)_{bf}+\phi_p(\rho\beta)_p \tag{7}$$

where ϕ is volume fraction of nanoparticles and the subscripts 'bf', 'p' and 'nf' denote the base fluid, nanoparticle and nanofluid, respectively.

Furthermore, dynamic viscosity of the nanofluid according to the Brinkman [31] model is represented as:

$$\mu_{nf}=\frac{\mu_{bf}}{(1-\phi)^{2.5}} \tag{8}$$

Thermal conductivity of the nanofluid by using uniform spherical shape of nanoparticles according to Wasp [32] can be expressed as:

$$\frac{k_{nf}}{k_{bf}}=\frac{k_p+2k_{bf}-2\phi_p(k_{bf}-k_p)}{k_p+2k_{bf}+\phi_p(k_{bf}-k_p)} \tag{9}$$

Electrical conductivity of the nanofluid due to the Maxwell [33] model is:

$$\frac{\sigma_{nf}}{\sigma_{bf}}=1+\frac{3\left(\frac{\sigma_p}{\sigma_{bf}}-1\right)\phi_p}{\left(\frac{\sigma_p}{\sigma_{bf}}+2\right)-\left(\frac{\sigma_p}{\sigma_{bf}}-1\right)\phi_p} \tag{10}$$

2. 1. Non-dimensional Equations By defining non-dimensional parameters and substituting in the equations of (1-4), the dimensionless equations can be written as follows:

$$X=\frac{x}{2H},Y=\frac{y}{2H},U=\frac{u}{V_{in}},V=\frac{v}{V_{in}}$$
$$P=\frac{p}{\rho V_{in}^2},\theta=\frac{T-T_{in}}{T_h-T_{in}},\mathrm{Re}=\frac{2HV_{in}}{\nu_{nf}},\mathrm{Pr}=\frac{k_{nf}}{\rho_{nf}c_{p,nf}} \tag{11}$$
$$Ha=2BH\sqrt{\frac{\sigma_{nf}}{\mu_{nf}}},Gr=\frac{g\beta_{nf}(T_h-T_{in})(2H)^3}{\nu_{nf}^2}$$

$$\frac{\partial U}{\partial X}+\frac{\partial V}{\partial Y}=0 \tag{12}$$

$$\frac{\rho_{nf}}{\rho_{bf}}\left(U\frac{\partial U}{\partial X}+V\frac{\partial U}{\partial Y}\right)=-\frac{\partial P}{\partial X}+\frac{\mu_{nf}}{\mu_{bf}}\frac{1}{\mathrm{Re}}\left(\frac{\partial^2 U}{\partial X^2}+\frac{\partial^2 U}{\partial Y^2}\right) \tag{13}$$

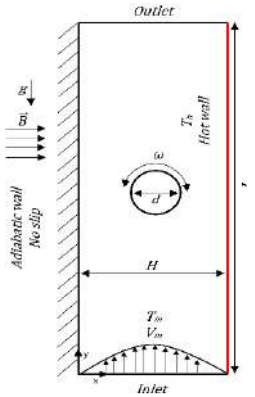

Figure 1. Schematic diagram of vertical channel with an inner rotating cylinder

TABLE 1. Thermophysical properties of water and Cu nanoparticles

	$\rho(\frac{kg}{m^3})$	$c_p(\frac{J}{kgK})$	$k(\frac{W}{mK})$	$\sigma(\frac{1}{\Omega.m})$	$\beta(\frac{1}{K})$
Water	996	4178	0.615	0.05	2.94×10^{-4}
Copper	8933	385	401	5.96×10^{7}	1.67×10^{-5}

$$\frac{\rho_{nf}}{\rho_{bf}}\left(U\frac{\partial V}{\partial X}+V\frac{\partial V}{\partial Y}\right)=-\frac{\partial P}{\partial Y}+\frac{\mu_{nf}}{\mu_{bf}}\frac{1}{\mathrm{Re}}\left(\frac{\partial^2 V}{\partial X^2}+\frac{\partial^2 V}{\partial Y^2}\right)-\frac{\sigma_{nf}}{\sigma_{bf}}\frac{Ha^2}{\mathrm{Re}}V+\frac{\beta_{nf}}{\beta_{bf}}\frac{Gr}{\mathrm{Re}^2}\theta \quad (14)$$

$$\frac{(\rho c_p)_{nf}}{(\rho c_p)_{bf}}\left(U\frac{\partial \theta}{\partial X}+V\frac{\partial \theta}{\partial Y}\right)=\frac{k_{nf}}{k_{bf}}\frac{1}{\mathrm{Re}\,\mathrm{Pr}}\left(\frac{\partial^2 \theta}{\partial X^2}+\frac{\partial^2 \theta}{\partial Y^2}\right) \quad (15)$$

2. 2. Boundary Conditions Non-dimensional boundary conditions of the channel with an inner rotating cylinder are:

Left wall:

$U=V=0,\ \frac{\partial \theta}{\partial X}=0$ & Right wall: $U=V=0,\ \theta=1$

Inlet condition: $U=0,\ V=1,\ \theta=0$

Cylinder: $\omega=\Omega,\ \frac{\partial \theta}{\partial \eta}=0$

where η is the normal vector to the surface and non-dimensional rotational speed of the cylinder can be obtained from: $\Omega=\frac{\omega d}{2V_{in}}$.

Local Nusselt number along the vertical hot wall of the channel is:

$$Nu_{local}=\frac{-k_{nf}}{k_f}\frac{\frac{\partial \theta}{\partial x}}{(1-\theta_b)} \quad (16)$$

Furthermore, by integrating the local Nusselt number along the hot wall, the average Nusselt number can be expressed as:

$$Nu_{avg}=\frac{2H}{L}\int_0^{\frac{L}{2H}} Nu_{local}\,dY \quad (17)$$

Lift and Drag coefficients over the cylinder due to the Magnus and the flow separation effects are respectively presented as follows:

$$C_L=\frac{2F_{lift}}{\rho_{nf}V_{in}^2 d} \quad (18)$$

$$C_D=\frac{2F_{drag}}{\rho_{nf}V_{in}^2 d} \quad (19)$$

3. NUMERICAL PROCEDURE

Non-dimensional governing Equations 12-15 along with the corresponding non-dimensional boundary conditions are solved by using the Galerkin finite element method. Modification of the computed field variables and leading the residual to be zero over the computational domain is accomplished by using weighted functions.

$$\int_\Omega wf(x)Rd\omega=0 \quad (20)$$

where w, f, R, ω and Ω are weight function, residual, location variables and entire domain, respectively. Using weighted residual scheme, governing PDEs are simplified to integral equations, which are then solved in a matrix by the Newton-Raphson iteration method. The relative error for each field variable (Γ) should satisfy:

$$\left|\frac{\Gamma^{n+1}-\Gamma^n}{\Gamma^{n+1}}\right|<10^{-5} \quad (21)$$

where n represents the iteration number. The velocity components and pressure are discretized by utilizing P2-P1 Lagrange finite elements. In addition, Lagrange quadratic finite element was used to discretize temperature. Unstructured triangular grids are employed to the domain, which consisted higher resolution near the walls and the cylinder to augment precision at positions of higher gradients.

3. 1. Validation To ensure the accuracy of the numerical solution, the problem of Park et al. [34] is modeled to validate the present code results.

Figures 2 and 3 demonstrate the comparison of the streamlines and the isotherm contours versus different Rayleigh numbers for the present work and those of Park et al. [34] Furthermore, Figure 4 illustrates the Nusselt number variation along the walls of the cavity at $Ra=10^3$. According to these figures, the results of the present computational code are precise enough and are in excellent agreement with those of [34].

3. 2. Grid Independency In this study, to find out the solution mesh independency, the domain discretized to various numbers of elements. Figure 5 demonstrates the average Nusselt number in terms of element numbers of 2090, 4608, 7434, 11372, 52032 and 195692. According to this figure, by considering finer elements, results converge to a specific value and do not change significantly by increasing the numbers of

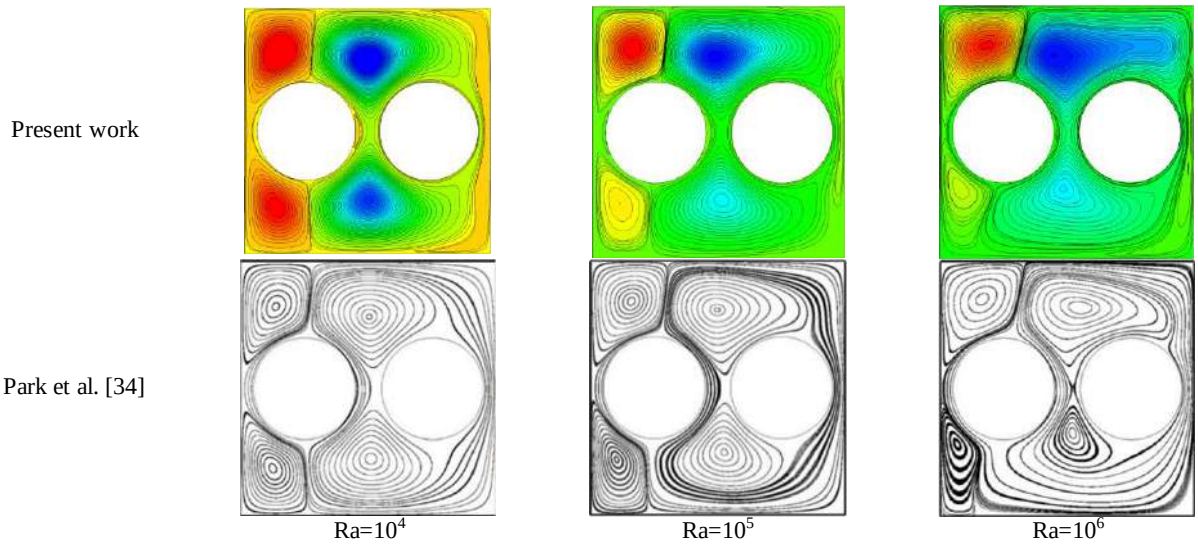

Figure 2. Comparison of streamlines for present work and that of Park et al. [34] in a square cavity with hot and cold inner stationary cylinder for different range of Rayleigh numbers

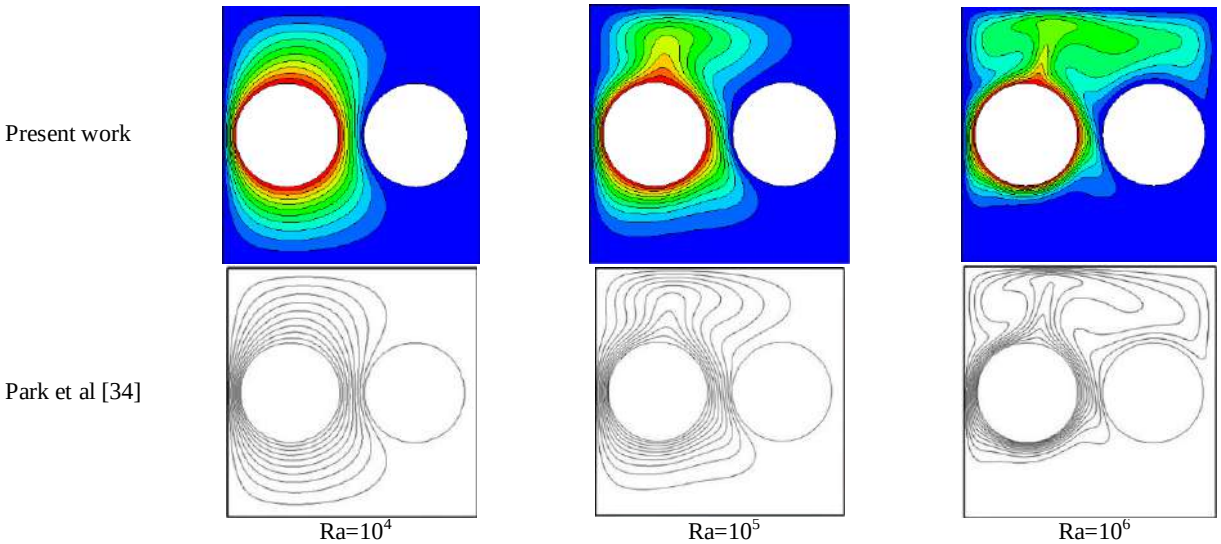

Figure 3. Isotherm contours comparison in square cavity with cold and hot inner stationary cylinder with present work and Park et al. [34] versus varying Rayleigh numbers

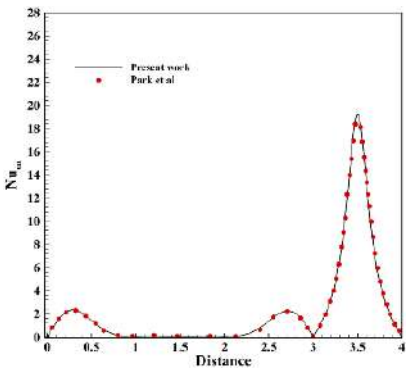

Figure 4. Comparison of the Nusselt number between present work and Park et al. [34] at $Ra=10^3$

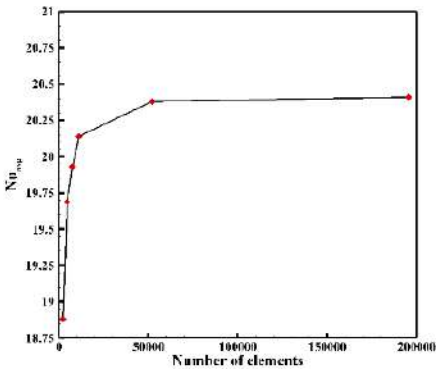

Figure 5. Average Nusselt number versus elements number for Ha = 60 and $\Omega = -10$

elements. As the figure shows, the average difference between Nusselt numbers for 52032 and 195692 grids is less than 0.15%. Thus, the 52032 grid is used in the rest of the simulations.

4. RESULTS AND DISCUSSION

The study aims to investigate the effects of Hartmann number ($0 \leq Ha \leq 60$) and non-dimensional angular velocity of the cylinder ($-10 \leq \Omega \leq 10$) on the fluid flow and heat transfer in the channel. Simulation results are carried out for constant parameters of Re = 200, ϕ =0.04 for all cases.

4. 1. Effects of Hartmann Number Figure 6 illustrates the effects of different Hartmann numbers on the flow structure and isotherm contours. Constant parameters of $\Omega = 3$ and varying Ha = 0, 20, 40, 60 are considered for these simulations. As the streamlines show, in the case of no magnetic field (Ha = 0), a large vortex is formed before the outlet on the hot wall. This vortex is formed because the separation occurs after the cylinder. As it can be observed, by raising the Hartmann number, due to the flow momentum reduction, the flow structure changes to a uniform configuration and the vortices eliminate disappear. In addition, there are two stagnation points in the flow field. The first stagnation point is at front of the cylinder and the second one is located at the left side of the cylinder, due to the counterclock-wise rotation of the cylinder. It can be seen, by augmenting the Hartmann number that locations of the stagnation points change and move toward the centerline of the channel. Despite the flow around the cylinder, the flow far away from the cylinder is not affected by the cylinder rotation in the higher Hartmann numbers. As evident from Figure 6, the cylinder rotation in the center of the channel causes to temperature boundary layer clings to the hot wall and consequently accelerate the convection heat transfer. As it is obvious from streamlines, the cylinder counterclockwise rotation conducts fluid flow from the hot wall to the adiabatic wall and leads to temperature layer thickness increment. Furthermore, at the front of the cylinder, the isotherms are squeezed gradually toward the hot wall by augmenting the Hartmann number. Similarly, the Lorentz force suppress the vorticities behind the cylinder, with this in mind that the size of the recirculation zones restrain as the Hartmann number increase.

Effects of the Hartmann number on the velocity profile at y/L=0.125 are depicted in Figure 7. As the figure shows, the Hartmann number increment results in flattering of the velocity profile at the mid-section of the channel, and accordingly, the velocity gradient adjust the walls increases. Similar conclusions have been reported in previous works as well. [20-21, 23, 25]

Figure 8 reveals the effects of Hartmann number variation on the local Nusselt number. As this figure shows, at the entry region of flow, by raising the Hartmann number, the local Nusselt number increment. This is due to the velocity increment at the vicinity of walls, resulting in improvement in the convective heat transfer.

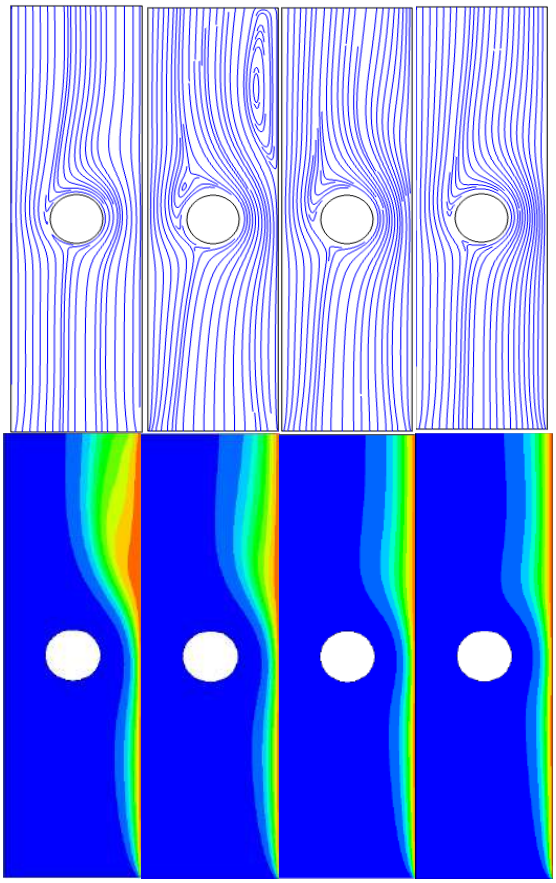

Figure 6. Streamlines and isotherm contours for numerous values of Hartmann number for $\Omega = 3$

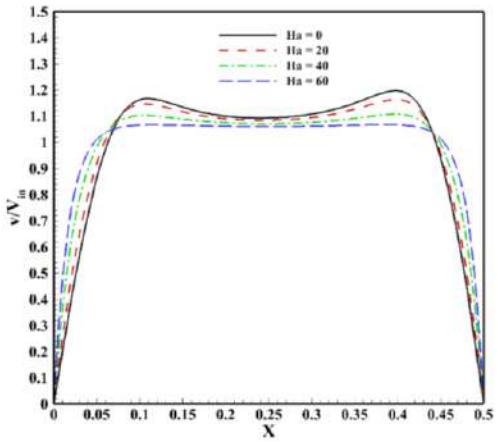

Figure 7. Influences of the Hartmann number on velocity profile at Y = 0.125 for $\Omega = 3$

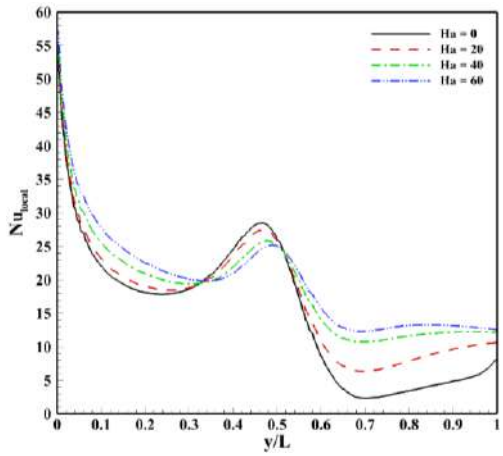

Figure 8. Local Nusselt number variation along the hot wall against varying Hartmann number for Ω = 3

However, at the location of the cylinder, the flow structure is in the opposite of the entrance region. In where, the flow section area is smaller which leads to higher velocity on the hot wall and applying the magnetic field causes to reduce the velocity so as the Nusselt number. Furthermore, as shown in Figure 7, at the back of the cylinder, further raising in Hartmann number yields in local Nusselt number enhancement. This phenomenon corresponds to suppression of the vortices by increasing Hartmann number that leads to improve convection heat transfer efficiency.

4. 2. Effects of Non-dimensional Angular Velocity of the Cylinder Figure 9 demonstrates the effects of the cylinder rotation on the structure of flow and the isotherm contours for different non-dimensional angular velocity. Positive and negative values of Ω represent counterclockwise and clockwise rotation of cylinder, respectively. As shown by streamlines, in the case of Ω = 0, there is one stagnation point at the channel which takes place in front of the cylinder. This point appears when free stream encounters the cylinder. In addition, by enhancing non-dimensional velocity, second stagnation point appears at the left of the cylinder due to the counterclockwise rotation of the cylinder. Nonetheless, the density of the streamlines at the right side of the cylinder increases as the non-dimensional angular velocity increases, and hence the local velocity at this region rises. Furthermore, in the cases of CCW, the cylinder rotation diverts fluid flow from the hot wall to the adiabatic wall, which causes a recirculation zone to form behind the cylinder. In the cases of CW, however, the aforementioned influences are in opposite with CCW cases. According to the isotherms, in the direction of CCW, at the location of the cylinder, the cylinder rotation pushes isotherms to the hot wall which leads to a thin

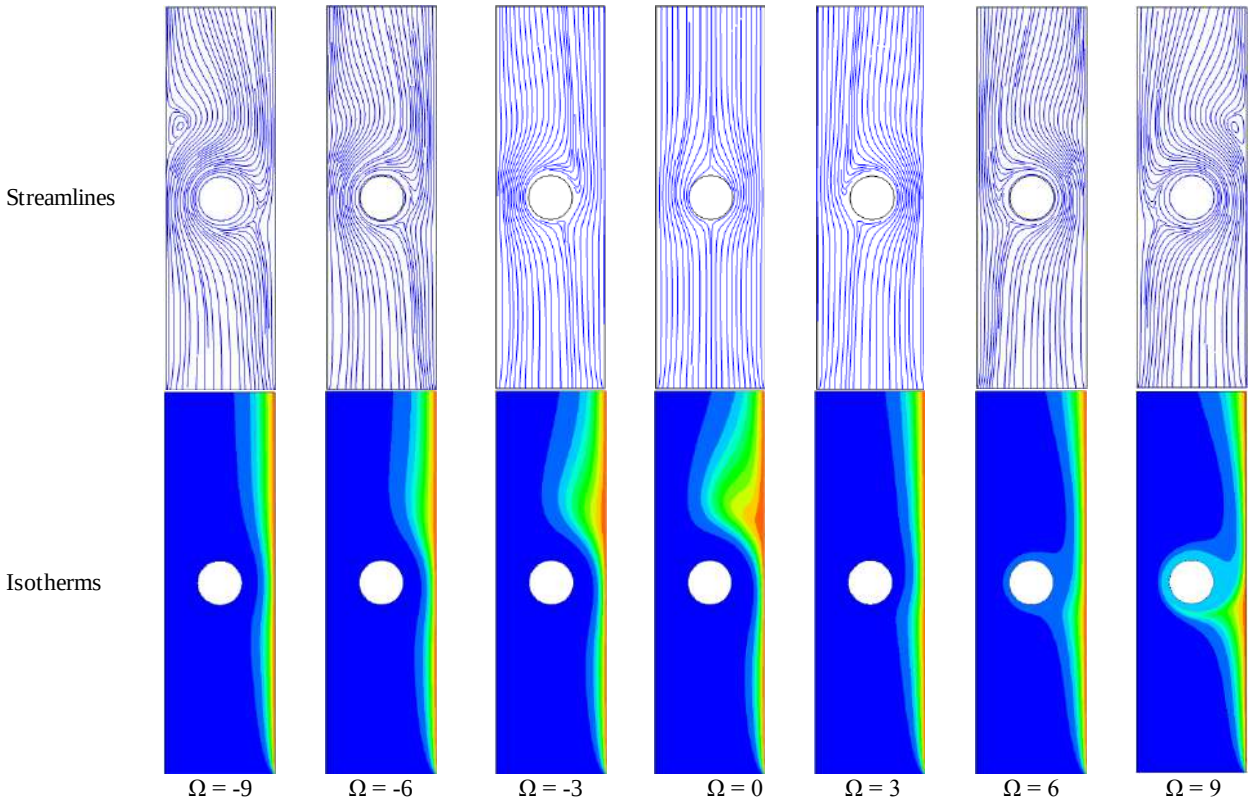

Figure 9. Impacts of the cylinder rotation on streamlines and isotherm contours for Ha = 30

temperature layer. In addition, as mentioned in the previous section, the cylinder rotation forms a vortex behind the cylinder and this phenomenon widens the isotherms behind the cylinder.

However, in the cases of CW rotation of the cylinder, due to the streamlines, the net effect of the inlet velocity and the cylinder rotation causes the creation of a stagnation point before the cylinder. Therefore, the dominant heat transfer mechanism in this region is conduction. Moreover, due to the streamline compression after the cylinder on the hot wall, thickness of the isothermal lines decrease and therefore the convective heat transfer mechanism share increases.

The variations of the local Nusselt number alongside the hot wall with respect to the effects of counterclockwise rotation of the cylinder are demonstrated in Figure 10. As the results show, before the cylinder, any increment in Ω has positive effects on the Nusselt number. It is due to the rotational velocity increment of the cylinder that pushes fluid flow to the hot wall and reduces the thermal boundary layer thickness. Oppositely, at the behind of the cylinder due to vortex generation on the hot wall, raising Ω leads to reduce local Nusselt number.

Influences of the clockwise rotation of the cylinder on the local Nusselt number are illustrated in Figure 11. According to this figure, at the front of the cylinder, increment in angular velocity yields to the Nusselt number reduction. Because the net fluid flow velocity decreases by raising angular velocity that causes to thicken the thermal boundary layer. in contrast to the front region, at the back of the cylinder, increment in angular velocity has positive effects on the Nusselt number. The reason for the mentioned influence is related to pushing fluid flow to the hot wall by the cylinder which makes the thermal boundary layer thin and increases convective heat transfer.

Figure 12 represents the effect of Ω on the average Nusselt number for different Hartmann numbers. As this figure depicts, in the condition of no magnetic field (Ha = 0), in the ranges of $-2 \leq \Omega \leq 0$ and $0 < \Omega \leq 3$, any change in the rotational speed of the cylinder has negative impact on the average Nusselt number. Additionally, in higher values of Ω, due to the thermal boundary layer thickness reduction in the back of the cylinder, the average Nusselt number for both cases of CCW and CC rotations enhances. Furthermore, as the magnetic field augments, the effects of Ω on the average Nusselt number is insignificant. For instance, at Ha = 45 and 60, the effects of Ω on the average Nusselt number have almost been eliminated and its variations are independent of Ω.

4. 3. Lift and Drag Coefficients The effects of the non-dimensional angular velocity with varying Hartmann number on the lift coefficient are shown in

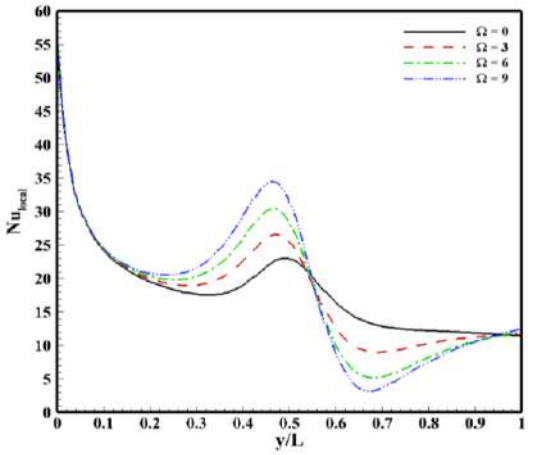

Figure 10. Effects of non-dimensional angular velocity of the cylinder in direction of counterclockwise rotation on the local Nusselt number for Ha = 30

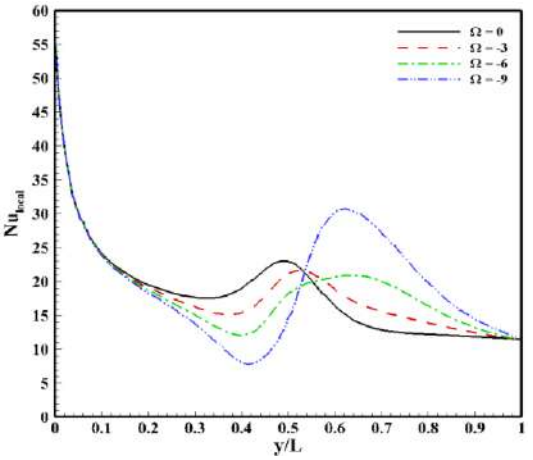

Figure 11. Variation of non-dimensional angular velocity of the cylinder in direction of clockwise rotation with the local Nusselt number for Ha = 30

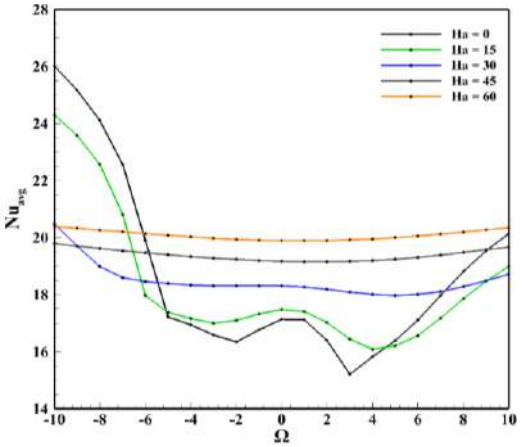

Figure 12. Average Nusselt number variation versus the cylinder rotation against various Hartmann numbers

Figure 13. As this figure illustrates, any increase in Ω in terms of CCW and CW rotations of the cylinder causes to decrease and increase lift coefficient, respectively. In contrast to CW rotation, as Ω rises in CCW direction, the flow at the right side of the cylinder accelerates which forces the pressure gradient to lower and consequently, the lift force becomes higher. Moreover, as the magnetic field strength increases, the magnitude of C_L at both rotation directions decrease. This phenomenon corresponds to the momentum reduction due to the higher Hartmann number that leads to a decrease in lift force. Moreover, the negative values of the lift coefficient represent the opposite direction of the lift force. Additionally, it is worth to mention that, the value of the lift coefficient at stationary case of the cylinder (Ω = 0) is zero and does not changes with the Hartmann number. It is due to symmetric fluid flowing on the stationary cylinder.

Figure 14 demonstrates the effect of varying Ω on the drag coefficient for different Hartmann numbers. As shown in this figure, in the case of no magnetic field (Ha = 0), any enhancement in Ω magnitude, in turn, increases the drag coefficient. Moreover, by increasing Ω, the rotational cylinder causes to guide the flow to the back of the cylinder that leads to creating a negative pressure gradient and therefore the drag force increases. Similarly, as the magnetic field is increased, for lower numbers of Ω ($-5 \leq \Omega \leq 5$) drag coefficient increases. It is worth to say that applying the magnetic field eliminates wake regions behind the cylinder. As Figure 14 shows, any increment in the Hartmann number results in a uniform distribution of the drag coefficient. In other words, the Hartmann number decreases the dependence of the drag coefficient on non-dimensional velocity. This phenomenon is due to the braking action of the Lorentz force that controls fluid flow and restrains fluctuations.

5. CONCLUSION

Heat transfer and fluid flow of the straight vertical channel with adiabatic rotating cylinder utilizing nanofluid affected by uniform magnetic field are numerically studied. Effective parameters such as Hartmann number and direction of rotation are examined. Following points can be concluded from this study:

- Magnetic field reduces the velocity of the core flow while it increases the velocity near walls, and therefore enhances the convection heat transfer.
- In absence of the magnetic field, the cylinder rotation causes vortex to form behind the cylinder near the walls. However, by applying magnetic field the vortex weakens.
- The highest Nusselt numbers achived at Ω = -10 in the case of no magnetic field and enhancement due to the motionless cylinder is 51%.
- In higher Hartmann numbers, the average Nusselt number does not change remarkbaly with Ω .
- Magnitude of the drag and the lift coefficients of the cylinder increased in higher Ωs. In addition, applying the magnetic field leads to a decrease in lift coefficient and reduces the dependency of the drag coefficient to Ω.

5. REFERENCES

1. Ganvir, R., P. Walke, and V. Kriplani, "Heat transfer characteristics in nanofluid—a review", ***Renewable and Sustainable Energy Reviews***, Vol. 75, (2017), 451-460, https://doi.org/10.1016/j.rser.2016.11.010
2. Hussein, A.M., K. Sharma, R. Bakar, and K. Kadirgama, "A review of forced convection heat transfer enhancement and hydrodynamic characteristics of a nanofluid", ***Renewable and Sustainable Energy Reviews***, Vol. 29, (2014), 734-743, https://doi.org/10.1016/j.rser.2013.08.014
3. Kakaç, S. and A. Pramuanjaroenkij, "Review of convective heat transfer enhancement with nanofluids", ***International Journal of Heat and Mass Transfer***, Vol. 52, (2009), 3187-3196, https://doi.org/10.1016/j.ijheatmasstransfer.2009.02.006
4. Li, Y., S. Tung, E. Schneider, and S. Xi, "A review on development of nanofluid preparation and characterization", ***Powder Technology***, Vol. 196, (2009), 89-101, https://doi.org/10.1016/j.powtec.2009.07.025
5. Tawfik, M.M.,"Experimental studies of nanofluid thermal conductivity enhancement and applications: a review", ***Renewable and Sustainable Energy Reviews***, Vol. 75, (2017), 1239-1253, https://doi.org/10.1016/j.rser.2016.11.111
6. Yu, W., D.M. France, J.L. Routbort, and S.U. Choi, "Review and comparison of nanofluid thermal conductivity and heat transfer enhancements", ***Heat Transfer Engineering***, Vol. 29, (2008), 432-460, https://doi.org/10.1080/01457630701850851
7. Gravndyan, Q., O.A. Akbari, D. Toghraie, A. Marzban, R. Mashayekhi, R. Karimi, and F. Pourfattah,"The effect of aspect ratios of rib on the heat transfer and laminar water/TiO_2 nanofluid flow in a two-dimensional rectangular microchannel", ***Journal of Molecular Liquids***, Vol. 236, (2017), 254-265, https://doi.org/10.1016/j.molliq.2017.04.030
8. Ahmadi, A.A., E. Khodabandeh, H. Moghadasi, N. Malekian, O.A. Akbari, and M. Bahiraei, "Numerical study of flow and heat transfer of water-Al_2O_3 nanofluid inside a channel with an inner cylinder using Eulerian–Lagrangian approach", ***Journal of Thermal Analysis and Calorimetry***, Vol. 132, (2018), 651-665, https://doi.org/10.1007/s10973-017-6798-y
9. Bahiraei, M. and P.R. Mashaei, "Using nanofluid as a smart suspension in cooling channels with discrete heat sources", ***Journal of Thermal Analysis and Calorimetry***, Vol. 119, (2015), 2079-2091, https://doi.org/10.1007/s10973-015-4414-6
10. Ho, C.-J., L. Wei, and Z. Li, "An experimental investigation of forced convective cooling performance of a microchannel heat sink with Al_2O_3/water nanofluid", ***Applied Thermal Engineering***, Vol. 30, (2010), 96-103, https://doi.org/10.1016/j.applthermaleng.2009.07.003
11. Heidary, H. and M. Kermani, "Heat transfer enhancement in a channel with block (s) effect and utilizing Nano-fluid", ***International Journal of Thermal Sciences***, Vol. 57, (2012), 163-171, https://doi.org/10.1016/j.ijthermalsci.2012.02.001
12. Khanafer, K., K. Vafai, and M. Lightstone, "Buoyancy-driven heat transfer enhancement in a two-dimensional enclosure utilizing nanofluids", ***International Journal of Heat and Mass***

Transfer, Vol. 46, (2003), 3639-3653, https://doi.org/10.1016/S0017-9310(03)00156-X

13. Santra, A.K., S. Sen, and N. Chakraborty, "Study of heat transfer due to laminar flow of copper–water nanofluid through two isothermally heated parallel plates", ***International Journal of Thermal Sciences***, Vol. 48, (2009), 391-400, https://doi.org/10.1016/j.ijthermalsci.2008.10.004
14. Roslan, R., H. Saleh, and I. Hashim,"Effect of rotating cylinder on heat transfer in a square enclosure filled with nanofluids", ***International Journal of Heat and Mass Transfer***, Vol. 55, (2012), 7247-7256, https://doi.org/10.1016/j.ijheatmasstransfer.2012.07.051
15. Chen, C.-H., "Heat and mass transfer in MHD flow by natural convection from a permeable, inclined surface with variable wall temperature and concentration", ***Acta Mechanica***, Vol. 172, (2004), 219-235, https://doi.org/10.5281/zenodo.1091654
16. Daniel, Y.S., Z.A. Aziz, Z. Ismail, and F. Salah, "Effects of thermal radiation, viscous and Joule heating on electrical MHD nanofluid with double stratification", ***Chinese Journal of Physics***, Vol. 55, (2017), 630-651, https://doi.org/10.1016/j.cjph.2017.04.001
17. Ma, Y., R. Mohebbi, M. Rashidi, Z. Yang, and M.A. Sheremet,"Numerical study of MHD nanofluid natural convection in a baffled U-shaped enclosure", ***International Journal of Heat and Mass Transfer***, Vol. 130, (2019), 123-134, https://doi.org/10.1016/j.ijheatmasstransfer.2018.10.072
18. Mabood, F. and W. Khan,"Analytical study for unsteady nanofluid MHD Flow impinging on heated stretching sheet", ***Journal of Molecular Liquids***, Vol. 219, (2016), 216-223, https://doi.org/10.1016/j.molliq.2016.02.071
19. Makinde, O. and I. Animasaun,"Bioconvection in MHD nanofluid flow with nonlinear thermal radiation and quartic autocatalysis chemical reaction past an upper surface of a paraboloid of revolution", ***International Journal of Thermal Sciences***, Vol. 109, (2016), 159-171, https://doi.org/10.1016/j.ijthermalsci.2016.06.003
20. Aminossadati, S., A. Raisi, and B. Ghasemi,"Effects of magnetic field on nanofluid forced convection in a partially heated microchannel", ***International Journal of Non-Linear Mechanics***, Vol. 46, (2011), 1373-1382, https://doi.org/10.1016/j.ijnonlinmec.2011.07.013
21. Heidary, H., R. Hosseini, M. Pirmohammadi, and M. Kermani,"Numerical study of magnetic field effect on nano-fluid forced convection in a channel", ***Journal of Magnetism and Magnetic Materials***, Vol. 374, (2015), 11-17, https://doi.org/10.1016/j.jmmm.2014.08.001
22. Selimefendigil, F. and H.F. Öztop,"Numerical study of MHD mixed convection in a nanofluid filled lid driven square enclosure with a rotating cylinder", ***International Journal of Heat and Mass Transfer***, Vol. 78, (2014), 741-754, https://doi.org/10.1016/j.ijheatmasstransfer.2014.07.031
23. Hosseini, S., M. Sheikholeslami, M. Ghasemian, and D. Ganji, "Nanofluid heat transfer analysis in a microchannel heat sink (MCHS) under the effect of magnetic field by means of KKL model", ***Powder Technology***, Vol. 324, (2018), 36-47, https://doi.org/10.1016/j.powtec.2017.10.043
24. Oztop, H.F., K. Al-Salem, and I. Pop, "MHD mixed convection in a lid-driven cavity with corner heater", International Journal of ***Heat and Mass Transfer***, Vol. 54, (2011), 3494-3504, https://doi.org/10.1016/j.ijheatmasstransfer.2011.03.036
25. Aminfar, H., M. Mohammadpourfard, and F. Mohseni, "Two-phase mixture model simulation of the hydro-thermal behavior of an electrical conductive ferrofluid in the presence of magnetic fields", ***Journal of Magnetism and Magnetic Materials***, Vol.324, (2012), 830-842, https://doi.org/10.1016/j.jmmm.2011.09.028
26. Ma, Y., R. Mohebbi, M. Rashidi, and Z. Yang,"MHD convective heat transfer of Ag-MgO/water hybrid nanofluid in a channel with active heaters and coolers", ***International Journal of Heat and Mass Transfer***, Vol. 137, (2019), 714-726, https://doi.org/10.1016/j.ijheatmasstransfer.2019.03.169
27. Mahmoudi, A.H., I. Pop, and M. Shahi, "Effect of magnetic field on natural convection in a triangular enclosure filled with nanofluid", ***International Journal of Thermal Sciences***, Vol. 59, (2012), 126-140, https://doi.org/10.1016/j.ijthermalsci.2012.04.006
28. Bianco, V., F. Chiacchio, O. Manca, and S. Nardini, "Numerical investigation of nanofluids forced convection in circular tubes", ***Applied Thermal Engineering***, Vol. 29, (2009), 3632-3642, https://doi.org/10.1016/j.applthermaleng.2009.06.019
29. Garoosi, F., F. Hoseininejad, and M.M. Rashidi,"Numerical study of natural convection heat transfer in a heat exchanger filled with nanofluids", ***Energy***, Vol.109, (2016), 664-678, https://doi.org/10.1016/j.energy.2016.05.051
30. Pak, B.C. and Y.I. Cho,"Hydrodynamic and heat transfer study of dispersed fluids with submicron metallic oxide particles", ***Experimental Heat Transfer an International Journal***, Vol. 11, (1998), 151-170, https://doi.org/10.1080/08916159808946559
31. Brinkman, H.,"The viscosity of concentrated suspensions and solutions", ***The Journal of Chemical Physics***, Vol. 20, (1952), 571-571, https://doi.org/10.1063/1.1700493
32. Wasp, E.J., J.P. Kenny, and R.L. Gandhi,"Solid--liquid flow: slurry pipeline transportation.[Pumps, valves, mechanical equipment, economics]", Ser. Bulk Mater. Handl.;(United States), Vol. 1, (1977), https://www.osti.gov/biblio/6343851
33. Maxwell, J.C., A treatise on electricity and magnetism. Vol. 1. 1873: Oxford: Clarendon Press.
34. Park, Y.G., H.S. Yoon, and M.Y. Ha,"Natural convection in square enclosure with hot and cold cylinders at different vertical locations", ***International Journal of Heat and Mass Transfer***, Vol. 55, (2012), 7911-7925, https://doi.org/10.1016/j.ijheatmasstransfer.2012.08.012

Persian Abstract

چکیده

امروزه تحلیل انتقال حرارت در کانال‌ها و محفظه‌ها مورد توجه بسیاری از پژوهش‌گران قرار گرفته است. در کار حاضر جریان و انتقال حرارت نانوسیال در یک کانال عمودی که شامل یک استوانه‌ی چرخان می باشد، به صورت عددی مطالعه گردیده است. میدان مغناطیسی یک‌نواخت به سیال اعمال شده و تاثیر جهت‌های مختلف چرخش استوانه عدد هارتمن و سرعت دورانی استوانه بررسی شده‌است. نتایج نشان می‌دهد که با افزایش عدد هارتمن در سرعت‌های دورانی کم استوانه عدد ناسلت متوسط افزایش می یابد. برخلاف آن در اعداد هارتمن بالاتر عدد ناسلت متوسط تغییرات چشمگیری با سرعت زاویه‌ای بی‌بعد ندارد. علاوه برآن مطالعه‌ی ضرایب درگ و برآ نشان می‌دهد که در عدد هارتمن ثابت بیشترین ضریب درگ در بیشترین سرعت زاویه‌ای استوانه اتفاق می‌افتد. به همین ترتیب توزیع تقریباً یک‌نواخت ضریب درگ در اعداد هارتمن بزرگتر مشاهده می‌شود. نتایج عددی با گزارش‌های گذشته مقایسه شده و این مقایسه تطابق بسیار مناسب بین آنها را نشان می‌دهد.

International Journal of Engineering

Journal Homepage: www.ije.ir

Development of a New Supersonic Rotor-vane Ejector using Computational Fluid Dynamics

M. Sarvalishah, S. Niazi*, Y. Bakhshan

Department of Mechanical Engineering, University of Hormozgan, Bandar Abbas, Iran

P A P E R I N F O

Paper history:
Received 29 February 2020
Received in revised form 04 September 2020
Accepted 30 October 2020

Keywords:
Ejector
Rotor
Viscous
Compressible
Entrainment Ratio
Supersonic

A B S T R A C T

An innovative design of a supersonic rotor pressure-exchange ejector is introduced in this paper. In this design, momentum is exchanged between supersonic primary flow and secondary flow using an idle rotor. A CFD code developed to model the 3-D compressible, viscous and turbulent flow of air inside the new design of ejector. Roe approach and Spallart-Allmaras methods used to analyze flow inside the ejector. The flow inside the ejector was modeled by using a structured grid and air was employed as the working fluid in both primary and secondary streams. The Mach number of the motive flow was set at 2. Momentum exchanged between the primary and secondary flows because of direct contact between those. In addition to that, rotation of idle rotor and mechanical blades entrained the secondary flow to the ejector. Enthalpy, entrained mass flow rate and created vacuum presented for the flow inside the ejector for different configurations of the rotor and ejector until an optimum case was achieved. Also, uniformity of the flow at discharge section compared between ejectors. For the optimum case with the presented geometry, the ultimate rotor speed of 50000 rpm was obtained and an increase of 47% in entrainment ratio achieved with respect to the stationary blades. To study the flow field in more details, the contours of the Mach number and stagnation pressure were compared according to the different sections of computational domain.

***doi**: 10.5829/ije.2021.34.01a.26*

NOMENCLATURE

Q	Primitive variable matrix	e	Total energy per unit mass
E, F, G	Inviscid fluxes	q_i	Heat flux
E_v, F_v, G_v	Viscous stresses and heat fluxes	**Greek Symbols**	
x, y, z	Cartesian coordinates	ρ	Density
t	Time	τ_{ij}	Viscous stress tensor
u, v, w	Cartesian velocity components	υ	Kinematic viscosity
p	Pressure	υ_t	Turbulent viscosity
W_{ij}	Vorticity tensor	$\bar{\upsilon}$	Working variable in Spalart-Allmaras turbulence model
d	Distance from nearest wall	Ω	Magnitude of vorticity

1. INTRODUCTION

Ejectors are widely used in different industries. This device can convert low-grade energies into power. In addition to the ability of creating compression without using any moving parts, ejectors have the advantage of a simple structure causing their manufacturing, installations and operations to be simpler than those of other compression systems.

One of the major applications of ejectors is in Ejector Refrigeration Systems (ERS). Le Blanc and Parson developed the first steam jet refrigerator in the early 1900s. It has experienced great popularity during the early 1930s for the air conditioning systems of large buildings. Ejectors are also utilized in vacuum systems

*Corresponding Author Institutional Email: *s.niazi@hormozgan.ac.ir* (S. Niazi)

Please cite this article as: M. Sarvalishah, S. Niazi, Y. Bakhshan, Development of a New Supersonic Rotor-vane Ejector using Computational Fluid Dynamics, International Journal of Engineering, Transactions A: Basics Vol. 34, No. 01, (2021) 234-242

like steam surface condensers. In this way, ejector reduces the pressure and temperature in condenser and therefore, smaller sizes of condensers can be employed to perform the same duty of condensation. Moreover, ejectors are also applied for evacuation of vessels containing toxic or flammable gases.

The streams passing through ejectors include high and low energy streams in which a high pressure flow is converted into a high speed flow after passing through the convergent-divergent motive nozzle of an ejector. This flow entrains a secondary flow through the suction nozzle and after exchanging power and mixing high and low energy streams in the mixing chamber, there will be an intermediate pressure in the discharge nozzle. In other words, ejectors can entrain a secondary flow and increase its pressure through a high energy flow at the primary nozzle.

In spite of all the benefits of ejectors, they have low efficiencies. Therefore, many researches are being conducted on ejectors to improve their efficiencies and entrainment ratios. Some of these studies are reported hereunder.

Suvarnakuta et al. [1] have used the computational fluid dynamics (CFD) to investigate the performance of a steam ejector employed in a refrigeration system to increase its functionality and coefficient of performance (COP). They modeled a 2D-axisymmetric two stage ejectors and performance compared with the available single stage ejector refrigeration system. CFD results provided high entrainment ratio of 77.2% and 21.9% decrease in back pressure of ejector system. In this research, they achieved high refrigeration capacity and low condensing pressure.

Meyer et al. [2] established an experimental setup of a small-scale steam jet ejector. They studied the Coefficient of Performance (COP) of their ejector with changing the primary and secondary throat diameters, boiler temperature, motive nozzle discharge position and condenser pressure.

XChen et al. [3] provided a literature review on the recent development of ejectors and refrigeration systems. They reported several useful researches in their review articles, including refrigerant selections, mathematical modeling and numerical simulation of ejector systems, geometric optimizations, modification of operating conditions and combinations with other refrigeration systems.

Hong et al. [4] presented a computational and experimental program for designing a rotor-vane/pressure-exchange ejector for thermally driven ejector refrigeration systems. In their research, careful management was performed to control the entropy rise through the oblique shocks and boundary layers. They focused on the selection, design and optimization of their ejector rotor and blades. In addition, total pressure distribution for different blade spin angles and different rotor speeds were compared.

Gould and Garris [5] worked on the computer simulation and theoretical analysis of a steam pressure exchange ejector for an automobile. Waste heat from the internal combustion engine exhaust was captured to run the boiler of the steam ejector refrigeration system. In their study, theoretical and numerical results compared with the experimental data from an existing ejector refrigeration system for the automobile.

Chenghua et al. [6] used CFD methods to study the entropy production and pressure loss in a supersonic rotor-vane ejector. The expansion shock waves at the rotor tails induced the secondary flow and enhanced the mixing of two flows at a short distance. They showed that turbulence effects were weak and negligible. They had also studied effects of vane configuration and speed on ejector efficiency.

2. TURBO-EJECTOR

To resolve the problem of low efficiency and small entrainment ratio in ejectors, a new configuration was presented for them. In this configuration, an integrally turbine-compressor blade was located in front of the primary flow. In fact, the rotor blades played the roles of both turbine and compressor blades. Figure 1 shows a schematic view of the desired turbo-ejector. In this model, a high pressure-flow enters the motive nozzle and expands to supersonic speed after passing through the convergent-divergent primary nozzle.

Same as the turbine, admission of the high-velocity flow to the inner part of the blades caused the cascade to rotate around the frictionless shaft. Thus, the outer part acted as a compressor blade and entrained the flow from the suction chamber. In this way, two different natures of flow entrainment were employed. The first was the shear stresses at the tangential interface between the primary and secondary flows as a result of turbulence and viscosity, and the work of normal pressure forces. This is the same scenario that appears in common ejectors. The second was the solid vanes that transferred momentum

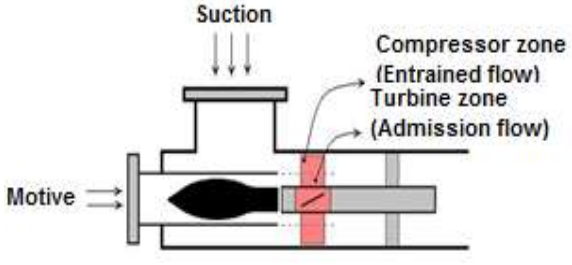

Figure 1. A schematic view of turbo-ejector

and energy to the fluid in contact, like the turbo-machines.

In this study, a CFD code named HORMOZ 3-D was developed for analyzing and modeling 3-D turbulent compressible flow inside the introduced turbo-ejector.

3. GOVERNING EQUATIONS

To model the flow inside the turbo-ejector, the system of partial differential equations for the conservation of mass, momentum and energy, known as the Navier-Stokes equations, were employed. The complex nature of the governing equations limits the analytical solutions to simple flows and configurations. Therefore, numerical techniques are required for more complex problems. The control volume procedure used in Roe's method [7, 8, 9] was applied to model a three-dimensional compressible flow inside the turbo-ejector. The Spalart-Allmaras method was also employed with some modifications to model the turbulent flow inside the domain [10].

In the three-dimensional Cartesian coordinates, the conservative form of the equations is given in a vector form as follows:

$$Q_t + (E - E_v)_x + (F - F_v)_y + (G - G_v)_z = 0 \quad (1)$$

where Q is the primitive variable matrix, t time and x, y, z are the three directions in the Cartesian coordinate. Matrices E, F and G are inviscid flux terms, and E_υ, F_υ and G_υ represent viscous terms. Matrix Q and inviscid flux terms are:

$$Q = \begin{Bmatrix} \rho \\ \rho u \\ \rho v \\ \rho w \\ \rho e \end{Bmatrix}, E = \begin{Bmatrix} \rho u \\ \rho u^2 + p \\ \rho uv \\ \rho uw \\ \rho(e + \frac{p}{\rho})u \end{Bmatrix},$$
$$F = \begin{Bmatrix} \rho v \\ \rho uv \\ \rho v^2 + p \\ \rho vw \\ \rho(e + \frac{p}{\rho})v \end{Bmatrix}, G = \begin{Bmatrix} \rho w \\ \rho uw \\ \rho vw \\ \rho w^2 + p \\ \rho(e + \frac{p}{\rho})w \end{Bmatrix} \quad (2)$$

where e is total energy per unit mass.

The viscous terms are:

$$E_v = \begin{Bmatrix} 0 \\ \tau_{xx} \\ \tau_{xy} \\ \tau_{xz} \\ u\tau_{xx} + v\tau_{xy} + w\tau_{xz} - q_x \end{Bmatrix},$$
$$F_v = \begin{Bmatrix} 0 \\ \tau_{yx} \\ \tau_{yy} \\ \tau_{yz} \\ u\tau_{yx} + v\tau_{yy} + w\tau_{yz} - q_y \end{Bmatrix}, \quad (3)$$
$$G_v = \begin{Bmatrix} 0 \\ \tau_{zx} \\ \tau_{zy} \\ \tau_{zz} \\ u\tau_{zx} + v\tau_{zy} + w\tau_{zz} - q_z \end{Bmatrix}$$

General form of the Spalart-Allmaras turbulence model with the assumption of turbulence flow at the entrance to the blades is:

$$\frac{D\bar{\upsilon}}{Dt} = C_{b1}\bar{\Omega}\bar{\upsilon} + \frac{1}{\sigma}\left[\nabla.\left((\upsilon + \bar{\upsilon})\nabla\bar{\upsilon} + C_{b2}(\nabla\bar{\upsilon})^2\right)\right] - C_{w1}f_w\left[\frac{\bar{\upsilon}}{d}\right]^2 \quad (4)$$

where turbulent kinematic viscosity is:

$$\upsilon_t = \bar{\upsilon}f_{\upsilon 1}, f_{\upsilon 1} = \frac{X^3}{X^3 + C_{\upsilon 1}{}^3}, X = \frac{\bar{\upsilon}}{\upsilon} \quad (5)$$

and

$$\bar{\Omega} = \Omega + \frac{\bar{\upsilon}}{K^2 d^2}f_{\upsilon 2}, f_{\upsilon 2} = 1 - \frac{X}{1 + Xf_{\upsilon 1}},$$
$$f_w = g\left[\frac{1 + C_{w3}{}^6}{g^6 + C_{w3}{}^6}\right]^{1/6}, g = r + C_{w2}(r^6 - r), \quad (6)$$
$$r = \frac{\bar{\upsilon}}{\bar{\Omega}K^2 d^2}, \Omega = \sqrt{2W_{ij}W_{ij}}$$

W_{ij} is the vorticity tensor. To solve the equation, $\bar{\upsilon}$ was set to zero for the wall boundary conditions. Other constant parameters were set as below:

$$\sigma = 2/3, C_{b1} = 0.1355, C_{b2} = 0.622,$$
$$K = 0.41, C_{w1} = \frac{C_{b1}}{K^2} + \frac{(1 + C_{b2})}{\sigma}, C_{w2} = 0.3, C_{w3} = 2, C_{\upsilon 1} = 7.1 \quad (7)$$

As stated before, one of the major roles of ejectors is to transfer power from high-energy (motive) zone to the low-energy (suction) zone. In other words, it is favorable to have a uniform distribution of stagnation enthalpy at the discharge section. To count the uniformity, two parameters of $H_{0,outlet}$ (summation of stagnation enthalpy at the discharge section) and $H_{0,non-uniformity}$ (summation of enthalpy deviation from the average value) are defined as follows:

$$H_{0,outlet} = \left(\sum \dot{m} C_p T_0\right)_{outlet\ section} \quad (8)$$

$$H_{0,non-uniformity} = \sum \dot{m}\left(\frac{H_{0,outlet}}{\dot{M}_{outlet}} - C_p T_0\right)_{outlet\ section} \quad (9)$$

The above equations were employed to compare the enthalpy distribution in different turbo-ejector models. It is also noticeable that the above mentioned stagnation enthalpies were based on the absolute velocities in the ejector.

Entrainment ratio is defined as:

$$Entrainment\ ratio = \frac{\dot{M}_{suction\ zone}}{\dot{M}_{motive\ zone}} \quad (10)$$

where $\dot{m}$ and $\dot{M}$ are mass flow rates at each cell and at the specified section, respectively.

Navier-Stokes equations were written in the Rotating Reference Frame (RRF) for both stationary and moving parts. Explicit discretization was used for Navier-Stokes equations and turbulence modeling.

For the code validation, the experiment results of some internal and external flows were compared with the code solutions. Also, convergence history and grid independency were reviewed and checked for the solutions achieved from this code.

4. TURBO-EJECTOR GEOMETRY

To analyze the flow in turbo-ejectors, the domain between two adjacent blades, including inlet and outlet zones, was chosen as shown in Figure 2. A structural grid with the dimensions of $105 \times 40 \times 40$ in X, Y and Z directions was employed as displayed in the following figure (Figure 2).

In this research, the following geometries were analyzed and studied for the flow inside the turbo-ejector. Rotor had the inner and outer blade diameters of 6 cm and 10 cm, respectively with the width of 2 cm. The lengths of the stationary zone at the blade upstream and downstream were 1cm and 5cm, respectively. The blade orientations with respect to the rotation axis were 10° and 20° and the flow direction at the entrance was in the positive X direction which is the rotation axis. Figure 3 represents a schematic view of four turbo-ejector rotors with different configurations.

All these rotors were located in the ejectors with similar configurations and some comparisons were made between those to find the best solution for the turbo-ejector.

5. CODE VALIDATION

To validate the in-house developed code, grid independencies were checked for different cases and the same results achieved for pressure, density, temperature and velocity components in the flow field. In addition, graphs of convergence history depicted the smooth convergence of the code to the final solutions. As a sample, convergence history for Ejector B is represented in Figure 4, where the vertical axis (Error) is the difference between two alternative iterations for the summation of the desired parameter in the whole domain and the axial axis is the number of iterations.

As shown here, this case is converged in less than 30000 iterations for the grid dimensions of $105 \times 40 \times 40$ in X, Y and Z directions.

In addition to above, this code was checked and proved for some other internal and external flows. A sample is shown in Figure 5 that is the supersonic flow on a cone with different attack angles [11].

Mach number for air at the entrance to the cone was 2.72 and as shown in Figure 6, a structured grid with the dimensions of $30 \times 70 \times 20$ in axial, radial and circumferential directions was employed.

Figure 7 shows the results for pressure coefficient on the cone body in circumferential direction for the various angles of attack as $a = 0° \sim 30°$.

Results showed acceptable conformity of experimental and numerical results.

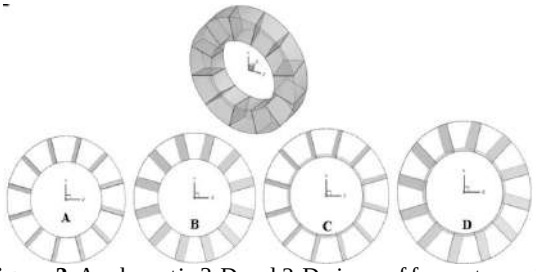

Figure 3. A schematic 3-D and 2-D views of four rotors with different configurations
A: Pitch angle 10°; B: Pitch angle 20°; C: Pitch angle 10° with conical hub angle of 28°; D: Pitch angle 20° with conical hub angle of 28°

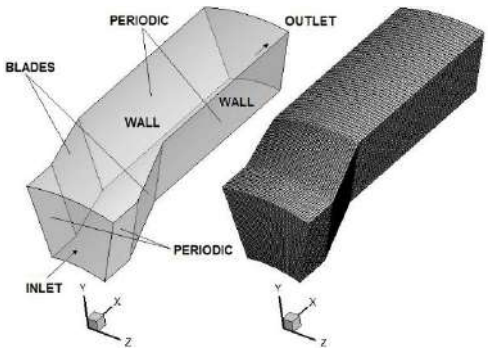

Figure 2. Computational domain of ejector and the structured grid

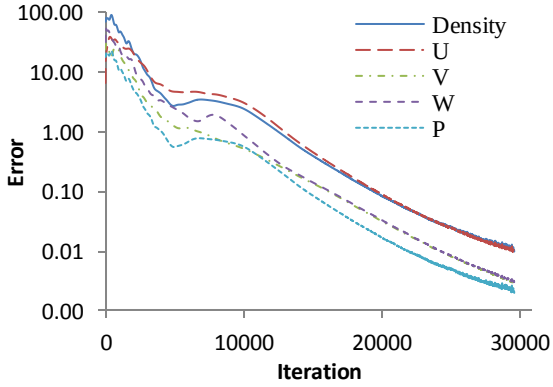

Figure 4. Convergence history of the flow in Ejector B

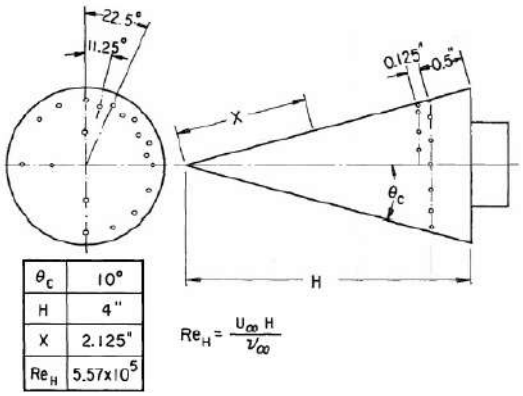

Figure 5. Cone geometry and the location of pressure probes

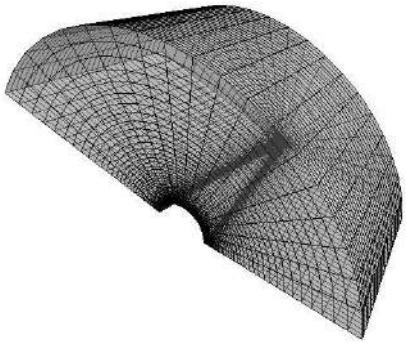

Figure 6. Structured grid on the cone with dimensions of $30 \times 70 \times 20$ in axial, radial and circumferential directions

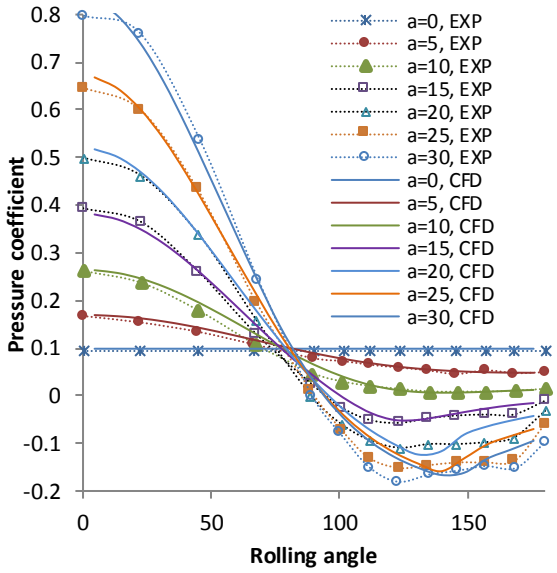

Figure 7. Circumferential pressure distribution for the cone at various angles of attack

Generally, results for grid independency, convergence history and different case studies depicted the acceptable solutions of this code.

6. BOUNDARY CONDITIONS

Air was the working fluid for both the admitted and entrained sections of the ejector. Mach number at the entrance to the admission zone was 2 with the static pressure and temperature of 100KPa and 300K, respectively. The stagnation pressure and temperature at the entrance to the entrained part of the turbo-ejector were 100KPa and 300K, respectively. The one-dimensional Riemann characteristic equation was used to find the entrained flow velocity [12, 13]. For the outlet section, the supersonic flow parameters were extrapolated from the properties inside the domain and back pressure of 100Kpa was set for the subsonic region. Periodic boundary conditions were considered for the side walls of the inlet and outlet zones and no slip condition was set for the flow on the blade walls.

7. RESULTS

In this part, all Ejectors A, B, C and D were analyzed and flow parameters compared between ejectors. Then, the best case was chosen to study the flow field in more details. High energy admission to the ejector caused the rotor to reach its final speed when began to rotate idly around its axis. To find the final speed using CFD analysis, the speed was increased from zero and the resultant momentum on the rotor in axial direction (rotation axis) was calculated in each stage. The final speed occurred when the resultant momentum on the rotor equaled zero. Figure 8 shows a sample of momentum variation with regard to the rotor speed for Ejector B. As shown in this figure, final speed of 50000 rpm was achieved, where axial momentum on the rotor became zero.

Figure 9 shows the variations of enthalpy non-uniformity, $H_{0,non-uniformity}$, with regard to the rotor speed for all the ejectors. In this diagram, speed increased from zero to the final speed of ejector.

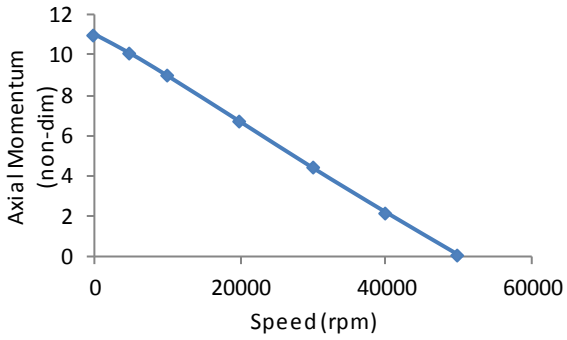

Figure 8. Variations of the torque on the rotor of ejector B with respect to its speed

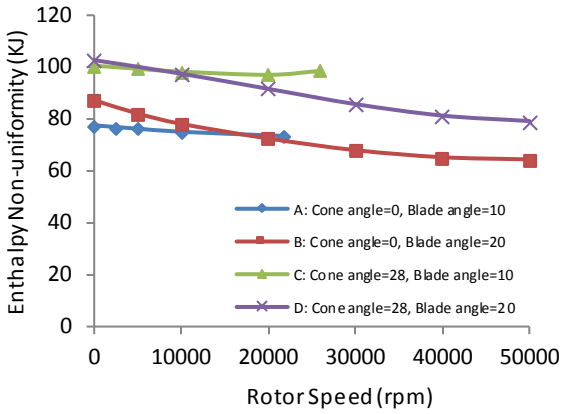

Figure 9. Variation of stagnation enthalpy non-uniformity for the ejectors with respect to the rotor speed

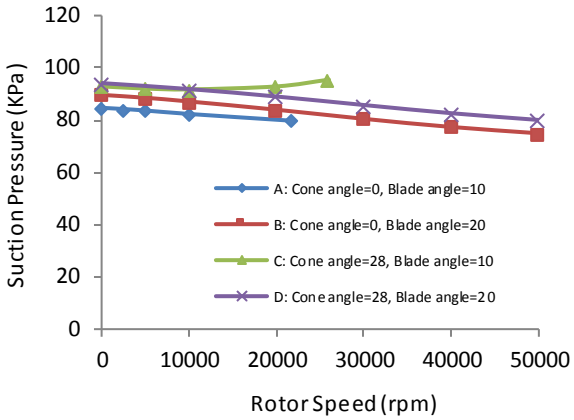

Figure 11. Variation of suction static pressure for the ejectors with respect to the rotor speed

As shown in this figure, non-uniformities for Ejectors A and B are less than Ejectors C and D. In other words, Ejectors A and B have more uniform distributions of stagnation enthalpy at the outlet section compared to those of Ejectors C and D. Also, Ejector B displayed a slightly better operation than Ejector A.

One of the modifications on ejectors is to suction more flow through suction nozzle and to create more vacuum in this region. Figures 10 and 11 represent and compare the mass flow rate and suction pressure in entrained region between different configurations of ejectors.

As shown in Figure 10, the highest entrained flow appears in Ejector B. It is such that the motive mass flow rates are the same for all ejectors. Results show that mass flow rate for Ejectors A and B are higher than those for C and D. This means that conical hub and created oblique shock wave has reduced the entrained mass flow rate through suction zone.

Suction pressure in the region of entrained flow is presented and compared for all ejectors in Figure 11.

As shown in this figure, the same as previous results, Ejectors A and B have created higher vacuum (lower suction pressure) with respect to Ejectors C and D.

Entrainment ratio of Ejectors for speed variations from zero to final speed is prototyped in Figure 12.

As shown in this figure, increase in rotor speed and blade rotation cause enhancement of the entrainment ratio. It means that mass flow rate in suction side of the ejector increases by raising the rotor speed from zero to the final speed. As a sample for Ejector B, the entrainment ratio was 0.36 for the rotor final speed of 50000 rpm. It is such that, an increase of 47% in entrainment ratio achieved with respect to the stationary blades of this ejector.

All above results obtained in Figures 9, 10, 11 and 12 prove that Ejector B has shown better results than other ejectors. Thus, the CFD results of Ejector B were focused on.

To study the ejector in more details, some sections depicted in Figure 13 were selected for reporting flow properties inside the domain.

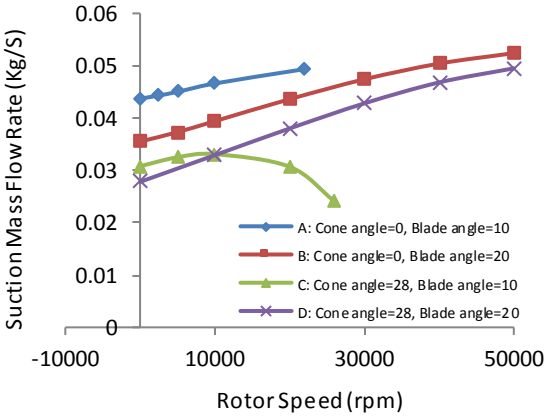

Figure 10. Variation of suction mass flow rate for the ejectors with respect to the rotor speed

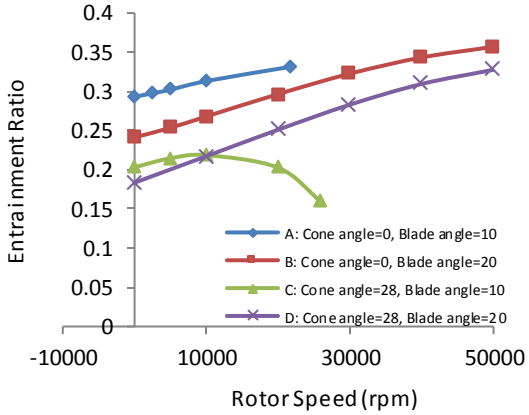

Figure 12. Entrainment ratio variations with respect to the rotor speed for all ejectors

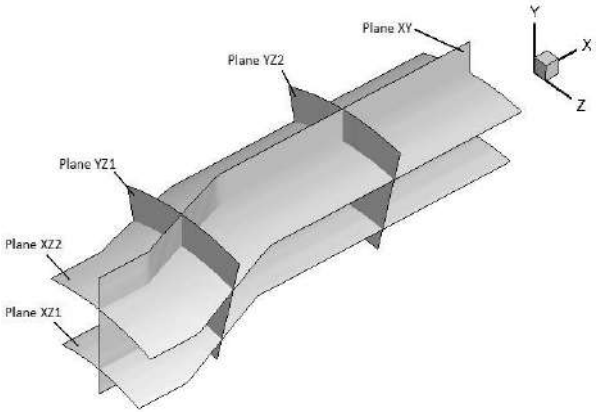

Figure 13. A schematic view of some selected sections

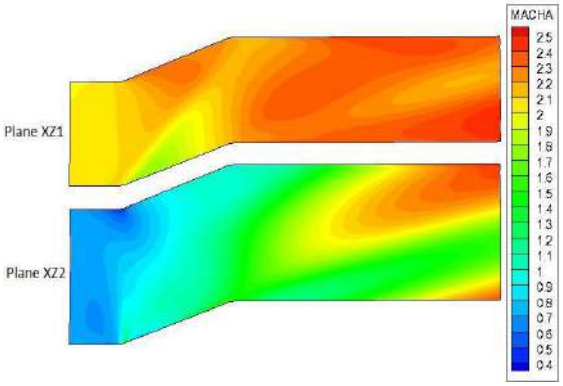

Figure 15. Contours of Mach number on Planes XZ1 and XZ2 inside the domain

As can be seen, Plane XY is located at the middle of the domain in axial direction. Planes XZ1 and XZ2 are at middles of admission domain and suction zone in radial direction, respectively. In the same manner, Planes YZ1 and YZ2 are at the middles of the blade section and discharge zone in circumferential direction, respectively.

In Figure 14, the streamlines on some planes are displayed based on the absolute velocities. As shown in this figure, the secondary flows appear in the blade and discharge zones in the axial direction. These secondary flows can mix the high and low energy streams in the flow field and improve the uniformity of enthalpy at the discharge section. In addition, there is a tendency of the motive flow to expand towards the suction zone on Plane XY.

The contours of the absolute Mach number on two different planes in the axial direction are prototyped in Figure 15. Creations of the oblique shock waves at the edges of the blades in the admission zone are shown in Plane XZ1. As can be seen in plane XZ2 that is located in the entrained zone, Mach number increases gradually from the inlet to the outlet section of the ejector.

However, as shown in this figure, there are some secondary flows that are mixing the primary and secondary streams at the downstream of the blades. The detailed contours of Mach number on Plane XY are shown in Figure 16. Mach number at the entrance to the ejector is 2 for motive flow and nearly 1 for the suction flow. The secondary flows are also shown at the downstream of the blade. In this figure the contour of Mach number for the rotor with zero speed is compared with its final speed. As shown, the Mach number of the entrained flow at the inlet to the ejector is about 0.4 for Plane XY in the second case when the rotor is fixed. In a way that same value of about 1 has been obtained for the rotor final speed of 50000 rpm. In other words, rotation of the blades has increased the Mach number of the entrained stream to the sonic flow and thus, a higher entrainment ratio has been achieved.

Counters of the stagnation pressure on three sections of the inlet, outlet and Plane XY are displayed in Figure 17. This figure shows the variation of total pressure through ejector. Contours of P_0 in the inlet section represent the huge difference between momentums of the motive and suction flows. Similar results for Plane XY indicate the momentum exchange between the high and low energy streams when passing through the turbo-ejector.

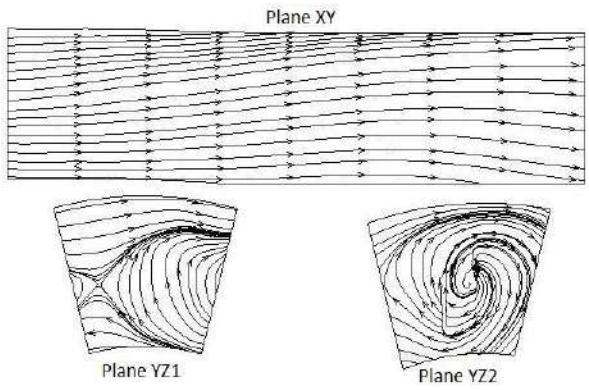

Figure 14. Streamlines on the planes XY, YZ1 and YZ2

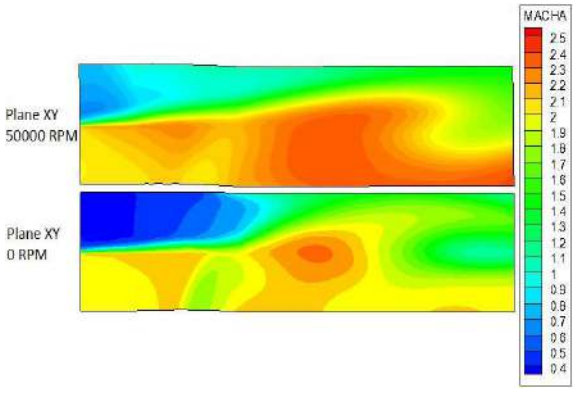

Figure 16. Contours of Mach number on Plane XY inside the domain the for stationary and rotating blades

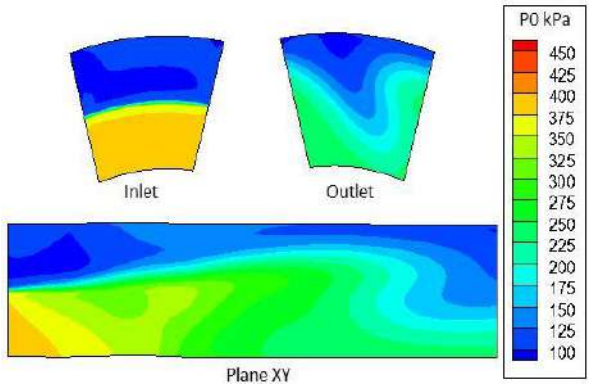

Figure 17. Contours of stagnation pressure on planes XY, inlet and outlet

P_0 distribution is also depicted in the outlet section of the ejector. Comparison between inlet and outlet sections shows the momentum exchange between primary and secondary flows. However, the flow at the discharge is not uniform and more power exchange can occur at the downstream of the ejector.

8. CONCLUSION

In this investigation, a new configuration has been presented for an ejector equipped with an idle rotor. To analyze the flow inside the rotor, a CFD code of HORMOZ 3-D was developed to model the 3-D compressible, viscous and turbulent flow. Four ejectors with different rotor configurations were modeled and the best case was selected to study the flow in more detail. Entrainment ratio variations with respect to the rotor speed were reported for the ejectors. The rotor speed ramped to the final speed where the torque on the rotor was zero and a speed of 50000 rpm was achieved for Ejector B. At this speed, the streamlines and contours of Mach number and stagnation pressure on different sections of the flow field were examined. The contours clearly revealed the creations of compression and expansion oblique shock waves. Results indicated that motive flow at the outlet of the ejector, still have more power to be exchanged with the entrained flow, while some further exchange power could occur downstream of the rotor to provide better efficiencies. In addition, higher efficiencies could result from rotor geometry optimization.

9. REFERENCES

1. Suvarnakuta, N., Pianthong, K., Sriveerakul, T., &Seehanam, W.," Performance analysis of a two-stage ejector in an ejector refrigeration system using computational fluid dynamics", ***Journal of Engineering Applications of Computational Fluid Mechanics***, Vol. 14, (2020), 669-682, doi: 10.1080/19942060.2020.1756913
2. Meyer, A. J., Harms, T. M., Dobson, R. T., "Steam jet ejector cooling powered by waste or solar heat", ***Journal of Renewable Energy***, Vol. 34, (2009), 297-306, doi: 10.1016/j.renene.2008.03.020
3. Chen, X., Omer, S., Worall, M., Riffat, S., "Recent Developments in ejector refrigeration technologies", ***Journal of Renewable and Sustainable Energy Reviews***, Vol. 19, (2013), 629-651, doi: 10.1016/j.rser.2012.11.028
4. Hong, W. J., Alhussan, Kh., Zhang, H., Garris, C. A., "A novel thermally driven rotor-vane/pressure-exchange ejector refrigeration system with environmental benefits and energy efficiency", ***Journal of Energy***, Vol. 29, (2004), 2331-2345, doi: 10.1016/j.energy.2004.03.050
5. Gould, D., Garris, C., "Theoretical analysis of the pressure exchange ejector for an automotive car conditioning applications", George Washington University, Master of Science thesis, (2009).
6. Chenghua, C., Qiang, P., Xingyou, Y., & Juan, Z., "Numerical simulation of flow mechanism of unsteady supersonic rotor-vane ejector", ***Journal of High Power Laser and Particle Beams***, Vol. 26, (2014), 039001, doi: 10.2514/6.2001-858.
7. Chackravarthy, S. R., Szema, K. Y., "Euler Solver for Three-Dimensional Supersonic Flows with Subsonic Pockets", ***Journal of Aircraft***, Vol. 24, No. 2, (1987), 73-83.
8. Farhanieh, B., Amanifard, N., Ghornanian, K., "Numerical Investigation on Compressible Flow Characteristics in Axial Compressors Using Multi-Block Finite Volume Scheme", ***International Journal of Engineering, Transactions A: Basics,*** Vol. 15, (2001), 91-104.
9. Bagheri-Esfe, H.,DehghanManshadi, M., "A Low Cost Numerical Simulation of a Supersonic Wind-tunnel Design", ***International Journal of Engineering, Transactions A: Basics,*** Vol. 31, No. 1, (2018), 128-135, doi: 10.5829/ije.2018.31.01a.18
10. Allmaras, S. R., Johnson, F. T., Spalart, P. R., "Modification and Clarification for the Implementation of the Spalart-Allmaras Turbulence Model", 7th international conference on Computational Fluid Dynamics, Big Island, Hawaii, (July 9-13, 2012), 2012.
11. R. Yahalom, "An experimental investigation of supersonic flow past yawed cones", College of engineering, University of Calofornia, Berkeley, Report No. AS-71-2, (1971).
12. Adel Zaki, M., "Physics Based Modeling of Axial Compressor Stall", Georgia Institute of Technology, PHD thesis, (2009).
13. Niazi, S., "Numerical Simulation of Rotating Stall and Surge Alleviation in Axial Compressors", Georgia Institute of Technology, PHD thesis, (2000).

Persian Abstract

چکیده

در این تحقیق یک طرح جدید از اجکتور پره‌دار فراصوتی ارائه شده است که در آن از یک روتور هرزگرد برای انتقال ممنتم از جریان فراصوتی اولیه به جریان ثانویه کمک گرفته شده است. برای بررسی و مدل‌سازی جریان درون این نوع اجکتور یک کد CFD تولید شده که قادر است جریان سه‌بعدی، تراکم‌پذیر، گران‌رو و متلاطم را درون اجکتور شبیه‌سازی کند. در این کد از روش Roe و مدل تلاطمی Spallart-Allmaras برای مدل‌سازی جریان تراکم‌پذیر و متلاطم درون اجکتور استفاده شده است. برای این کار از یک شبکه‌ی سازمان‌یافته استفاده شده و هوا به عنوان جریان اولیه و ثانویه به کار گرفته شده است. عدد ماخ هوا در خروجی نازل جریان اولیه و در ورودی به پره های روتور ۲ می‌باشد. این جریان علاوه بر این که با جریان ثانویه در تماس است و انتقال ممنتم از طریق تماس آنها رخ می دهد، سبب چرخش روتور هرزگرد نیز می‌شود که در پی آن جریان ثانویه به کمک پره‌های مکانیکی به درون اجکتور مکیده می شود. در این تحقیق چندین هندسه متفاوت از اجکتور بررسی شده و میزان آنتالپی، جریان مکش شده و فشار مکش برای حالت‌های مختلف مقایسه شده است. همچنین، معیاری برای مقایسه و اندازه‌گیری میزان یک‌نواختی جریان در خروجی از اجکتورها ارائه شده است. طبق نتایج به دست آمده در بهترین حالت از گزینه‌های مورد بررسی، سرعت روتور ۵۰۰۰۰ دور بر دقیقه بوده و نسبت مکش در مقایسه با همان اجکتور با روتور ثابت، ٤٧٪ افزایش نشان می‌دهد. برای بررسی جریان با جزئیات بیشتر، کانتورهای ارائه شده میزان تغییرات عدد ماخ و فشار کل را در مقاطع و صفحات مختلف از اجکتور نشان می‌دهد.

International Journal of Engineering

Journal Homepage: www.ije.ir

Elastic Buckling Response of a Composite Panel Stiffened Around Cutouts

S. B. Rayhan*

School of Aeronautics, Northwestern Polytechnical University, Xi'an, China

P A P E R I N F O

Paper history:
Received 22 August 2020
Received in revised form 20 September 2020
Accepted 30 October 2020

Keywords:
Critical Buckling Load
Perforated Composite Panel
Stiffener
Reinforcement
Finite Element Analysis
Fiber Orientation

A B S T R A C T

Perforated composite panels are widely used in many engineering applications as subcomponents of complex structures including aircraft, ships, and other transport vehicles. In many of these applications, the primary objective of using the panel is to resist buckling. In this present study, a finite element analysis is performed adopting popular commercial software code Ansys on the buckling behavior of a simply supported quasi-isotropic symmetric composite panel with central circular cutouts, reinforced with stiffeners on both sides of the cutouts under uniaxial, biaxial and combined loading conditions. The main objective is to achieve the elastic buckling response of the perforated composite panels considering some important aspects of the stiffener as follows: (1) effect of the presence of reinforcement, (2) effect of stiffener area, (3) effect of stiffener thickness, (4) effect of stiffener material and (5) effect of fiber orientation angle. It is observed that reinforcement can significantly improve the critical buckling load of a panel, which is already reduced due to cutouts. Then, increasing the area of the stiffener does not have a major impact on the buckling stability of the panels. However, increasing the thickness can play a crucial role to strengthen the buckling stability. Finally, it is found that in comparison to aluminum and titanium alloys, epoxy-carbon is more practical as a stiffener material with correct fiber orientation angle (90°), considering the low weight increment and higher buckling achievability.

doi: *10.5829/ije.2021.34.01a.27*

1. INTRODUCTION

Composite panels are often used as fundamental structural components in both the transportation and infrastructure industries. Cutouts are frequently found in these panels to meet the specific requirements based on applications like maintenance, pipe and cable access, hydraulic lines, weight reduction, etc. However, due to cutouts, in-plane compressive loading capability (also known as critical buckling) of thin-walled panels, reduces significantly with increasing cutout diameter [1-3]. Besides, various cutout shapes (circular, elliptical, square, triangular, etc.) present in the panel can significantly affect the critical buckling load [4], in some cases up to 50% [5]. In general, both circular and elliptical cutouts provide optimum buckling load [6] while their location in the panel is also crucial [7].

Among other important parameters, boundary and loading conditions have a great influence in the buckling load assessment of composite panels [8-11]. For instance, buckling load of a rectangular panel with clamped-clamped type boundary condition is twice that of clamped-simply supported condition, irrespective of various linearly varying in-plane compressive loads [12]. Furthermore, square panels with partial edge compression showed completely different behavior compared to those with full edge compression [13].

It is not always feasible to determine buckling strength of composite panels due to the complex setups (e.g., poor hand layup manufacturing process of composite panels [14], shear loading [15], etc.) and costs involved. On the other hand, readily available analytical formulas are not always applicable for panels, especially with cutouts [16]. Therefore, commercial finite element analysis (FEA) packages, namely, Abaqus, Ansys, MSC Nastran, etc., are widely adopted to conduct various parametric studies on the buckling strength of panels [17-22]. In most cases, the predicted buckling [23, 24] and

*Corresponding Author Institutional Email: *rayhan,saiaf@mail.nwpu.edu.cn* (S. B. Rayhan)

Please cite this article as: S. B. Rayhan, Elastic Buckling Elastic Buckling Response of a Composite Panel Stiffened Around Cutouts, International Journal of Engineering, Transactions A: Basics Vol. 34, No. 01, (2021) 243-252

post-buckling [25] strength using FEM agrees quite well with the experiments. However , in some particular instances, the discrepancy may reach up to 30% due to imperfections found in the tested specimen, material and experimental boundary conditions [26].

As described earlier, cutouts are inevitable in panels, which eventually decrease the in-plane compressive loading capability of structures. Therefore, it is common in offshore structures to adopt various reinforcement types to strengthen the buckling load capability of isotropic panels, which are mainly selected based on loading conditions [27]. Apart from that, perforated composite panels can also be strengthened with flange reinforcement, ring reinforcement, flange and ring reinforcement, and double ring reinforcement. It is reported that for composite panels under shear loading, double ring reinforcement is most effective; when considering both stress reduction and buckling stability [28]. Subsequent research reveals that the critical buckling load of a composite C-section flange can be increased by 20.9% with a reinforcing L-shape stiffener [29]. More recent investigation on the reinforcement of composite perforated panels suggests that longitudinal and planer type stiffener can improve the buckling load capacity of panels by 2.8 and 1.9 times in contrast to the panel without the stiffener, respectively [30].

While several contributions] are made to investigate the critical buckling load of the panels, only a few studies are reported to reinforce the cutouts and improve the buckling stability of the panels [1-13, 17-21, 23-30]. Moreover, no investigations are found to address the effect of reinforcement parameters like area and thickness of stiffener, stiffener material and fiber orientation angle of composite stiffener on the buckling stability of the panels. Therefore, the main objective of this current research is to study the critical buckling improvement of simply supported composite panels, while reinforcing planer type stiffeners on both sides of the panel around the cutout under three different loading conditions, namely uniaxial, biaxial, and combined loading, based on commercial finite element code Ansys.

2. PROBLEM STATEMENT

A quasi-isotropic symmetric layup $[0°/45°/-45°/90°]_{2s}$ is considered as a composite panel with a dimension of 300 mm (length, a) × 200 mm (width, b) × 3 mm [total thickness of the panel, 0.1875 mm (= t_{ply}) × 16] along with central circular cutouts having a diameter (d) of 20 mm, 40 mm, 60 mm, 80 mm, 100 mm and 120 mm. The cutouts are reinforced from both sides of the panel with square planer type stiffeners. These stiffeners have the same circular cutouts as the panels to which they are affixed. The length of each side of the stiffener is defined as 10 mm + d + 10 mm (see Figure 1). The thickness of each stiffener attached on both sides of the panel is 0.1875 mm (the same as a single ply thickness of composite laminate).

First, to study the effect of the area of the stiffeners, the horizontal sides are increased by 5 mm intervals up to 30 mm while the lengths of the vertical sides are kept fixed. Then, the vertical sides are lenghthened by similar 5 mm intervals while the lengths of the horizontal sides are kept constant. Next, both the horizontal and vertical sides are lengthened together in such a way that the area increase matches the area of the stiffeners in the previous steps of lengthening the horizontal or vertical sides. In summary, the buckling load due to cutout reinforcement is studied in the cases of incremental lengthening of the horizontal side of the planer stiffener, incremental lengthening of the vertical side of the planer stiffener, and incremental lengthing of both sides simultaneously (Figure 2). In addition, when investigation is conducted on the stiffener thickness, the initial area of the stiffener, that is, 10 mm + d + 10 mm, is kept constant while the thickness is increased as doubled, tripled and quadrupled for both the affixed stiffeners. Similarly, during the investigation of the area increment of stiffener, the initially assumed thickness of the stiffener is kept fixed, to be precise, 0.1875 mm. Finally, to study the effect of

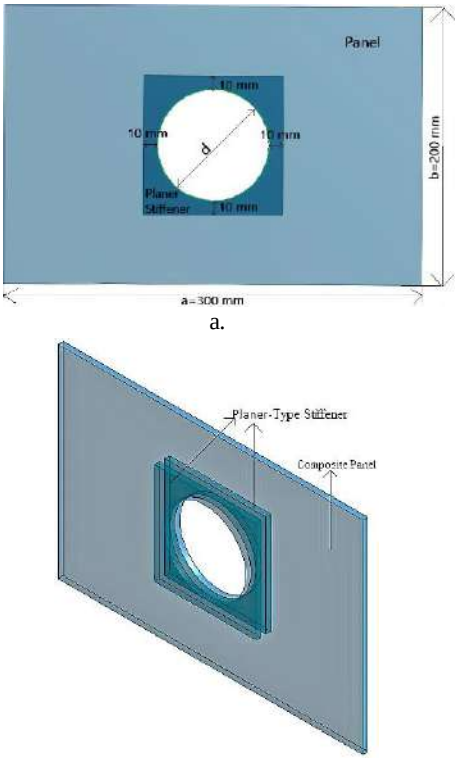

Figure 1. Composite panel with circular cutouts and reinforced stiffeners; a: 2D view of the composite panel with stiffener and dimensions, b: 3D view of the stiffeners bonded with composite panels

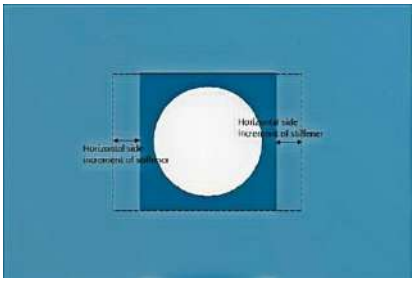

a.

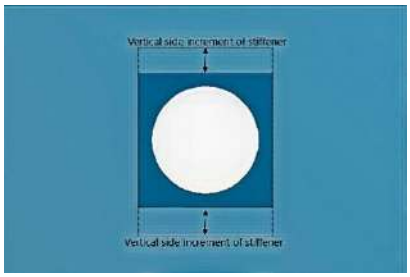

b.

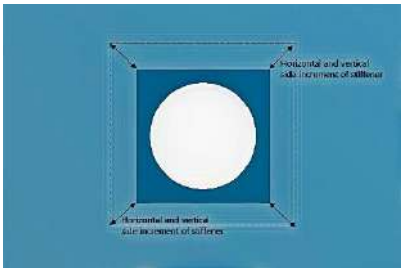

c.

Figure 2. Area increment plan of stiffeners; a: Horizontal side increment plan, b: Vertical side increment plan, c: Simultaneous horizontal and vertical side increment plan

the material, both initial thickness and stiffener area are kept constant. The following assumptions are made to carry out the critical buckling investigations of the perforated panel:-

(1) The Planer stiffener is perfectly bonded with the panel around the cutouts. This assumption is valid since the study is limited to critical buckling which occurs in the elastic zone and does not have any effect on the connection until the sudden post-buckling collapse takes place in the plastic region [31].

(2) This investigation is limited to critical buckling only. Further first ply failure, damage, etc. are not sought since critical buckling itself is a type of failure which takes place far before the damage is initiated in the composite panels [32-34].

The material of the composite panel is assumed to be epoxy-carbon while for reinforced stiffener, aerospace type aluminum alloy T3-2024 is adopted. To compare the effect of the stiffener material on the buckling behavior of the perforated panel, apart from aluminum alloy, the same composite material of the panel with ply orietation of 0°,30°,45°,60°, 90°, and titanium alloy is chosen. The mechanical properties of all the materials used for this case study are given below in Table 1.

3. FINITE ELEMENT PROCEDURE

Commercial FE code Ansys is employed to investigate the eigenvalue buckling of the reinforced composite panel. Meshing the structure to prepare for finite element analysis is one of the most crucial steps since poor meshing adoption often leads to inappropriate results and special consideration should be taken for structures with discontinuity, for instance, the panel with holes. Therefore, for meshing the panel and the stiffener, mapped face meshing with quadrilateral shell elements is applied. Since the cutouts are sensitive, meshing is more refined towards the cutout (Figure 3). Besides, for each cutout ratio, the mesh element number is kept in such that increasing the element number would not lead to any further change in eigenvalue buckling.

For the boundary conditions of the panel, all edges are considered as simply supported since most aerospace panels are simply supported [35]. Three loading cases are considered for the panel, namely, uniaxial, biaxial, and combined loading (shear and uniaxial together), (see Figure 4).

3. VALIDATION OF THE PRESENT STUDY

The present finite element analysis results are validated with available experimental data for various composite panels with central circular cutouts found in literature [36], (see Table 2). It can be observed that most of the current finite element predictions are closer to the experimental results than the author's finite element results.

TABLE 1. Mechanical properties of Epoxy-Carbon Unidirectional, Aluminum and Titanium Alloy

Material	Density, P (Kg/m^3)	E_{11} (GPa)	$E_{22}=E_{33}$ (GPa)	$G_{12}=G_{13}$ (GPa)	G_{23} (GPA)	$V_{12}=V_{13}$	V_{23}
Epoxy-Carbon	1490	121	86	4.7	3.1	0.27	0.4
Aluminum Alloy	2780	73.1		27.481		0.33	
Titanium Alloy	4620	96		35.3		0.36	

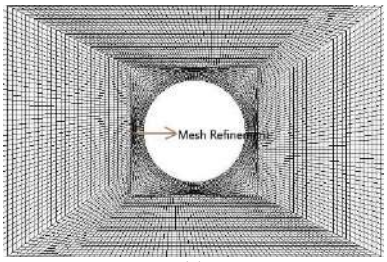

(a)

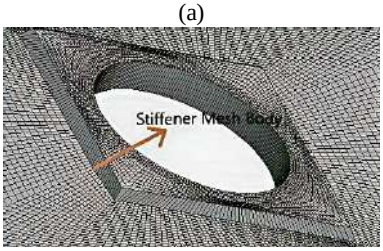

(b)

Figure 3. Composite panel meshing with stiffeners; a: Composite panel meshing with refinements, b: Closure view of stiffener meshed body

5. NUMERICAL RESULTS AND DISCUSSIONS

5. 1. Effect of Reinforcement Firstly, a comparative study of perforated composite panels with and without reinforcement is carried out to investigate the influence of stiffeners on the critical buckling load for cutout ratios (d/b) 0.1 to 0.6 as shown in Figure 5. It is observed that for all loading cases, stiffened panels show better critical buckling stability than panels without having stiffeners. The studies also revealed that, as the cutout ratio increases, due to the reinforcement, the percentage of buckling stability of a panel increases significantly compared to the same panel without having stiffeners (see Figure 6). The highest buckling achievement occurs for a combined loading case with the cutout ratio 0.6. In this case, reinforcing the panel improves buckling stability by 26%. However, for biaxial loading, the increment percentage is relatively low compared with other loading cases. Besides, for the cutout ratio of 0.1, reinforcement does not greatly affect the critical buckling load; it only changes by an increment of around 5% for all loading cases.

(a) (b)

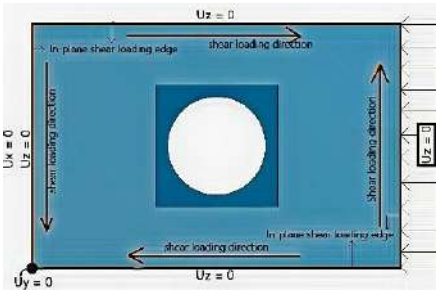

(c)

Figure 4. Boundary conditions of the panel; a: Uniaxial loading, b: Biaxial loading, c: Combined loading

TABLE 2. Comparison of buckling loads with central circular cutouts

Plate length by plate thickness	Laminate Code	Boundary Condition	Author FE results, N	Experimental results, N	Present Study, N
75	$[90°/45°/-45°/0°]_s$	Clamped-Clamped	377.4	410	458.2
	$[90°/45°/-45°/0°]_{as}$		540.65	465	510.77
	$[90°/45°/-45°/0°]_s$	Clamped-Pinned	185.2	215	222.78
	$[90°/45°/-45°/0°]_{as}$		277.3	240.6	262.2
	$[90°/45°/-45°/0°]_s$	Pinned-Pinned	94.2	89.1	101.7
	$[90°/45°/-45°/0°]_{as}$		133.7	144.69	125.1
37.5	$[90°/45°/-45°/0°]_s$	Clamped-Clamped	1608.7	1326	1571
	$[90°/45°/-45°/0°]_{as}$		2120.3	2209	2000
	$[90°/45°/-45°/0°]_s$	Clamped-Pinned	792.7	759	755
	$[90°/45°/-45°/0°]_{as}$		1096.7	1244	1033.9
	$[90°/45°/-45°/0°]_s$	Pinned-Pinned	414.5	358	395.76
	$[90°/45°/-45°/0°]_{as}$		520.8	518	488

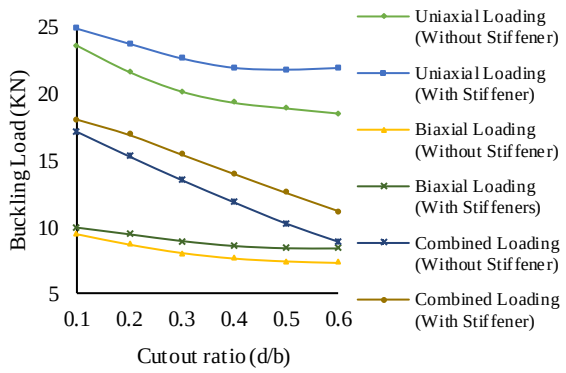

Figure 5. Buckling load of perforated panels with and without stiffeners

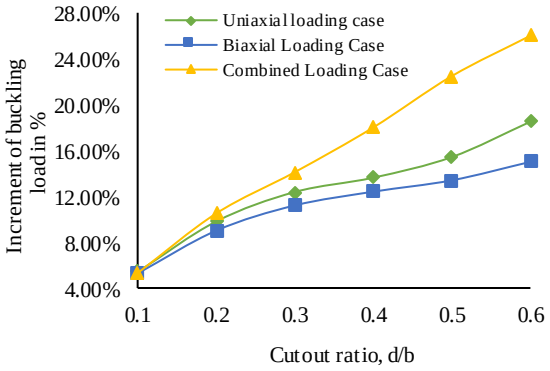

Figure 6. Cutout ratio vs. buckling load increment under various loading conditions

5. 2. Effect of Increasing the Area of Stiffeners

Since the reinforcement has a positive impact on the buckling load of perforated panels, a further investigation is performed by increasing the area of the stiffener to check whether additional area provides better stability to the panels. The results suggest that for any loading condition, increasing the area horizontally, vertically, or simultaneously does not have a major effect on the buckling behavior of reinforced panels with cutout ratio 0.1 and 0.2 as shown in Figures 7(a) and 7(b). Similar trends can be observed for cutout ratios 0.3 and 0.4 except for the uniaxial loading case, where the maximu m increment of the vertical area provides an increment of 8% critical buckling value to the panel as illustrated in Figures 7(c) and 7(d). This trend continues for cutout ratios 0.5 and 0.6 too, where buckling strength can be further increased by 12 and 13.5%, respectively; for the highest increment of the area, as shown in Figures 7(e) and 7(f). For the other two loading conditions, the increment of the area of any form has minor effects on the overall critical buckling value of the panel observed in Figures 7(e) and 7(f).

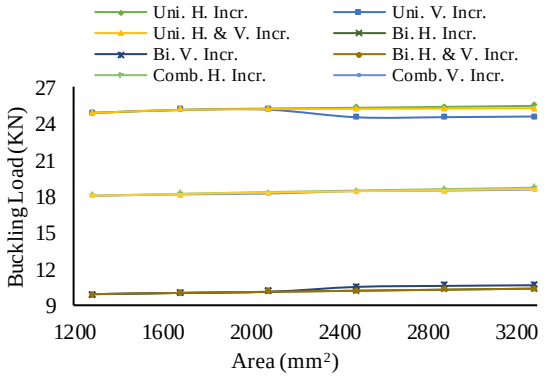

(a)

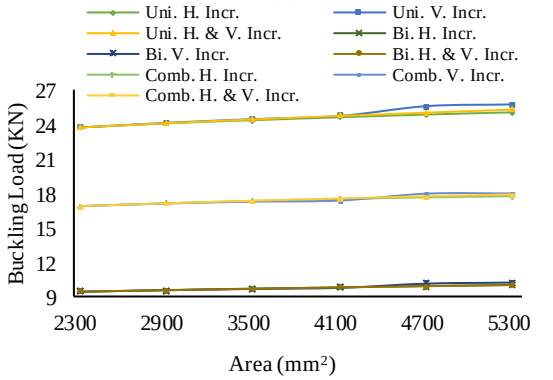

(b)

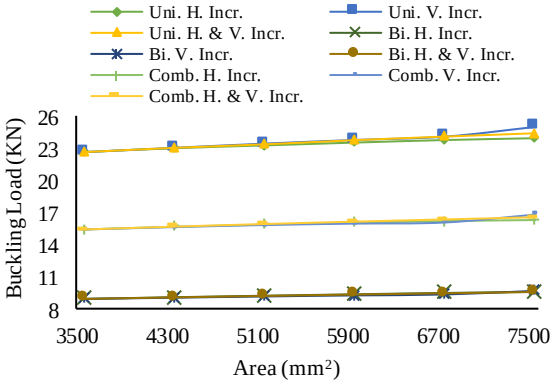

(c)

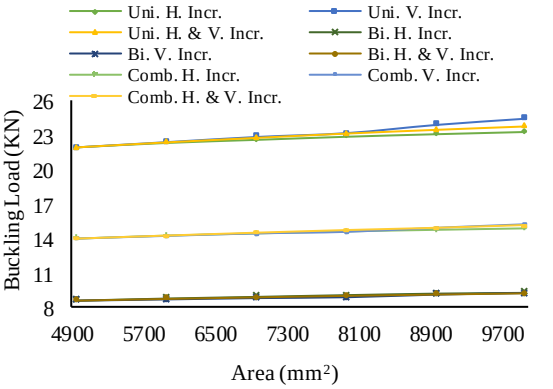

(d)

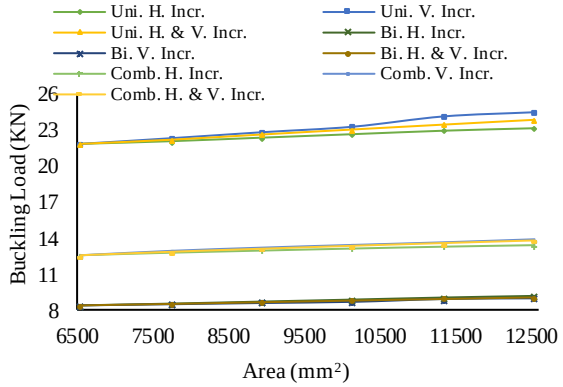

(e)

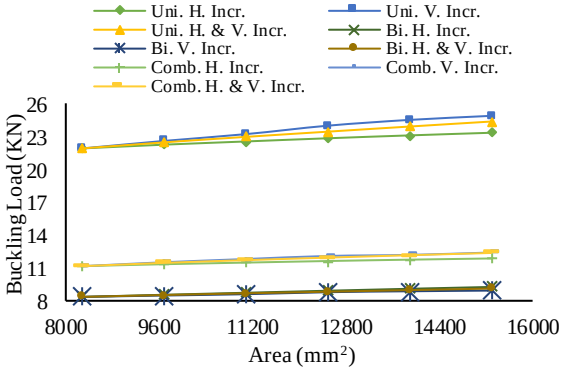

(f)

Figure 7. Effect of area increment of stiffener on the buckling load of panels; (a) Cutout ratio, d/b=0.1, (b) Cutout ratio, d/b=0.2, (c) Cutout ratio, d/b=0.3, (d) Cutout ratio, d/b=0.4, (e) Cutout ratio, d/b= 0.5, (f) Cutout ratio, d/b=0.6.

5. 3. Effect of Thickness of the Stiffener Unlike the previously discussed case, increasing the thickness of the stiffeners has a major impact on the critical buckling load of the composite panels illustrated in Figures 8(a), 8(b), and 8(c). Even though, for cutout ratio 0.1, no significant load increase is observed. However, improvement of the buckling stability starts to take place from cutout ratio 0.2. For cutout ratio 0.3, for a thickness of 0.75 mm (×2) stiffener, the increment can be achieved up to 22.9, 27.1, and 29.87% for uniaxial, biaxial and combined loading, respectively. The highest impact on the critical buckling load due to increasing the thickness occured for cutout ratio 0.6 when doubling the thickness from 0.1875 to 0.375 mm for both the stiffeners will strengthen the buckling capacity of panels by 16.1, 13.67 and 22% for uniaxial, biaxial and combined loading cases, respectively. For a thickness of 0.75 mm (×2) stiffener, buckling strength can be increased further up to 49.5, 43.4 and 70% for uniaxial, biaxial and combined loading cases, respectively. Besides, for the uniaxial loading case, when the thickness of the stiffeners is 0.1875 mm × 6 and 0.1875 mm × 8, buckling load increases with the cutout ratios. A similar conclusion can be made for the biaxial loading caseas well , when 0.1875 mm × 8 reinforced stiffeners provide a rise in buckling load with the increase of cutout ratios. However, no such increase is observed for the combined loading case. Finally, it is important to note that increasing the thickness of stiffeners is most beneficial for strengthing stability of combined loaded panels.

5. 4. Effect of Stiffener Material and Fiber Orientation Reinforcement on a composite panel will definitely add up weights to the structure which should be minimized to achieve the desired strength of the panel. Material plays an important role to achieve the

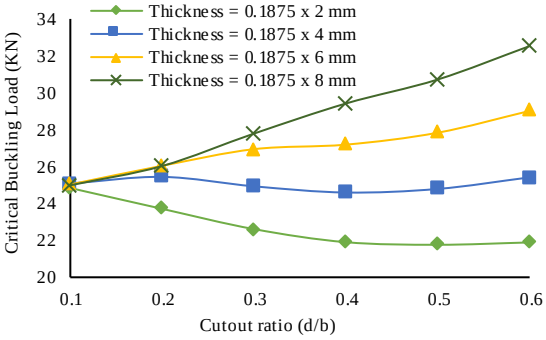

(a)

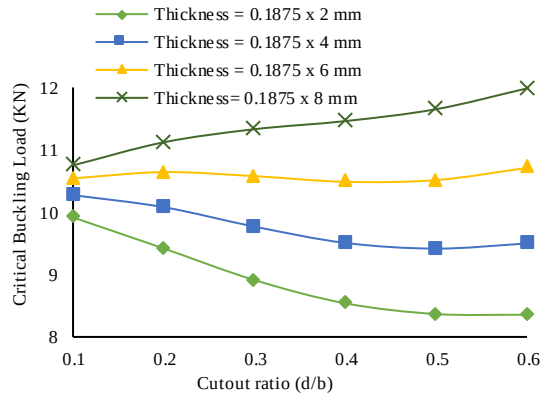

(b)

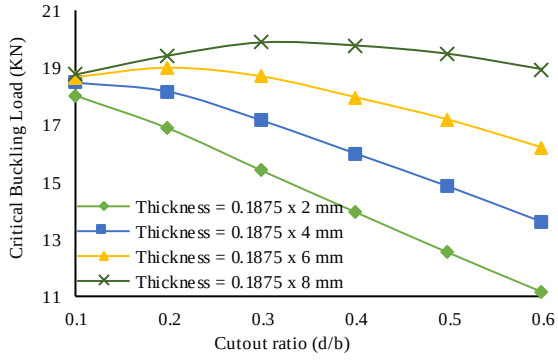

(c)

Figure 8. Buckling load at various thickness of stiffeners and cutout ratios at various loading conditions; (a) Uniaxial loading, (b)Biaxial loading; (c) Combined loading

convenient strength to weight ratio of a panel. Therefore, a detailed study is carried out on the stiffener material and it can be observed that, in case of composite stiffener, fiber orientation angle has a strong influence on the critical buckling load of composite panels. For all the loading cases and cutout ratios, changing the fiber orientation angle from 0° to 90°, leads to a sharp increase in the critical buckling load of the panels (see Figure 9). In comparison with the aluminum alloy, for all loading cases and cutout ratio, 90° fiber orientation performs slightly better than the alloy except for cutout ratio 0.6 when aluminum alloy provides a better stability to the uniaxial and combined loading cases up to 4.5 and 3.8%, respectively. Along with aluminum alloy and epoxy-carbon, titanium alloy is also investigated which outperforms both of them providing better stability to the panels. However, as described earlier, a strength to weight ratio must be maintained for lightweight structure; therefore, a comparison of weight increment and buckling load increment in percentage for all cutout ratios is shown in Figure 10. Interestingly, up until cutout ratio 0.3, for all loading cases, epoxy-carbon provides almost similar buckling strength to the panel compared with titanium alloy. However, for cutout ratio 0.4 and greater, titanium alloy provides increasingly more stability to the panels. This is most severe for uniaxial and combined loading cases and cutout ratio 0.6, when using titanium alloy provides almost 16.29 and 13% more stability to the panels. Nevertheless, looking at the weight increment, epoxy-carbon is more practical than titanium alloy because of its lower density.

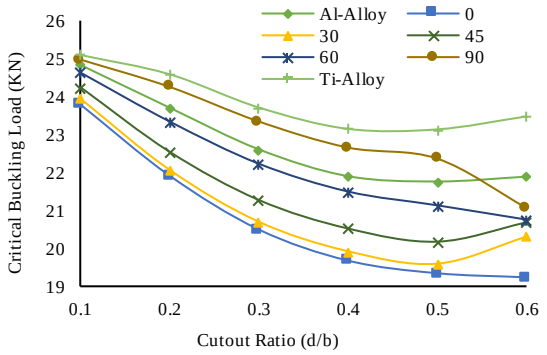

(a)

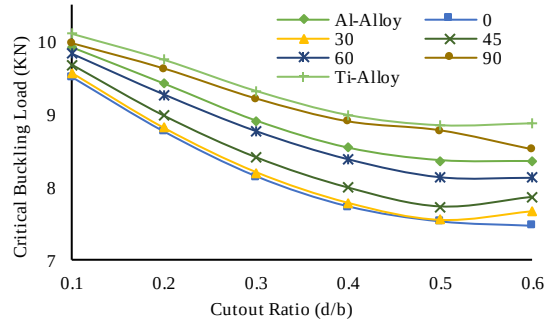

(b)

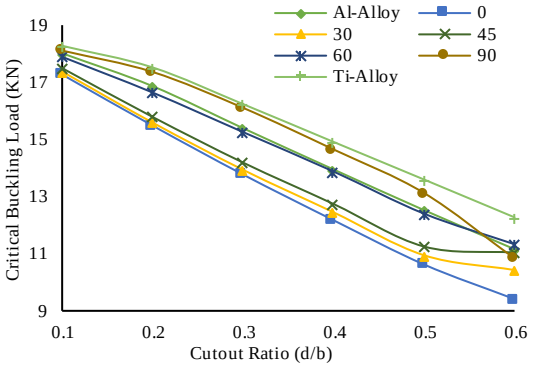

(c)

Figure 9. Stiffener material and fiber orientation angle on the buckling load at various loading condition; (a) Uniaxial loading, (b) Biaxial loading; (c) Combined loading

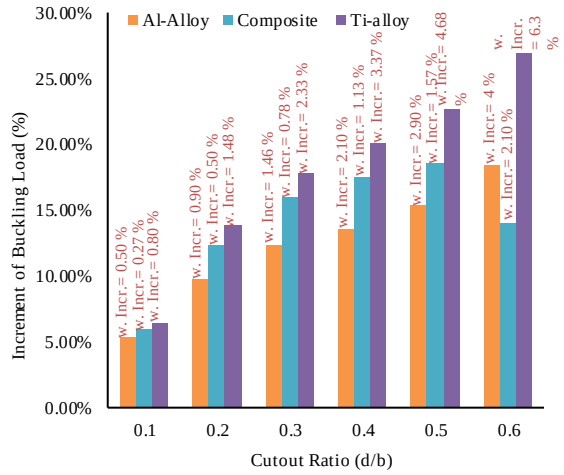

(a)

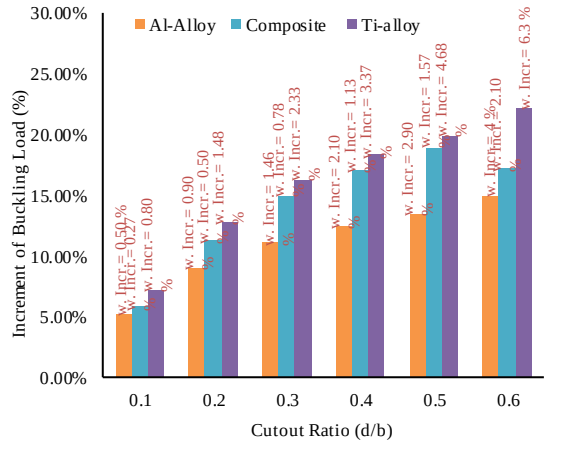

(b)

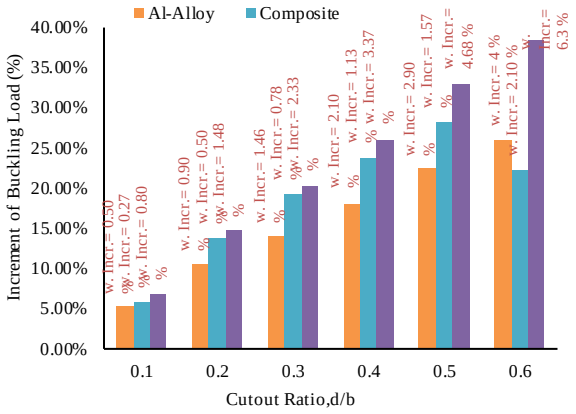

(c)

Figure 10. Effect of stiffener material weight and corresponding buckling increment; (a)Increment of Buckling load (in %) and weight increment (in %) at various cutout ratios under uniaxial loading case, (b) Increment of buckling load (in %) and weight increment (in %) at various cutout ratios under biaxial loading case, (c) Increment of buckling load (in %) and weight increment (in %) at various cutout ratios under combined loading case

6. CONCLUSION

A large number of simulations are carried out to investigate the effect of planer type stiffener as reinforcement to the quasi-isotropic perforated composite panels. Based on the investigations, key findings are outlined as follows.

1. Buckling stability of panels with smaller cutout ratios (0.1 and 0.2) does not improve greatlydue to reinforcement. Even increasing the stiffener thickness or choosing strong material like titanium alloy fails to increase the stability of the panels significantly. In summary, planar type stiffeners should not be chosen asreinforcement for smaller cutouts.
2. Planer reinforcement improves the buckling stability of the simply supported panels with central circular holes under any loading conditions.
3. The percentage of buckling stability that is due to reinforcement increases with increasing cutout area.
4. Increasing the area of the stiffener does not have a significant effect on the critical buckling load of the reinforced panels.
5. Increasing the thickness of the stiffener has a major impact on the critical buckling load of the panels.

For the uniaxial loading case, when the stiffener thickness is tripled and quadrupled, the critical buckling load of the panels increases with the cutout ratio.

6. In the case of choosing composite (epoxy-carbon) as stiffener material, fiber orientation has a great impact on the overall buckling stability of the panels.
7. For weight reduction and maximizing the critical buckling capability, composite (epoxy-carbon) material is preferable to metals (aluminum and titanium alloy)
8. Among all loading cases, the stability of stiffened panels under combined loading condition is mostly benefited from the reinforcement.

7. ACKNOWLEDGEMENTS

The author is grateful to China Scholarship Council (CSC) for financing his research at Northwestern Polytechnical University, China (CSC grant No. GXZ023506).

8. REFERENCES

1. Aydin Komur, M., Sonmez, M.,"Elastic buckling of rectangular plates under linearly varying in-plane normal load with a circular cutout." ***Mechanics Research Communications***, Vol. 35, No. 6, (2008), 361-371. DOI: 10.1016/j.mechrescom.2008.01.005.
2. Aydin Komur, M., Sen, F., Ataş, A., Arslan, N., "Buckling analysis of laminated composite plates with an elliptical/circular cutout using FEM. " ***Advances in Engineering Software***, Vol. 41, No. 2, (2010), 161-164. DOI: 10.1016/j.advengsoft.2009.09.005.
3. Onkar, A., Upadhyay, C., Yadav, D., "Stochastic Finite Element Buckling Analysis of Laminated Plates with Circular Cutout under Uniaxial Compression." ***Journal of Applied Mechanics***, Vol. 74, No. 4, (2006), 798-809. DOI: 10.1115/1.2711230.
4. Erkliğ, A., Yeter, E., "The effects of cutouts on buckling behavior of composite plates." ***Science and Engineering of Composite Materials***, Vol. 19, No. 3, (2012), 323-330. DOI: 10.1515/secm-2012-0011.
5. Rayhan, S., "A comprehensive study on the buckling behaviour of woven composite plates with major aerospace cutouts under uniaxial loading." ***Journal of Mechanical Engineering and Sciences***, Vol. 13, No. 2, (2019), 4756-4776. DOI: 10.15282/jmes.13.2.2019.01.0398.
6. Tercan, M., Aktaş, M., "Buckling behavior of 1×1 rib knitting laminated plates with cutouts." ***Composite Structures***, Vol. 89, No. 2, (2009), 245-252. DOI: 10.1016/j.compstruct.2008.07.030.
7. Jana, P., "Optimal design of uniaxially compressed perforated rectangular plate for maximum buckling load." ***Thin-Walled Structures***, Vol. 103, (2016), 225-230. DOI: 10.1016/j.tws.2015.12.027.
8. Ghannadpour, S., Najafi, A., Mohammadi, B., "On the buckling behavior of cross-ply laminated composite plates due to circular/elliptical cutouts." ***Composite Structures***, Vol. 75, (2006), 3-6. DOI: 10.1016/j.compstruct.2006.04.071.
9. Topal, U., Uzman, Ü., "Effects of nonuniform boundary conditions on the buckling load optimization of laminated composite plates." ***Materials & Design***, Vol. 30, No. 3 (2009), 710-717. DOI: 10.1016/j.matdes.2008.05.012.
10. Rajanna, T., Banerjee, S., Desai, Y., Prabhakara, D., "Effect of boundary conditions and non-uniform edge loads on buckling characteristics of laminated composite panels with and without cutout." ***International Journal for Computational Methods in Engineering Science and Mechanics***, Vol. 18, No. 1, (2017), 64-76. DOI: 10.1080/15502287.2016.1276350.
11. Maarefdoust, M., Kadkhodayan, M., "Elastoplastic Buckling Analysis of Plates Involving Free Edges by Deformation Theory

of Plasticity." ***International Journal of Engineering, Transections A: Basics***, Vol. 26, No. 4, (2013), 421-432. DOI: 10.5829/idosi.ije.2013.26.04a.11

12. Narayana, A., Rao, K., Kumar, R., "Buckling analysis of rectangular composite plates with rectangular cutout subjected to linearly varying in-plane loading using fem.", ***Sadhana***, Vol. 39, No. 3, (2014), 583-596. DOI: 10.1007/s12046-014-0250-9.
13. Singh, S., Kulkarni, K., Pandey, R., Singh, H., "Buckling analysis of thin rectangular plates with cutouts subjected to partial edge compression using FEM." ***Journal of Engineering, Design and Technology***, Vol. 10, No. 1, (2012), 128-142. DOI: 10.1108/17260531211211935.
14. Elkington, M., Bloom, D., Ward, C., Chatzimichali, A., Potter, K., "Hand layup: understanding the manual process." ***Advanced Manufacturing: Polymer & Composites Science***, Vol. 1, No. 3, (2015), 38-151. DOI: 10.1080/20550340.2015.1114801.
15. Islam, M., khan, A., Walter, S., Jian, L., "A Study of Shear Stress Intensity Factor of PP and HDPE by a Modified Experimental Method together with FEM", ***International Journal of Mechanical, Aerospace, Industrial and Mechatronics Engineering***, Vol. 7, No. 11 (2013), 1177-1178. DOI: 10.5281/zenodo.1088948.
16. Kassapoglou, C., Design and Analysis of Composite Structures, John Wiley and Sons Ltd, West Sussex, 2010. DOI: 10.1002/9781118536933.
17. Özben, T., "Analysis of critical buckling load of laminated composites plate with different boundary conditions using FEM and analytical methods." ***Computational Materials Science***, Vol. 45, No. 4, (2009), 1006-1015. DOI: doi.org/10.1016/j.commatsci.2009.01.003.
18. Mohtaram, Y., Kahnamouei, J., Shariati, M., Behjat, B., "Experimental and numerical investigation of buckling in rectangular steel plates with groove-shaped cutouts." ***Journal of Zhejiang University Science A***, Vol. 13, No. 6 (2012), 469-480. DOI: 10.1631/jzus.A1100226.
19. Okutan Baba, B., Baltaci, A., "Buckling Characteristics of Symmetrically and Antisymmetrically Laminated Composite Plates with Central Cutout." ***Applied Composite Materials***, Vol. 14, No. 4, (2007), 265-276. DOI: 10.1007/s10443-007-9045-z.
20. Baba, B., "Buckling Behavior of Laminated Composite Plates." ***Journal of Reinforced Plastics and Composites***, Vol. 26, No. 16, (2007), 1637-1655. DOI: 10.1177/0731684407079515.
21. Geng, X., Zhao, L., Zhou, W., "Finite-element buckling analysis of functionally graded GPL-reinforced composite plates with a circular hole." ***Mechanics Based Design of Structures and Machines***, Vol. 48, No. 1, (2020), 1-17. DOI: 10.1080/15397734.2019.1707688.
22. Yousefi Khatuni, S., Showkati, H., "Buckling Behavior of Semi-scale Steel Tank with Carbon Fiber Reinforced Polymer Ring Subjected to Lateral Uniform Pressure Loading." ***International Journal of Engineering, Transections A: Basics***, Vol. 32, No. 10, (2019), 1407-1415. DOI: 10.5829/ije.2019.32.10a.10.
23. Yazici, M., "Influence of Cut-Out Variables on Buckling Behavior of Composite Plates." ***Journal of Reinforced Plastics and Composites***, Vol. 28, No. 19, (2008), 2325-2339. DOI: 10.1177/0731684408092058.
24. Turan, K., "Buckling behavior of adhesively patch-repaired composite plates." ***Journal of Composite Materials***, Vol. 48, No. 26, (2013), 3253-3261. DOI: 10.1177/0021998313508801.
25. Erdem, S., Kaman, M. and Gur, M., "Post-buckling behavior of carbon fiber epoxy composite plates." ***Journal of Mechanical Science and Technology***, Vol. 33, No. 4, (2019), 1723-1730. DOI: 10.1007/s12206-019-0324-z.
26. Baba, B., "Buckling Response of Rectangular Laminated Composite Plates with Cutouts". ***Science and Engineering of Composite Materials***, Vol. 14, No. 1, (2007), 17-24. DOI: 10.1515/SECM.2007.14.1.17.
27. Kim, J., Jeon, J., Park, J., Seo, H., Ahn, H., Lee, J., "Effect of reinforcement on buckling and ultimate strength of perforated plates." ***International Journal of Mechanical Sciences***, Vol. 92, (2015), 194-205. DOI: 10.1016/j.ijmecsci.2014.12.016.
28. Guo, S., "Stress concentration and buckling behaviour of shear loaded composite panels with reinforced cutouts." ***Composite Structures***, Vol. 80, No. 1, (2007), 1-9. DOI: 10.1016/j.compstruct.2006.02.034.
29. Guo, S., Li, D., Zhang, X., Xiang, J., "Buckling and post-buckling of a composite C-section with cutout and flange reinforcement." ***Composites Part B: Engineering***, Vol. 60, (2014), 119-124. DOI: 10.1016/j.compositesb.2013.12.055.
30. Shojaee, T., Mohammadi, B., Madoliat, R., "Experimental and numerical investigation of stiffener effects on buckling strength of composite laminates with circular cutout". ***Journal of Composite Materials***, Vol. 54, No. 9, (2019), 1141-1160. DOI: 10.1177/0021998319874101.
31. Zhu, S., Yan, J., Chen, Z., Tong, M., Wang, Y., "Effect of the stiffener stiffness on the buckling and post-buckling behavior of stiffened composite panels – Experimental investigation." ***Composite Structures***, Vol. 120, (2015), 334-345. DOI: 10.1016/j.compstruct.2014.10.021.
32. Kong, C., Hong, C., Kim, C., "Postbuckling Strength of Composite Plate with a Hole." ***Journal of Reinforced Plastics and Composites***, Vol. 20, No. 6, (2001), 466-481. DOI: 10.1177/073168401772678652.
33. Kumar, D. and Singh, S., "Postbuckling strengths of composite laminate with various shaped cutouts under in-plane shear." ***Composite Structures***, Vol. 92, No. 12, (2010), 2966-2978. DOI: 10.1016/j.compstruct.2010.05.008.
34. Vummadisetti, S. and Singh, S., "Buckling and postbuckling response of hybrid composite plates under uniaxial compressive loading." ***Journal of Building Engineering***, Vol. 27, (2020). DOI: 10.1016/j.jobe.2019.101002.
35. Ion, D., "Buckling of Flat Thin Plates under Combined Loading." ***Incas Bulletin***, Vol. 7, No. 1, (2015), 83-96. DOI: 10.13111/2066-8201.2015.7.1.8.
36. Okutan Baba, B., Baltaci, A., "Buckling characteristics of symmetrically and antisymmetrically laminated composite plates with central cutout." ***Applied Composite Materials***, Vol. 14, No. 4, (2007), 265-276. DOI: 10.1007/s10443-007-9045-z.

Persian Abstract

چکیده

پانل های کامپوزیت سوراخ دار به طور گسترده ای در بسیاری از برنامه های مهندسی به عنوان زیرمجموعه های سازه های پیچیده از جمله هواپیما ، کشتی و سایر وسایل نقلیه حمل و نقل مورد استفاده قرار می گیرند. در بسیاری از این برنامه ها ، هدف اصلی استفاده از پانل مقاومت در برابر کمانش است. در این مطالعه حاضر ، تجزیه و تحلیل عناصر محدود با استفاده از کد نرم افزار محبوب تجاری Ansys در مورد رفتار کمانش یک صفحه مرکب متقارن شبه ایزوتروپیک متقارن با برش های دایره ای مرکزی ، تقویت شده با سخت کننده های دو طرف بریدگی تحت تک محوری ، دو محوری و شرایط بارگیری ترکیبی هدف اصلی دستیابی به پاسخ کمانش الاستیک صفحات کامپوزیت سوراخ دار با در نظر گرفتن برخی از جنبه های مهم ماده سخت کننده به شرح زیر است: ، (٤) اثر ماده سخت کننده و (٥) اثر زاویه جهت الیاف. مشاهده شده است که آرماتورها می توانند بار بحرانی کمانش یک صفحه را بهبود بخشند ، که در حال حاضر به دلیل بریدگی کاهش یافته است. سپس ، افزایش سطح ماده سخت کننده تأثیر زیادی در پایداری کمانش صفحات ندارد. با این حال ، افزایش ضخامت می تواند نقشی اساسی در تقویت ثبات کمانش داشته باشد. سرانجام ، مشخص شد که در مقایسه با آلیاژهای آلومینیوم و تیتانیوم ، با توجه به افزایش وزن کم و قابلیت کمانش بالاتر ، اپوکسی کربن به عنوان یک ماده سفت کننده با زاویه جهت الیاف صحیح (۹۰ درجه) عملی تر است..

IJE TRANSACTIONS A: Basics Vol. 34, No. 01, (January 2021) 253-262

International Journal of Engineering

Journal Homepage: www.ije.ir

Reliability Analysis of Notched Plates under Anisotropic Damage Based on Uniaxial Loading using Continuum Damage Mechanics Approach

M. Nadjafi*[a], P. Gholami[b]

[a] *Aerospace Engineering, Aerospace Research Institute (Ministry of Science, Research and Technology), Tehran, Iran*
[b] *Aerospace Engineering, Department of Aerospace Engineering, Sharif University of Technology, Tehran, Iran*

P A P E R I N F O

Paper history:
Received 08 June 2020
Received in revised form 28 September 2020
Accepted 30 October 2020

Keywords:
Anisotropic Damage
Continuous Damage Mechanics
Energy Density Release Rate
First Order Reliability Method
Second Order Reliability Method

A B S T R A C T

Extensive recent researches have been underway to model the fracture mechanics degradation based on continuum damage mechanics (CDM) technique. CDM theory is a powerful tool for solving problems such as large plastic deformations that the fracture mechanics is unable to solve. This model is derived by means of the thermodynamics internal variable theory and based on the experimental results on material properties. In this paper, the reliability of rectangular plates containing a central circular hole under static tensile load using the CDM approach for ductile fracture has been studied. To investigate the initiation and evolution of damages, anisotropic damage expressed by second order damage tensor is used to derive constitutive equations. Then, these relationships together with material constants are implemented with subroutine in ABAQUS software. The reliability assessment has been investigated using first order reliability method (FORM) and second order reliability method (SORM). Based on the FORM and SORM, the limit state functions and random variables have been obtained according to the energy density release rate. The probability of failure of each plate with different hole sizes is estimated based on the anisotropic damage theory, and the results are compared with the isotropic damage model. Finally, the sensitivity analysis of the coefficient of variation is performed.

***doi**: 10.5829/ije.2021.34.01a.28*

NOMENCLATURE

b	Isotropic hardening exponents	X	Random variable
D	Scalar damage variable	Y	Energy density release rate
D_c	Critical damage	**Greek Symbols**	
D_H	Hydrostatic damage	α	Damage exponent
E	Young modulus of elasticity	β	Reliability index
f	Yield function of plastic criterion	Γ	Gibbs free energy
F	Dissipative potential function	ε	Uniaxial total strains
F_D	Damage potential function	ε_p	Plastic strain
F_P	Plastic potential function	ε_{pD}	Damage threshold plastic strain
g	Performance function	ε_{pR}	Rupture plastic strain
k	Curvature of the performance function	η	hydrostatic sensitivity parameter
p	Accumulated plastic strain	Φ	Cumulative distribution function
P	Probability of failure	λ	Plastic multiplier
R	Isotropic hardening	ν	Poisson ratio
$\boldsymbol{R}$	Reliability	ρ	Mass density
R_∞	Saturated isotropic hardening parameter	σ	Uniaxial and tensorial stresses
s	Unified damage law exponent	σ_{eq}	Von Mises equivalent stress
S	Energetic damage law parameter	σ_Y	Yield stress

*Corresponding Author Email: *m.nadjafi@ari.ac.ir* (M. Nadjafi)

Please cite this article as: M. Nadjafi, P. Gholami, Reliability Analysis of Notched Plates under Anisotropic Damage Based on Uniaxial Loading using Continuum Damage Mechanics Approach, International Journal of Engineering, Transactions A: Basics Vol. 34, No. 01, (2021) 253-262

1. INTRODUCTION

Ductile failure and its criteria are very important in fracture mechanics due to the importance of its engineering, and extensive researches have been done in this field [1]. Low weight metals under ductile fractures are assumed as a criterion for an anisotropic ductile fracture. This criterion considers the interactions between surfaces with shear connections and shear stress [2]. In this regard, comprehensive mathematical model has been extracted from the point of theoretical and experimental views to evaluate ductile fracture of anisotropic materials [3]. In structural systems, there are uncertainties in the system parameters that must be considered to describe the behavior of the system. In these systems, load variation and distribution, boundary conditions, material properties, and constants, environmental conditions and etc. are uncertainties that cause the random behavior of structures. Therefore, it is very important to study the reliability and consider the source of the uncertainties, and these propagation effects on the system reliability.

It is very common to use classical fracture mechanics models to demonstrate material degradation, and great efforts have been made to develop new models of fracture mechanics [4-7]. Most research and studies have been done to demonstrate the fracture behaviors under various stress shearing loads. In these studies, anisotropic states were investigated in the various directions of the tension test angles, and the results are examined from different angles [8]. Despite some successful applications of fracture mechanics, the results show that it is difficult to apply the theory of classical fracture mechanics to practical applications. As a result, damage models have been developed as an alternative method for modeling material degradation based on the irreversible thermodynamic process. In this context, accurate and correct failure modeling is one of the main topics in the formation of the metal. For this purpose, various categories have been extracted for failure states and modes during metal formation. In this regard, ductile fracture was no exception to this rule and has been studied in numerical, experimental and analytical forms [9]. Mechanical behavior based on the uniaxial tensile tests of the anisotropic in the ductile fracture and plastic deformation has been investigated as well [10].

Kachanov [11] proposed the concept of damage models for the first time and expressed the isotropic damage model with a scalar variable, which defined the surface density of microvoids per unit volume [12, 13]. In this model, it is assumed that the start of microvoids in the rupture process from the very beginning of loading consists of two stages. The first stage is the regular growth of microvoids and the second stage is the acceleration of fracture. Therefore, the probability of growth of microvoids is more than the surface of the body if there is an aggressive environment. As a result, the scalar damage variable was specified as the ratio of the surface area of the damage to the whole surface. This theory is determined by considering the equivalence between the state of a body with not damaged fancied and the real damaged state. Later, the effective stress concept was proposed by Rabotnov [14] in continuum damage mechanics (CDM).

Many researchers have used continuum mechanics and scalar damage variables to properly solve many mechanical problems [15, 16]. Van Do [17] investigated the evolution of damage and the onset of failure in notched specimens using finite element model (FEM) analysis and CDM approach. The simulations were compared with the numerical and experimental results of earlier works and good agreements were found between them. Using the concepts of CDM approach, Majzoobi et al. [18] investigated the equivalent plastic strain to the failure of notched aluminum specimens and introduced a relation to express the effect of triaxial stress coefficient in the medium range of stress triaxiality. Razanika et al. [19] proposed an enhanced CDM formulation based on novel damage driving energy, which includes that involves both stored energy and dissipative contributions. The applicability of proposed model was validated by FEM analysis. Bonora et al. [20] have shown that the strain required to initiate damage in ductile materials decreases exponentially with increasing stress triaxiality. As a result, they combined this feature with the concepts of CDM approach, and provided a phenomenological relationship for the dependence of the damage threshold strain on stress triaxiality. Ganjiani [21] also proposed a generalized ductile fracture model for ductile materials coupling with stress triaxiality and Lode angle parameter using CDM approach.

Nevertheless, in practical problems, it has been shown that the damage behavior of all materials are in fact anisotropic. On the other hand, by careful attention to isotropic damage models, it can be understood that these models have less ability to describe material damage than anisotropic damage models. In addition, in multiaxial loading, the results of the isotropic damage models in comparison to anisotropic damage models are very significant. Therefore, to describe the behavior of materials, it has been suggested that damage tensors be used as damage state variables, but the use of damage tensors is complex [22]. In this context, some recent studies have been done and the most practical of them is the hybrid numerical and experimental assessment in order to determine the behavioral characteristics of the plasticity of anisotropic and ductile fracture upon the high-strength materials [23]. To study the effects of anisotropic plasticity on ductile fracture, Keshavarz and Ghajar [24] proposed modified CDM approach based on the isotropic and anisotropic damage. Developed CDM formulations were implemented in Abaqus software by subroutine and the results have been verified with

experimental results. For accurate investigation, various tensile tests on different loading directions have been performed. In these studies, the mechanical model of the anisotropic damage with respect to the states of the stress and anisotropy are predicted and simulated the material fracture by some researchers.[25, 26]. Surmir et al. [27] coupled nonlinear kinematic hardening model with anisotropic damage model to predict ratcheting strain of different loading paths.

This paper represents a method for reliability analysis of a plate containing a central circular hole using CDM-based anisotropic damage model coupled with the FEM for the first time. A performance function using the energy density release rate based on the anisotropic damage is formulated within the basic thermodynamic framework. This proposed reliability relationship can be used to predict the fracture probability of structure systems. The second law of thermodynamics has been used to determine the internal energy of materials with Gibbs free energy. Then, by using Gibbs free energy, the variables that can be used to show the growth of material damage are introduced. In the framework of irreversible thermodynamic processes, thermodynamically associated variables are obtained using the dissipation potential function. Therefore, the finite element simulation of material behavior based on the evolution of damage and constitutive equation by the CDM approach during failures is implemented by a subroutine in ABAQUS software. The results of the FEM are compared with experimental results reported by other researchers and the FEM models of the notched tension tests are validated. Finally, using the FORM and SORM, the limit state functions and random variables will be obtained according to the CDM approach.

2. RELIABILITY ASSESSMENT

Reliability is defined as the capability of an item or equipment to perform the required activities successfully within a specified and predefined time period and operating conditions [28]. In fact, reliability refers to the probability of the proper function of a system or item without failures in specific and predetermined conditions for a given length of time. There are several ways to analyze the structural reliability of a system, the most important of which are FORM and SORM methods [29]. In reliability assessment, the failure probability measurements of a system or structure have been evaluated based on the respective failure rate/function. In this study, FORM and SORM has been used to obtain the probability of ductile fracture of the rectangular plate containing various hole size which is subjected to uniaxial tensile loading.

2. 1. First Order Reliability Method (FORM) In the FORM model, the function of the limit state is based on the first order Taylor expansion, which is expressed by the following relation [30]:

$$g(X) = Z(X) - S(X) \tag{1}$$

Here, X denotes the random variables of the limit state function, while Z and S are resistance and load, respectively, which are assumed to be functions of random variables.

In the FORM, at first, random variables are transferred using Rosenblatt's transformation of the main random space (X) into the normal standard space (U) with zero mean and standard deviation 1. The main goal in the FORM is to obtain the most probable point (MPP), i.e., U^* as the minimal distance of the limit state surface to the origin in the normal standard space. This shortest distance is called the index of reliability or (β). So, in this method, while g(X) is less than zero and failure occurs, then the P_f (failure likelihood) and subsequently reliability $\boldsymbol{R}$, by using the reliability index is estimated as follows:

$$\boldsymbol{R} = 1 - P_f = 1 - \Phi(-\beta) = \Phi(\beta) \tag{2}$$

where Φ is the cumulative distribution function of standard normal distribution.

2. 2. Second Order Reliability Method (SORM) In the case of nonlinear limit state function, the probability of failure should be less than that of the linear one. In FORM approach, because of the MPP using first order approximation, the curvature of the nonlinear state function is ignored. Therefore, SORM approach was studied to consider curvature information. So, SORM uses second order Taylor expansion to calculate the failure probability as following [30]:

$$P_f = P\{g(x) < 0\} = \Phi(-\beta)\prod_{i=1}^{n-1}(1+\beta k_i)^{1/2} \tag{3}$$

In this relation, k_i denotes the performance function of the ith main curvature at the MPP.

For linear limit state functions, FORM solution is exact. For non-linear failure functions, the exact calculation of the failure probability or the reliability generally involves mathematical and computational difficulties. Based on the number of random variables and the linearity (or not) of the failure function, FORM can be seen to have limitations for non-linear failure functions having a large number of random variables. Nevertheless, accuracy of SORM due to its approximation of the performance function is generally more than that of FORM. However, since SORM requires the second order derivative, it is not as efficient as FORM when the derivatives are evaluated numerically and its use is complex and expensive. On the other hand, several algorithms have been proposed for approximation of the most probable failure point and the β index,

therefore the decision as to which is the most effective algorithm depends on the limit state function of interest.

3. MECHANICS OF THE CONTINUUM DAMAGE

Classical fracture mechanics models that were originally developed for demonstrating material degradations required prior knowledge of location and geometry of the microcracks, which is difficult to assess before they are formed. The CDM approaches were proposed to create an alternative towards modeling material degradation based on the thermodynamics framework. The procedure of the CDM approach is to illustrate first the damage state of a material in terms of properly specified damage variables (D) and then to explain mechanical behavior of the damaged material and further development of the damage by the use of these damage variables. Therefore, CDM approach provides a tool that can simulate damage from the beginning of loading to final fracture.

State of damage is one of the main factors that effects on mechanical properties of materials, which is determined by the density, distribution, type and direction of microvoids. According to the size and orientation of microvoids, some of them will start to develop under specified loading and environmental conditions. The CDM approach provides a new glance for the initiation and evaluation of damage. The CDM approach uses the concepts of continuum physics by defining internal field or damage variables to describe the process of material defeat and fracture.

The change of internal field of material generally depends on the direction of stress and/or strain, and therefore it can be said that the internal field is an anisotropic phenomenon. Therefore, a proper description of material behavior necessitates vectorial or tensorial damage variables. In the CDM approach, using the strain equivalence hypothesis and equivalence between the fictitious undamaged state of a body and the real damaged state, the 2nd order damage variable D by means of the effective area reduction is defined as $(\delta_{ij} - D_{ij})n_j \delta S = \tilde{n}_i \delta \tilde{S}$, where δS is total surface area with normal n, and $\delta \tilde{S}$ is surface of effective area with normal $\tilde{n}$, while δ_{ij} represent the Kronecker delta [31]. It is worth mentioning that, effective area is an area where internal force is applied. So, based on the stress σ applied to the total surface area, the effective stress $\tilde{n}$ on this effective area according to the tensor of the 2nd order damage is expressed as $\tilde{\sigma}_{ij} = \sigma_{ik}(1-\mathrm{D})^{-1}_{kj}$.

The CDM approach is related to thermodynamics, and the irreversible thermodynamic theory is used as a logical framework for explaining the damaged elastic-plastic material behavior. As a result, Gibbs free energy must first be defined for anisotropic damage. Then, the dissipation function is expressed to characterize the estimation of state variables and determine the load level that denotes the elastic region.

3. 1. Gibbs Free Energy The free energy stored in the damaged material is determined by various factors such as strain, damage and dislocation structure state, etc. Therefore, the Gibbs free energy function according to the principle of strain equivalence between the undamaged and damaged configuration, with the definition of the anisotropic damage, may be considered as follow [32]:

$$\rho\Gamma = \frac{1+\nu}{2E} H_{ij}\sigma^D_{jk} H_{kl}\sigma^D_{li} + \frac{3(1-2\nu)}{2E}\frac{\sigma_H^2}{1-\eta D_H} \tag{4}$$

In the above equation, v, E, and η represent Poisson ratio, Young's modulus, and hydrostatic sensitivity parameter, respectively, while $D_H = D_{kk}/3$ is hydrostatic damage, $\sigma_H = \sigma_{kk}/3$ hydrostatic stress, σ^D_{ij} deviatoric stress, and $H_{ij} = (1-\mathrm{D})^{-1/2}_{ij}$ effective damage tensor.

Based on the thermodynamic formulation, the equation of constitutive elasticity and effective stress of the material under damage has the following form:

$$\varepsilon^e_{ij} = \rho\frac{\partial\Gamma_e}{\partial\sigma_{ij}} = \frac{1+\nu}{E}\tilde{\sigma}_{ij} - \frac{\nu}{E}\tilde{\sigma}_{kk}\delta_{ij} \tag{5}$$

$$\tilde{\sigma}_{ij} = \left(H_{ik}\sigma^D_{kl}H_{lj}\right)^D + \frac{\sigma_H}{1-\eta D_H}\delta_{ij} \tag{6}$$

The rate of released density energy (Y) is depended with the damage variable D, that can be extracted from the function of Gibbs free energy as follows:

$$Y_{ij} = \rho\frac{\partial\Gamma}{\partial D_{ij}} = \frac{1+\nu}{E}\sigma^D_{kp}H_{pq}\sigma^D_{ql}A^{-1}_{klmn}H^2_{mi}H^2_{jn} + \frac{\eta(1-2\nu)}{2E}\frac{\sigma_H^2}{(1-\eta D_H)^2}\delta_{ij} \tag{7}$$

with $A_{klmn} = (1/2)(H_{km}\delta_{\ln} + H_{\ln}\delta_{km} + H_{kn}\delta_{lm} + H_{lm}\delta_{kn})$.

It is worth noting that the role of the rate of released density energy in the CDM approach that is a similar role as the rate of released strain energy G in the mechanics of the fracture.

3. 2. Dissipative Potential Function Based on the standard thermodynamics principles, the total dissipation potential function F may be presented by the plastic deformation function F^P in sum with damage function F^D. By taking account of isotropic hardening R and yield stress σ_Y, the plastic dissipation potential function based on the von Mises criterion is determined by [32]:

$$F^p = \tilde{\sigma}_{eq} - R - \sigma_Y \tag{8}$$

where $\tilde{\sigma}_{eq} = (H\sigma^D H)_{eq}$ shows the effective von Mises equivalent stress. Isotropic Hardening indicates the density of the dislocations, and exponential isotropic hardening is written as $R = R(r) = R_\infty[1-\exp(-br)]$, where r is isotropic hardening state variable, while R_∞ and b represent saturated isotropic hardening parameters and isotropic hardening exponents, respectively. Based on the thermodynamic rules, the evolution equation of the isotropic hardening variable is obtained in the form:

$$\dot{r} = -\dot{\lambda}\frac{\partial F}{\partial R} = -\dot{\lambda}\frac{\partial F^p}{\partial R} = \dot{\lambda} \tag{9}$$

where $\dot{\lambda}$ is plastic multiplier. So, by using Equation (9), the constitutive equation of the strain rate of the plastic that is stated as:

$$\dot{\varepsilon}_{ij}^p = \dot{\lambda}\frac{\partial F}{\partial \sigma_{ij}} = \dot{\lambda}\frac{\partial F^p}{\partial \sigma_{ij}} = \left[H_{ik}\dot{e}_{kl}^p H_{lj}\right]^D \tag{10}$$

with $\dot{e}_{kl}^p = (3\tilde{\sigma}_{ij}^D / 2\tilde{\sigma}_{eq})(\dot{r})$.

4. DAMAGE MECHNISM

4. 1. Damage Threshold Experimental results from measuring damage in plastic region show that mechanical damage occurs when the plastic strain in the material reaches the irreversible or accumulated plastic strain ε_{pD} [33]. It can be said that this damage threshold accumulated plastic strain is almost the properties of materials. On the other hand, the strain rate of accumulated plastic $\dot{p}$ is defined according to the yield criterion. So, exposed on the anisotropic damage and based on the von Mises criterion with Equation (10), it can be expressed as follows [32]:

$$\dot{p} = \frac{\left[\mathrm{H}\tilde{\sigma}\mathrm{H}\right]_{eq}}{\tilde{\sigma}_{eq}}\dot{r} \tag{11}$$

4. 2. Damage Evolution According to thermodynamic relations in the framework of CDM approach, the evolution equations of the damage variable are governed by damage dissipation function. As result, it may be written as follows [32]:

$$\dot{D}_{ij} = \dot{\lambda}\frac{\partial F_D}{\partial Y_{ij}}; \quad r > \varepsilon_{pD} \tag{12}$$

Based on the experimental results damage dissipation function can be postulated as follows [34]:

$$F_D = \left(\frac{\bar{Y}\left(\varepsilon^e\right)}{S}\right)^s Y_{ij}\left|\frac{d\varepsilon^p}{dr}\right|_{ij} \tag{13}$$

In above, $|\cdot|$ represents the principal components in absolute form, s denotes the law unified damage, and S is defined as the parameter of the law of energy damage. On the other hand, $\bar{Y}$ is the elastic density of the effective energy that can be expressed as follows:

$$\bar{Y} = \int \tilde{\sigma}_{ij} d\,\varepsilon_{ij}^e = \frac{1}{2}E_{ijkl}\varepsilon_{ij}^e\varepsilon_{kl}^e = \frac{\tilde{\sigma}_{eq}^2\tilde{R}_v}{2E} \tag{14}$$

where $\tilde{R}_v$ is known as the effective stress triaxiality function and can be written as $\tilde{R}_v = \frac{2}{3}(1+v) + 3(1-2v)(\frac{\tilde{\sigma}_H}{\tilde{\sigma}_{eq}})^2$ with $\tilde{\sigma}_H = \sigma_H/(1-\eta D_H)$. Then, by using Equations (9), (11) and (12), the damage evolution law is given by:

$$\dot{D}_{ij} = (\frac{\bar{Y}}{S})^s \left|\dot{\varepsilon}^p\right|_{ij}; \quad \varepsilon_p > \varepsilon_{pD} \tag{15}$$

If damage occurred in one of the plane and causes critical conditions, it is defined as the condition of fracture in material. As a result, the onset of the fracture occurs while the damage vector in norm state ($D_{ij}n_j$) or the damage biggest principal value (D_I) reaches D_c (i.e. $\max D_I = D_c;\ I = 1,2,3$). In other words, from the point view of the rate of released density energy, the main criterion of fracture in a material with damage can also be defined as follows:

$$Y_I = Y_{Ic};\ I = 1,2,3 \tag{16}$$

5. PROPOSED METHODOLOGY

The finite element simulation of material behavior based on the evolution of damage and constitutive equation by CDM approach during failures is carried out by subroutine in ABAQUS software. In the proposed subroutine, the rate of released density energy is calculated, and the amount of damage growth in each of the principal directions is obtained and checks if damage has reached the specified critical damage or not. In the event of damage in the principal direction, the equations and behavior of the material are affected based on the updated damage mode.

A rectangular plate containing a circular hole located in the center of the plate with the principal coordinate is shown in Figure 1. If the damage is anisotropic for the uniaxial tension at direction-1, then $D_2 = D_3 = D_1/2$ and $D_H = 2D_1/3$. Therefore, effective equivalent stress, effective stress triaxiality function, and evolution law lead to:

$$\tilde{\sigma}_{eq} = \frac{2}{3}\frac{\sigma_1}{1-D_1} + \frac{1}{3}\frac{\sigma_1}{1-D_2} \tag{17}$$

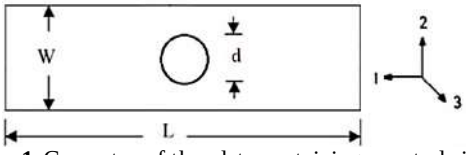

Figure 1. Geometry of the plate containing a central circular hole

$$\tilde{R}_v = \frac{2}{3}(1+\nu)+3(1-2\nu) \times\left[\left(1-\frac{2\eta}{3}D_1\right)\left(\frac{2}{1-D_1}+\frac{1}{1-D_2}\right)\right]^{-2} \quad (18)$$

$$\dot{D}_1 = \left(\frac{\bar{Y}}{S}\right)^s \left|\dot{\varepsilon}^p\right| \quad (19)$$

Using initial condition $\varepsilon = \varepsilon_{pD}$, $D = D_0$ and fracture condition $\varepsilon = \varepsilon_{pR}$, $D = D_c$, the integration of the damage evolution equation in direction-1 gives:

$$D_C = \left(\frac{\bar{Y}}{S}\right)^s (\varepsilon_{pR} - \varepsilon_{pD}) \quad (20)$$

Due to the symmetric conditions of the model, a quarter of the specimen was modelled in the FEM, to save computing resources. Consequently, symmetric boundary conditions are applied to the model and a unit displacement is applied to tits free edge. The specimens have been meshed with four-node S4R elements, and the meshes near the notches were refined, as shown in Figure 2. The meshes were refined until the maximum equivalent stress converged. In order to analyze the reliability, a proper function for the limit state is required in accordance with the systems structure. For this purpose, the fracture criterion introduced in the previous section is used to forecast damage in ductile materials based on the CDM approach. Therefore, when the rate of released density energy exceeds its threshold in each principal direction, the fracture will occur. So, the function for the limit state of this condition can be expressed as:

$$g(X) = Y_{Ic} - Y \; ; \quad I = 1,2,3 \quad (21)$$

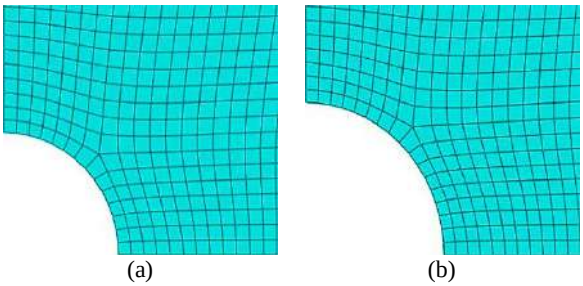

(a) (b)

Figure 2. Mesh design of notched specimens (a) 5 mm, (b) 10 mm

TABLE 1. Statistical properties and material characteristics of aluminum alloy 2024-T3 [32, 35]

Random variables	Mean value	Coefficient of Variation	Distribution type
Critical damage, D_c	0.209	8×10^{-2}	Normal
Young's modulus, E (GPa)	75	5×10^{-2}	″
Energetic damage law parameter, S	1.7	10^{-2}	″
hydrostatic sensitivity parameter, η	3	10^{-2}	″
Poisson's ratio, ν	0.3	5×10^{-2}	″
Rupture plastic strain, ε_{pR}	0.33	5×10^{-2}	″
Damage threshold plastic strain ε_{pD}	0.031	5×10^{-2}	″

According to Equations (7) and (20), in the function of the limit state, the uncertainty sources and the random variables vector is equal to:

$X = (\nu, E, \eta, D_c, \varepsilon_{pD}, \varepsilon_{pR})$.

For the aluminum 2024 plate under tensile loading, mechanical properties and their statistics data (i.e. the mean value and coefficient of variation), are presented in Table 1. Sensitivity index is another parameter that is used to evaluate the failure probability of the random variables, which is obtained using Equation (22), in which SI_X is the sensitivity index of random variable X_i [36, 37].

$$SI_{X_i} = \frac{\left(\frac{\partial g(X)}{\partial X_i}\right)}{\left(\sqrt{\sum\left(\frac{\partial g(X)}{\partial X_i}\right)}\right)} \quad (22)$$

6. STATISTICAL STUDY OF RESULTS

This paper studies the fracture probability and reliability evaluation of a plate containing a central circular hole with various sizes of diameters under uniaxial tensile loading. To calibrate the FEM, the simulation results are compared with the experimental data in [38] and [39]. Figure 3 demonstrates this comparison for force-displacement responses between experiment and simulation at direction-1 for the notched specimen with a diameter of 10 mm which shows good agreement. Therefore, the FEM models of the notched tension tests are validated. The evolution of the damage variable obtained in the simulation for the specimens containing holes with diameters of 5 and 10 mm in direction-1 is shown in the contour plots in Figure 2. It can be seen that the maximum damage is detected near the edge of the

notch. As the specimen is gradually pulled, the maximu m damage zone moves slowly towards the free edge of the specimen and localizes there.

Table 2 shows comparisons of the probability of failure between the isotropic and anisotropic damage model based on the FORM and SORM for various sizes of diameters. Under the same conditions and the same critical ratio (D/D_C) for both cases of damage models, the failure probability in the damage model of anisotropic is higher than that in isotropic one. In addition, as can be seen, the SORM indicates a higher probability of failure than FORM, and by increasing diameter size, the probability of failure for both methods increases.

The effect of change in the critical ratio (D/D_C) on the failure probability of a plate under uniaxial loading for various sizes of diameter in the principal directions-1 and -2 are depicted in Figures 5 and 6, respectively. The results show that the probability of failure in direction-1

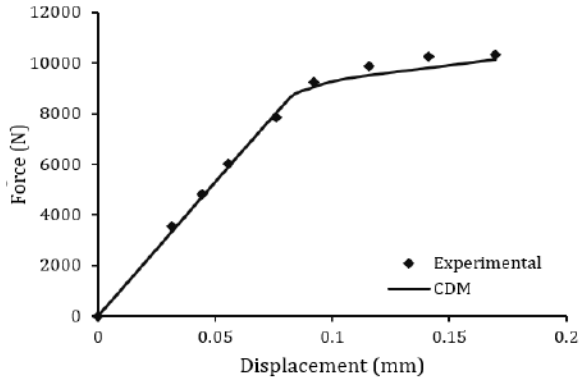

Figure 3. Comparison of force–displacement responses between experiment and simulation

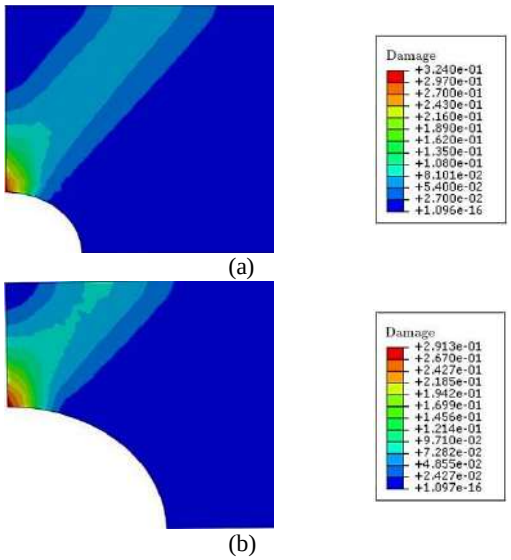

Figure 4. Damage contour plots, (a) 5 mm, (b) 10 mm

TABLE 2. Comparison of probability of failure between isotropic damage model and anisotropic damage model using FORM/SORM ($x10^{-2}$)

d (mm)	Isotropic damage		Anisotropic damage	
	FORM	SORM	FORM	SORM
2	4.8951	5.1994	5.5837	5.8025
3	5.7938	6.1994	6.3987	6.6496
5	7.9279	8.3672	8.9951	9.3477
8	8.3898	8.7268	9.4816	9.8533
10	8.6908	9.0315	9.7182	10.0992

is greater than direction-2, and as the diameter increases, the probability of failure increases. Figure 7 shows the relationship between the probability of failure and the variation coefficient for a plate under uniaxial loading. It is obvious that the critical damage D_c, rupture the strain of plastic ε_{pR} and the damage threshold plastic strain ε_{pD} have the lowest sensitivity; however, by increasing the coefficient of variation, other variables become more sensitive to the dispersion of the data.

Sensitivity analysis was performed according to Equation (22) and the sensitivity index for each random variable was obtained. As it is obvious in Figure 8, among the random variables determined in the problem, the critical damage D_c, rupture plastic strain ε_{pR} have the highest sensitivity index and it can be said that these two variables have the most effect on the reliability of rectangular plates under uniaxial tensile loading. Other available variables have lower sensitivity index, and, in other words, the least effect on the reliability of the problem.

At the end, it should be noted that these results are obtained for a plate containing a central hole made of aluminum under specific uniaxial loading based on anisotropic damage and it may be different for other of conditions. Therefore, the proposed method provides a

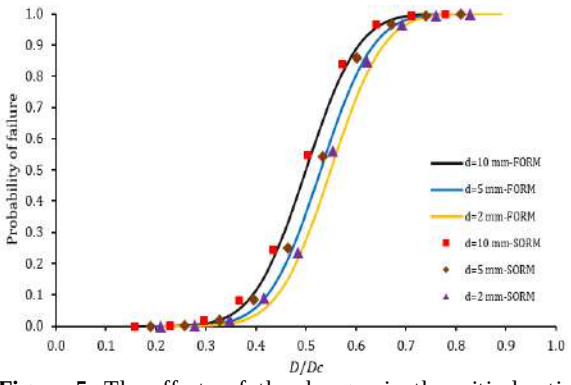

Figure 5. The effects of the changes in the critical ratio (D/D_C) on Probability of failure in direction-1

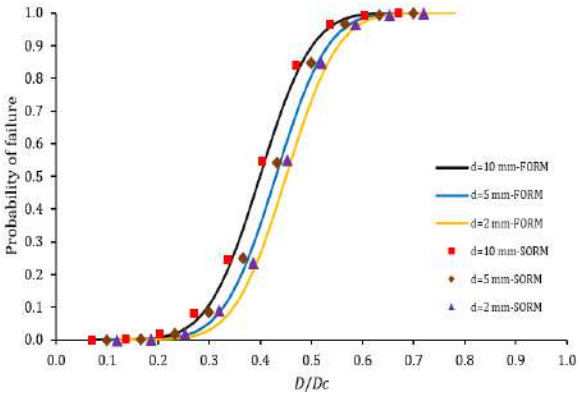

Figure 1. The effects of the changes in the critical ratio (D/D_C) on Probability of failure in direction-2

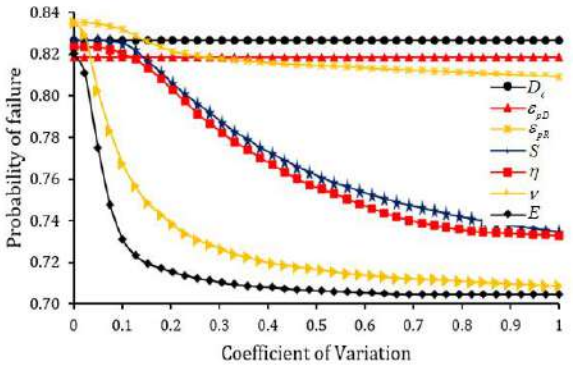

Figure 2. Relationship between the probability of failure and coefficient of variation for random variables of uniaxial loading

tool that can provide probability of damage from the beginning of the loading to final fracture. On the other hand, in this study, anisotropic damage is used which can simulate mechanical behavior in practical applications because of multiaxial loading. Therefore, use of multiaxial loads and various material types are suggested to analyze the reliability of structural systems based on the CDM approach.

As a general conclusion, this study proposed a method for calculating the reliability of the structural system, but the result depends on the choice of performance function, selection of variables, and its approximation algorithm to obtain reliability.

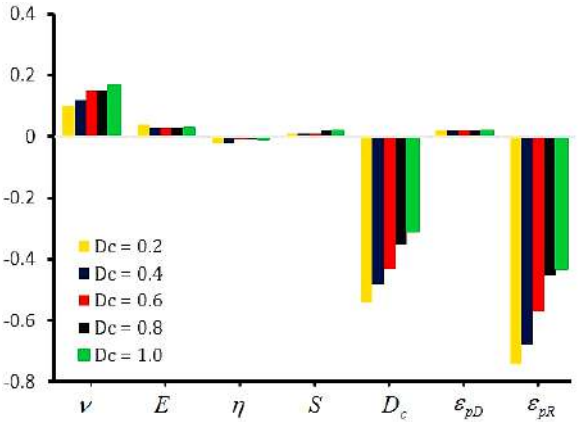

Figure 8. Sensitivity index of random variables by increasing critical damage for uniaxial loading

7. CONCLUSION and FUTURE WORK

This paper introduces a framework for analyzing the reliability of a plate containing a hole on center under tensile loading using the theory of damage on anisotropic elastic-plastic based on the FORM and SORM models.

Reliability analysis was performed using the FORM and SORM. At first, based on the thermodynamic framework by the CDM approach, constructive equations, and the development of ductile elastic and plastic damage are obtained. It is then implemented using a subroutine code in the ABAQUS software to drive the stress-strain relationship and the onset of fracture. The probability of fracture of a plate containing a central circular hole with different diameters has been compared between the anisotropic and isotropic damage models. Results show that while the model of damage follows an anisotropic path, the probability of failure is higher. And, in different directions in the principal coordinates, this probability of failure is different. Next, based on the sensitivity analysis of variables, the critical damage and rupture plastic strain have the most sensitivity index. In the future work, we will extend the CDM approach more precisely over the notched composite laminates and isotropic damage under uniaxial loading to evaluate reliability analysis.

8. REFERENCES

1. Alijani, H., "Evaluation of ductile damage criteria in hot forming processes", ***International Journal of Engineering, Transactions A: Basics***, Vol. 29, No. 10, (2016), 1441-1449.
2. Lou, Y. and Yoon, J.W., "Anisotropic ductile fracture criterion based on linear transformation", ***International Journal of Plasticity***, Vol. 93, (2017), 3-25, doi: 10.1016/j.ijplas.2017.04.008.
3. Stormont, C., Gonzalez, H. and Brinson, H., "The ductile fracture of anisotropic materials", ***Experimental Mechanics***, Vol. 12, No. 12, (1972), 557-563, doi: 10.1007/BF02320599.
4. Farrahi, G. and Mohajerani, A., "Numerical investigation of crack orientation in the fretting fatigue of a flat rounded contact", ***International Journal of Engineering, Transactions C: Aspects***, Vol. 23, No. 3, (2010), 223-232.
5. Vossoughi Shahvari, F. and Kazemi, M., "Mixed mode fracture in reinforced concrete with low volume fraction of steel fibers", ***International Journal of Engineering, Transactions A: Basics***, Vol. 24, No. 1, (2011), 1-18, doi.

6. Hassan Ghasemi, M., Mofid Nakhaei, A. and Dardel, M., "A simple method for modeling open cracked beam", ***International Journal of Engineering, Transactions B: Applications***, Vol. 28, No. 2, (2015), 321-329.
7. Fallah, N., "A development in the finite volume method for the crack growth analysis without global remeshing", ***International Journal of Engineering, Transactions A: Basics***, Vol. 29, No. 7, (2016), 898-908.
8. Zhang, H., Zhang, H., Li, F. and Cao, J., "A novel damage model to predict ductile fracture behavior for anisotropic sheet metal", ***Metals***, Vol. 9, No. 5, (2019), 595, doi: 10.3390/met9050595.
9. Lou, Y., Chen, L., Clausmeyer, T., Tekkaya, A.E. and Yoon, J.W., "Modeling of ductile fracture from shear to balanced biaxial tension for sheet metals", ***International Journal of Solids and Structures***, Vol. 112, (2017), 169-184, doi: 10.1016/j.ijsolstr.2016.11.034.
10. Lou, Y.S. and Yoon, J.W., "Anisotropic behavior in plasticity and ductile fracture of an aluminum alloy", in Key Engineering Materials, ***Trans Tech Publications*** Vol. 651, (2015), 163-168, doi: 10.4028/www.scientific.net/KEM.651-653.163.
11. Kachanov, L., "On creep rupture time", Izv. Acad. Nauk SSSR, Otd. Techn. Nauk, Vol. 8, (1958), 26-31.
12. Oucif, C., Voyiadjis, G.Z., Kattan, P.I. and Rabczuk, T., "Investigation of the super healing theory in continuum damage and healing mechanics", ***International Journal of Damage Mechanics***, Vol. 28, No. 6, (2019), 896-917, doi: 10.1177/1056789518799822.
13. Voyiadjis, G.Z. and Kattan, P.I., "Fundamental aspects for characterization in continuum damage mechanics", ***International Journal of Damage Mechanics***, Vol. 28, No. 2, (2019), 200-218, doi: 10.1177/1056789517752524.
14. Rabotnov, Y., *On the equations of state for creep. Progress in applied mechanics. Prager anniversary vol*. 1963, New York: Macmillan.
15. Lemaitre, J., "How to use damage mechanics", ***Nuclear Engineering and Design***, Vol. 80, No. 2, (1984), 233-245.
16. Saboori, B. and Moshrefzadeh-sani, H., "A continuum model for stone-wales defected carbon nanotubes", ***International Journal of Engineering, Transactions C: Aspects***, Vol. 28, No. 3, (2015), 433-439.
17. Van Do, V.N., "The behavior of ductile damage model on steel structure failure", ***Procedia Engineering***, Vol. 142, (2016), 26-33, doi: 10.1016/j.proeng.2016.02.009.
18. Majzoobi, G., Kashfi, M., Bonora, N., Iannitti, G., Ruggiero, A. and Khademi, E., "Damage characterization of aluminum 2024 thin sheet for different stress triaxialities", ***Archives of Civil and Mechanical Engineering***, Vol. 18, (2018), 702-712, doi: 10.1016/j.acme.2017.11.003.
19. Razanica, S., Larsson, R. and Josefson, B., "A ductile fracture model based on continuum thermodynamics and damage", ***Mechanics of Materials***, Vol. 139, (2019), 103197, doi: 10.1016/j.mechmat.2019.103197.
20. Bonora, N., Testa, G., Ruggiero, A., Iannitti, G. and Gentile, D., "Continuum damage mechanics modelling incorporating stress triaxiality effect on ductile damage initiation", ***Fatigue & Fracture of Engineering Materials & Structures***, (2020), doi: 10.1111/ffe.13220.
21. Ganjiani, M., "A damage model for predicting ductile fracture with considering the dependency on stress triaxiality and lode angle", ***European Journal of Mechanics-A/Solids***, (2020), 104048, doi: 10.1016/j.euromechsol.2020.104048.
22. Krajcinovic, D., Damage mechanics, Elsevier, (1996).
23. Park, S.-J., Lee, K., Choung, J. and Walters, C.L., "Ductile fracture prediction of high tensile steel EH36 using new damage functions", ***Ships and Offshore Structures***, Vol. 13, No. sup1, (2018), 68-78, doi: 10.1080/17445302.2018.1426433.
24. Keshavarz, A. and Ghajar, R., "Effect of isotropic and anisotropic damage and plasticity on ductile crack initiation", ***International Journal of Damage Mechanics***, Vol. 28, No. 6, (2019), 918-942, doi: 10.1177/1056789518802625.
25. Kõrgesaar, M., "The effect of low stress triaxialities and deformation paths on ductile fracture simulations of large shell structures", ***Marine Structures***, Vol. 63, (2019), 45-64, doi: 10.1016/j.marstruc.2018.08.004.
26. Shen, F., Muenstermann, S. and Lian, J., "Investigation on the ductile fracture of high-strength pipeline steels using a partial anisotropic damage mechanics model", ***Engineering Fracture Mechanics***, Vol. 227, (2020), 106900, doi: 10.1016/j.engfracmech.2020.106900.
27. Surmiri, A., Nayebi, A. and Rokhgireh, H., "Application of anisotropic continuum damage mechanics in ratcheting characterization", ***Mechanics of Advanced Materials and Structures***, (2020), 1-8, doi: 10.1080/15376494.2020.1751353.
28. Modarres, M., Kaminskiy, M.P. and Krivtsov, V., Reliability engineering and risk analysis: A practical guide, CRC press, (2016).
29. Silva, J., Garbatov, Y. and Soares, C.G., "Reliability assessment of a steel plate subjected to distributed and localized corrosion wastage", ***Engineering Structures***, Vol. 59, (2014), 13-20, doi: 10.1016/j.engstruct.2013.10.018.
30. Melchers, R.E. and Beck, A.T., Structural reliability analysis and prediction, John wiley & sons, (2018).
31. Murakami, S. and Ohno, N., A continuum theory of creep and creep damage, in Creep in structures. 1981, Springer.422-444.
32. Lemaitre, J. and Desmorat, R., Engineering damage mechanics: Ductile, creep, fatigue and brittle failures, Springer Science & Business Media, (2005).
33. Benzerga, A., Besson, J. and Pineau, A., "Anisotropic ductile fracture: Part i: Experiments", ***Acta Materialia***, Vol. 52, No. 15, (2004), 4623-4638, doi: 10.1016/j.actamat.2004.06.020.
34. Lemaitre, J., Desmorat, R. and Sauzay, M., "Anisotropic damage law of evolution", ***European Journal of Mechanics-A/Solids***, Vol. 19, No. 2, (2000), 187-208, doi: 10.1016/S0997-7538(00)00161-3.
35. Bonora, N., "A nonlinear cdm model for ductile failure", ***Engineering Fracture Mechanics***, Vol. 58, No. 1-2, (1997), 11-28, doi: 10.1016/S0013-7944(97)00074-X.
36. Haldar, A. and Mahadevan, S., Reliability assessment using stochastic finite element analysis, John Wiley & Sons, (2000).
37. Haldar, A. and Mahadevan, S., Probability, reliability, and statistical methods in engineering design, John Wiley, (2000).
38. Farsi, M.A. and Sehat, A.R., "Experimental and numerical study on aluminum damage using a nonlinear model of continuum damage mechanics", ***Journal of Applied and Computational Sciences in Mechanics***, Vol. 27, No. 2, (2016), 41-54, (in Persian).
39. Farsi, M.A. and Sehat, A.R., "Comparison of nonlinear models for prediction of continuum damage in aluminum under different loading", ***Joural of Mechanical Engineering***, Vol. 46, No. 4, (2017), 211-220, (in Persian).

Persian Abstract

چکیده

در دهه‌های اخیر، مدل‌های تخریب بر اساس رویکرد مکانیک آسیب پیوسته توسط پژوهش‌گران در زمینه‌ی مکانیک شکست مورد توجه قرار گرفته است. تئوری مکانیک آسیب پیوسته ابزاری قدرتمند برای حل مسائلی مانند تغییر شکل‌های موم‌سان بزرگی است که مکانیک شکست قادر به حل آن نیست. این مدل در چارچوب تئوری متغیر داخلی ترمودینامیک استخراج می‌شود و بر اساس نتایج تجربی که بر روی خواص ماده انجام شده است توسعه داده می‌شود. در این مقاله، قابلیت اطمینان یک صفحه‌ی مستطیل شکل حاوی سوراخ دایره‌ای مرکزی تحت بار کششی ایستا، با استفاده رویکرد مکانیک آسیب پیوسته برای شکست نرم بررسی شده است. برای بررسی شروع و پیشروی آسیب، از مدل آسیب ناهمسان‌گرد بیان شده توسط تانسور مرتبه‌ی دوم برای استخراج معادلات سازگاری استفاده می‌شود. سپس، این روابط به همراه ثابت‌های ماده با استفاده از زیربرنامه در نرم افزار آباکوس اجرا می‌شوند. ارزیابی قابلیت اطمینان با استفاده از روش قابلیت اطمینان مرتبه‌ی اول (FORM) و روش قابلیت اطمینان مرتبه‌ی دوم (SORM) انجام شده است. بر اساس روش قابلیت اطمینان مرتبه‌ی اول/دوم، تابع عملکرد و متغیرهای تصادفی با توجه به نرخ آزادسازی چگالی انرژی به‌دست آمده است. احتمال خرابی صفحه با اندازه‌ی سوراخ‌های مختلف بر اساس تئوری آسیب ناهمسان‌گرد محاسبه و نتایج با مدل آسیب همسان‌گرد مقایسه می‌شوند. سرانجام، تحلیل حساسیت بر روی ضریب تغییرات انجام می‌شود.

International Journal of Engineering

Journal Homepage: www.ije.ir

Towards a Uncertainty Analysis in Thermal Protection using Phase-change Micro/Nano Particles during Hyperthermia

A. A. Taheri*, M. Taghilou

Department of Mechanical Engineering, Faculty of Engineering, University of Zanjan, Zanjan, Iran

P A P E R I N F O

Paper history:
Received 25 August 2020
Received in revised form 25 September 2020
Accepted 30 October 2020

Keywords:
Electromagnetic Field
Hyperthermia
Phase-Change Micro/Nano Martials
Superparamagnetic Micro/Nano Particles
Uncertainty Analysis

A B S T R A C T

In thermal protection of healthy tissues during hyperthermia with the phase-change micro/nano-materials, the impossibility of performing a similar experiment with the theoretical parameters is inevitable because of different errors such as modeling, measuring, particle deposition area, etc. These errors may affect the practical thermal protection from damaging the healthy tissue or not destroying the tumor tissue. To perform a numerical procedure, the electrical potential is obtained solving the Laplace equation and the Pennes Biothermal equation is used to find the temperature distribution in the tissue using the finite difference method. The Pennes equation is transiently resolved by considering intracellular conductance, blood perfusion, and metabolic heating. Consequently, the deviation and the uncertainty of each parameters in the thermal protection including the concentration of the phase change material, the radius of microcapsules, the latent heat, the melting point, the temperature range of phase change of micro/nanoparticles, and the concentration and the radius of the superparamagnetic materials are investigated. According to the results of the uncertainty analysis, the radius of the superparamagnetic materials is the most important parameter so that a 20% deviation from the numerical value changes the temperature of the tissue up to 4 °C.

doi: *10.5829/ije.2021.34.01a.29*

1. INTRODUCTION

Based on the statistics released by the International Agency for Research on Cancer (IARC), about 110,000 cases of cancer occurred in Iran and about 56,000 of them have passed away [1]. These statistics demonstrate the importance of research on cancer and its treatment [2-4]. Hyperthermia that is known as thermotherapy is a technique for cancer treatment. In this treatment, cancerous tissue or the whole body through the use of electromagnetic energy are exposed to temperatures between 41-43 ºC to damage or kill the cancer cells. Higher than this temperature range, the heat would kill tumor and healthy cells, and this known as thermal ablation. Nowadays, hyperthermia is always used together with other forms of cancer treatment methods which allows more synergy with different proceedings of conventional treatments [5].

The treatment of cancer, based on nanotechnology is a specific form of interstitial thermotherapy with the advantage of selective heat deposition to the tumor cells [6]. This technique is made by the injection of Super-Paramagnetic Materials (SPMs) into the tumor tissue and then applying an external magnetic field which leads to heat generation. Delivery of the treatment agent to the target area is the key points to effective treatment [7]. Despite the advantage of selective heat deposition, overheating of healthy tissues are possible that could cause burn, blister, and pain [6, 8]. The electromagnetic field can itself, causes cancer depending on how they are produced [9] or improve body behavior [10]. Also, the nanoparticles should not have a toxic effect on the body [11, 12]. Cobalt ferrite (CoFe2O4) is one of these nanoparticle that can be used in hyperthermia [13].

Phase-Change Materials (PCMs) store energy at a constant temperature so that, an increase in tissue temperature during the hyperthermia will be low. Additionally, because of the low thermal conductivity of the PCMs, they prevent heat conduction from the cancerous tissues to the healthy tissues [14]. Sezgin et al.

*Corresponding Author Email: *aliasghartaheri310@gmail.com* (A. A. Taheri)

Please cite this article as: A. A. Taheri, M. Taghilou, Towards a Uncertainty Analysis in Thermal Protection using Phase-change Micro/Nano Particles during Hyperthermia, International Journal of Engineering, Transactions A: Basics, Vol. 34, No. 1, (2021) 263-271

[15] investigated hyperthermia in combination with chemotherapy mediated by gold nanoparticles. They concluded that the presence of nanoparticles increases the treatment efficacy. Lv et al. [14] injected the PCM around the tumor by the goal of protecting healthy tissues during the hyperthermia. The results showed that the PCM can significantly reduce the temperature around the tumor tissue. Lv et al. [16] also proposed a new model for utilizing of the micro/nanomaterials in the living tissue using Monte Carlo's method. Deng and Liu [17] investigated uncertainty analysis during induction hyperthermia using SPM. They concluded that uncertainty analysis should be applied when designing the treatment plan. Majchrzak et al. [18] studied induction hyperthermia with choosing a two dimensional model and applying the electromagnetic field using Boundary Element Method (BEM). They examined different voltages and frequencies and showed that the optimum value for these parameters must be determined to achieve the optimal treatment.

Majchrzak and Paruch [19, 20] applied the Finite Element Method (FEM) to examine the effect of location and size of the external electrodes on the temperature distribution in the tumor tissue. Zhao et al. [21] conducted a study about hyperthermia using magnetic nanoparticles on the laboratory mice. Experimental results showed that within the first 5-10 minutes the temperature of the tumor center reached about 40 ºC. Taheri and Talati [22] obtained the temperature distribution in the tissue by injecting electromagnetic micro/nanomaterials and then applying the electromagnetic field. The results showed that inserting the nanoparticles into the tumor significantly increases the temperature in this tissue and transmits the maximu m temperature to the tumor center. Taheri and Talati [23] also investigated the uncertainty of the effective parameters during hyperthermia with SPM nanoparticles. They concluded that uncertainties in the measurement of some parameters, such as strength of electromagnetic field, radius, and area of the micro/nanoparticle severely affect the temperature distribution in the tissue. In other work, Taheri and Talati [24] examined the hyperthermia cancer treatment by considering the two-dimensional transient model of biological tissue with SPM and PCM. Results showed that the use of the PCM reduces the temperatures up to 3°C. Nemati et al. [25] showed that by deforming the spherical SPMs into the cubes (octopods) ones, their specific rate of absorption could be increased by 70%. Wang et al. [26] obtained an optimal temperature distribution for a 3D triple-layered skin structure that is embedded with multi-level blood vessels considering electromagnetic radiation heat source. The effects of geometric structures of vascular trees and blood flow are investigated by Li et al. [27]. They derived a fractal model for the effective thermal conductivity of the living biological tissue and found that the blood flow highly affects the effective thermal conductivity. Despite the thermal protection of PCMs, the incompatibility of the practical parameters with the numerical estimations could make it problematic for the treatment procedure. Therefore, for designing a decent therapeutic pattern in laboratory conditions, the possible deviations from the numerical values should be examined.

In this study, the deviation and the uncertainty analysis of each effective parameters in thermal protection including the concentration, the radius of microcapsules, the latent heat, the melting point, the temperature range of phase change of micro/nanoparticles, and also the effect of the concentration and the radius of superparamagnetic materials are investigated. For this purpose, the distribution of electrical potential within the tissue is first obtained using Laplace equation. As the potential distribution is determined, the heat production in the different regions of the tissue will be obtained. This heat, together with the metabolic heat of the body, enters into the biothermal equation of Pennes. This equation provides a transient temperature distribution in the tissue, taking into account the conductivity of the tissue as well as blood perfusion. After determining the temperature distribution, the uncertainties of each of the important parameters with a 20% tolerance have been investigated.

The rest of the paper has been compiled in this way. Section 2 expresses the problem geometry with details of the governing equations. Uncertainty analysis is defined in section 3 and numerical procedure with mesh independency and verification tests are provided in section 4. Numerical results are presented in section 5 and general conclusions are given in section 6.

2. THEORETICAL MODEL

Here, three regions with different properties including healthy tissue without PCM, tumor with SPMs, and healthy tissue with PCMs are considered. Figure 1 shows these regions by Ω_1, Ω_2, and Ω_3, respectively.

To prevent damage caused by overheating, two pads cool down the surface of the skin. Also, paraffin wax with a melting temperature of 38-42 ºC is assumed as the PCM and injected around the tumor with high concentration (see Figure 1). Details of geometric information and thermophysical properties of three regions are reported in section 5. If the permittivity of the dielectric is constant, the potential within the tissue, φ could be determined using the Laplace equation [16]:

$$\nabla^2\varphi(x,y)=0 \tag{1}$$

$$\varphi(x,y)=\pm U, \qquad (x,y)\in\Omega_h$$
$$\frac{\partial\varphi(x,y)}{\partial q}=0, \qquad (x,y)\notin\Omega_h \tag{2}$$

where U is the voltage of the electrodes, q is the direction normal to the boundaries, and Ω_h is area of the electrodes. The strength of the electric field is determined as [16]:

$$\mathbf{E}(x,y) = -\nabla\varphi(x,y) \tag{3}$$

Heat generation in the tissues without SPM particles depends on the electrical conductivity and strength of the electric field $\boldsymbol{E}$. Thus, volumetric heat generation in these regions could be determined for electric field $\boldsymbol{E}$, roughly [16]:

$$Q_r = \sigma_i \frac{|\mathbf{E}(x,y)|^2}{2} = \frac{\sigma_i\left[|E_x|^2 + |E_y|^2\right]}{2} \quad (x,y) \in \Omega_{1,3}. \tag{4}$$

where σ_i is the electrical conductivity of the region . Properties in each subdomain are constant but different from other subdomains. Subscripts of 1, 2, 3 and 4 are used to show the features of the healthy tissue, cancerous tissue, SPMs, and PCMs, respectively. Also, subscripts 5 and 6 are used to show the effective properties of the cancerous tissue filled with SPM particles and the effective properties of healthy tissue filled with PCM particles. The heat generated in the tumor tissue with SPM could be gained using [16]:

$$Q_r = \left[\frac{3n_3 r_3^3 \chi''}{4\mu_0 f R^2} + (1-\eta_3)\frac{\sigma_5}{2}\right].\left[|E_x|^2 + |E_y|^2\right] \quad (x,y) \in \Omega_2. \tag{5}$$

where μ_0 is the permeability of the free space ($\mu_0 = 4\pi\times10^{-7}\ \mathrm{T\cdot m\cdot A^{-1}}$), f is the frequency of the electromagnetic field, R is the radius of the magnetic induction loop, χ'' is the susceptibility of electromagnetic nanoparticles, σ_5 is the effective electrical conductivity in the tumor tissue, $\eta_3 = 4\pi n_3 r_3^3 / 3$ is the SPM ratio in a volume of tissue, r_3 is the radius of the SPM micro/nanoparticles, and n_3 is the concentration of the SPM micro/nanoparticles in the tumor tissue.

Pennes equation determines the temperature distribution within the tissue [14]:

$$\begin{aligned} c\frac{\partial T(x,y,t)}{\partial t} &= \nabla\cdot\left(k(x,y)\nabla T(x,y,t)\right) \\ &-\omega_b(x,y)c_b T(x,y,t) + \omega_b(x,y)c_b T_a \\ &+Q_m(x,y,t) + Q_r(x,y,t) \quad (x,y)\in\Omega. \end{aligned} \tag{6}$$

where Ω is the solution domain, c and c_b are the heat capacity of the tissue and blood respectively, T_a is the temperature of the supplier artery which is assumed to be constant, T is the temperature of tissue, k is the thermal conductivity, ω_b is the blood perfusion, Q_m is the heat generation and resulted from the body metabolism, and Q_r is the heat source comes from the electromagnetic field.

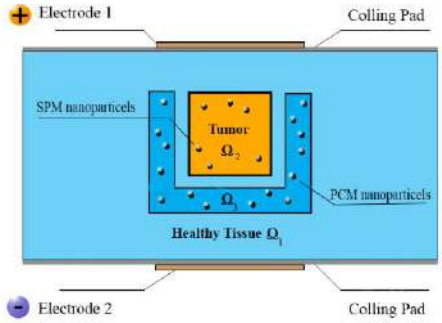

Figure 1. The regions of healthy tissue without PCM Ω_1, tumor with SPM Ω_2, and healthy tissue with PCMs Ω_3

The heat capacity c_4 and the thermal conductivity k_4 are estimated by [14]:

$$c_4 = \begin{cases} c_{4s}, & T < T_s \\ \dfrac{Q_l}{(T_l - T_s)} + \dfrac{c_{4s}+c_{4l}}{2}, & T_s \le T \le T_l \\ c_{4l}, & T > T_s \end{cases} \tag{7}$$

$$k_4 = \begin{cases} k_{4s}, & T < T_s \\ \dfrac{k_{4s}+k_{4l}}{2}, & T_s \le T \le T_l \\ k_{4l}, & T > T_s \end{cases} \tag{8}$$

where c_{4s}, c_{4l}, k_{4s}, and k_{4l} are the heat capacity of liquid and solid PCM, the thermal conductivity of liquid and solid PCM, respectively, and Q_l indicates the latent heat of the PCM [14]. Also, the effective electrical and thermal properties of the tissues with SPMs and PCMs are estimated as follows [9]:

$$\begin{aligned} c_2 &= (1-\eta_5)c_4 + \eta_5 c_5, \quad (x,y)\in\Omega_2 \\ c_3 &= (1-\eta_6)c_1 + \eta_6 c_6, \quad (x,y)\in\Omega_3 \end{aligned} \tag{9}$$

$$\begin{aligned} k_2 &= \left(\frac{1-\eta_5}{k_1} + \frac{\eta_5}{k_5}\right)^{-1}, \quad (x,y)\in\Omega_2 \\ k_3 &= \left(\frac{1-\eta_6}{k_1} + \frac{\eta_6}{k_6}\right)^{-1}, \quad (x,y)\in\Omega_3 \end{aligned} \tag{10}$$

$$\begin{aligned} \sigma_2 &= \left(\frac{1-\eta_5}{\sigma_4} + \frac{\eta_5}{\sigma_5}\right)^{-1}, \quad (x,y)\in\Omega_2 \\ \sigma_3 &= \left(\frac{1-\eta_6}{\sigma_1} + \frac{\eta_6}{\sigma_6}\right)^{-1}, \quad (x,y)\in\Omega_3 \end{aligned} \tag{11}$$

The boundary conditions for Equation (6) are defined as follows [14]:

$$\begin{aligned} -k\frac{\partial T}{\partial y} &= h_f(T_f - T), \quad y = 0\ \mathrm{m},\ y = 0.04\ \mathrm{m}, \\ -k\frac{\partial T}{\partial x} &= 0 \qquad\qquad x = 0\ \mathrm{m},\ x = 0.08\ \mathrm{m}. \end{aligned} \tag{12}$$

where h_f is the heat convection coefficient between the surface of the skin and water and T_f is the temperature of

the water. The details of discretization of equations and temperature distribution in the tissue are given in literature [22, 23], and the uncertainty analysis of thermal protection using PCM is studied here.

3. UNCERTAINTY ANALYSIS

The errors occur in the measurement of parameters are one of the important reasons that cause the difference between the results of the numerical results and the laboratory ones. Generally, the temperature could be defined by [17]:

$$T = f(w_1, w_2, ..., w_m) \tag{13}$$

where $w_1, w_2, \ldots, w_m$ indicate m parameters in the problem. Accordingly, the total uncertainty for temperature of the tissue can be obtained using the following equation [17]:

$$\Delta T = \sqrt{\left(\frac{\partial f}{\partial w_1}\Delta w_1\right)^2 + \left(\frac{\partial f}{\partial w_2}\Delta w_2\right)^2 + \ldots + \left(\frac{\partial f}{\partial w_m}\Delta w_m\right)^2} \tag{14}$$

where $\frac{\partial f}{\partial w}$ and Δw are the sensitivity coefficient and the uncertainty of the parameter, respectively.

4. NUMERICAL SOLUTION

Pennes Biothermal equation can be discretized by the finite difference method with a second-order accuracy considering $\Delta x = \Delta y$.

$$T_{i,j}^{s+1} = Fo\left(T_{i+1,j}^{s} + T_{i-1,j}^{s} + T_{i,j+1}^{s} + T_{i,j-1}^{s}\right) + (1 - 4Fo - W)T_{i,j}^{s} + \frac{\Delta t}{c}Q \tag{15}$$

where s denotes the time increment, $Fo = k\Delta t / c\Delta x^2$ is the Fourier number and $W = \omega_b c_b \Delta t / c$. Also, the discretized form of the boundary conditions are written as follows:

$$\begin{aligned} &T_{i,1}^{s} = \left(\frac{h_f \Delta x T_f}{k_1} + T_{i,2}^{s}\right) / \left(1 + \frac{h_f \Delta x T_f}{k_1}\right), \\ &T_{i,N}^{s} = \left(\frac{h_f \Delta x T_f}{k_1} + T_{i,N-1}^{s}\right) / \left(1 + \frac{h_f \Delta x T_f}{k_1}\right), \\ &T_{1,j}^{s} = T_{2,j}^{s}, \\ &T_{M,j}^{s} = T_{M-1,j}^{s}. \end{aligned} \tag{16}$$

The average of absolute error in each iteration (p) for the potential equation [28] is computed by.

$$\varepsilon^p = \frac{\sum_{i=1}^{M}\sum_{j=1}^{N}\left|T_{i,j}^{p+1} - T_{i,j}^{p}\right|}{M \times N} \tag{17}$$

The calculations stop, if the average of the absolute error falls below the concurrency criterion of 10^{-6}. The mesh independency is investigated for the temperature difference between two cases, tissue with PCM and tissue without PCM. For the same condition, Figure 2a displays the temperature difference on the vertical lines passing through the x=0.02 m and x=0.04 m and Figure 2b plots the temperature differences on the horizontal lines passing through the y=0.01 m and y=0.02 m for dx=0.0008 (101×51), dx=0.0005 (161×81), dx=0.0004 (201×101), and t= 500 seconds. As can be seen, with the change in the mesh resolution, the results do not change significantly, which results in mesh independency of the numerical results. Numerical validation has already been performed by the authors [19] for $R = 4.2\times10^{-8}\,m$ and $n = 4.8\times10^{6}\,m$ [15]. Figure 3 shows the flowchart for implementation of the numerical process.

5. RESULTS AND DISCUSS

The solution domain is rectangular with a dimension of 0.08×0.04 m^2. The heating area Ω_h is limited to 0.032 ≤ x≤.048 m, y=0 and 0.032 ≤x≤0.048m, y=0.04 m, and tumor area Ω_2 is limited to 0.032 ≤ x≤.048 m, 0.16 ≤ y≤.048m. The PCM area Ω_3 is specified in Table 1.

It is recognized that the presence of malignant tumor in the tissue changes the blood perfusion, heat capacity and heat of metabolism in the region of the tumor. For the healthy tissue and tissue with the tumor the magnetic and thermal properties are reported in Table 2. Also, the blood temperature is T_a=37 °C and the heat capacity of blood is c_b=4200 $kJ/m^3.K$. The boundary condition on the surface of the skin is the third kind with h_f =45 $W/m^2.K$ and T_f=20 °C, and other boundary conditions are assumed to be insulated [18]. The radius of the magnitude induction loop is R=0.01 m, voltage of the electrodes is U=8 V, and frequency of the electromagnetic domain is f=1 MHz. The thermophysical and electrical properties of the SPM and PCM are reported in Table 3. The susceptibility of electromagnetic nanoparticles is $\chi'' = 18$. Experimental results show that the nanoparticle size for cancer treatment should ideally be in the range of 10 to 100 nm [29].

The difference of temperature distribution between two cases, tissue with PCM and tissue without PCM is shown in Figure 4. According to this figure, it is observed that the injection of the PCM reduces the tissue temperature by more than 2 degrees, which justifies the use of PCM to control the temperature of the tissue during the hyperthermia.

To investigate the uncertainty analysis, a 20% tolerance has been assumed for each parameter. The positive or negative value of the uncertainty is so chosen to have the worst effect on thermal protection. Therefore

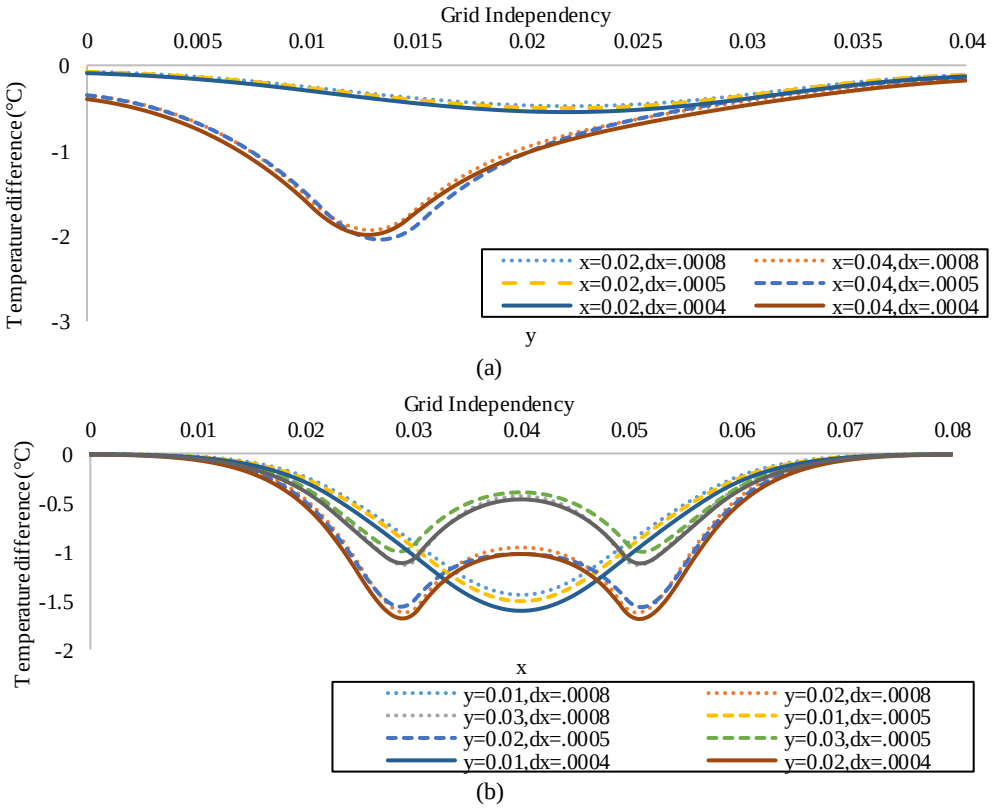

Figure 2. Investigation of the mesh independency at t=500 s for a) sections along the *x*-axis and b) sections along the *y*-axis

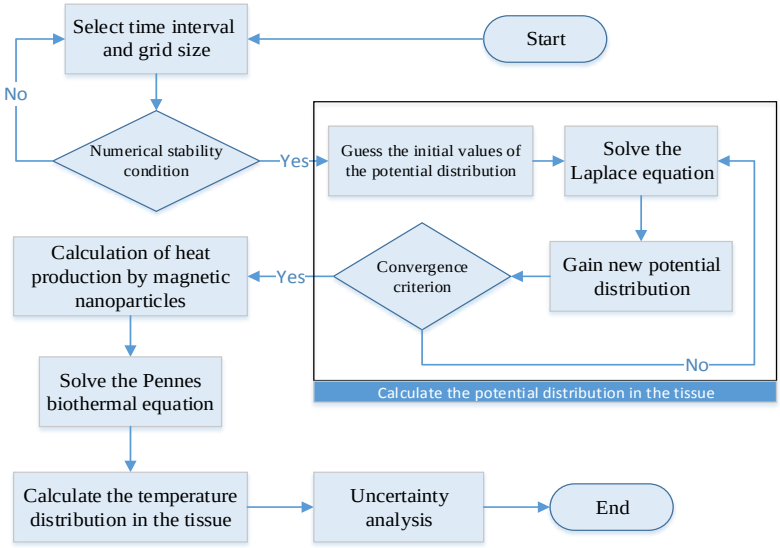

Figure 3. Flowchart of the numerical process for reaching the uncertainty analysis

TABLE 1. The area in which the PCM is injected into the tissue

$\Omega_3 = A \cap \overline{B}$
$A = \{(x, y) \mid 0.022 \le x \le 0.058 \text{ m}, 0.011 \le y \le 0.032 \text{ m}\}$
$B = \{(x, y) \mid 0.03 \le x \le 0.05 \text{ m}, 0.015 \le y \le 0.032 \text{ m}\}$

TABLE 2. Magnetic and thermal properties of healthy tissue and tissue with tumor [18]

	k (W/m.K)	c (J/m^3.K)	σ (S/m)	ω_b (1/s)	Q_m (W/m^3)
Healthy tissue	0.5	4.2×10^6	0.4	0.0005	4200
Tissue with tumor	0.6	4.2×10^6	0.48	0.002	42000

TABLE 3. Thermophysical and electrical properties of SPM and PCM [14]

	k (W/m.K)	c (J/m^3.K)	σ (S/m)	T_s (°C)	T_l (°C)	Q_l (J/m^3)	r (nm)	n (m^{-3})
SPM	40	2.072×10^7	25000	---	---	---	10	1×10^{19}
PCM	k_s=0.35 k_l=0.1	$c_s=2.56\times10^6$ $c_l=2.2\times10^6$	10^{-11}	38	42	1×10^8	10	1×10^{23}

all uncertainty values for the PCM are selected negative except the melting temperature, and uncertainty values for the SPM are selected positive. The uncertainty analysis of the concentration of micro/nanoparticles is shown in Figure 5. It is seen that the maximum temperature change in this case is only 0.22 °C, which is negligible.

The uncertainty analysis for the radius of the microcapsules is shown in Figure 6. The micro-capsulation of phase-change micro/nanoparticles should be in such a way that their radius not to be lower than the numerical value. It is seen that the difference from the numerical values is not perceptible so that a change of 20% of this parameter can affect the temperature distribution by about 0.5˚C.

Figure 7 shows the uncertainty analysis of the latent heat estimation. It is seen that a small deviation from the numerical values would not affect the results, and its impact can be ignored.

Uncertainty analysis of the melting temperature of micro/nanoparticles is shown in Figure 8. According to this figure, an imprecise estimation of the melting temperature affects the thermal protection over 1.1 °C. Hence to gain a similar results between the numerical and experimental data, the melting temperature should be estimated more accurately.

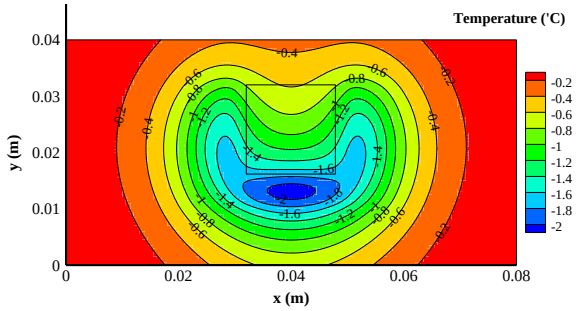

Figure 4. The difference of temperature distribution between two cases, tissue with PCM and tissue without PCM

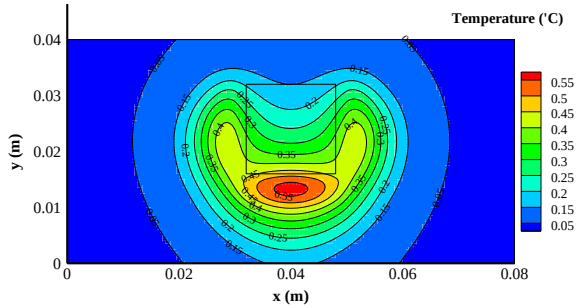

Figure 6. Temperature changes in the tissue due to a 20% change in the micro-capsulation radius of the PCM

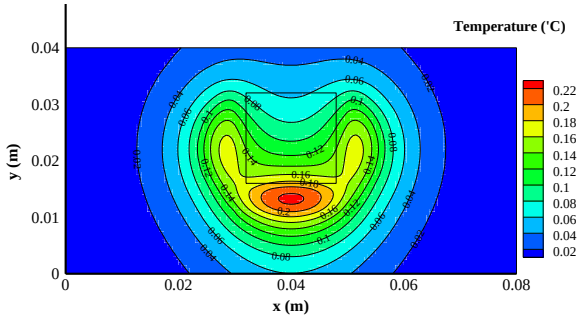

Figure 5. Temperature changes in the tissue due to a 20% change in the PCM concentration

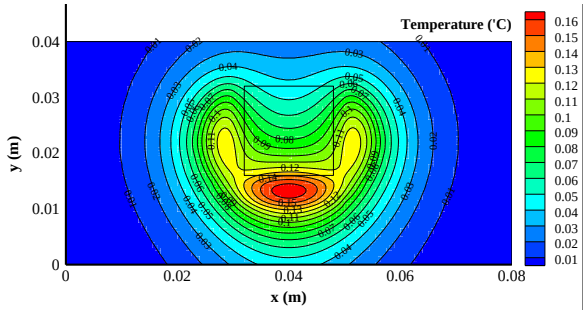

Figure 7. Temperature changes in the tissue due to a 20% change in the latent heat of the PCM

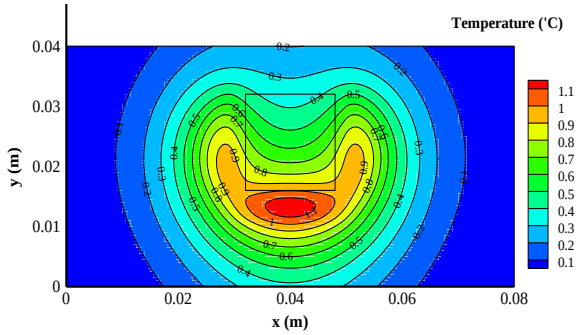

Figure 8. Temperature changes in the tissue due to a 20% change in the melting temperature of the PCM

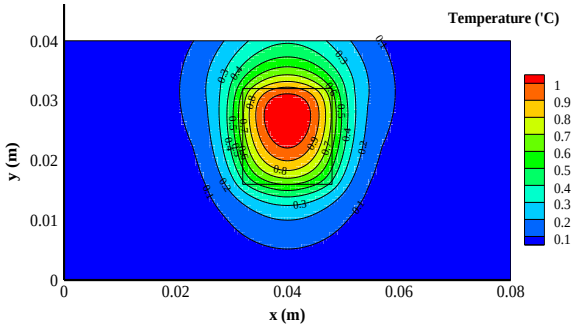

Figure 10. Temperature changes in the tissue due to a 20% change in the concentration of the SPM

Figure 9 shows the temperature changes in the tissue due to a 20% changes in the, solidus and liquidus temperatures of the phase-change micro/nanoparticles (the range of phase-change). Based on this figure, the deviation from the numerical values for the solidus and liquidus temperatures is so small, and there is no sensitivity to determine it precisely in the laboratory. As was shown in the previous study [23], the concentration and radius of SPM can also affect the thermal protection of the healthy tissue during the hyperthermia, thus the uncertainty analysis for these parameters are presented.

Figure 10 shows the temperature changes after 20% change of the concentration of the SPM. According to this figure, any small deviation from numerical values is negligible because the temperature change in the healthy tissues around the tumor is not significant.

Uncertainty of the radius of the SPM micro/nanoparticles has increased the temperature in the tumor tissue and also in the healthy tissues about 4˚C and 3˚C, respectively. This shows that the radius of the SPM micro/nanoparticles should be estimated accurately. The uncertainty of the radius of SPM micro/nanoparticles is shown in Figure 11. A summary of uncertainty analyzes is given in Table 4. These results are also graphically plotted in Figure 12.

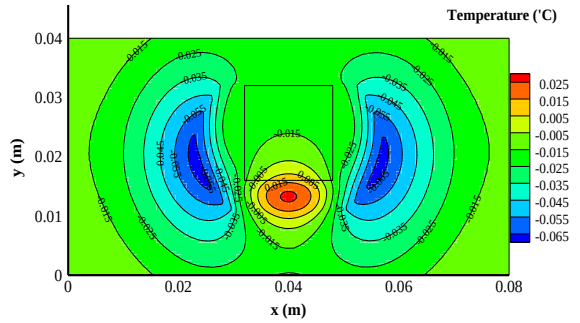

Figure 9. Temperature changes in the tissue due to a 20% change in the solidus and liquidus temperatures of the PCM

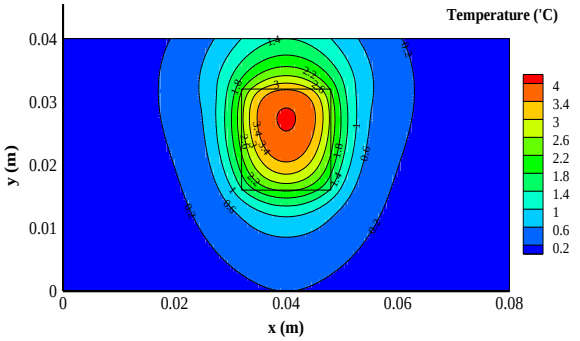

Figure 11. Temperature changes in the tissue due to a 20% change in the radius of the SPM

TABLE 4. Temperature variations in the tissue due to 20% changes in effective parameter at t=1000 (s)

Region	Maximum Temperature variation ˚C						
	Concentration of the PCM	Micro-capsulation radius of the PCM	Latent heat of the PCM	Melting temperature of the PCM	Range of solidus and liquidus temperatures of the PCM	Concentration of the SPMs	Radius of the SPM
Healthy tissue	0.22	0.47	0.17	1.15	0.065	0.6	3.2
Tumor tissue	0.17	0.57	0.14	0.98	0.025	1.12	4.1

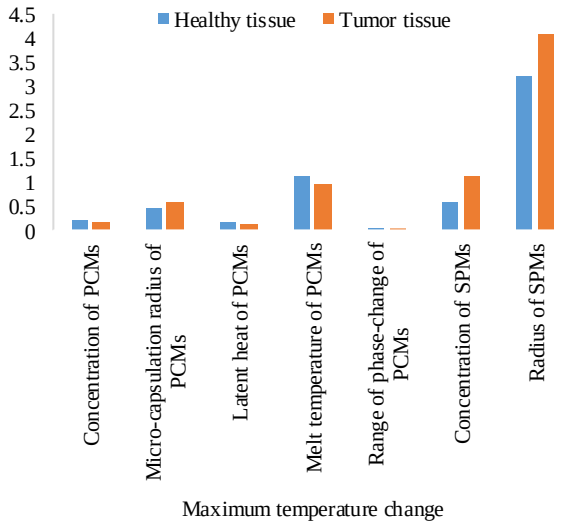

Figure 12. Temperature variations in the tissue due to 20% changes for the effective parameters at t=1000 (s)

6. CONCLUSION

In the present study, the inevitable deviation of the laboratory values with the numerical ones is investigated for the SPM and PCM. The results show that the deviation of some quantities affect the protection of healthy tissues during the hyperthermia and therefore need more precision in measurement of parameters for the practical condition. According to the obtained results, the deviation of the concentration, the radius of micro-capsulation, the latent heat and the range of the melting temperature have no significant effect on the thermal protection of healthy tissues. But the melting temperature of the PCM, the concentration of the SPM and the radius of SPM must be measured more accurately to gain the equal numerical and experimental results.

According to the results, a 20% difference between the numerical and laboratory values can cause a significant temperature change in the tissue. Uncertainties in measuring the concentration of the PCM, the radius of the micro-capsulation, the latent heat of the PCM, the melting temperature, the concentration of the SPM, and the radius of the SPM cause temperature change about 0.22 °C, 0.55 °C, 0.16 °C, 1.1 °C, 1 °C and 4 °C, respectively. Therefore, the radius of the SPM, the melting temperature and the concentration of the SPM should be more accurately measured.

7. REFERENCES

1. Zendehdel, K., "Cancer statistics in ir iran in 2018", ***Basic & Clinical Cancer Research***, Vol. 11, No. 1, (2019). https://doi.org/10.18502/bccr.v11i1.1645.
2. Pala, T., Ycedag, I. and Biberoglu, H., "Association rule for classification of breast cancer patients", ***Sigma Journal of Engineering and Natural Sciences***, Vol. 8, No. 2, (2017), 155-160.
3. Ozkan, E., Erdemir, A., Torer, B.D., Tasci, A.I., Baskin, Y., Ellidokuz, H. and Balik, D.T., "Genotyping and analysis of rs7501939 polymorphism for prostate cancer", ***Sigma Journal of Engineering and Natural Sciences***, Vol. 6, No. 1, (2015), 101-107.
4. Kizilbey, K. and Akdeste, Z.M., "Melanoma cancer", ***Sigma Journal of Engineering and Natural Sciences***, Vol. 31, No. 4, (2013).
5. Cabuy, E., "Reliable cancer therapies", ***Energy-Based Therapies. Hyperthermia in Cancer Treatment, RCT Summary for Professionals***, Vol. 1, No. 2, (2011), 1-48.
6. van der Zee, J., González, D., van Rhoon, G.C., van Dijk, J.D., van Putten, W.L. and Hart, A.A., "Comparison of radiotherapy alone with radiotherapy plus hyperthermia in locally advanced pelvic tumours: A prospective, randomised, multicentre trial", ***The Lancet***, Vol. 355, No. 9210, (2000), 1119-1125. https://doi.org/10.1016/s0140-6736(00)02059-6.
7. Pirouz, F., Najafpour, G., Jahanshahia, M. and Sharifzadeh Baei, M., "Plant-based calcium fructoborate as boron-carrying nanoparticles for neutron cancer therapy", ***International Journal of Engineering, Transactions A: Basics***, Vol. 32, No. 4, (2019), 460-466. https://dx.doi.org/10.5829/ije.2019.32.04a.01.
8. Falk, M. and Issels, R., "Hyperthermia in oncology", ***International Journal of Hyperthermia***, Vol. 17, No. 1, (2001), 1-18. https://doi.org/10.1080/02656730118511.
9. Javadi, K. and Komjani, N., "Investigation into low sar pifa antenna and design a very low sar u-slot antenna using frequency selective surface for cell-phones and wearable applications", ***Emerging Science Journal***, Vol. 1, No. 3, (2017), 145-157. https://doi.org/10.28991/ijse-01117.
10. Zhang, S., Clark, M., Liu, X., Chen, D., Thomas, P. and Ren, L., "The effects of bio-inspired electromagnetic fields on healthy enhancement with case studies", ***Emerging Science Journal***, Vol. 3, No. 6, (2019), 369-381. https://doi.org/10.28991/esj-2019-01199.
11. Priscilla, S.J., Judi, V.A., Daniel, R. and Sivaji, K., "Effects of chromium doping on the electrical properties of zno nanoparticles", ***Emerging Science Journal***, Vol. 4, No. 2, (2020), 82-88. https://doi.org/10.28991/esj-2020-01212.
12. Manikandan, G., Yuvashree, M., Sangeetha, A., Bhuvana, K. and Nayak, S.K., "Liver tissue regeneration using nano silver impregnated sodium alginate/pva composite nanofibres", ***SciMedicine Journal***, Vol. 2, No. 1, (2020), 16-21. https://doi.org/10.28991/SciMedJ-2020-0201-3.
13. Puspitasari, P. and Budi, L., "Physical and magnetic properties comparison of cobalt ferrite nanopowder using sol-gel and sonochemical methods", ***International Journal of Engineering, Transactions B: Applications***, Vol. 33, No. 5, (2020), 877-884. https://dx.doi.org/10.5829/ije.2020.33.05b.20.
14. Lv, Y., Zou, Y. and Yang, L., "Theoretical model for thermal protection by microencapsulated phase change micro/nanoparticles during hyperthermia", ***Heat and Mass Transfer***, Vol. 48, No. 4, (2012), 573-584. https://doi.org/10.1007/s00231-011-0907-4.
15. Sezgin, E., Karatas, O., Çam, D., Sur, İ., Sayin, İ. and Avci, E., "Interaction of gold nanoparticles with living cells", ***Sigma***, Vol. 26, (2008), 227-246.
16. Lv, Y.-G., Deng, Z.-S. and Liu, J., "3-d numerical study on the induced heating effects of embedded micro/nanoparticles on human body subject to external medical electromagnetic field",

IEEE Transactions on Nanobioscience, Vol. 4, No. 4, (2005), 284-294. https://doi.org/10.1109/TNB.2005.859549.

17. Deng, Z.-S. and Liu, J., "Uncertainties in the micro/nano-particles induced hyperthermia treatment on tumor subject to external em field", in 2006 1st IEEE International Conference on Nano/Micro Engineered and Molecular Systems, IEEE, (2006), 851-855. https://doi.org/10.1109/NEMS.2006.334910.
18. Majchrzak, E., Dziatkiewicz, G. and Paruch, M., "The modelling of heating a tissue subjected to external electromagnetic field", ***Acta of Bioengineering and Biomechanics***, Vol. 10, No. 2, (2008), 29-37. PMID: 19031995.
19. Majchrzak, E. and Paruch, M., "Numerical modelling of temperature field in the tissue with a tumor subjected to the action of two external electrodes", ***Scientific Research of the Institute of Mathematics and Computer Science***, Vol. 8, No. 1, (2009), 137-145.
20. Majchrzak, E. and Paruch, M., "Application of evolutionary algorithms for identification of number and size of nanoparticles embedded in a tumor region during hyperthermia treatment", Evolutionary and Deterministic Methods for Design, Optimization and Control with Applications to Industrial and Societal Problems (eds. T. Burczyński and J. Periaux), CIMNE, Barcelona, Spain, A Series of Handbooks on Theory and Engineering Applications of Computational Methods, (2011), 310-315.
21. Q. Zhao, L. Wang, R. Cheng, L. Mao, R.D. Arnold, E.W. Howerth, Z.G. Chen, S. Platt, Magnetic nanoparticle-based hyperthermia for head & neck cancer in mouse models, ***Theranostics***, Vol. 2, No. 1, (2012). https://doi:10.7150/thno.3854.
22. F. Talati, A.A. Taheri, Numerical study of induction heating by micro/nano magnetic particles in hyperthermia, ***Journal of Computational & Applied Research in Mechanical Engineering (JCARME)***, (2019). https://doi.org/10.22061/JCARME.2019.3961.1465.
23. Talati, F. and Taheri, A.A., "Uncertainty analysis in induction heating by magnetic micro/nanoparticles during hyperthermia", ***Journal of Mechanical Engineering***, Vol. 48, No. 4, (2019), 195-201.
24. Taheri, A.A. and Talati, F., "Fdm-based 2d numerical study of hyperthermia cancer treatment by micro/nano-phase-change materials", ***Iranian Journal of Science and Technology, Transactions of Mechanical Engineering***, (2019), 1-13. https://doi.org/10.1007/s40997-019-00314-y.
25. Nemati, Z., Alonso, J., Martinez, L., Khurshid, H., Garaio, E., Garcia, J., Phan, M. and Srikanth, H., "Enhanced magnetic hyperthermia in iron oxide nano-octopods: Size and anisotropy effects", ***The Journal of Physical Chemistry C,*** Vol. 120, No. 15, (2016), 8370-8379. https://doi.org/10.1021/acs.jpcc.6b01426.
26. Wang, H., Dai, W. and Bejan, A., "Optimal temperature distribution in a 3d triple-layered skin structure embedded with artery and vein vasculature and induced by electromagnetic radiation", ***International Journal of Heat and Mass Transfer,*** Vol. 50, No. 9-10, (2007), 1843-1854. https://doi.org/10.1016/j.ijheatmasstransfer.2006.10.005.
27. Li, L., Yu, B., Liang, M., Yang, S. and Zou, M., "A comprehensive study of the effective thermal conductivity of living biological tissue with randomly distributed vascular trees", ***International Journal of Heat and Mass Transfer,*** Vol. 72, (2014), 616-621. https://doi.org/10.1016/j.ijheatmasstransfer.2014.01.044.
28. Ferziger, J.H. and Perić, M., "Computational methods for fluid dynamics, Springer, Vol. 3, (2002).
29. Kazemi, S., Rezaei, S., Mohammadi, M. and Nikzad, M., "Separation of curcumin from curcuma longa l. And its conjugation with silica nanoparticles for anti-cancer activities", ***International Journal of Engineering, Transactions C: Aspects***, Vol. 31, No. 9, (2018), 1803-1809.

Persian Abstract

چکیده

در محافظت گرمایی از بافت‌های سالم در طول هایپرترمیا به‌وسیله مواد میکرو/نانو تغییر فاز دهنده (PCM)، انحراف از مقادیر نظری در شرایط آزمایشگاهی به دلیل خطاهای مختلف مانند مدلسازی، اندازه‌گیری، جابجایی ذرات و غیره اجتناب‌ناپذیر است. این انحراف‌ها می‌توانند محافظت گرمایی عملی را با آسیب به سلولهای سالم یا عدم تخریب سلولهای تومور تحت تأثیر قرار دهند. برای انجام روش عددی، با استفاده از روش اختلاف محدود، توزیع پتانسیل با حل معادله لاپلاس و برای یافتن توزیع دما در بافت معادله زیست گرمایی پنس استفاده شده است. معادله پنس با در نظر گرفتن رسانش درون بافت، پرفیوژن خون و گرمای متابولیک بدن به صورت گذرا حل شده است. در نتیجه انحراف و عدم قطعیت هر یک از عوامل موثر در محافظت گرمایی شامل غلظت مواد تغییر فاز دهنده، شعاع میکروکپسوله کردن، گرمای نهان، دمای ذوب و گستره تغییر فاز میکرو/ نانوذرات تغییر فاز دهنده و همچنین تأثیر غلظت و شعاع مواد سوپر پارامغناطیس (SPM) بررسی شده است. مطابق نتایج به دست آمده از آنالیز عدم قطعیت، شعاع SPMs پر اهمیت ترین پارامتر است و انحراف ۲۰ ٪ از مقدار عددی این پارامتر میتواند تا میزان ٤ درجه سیلسیوس بر روی دمای بافت تاثیرگذار باشد.

IJE TRANSACTIONS A: Basics Vol. 34, No. 1, (January 2021) 272-282

International Journal of Engineering

Journal Homepage: www.ije.ir

Fused Deposition Modeling of an Aircraft Wing using Industrial Robot with Non-linear Tool Path Generation

S. Harsha Arigela*[a], V. Kumar Chintamreddy[b]

[a] *Department of Mechanical Engineering, Jawaharlal Nehru Technological University Anantapuramu, Ananthapur Dt., Andhra Pradesh, India*
[b] *Department of Mechanical Engineering, N.B.K.R.I.S.T., Vidyanagar, Nellore Dt., Andhra Pradesh, India*

P A P E R I N F O

Paper history:
Received 24 September 2020
Received in revised form 16 October 2020
Accepted 30 October 2020

Keywords:
Additive Manufacturing
Fused Deposition Modelling
Industrial Robot
Robotics
Three Dimensional Printing
Toolpath Generation

A B S T R A C T

Fused Deposition Modelling (FDM) is an additive manufacturing process to build 3D objects on a horizontal plane from bottom to top. In the conventional FDM process, the printing of curved objects causes the staircase effect and results in poor surface finish. In this work, the FDM process integrated with a 6-DOF Industrial robot is used to print the curved objects by generating non-linear tool paths to avoid the staircase effect. A standard NACA 0015 aircraft wing having curved surfaces is printed without staircase effect at a uniform deposition rate using an industrial robot. The wing is sliced into concentric curved layers either in the form of convex or a concave shape. A new methodology is developed by combining the non-linear toolpaths with the change in extruder orientation to print curved objects at a uniform deposition without any staircase effect. ABB Robotstudio simulation software is used for simulating the printing process and simulation results are validated by printing the portion of the wing using the Industrial robot with an FDM extruder as an end effector. The experimental results showed that the aircraft wing is printed successfully with uniform deposition at constant velocity without any staircase effect.

doi: *10.5829/ije.2021.34.01a.30*

NOMENCLATURE

FDM	Fused Deposition Modelling	PLA	Polylactide
DOF	Degrees of Freedom	STL	Standard Triangle Language
NACA	National Advisory Committee for Aeronautics	MATLAB	Matrix Laboratory software
CAD	Computer-Aided Design	TCP	Tool Centre Point

1. INTRODUCTION

Fused Deposition Modelling (FDM) is a widely used additive manufacturing technology. It is less expensive compared to other 3D printing processes. FDM machines consist of an extruder (generally having two nozzles) and a horizontal printing bed. The degree of freedom for the conventional FDM machine is limited to three. Those are the movement of the extruder along the X and Y axes, and the movement of the bed along the Z-axis. In the conventional FDM machine, the orientation of the extruder is always perpendicular to the printing bed and the object is printed in a layered fashion from bottom to top.

The processing steps involved in the conventional FDM process are shown in Figure 1. The first step involved in the FDM process is to generate or create a virtual model or CAD model of the physical object. This CAD model is converted into STL (Standard Triangle Language) format. In the STL format, the entire surface of the object is approximated by triangles. The object in STL format is sliced into horizontal layers based upon the layer thickness. In the third step, the toolpath is generated for each layer in terms of G and M code instructions to the machine to print the desired object. The post-processing step is the removal of support material.

*Corresponding Author Email: *sriharsha.arigela@gmail.com* (S. Harsha Arigela)

Please cite this article as: S. Harsha Arigela, V. Kumar Chintamreddy, Fused Deposition Modeling of an Aircraft Wing using Industrial Robot with Non-linear Tool Path Generation, International Journal of Engineering, Transactions A: Basics, Vol. 34, No. 1, (2021) 272-282

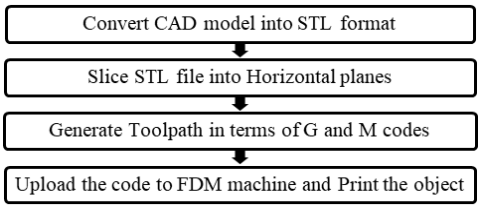

Figure 1. FDM Process

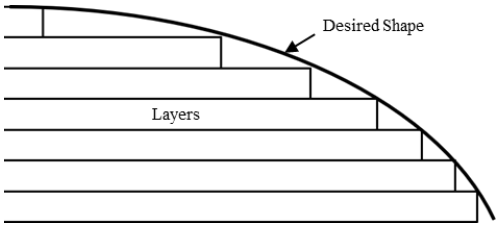

Figure 2. Staircase effect

In a conventional FDM process, while printing the objects with curved surfaces, the staircase effect is one of the common defects. For the curved surfaces, as the material deposition is carried out in layer-by-layer fashion, there is a presence of offset between two adjacent layers as shown in Figure 2. Steps are formed instead of the desired curved shape that results in poor surface finish as shown in the figure.

Tyberg and Bohn [1] developed an adaptive slicing methodology to reduce the staircase effect for curved surfaces. In this method, the slicing thickness is varied throughout along the curved surface. When the curvature is more the slice thickness is reduced to minimize the offset between the adjacent layers and in other cases default layer thickness is considered. The other way to minimize or eliminate the staircase effect is to adopt the non-linear toolpath generation [2]. For the conventional FDM machine, a non-linear toolpath can be generated with the three simultaneous translation movements in x, y, and z directions. But the orientation of the extruder cannot be changed and hence it may lead the extruder to collide with the previously deposited layers during the printing of curved surfaces. At the same time, the extruder's orientation needs to be maintained perpendicular to the printing surface to get homogeneous deposition. Due to the limitation of the orientation using conventional FDM, at some places, the excess of material will be deposited or an inadequate amount of material will be deposited. It results in the variation of part geometry and mechanical properties. Hence the conventional FDM machines are not suitable to produce uniform deposition of curved surfaces due to the limitation of extruder orientation. Shembekar et al. [3] proposed a collision-free trajectory planning for printing using a non-planar deposition. It indicated that collision with the printing surface can be avoided by properly controlling the trajectory parameters with respect to surface curvature. The proposed approach is implemented by using a 6-DOF robot arm. STL files of non-planar surfaces were generated with information of unit normal vectors set and the information on vertices of each triangle in 3D Cartesian coordinates. By projecting this data on the 2D Cartesian coordinate plane, the shape of the projected surface is obtained. In this way, all the surfaces (slices) were obtained for the 3D structure. Complex 3D structures with various curvatures like Curved beam, Mini armor chest protector, Wind turbine blade, Mini Car Bonnet were successfully fabricated using the proposed collision-free trajectory and a satisfactory surface finish is accomplished. Bhatt et al. [4] proposed a robotic cell for multi-resolution AM (Additive manufacturing with two different nozzle sizes). The proposed cell consists of two 6 degrees of freedom (DOF) robot manipulators. Algorithms were developed for decomposing parts into multi-resolution layers and generating collision-free trajectories for these robot manipulators. Euclidean distance transform (EDT) based layering algorithm is used to generate non-planar layers required for printing. EDT is used to construct the 3D transform distance from the 2D transform distance. Sample specimens like Mini car bonnet, Mini airplane wing, Composite slider, and Helix shape slider were printed with non-planar layers for the exterior regions with the ABB IRB 120 robot. The planar layers were printed for the interior regions of those specimens with the ABB IRB 2600 robot. While printing the airplane wing with the proposed slicing technique, non-planar layers for the outer region and planar layers for the inner region were generated. This will eliminate the staircase effect but the mechanical properties of the wing will be the same just like the same wing printed with the conventional FDM process. Jensen et al. [5] introduced two new deposition-strategies for 5 DOF (five degrees of freedom) and 6 DOF extrusion-based additive manufacturing (AM) process. The 5 DOF extrusion-based additive manufacturing strategy is called the tool path projection approach. This approach was inspired by the texturing of 3D bodies used in computer-generated imagery (CGI) for generating layers. This approach follows a sequence in which the surface of the geometry is unwrapped, and in its flattened form, texturized, and then the geometry is wrapped back to its 3-dimensional shape. This is done for each layer. The 6 DOF extrusion-based additive manufacturing strategy is called parent-child-approach. This approach allows local features of the workpiece to be built in different directions by reorienting the workpiece accordingly, exploiting the 6DOF of the system. It indicated that the proposed automated tool path projection method to generate concentric shell layers as a remedy for the staircase effect. Ishak et al. [6] integrated six degrees of a freedom robot arm with a fused deposition modeling

system for multi-plane and 3D lattice structure printing applications. The proposed system has the advantage of printing in multiple planes over a conventional Cartesian 3D printer platform which is limited to single-plane layering for the printing of 3D objects. 3D lattice structures and an object with an overhang structure were printed with the proposed platform. Ahlers et al. [7] presented a slicer (slices generating algorithm) that is capable of generating non-planar toolpaths from any object to avoid the staircase effect. In this work, first object is sliced with the regular layer generation to generate the planar layers. And then the top and shell areas are removed and replaced by nonplanar layers to generate the needed space for the nonplanar extrusions. The replacement is done by first finding the layer where the nonplanar surface should be generated. In this way, nonplanar layers are generated. Collision prevention while printing nonplanar layers is also taken care of in the proposed printing approach. The objects printed with the nonplanar layers by the proposed approach have shown better surface quality compared with objects printed with conventional planar layers. Kubalak et al. [8] have presented a multi-axis toolpath generation algorithm and it is implemented on a 6-DOF robotic arm ME (Material Extrusion) system to fabricate tensile specimens at different global orientations. ABS tensile specimens at various inclination angles were printed using the proposed multi-axis technique. The results showed that the multi-axis specimens had similar performances regardless of orientation and were equivalent to the 3-DOF specimens printed with the conventional FDM machine. Balogun et al. [9] developed a generic electrical energy model for the 3D printing process and indicated the warm-up time for the FDM machine is considerably high and suggested that energy efficiency can be improved without cooling down the 3D printer to room temperature before the next part is printed. Kumar et al. [10] examined the tribological behaviour of Ultra High Molecular Weight Polyethylene (UHMWPE) and Polyether ether ketone (PEEK) biopolymers which are mostly used for prosthesis used in Total Knee Replacement (TKR). The test specimens were fabricated using Direct Laser Metal Sintering (DMLS) and indicated that PEEK is a suitable material for TKR due to less wear rate compared to the UHMWPE. Kumar et al. [11] developed a robotic manipulator to recognize the speech and n write letters by using a pen as an end effector. In this work, a dynamic time warping (DTW) algorithm is used for recognizing the sound signal and to generate the executable command to move the robot in its workspace. Moradi et al. [12] statistically analysed 3D printing of PLA (Polylactic acid) by the Fused Deposition Modelling process. The honeycomb pattern is selected in this work for infill. It indicated that layer thickness is the major control variable. It also indicated that the infill percentage and extruder's temperature had a significant influence on the tough fracture of printed parts. Moradi et al. [13] investigated the influence of layer thickness, infill percentage, and extruder temperature on the failure load, thickness, and build time of bronze polylactic acid (Br-PLA) composites 3D printed by the fused deposition modeling (FDM). The failure load and build time were considered as objective functions. In this work, a comparison was made between PLA and Br-PLA in terms of failure load. Moradi et al. [14-17] investigated the post-processing of 3D printed PLA (polylactic acid) parts. To remove the defects of workpieces printed by the FDM process, a post-processing operation is introduced in this work that uses a low power CO_2 laser. Optimum values of the process parameters were obtained in this work from the DOE analysis.

In the FDM process, an alternative slicing technique is needed to generate nonplanar layers for objects having curved surfaces to eliminate the staircase effect. In the conventional FDM machine, due to limited degrees of freedom (3), it is not possible to print the curved objects without staircase effect. The objective of the present work is to develop a new slicing methodology to print the objects having curved surfaces without staircase effect using the Industrial robot. The curved surface object is sliced into nonplanar layers that are concentric to the shape of the object. These nonplanar layers are printed by generating non-linear toolpaths using the Industrial robot with an FDM extruder as the end-effector. To obtain uniform and homogeneous deposition along the nonplanar layers, the extruder needs to move with constant velocity and its orientation needs to be maintained perpendicular to printing surfaces. The proposed methodology is applied to print a segment of an aircraft wing having NACA 0015 [18] Airfoil shape. The NACA aircraft wings are developed by the National Advisory Committee for Aeronautics [18]. Data for these Airfoil shapes are available on the UIUC Airfoil Coordinates Database [19]. Simulation of the extruder's movement along the generated toolpath is carried out in ABB Robotstudio software for validation. The simulation results showed that there is no presence of singularity errors and the generated toolpath is within the range of the robot's workspace. The actual printing of the aircraft wing is done successfully without the staircase effect. The methodology followed in slicing and printing the segment of the aircraft wing is presented in this paper.

2. METHODOLOGY

2. 1. Nomenclature of the Wing A wing is a type of fin that produces lift force to fly while moving through the air [20]. The wing has curved surfaces on

the upper and the lower portions, designed to give an adequate ratio of lift to drag. The cross-sectional shape of a wing is called Airfoil. Wings are classified as symmetric and asymmetric Airfoil-shaped wings. Figure 3 shows the nomenclature of an asymmetric Airfoil-shaped wing and Figure 4 shows the nomenclature of a symmetric Airfoil-shaped wing. The lower surface of the wing is subjected to higher static pressure compared to the upper surface. The lift force is generated due to the pressure difference between these two surfaces of the Airfoil. The leading edge is situated at the front part of the Airfoil and it has maximum curvature. The trailing edge is situated at the rear part of the Airfoil. These two edges are connected by a straight line called chord line. Angle "α" is called the angle of attack that is measured between the direction of the relative wing and chord line. The camber line is constructed by joining the locus of points midway between the upper and lower surfaces. If the Airfoil is symmetric, then both the camber line and the chord line will coincide. In this work, the symmetric Airfoil NACA 0015 [18] wing is selected for printing.

2. 2. Selection of Aircraft Wing's Orientation for Slicing In this work, a symmetric Airfoil-shaped wing as shown in Figure 4 is selected for printing using the Industrial robot. In the conventional FDM process, the wing can be sliced into three possible ways with respect to two reference planes viz. "S" and "R" as shown in Figure 5.

The reference plane "R" is considered as a plane parallel to the flat base of the wing as shown in Figure 5. Another reference plane "S" is considered as a plane containing the chord lines and perpendicular to the reference plane "R".

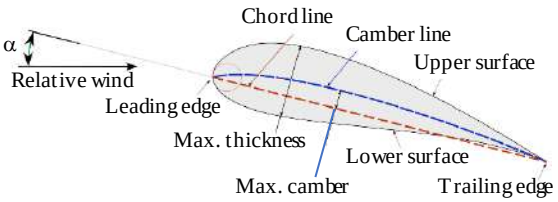

Figure 3. Airfoil Nomenclature (asymmetric type) [17]

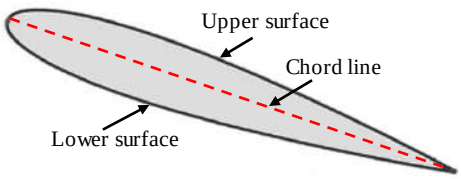

Figure 4. NACA 0015 (Symmetric type Airfoil) [18]

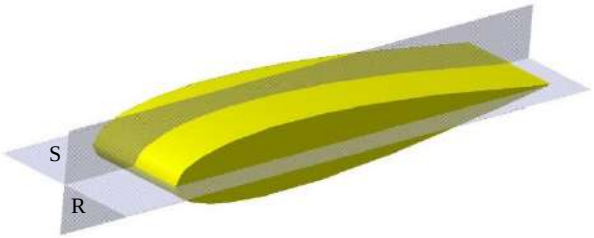

Figure 5. A portion of the wing with plane "S" passing through chord line and plane "R" parallel to the wing base

For conventional FDM, the selected aircraft wing can be sliced and printed in three possible orientations with minimum support structure with reference to planes "R" and "S" as shown in Figure 6, Figure 7 and Figure 8. In all these three cases, slicing is carried out with a plane parallel to the horizontal printing bed. The boundaries (shells) for each of these layers are shown in red color and the infill is shown in yellow color for these three cases as shown in Figures 6, 7 and 8.

In the first orientation, as shown in Figure 6, the slicing is carried out parallel to plane "S" and perpendicular to plane "R". In this orientation the cross-sectional area of each sliced layer is different and it produces the staircase effect. Due to variation in the cross-sectional area of each layer, the object may not have uniform strength. In this orientation, the support structure is required to build the wing up to the chord length's height.

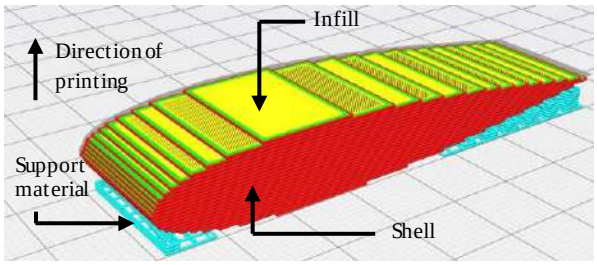

Figure 6. Case 1: Slicing perpendicular to plane "R" and parallel to plane "S"

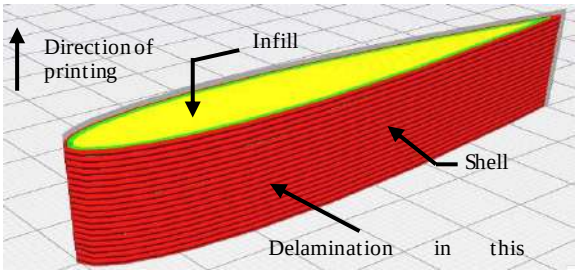

Figure 7. Case 2: Slicing perpendicular to plane "S" and parallel to plane "R"

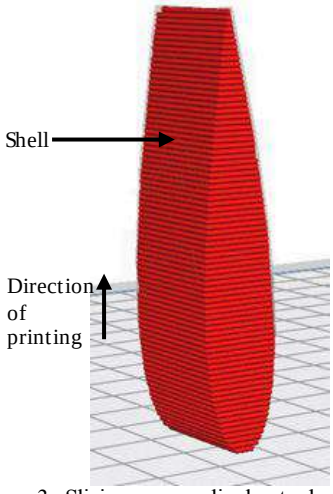

Figure 8. Case 3: Slicing perpendicular to both plane "R" and plane "S"

In the second orientation, as shown in Figure 7, the slicing is carried out perpendicular to plane "S" and parallel to the plane "R". In this orientation, the objects can be printed without staircase effect and support structure but the tensile strength is poor along the direction of printing. Zhao et al. [21] studied the tensile strength and elastic property of PLA material printed with different angles and layer thicknesses through the FDM process. It indicated that the tensile strength and Young's modulus of PLA specimen increased with the increase in the printing angle or decrease in layer thickness. It also indicated that the specimen printed at 0^0 angle (i.e. layers are parallel to tensile load direction) having comparatively less tensile strength compared to specimen printed at other angles (15^o, 30^o, 60^o, 90^o). At 90^o the printed layers are perpendicular to tensile load direction. Moreover, in this orientation, the aircraft wing will suffer a serious delamination effect due to the action of high static pressure (load) on the lower surface. Perkowski [22] indicated that the part printed by the FDM process with PLA material will fail, if it is subjected to the compressive load applied perpendicular to the direction of printing due to the buckling of layers. This is caused by the layers delaminating and bending out of the plane of the applied stress.

In the third possible orientation, as shown in Figure 8, the slicing is carried out perpendicular to both plane "R" and plane "S". In this case, the support structure is required to build up to the maximum thickness of the wing. The major drawback of this orientation is that the staircase effect and poor tensile strength along the direction of printing. The cross-section of each layer is not uniform and the wing may not have uniform strength.

In the present work, a new methodology is adopted for slicing and printing of the wing as shown in Figure 9 using the Industrial robot. The slicing is carried out parallel to the outer curved surfaces of the wing i.e. in the concentric form. In this orientation, the support structure is required up to the chord line's height. In this slicing method, each layer is having maximum surface area contact to adjacent layers and results in comparatively higher strength in perpendicular directions along the curved surfaces than the conventional orientations as shown in Figures 6, 7 and 8. This slicing method also avoids staircase effect. For the support structure, the slicing is carried out in a conventional horizontal slicing, and to eliminate the staircase effect in the lower surface of the wing two nonplanar layers are required as shown in Figure 9. The layers of the support structure are represented in red color and the layers of the wing are represented in green color as shown in Figure 9. Due to limited degrees of freedom, in the conventional FDM machine, the change in orientation of the extruder is not possible to print the nonplanar layers that are shown in Figure 9. The layers in this orientation have stronger bonding and minimum delamination due to nonplanar type and maximum surface area contact.

The relative merits and demerits of the mentioned slicing methodologies and orientations are shown in Table 1.

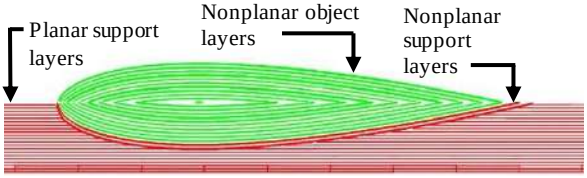

Figure 9. Slicing along the contour of the wing (nonplanar slicing)

TABLE 1. Relative merits and demerits of slicing

	Case 1 Figure 6	**Case 2 Figure 7**	**Case 3 Figure 8**	**Slicing along the contour of the wing Figure 9**
Staircase effect	Yes	No	Yes	No
Strength	Moderate	Poor	Poor	High
Slicing	Linear	Linear	Linear	Both Linear and Non-Linear
Printing with Conventional FDM	Possible	Possible	Possible	Not possible
Extruder's Orientation when printing	No Change	No Change	No Change	Changes when printing nonplanar layers
Support structure	Required	Not Required	Required	Required
Type of support structure	Planar Layers	Not Required	Planar Layers	Both planar and non-planar layers

2. 3. Steps Involved in Printing the Aircraft Wing using Industrial Robot In this work, the aircraft wing is printed with an Industrial robot using the extruder as an end effector. In this work, a small segment of the wing is printed. Various steps involved in printing the aircraft wing [18] are presented in this section and they are 1) Layer generation 2) Toolpath generation 3) Simulation of Printing in ABB Robotstudio software and 4) Printing using the Robot.

2. 3. 1. Layer Generation The data points for the lower surface and upper surface of the Airfoil of NACA 0015 [18] wing are shown in the following Table 2. Data for this Airfoil shape is taken from the UIUC Airfoil Coordinates Database by considering the value of chord length as 80 mm.

1. Based on the data points, two splines are fitted for both the lower surface and upper surface respectively. The obtained Airfoil shape or cross-section of the wing is shown in Figure 10. These two splines are considered as base splines.
2. Normal vectors at discrete intervals (0.5 mm) to the lower base spline are generated. The direction of each normal vector is reversed (towards the chord line) and the obtained vectors for the base spline are shown in Figure 11.

TABLE 2. Data Points [18]

S. No.	Lower Surface		Upper Surface	
	X	Z	X	Z
1	15	8.7016	15	8.7016
2	16	6.808	16	10.5952
3	17	6.0872	17	11.316
4	19	5.1472	19	12.256
5	21	4.5016	21	12.9016
6	23	4.0192	23	13.384
7	27	3.356	27	14.0472
8	31	2.964	31	14.4392
9	35	2.76	35	14.6432
10	39	2.7	39	14.7032
11	47	2.8984	47	14.5048
12	55	3.408	55	13.9952
13	63	4.1384	63	13.2648
14	71	5.0376	71	12.3656
15	79	6.0784	79	11.3248
16	87	7.2536	87	10.1496
17	91	7.8952	91	9.508
18	95	8.5752	95	8.828

3. On each obtained vector, a new point is determined at a certain distance from the origin of the respective vector towards the chord line. This distance is equal to the layer thickness. The layer thickness considered in this work is 0.5 mm. Again, one more spline is fitted through the newly obtained points. Figure 12 shows the newly obtained spline over the base spline that is separated by 0.5 mm.
4. By repeating the above step and by considering the distance as multiples of 0.5 mm, new splines are created. The extended portion of each spline beyond the chord length is trimmed off. Following the same procedure for the upper surface, concentric splines are generated. Figure 13 shows the final set of splines that are obtained for the cross-section of the wing.
5. From the obtained set of splines, each spline is swept along a line segment towards the depth direction to generate a layer. All the splines are swept in the same way to generate a set of layers. Figure 14 shows a generated layer obtained by sweeping a spline.

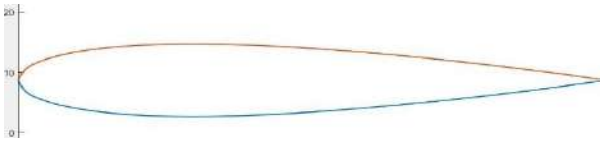

Figure 10. Airfoil Shape

Figure 11. Vectors along the Lower surface

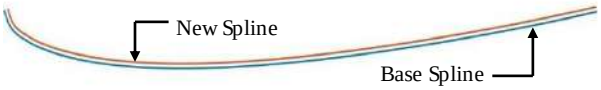

Figure 12. New obtained spline above the Base spline

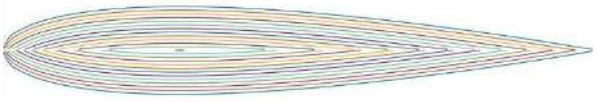

Figure 13. Set of splines

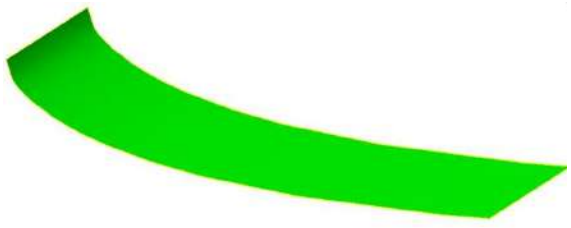

Figure 14. Generated layer

2. 3. 2. Toolpath Generation The sliced layers of the aircraft wing consist of concave shapes below the chord line and convex shapes above the chord line. To print the concave-shaped layers below the chord line need supporting structure. The support structure consists of both planar (flat) and non-planar (curved) type of layers. Two concave-shaped layers were generated to support the aircraft wing's bottom layer to eliminate the staircase effect at the bottom portion. After completion of printing the aircraft wing, the entire support structure is removed. The cross-sectional view of the aircraft wing with support structure is shown in Figure 15. In the figure, it can be observed that a support structure having nonplanar layers are used at the lower surface of the aircraft wing in order to eliminate the staircase effect. 3D view of the aircraft wing is shown in Figure 16. In this work, both wing and support structure are printed using a robot and the tool path is generated separately for both support structure and wing.

For printing the portion of the support structure with flat horizontal layers, a CAD model up to that portion is developed based on data points shown in Table 2. In this work, a chord line length of 80 mm is considered. The width of the wing segment is considered as 20 mm. The CAD model is converted into STL format and it is sliced into horizontal layers as shown in Figure 17.

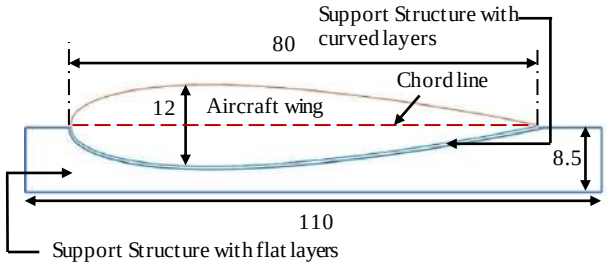

Figure 15. The cross-sectional view of the aircraft wing with the support structure

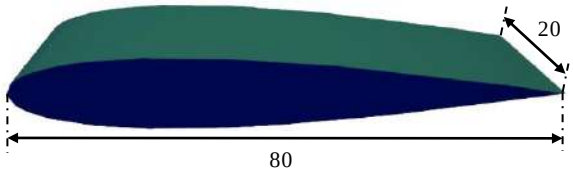

Figure 16. 3D view of the aircraft wing

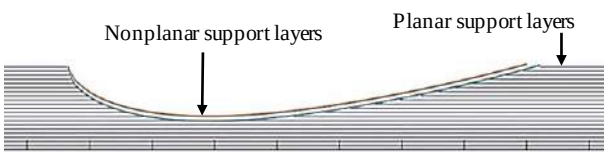

Figure 17. Front view of the slices of support

Each layer's toolpath is generated in a zig-zag fashion based upon the scan-line polygon filling algorithm [23]. The fill density of the support structure is taken as 50% to save the material and time and for ease of cleaning. The toolpath is converted into rapid commands (MoveL) for the ABB Industrial robot to print the support structure. For generating the two curved (concave-shaped) layers of the support structure, the proposed layer generation technique in the above section is used. The toolpath generation for these two layers is similar to the aircraft wing's layers, which is explained in the remaining part of this section.

The tool path for printing the wing is generated by combining the non-linear motion of the robot wrist combined with continuous change in orientation. As shown in Figure 11, the set of layers were generated by sweeping the splines. In generating non-linear toolpath for each layer, the extruder needs to move in all the x, y and z coordinates simultaneously. At the same time, the orientation of the extruder needs to vary to maintain perpendicular orientation to layer to get uniform deposition and to avoid collision with the previously printed layers. The maximum rotation (roll) along the x-axis considered in this work is $\pm 45^0$. Figure 18 shows the schematic view of the tool (Extruder) moving along a nonplanar layer in a nonlinear fashion keeping the orientation perpendicular to the layer. The extruder keeps on changing the orientation along with the movement at constant velocity to facilitate homogeneous deposition of material as shown in the figure.

Two types of toolpaths that are considered alternatively for generating the toolpaths while depositing the material along the curved layers. A MatLab program is developed to generate these toolpaths. This MatLab program takes the coordinates on the layer as input and joins them logically to create the path. If the tool is required to move from the first coordinate to the second coordinate, the MatLab program generates the output in the form of MoveL (rapid code for the robot) statement which will make the robot move from the first coordinate to the second coordinate in a linear fashion. In this way, the toolpath is created for the entire layer. The first type of the toolpath is generated in such a way that the tool moves along the curved layer (treating the movement along the y-axis) and changes its orientation while moving from

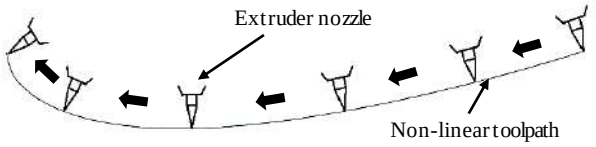

Figure 18. Schematic view of the tool moving along a curved layer

one position to another. This movement is incremented along the other axis (x-axis) for generating the toolpath for that layer. The isometric view of this type of toolpath is shown in Figure 19. Schematically the toolpath is drawn along the layer in Figure 19 for representation purpose. The top view of the actual toolpath is shown in Figure 20.

The second type of toolpath is generated by changing the direction of the movement of the extruder is along the depth direction (x-axis) with constant orientation. This movement is incremented towards the curve (towards the y-axis) by changing the orientation for each increment. The isometric view of this toolpath is shown in Figure 21. Schematically the toolpath is drawn along the layer in Figure 21 for representation purpose. The top view of the actual toolpath is shown in Figure 22.

These two types of toolpaths are used alternatively for consecutive layers to produce stronger bonds between layers and result in an increase in the strength of the wing. For the outer layers of the wing, the first type of toolpath is used for printing to avoid the staircase effect.

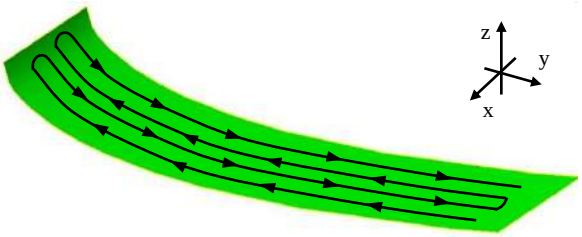

Figure 19. Isometric view of Toolpath type 1

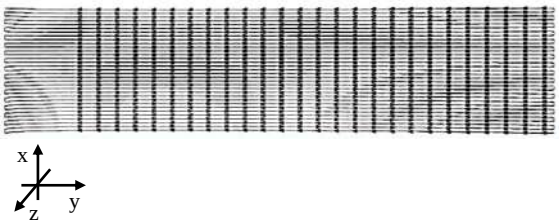

Figure 20. Top view of Toolpath type 1

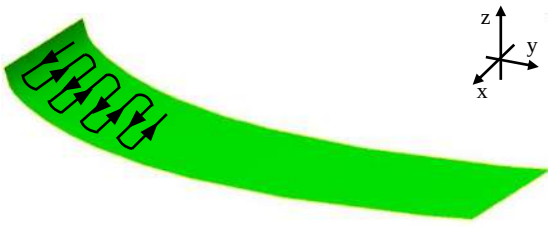

Figure 21. Isometric view of Toolpath type 2

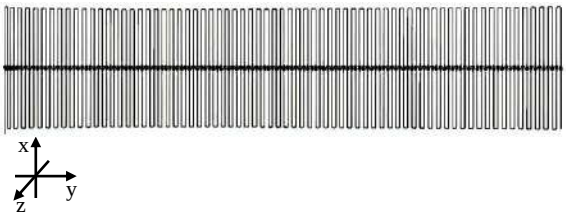

Figure 22. Top view of Toolpath type 2

2. 3. 3. Simulation of Printing in ABB Robotstudio Software In this work, ABB make IRB 1600 robot acts as a fused deposition modeling machine with a higher degree of freedom (6) by attaching the extruder as an end effector. Before carrying out the actual printing process, simulation of the toolpath movement is done in ABB Robotstudio simulation software for validation. This simulation is helpful for checking out the presence of any singularity errors. This can be also useful to check whether all the positions were within the reach of the robot or not. For simulation, a model of the extruder is built and attached to the IRB 1600 robot and it acts as a tool. The tip of the nozzle is defined as the TCP (Tool Centre Point).

2. 3. 4. Printing using the Robot A dual nozzle extruder is attached to the flange of the ABB IRB 1600 robot's wrist to facilitate Fused deposition modeling. TCP (Tool Centre Point) is defined at the tip of nozzle 1. This setup is shown in Figure 23.

The toolpath that has been generated in terms of Rapid commands is given as input to the ABB IRC5 controller. These rapid commands do contain both motion instructions and digital output signals. The motions instructions in the form of MoveL (Move Linear) are used to control the movement of the robot. As the TCP (Tool Centre Point) is defined at the tip of the nozzle, the nozzle follows the defined toolpath.

Figure 23. Extruder attached to the robot

The other rapid commands are digital output signals. These signals are being used to control material deposition. Here the material used for printing is PLA (Polylactic acid) with a melting point of 195^0. This digital output signal is in binary form i.e. either 0 or 1, a simple off or on. The digital output signal is fed to the Arduino Uno board's digital input pin. Here the Arduino board does contain an L293D Motor Driver for stepper motor control. A program is dumped into this Arduino board to rotate the stepper motor at specific constant rpm if the digital output from the controller is 1. This rotation is only in one direction. If the digital output signal is 0, the stepper motor stops rotating and holds its position. When the stepper motor is in ON state, the material in the form of wire will pass through the heat block and gets melted and gets deposited through the nozzle. Once the material leaves the nozzle and gets exposed to the atmosphere, it gets solidified instantly within 0.1s. These digital output signals are passed logically so that wherever there is a need the material gets deposited in between two specific points along the toolpath. If not, the material won't get deposited. In this way, the stepper motor will be controlled. Process parameters that were considered for the FDM process in this work are shown in Table 3. Layer thickness is one of the important process parameters for the FDM process. Total printing time is also affected by layer thickness. In this work, is used to print layers of thickness 0.5 mm and deposition speed i.e TCP (Extruder's nozzle tip) speed is considered to be 40 mm/s. Infill density for support is considered as 50%. This will ensure the easy removal of the support structure after the printing process is completed. The aircraft wing is printed with 100% infill density. The extrusion temperature is maintained at 195^0 C. This is done by using Arduino Atmega 2560 board and Ramps 1.4 Shield. All the time there is continuous feedback from the heat block to maintain a constant temperature. To take away excessive heat from the nozzle's heat block, a cooling fan is also being controlled by this Arduino board. Using this same feedback system the bed temperature is also maintained at 70^0 C.

TABLE 3. Process parameters

S. No	Process Parameter	Value
1	Layer Thickness (For both planar and nonplanar layers)	0.5 mm
2	Deposition speed	40 mm/s
3	Infill density for support	50%
4	Infill density for aircraft wing	100%
5	Nozzle Diameter	0.5 mm
6	Extrusion Temperature	195^0
7	Bed Temperature	70^0

The relative advantage of the methodology adopted to print the aircraft wing in this work over and the methodology adopted by Bhatt et al. [4] is shown in Table 4.

3. RESULTS AND DISCUSSION

Simulation is carried out in Robotstudio software to check the movement of the tool along the defined toolpath. The generated toolpath in the form of rapid commands is uploaded to the software environment. The movement of the tool speed is maintained at 40 mm/s. Simulation is carried out in two stages. In the first stage, the simulation of the tool moving along the toolpath for the support is checked. For this movement, the tool remains in the same perpendicular orientation to the planar toolpath throughout the simulation with a movement speed of 40 mm/s. Tool moving along the two nonplanar layers in the support structure is also simulated in this stage at the same speed but with a change in the tool's orientation. The toolpath generated in the robotstudio simulation environment for the support is shown in Figure 24.

In the second stage, the simulation of the tool moving along the toolpath for the wing segment is checked. In this movement, the tool changes its orientation perpendicular to the non-linear toolpath throughout the simulation with a movement speed of 40 mm/s. The toolpath generated in the robotstudio simulation environment for the aircraft wing segment is shown in Figure 25.

TABLE 4. Relative advantages of the present methodology

	Aircraft wing printed through proposed methodology in this work	Aircraft wing printed through the methodology presented by Bhatt et al. [4]
Type of layers used to print the aircraft wing	Non-planar layers only	Both planar and nonplanar layers
Type of slicing	Based on Splitting the part into a set of splines	Based on Euclidean distance transform
Nozzle diameter	0.5 mm	0.4 mm and 0.8 mm
Robot end effector velocity	40 mm/s	25 mm/s
Number of Robots used	1	2

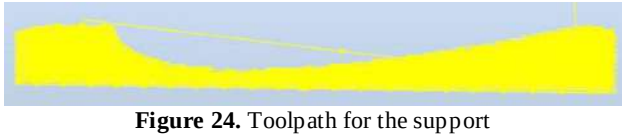

Figure 24. Toolpath for the support

Figure 25. Toolpath for the Aircraft wing segment

The simulation results showed that the TCP (tip of the nozzle) followed the toolpath with desired orientations at every position without singularity errors. All the positions are within reach. Hence the generated toolpath for both the support and wing segment is validated.

After validating the simulation results, the printing of the segment of the NACA 0015 [18] Airfoil shaped wing is carried out successfully with the robot without any singularity errors. The tip of the extruder reached every desired position with the corresponding orientation. Figure 26 shows the printed model with the support structure. Black-colored PLA is used to print the aircraft wing and yellow-colored PLA is used to print the support structure.

Thermal stresses will be induced as the non-planar surfaces were printed. This results in warping of the support structure. To eliminate this warping Thermo plasters (acts like fixtures) were used to fix the position of the support before printing the wing segment. The support structure is removed once the printing of the wing segment is completed. The aircraft wing printed through this proposed slicing method will have good mechanical properties compared to the aircraft wing printed with both planar and nonplanar layers through the methodology presented by Bhatt et al. [4]. Voids will be created between planar and nonplanar layers if the aircraft wing is printed through the methodology developed by Bhatt et al. [4]. This can be overcome by adopting the slicing technique presented in this paper.

One of the major drawbacks of conventional FDM machine is that it produces staircase effect while printing curved surfaces. Therefore, rough surfaces are obtained. This is due to the limited degree of freedom of the FDM machine. The orientation of the extruder remains the same throughout the printing process. If the orientation doesn't change, the homogeneous distribution of the material is not possible while printing is carried out over curved surfaces. Hence a higher degree of freedom machine is required to change the orientation of the robot. Nonplanar layers are supposed to be generated instead of conventional planar layers to eliminate the staircase effect. A six-axis industrial robot is considered in this work to meet the requirement. Non-planar layers were generated based upon the proposed nonplanar layer generating strategy and toolpath is generated for these layers with the extruder having a perpendicular orientation with respect to the surface to get the homogeneous distribution of the material. After validating the simulation results, the printing of the Airfoil shaped wing is carried out successfully.

Figure 26. Printed Aircraft wing

4. CONCLUSIONS

1. In this paper, a new nonplanar layer generating strategy is developed and it is applied to a NACA 0015 [18] aircraft wing to generate nonplanar layers along the curved surface. Printing is done by using the extruder as the end effector of the robot.
2. The staircase effect, the major drawback of the conventional FDM process can be overcome by making use of the Industrial robot's extra degree of freedom by adopting the proposed layer generating and printing strategy, and hence good surface finish is obtained.
3. Homogenous deposition of material along the non-linear toolpaths is possible through the continuous change of the extruder's orientation with the help of the robot, which can't be done in the conventional FDM process.
4. Future work can be focused on generating toolpaths for the wing segment with a variable cross-sectional area along the depth direction.

5. REFERENCES

1. Tyberg, J. and Bøhn, J. H., "FDM systems and local adaptive slicing", ***Materials & Design,*** Vol. 20, No. 2, (1999), 77-82, DOI: 10.1016/S0261-3069(99)00012-6.
2. Gibson, I., Rosen, D. W. and Stucker, B., "Additive Manufacturing Technologies", Springer, **(**2010), ISBN: 978-1-4419-1119-3.
3. Shembekar, A. V., Yoon, Y. J., Kanyuck, A. and Gupta, S. K., "Trajectory Planning for Conformal 3d Printing Using Non-Planar Layers", ASME 2018 International Design Engineering Technical Conferences and Computers and Information in Engineering Conference IDETC/CIE, Quebec City, Quebec, Canada, (August 26-29, 2018), DOI: 10.1115/DETC2018-85975.
4. Bhatt, P. M., Kabir, A. M., Malhan, R. K., Shah, B., Shembekar, A. V., Yoon, Y. J. and Gupta, S. K., "A Robotic Cell for Multi-Resolution Additive Manufacturing", International Conference on Robotics and Automation (ICRA), Montreal, QC, Canada, (2019), 2800-2807, DOI: 10.1109/ICRA.2019.8793730.
5. Jensen, M.L., Mahshid, R., D'Angelo, G., Walther, J.U., Kiewning, M.K., Spangenberg, J., Hansen, H.N. and Pedersen, D.B., "Toolpath Strategies for 5DOF and 6DOF Extrusion-Based Additive Manufacturing", ***Applied Sciences***, Vol. 9, No. 19, (2019), DOI: 10.3390/app9194168.

6. Ishak, I. B. and Larochelle, P., "MotoMaker: a robot FDM platform for multi-plane and 3D lattice structure printing", ***Mechanics Based Design of Structures and Machines,*** Vol. 47, No. 6, (2019), 703-720, DOI: 10.1080/15397734.2019.1615943.
7. Ahlers, D., Wasserfall, F., Hendrich, N. and Zhang, J., "3D Printing of Nonplanar Layers for Smooth Surface Generation", IEEE 15th International Conference on Automation Science and Engineering (CASE), Vancouver, BC, Canada, (2019), 1737-1743, DOI: 10.1109/COASE.2019.8843116.
8. Kubalak, J. R., Wicks, A.L. and Williams, C. B., "Exploring multi-axis material extrusion additive manufacturing for improving mechanical properties of printed parts", ***Rapid Prototyping Journal,*** Vol. 25, No. 2, (2019), 356-362, DOI: 10.1108/RPJ-02-2018-0035.
9. Balogun, V. A. and Oladapo, B. I., "Electrical Energy Demand Modeling of 3D Printing Technology for Sustainable Manufacture", ***International Journal of Engineering, Transactions A: Basics,*** Vol. 29, No. 7, (2016), 954-961, DOI: 10.5829/idosi.ije.2016.29.07a.10.9.
10. Sandeep Kumar, Y., Rajeswara Rao, K .V. S. and Sunil, R. Y., "Investigation of Wear Behavior of Biopolymers for Total Knee Replacements Through Invitro Experimentation", ***International Journal of Engineering, Transactions B: Applications,*** Vol. 33, No. 8, (2020), 1560-1566, DOI: 10.5829/ije.2020.33.08b.14.
11. Manoj Kumar, V. and Srii Hari Thipesh, D., "Robot Arm Performing Writing through Speech Recognition Using Dynamic Time Warping Algorithm", ***International Journal of Engineering, Transactions B: Applications,*** Vol. 30, No. 8, (2017), 1238-1245, DOI: 10.5829/ije.2017.30.08b.17.
12. Moradi, M., Meiabadi, S. and Kaplan, A., "3D Printed Parts with Honeycomb Internal Pattern by Fused Deposition Modelling; Experimental Characterization and Production Optimization", ***Metals and Materials International,*** Vol. 25, No. 5, (2019), 1312–1325, DOI: 10.1007/s12540-019-00272-9.
13. Moradi, M., Karami Moghadam, M., Shamsborhan, M. and Bodaghi, M., "The Synergic Effects of FDM 3D Printing Parameters on Mechanical Behaviors of Bronze Poly Lactic Acid Composites", ***Journal of Composites Science,*** Vol. 4, No. 1, (2020), DOI: 10.3390/jcs4010017.
14. Moradi, M., Karami Moghadam, M., Shamsborhan, M., Bodaghi, M. and Falavandi, H., "Post-Processing of FDM 3D-Printed Polylactic Acid Parts by Laser Beam Cutting", ***Polymers,*** Vol. 12, No. 3, (2020), DOI: 10.3390/polym12030550.
15. Moradi, M. and Karami Moghadam, M., "High power diode laser surface hardening of AISI 4130; statistical modelling and optimization", ***Optics & Laser Technology,*** Vol. 111, (2019), 554-570, DOI: 10.1016/j.optlastec.2018.10.043.
16. Moradi, M., Moghadam, M. K., Shamsborhan, M., Beiranvand, Z. M., Rasouli, A., Vahdati, M., Bakhtiari, A. and Bodaghi, M., "Simulation, statistical modeling, and optimization of CO2 laser cutting process of polycarbonate sheets", ***Optik***, Vol. 225, (2021), DOI: 10.1016/j.ijleo.2020.164932.
17. Moradi, M., Falavandi, H., Moghadam, M. K. and Shaikh Mohammad Meiabadi, M., "Experimental Investigation of Laser Cutting Post Process of Additive Manufactured Parts of Poly Lactic Acid (PLA) by 3D Printers Using FDM Method", ***Modares Mechanical Engineering,*** Vol. 20, No. 4, (2020), 999-1009.
18. "NACA 0015 Airfoil", In UIUC Airfoil Coordinates Database (Accessed on 2020, August 10) Retrieved from https://m-selig.ae.illinois.edu/ads/coord/naca0015.dat
19. "Wing", In Wikipedia (Accessed on 2020, August 10) Retrieved from https://en.wikipedia.org/wiki/Wing
20. "Airfoil", In Wikipedia (Accessed on 2020, August 10) Retrieved from https://en.wikipedia.org/wiki/Airfoil
21. Zhao, Y., Chen, Y. and Zhou, Y., "Novel mechanical models of tensile strength and elastic property of FDM AM PLA materials: Experimental and theoretical analyses", ***Materials & Design,*** Vol. 181, (2019), DOI: 10.1016/j.matdes.2019.108089.
22. Perkowski, C., "Tensile-Compressive Asymmetry and Anisotropy Of Fused Deposition Modeling PLA Under Monotonic Conditions", Master Thesis submitted to University of Central Florida, (2017), Retrieved from https://stars.library.ucf.edu/etd/5576.
23. Sri Harsha, A. and Vikram Kumar, C., "Fused Deposition Modeling Using 6-Axis Industrial Robot", Advances in Additive Manufacturing and Joining, Lecture Notes on Multidisciplinary Industrial Engineering, Springer, Singapore, (2020), DOI: 10.1007/978-981-32-9433-2_13.

Persian Abstract

چکیده

مدل‌سازی رسوب Fusion (FDM) یک فرآیند تولید مواد افزودنی برای ساخت اشیا سه بعدی D۳ در یک صفحه افقی از پایین به بالا است. در فرآیند متداول FDM، چاپ اشیا cur منحنی باعث اثر راه پله می‌شود و منجر به پایان ضعیف سطح می‌شود. در این کار، از فرآیند FDM یکپارچه شده با یک ربات ٦-DOF Industrial برای چاپ اشیا cur منحنی با ایجاد مسیرهای ابزار غیر خطی استفاده می‌شود تا از اثر پله جلوگیری شود. یک بال هواپیمای استاندارد NACA 0015 که دارای سطوح منحنی است بدون اثر راه پله با سرعت رسوب یکنواخت با استفاده از یک ربات صنعتی چاپ می‌شود. بال به صورت محدب یا مقعر به لایه‌های منحنی متحدالمرکز تقسیم می‌شود. یک روش جدید با ترکیب مسیرهای ابزار غیر خطی با تغییر جهت اکسترودر برای چاپ اشیا cur منحنی در یک رسوب یکنواخت و بدون اثر پله‌ای ایجاد شده است. از نرم‌افزار شبیه‌سازی ABB Robotstudio برای شبیه‌سازی فرآیند چاپ استفاده می‌شود و نتایج شبیه‌سازی با چاپ بخشی از بال با استفاده از ربات Industrial با اکسترودر FDM به عنوان اثر نهایی تأیید می‌شود. نتایج تجربی نشان داد که بال هواپیما با رسوب یکنواخت با سرعت ثابت و بدون هیچگونه اثر پله‌ای با موفقیت چاپ می‌شود.

International Journal of Engineering

Journal Homepage: www.ije.ir

The Influence of Overburden Structure on Mine Ground Pressure Appearance in Working Face with Super-large Mining Height: a Case Study in Shendong Mining Area

C. Li*[a], C. W. Zhao[b], J. J. Ren[a], L. Tao[a]

[a] School of Resources & Mining, China University of Mining and Technology, Beijing, China
[b] State Key Laboratory for Geomechanics and Deep Underground Engineering, China University of Mining and Technology, Beijing, China

PAPER INFO

Paper history:
Received 02 May 2020
Received in revised form 30 June 2020
Accepted 03 September 2020

Keywords:
Super-large Mining Height
Mine Ground Pressure Appearance
Periodic Weighting
Key Stratum

ABSTRACT

The Shendong mining area where is located in the northwest of China has the highest fully mechanized working face in the world. The purpose of this paper is to understand the causes of abnormal mine ground pressure appearance (MGPA) on the fully mechanized mining working face with super-large height in Shendong mining area. Field monitoring, physical similarity material test and UDEC numerical simulation were used to investigate the influencing factors of abnormal MGPA on the super-large mining height working face. The results show that the simultaneous breaking movement of multiple key strata will transfer more load than that of a single key stratum, which intensifies the MGPA in working face. The distance between primary key stratum and coal seam determines MGPA, but this distance is limited to 115 m above the coal seam. The results of this study are of guiding significance to control the MGPA in Shendong mining area.

doi: *10.5829/ije.2021.34.01a.31*

1. INTRODUCTION

China Shendong mining area is located in northern Shaanxi province and southeast of the Inner Mongolia autonomous region, as shown in Figure 1. The geological reserves of coal seams with thickness over 7 m and 8 m are 976 million tons and 350 million tons, respectively. Most of these coal seams are characterized by shallow burial, small dip angle and high hardness [1, 2]. It is suitable for fully mechanized mining with super-large mining height [3].

To improve production and efficiency, the mining height of fully-mechanized working face in Shendong mining area has increased from 7 m in 2009 to 8.8 m in 2019, which is the highest mining face in the world [4-6]. However, an increase in mining height sometimes causes abnormal MGPA in the working face and leads to the dynamic pressure problems such as coal wall caving, roof falling and large shrinkage of hydraulic support column [7, 8]. In recent years, many experts and scholars have studied the law of MGPA and overburden structure of the super-high working face. Huang et al. [9] studied the roof advanced breaking position and influences of large mining height working face in the shallow coal seam. Their research results can provide early warning for safety problems related to the large height working face of the shallow coal seam, but there is still no clear conclusion for the existence of multiple key strata in overlying strata [9]. Ju et al. [10] summarized the law of MGPA in different mining stages of the world's first 7 m supporting working face and concluded that the distance between a single key stratum and coal seam was the main factor affecting the mining pressure; but did not quantify the factor. By establishing a simplified dynamic model of surrounding rock and support, Pang et al. [11] proposed a two-factor control method to calculate working resistance of hydraulic support, which was successfully applied to working face with super-large mining height of 8 m. However, the mechanism of overburden movement has

*Corresponding Author Email: *1627365221@qq.com* (C. Li)

Please cite this article as: C. Li, C. W. Zhao, J. J. Ren, L. Tao, The Influence of Overburden Structure on Mine Ground Pressure Appearance in Working Face with Super-large Mining Height: a Case Study in Shendong Mining Area, International Journal of Engineering, Transactions A: Basics Vol. 34, No. 01, (2021) 283-291

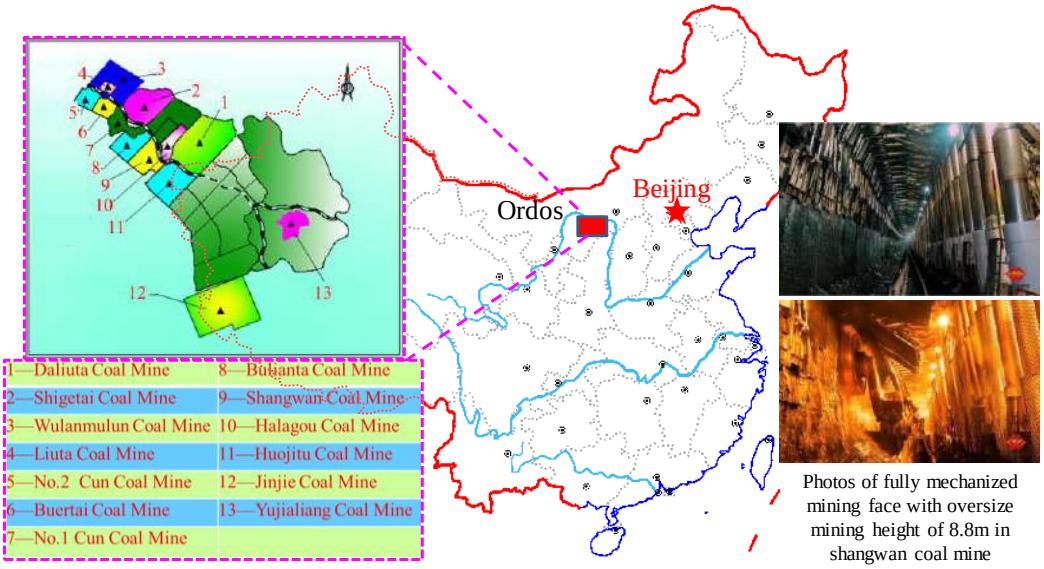

Figure 1. Location of the Shendong mining area and site photos of the Shangwan coal mine

not been studied in depth [11]. Duan [12] obtained the law of weighting interval in the mining period by monitoring the hydraulic support load of working face, but he did not investigate its mechanism. Zhu et al. [13] studies fracture form of the key stratum in the Datong mining area and its influencing mechanism on the stope MGPA, but the difference of geological conditions makes it not applicable to Shendong mining area [14].

The above results provide some references for studying the influence of overburden structure on MGPA in fully mechanized mining face with super-large mining height. However, there is a lack of a unified recognition of the MGPA of several mines in Shendong mining area. In addition, with the gradually entering into deep mining, the roof overburden structure of the coal seam also becomes more complex and the mining pressure law of the working face will be more complicated [15]. This has caused some troubles to Shendong Group's unified management of multiple mines. Therefore, it is necessary to further study the causes of MGPA difference in super-high working face. This paper can guide the actual production and management.

2. MONITORING & ANALYSIS OF MGPA

2. 1 Theory of MGPA and its Monitoring Content

Under the action of mine pressure, the phenomenon of mine pressure manifested in the form of surrounding rock movement and support stress is called MGP, such as roadway floor heave, deformation of the two ribs, roof falling, coal wall caving and support stress.

About stope MGPA, Qian Minggao successively proposed "masonry beam theory" and "key strata theory", which can well explain the movement characteristics of overlying rocks in goaf [8, 16-18], as shown in Figure 2. According to the existing theoretical basis, the corresponding data on-site were monitored. The monitoring content and its definition are as follows.

First weighting (FW): When the basic roof (key stratum) of goaf is broken for the first time and caved in a large area, strong MGPA will be caused in the working face, which is called FW.

First weighting step distance (FWSD): The distance between the open-off cut and the breaking line of the basic roof is called the FWSD.

Periodic weighting (PW): After the FW, when the working face continues to advance and the span of the basic roof overhanging surface reaches a certain length, it breaks and collapses under the action of its weight and overburden. This phenomenon of periodic basic roof breaking and caving is called PW.

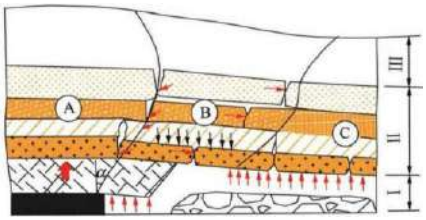

Figure 2. Conceptual model of overburden strata movement (I, II, III represent the caving zone, fractured zone, bending subsidence zone. A, B and C represent the area affected by mining abutment pressure, the rock strata vigorous movement area and the re-compaction area, respectively)

Periodic weighting step distance (PWSD): The distance between the two PW is called PWSD.

Dynamic load coefficient (DLC): The ratio of hydraulic support load during weighting to no weighting.

Column shrinkage of hydraulic support (CSHS): Cylinder shrinkage value of hydraulic support when weighting comes.

2. 2. Monitoring of MGPA (1) MGPA of panel 12106 in the Shangwan coal mine

The average thickness and buried depth of panel 12106 were 7.3 m and 90.2 m, respectively. The strike and dip length of panels were 2984 m and 298 m, respectively. There were two key strata in the overlying strata. The primary key stratum was medium sandstone with a thickness of 11.5 m, 41.9 m away from the coal seam. The inferior key stratum was siltstone with a thickness of 12.4 m, 3.2 m away from the coal seam.

The FW occurred when the working face was advanced to 43 m, and the FWSD was about 53 m. The PWSD was 9.5-11.4 m with an average of 10.3 m, and the persistence length (PL) was 2.5-4.5 m. During PW, the DLC was 1.16, the CSHS was about 6-8 mm. There was not coal wall caving or roof falling occurred in the working face.

(2) MGPA of panel 12401 in the Shangwan coal mine

The average thickness and buried depth of panel 12401 were 8.9 m and 160.6 m, respectively. The strike and dip length of panels are 5400 m and 260 m, respectively. There were two key strata in the overlying strata. The primary key stratum was medium sandstone with a thickness of 8.1 m, 87.2 m away from the coal seam. The inferior key stratum was siltstone with a thickness of 13.7 m, 9.3 m away from the coal seam.

The FW occurred when the working face was advanced to 49 m, and the FWSD was about 51 m. PWSD was 20.4-22 m with an average of 21 m, and the PL was 2.5-4.8 m. During PW, the average DLC was 1.08, and the CSHS was about 6-10 mm. There was not coal wall caving or roof falling occurred in the working face.

(3) MGPA of panel 52303 in the Daliuta coal mine

The average thickness and buried depth of panel 52303 were 7.0 m and 220.4 m, respectively. The strike and dip length of panels were 4443 m and 301.5 m, respectively. There were three key strata in the overlying strata. The primary key stratum was coarse sandstone with a thickness of 13.4 m, 101.7 m away from the coal seam. The inferior key stratum 1 was fine sandstone with a thickness of 6.9 m, 21 m away from the coal seam. The inferior key stratum 2 was siltstone with a thickness of 9.1 m, 83.5 m away from the coal seam.

The FW occurred when the working face was advanced to 62 m, and the FWSD was about 71 m. During the FW, there were some problems in the middle of the working face, such as coal wall caving and roof falling. The depth of coal wall caving was 200-400 mm. PWSD was 13.3-26.1 m with an average of 16 m, and the PL was 2.5-4.7 m. During PW, the average DLC was 1.55, and the CSHS was about 300-500 mm. The MGPA was severe, and the maximum depth of coal wall caving and roof falling can reach 1000 mm and 800 mm, respectively.

(4) MGPA of panel 12511 in the Bulianta coal mine

The average thickness and buried depth of panel 12511 were 7.8 m and 252.1 m, respectively. The strike and dip length of panels are 3193.3 m and 319 m, respectively. There were four key strata in the overlying strata. The primary key stratum was medium sandstone with a thickness of 28.9 m, 186.7 m away from the coal seam. The inferior key stratum 1 was medium sandstone with a thickness of 11.2 m, 5.1 m away from the coal seam. The inferior key stratum 2 was medium sandstone with a thickness of 19.1 m, 28.1 m away from the coal seam. The inferior key stratum 3 was siltstone with a thickness of 24.6 m, 106.1 m away from the coal seam.

The FW occurred when the working face was advanced to 40 m, and the FWSD was about 52 m. The CSHS is about 100 mm at most. PWSD was 7.2-16.8 m with an average of 10.6 m, and the PL was 2.5-4.2 m. During PW, the average DLC 1.48. The mine ground pressure was strong, but the support column did not appear the phenomenon of large shrinkage.

2. 3. Comparative Analysis of MGPA The MGPA characteristics of the above four working faces is shown in Table 1.

It can be seen from Table 1 that the four working faces were all super-large mining height working faces, but there were great differences in the intensity degree of MGPA. In general, the MGPA of the deep-buried working face was more obvious than that of shallow buried working face [8, 12, 19]. After entering PW, the working faces were greatly different from each other. At the same time, we can also see that the panel 52303 of the Daliuta coal mine showed stronger MGPA in all mines. According to the basic geological data, with the increase of burial depth, the number of the key strata of overburden increases correspondingly, and the relative position of primary key stratum changes obviously [3, 5]. The buried depth of panel 52303 and the number of the key strata above panel 52303 ars less than panel 12511, but the MGPA of panel 52303 is stronger. Therefore, we believe that the number of key strata and the distance between the primary key stratum and the coal seam will have important influences on MGPA.

3. PHYSICAL SIMILARITY MATERIAL TEST

The physical similarity material simulation test is to

make a prototype similar model according to the similarity principle in the laboratory [20]. The mechanical parameters and their distribution in the model were observed utilizing measuring instruments. The results of the model are used to deduce the possible mechanical phenomena and the law of rock mass pressure distribution in the prototype, so as to solve the practical problems in rock mass engineering [21]. In this test, with the help of the independently developed physical similar material test system, we studied the impact of the key strata fractures above the coal seam roof on MGPA.

3. 1. Establishment of Physical Similarity Material Model The test conditions and rock parameters refer to the engineering practice of panel 52303 of the Daliuta coal mine [22, 23]. The length, width and height of the model were 2.5 m, 0.3 m and 2 m, respectively. The model geometry similarity ratio, density similarity ratio, stress similarity ratio and time similarity ratio were 1:100, 1:1.6, 1:1.6 and 1:10, respectively. To facilitate qualitative analysis, the thickness and position of each key stratum in the model were adjusted. Similar material arrangements for each stratum in the model are shown in Table 2.

The established physical model of similar materials is shown in Figure 3. In the process of coal mining, a self-made small hydraulic support model with a pressure sensor was used to support the working face, and the support resistance data of the support was monitored and collected.

TABLE 1. Periodic weighting characteristics of working face

Name of panel	Mining height/ m	Buried depth/ m	Distance from the primary key stratum	No. of the key strata	PWSD/ m	PL/ m	Support force/ kN	DLC	Depth of wall caving /mm	CSHS/ mm	Depth of roof falling/ mm
12106	7.0	90.2	41.9	2	10.3	2.5-4.5	11775-13737	1.16	--	6-8	--
12401	8.8	160.6	87.3	2	21.0	2.5-4.8	25865-28243	1.08	--	6-10	--
52303	7.0	220.4	101.7	3	16.0	2.5-4.7	17670-18089	1.55	1000	300-500	500
12511	8.0	252.1	186.9	4	10.6	2.4-4.2	20874-21562	1.48	200	10-100	150

TABLE 2. Ratio table of rock similar material

No.	Stratum	Thickness/cm	Ratio number	Sand/kg	Carbonate/kg	Gesso/kg	Water/L
1	Incompetent bed	60	673	617.14	72	30.86	80.00
2	Primary key stratum	9	373	81.00	18.9	8.10	12.00
3	Incompetent bed	50	673	370.29	43.2	18.51	48.00
4	Inferior key stratum 2	8	337	67.20	11.76	5.04	9.33
5	Incompetent bed	34	673	349.71	40.8	17.49	45.33
6	Inferior key stratum 1	5	437	48.00	3.6	8.40	6.67
7	Incompetent bed	12	673	123.43	14.4	6.17	16.00
8	Coal seam	7	773	73.50	7.35	3.15	9.33

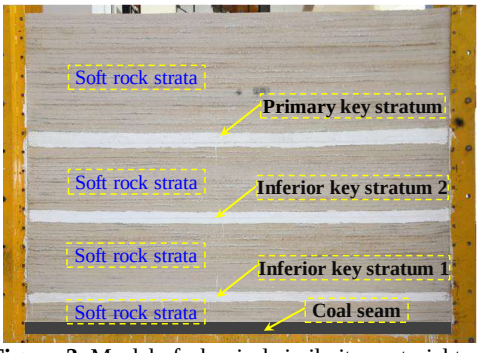

Figure 3. Model of physical similarity material test

3. 2. Analysis of Dynamic Overburden Migration The fracture patterns of key strata at different locations during model excavation are shown in Figure 4. A total of nine fractures occurred in the inferior key stratum 1 during the excavation process of the whole physical model, and drastic changes in support resistance were observed for 8 times. The detailed data are shown in Table 3. The working resistance data collected by self-made small support models were sorted out, as shown in Figure 5.

Before the key strata were broken synchronously, the resistance of support and DLC were not large, as

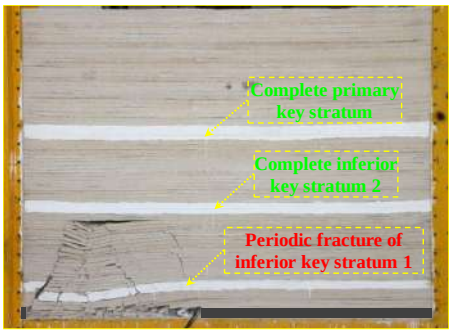

(a) Inferior key stratum 1 is broken separately

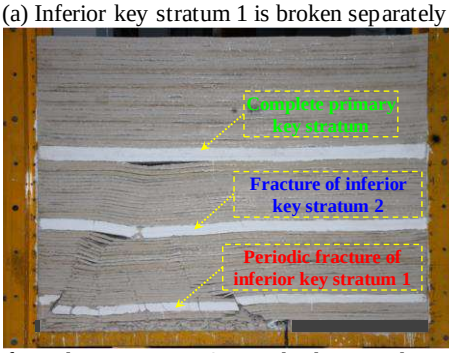

(b) Inferior key stratum 1 & 2 are broken synchronously

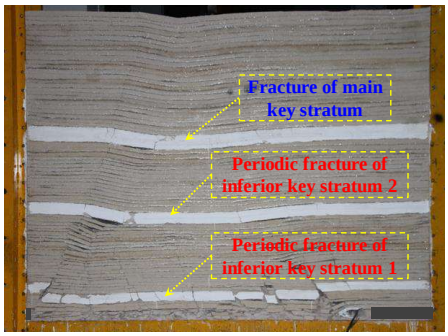

(c) Three key strata are broken synchronously

Figure 4. Test results of different key strata breaking forms

shown in Table 3. During the synchronous breaking of key strata, the resistance of support increased sharply and DLC also increased dramatically to 2.12-2.40, and the support was failed twice under weighting.

When inferior key stratum was broken alone, the pressure zones were marked as 1, 2, 3 and 4, respectively. When inferior key strata were broken synchronously, the pressure zone was marked as 5.

TABLE 3. Statistics of key stratum breakage

Excavation length /cm	Breaking type			Support resistance /kPa	DLC	Comment
	Inferior key stratum 1	Inferior key stratum 2	Primary key stratum			
75	FW	/	/	320	1.28	
85	PW	/	/	352	1.40	
100	PW	/	/	450	1.80	
130	PW	/	/	484	1.92	
145	PW	FW	/	530	2.12	Synchronous breaking
174	PW	PW	FW	600	2.40	Synchronous breaking& support crushed
190	PW	PW	/	548	2.20	Rotation of Primary key stratum
205	PW	PW	PW	600	2.40	Synchronous breaking & support crushed

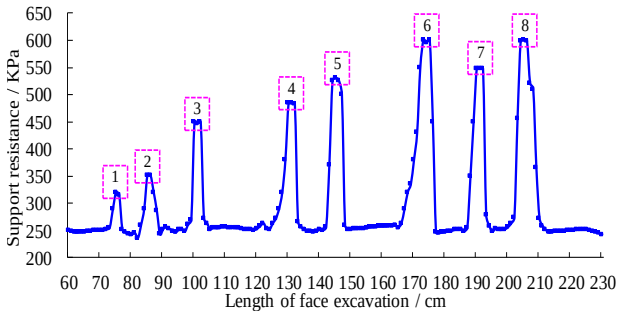

Figure 5. Support resistance curve of support

When the three key strata were broken synchronously, the pressure zones were marked as 6, 7 and 8, respectively. The breaking photos of each stage are shown in Figure 4. By comparing the relevant data of each pressure zone, it can be obtained that the intensity degree of MGPA in the working face caused by the simultaneous breaking of multiple key strata was greater than that of a single key stratum. The greater the number of key strata in which synchronous breaking occurs, the greater the intensity degree of MGPA in the working face.

4. NUMERICAL SIMULATION

4. 1. Establishment of Numerical Model UDEC 6.0 numerical simulation software was used to study the effect of primary key stratum on MGPA [24, 25]. We kept the position of inferior key stratum immovable and changed the distance between primary key stratum and coal seam. The coal seam was buried 200 m underground, the mining height of the coal seam was 7 m, and the top of the model was unconsolidated formation. There were two key strata in the overlying strata. The thickness of the inferior key stratum was 5, 12 m from the coal seam, and the thickness of the primary key stratum was 9 m, as shown in Figure 6. In the numerical simulation, the coal seam was excavated 20 times in total and each time excavated 10 m. The coal seam was excavated from left to right. The model parameters are shown in Table 4.

The length and height of the model were 300 m and 230 m, respectively. To eliminate the boundary effect, a 50 m boundary coal pillar was set on both sides. The model was calculated using the Mohr-Coulomb criterion. The hydraulic support was stimulated by the "Beam" built-in UDEC and the data was recorded automatically in UDEC. A total of 7 simulations schemes were established. The distance between the primary key stratum and coal seam of each plan was 55, 75, 95, 115, 135, 155 and 175 m, respectively.

4. 2. Analysis of Numerical Simulation Results Three representative calculation results were selected from the 7 simulation schemes, as shown in Figure 7. The blue part of coal seam in the figure represented a hydraulic support model, and the red part represented mining-induced fracture. Compared with Figures 7(a) and 7(b), the farther the primary key stratum is from the coal seam, the wider the goaf roof failure range. However, when Figure 7(b) is compared with Figure 7(c), the law is reversed.

The support strength of simulated results in each scheme is arranged as shown in Table 5, and the obtained data is shown in Figure 8. The following conclusions can be drawn from Figure 8. when the distance between primary key stratum and coal seam was 115 m, the support resistance of hydraulic support reached to the maximum, with an average of 1.88 MPa. Meanwhile, when the distance between primary key stratum and coal seam was 55 m, the support resistance of hydraulic support was only 1.09 MPa. The difference between the two values was 1.72 times. After the distance between primary key stratum and coal seam was more than 115 m, the support resistance of

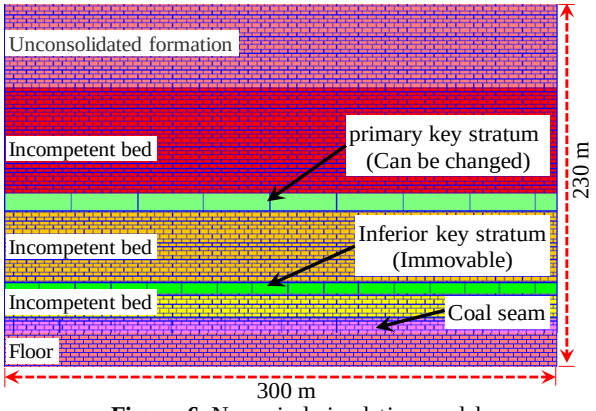

Figure 6. Numerical simulation model

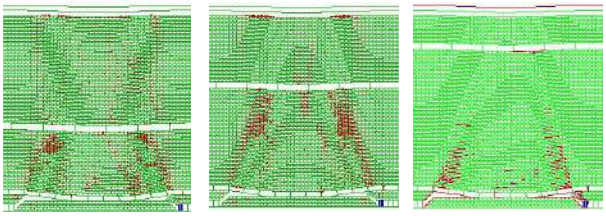

(a) 75m (b) 115m (c) 155m

Figure 7. Mining-induced fracture in primary key stratum at different positions

TABLE 4. Mechanical and physical parameters of the numerical models

Stratum	bulk modulus/ GPa	Shear modulus/ GPa	Density/ (kg·m^{-3})	internal friction angle/ (°)	Tensile strength/ MPa
Unconsolidated formation	10	36	1500	10	1.1
Incompetent bed	15	8	2100	20	3.2
Primary key stratum	45	26	2500	35	6.7
Incompetent bed	15	8	2100	20	3.2
Inferior key stratum	40	25	2500	30	5.6
Incompetent bed	15	8	2100	23	3.2
Coal seam	12	5	1500	17	1.7
Floor	50	28	2500	35	5.8

TABLE 5. Supporting strength of working face at different primary key stratum locations

Distance between primary key stratum & coal seam /m	Support resistance of each hydraulic support/ MPa					Average/ MPa
	1	2	3	4	5	
55	1.18	1.17	1.06	1.02	0.97	1.09
75	1.40	1.27	1.38	1.25	1.15	1.29
95	1.75	1.78	1.66	1.61	1.55	1.67
115	1.92	2.03	1.85	1.85	1.77	1.88
135	1.26	1.39	1.41	1.21	1.18	1.29
155	1.40	1.40	1.27	1.22	1.16	1.29
175	1.40	1.40	1.27	1.22	1.16	1.29

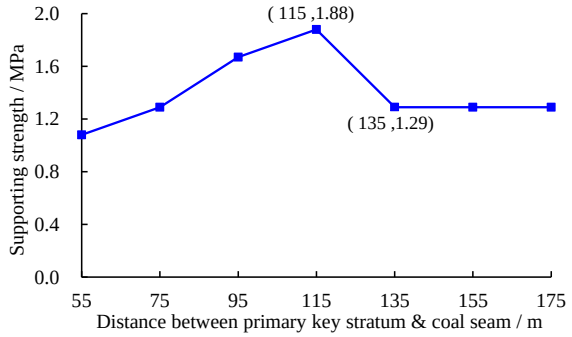

Figure 8. The average support strength of the primary key stratum at different positions

hydraulic support decreased gradually, and the support strength tended to be stable when the distance was 135-175 m.

The MGPA of the working face was affected by the primary key stratum and there was a critical limit height. When the primary key stratum was located within the critical height limit, the fracture of primary key stratum would aggravate MGPA in the working face, while when the primary key stratum was located outside the critical height limit, the fracture of primary key stratum would not aggravate MGPA. When the primary key stratum in this model was 115 m away from the coal seam, the MGPA was the most severe, and when the distance was greater than 115m, the hydraulic support gradually returned to normal support strength. The numerical simulation results are in good agreement with the field practice. Therefore, under this condition, the critical height of MGPA in the working face affected by the primary key stratum was 115 m.

5. DISCUSSION

Physical similarity material test results show that the number of key strata is positively correlated with the MGPA of the working face. Because the key stratum is usually composed of rocks with hard and thick lithology. Therefore, the immediate roof collapses immediately after coal mining, while the key strata form a suspended roof above the goaf. The key strata of the overhang hold huge amounts of energy until it can no longer withstand the load of itself and its overlying layers before suddenly breaking. Therefore, for field engineering, if the number of key strata is large, the roof management of coal mining working face should be strengthened, such as weakening the powerful MGPA employing supports selection and hydraulic fracturing.

The UDEC numerical simulation with simplified geological conditions shows that the influence of the primary key stratum on MGPA has a limit influence distance. Therefore, after deep mining, although the key strata overlying the coal seam also becomes complex, including the distance between the primary key stratum and the coal seam, the number of key strata and the rock strength, then the key strata will not affect MGPA indefinitely. This could be because the rock collapse beneath the higher key strata is filled with goaf, i.e., the broken and swelling rock blocks in the goaf form support for the goaf roof, so that the key layer is no longer broken or the rotation angle is small after being broken.

In this paper, the influence mechanism of key strata on MGPA in Shendong mining area has been preliminarily obtained. However, due to the limitations of the physical similarity material test system and the idealized simplification of the numerical model, there are still some deficiencies. Factors such as the number of key layers, rock strength and relative distance of each key layer are complex and changeable, so it is temporarily impossible to conduct quantitative analysis on various influencing factors, which is also the research direction of this paper in the future.

6. CONCLUSION

1) The field measurement of four super-large working faces in the Shendong mining area shows that the MGPA law of super-large working faces is complicated.

Relative to the buried depth and mining height of coal seam, the number of key stratum and the location of the primary key stratum have a more drastic influence on MGPA.

2) In the case of larger buried depth, the overburden load of synchronous fracture of multi-layer key strata in working face with large mining height is larger than that of the single fracture of key stratum, which results in more severe MGPA in working face.

3) The position change of primary key stratum will affect MGPA in working face, and there is a critical limit height. The critical height is 115 m according to the numerical simulation results in Shengdong mining area.

7. ACKNOWLEDGEMENT

This study was financially supported by the Basic scientific research operating expenses of China University of Mining and Technology (Beijing) (2020YJSNY09).

8. REFERENCES

1. Du, F. and Syd S., "Change rule of physical and mechanical property of rock mass in Shendong mine", ***Journal of Mining & Safety Engineering***, Vol. 36, No. 5, (2019), 1009-1015. DOI: 10.13545/j.cnki.jmse.2019.05.019
2. Zhao, Y., Liu, B., Yang, Z., Song, G. and Yang, D., "Tensile strength and fracture toughness of sedimentary rocks at different buried depths in Shendong coal field", ***Journal of china coal society***, Vol. 46, No. 1, (2019), 1732-1741. DOI: 10.13225/j.cnki.jccs.2018.9031
3. Yang, J. and Liu, Q., "Analysis and measured of strata behavior law and mechanism of 8.8 m ultra-high mining height working face", ***Coal Science and Technology***, Vol. 48, No. 1, (2020), 69-74. DOI: 10.13199/j.cnki.cst.2020.01.009
4. Yin, X., "Research status of strata control and large mining height fully mechanized mining technology in China", ***Coal Science and Technology***, Vol. 47, No. 8, (2019), 37-45. DOI: 10.13199/j.cnki.cst.2019.08.002
5. Yang, J., "Key technologies and equipment for 8.8 m intelligent super large mining height fully mechanized mining face mining", ***Coal Science and Technology***, Vol. 47, No. 10, (2019), 116-124. DOI: 10.13199/j.cnki.cst.2019.10.014
6. Wang, G. and Pang, Y., "Development and application of complete equipment for fully mechanized mining with 8.2m super-large mining height", ***Coal Engineering***, Vol. 49, No. 11, (2017), 1-5. DOI: CNKI:SUN:MKSJ.0.2017-11-002
7. Xu, J., Zhu, W. and Ju, J., "Supports crushing types in the longwall mining of shallow seams", ***Journal of China Coal Society***, Vol. 39, No. 8, (2014), 1625-1634. DOI: 10.13225/j.cnki.jccs.2014.9006
8. Qian, M., Shi, P. and Xu, J., "Mining Pressure and Strata Control", China University of Mining and Technology Press, Xu Zhou (2010).
9. Huang, Q., He, Y. and Li, F., "Research on the roof advanced breaking position and influences of large mining height working face in shallow coal seam", ***Energies***, Vol. 13, No. 7, (2020), 1-15. DOI: 10.3390/en13071685
10. Ju, J., Xu, J., Zhu, W. and Wang, Q., "Strata Behavior of Fully Mechanized Face with 7.0 m Height Support", ***Journal of Mining & Safety Engineering***, Vol. 29, No. 3, (2012), 344-350. DOI: CNKI:SUN:KSYL.0.2012-03-010
11. Pang, Y., Wang, G. and Yao, Q., "Double-factor control method for calculating hydraulic support working resistance for longwall mining with large mining height", ***Arabian Journal of Geosciences***, Vol. 13, No. 6, (2020), 1-16. DOI: 10.1007/s12517-020-5208-0
12. Duan, W., "Study on the Mining Pressure Law of 8.8m Fully Mechanized Mining Face in Shangwan Coal Mine", ***Coal Engineering***, Vol. 51, No. 11, (2019), 55-59. DOI: 10.11799/ce201911013
13. Zhu, W. and Yu, B. "Breakage form and its effect on strata behavior of far field key stratum in large space stope", ***Coal Science and Technology***, Vol. 46, No. 1, (2018), 99-104. DOI: 10.13199/j.cnki.cst.2018.01.014
14. Gong, P. and Jin, Z., "Study on the structure characteristics and movement laws of overlying strata with large mining height", ***Journal of China Coal Society***, Vol. 29, No. 1, (2004), 7-11. DOI: 10.3321/j.issn:0253-9993.2004.01.002
15. Yu, B., Zhu, W., Li, Z. and Gao, D. "Mechanism of the instability of strata structure in far field for super-thick coal seam mining", ***Journal of China Coal Society***, Vol. 43, No. 9, (2018), 2398-2407. DOI: 10.13225/j.cnki.jccs.2017.1037
16. Qian, M., "Theory and Practice of Surrounding Rock Control in Stope", ***Journal of Mining & Safety Engineering***, Vol. 16, No. Z1, (1999), 12-15. DOI: 10.3321/j.issn:1000-1964.2000.01.001
17. Liao, X., Chen, H., Pu, H. and Qian, M., "Analysis of breakage and collapse of thick key strata around coal face", ***Chinese Journal of Rock Mechanics and Engineering***, Vol. 24, No. 8, (2005),1289-1295. DOI: 10.3321/j.issn:1000-6915.2005.08.003
18. Qian, M. and Xu, J. "Behaviors of Strata movement in coal mining", ***Journal of China Coal Society***, Vol. 44, No. 4, (2019),973-984. DOI: 10.13225/j.cnki.jccs.2019.0337
19. Zhang, G., Guo, G., Lv, Y., and Gong, Y., "Study on the strata movement rule of the ultrathick and weak cementation overburden in deep mining by similar material simulation: a case study in china", ***Mathematical Problems in Engineering***, Vol. 2020, No. 4, (2020), 1-21. DOI: 10.1155/2020/7356740
20. Jing, H., Xiang, Y., Yi, Y., and Zeng, Q., "Physical simulation and theoretical evolution for ground fissures triggered by underground coal mining", ***Plos One***, Vol. 13, No. 3, (2018), e0192886. DOI: 10.1371/journal.pone.0192886
21. Chai, J., Du, W., Yuan, Q. and Zhang, D., "Analysis of test method for physical model test of mining based on optical fiber sensing technology detection", ***Optical Fiber Technology***, Vol.48, No.3, (2019), 84-94. DOI: 10.1016/j.yofte.2018.12.026
22. Zhang, J. and Shi, X. "Failure of overburden rock under large mining height in shallow buried goaf area", ***The Chinese Journal of Geological Hazard and Control***, Vol. 30, No. 5, (2019), 92-97. DOI: 10.16031/j.cnki.issn.1003-8035.2019.05.12
23. Wu, F., Liu, C. and Yang, J. "Mode of overlying rock roofing structure in large mining height coal face and analysis of support resistance", ***Journal of Central South University***, Vol. 23, No. 12, (2016), 3262-3272. DOI: 10.1007/s11771-016-3392-6
24. Saeedi, G., Shahriar, K. and Rezai, B., "Estimating volume of roof fall in the face of longwall mining by using numerical methods", ***Archives of Mining Sciences***, Vol. 58, No. 3, (2013), 767-778. DOI: 10.2478/amsc-2013-0053
25. Khaboushan, A.S. and Osanloo, M., "An uncertainty-based transition from open pit to underground mining", ***International Journal of Engineering-Transactions B: Applications***, Vol. 32, No. 8, (2019), 1668-1676. DOI: 10.5829/ije.2020.33.08b.26

Persian Abstract

چکیده

منطقه معدنکاری شندونگ که در شمال غربی چین واقع شده دارای بالاترین سطح کار کاملاً مکانیزه در جهان است. هدف از این مقاله درک علل ظاهر غیر طبیعی فشار مین (MGPA)بر روی سطح معدن کاملاً مکانیزه کار با ارتفاع فوق العاده بزرگ در منطقه معدن شندونگ است. برای بررسی عوامل تأثیرگذار MGPA غیرطبیعی روی سطح کار بسیار بزرگ استخراج از مانیتورینگ میدانی ، آزمون ماده تشابه فیزیکی و شبیه سازی عددی UDEC استفاده شد. نتایج نشان می دهد که حرکت شکستن همزمان چندین لایه کلیدی بار بیشتری نسبت به یک لایه کلیدی را منتقل می کند ، که باعث تشدید MGPA در چهره کار می شود. فاصله لایه اصلی کلید و درز ذغال سنگ MGPA را تعیین می کند ، اما این فاصله به ۱۱۵ متر بالاتر از درز ذغال سنگ محدود می شود. نتایج این مطالعه برای کنترل MGPA در منطقه استخراج شندونگ از اهمیت بالایی برخوردار است.

IJE TRANSACTIONS A: Basics Vol. 34, No. 1, (January 2021) 292-304

International Journal of Engineering

Journal Homepage: www.ije.ir

Korkinsk Brown Coal Open Pit as a Case Study of Endogenous Fires

C. Drebenstedt[a], K. R. Argimbaev*[b]

[a] *Institute for Mining and Civil Engineering, Technical University Bergakademie Freiberg, Freiberg, Germany*
[b] *Faculty of Mining, Saint Petersburg Mining University, St. Petersburg, Russia Federation*

P A P E R I N F O

Paper history:
Received 17 September 2020
Received in revised form 21 October 2020
Accepted 30 October 2020

Keywords:
Antipyrogen
Coal Open Pit
Endogenous Fire
Korkinsk Brown Coal

A B S T R A C T

Abrupt termination of the coal open pit operation is complicated in many cases by endogenous fires that not only cause significant damage to property but also worsen sanitation and hygienic conditions for human life in nearby settlements, as well as those for fauna and flora. Therefore, the purpose of the research was to prevent endogenous fires at Korkinsk brown coal open pit. In this connection, we used an analytical method to process the statistical data obtained from observations. The laboratory method included the study of coal samples for moisture exchange intensity by creating conditions with relative humidity up to 97%, temperature up to plus 50°C and air speed up to 0.5 l/minute. Dependencies were determined for fire occurrence frequency, relative humidity, and average temperature of the air upon the time of day, the intensity of moisture evaporation and initial coal humidity on equilibrium coal humidity as well as the intensity of moisture absorption and equilibrium coal humidity upon initial humidity in different temperature periods. An environmentally friendly solution was created that featured good adhesion to the materials being coated, fire and explosion resistance. The results obtained make it possible to understand the causes and methods of fighting endogenous fires.

doi: *10.5829/ije.2021.34.01a.32*

1. INTRODUCTION

There is a fair amount of scientific theories and reasons for spontaneous coal combustion. The theory of absorption is the most credible and is based on oxygen absorption by coal matter. According to research, coal reacts not only with atmospheric oxygen but also with one contained in water [1]. Practical experience confirms this fact as wet coal self-ignites easier. Oxygen sorption by coal increases with the moisture content increase in the mineral to a particular value and vice versa. This is due to the intensification of electrochemical processes in the presence of a certain moisture amount.

As of now, numerous studies of coal self-ignition have been carried out. The issue was studied by leading scientists like Skochinsky and Makarov [1] and others [2-9]. Examinations have shown that coal adsorbs oxygen by its surface resulting in an exothermic reaction of carbon with oxygen ($C+O_2 \rightarrow CO_2$). Therefore, two factors caused the self-ignition process – the surface area of coal matter and the amount of oxygen contacting it. The higher is coal area, the more is the probability of its spontaneous combustion with approximately the same oxygen amount [1-8].

Spontaneous coal combustion may occur not only in areas of direct coal contact with airflows that are insufficiently intensive to remove accumulated heat. It may take place in areas well isolated at first glance and containing coal residues. The oxygen amount necessary for the reaction often penetrates a coal block through cracks during fluctuations of barometric pressure. The atmospheric pressure drop causes a pressure decrease in it. Air pressure in the confined area, which is in equilibrium with initial pressure in the open area, tends to equalize the resulting difference. At the same time, coal oxidation products pass via cracks in rocks [9-14].

Based on the theory of the "coal-oxygen" complex, coal ignitability depends on the intensity of oxidation process during coal reaction with atmospheric oxygen. The more intensive oxidation reaction, the more coal tends to spontaneous ignition [1, 5, 8].

*Corresponding Author Institutional Email: *diamond-arg@mail.ru* (K. R. Argimbaev)

Please cite this article as: C. Drebenstedt, K. R. Argimbaev, Korkinsk Brown Coal Open Pit as a Case Study of Endogenous Fires, International Journal of Engineering, Transactions A: Basics Vol. 34, No. 1, (2021) 292-304

There are three phases of oxidation progress when using methodology [1], which allows observations over the coal self-heating process and is widely tested in practice: moisture evaporation from coal, intensive oxidation, and low-temperature combustion.

The first phase – moisture evaporation from coal – features insignificant oxygen sorption and emission of gaseous oxidation products. Oxygen taken by coal is consumed for adsorption, formation of water CO and CO_2. Adsorption prevails during this phase.

The second phase features an intensive increase of coal heating rate, oxygen uptake, and emission of CO and CO_2. During this phase, chemisorption is simultaneously observed with adsorption since oxygen is not only adsorbed but also significantly consumed to form CO and CO_2.

The third phase features decreased coal heating rate and intensive CO and CO_2 emission due to insufficient oxygen supply.

Temperature ranges for the above phases depend on coal metamorphism and atmospheric oxygen sorptivity [5,7,9,10,15]. Decreased metamorphism shifts these intervals to lower values and increases coal heating rate as well as the amount of absorbed oxygen and emission of oxidation products – CO and CO_2 per 1g of coal. Intensive oxidation of Korkinsk brown coals takes place at a temperature of >49 °C to > 69 °C [16].

Mining completion at Korkinsk brown coal open pit resulted in the appearance of endogenous fire seats that polluted the environment in the neighboring settlements and caused sliding of quarry benches. Up to now, there are no efficient methods and means to fight endogenous fires, which are acceptable for open pit conditions [16].

In this regard, the purpose of the research was to prevent endogenous fires at Korkinsk brown coal open pit aiming at improvement of the environmental situation in neighboring areas as well as the bench sliding prevention.

This article contains the data regarding endogenous fires at Korkinsk brown coal open pit over the period of 2012 to 2014. It identifies places of spontaneous combustion and evaluates antipyrogens used in Russia and abroad. Experimental data processing made it possible to determine dependencies for fire occurrence frequency, relative humidity, and average temperature of the air on the time of day, the intensity of moisture evaporation and initial coal humidity upon equilibrium coal humidity as well as the intensity of moisture absorption and equilibrium coal humidity upon initial humidity in different temperature periods.

Based on the results, an environmentally friendly solution was created that combines positive properties of all existing antipyrogens and inhibitors, varies in the composition according to application conditions, and features good adhesion to the materials being covered.

Practical relevance of the study covers the determination of parameters and conditions for spontaneous ignition of brown coal using Korkinsk open pit as an example and finding the solution with high adhesion, stability to high temperatures, and water repellence.

2. MATERIALS AND METHODS

The study covered 3 periods: analytical period, field period and laboratory period. During the analytical period, the data were assessed regarding endogenous fires at the open pit over the period of 2012 to 2014; the annual fire frequency was defined; climatic conditions were assessed in the open pit region.

This period also included evaluation of existing antipyrogens for brown coal and processing of laboratory results.

During the laboratory period, samples were prepared for laboratory tests to study the impact of the particle size distribution (0.25 mm to 0.5 mm, 0.5 mm to 1.0 mm, 1.0 mm to 2.0 mm, 1.0 mm to 3.0 mm, 0.0 mm to 6.0 mm, and 0.0 mm to 10.0 mm) on the intensity of moisture exchange by creating relative air humidity up to 97 %, at temperatures up to 50 ˚C and air speed up to 0.5 l/minute.

We studied the change in sorption capacity and chemical activity of usual Korkinsk coal and one activated by preliminary heating (50 to 70˚C) using the procedure developed at Skochinsky Institute of Mining [1, 17, 18].

Strength indicators of the designed formulation were measured by destructing 5 cylindrical specimens (50 mm in diameter, 100 mm long) by co-axial counter-directed indenters. The method comprised testing the specimens by the axial force created by two indenters (steel balls of 15 mm in diameter) until samples splitting, recording destructive force, measuring the separation surface areas according to Russia's State Standard (GOST) 24941-81 rocks. Methods for determination of mechanical properties by pressing with spherical indenters. Additionally, the area was measured for destructed rock zones in contact with indenters [19-22].

Ultimate strength during uniaxial expansion was measured according to Russian Patent No. 2435955. Ultimate strength during uniaxial compression and ultimate shear resistance without normal stresses (cohesion) were measured according to Russian Patent No. 2521116 [19-22].

The solution was testing for fire resistance and explosion safety by its application on the flammable surface and exposing to direct fire from a gas burner.

During the field period, brown coal samples weighing 25 kg each were taken from four quarry faces.

3. RESULTS

3. 1. Deposit Features Spontaneous coal ignition (endogenous fire) is typical for many collieries both in Russia and abroad.

Coal combustion on exposed coal surfaces, at warehouses and in coal piles, overburden spoil heaps cause both economic loss and environmental problems.

Korkinsk brown coal open pit is among the main environmental problems of the Chelyabinsk Region in Russia. Endogenous fires occurred at the open pit pollute the air in the town of Korkino and other regional settlements as well as in Chelyabinsk. Coal combustion products released into the atmosphere may affect humans, crops, fauna, and different materials [23, 24, 25].

Slides on pit walls threaten destruction of residential buildings and social facilities in nearby settlements [26, 27].

Brown coal from Korkinsk open pit contains rock and mineral inclusions (Figure 1): Al, Fe, Ca, Mg, Na, and K silicates, carbonates ($CaCO_3$, $MgCO_3$, $FeCO_3$, etc.), sulphates ($CaSO_4$, $FeSO_4$, $Al_2(SO_4)_3$, etc.), oxides (FeO, CaO, etc.), sulphides (FeS_2), organic minerals – humic acid salts (humates) and 46 % of carbon. Combustion heating value is 29 MJ/kg [16, 28].

There were 10 sites in the open pit prone to spontaneous combustion, where oxidation processes and fire spots emitted much heat, which resulted in the formation of carbon dioxide, benzapyrene, sulphur dioxide, hydrogen sulphide, sulphurous oxide (near fire-impacted areas). Their concentration exceeds MAC and causes rheum, cough, hoarseness, throat irritation, and specific after-taste. The last one is typical for high concentrations of bituminous substances, bleedings at a depth of 265 m to 345 m, which are linked genetically with oil shows. The issue of combating endogenous fires has become especially topical due to significant depth and closing the open pit (Figure 2).

3. 2. Evaluation of Climatic Conditions at Korkinsk Open Pit Taking into account the coal self-ignition theory, we studied climatic conditions at Korkinsk brown coal open pit, which featured meteorological variability. Climatic properties at the quarry depend upon atmospheric conditions in the neighboring area and are caused by various terrain forms, including mined-out area.

Figure 1. Brown coal mined at Korkinsk open pit

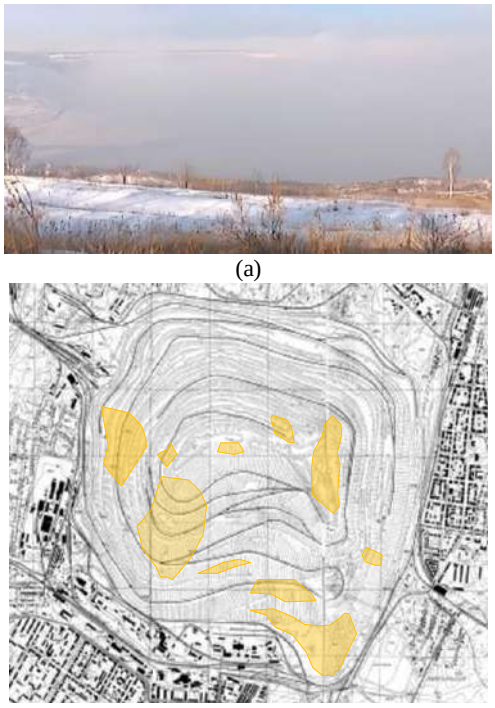

(a)

(b)

Figure 2. Korkinsk brown coal open pit: a – smog at Korkinsk open pit (March 2014); b – layout of possible self-heating areas

The largest amplitudes of temperature fluctuations were observed during summer and fall and were plus 12° to plus 15°, sometimes plus 20˚C to plus 25˚C. The amplitude of relative humidity daily fluctuations was 40 to 45% [29, 30].

Airflows moving over the open pit space and local flows formed due to uneven heating of individual quarry areas with specific terrain built the quarry wind pattern [31].

The intensity of local flows decreased at the quarry during winter. Moreover, temperature inversions appeared at its bottom after long cold periods and during gentle breeze/still air. During inversions, wind did not remove all harmful impurities from the quarry atmosphere, and they were accumulated in concentrations hazardous for human health. When winding, their large quantities were blown out of the open pit towards nearby settlements. During those periods, there were favorable conditions to form fog or smog as well as man-induced fires (Figure 2a).

Temperature increase in the inversion layer at the bottom of Korkinsk open pit-earth surface was up to plus 9˚C. Simultaneously, there was fog in the quarry that reduced visibility up to 4 m [16, 32].

Thus, different steps of oxidation process were the main sources of the quarry pollution.

Calculations have shown that up to 0.00135 m^3/hour of carbon monoxide may emit from one square meter of a fire-impacted zone [16].

Statistical data featured the number and locations of fires occurrence at Korkinsk open pit are given in Table 1.

Table 1 illustrates that most fires appear in burden-coal piles, coal slides, caved benches, broken faces, and coal storage sites.

Existing layer-by-layer mining of thick coal beds and using rock mass as a basis for placing railroads promoted the accumulation of significant pile volumes inside the quarry.

Coal outbreaks make a significant fire hazard, especially when the part of their thickness was mined in closed long faces. In certain cases, loosen coal was left in solid one due to poor bench dressing by a shovel bucket.

Previous observations at Korkinsk open pit have shown that the latent duration depended on the pile shape and dimensions, coal compaction degree and particle size distribution [32]. The above factors adjusted fresh air inflow into the mass and dissipation of generated heat.

Compaction of rocks and increasing their outer surface promoted the fire hazard decrease. On the contrary, coarse rock pieces in the lower part of piles(material segregation) and their significant height created favorable conditions for spontaneous combustion seats [33-36].

In addition to the above factors, quarry microclimate significantly affected the fire hazard of mining operations. It featured extreme variability of air temperature and humidity, wind speed and direction, solar radiation and other factors [34].

The frequency of endogenous fires increases during the periods with increased air humidity at the quarry, especially during autumn and spring, when air humidity drastically increases after warm sunny days. In this case, somewhat dried coal intensively absorbs water vapor and causes the temperature increase inside the loosed rock pile [32].

However, Figure 3 illustrates the different numbers of fire seats in different years. This is due to the implementation of fire-fighting measures in different quarters. At the same time, the intensity of further self-ignition progress at high temperatures poorly depended upon air temperature that could explain the appearance of endogenous fires in quarries during the cold period [12, 15].

TABLE 1. Data about endogenous fires at Korkinsk brown coal open pit over 2012 to 2014

Observation period	Number of fires				Total area of a fire-impacted zone, m^2
	Total	In piles	In coal blocks	In slides	
			2012		
Quarter 1	44	22	20	2	199435
Quarter 2	37	18	17	2	171710
Quarter 3	28	15	12	2	164910
Quarter 4	15	12	1	2	104660
			2013		
Quarter 1	15	12	2	1	92400
Quarter 2	30	25	4	1	109100
Quarter 3	27	22	4	1	104600
Quarter 4	23	20	2	1	23000
			2014		
Quarter 1	19	12	6	1	104200
Quarter 2	19	12	6	1	104200
Quarter 3	18	11	6	1	10320
Quarter 4	17	12	3	2	7360

3. 3. The Study of Brown Coal at Korkinsk Open Pit Laboratory study of the effect of the particle size distribution on moisture exchange intensity has shown that the air volume passed through coal particles sized 0.25 to 0.5 mm; 0.5 to 1.0 mm; 1.0 to 2.0 mm; 1.0 to 3.0 mm; 0.0 to 6.0 mm and 0.0 to 10.0 mm was 0.7 l per minute.

At the same time, coal particles sized 0.25 to 0.5 mm featured maximum evaporation intensity. For the first 3 hours, it was 1.1% per hour. The maximum evaporation intensity (0.8 % per hour) was for coal particles 3 to 6 mm.

Thus, the particle size distribution of coal significantly affected moisture absorption intensity. This impact was explained by the fact that the total surface area of coal particles per volume unit increased with the particle size decrease. On that basis, fine coal fractions were more dangerous regarding fire occurrence. Visual observations over the places, where endogenous fire occurred, have confirmed this conclusion (Figure 4).

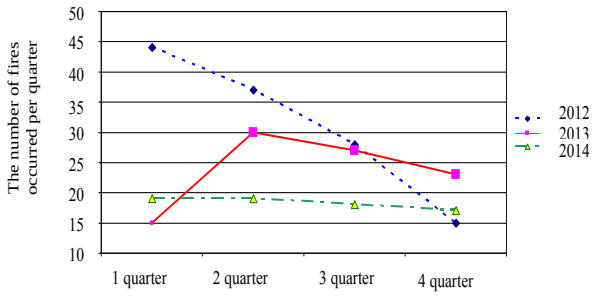

Figure 3. The fire occurrence frequency at Korkinsk brown coal open pit

Figure 4. Self-heating area (March 2014)

Fire seats in loosen coal piles, burden-coal piles and in slides occurred usually at the border between the lower coarse part and upper fine fractions.

At the same time, increased airflow speed resulted into increased moisture exchange intensity (Figure 5).

Hygroscopic equilibrium (complete termination of moisture exchange) attained between coal and air at a temperature of plus 40, plus 25, plus 10, 0 and minus 10˚C. Coal particles sized 1mm to 3mm were put in vessels, and air with different moisture content was pumped through them at a speed of 0.5 l per minute.

Research results have shown that coal hygroscopic equilibrium was caused mainly by relative air humidity. Meanwhile, it depended upon ambient temperature. At the same time, evaporation of moisture from Korkinsk coal, which was pumped with completely dry air, stopped at moisture content 1.5 to 2.1% in coal.

The intensity of moisture exchange decreased in due time, when coal humidity became close to the moisture content in the equilibrium state. In certain cases, coal could lose more than 1% of moisture during the first hour. In 20 to 50hours, coal lost moisture 0.005% and less per hour.

Maximum evaporation intensity was at a temperature exceeding plus 40˚C. Moisture evaporated less intensively at a temperature of plus 25, plus 10, 0 and minus 10˚C. Experiments have shown that temperature insignificantly affected evaporation intensity within these limits.

It was found out that the maximum intensity of moisture absorption took place at a temperature of 0 to plus 25˚C. Moisture was absorbed with less intensity at a negative temperature. Coal virtually did not absorb moisture at plus 40˚C.

Relative humidity and temperature were taken for Korkinsk open pit using statistical meteorological data typical for Chelyabinsk (Figures 6 and 7), which were used when calculating hygroscopic characteristic [29].

Precipitation factor played an important role in activating the self-ignition process during moisture decrease in oxidizing coal. At the same time, fall-out ambivalently influenced the temperature behavior of self-heating minerals in bulk (Figure 8). Self-heating temperature dropped during the initial rainfall period due to heat absorption by moisture. After a certain period, self-heating intensity drastically increased that may be explained by intensification of electrochemical oxidation taking into account oxygen content up to 30% in rainwater. However, self-heating can attenuate and completely stop during long periods and significant precipitation amounts. It was noted that moisture content in ore could increase from (6 to 7%) up to (14 to 20%).

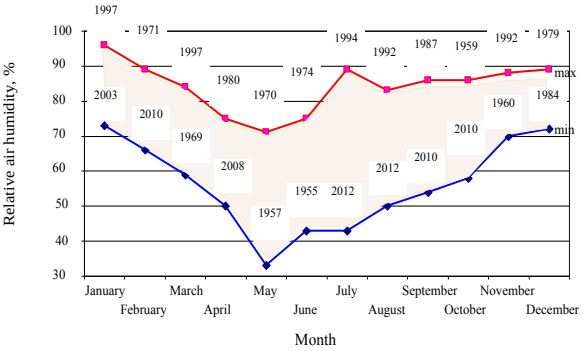

Figure 6. Relative humidity, %

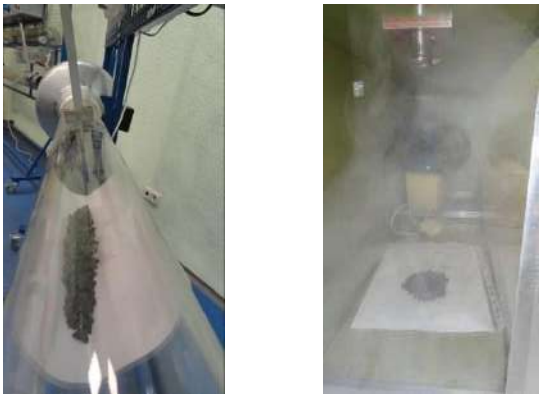

Figure 5. Laboratory study of the size distribution effect on moisture exchange intensity

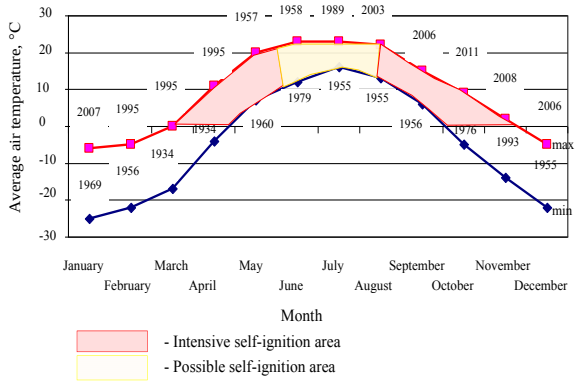

Figure 7. Average air temperature, °C

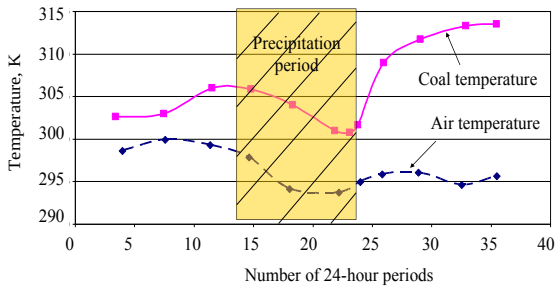

Figure 8. Change in coal and air temperature during the precipitation period

Experimental data processing made it possible to determine the following coal hygroscopic characteristic as a function of ambient relative humidity and temperature (Figure 9).

Figure 10 illustrates the function of moisture evaporation intensity.

Figure 10 shows that the intensity of moisture evaporation from coal depends on the initial and equilibrium moisture content. A sharp increase in moisture evaporation up to 0.6% per an hour in the temperature range from minus 10 to plus 25˚C is due to an increase in the initial moisture content of the coal over 2%, with a constant value of equilibrium moisture content (4%). The reverse process is observed when the equilibrium moisture content of coal rises above 4%, and when the equilibrium moisture content reaches 12%, the evaporation rate stops.

Figures 11 and 12 show the function of moisture absorption intensity.

When the evaporation rate decreases (Figure 10), the process of moisture absorption rate starts (Figure 11).

That is, in the temperature range from 0 to plus 25˚C, equilibrium moisture content of 12% and initial moisture coal content of 2%, the maximum intensity of moisture absorption occurs (1% per an hour, while the intensity of moisture evaporation is stopped). The process of moisture absorption intensity decreases up to 0.6% per an hour when the temperature drops from 0 to minus 10˚C (Figure 12).

The above dependences allowed defining quantitative significance of moisture exchange in the heat balance of self-heating coal for particular conditions.

The moisture exchange share may be set in the heat balance only by comparing this value with oxygen sorption heat by coal. The last one depends upon oxygen sorption rate that features the coal chemical activity.

Changes in sorption capacity and chemical activity have shown that even insignificant heating increased the chemical activity of brown coal several times. This property explained frequent fire repetitions in the areas located in immediate vicinity of fire-impacted zone.

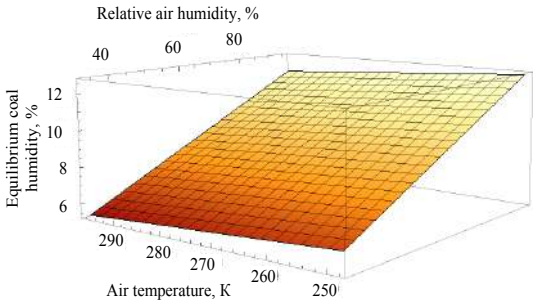

Figure 9. Moisture content in coal in equilibrium state (equilibrium coal humidity)

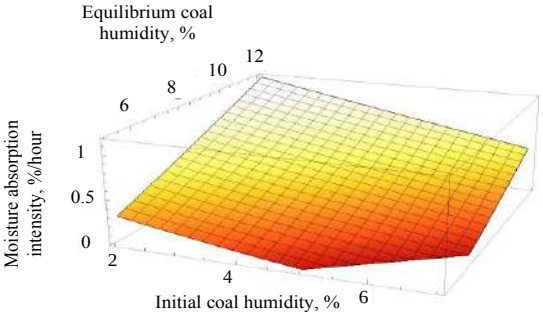

Figure 11. Moisture absorption intensity at temperatures from 0 to plus 25°C

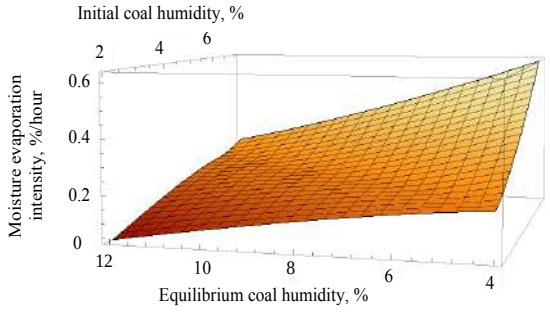

Figure 10. Moisture evaporation intensity at temperatures of minus 10 to plus 25°C

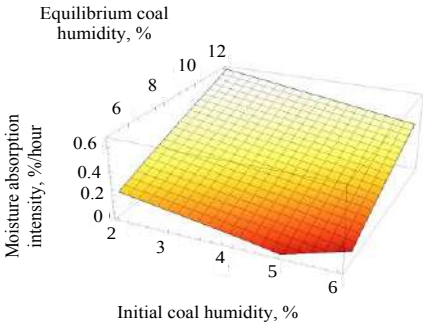

Figure 12. Moisture absorption intensity at a temperature minus 10 to 0°C

Sorption rate constant calculated by the specified procedure was (0.07 to 0.12mm/g.h).

Calculations performed using the above data have established that minor (less than 0.02%/h) intensity of moisture evaporation from coal was necessary to compensate oxygen sorption heat. However, the coal open pit featured extreme variability in microclimate parameters that created conditions, where sorption heat of water vapor could significantly exceed oxygen sorption heat.

Thus, laboratory tests have confirmed that moisture exchange at Korkinsk open pit could affect the initial period (1st and 2nd phases) of self-heating quite significantly and even decisively in some cases.

Taking the foregoing into consideration, the possibility to decrease the intensity of moisture exchange between air, water, and coal due to its treatment with solutions is of significant interest when designing means and ways for endogenous fire prevention. That is why antipyrenes to be tested should satisfy the following requirements: to prevent oxygen sorption by coal with simultaneous decrease of the moisture exchange intensity, and to save moisture sometimes by preventing its evaporation from coal.

3. 4. Analysis of Existing Antipyrogens for Brown Coal Numerous methods and ways were used for endogenous fire prevention at Korkinsk open pit, both engineering methods and chemical/mineral substances capable to decelerate initiating effect of coal active organic and mineral ingredients, for example, peroxides and iron compounds, etc. [15, 16, 32].

Various reagents were analyzed as antipyrogens (Table 2) in different combinations and concentrations, neutralized black contact (NBC), the NBC mixture with calcium chloride ($CaCl_2$) as well as aqueous solutions of organic and inorganic acids, chlorides, ammonium salts, sodium fluoride, triethanolamine, polyvinyl acetate, polyacrylamide, K-4, production wastes for oxyethylated fatty acids, carboxymethyl cellulose [37-46].

TABLE 2. Antipyrogen solutions used in the world

No.	Antipyrogen solution	Actual ignition point, °C
1.	Coal impregnated with tap water	192
2.	Dry coal	243
3.	Coal impregnated with 1 % solution of MF-17 resin	287
4.	Coal impregnated with 2 % solution of MF-17 resin	250
5.	Coal impregnated with 3 % solution of MF-17 resin	262
6.	Coal impregnated with 1 % solution of MF-17 resin with oxalic acid addition	299
7.	Coal impregnated with 2 % solution of MF-17 resin with oxalic acid addition	283
8.	Coal impregnated with 1 % liquid glass solution	250
9.	Coal impregnated with 3 % liquid glass solution	250
10.	Coal impregnated with 5 % liquid glass solution	287
11.	Coal impregnated with 7 % liquid glass solution	225
12.	Coal impregnated with aqueous solution (5 % $CaCl_2$, 2.5 % liquid glass)	275
13.	Coal impregnated with aqueous solution (10 % $CaCl_2$, 1 % MF-17 resin)	350
14.	Coal impregnated with aqueous solution (10 % $CaCl_2$, 1 % MF-17 resin)	260
15.	Coal impregnated with aqueous solution (10 % $CaCl_2$, 1 % MF-17 resin, 1 % liquid glass)	323
16.	Coal impregnated with aqueous solution (5 % $CaCl_2$, 1 % MF-17 resin)	320
17.	Coal impregnated with aqueous solution (5 % $CaCl_2$, 1 % MF-17 resin, 1 % liquid glass)	290
18.	Coal impregnated with aqueous solution (5 % $CaCl_2$, 1 % liquid glass)	280
19.	Coal impregnated with aqueous solution (10 % $CaCl_2$, 1 % liquid glass)	295
20.	Coal impregnated with 1 % soda solution (Na_2CO_3)	310
21.	Coal impregnated with 5 % soda solution (Na_2CO_3)	310
22.	Coal impregnated with 10 % soda solution (Na_2CO_3)	320
23.	Coal impregnated with 20 % soda solution (Na_2CO_3)	330
24.	Coal impregnated with aqueous solution (1 % soda Na_2CO_3, 1 % liquid glass)	315
25.	Coal impregnated with aqueous solution (20 % soda Na_2CO_3, 1 % liquid glass)	320
26.	Coal impregnated with 10 % table salt solution (NaCl)	315
27.	Coal impregnated with 1 % table salt solution (NaCl)	-
28.	Coal impregnated with 5 % table salt solution (NaCl)	-

NBC both pure and mixed with $CaCl_2$, lime were the most promising antipyrogens among the studied ones [15, 16, 32].

The NBC demulsifier is an aqueous solution of ammonium salts of water-soluble sulphonic acids, an oil-refining product. It is a dark brown liquid with ammonia odor, non-toxic, free from resorptive impact, non-flammable, soluble in water in any proportions. Its freezing point is minus 17˚C, the reagent has good wetting and adhesion properties.

NBC antipyrogen was successively used previously for fire prevention at Korkinsk open pit but was not widely used due to its low applicability. [16].

After studying the effect of different substances on coal porosity, it was found that film-forming compositions decreased the intensity of moisture exchange between coal and air while $CaCl_2$ featured plugging properties. Blocking the access of air oxygen to active surfaces was carried out by forming hardly soluble calcium sulphate and calcium salts of sulphonic acids due to NBC interaction with $CaCl_2$ [37].

$$2RSO_3NH_4 + CaCl_2 \rightarrow (RSO_3)_2Ca\downarrow + 2NH_4Cl$$

However, coal treatment with NBC+$CaCl_2$ mixture made it impossible due to high reaction rate with sedimentation.

It is possible to use appropriate oxidants (more active than water) in the low-temperature oxidation zones and to create a thickened film near coal surface, which prevents further oxidation in coal depth.

Lime as a chemically active oxidant reacts with brown coal 3 to 9 times more intensively than with hard coal. [32] Owing to high dispersion, lime is the best isolating material for the medium-temperature oxidation zone as compared with sandy-argillaceous or argillaceous pulps.

For ignition and combustion, lime (in particular, white lime or limestone) is a good fire extinguisher. Lime solution successfully prevents gas flares and explosions when extinguishing seats with high temperature [15].

Lime has a significant drawback – it quickly precipitates from the solution and may be neutral regarding coal oxidation or catalyze oxidation in certain conditions. [1, 40, 41, 45] Even 7 to 10% lime solutions should be intensively mixed to supply the suspension with desired concentration into coal block. The lack of mixing results in the lime content in the solution and injection quality.

Liquid glass solutions 1 to 7% do not yield good results when treating brown coal. Application of liquid nitrogen is short-term during extinguishing endogenous fire, which is accompanied with temperature drop inside the block and strong deoxidation that results in more powerful new fire after a while [42, 45- 48].

All the above solutions have a common shortage: they turn in gels after exceeding the flash point for impregnated brown coal. Gels are decomposed in the fire seat (plus 500 to plus 1000˚C) and turn into grey sand-like substance [1].

Mud accumulation widely used in flat-lying seams is not efficient since it is difficult to achieve uniform distribution of slushing pulp over cracks. Besides, clay and sand precipitate, filled cavities and cracks may be easily washed with water [15, 17, 49].

Efficiency of fire isolation using clay depends upon the layer thickness and particle size of inert material. Non-uniform stocking thickness is a significant drawback for this method as well as high transportation costs. Due to the difference between the slope angle for inert material (30° to 40°) and bench (75° to 80°), most clay drops to the bench basis and forms a thick layer there. The upper part of the bench is not covered. Material loses its properties when exposed by precipitate and solar radiation.

Fire extinguishing with water does not yield the result since self-ignition seats become more active with the increase of pit water acidity. [50, 51] Thus, there were attempts to extinguish endogenous fire seats using quarry water with pH 2 to 3 at Korkinsk open pit. However, flooding the seat with water resulted in temperature drop at first and abrupt repeat of endogenous fire soon. That is why using water (quarry or process) to extinguish endogenous fire events is inappropriate; its result is temporary (5 to 7 days). It should be noted that the most intensive coal self-ignition was observed at coal moisture approx. 2 to 4% [32, 35, 42, 50].

3. 5. Surveying a New Way to Fight Man-Induced Fires at Korkinsk Coal Open Pit Today, preventing treatment with antipyrogens or inhibitors does not have a meaningful effect in decreasing the number of self-ignition seats for coal pillars of Korkinsk open pit. Due to rock pressure, coal block crumbles away and form new non-treated surfaces accessible for oxygen effect, which may result in coal spontaneous ignition under certain conditions.

Examinations have established that the treatment with film-forming and plugging substances provided the decease of coal chemical activity by 85%. Moreover, the solution resulted during the treatment formed an airtight layer. However, insulating film lost its tightness after a short time, allowed air and water to pass through due to its destruction caused by various factors (water flow, cliff debris, block motion, wind) [6, 9].

It is possible to prevent coal spontaneous combustion by its strengthening with solidifying solutions featuring high adhesion, stability to high/low temperature, outside environment and rockslides. [5, 10, 15, 30, 32] In this case, it was possible to attain the

decrease in the susceptibility to spontaneous combustion for the coal treated with such solutions due to increase of the coal block strength and stability, formation of predominantly coarse fractions during its destruction and decreasing coal sorption capacity. Neutral metals could prevent oxidation processes.

An environmentally friendly solution was designed for Korkinsk open pit. It combined positive properties of all existing antipyrogens and inhibitors and varied in composition according to the above factors (Figure 13).

Dissolution of used components results in formation of calcium acetate $(C_2H_3O_2)_2Ca$, silicic acid H_2SiO_3, lactic acid $nC_3H_6O_3$. Depending upon coal oxidation degree, neutral metal Al may be also used.

The designed solution was tested to define the efficiency of its application in simulated process and climatic conditions.

All experiments were carried out using heated activated (plus 227˚C) and non-activated samples of coal taken from Korkinsk open pit (Figure 14).

Initially, we measured coal self-ignition temperature by putting samples into a metallic cylinder and uniform heating. When the first ignition signs appeared, fire supply was stopped, and the temperature was measured using the laser pyrometer, which was plus 227˚C.

Then, work solution was supplied on heated sample using a compressor and a hopper gun.

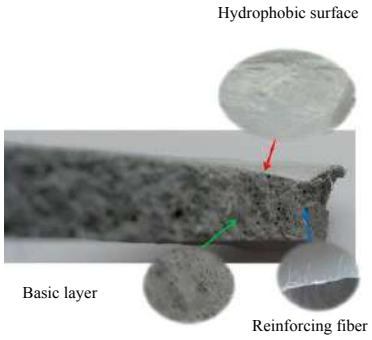

Figure 13. Solution for endogenous firefighting at Korkinsk coal open pit

Figure 14. Coal activated samples with temperature plus 227 °C

When the ignition area surface was treated with the prepared solution, significant extinguishing was observed as well as considerable heat absorption from 4,500 to 6,000kJ. Besides, solid dense coating was formed (Figure 15) and prevented oxygen and water ingress.

The material hardened when coating the entire surface or after it. According to exact composition of the solution, it looked like a point coagulant during application, which adhered to the rock and to itself. As a rule, the material dried in the air and solidified during (8 to 24) hours depending on the additives used. To visualize the application place, it is possible to use a dye.

The resulting hard coating was tested for strength, dissolution (decrease of water permeability due to the particle void decrease) and ignitability.

High content of solids in the solution was ideal for fire extinguishing or fighting. The natural mineral basis did not ignite by its nature even after long and direct exposure by a burner, which was also revealed during the experiment (Figure 16).

Solidified solution may form long-time coating or membrane over the material being protected, thus preventing emission of any harmful substances, gases, and smells; prevents the possibility of fire occurrence; material moving or spraying, for example, due to wind or precipitation. It prevents penetration of any substances in the material and strengths solid mass slopes.

Figure 17 and Table 3 illustrates the research results for the solidified solution.

Figure 15. Solid surface formation over the coal ignition area

(a) (b)

Figure 16. Solution during ignition testing

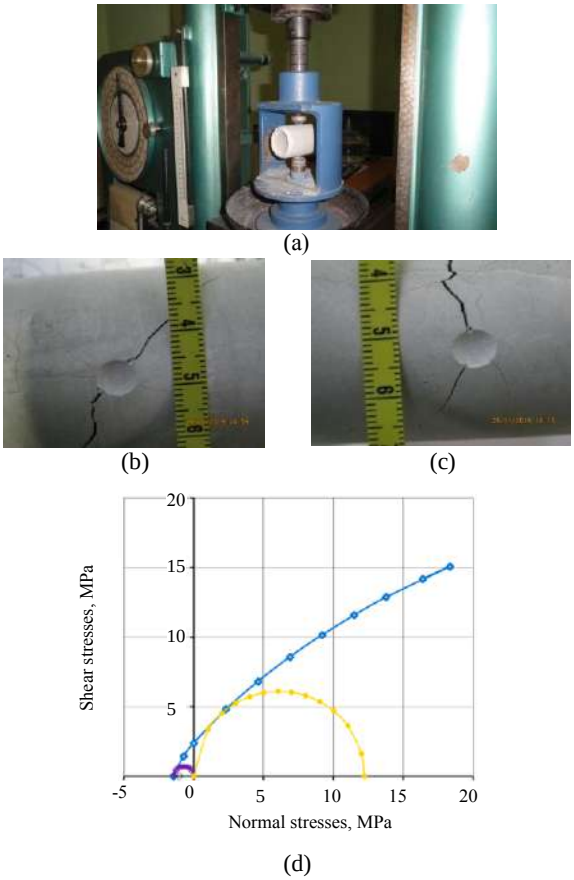

Figure 17. Results of physical and mechanical tests of solution samples: a – hydraulic press; b, c – crack formation in samples; d – strength certificate.

TABLE 3. Strength indexes of KKV solution

Sample number	Ultimate strength during uniaxial extension, MPa	Ultimate strength during uniaxial compression, MPa	Ultimate shear resistance without normal stresses, MPa
1	1,81	13,18	3,15
1-1	1,24	8,64	2,12
2	1,45	14,45	2,98
2-1	1,35	11,68	2,58
3	1,41	13,14	2,80
Average value	1,46	12,22	2,73
Number of tests		5	
Variation factor	14,6	18,3	14,7

By analyzing results given in Figure 17 and Table 3 it is possible to conclude that the solution is ductile (ultimate strength during uniaxial extension is 1.46 MPa) and rigid (ultimate strength during uniaxial compression is 12.22 MPa, shear resistance without normal stresses is 2.73 MPa).

Thus, the recommended thickness of the applied solution layer on the treated surface depends upon the time, when the material should remain coated. For example, the layer thickness should be 5 mm to isolate the material for up to 30 days, 10 mm – for 31 to 180 days, 15 mm – 181 and more days.

4. DISCUSSION

Anthropogenic fires are a serious factor of environment contamination, and there is still no universal way to fight them [52-56]. Most miners face this problem, especially when mining works stop in an open pit. Man-induced fires in Korkinsk brown coal open pit are very dangerous; approximately 0.00135 m^3/hour may emit from 1 m^2 of a fire-impacted zone; and totally, up to 140 m^3/hour of harmful impurities may release due to coal spontaneous ignition and affect nearby settlements.

It was found that coal grain size distribution considerably affects the intensity of moisture evaporation, which was observed as the highest for coal fineness of 0.258 mm to 0.5 mm and is the lowest for coarseness of 3.0 mm to 6.0 mm. This phenomenon is explained by increase in total area per volume unit for the surface, which is the most prone to self-ignition. Therefore, it may be considered that fine coal fractions are the most dangerous regarding the fire. In most cases, they are in rockslides on the border between upper and lower coarse-size fractions as well as in burden-coal piles, abandoned faces. At the same time, the intensity of moisture absorption is observed at a temperature of 0˚C to plus 25˚C and is virtually stopped at plus 40˚C.

During rainfall, self-heating temperature decreases due to heat absorption by water. After a certain period, the intensity of self-heating drastically increases. This phenomenon may be explained by the intensification of electrochemical oxidation processes considering the oxygen content up to 30% in rainwater. However, self-heating may completely stop during long precipitation, but coal humidity may increase up to 20%.

Our study has confirmed that moisture exchange could affect the initial period (1st and 2nd oxidation phases) of self-heating quite significantly and even decisively in some cases.

The assessment of antipyrogens that are applied globally revealed that the materials with film-forming effect and plugging properties are the most efficient and make it possible to decrease coal activity by 85%. The solution combines all positive properties of all existing antipyrogens and forms a rigid (ultimate strength during uniaxial compression is 12.22 MPa, shear resistance without normal stresses is 2.73 MPa), non-combustible, explosion-safe, ductile (ultimate strength during

uniaxial extension is 1.46 MPa) layer, which is formed by calcium acetate $(C_2H_3O_2)_2Ca$, silicic acid H_2SiO_3, lactic acid $nC_3H_6O_3$. Depending on coal oxidation degree, neutral metal Al may be used as well.

5. CONCLUSIONS

Summing up, we can conclude that the fractional composition of coal significantly affects the intensity of moisture evaporation: the maximum was observed for coal with fractions of 0.258-0.5 mm, the minimum was 3.0-6.0 mm. This is due to the increase in the total surface area, which is most likely to spontaneous combustion, per unit volume. Therefore, areas with talus, rock-coal heaps, abandoned slaughterhouses, in which the bulk of the fine fraction is concentrated, can be attributed to the most fire hazardous items . At the same time, the intensity of moisture absorption is observed at the temperatures from 0˚C to plus 25˚C and varies from 0 to 1% per an hour, and when it reaches plus 40˚C it practically stops. However, a negative temperature from 0˚C to minus 10˚C slows down the process of moisture absorption by 40 %.

The data obtained confirm that, under the conditions of the Korkinsky coal mine, moisture exchange can have a significant effect on the self-heating of coals.

Taking into account the above, as well as the advantages and disadvantages of antipyrogens existing in the world for brown coals, a solution has been developed that has the following strength properties, namely: tensile strength in uniaxial tension is 1.46 MPa, ultimate strength in uniaxial compression is 12.22 MPa and average tensile strength shear without normal stresses is 2.73 MPa. It will be possible to strengthen the slopes and isolate them from external influences, which will lead to a reduction in the number of endogenous fires in the Korkinsky open-pit mine, and as a result, to a decrease in emissions of pollutants from coal combustion into the atmosphere.

The dependencies for fire occurrence frequency, relative humidity and average temperature of the air upon the time of day, the intensity of moisture evaporation and initial coal humidity on equilibrium coal humidity as well as the intensity of moisture absorption and equilibrium coal humidity upon initial humidity in different temperature periods contribute to the theoretical study of endogenous fires and makes it possible to understand the essence of their occurrence and design efficient ways and means to fight them under various conditions.

6. REFERENCES

1. Skochinsky A.A., Makarov S.Z., "Research in the field of application of antipyrogens in the fight against mine fires of endogenous origin", ***Academy of Sciences of the USSR***, Moscow, (1947), 750
2. Saranchuk VI, Galushko L.Ya., Pashchenko LV, Lukyanenko LV, "Influence of water on the process of low-temperature oxidation of coal", ***Solid Fuel Chemistry***, Vol. 1, (2005), 9-12
3. Maier Patrick, Hartlieb Philipp, Brune Jurgen, "Laboratory Scaled Coal Dust Explosions and Physical Test Results for CFD Explosion Models", ***BHM Berg- und Hüttenmännische Monatshefte***, (2020). doi: 10.1007/s00501-020-00985-0
4. Vylegzhanin, V., "Effect of mechanical processes on development of the centers of endogenous fires", ***Soviet Mining***, Vol. 18, (1982), 163-167. doi: 10.1007/BF02528524
5. Tóth, J. & Matei, A. & Traistã, E., "Study of endogenous fires on the basis of fire indices", Vol. 108, (2002), 512-514.
6. Sofranko Marian, "Methodology of Risk Analysis of Endogenous Fire in Coal Mines", ***Advanced Materials Research***, (2014), 962-965. doi: 10.4028/www.scientific.net/AMR.962-965.1153
7. Xiao G.Q., Wen L.M., Zhang P.H., Chen B.Z., "Dynamic imitation study on fire effect in coal mine", (2001), 26
8. Zhou Lihong, Yuan Liming, Thomas Rick, Bahrami Davood, Rowland James., "An Improved Method to Calculate the Heat Release Rate of a Mine Fire in Underground Mines", ***Mining, Metallurgy & Exploration***, (2020), 113-123. doi: 10.1007/s42461-020-00276-9
9. Perera Eranda & Harris Marcia & Sapko Michael, "Examination of classified rock dust (treated and untreated) performance in a 20-L explosion chamber", ***Journal of Loss Prevention in the Process Industries***, Vol. 62, (2019), 103-943. doi: 10.1016/j.jlp.2019.103943
10. Zlochower Isaac, Sapko Michael, Perera Eranda, Brown Connor, Harris Marcia, Rayyan Naseem, "Influence of specific surface area on coal dust explosibility using the 20-L chamber", ***Journal of Loss Prevention in the Process Industries***, Vol. 54, (2018), 103-109. doi: 10.1016/j.jlp.2018.03.004.
11. Novoselov, S.V., Popov, V.B., Golik, A.S., "Risk assessment of endogenous fires in coal mines", ***Ugol'***, (2020), 21-25. Doi: 10.18796/0041-5790-2020-5-21-25
12. Portola V.A., Ovchinnikov A.E., Zhdanov A.N., "Evaluation of endogenous fire precautions in coal mines", ***Mining Informational and Analytical Bulletin***, Vol. 12, (2019), 205-214. doi: 10.25018/0236-1493-2019-12-0-205-214
13. Gogola Krzysztof, Rogala Tomasz, Magdziarczyk Małgorzata, Smoliński Adam, "The Mechanisms of Endogenous Fires Occurring in Extractive Waste Dumping Facilities", ***Sustainability***, Vol. 12, (2020), 28-56. doi: 10.3390/su12072856
14. Hudecek, V.; Cerna, K.; Adamec, Z., "Reclamation of the Central Hald in the Jan Švermy mine in Žaclé˙r", ***In˙zynieria Mineralna***, Vol. 1, (2012), 41–53
15. Ivashkin V.S., Liskin A.Z., "Analysis of the causes of endogenous fires in the Azeiskiy and Kharanor open-pit mines", ***Safety Precautions at Open Pit Works***, (2000), 65-69
16. Tynterov I.A., Kulmenko Yu.M., Shirkin G.G., "Korkinsky coal mine", Chelyabinsk Printing House, Chelyabinsk, (2000), 225
17. Conti R., Cashdollar K., Thomas R.., "Improved furnace for measuring the autoignition temperatures of dust clouds», Report of investigations, (1993), 200
18. Sarapulova G.I., "Environmental Geochemical Assessment of Technogenic Soils", ***Journal of Mining Institute***, Vol. 234, (2018), 658-662. doi:10.25515/PMI.2018.6.658
19. Korshunov V.A., Kartashov Yu.M., Kozlov V.A., "Determination of indices of strength certificate of rocks using the method of specimens failire with spherical indentors", ***Journal of Mining Institute***, Vol. 185, (2010), 41-45

20. Beron A.I., Koifman M.I., Chirkov S.E., Solomina I.A., "The method for determination of strength of rocks using the specimens of irregular form", ***The Institute of Mining named after A.A. Skochinski***, Moscow, 1976, 40
21. Korshunov V.A., "Determination of indices of volumetric strength of rocks under their loading with spherical indentors", ***Rock Geomechanics and Mining Surveying, Proc. VNIMI***, (1999), 70-75
22. Kartashov Yu.M., Matveev B.V., Mikheev H.V., Fadeev A.B., "Strength and deformability of rocks", Nedra, Moscow, (1979), 269
23. Matveeva V.A., Isakov A.E., Sverchkov I.P., "The reduction of negative impact on environment in the area of coal processing enterprises", Innovation-Based Development of the Mineral Resources Sector: Challenges and Prospects - 11th conference of the Russian-German Raw Materials, (2018), 425-440
24. Strizhenok A., Korelskiy D., "Improvement of the system of industrial environmental monitoring of atmospheric air in the area of anthropogenic arrays impact", ***Journal of Physics: Conference Series***, Vol. 1384, (2019), 120-133. doi: 10.1088/1742-6596/1384/1/012052
25. Kazanin O.I., Korshunov G.I., Rudakov M.L., "The implementation of modern occupational safety and health system as an element of sustainable development of coal mining enterprises", Innovation-Based Development of the Mineral Resources Sector: Challenges and Prospects-11th Conf. of the Russian-German Raw Materials, (2018), 571-577
26. Pasynkov A.V., Kuletskiy K.V., Zhunda S.V., Rudakov M.L., Sobyanin D.S., "Use of occupational risk management procedure with the aim of improving training on occupational safety for the employees of the open-pit coal mining organizations", ***Bezopasnost' Truda v Promyshlennosti***, №2, (2020), 74-79. doi: 10.24000/0409-2961-2020-2-74-79
27. Nureev R.R., Pashkevich M.A., Isakov A.E., "Assessment of the technogenic impact of the korkinsky coal mine", Topical Issues of Rational Use of Natural Resources - Proceedings Of The International Forum-Contest of Young Researchers, (2018), 50-68
28. Biryukov Yu.V., "On the chemical structure of coals", ***Chemistry of Solid Fuel***, No. 4, (1969), 90-94.
29. Weather statistics, Chelyabinsk (Chelyabinsk region), (2019) URL: http://www.atlas-yakutia.ru/weather/stat_weather_286420.php
30. Ivashkin A.Z., Dolganov V.N., "Extinguishing endogenous fires at the Azeisky open pit", TsNIEI coal, Collection of "Safety technology, labor protection and mine rescue business", No. 10, (1974), 20-34
31. Pandey, Jitendra, "Environmental impact of coal mine fire during excavation of developed galleries by opencast method", ***Journal of Mine Metal and Fuels***, Vol. 43, (2004), 30-35
32. Liskin A.Z., Burkov P.A., Demidov Yu.V., "Experience in extinguishing endogenous fires in the Korkinsky quarry", ***Safety, Labor Protection and Mine Rescue***, Vol. 2, (2000), 50-68
33. Ostr¸ega, A.; Uberman, R., "Directions of remediation and development—Selection methods, classification and examples", ***Min. Geoeng***, Vol. 4, (2010), 445–461
34. Tóth, J., Matei, A., Traistã, E., "Study of endogenous fires on the basis of fire indices", ***Magyar Kemiai Folyoirat***, Vol. 108, (2002), 512-514
35. Szurgacz Dawid, Sobik Leszek, Brodny Jarosław, "Inter gases as one of the ways to reduce the risk of endogenous fires in hard coal mines", ***Multidisciplinary Aspects of Production Engineering***, Vol. 2, (2019), 183-190. doi: 10.2478/mape-2019-0018
36. Michalski Stanley, "Coal-Mining Techniques and Coal Fires", ***Coal and Peat Fires: A Global Perspective***, Vol. 2, (2011), 29-46. doi: 10.1016/B978-0-444-52858-2.00002-5
37. Kozlyuk S.A., Kuzyaev L.S., Lyuev V.A., "Application of fast-hardening polymer solutions for the prevention of endogenous fires", ***Coal of Ukraine***, (2009), 31-35.
38. Pashkevich M.A., Alekseenko A.V., Petrova T.A., "Application of polymeric materials for abating the environmental impact of mine wastes", ***Journal of Physics: Conference Series***, Vol. 1384, (2019), 1-8. doi:10.1088/1742-6596/1384/1/012039
39. Portola V.A., Ovchinnikov A.E., Zhdanov A.N., "Evaluation of endogenous fire precautions in coal mines", ***Mining Informational and analytical bulletin***, Vol. 12, (2019). 205-214. doi: 10.25018/0236-1493-2019-12-0-205-214
40. Teacoach K.A., Rowland James, Smith A.C., "Improvements in conveyor belt fire suppression systems for U.S.A.", ***Coal mines. Trans. Soc. Min. Metall. Explor***, 328, (2011), 502-506
41. Vagapov R.R., Rodionov V.A., "New possibilities of fire-extinguishing performance improvement of water and water-based surfactant solutions", ***Neftyanoe khozyaystvo - Oil Industry***, No. 11, (2010), 110-115
42. Abiev Z.A., Rodionov V.A., Paramonov G.P., Chernobay V.I., "Method to investigate influence of inhibitory and phlegmatizing agents on ignitability and explosibility of coal dust", ***Mining Informational and Analytical Bulletin***, Vol. 5, (2018), 26-34. doi: 10.25018/0236-1493-2018-5-0-26-34
43. Coal mine methane in Russia: Capturing the safety and inveronmental benefits. International Energy Agency: Information paper, (2009), 66
44. Li Qingzhao, Zhai Cheng, Wu Haijin, "Investigation on coal dust explosion characteristics using 20 L explosion sphere vessels", ***Journal of China Coal Society***, Vol. 36, (2011), 119
45. Maevskaya V.M., "The search for antipyrogens for the prevention of endogenous fires", ***Safety, Labor Protection and Mine Rescue***, No. 7, (2007), 43-44
46. Kostyurin S.N., "Prevention of fires at the Kharanorsky open-pit mine", Labor safety in industry, Vol.3, (2010), 14-15
47. Tabatabaee Moradi S.S., Nikolaev N.I., Leusheva E.L., "Improvement of Cement Properties Using a Single Multifunctional Polymer", ***International Journal of Engineering, Transactions A: Basics***, Vol. 31, No. 1, (2018), 181-187. doi: 10.5829/ije.2018.31.01a.24
48. Krikunov G.N., Aleksandrov V.A., Polyanskaya L.Ya., "The effect of aqueous solutions of liquid glass on coal substance", Safety technology, labor protection and mine rescue, Proceedings of the Academy of Sciences of the USSR, (1969), 39-42.
49. Bessolitsina G.G., "Investigation of the action of the pulp during preventive silting", ***Technique and Technology of Development of Minerals***, No. 5, (1966), 284-289.
50. Saranchuk V.I., Galushko L.Ya., Pashchenko L.V., Lukyanenko L.V., "Influence of water on the process of low-temperature oxidation of coal", ***Chemistry of Solid Fuel***, No. 1, (2003), 9-12
51. Teacoach, K.A. & Rowland, James & Smith, A.C., "Improvements in conveyor belt fire suppression systems for U.S. Coal mines. Trans", ***Society for Mining Metallurgy and Exploration***, Vol. 328, (2011), 502-506
52. Rowland, James & Harteis, S.P. & Yuan, L., "A survey of atmospheric monitoring systems in U.S.A underground coal mines", ***Mining Engineering***. Vol. 70, (2018), 37-40. doi: 10.19150/me.8058
53. Dini, J.W., "Coal mine fires", ***Plating and Surface Finishing***, Vol. 94, No. 34, (2007), 34-37

54. Barone Teresa, Hesse Evelyn, Seaman Clara, Baran Anthony, Beck Timothy, Harris Marcia, Jaques Peter, Schwegler-Berry Diane, Mischler Steven, Gao Pengfe, "Real-time sizing of Airborne Coarse Coal Dust", ***Plating and Surface Finishing,*** No. 35, (2010), 160-168

55. Du Plessis, Johannes Jacobus., "Active explosion barrier performance against methane and coal dust explosions", ***International Journal of Coal Science & Technology***, Vol. 2, (2015), 261-268 doi: 10.1007/s40789-015-0097-7

56. Selçuk Bilgen, "The environmental effects of coal-related activities", ***Energy Sources, Part A: Recovery, Utilization, and Environmental Effects***, Vol. 38, No. 22, (2016), 3283-3289. doi: 10.1080/15567036.2016.1152328

Persian Abstract

چکیده

خاتمه ناگهانی عملیات استخراج روباز ذغال سنگ در بسیاری از موارد با آتش سوزی های درون زا پیچیده است که نه تنها صدمه قابل توجهی به اموال وارد می کند بلکه شرایط بهداشتی و بهداشتی را برای زندگی انسان در سکونتگاه های مجاور و همچنین شرایط مربوط به جانوران و گیاهان گیاهی بدتر می کند. بنابراین ، هدف از تحقیق جلوگیری از آتش سوزی های درون زا در گودال روباز زغال سنگ قهوه ای کورکینسک بود. در این ارتباط ، ما از یک روش تحلیلی برای پردازش داده های آماری بدست آمده از مشاهدات استفاده کردیم. روش آزمایشگاهی شامل مطالعه نمونه های ذغال سنگ برای شدت تبادل رطوبت با ایجاد شرایط با رطوبت نسبی تا ۹۷٪ ، دما تا ۵۰ درجه سانتیگراد و سرعت هوا تا ۰,۵ لیتر در دقیقه بود. وابستگی ها برای فرکانس وقوع آتش سوزی ، رطوبت نسبی و متوسط دمای هوا بر زمان روز ، شدت تبخیر رطوبت و رطوبت اولیه ذغال سنگ بر روی رطوبت ذغال تعادل و همچنین شدت جذب رطوبت و رطوبت ذغال تعادل بر اساس مقدار اولیه تعیین شد. رطوبت در دوره های مختلف دما یک راه حل سازگار با محیط زیست ایجاد شد که دارای چسبندگی مناسب به مواد پوشش داده شده ، مقاومت در برابر آتش و انفجار است. نتایج به دست آمده درک علل و روش های مبارزه با آتش سوزی های درون زا را ممکن می کند.

AIMS AND SCOPE

The objective of the International Journal of Engineering is to provide a forum for communication of information among the world's scientific and technological community and Iranian scientists and engineers. This journal intends to be of interest and utility to researchers and practitioners in the academic, industrial and governmental sectors. All original research contributions of significant value focused on basics, applications and aspects areas of engineering discipline are welcome.

This journal is published in three quarterly transactions: Transactions A (Basics) deal with the engineering fundamentals, Transactions B (Applications) are concerned with the application of the engineering knowledge in the daily life of the human being and Transactions C (Aspects) - starting from January 2012 - emphasize on the main engineering aspects whose elaboration can yield knowledge and expertise that can equally serve all branches of engineering discipline.

This journal will publish authoritative papers on theoretical and experimental researches and advanced applications embodying the results of extensive field, plant, laboratory or theoretical investigation or new interpretations of existing problems. It may also feature - when appropriate - research notes, technical notes, state-of-the-art survey type papers, short communications, letters to the editor, meeting schedules and conference announcements. The language of publication is English. Each paper should contain an abstract both in English and in Persian. However, for the authors who are not familiar with Persian, the publisher will prepare the latter. The abstracts should not exceed 250 words.

All manuscripts will be peer-reviewed by qualified reviewers. The material should be presented clearly and concisely:

- *Full papers* must be based on completed original works of significant novelty. The papers are not strictly limited in length. However, lengthy contributions may be delayed due to limited space. It is advised to keep papers limited to 7500 words.
- *Research* notes are considered as short items that include theoretical or experimental results of immediate current interest.
- *Technical notes* are also considered as short items of enough technical acceptability with more rapid publication appeal. The length of a research or technical note is recommended not to exceed 2500 words or 4 journal pages (including figures and tables).

Review papers are only considered from highly qualified well-known authors generally assigned by the editorial board or editor in chief. Short communications and letters to the editor should contain a text of about 1000 words and whatever figures and tables that may be required to support the text. They include discussion of full papers and short items and should contribute to the original article by providing confirmation or additional interpretation. Discussion of papers will be referred to author(s) for reply and will concurrently be published with reply of author(s).

INSTRUCTIONS FOR AUTHORS

Submission of a manuscript represents that it has neither been published nor submitted for publication elsewhere and is result of research carried out by author(s). Presentation in a conference and appearance in a symposium proceeding is not considered prior publication.

Authors are required to include a list describing all the symbols and abbreviations in the paper. Use of the international system of measurement units is mandatory.

- On-line submission of manuscripts results in faster publication process and is recommended. Instructions are given in the IJE web sites: www.ije.ir-www.ijeir.info
- Hardcopy submissions must include MS Word and jpg files.
- Manuscripts should be typewritten on one side of A4 paper, double-spaced, with adequate margins.
- References should be numbered in brackets and appear in sequence through the text. List of references should be given at the end of the paper.
- Figure captions are to be indicated under the illustrations. They should sufficiently explain the figures.
- Illustrations should appear in their appropriate places in the text.
- Tables and diagrams should be submitted in a form suitable for reproduction.
- Photographs should be of high quality saved as jpg files.
- Tables, Illustrations, Figures and Diagrams will be normally printed in single column width (8cm). Exceptionally large ones may be printed across two columns (17cm).

PAGE CHARGES AND REPRINTS

The papers are strictly limited in length, maximum 6 journal pages (including figures and tables). For the additional to 6 journal pages, there will be page charges. It is advised to keep papers limited to 3500 words.

Page Charges for Papers More Than 6 Pages (Including Abstract)	
For International Author ***	**$55 / per page**
For Local Author	**100,000 Toman / per page**

AUTHOR CHECKLIST

- Author(s), bio-data including affiliation(s) and mail and e-mail addresses).
- Manuscript including abstracts, key words, illustrations, tables, figures with figure captions and list of references.
- MS Word files of the paper.

International **J**ournal of **E**ngineering, P.O. Box 13145-1659, Tehran, I.R. Iran
Materials and Energy Research Center, 5 Ahuramazda St., Alvand Ave., Argentina Sq., Tehran, Islamic Republic of Iran
www.merc.ac.ir - www.emerc.ac.ir

THOMSON REUTERS

WEB OF SCIENCE

Scopus®

CAS®
A DIVISION OF THE
AMERICAN CHEMICAL SOCIETY

Google
Scholar